28 February 2014 | $10

Science

Ant Chemical Warfare

AAAS

EDITORIAL

949 Festival Lessons
Leszek Borysiewicz and Nicola Buckley

NEWS OF THE WEEK

954 A roundup of the week's top stories

NEWS & ANALYSIS

956 Science Misused to Justify Ugandan Antigay Law

957 New Review Slams Fusion Project's Management

958 Twitter Offers Entire Data Pool, but Some Wary of Diving In

959 E.U. Privacy Protection Bill Would Hamper Research, Scientists Warn

960 New Look at Ancient Mineral Could Scrap a Test for Early Oxygen

NEWS FOCUS

961 Welcome to Beringia
>> Perspective p. 979

964 Can Down Syndrome Be Treated?
>> Science *Podcast*

LETTERS

968 Raw Data: Access to Inaccuracy
A. C. J. W. Janssens

Raw Data: Research and Health Care Goals Differ
W. J. Dondorp et al.

Response
J. E. Lunshof et al.

969 CORRECTIONS AND CLARIFICATIONS

BOOKS *ET AL.*

970 The New Science of Cities
M. Batty, reviewed by M. Szell

971 Pests in the City
D. D. Biehler, reviewed by F. R. Davis

POLICY FORUM

972 A Better Route to Tech Standards
J. Lerner and J. Tirole

PERSPECTIVES

974 Meet the New Boss, Same as the Old Boss
M. Kaspari and M. D. Weiser
>> Report p. 1014

975 The Surface Mobility of Glasses
F. Chen et al.
>> Report p. 994

976 The Tropical Pacific Ocean—Back in the Driver's Seat?
A. Clement and P. DiNezio

978 The Neural Code That Makes Us Human
Y. Grodzinsky and I. Nelken
>> Report p. 1006

979 Out of Beringia?
J. F. Hoffecker et al.
>> News story p. 961

981 How Shape Affects Microtubule and Nanoparticle Assembly
M. J. Stevens

982 Signaling Shifts in Allergy Responses
M. Daëron
>> Report p. 1021

REVIEW

985 Solar Synthesis: Prospects in Visible Light Photocatalysis
D. M. Schultz and T. P. Yoon
Review Summary; for full text: http://dx.doi.org/10.1126/science.1239176

CONTENTS continued >>

pages 961 & 979

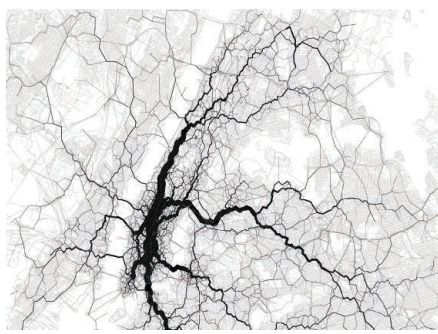

page 970

ON THE WEB THIS WEEK

>> *Science* Podcast
This week's show features a segment on recent research into treatments for Down syndrome and a roundup of shorts from our daily news site.

>> Find More Online
Check out the latest in a series of Perspectives on Challenges in Climate Science at **www.sciencemag.org/extra/climate**.

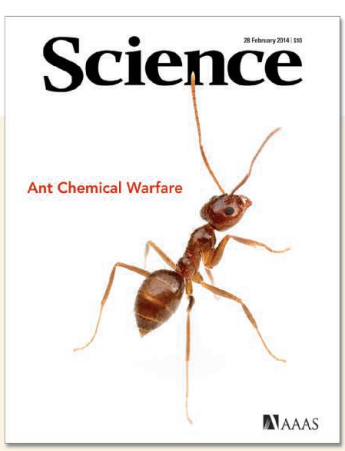

COVER

A portrait of a tawny crazy ant worker (*Nylanderia fulva*). Tawny crazy ants, native to central South America, are invading the southeastern United States and, in some places, displacing the current dominant South American ant invader, red imported fire ants (*Solenopsis invicta*). A notable ability to detoxify the venom of imported fire ants apparently underlies the success of tawny crazy ants. See pages 974 and 1014.

Photo: ©Alex Wild/alexanderwild.com

DEPARTMENTS

947 This Week in *Science*
950 Editors' Choice
952 *Science* Staff
984 AAAS News & Notes
1029 New Products
1030 *Science* Careers

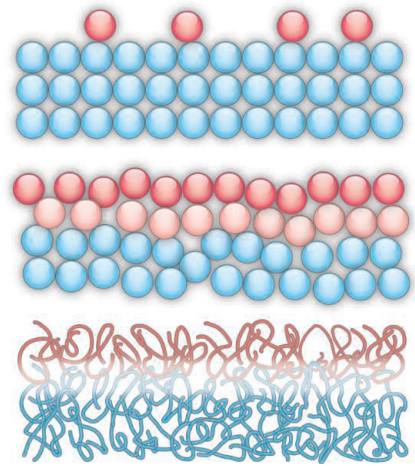

pages 975 & 994

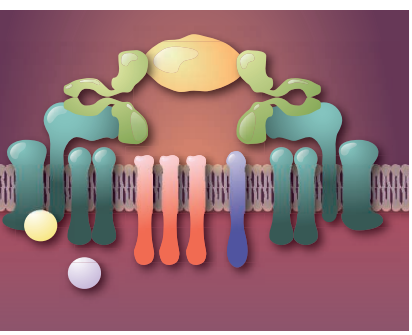

pages 982 & 1021

RESEARCH ARTICLES

986 ESCRT Machinery Is Required for Plasma Membrane Repair
A. J. Jimenez et al.
ESCRT proteins repair small wounds in the plasma membrane by shearing off damaged portions.
Research Article Summary; for full text: http://dx.doi.org/10.1126/science.1247136

987 Lost in Transition: Start-Up of Glycolysis Yields Subpopulations of Nongrowing Cells
J. H. van Heerden et al.
One source of nongenetic variation in yeast can be traced to distinct steady-state levels of glycolysis.
Research Article Summary; for full text: http://dx.doi.org/10.1126/science.1245114

REPORTS

988 Global Anisotropies in TeV Cosmic Rays Related to the Sun's Local Galactic Environment from IBEX
N. A. Schwadron et al.
Local interstellar conditions play a role in ordering very-high-energy cosmic rays in the Sun's immediate environment.

990 Nanoporous $BiVO_4$ Photoanodes with Dual-Layer Oxygen Evolution Catalysts for Solar Water Splitting
T. W. Kim and K.-S. Choi
A high-surface-area morphology of bismuth vanadate enhances the proportion of photogenerated holes that can oxidize water.

994 A Direct Quantitative Measure of Surface Mobility in a Glassy Polymer
Y. Chai et al.
A step geometry is used to probe the behavior of a glassy polymer above and below its glass transition temperature.
>> Perspective p. 975

999 Rapid Thinning of Pine Island Glacier in the Early Holocene
J. S. Johnson et al.
Pine Island Glacier in Antarctica thinned rapidly, as it is doing now, at least once before in the past 8000 years.

1002 Promoter-Bound Trinucleotide Repeat mRNA Drives Epigenetic Silencing in Fragile X Syndrome
D. Colak et al.
An abnormal activation of gene silencing underlies fragile X syndrome.

1006 Phonetic Feature Encoding in Human Superior Temporal Gyrus
N. Mesgarani et al.
The human auditory cortex encodes what speech sounds like.
>> Perspective p. 978

1010 Detection of a Recurrent *DNAJB1-PRKACA* Chimeric Transcript in Fibrolamellar Hepatocellular Carcinoma
J. N. Honeyman et al.
A rare form of liver cancer affecting young adults expresses a chimeric kinase that may contribute to pathogenesis.

1014 Chemical Warfare Among Invaders: A Detoxification Interaction Facilitates an Ant Invasion
E. G. LeBrun et al.
After fire ants invade, they can be invaded in turn by tawny crazy ants.
>> Perspective p. 974

1017 Resurrecting Surviving Neandertal Lineages from Modern Human Genomes
B. Vernot and J. M. Akey
Ancestral Neandertal sequences within extant humans reveal that positive and purifying selection has occurred.

1021 Molecular Editing of Cellular Responses by the High-Affinity Receptor for IgE
R. Suzuki et al.
One receptor uses different signals to achieve different outcomes.
>> Perspective p. 982

1025 Cell Surface ABP1-TMK Auxin-Sensing Complex Activates ROP GTPase Signaling
T. Xu et al.
An alternate signaling route for the plant hormone auxin goes directly inside from the cell surface.

SCIENCE (ISSN 0036-8075) is published weekly on Friday, except the last week in December, by the American Association for the Advancement of Science, 1200 New York Avenue, NW, Washington, DC 20005. Periodicals Mail postage (publication No. 484460) paid at Washington, DC, and additional mailing offices. Copyright © 2014 by the American Association for the Advancement of Science. The title SCIENCE is a registered trademark of the AAAS. Domestic individual membership and subscription (51 issues): $149 ($74 allocated to subscription). Domestic institutional subscription (51 issues): $990; Foreign postage extra: Mexico, Caribbean (surface mail) $55; other countries (air assist delivery) $85. First class, airmail, student, and emeritus rates on request. Canadian rates with GST available upon request, GST #1254 88122. Publications Mail Agreement Number 1069624. **Printed in the U.S.A.**

Change of address: Allow 4 weeks, giving old and new addresses and 8-digit account number. **Postmaster:** Send change of address to AAAS, P.O. Box 96178, Washington, DC 20090–6178. **Single-copy sales:** $10.00 current issue, $15.00 back issue prepaid includes surface postage; bulk rates on request. **Authorization to photocopy** material for internal or personal use under circumstances not falling within the fair use provisions of the Copyright Act is granted by AAAS to libraries and other users registered with the Copyright Clearance Center (CCC) Transactional Reporting Service, provided that $30.00 per article is paid directly to CCC, 222 Rosewood Drive, Danvers, MA 01923. The identification code for *Science* is 0036-8075. *Science* is indexed in the *Reader's Guide to Periodical Literature* and in several specialized indexes.

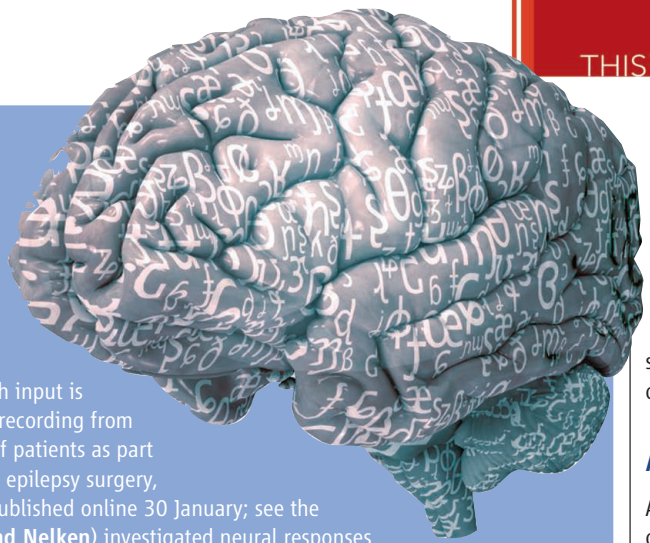

Deciphering Language >>

Consonants and vowels represent basic building blocks of human language. How their characteristics are extracted from acoustic speech input is not well understood. Directly recording from the superior temporal gyrus of patients as part of their clinical evaluation for epilepsy surgery, **Mesgarani *et al.*** (p. 1006, published online 30 January; see the Perspective by **Grodzinsky and Nelken**) investigated neural responses while the subjects listened to continuous speech. The findings reveal how both vowels and consonants of different phonetic categories are encoded.

Ordering Cosmic Rays

Earth and other planets are constantly bombarded by cosmic rays (charged particles from the cosmos). The flux of very-high-energy cosmic rays varies according to where we look in the sky. **Schwadron *et al.*** (p. 988, published online 13 February) show that recent measurements of the local interstellar parameters by NASA's Interstellar Boundary Explorer satellite are consistent with observed cosmic ray anisotropies at tera–electron volt energies, implying that local interstellar conditions play a role in ordering very-high-energy cosmic rays in our cosmic vicinity.

Polymer Film Behavior

An ongoing debate in the understanding of the behavior of thin-film glassy polymers is whether there is nanoconfinement of large molecules or enhanced mobility near a free surface. **Chai *et al.*** (p. 994; see the Perspective by **Chen *et al.***) prepared polymer films with a sharp step in the profile by depositing broken film fragments onto a uniform underlay. Atomic force microscopy revealed changes to the overall film profile with time at various temperatures. A transition was observed from localized motions to relaxation of the entire film at a temperature close to that of the bulk glass transition temperature.

Once in a While

Many regions at the edge of the Antarctic Ice Sheet have rapidly increased the rates at which they are sliding into the sea and thinning, raising concerns that global warming might cause the sudden collapse of some sections. **Johnson *et al.*** (p. 999, published online 20 February) present data from Pine Island Glacier, which has been thinning and retreating rapidly over the past two decades. The glacier experienced another rapid thinning around 8000 years ago, which occurred about as quickly as is happening now, and which lasted for 25 to 100 years.

A Boost for Bismuth Vanadate

In theory, given its light-absorption spectrum, bismuth vanadate should be an effective photoanode for solar water-splitting. However, in prior studies, few of the "holes" generated upon photoexcitation have persisted long enough to strip electrons from water. **Kim and Choi** (p. 990, published online 13 February) now show that the use of a hydrophobic vanadium source in the semiconductor's synthesis results in a high-surface-area morphology with substantially enhanced hole lifetimes. Deposition of two successive catalyst layers enhanced the proportion of holes that reacted with water at the surface, thereby raising the efficiency of the oxygen evolution reaction.

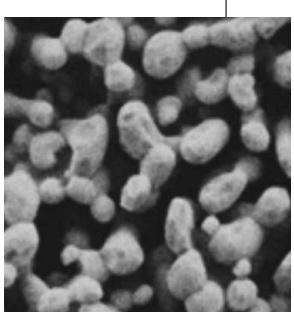

Oncogenic Suspect Exposed

It can be difficult logistically to study the genomics of rare variants of common cancers. Nevertheless, **Honeyman *et al.*** (p. 1010) studied fibrolamellar hepatocellular carcinoma (FL-HCC), a rare and poorly understood liver tumor that affects adolescents and young adults and for which there is no effective treatment. FL-HCCs from 15 patients all expressed a chimeric RNA transcript and protein containing sequences from a molecular chaperone fused in frame with sequences from the catalytic domain of protein kinase A. The chimeric protein retained kinase activity in vitro. Such recurrent gene fusions in cancer may signal a role in pathogenesis and provide an opportunity for therapeutic intervention.

Allergen Affinity

Allergic responses are initiated by interaction of allergens with immunoglobulin E (IgE) antibodies, which in turn bind to IgE receptors on the surface of mast cells. **Suzuki *et al.*** (p. 1021, published online 6 February; see the Perspective by **Daëron**) explored how the signaling properties of such receptor complexes differ, depending on the affinity of the IgE antibody for the antigen leading to different allergic responses.

Know Your Enemy

Fire ants accidentally introduced to North America from their native range in Argentina have been hugely invasive and difficult to eradicate and caused both environmental and economic damage. Recently, another accidentally introduced Argentine ant, the tawny crazy ant, appears to be displacing the fire ants. How? **LeBrun *et al.*** (p. 1014, published online 13 February; see the Perspective by **Kaspari and Weiser**) show that tawny crazy ants have a chemical and behavioral response to the toxic bite of fire ants that vastly reduces their mortality during confrontations and that allows the tawny crazy ants to outcompete their rivals.

Neandertal Shadows in Us

Non-African modern humans carry a remnant of Neandertal DNA from interbreeding events that have been postulated to have occurred as humans migrated out of Africa. While the total amount of Neandertal sequence is estimated to be less than 3% of the modern genome, the specific retained sequences vary among individuals. Analyzing the genomes of more than 600 Europeans and East Asians, **Vernot and Akey** (p. 1017, published online 29 January) identified Neandertal sequences within modern humans that taken together span approximately 20% of the Neandertal genome. Some Neandertal-derived sequences appear to be under positive selection in humans, including several genes associated with skin phenotypes.

CREDITS (TOP TO BOTTOM): XAVIER STUDIO; KIM AND CHOI

Downloaded from www.sciencemag.org on February 28, 2014

Additional summaries

Synthesis in the Spotlight

Most organic molecules absorb little or no visible light. Consequently, conventional organic photochemistry has relied on excitation in the ultraviolet regime, with the drawback that the high energy involved can lead to undesirable by-products. Over the past several years, an alternative strategy has emerged involving the visible excitation of metal complexes (primarily ruthenium and iridium) that can then engage in electron or energy transfer with organic compounds. The ensuing reactivity patterns complement thermally accessible outcomes without introducing detrimental quantities of excess energy. **Schultz and Yoon** (p. 985) review developments in this rapidly advancing area of photoredox catalysis.

ESCRT Your Wound Away

The ESCRT (endosomal sorting complex required for transport) protein complex plays a role in budding into multivesicular bodies, in cytokinesis, and in HIV budding. Now, **Jimenez *et al.*** (p. 986, published online 30 January) propose a role for ESCRT proteins in wound repair at the plasma membrane. In vivo imaging, modeling, and electron microscopy were used to reveal how the ESCRTs participate in a rapid energy-independent, calcium-dependent, membrane-shedding process at the plasma membrane that reseals small wounds caused by toxins or laser treatment.

Metabolic Heterogeneity

We commonly think of genetic or epigenetic sources of variation in cells and individuals. However, biochemical regulatory pathways can potentially also exist in multiple stable states and confer variable phenotypes on cells in a population. **Van Heerden *et al.*** (p. 987, published online 16 January) demonstrate such a phenomenon in yeast cells. Two distinct types of cell were observed that differed in the state of glycolysis, the central pathway in energy metabolism for these cells. This allowed some members of a population of cells to survive changes in glucose concentrations, whereas most cells did not.

Repeat Silencing

Fragile X syndrome, a genetic cause of many cases of autism and mental retardation, involves expansion of a trinucleotide repeat in the *fragile X mental retardation 1 (FMR1)* gene. Working with human embryonic stem cells, **Colak *et al.*** (p. 1002) found that the expanded repeat region was transcribed into the untranslated region of *FMR1* messenger RNA, which then bound to the DNA repeat region in the *FMR1* gene, inactivating the gene. The findings explain how the trinucleotide repeat expansion causes RNA-directed gene silencing during development in fragile X syndrome.

A Different Route

The plant hormone auxin regulates a variety of developmental processes and responses to environmental inputs, often via changes in gene transcription. **Xu *et al.*** (p. 1025) analyzed a signaling pathway involving ABP1 (auxin-binding protein 1) that affects the cytoskeleton and endocytosis in *Arabidopsis* without changing gene transcription. Instead, ABP1 functions at the cell surface to bind auxin and a family of membrane kinases, thereby activating intracellular guanosine triphosphatases to initiate important developmental changes in cell shape.

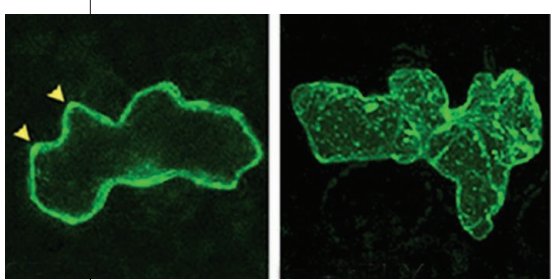

CREDIT: XU *ET AL.*

Sir Leszek Borysiewicz FRS is Vice-Chancellor of the University of Cambridge and a professor in the Department of Medicine at the University of Cambridge, Cambridge, UK.

Nicola Buckley is Head of Public Engagement at the University of Cambridge, Cambridge, UK. E-mail: nicola.buckley@admin.cam.ac.uk

Festival Lessons

FOR A UNIVERSITY THAT IS OVER 800 YEARS OLD, 20TH ANNIVERSARIES ARE RATHER MODEST. YET in March, the University of Cambridge will reflect on 20 years of organizing the Cambridge Science Festival in the United Kingdom. During this year's event, topics ranging from string theory to sustainability will be examined through talks, demonstrations, debates, theatre, music, exhibitions, and more. Hundreds of researchers and students will participate, and around 30,000 people are expected to attend. Over the past two decades, the festival has imparted many general lessons about how to successfully make science "public" and why this endeavor is important not only for the audience but for the research enterprise itself.

In 1994, the idea of a festival to communicate science to the public was still in its infancy in the United Kingdom. The modern concept of such a program had come about only a few years earlier in Edinburgh, with the idea that science could be packaged in a format from the arts. The first Cambridge Science Festival was attended by several hundred people, with a less ambitious scope and more dependence on straightforward public lectures. Since then, there has been growing recognition of the benefits of public engagement for researchers, and finding effective ways to showcase science and technology is now a priority. Research funders and universities in many nations are increasingly embedding requirements for public engagement within their funding programs and career advancement schemes, acknowledging the importance of making visible the processes of and outputs from research. The creative scaffold of most science festivals reflects this push to engage.

Today, there are several hundred festivals every year that enable millions of people worldwide to interact with those working in science. As part of the many science-in-society activities now taking place, festivals aim to nurture scientific literacy among attendees of all ages, to enthuse them with the wonder and excitement that scientists feel, and to help students and researchers appreciate how public engagement can help them view their own work in both interdisciplinary and social contexts. The core content of the Cambridge Festival is science and technology, but perspectives are drawn in from other fields too, and the presentation is influenced by the world of the arts. This weaving together of science and culture to communicate the relevance of science to everyday life seems to lie behind the growing international popularity of such festivals.

The Cambridge Festival has the advantage of pulling perspectives from the university's own researchers in social sciences, arts, and humanities together with those in the sciences and technology. The involvement of a university can also help to attract the participation of many partners beyond its own campus. In turn, a festival can make a university's research world less mysterious. The Cambridge Festival enables attendees to come into intimate contact with the people and setting of science at the University of Cambridge and to become part of discussions that have personal and global dimensions—from climate change and health to technologies that are part of their everyday lives.

Our experience has been that participants in science festivals are as diverse as the efforts that go into reaching out to them. Certainly, online dissemination is providing the University of Cambridge and the Festival with opportunities to reach an even wider audience. But successful outreach requires nurturing relationships with local communities, not only to support a yearly festival but also to maintain year-round public engagement activities. As such, science festivals such as the one in Cambridge have become central to many networks for informal science learning in the United Kingdom; this is perhaps the greatest lesson learned from organizing the Cambridge Festival. An honest dialogue between science and society comes through real experiences of engagement, and more than just once a year.

– Leszek Borysiewicz and Nicola Buckley

10.1126/science.1252251

CREDITS: (TOP LEFT) PHILIP MYNOTT; (BOTTOM LEFT) BECKY WIECZOREK; (RIGHT) UNIVERSITY OF CAMBRIDGE/SIR CAM

Downloaded from www.sciencemag.org on February 28, 2014

Published by AAAS

EDITORS' CHOICE

EDITED BY KRISTEN MUELLER AND JESSE SMITH

ECOLOGY

Diversity Down Below

Despite a surge of research efforts in recent years, the challenges faced by soil biologists remain daunting. Knowledge of even the basic elements of the biodiversity that is so visible above ground—in particular, species diversity and distribution—remains far more rudimentary where life below the soil surface is concerned. Soil fungi are a case in point. A key component of the soil ecosystem, its global species diversity, has tended to be estimated by various proxies. From a study of the fungi of boreal forest soils in Alaska, Taylor *et al*. suggest that previous estimates of fungal diversity, which hitherto hovered between 0.5 and 1.5 million, might need to be revised upward. Fungal DNA sequence data from their samples yielded just over 1000 discrete fungal taxa—many more than had been estimated from nonmolecular data. Within the soil, the fungal species communities were found to be highly structured and correlated with abiotic variables such as pH and soil horizon, and with the species composition of the understory plant community. The revealed fungus:plant ratio of 17:1, if reflected globally, would extrapolate to at least 6 million fungal species, suggesting in turn that 98% of fungi have yet to be described—a figure that remains to be corroborated by similarly detailed sampling across a range of other soil ecosystems. — AMS

Ecol. Monogr. **84**, 3 (2014).

IMMUNOLOGY

Amplifying Immunity

Antigen-specific T cells are important for the control and clearance of many types of infection. T cells that do not recognize the specific pathogen, however, often participate in getting rid of infections, but the specific mechanisms that regulate the activation of these so-called "bystander" T cells are less well understood. O'Donnell *et al*. used mice infected with *Salmonella* to better understand this phenomenon and found that detection of microbe-associated molecular patterns by Toll-like receptor 4 and components of the inflammasome in a T cell extrinsic pathway led to the production of several cytokines, including interleukin 18 (IL-18). IL-18 in turn acted on bystander $CD4^+$ T cells to amplify their antibacterial responses. In fact, mice in which the bystander activation of $CD4^+$ T cells was inhibited were impaired in their ability to control *Salmonella* infection. Although not formally demonstrated, this may be a way for the immune system to avoid being overwhelmed by a rapidly dividing pathogen and/or to protect the host against co-infection. — KLM

Immunity 10.1016/j.immuni.2013.12.013 (2014).

BIOMEDICINE

Counteracting Muscle Aging

Muscles tend to get weaker with age and also lose regenerative capacity. Studying young and old mice, Cosgrove *et al*. demonstrate that impaired muscle stem cell function is at least in part to blame. In aged mice, about two-thirds of the muscle stem cells were on their way to differentiation or senescence and thus were individually less effective at regenerating muscle fibers. However, even in the aged mice, a subset of muscle stem cells existed that showed youthful, enthusiastic muscle regeneration. Analysis of the differences between the two stem cell populations pointed to differences in the p38 mitogen-activated protein kinase (MAPK) pathway. Muscle stem cell populations from aged mice that were cultured on soft substrates and treated with a p38 MAPK inhibitor proliferated to produce more of the robust-regeneration stem cells, even though the source was aged mice. When transplanted into the muscles of aged mice, stem cells derived from this in vitro treatment engrafted enthusiastically, contributed to repair of muscle fibers, and restored muscle strength measurements to youthful levels. — PJH

Nat. Med. 10.1038/nm.3464 (2014).

EDUCATION

Teaching by Retraction

As funding for research grants becomes more competitive, the pressure to publish in top journals increases and may lead to an increase in ethical lapses. One way to overcome this may be through better education, but how best to teach it? Burnett *et al.* address this issue using research articles that have been retracted to highlight the types of ethical problems that can ultimately hinder scientific progress. Students in upper-level biology and chemistry courses were required to read a retracted research paper and the official retraction notice. Students then presented the ethical issues raised in the retraction and explained how these problems could have been avoided. This often led to class discussions, as the cause for retraction was not always clear. Instructors were able to take advantage of this process to teach about the scientific process and the importance of peer review, with students being able to see direct examples of how retractions alter scientific progress. Hopefully, by raising their awareness of ethical lapses that can derail research, the students can gain an appreciation for scientific ethics that they can carry with them throughout their careers. — MM

J. Coll. Sci. Teach. **43**, 24 (2014).

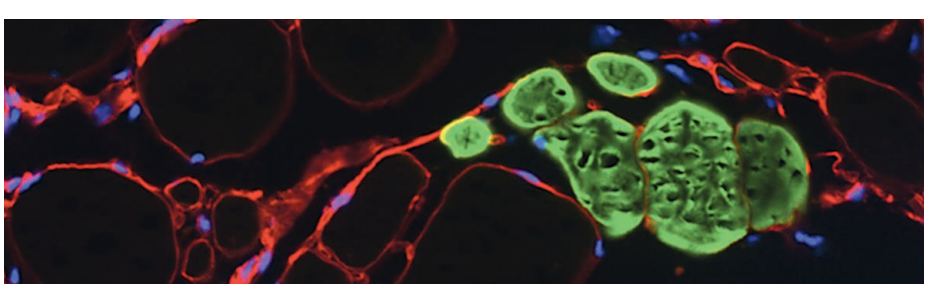

CREDITS (TOP TO BOTTOM): OKEA/THINKSTOCK; B. D. COSGROVE *ET AL.*, *NATURE MEDICINE* (16 FEBRUARY 2014)

Downloaded from www.sciencemag.org on February 28, 2014
© NATURE PUBLISHING GROUP

APPLIED PHYSICS

A Nanomechanical Phase Shifter

Information can be encoded in optical signals with a variety of parameters, usually wavelength, polarization, or phase. However, as signals propagate down optic fibers or around optical circuits, they can disperse; that is, they can acquire a phase shift that can then compromise the integrity of the encoded information. In other circumstances, one might want to control the phase of a signal to do a sort of analog computing by interfering the signal with reference signal and then monitoring the output as the subsequent changes in interference fringes. In each case, the ability to reliably control the phase

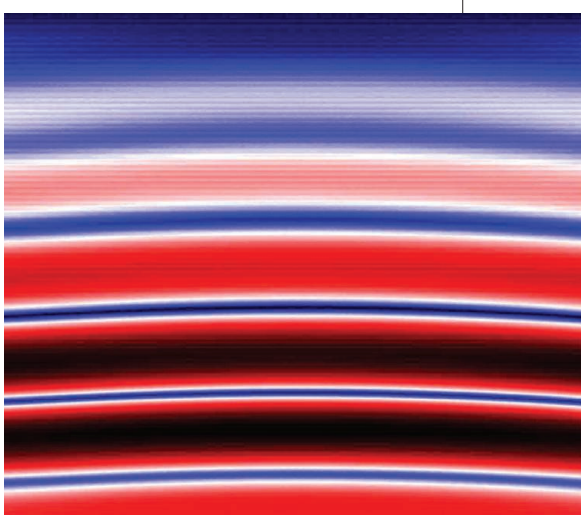

is crucial. Poot and Tang describe a broadband phase shifter based on a nanoelectromechanical controlled waveguide composed of two parts. By electrically switching one side of the waveguide and varying the separation, they change the effective refractive index of the waveguide and can induce a controlled phase shift in the propagating light signal. Such a nanoelectromechanical approach should prove useful as optoelectronics shrink and move from bulk-optical to low-power on-chip components. — ISO

Appl. Phys. Lett. **104**, 61101 (2014).

ENGINEERING

Safe, Selective, & Specific siRNA

RNA interference (RNAi) via small interfering (si) RNAs offers potential as a therapeutic tool for the specific knockdown of disease-associated genes. One limiting factor in the use of siRNAs as drugs involves delivering highly charged RNA molecules across cell membranes and into cells of the tissue of interest. Dong *et al*. used natural lipoprotein particles—which consist of apolipoprotein, phospholipid, cholesterol, and triglyceride and which have affinity for the liver—as a model for the design of an siRNA delivery system directed to the liver. They constructed lipopeptide nanoparticles (LPNs) by linking epoxide or aldehyde-derived lipid tails to amino acids or short peptides. Formulated with cholesterol, phospholipids, polyethylene glycol–lipid, and siRNA, the LPNs formed ~70-nm spheres, suspensions of which could be administered by injection. Lysine-based lipopeptides with tail lengths of 12 to 14 carbons proved highly effective at gene silencing specifically in liver hepatocytes. Furthermore, LPNs showed low toxicity and high gene-silencing activity in mice and cynomolgus monkeys. Apolipoprotein E facilitated both cell uptake and the escape of specific chemical classes of LPN-complexed siRNAs from endosomes into the cytoplasm. — GR

Proc. Natl. Acad. Sci. U.S.A. 10.1073/pnas.1322937111 (2014).

ASTROPHYSICS

Speedy Side-Kick

It is accepted that pulsars moving at high velocities through their surroundings received a kick at their birth from a core-collapse supernova, but details of this process remain under study. The presence of jets had been observed for rotation-powered pulsars either moving subsonically or still embedded in their supernova remnant, but not for pulsars moving at supersonic speeds. Pavan *et al.* report on radio and x-ray observations of the supersonic pulsar IGR J11014-6103, in which they detect its wind nebula and a jet, whose nature is supported by a counterjet in the opposite direction. Pulsar jets are usually difficult to observe because the pulsar spin axis is typically aligned with the direction of motion, so that the jet is disrupted, or hidden by shocked material in the wind nebula. However, this pulsar is unusual in that its direction of motion, and thus its probable kick direction from the supernova explosion, lies nearly perpendicular to the observed jet. The authors identify the corkscrew-shaped jet as originating with the pulsar and as consistent with modulation by a precessing spin axis. These findings suggest that such jets may be common, and the evidence of an apparently misaligned velocity kick will enable improvements to the core-collapse supernova model. — MMM

Astron. Astrophys. **562**, 10.1051/0004-6361/201322588 (2014).

CREDIT: COURTESY OF M. POOT

Published by AAAS

www.sciencemag.org

Science

1200 New York Avenue, NW
Washington, DC 20005
Editorial: 202-326-6550, FAX 202-289-7562
News: 202-326-6591, FAX 202-371-9227
Bateman House, 82-88 Hills Road
Cambridge, UK CB2 1LQ
+44 (0) 1223 326500, FAX +44 (0) 1223 326501

Subscription Services For change of address, missing issues, new orders and renewals, and payment questions: 866-434-AAAS (2227) or 202-326-6417, FAX 202-842-1065. Mailing addresses: AAAS, P.O. Box 96178, Washington, DC 20090-6178 or AAAS Member Services, 1200 New York Avenue, NW, Washington, DC 20005

Institutional Site Licenses please call 202-326-6755 for any questions or information

Reprints: Author Inquiries 800-635-7181
Commercial Inquiries 803-359-4578

Permissions 202-326-6765, permissions@aaas.org

Member Benefits AAAS Travels: Betchart Expeditions 800-252-4910; Apple Store www.store.apple.com/us/go/eppstore/aaas; NASA Federal, 1-888-NASA-FCU (1-888-627-2328) or www.nasafcu.com; Cold Spring Harbor Laboratory Press Publications www.cshlpress.com/affiliates/aaas.htm; Hertz 800-654-2200 CDP#343457; Seabury & Smith Life Insurance 800-424-9883; Subaru VIP Program 202-326-6417; Nationwide Insurance http://nationwide.com/aaas; Other Benefits: AAAS Member Services 202-326-6417 or http://membercentral.aaas.org/discounts.

science_editors@aaas.org	(for general editorial queries)
science_letters@aaas.org	(for queries about letters)
science_reviews@aaas.org	(for returning manuscript reviews)
science_bookrevs@aaas.org	(for book review queries)

Published by the American Association for the Advancement of Science (AAAS), *Science* serves its readers as a forum for the presentation and discussion of important issues related to the advancement of science, including the presentation of minority or conflicting points of view, rather than by publishing only material on which a consensus has been reached. Accordingly, all articles published in *Science*—including editorials, news and comment, and book reviews—are signed and reflect the individual views of the authors and not official points of view adopted by AAAS or the institutions with which the authors are affiliated.

AAAS was founded in 1848 and incorporated in 1874. Its mission is to advance science, engineering, and innovation throughout the world for the benefit of all people. The goals of the association are to: enhance communication among scientists, engineers, and the public; promote and defend the integrity of science and its use; strengthen support for the science and technology enterprise; provide a voice for science on societal issues; promote the responsible use of science in public policy; strengthen and diversify the science and technology workforce; foster education in science and technology for everyone; increase public engagement with science and technology; and advance international cooperation in science.

Information for Authors
See pages 680 and 681 of the 7 February 2014 issue or access www.sciencemag.org/about/authors

EDITOR-IN-CHIEF **Marcia McNutt**
EXECUTIVE EDITOR **Monica M. Bradford** NEWS EDITOR **Tim Appenzeller**
MANAGING EDITOR, RESEARCH JOURNALS **Katrina L. Kelner**
DEPUTY EDITORS **Barbara R. Jasny, Andrew M. Sugden, Valda J. Vinson, Jake S. Yeston**

Editorial senior editors/commentary Lisa D. Chong, Brad Wible; **senior editors** Gilbert J. Chin, Pamela J. Hines, Paula A. Kiberstis (Boston), Marc S. Lavine (Toronto), Kristen L. Mueller, Beverly A. Purnell, L. Bryan Ray, Guy Riddihough, H. Jesse Smith, Phillip D. Szuromi (Tennessee), Laura M. Zahn (San Diego); **associate editors** Melissa R. McCartney (Education Projects), Margaret M. Moerchen, Jelena Stajic, Sacha Vignieri (Oregon), Nicholas S. Wigginton (Michigan); **book review editor** Sherman J. Suter; **associate letters editor** Jennifer Sills; **editorial manager** Cara Tate; **senior copy editors** Jeffrey E. Cook, Chris Filiatreau, Cynthia Howe, Harry Jach, Lauren Kmec, Barbara P. Ordway, Trista Wagoner; **senior editorial coordinators** Carolyn Kyle, Beverly Shields; **editorial coordinators** RamatoulayeDiop, Joi S. Granger, Lisa Johnson, Anita Wynn; **publications assistants**, AneeraDobbins, Jeffrey Hearn, Dona Mathieu, Le-Toya Mayne Flood, Shannon McMahon, Scott Miller, Jerry Richardson, Brian White; **editorial assistant** Patricia M. Moore; **executive assistant** Alison Crawford; **administrative support** Maryrose Madrid

Senior web editor Sarah Crespi; **web development manager** Martyn Green **News managing editor** John Travis; **international news editor** Richard Stone; **deputy news editors** Robert Coontz, Elizabeth Culotta, David Grimm (Online), David Malakoff, Leslie Roberts; **senior correspondents** Eliot Marshall, Jeffrey Mervis, Elizabeth Pennisi **news writers** Yudhijit Bhattacharjee, Adrian Cho, Jennifer Couzin-Frankel, Carolyn Gramling, Jocelyn Kaiser, Richard A. Kerr, Robert F. Service (Pacific NW), Kelly Servick, Erik Stokstad, Emily Underwood; **web developer** Daniel Berger; **social media strategist** Meghna Sachdev; **interns** Thomas Sumner, Nadia Whitehead; **contributing correspondents** John Bohannon, Jon Cohen (San Diego, CA), Ann Gibbons, Sam Kean, Eli Kintisch, Andrew Lawler, Mitch Leslie, Charles C. Mann, Virginia Morell, Heather Pringle; **copy editors** Kara Estelle, Nora Kelly, Jennifer Levin; **administrative support** Scherraine Mack; **bureaus** San Diego, CA: 760-942-3252, FAX 760-942-4979; Pacific Northwest: 503-963-1940

Production director Wendy K. Shank; **assistant manager** Rebecca Doshi; **senior specialists** Steve Forrester, Anthony Rosen; **specialist** Jacob Hedrick **Preflight director** David M. Tompkins; **manager** Marcus Spiegler; **specialists** Jason Hillman, Tara Kelly

Art director Yael Fitzpatrick; **associate art director** Laura Creveling; **senior illustrators** Chris Bickel, Katharine Sutliff; **illustrator** Valerie Altounian; **senior art associates** Holly Bishop, Preston Huey; **art associates** Kay Engman, Garvin Grullón, Chrystal Smith; **photo editor** Leslie Blizard

***Science* International**

Europe (science@science-int.co.uk) **editorial: international managing editor** Andrew M. Sugden; **senior editor/commentary** Julia Fahrenkamp-Uppenbrink; **senior editors** Caroline Ash, Stella M. Hurtley, Ian S. Osborne, Peter Stern, Maria Cruz; **contributing editor** Helen Pickersgill; **editorial support** Rachel Roberts, Alice Whaley; **administrative support** Janet Clements, Joan Cuthbert, John Wood; **news: deputy news editor, u.k.** Daniel Clery; **contributing editor, europe** Martin Enserink; **contributing correspondents** Michael Balter (Paris), Kai Kupferschmidt (Berlin), Tania Rabesandratana (Brussels), Gretchen Vogel (Berlin)

Asia Japan Office: Asca Corporation, Tomoko Furusawa, Rustic Bldg. 7F, 77 Tenjin-cho, Shinjuku-ku, Tokyo 162-0808, Japan; +81 3 6802 4616, FAX +81 3 6802 4615, inquiry@sciencemag.jp; **contributing editor, asia** Mara Hvistendahl [China: mhvisten@aaas.org]; **contributing correspondents** Dennis Normile [Japan: dnormile@gol.com]; Christina Larson [China: christina.larson@gmail.com]; Pallava Bagla [South Asia: pallava.bagla@gmail.com]

Latin America contributing correspondent Lizzie Wade [Mexico City: lizziewade@outlook.com]

EXECUTIVE PUBLISHER **Alan I. Leshner**
PUBLISHER **Beth Rosner** CHIEF DIGITAL MEDIA OFFICER **Rob Covey**

Fulfillment Systems and Operations (membership@aaas.org); **customer service supervisor** Pat Butler; **specialists** LaToya Casteel, Michelle Ofordire, Javia Jennings, Chanta Stewart; **manager, data entry** Mickie Napoleoni; **data entry specialists** JJ Regan, Jaimee Wise, Fiona Giblin

Business Operations and Administration director Deborah Rivera-Wienhold; **business systems and financial analysis director** Randy Yi; **manager of fulfillment systems** Neal Hawkins; **systems analyst** Nicole Mehmedovich; **manager, business analysis** Eric Knott; **manager, business operations** Jessica Tierney; **business analysts** Cory Lipman, Cooper Tilton, Celeste Troxler; **financial analyst** Jeremy Clay; **rights and permissions: assistant director** Emilie David; **associate** Elizabeth Sandler; **marketing director** Ian King; **marketing managers** Alison Chandler, Julianne Wielga, Justin Sawyers; **marketing associates** Mary Ellen Crowley, Elizabeth Sattler, Rebecca Riffkin; **senior marketing executive** Jennifer Reeves; **director, site licensing** Tom Ryan; **director, corporate relations** Eileen Bernadette Moran; **senior publisher relations specialist** Kiki Forsythe; **publisher relations manager** Catherine Holland; **publisher relations, eastern region** Keith Layson; **publisher relations, western region** Ryan Rexroth; **customer relations manager** Iquo Edim; **customer relations analysts** Simon Chong, Lana Guz; **associate director, marketing** Christina Schlecht; **marketing associates** Paulina Curto, Mitchell Edmund; **electronic media: director** Lizabeth Harman; **assistant manager** Lisa Stanford; **production specialists** Antoinette Hodal, Nichele Johnston, Lori Murphy, Kimberly Oster; **web and new media: senior project manager** Trista Smith, **project leader** Luke Johnson **computer specialists** Walter Jones, Kai Zhang, **web developer** Chris Coleman; **program director, aaas member central** Peggy Mihelich

director, global collaboration, custom publications, advertising Bill Moran
editor, custom publishing Sean Sanders: 202-326-6430
assistant editor, custom publishing Tianna Hicklin 202-326-6463
sponsored content specialist Candice Nulsen 202-256-1528
associate director, collaboration, custom publications/china/taiwan/korea/singapore Ruolei Wu +86-1367-101-5294

Product (science_advertising@aaas.org); **midwest** Rick Bongiovanni: 330-405-7080, FAX 330-405-7081; **east coast/e. canada** Laurie Faraday: 508-747-9395, FAX 617-507-8189; **west coast/w. canada** Lynne Stickrod: 415-931-9782, FAX 415-520-6940; **uk europe/asia** Roger Goncalves: TEL/FAX +41 43 243 1358; **japan**, Makiko Hara: +81 (0) 3 6802 4616, FAX +81 (0) 3 6802 4615; ads@sciencemag.jp; **china/taiwan** Ruolei Wu: +86 1367 1015 294 rwu@aaas.org

worldwide associate director of *Science* Careers Tracy Holmes: +44 (0) 1223 326525, FAX +44 (0) 1223 326532

Classified (advertise@sciencecareers.org); **u.s./canada/south america** Tina Burks: 202-326-6577; **u.s. corporate** Candice Nulsen 202-256-1528; **sales administrator** Marci Gallun; **europe/row sales** Axel Gesatzki, Sarah Lelarge; **sales assistant** Kelly Grace; **japan** Yuri Kobayashi +81 (0)90-9110-1719; careerads@sciencemag.jp; **china/taiwan** Ruolei Wu: +86 1367 1015 294 rwu@aaas.org; **advertising support manager** Karen Foote: 202-326-6740; **advertising production operations manager** Deborah Tompkins; **senior production specialist/graphic designer** Amy Hardcastle; **production specialist** Yuse Lajiminmuhip; **senior traffic associate** Christine Hall; **sales coordinator** Shirley Young; **marketing manager** Allison Pritchard; **marketing associate** Aimee Aponte

AAAS Board of Directors retiring president, chair Phillip A. Sharp; **president** Gerald R. Fink; **president-elect** Geraldine (Geri) Richmond; **treasurer** David Evans Shaw; **chief executive officer** Alan I. Leshner; **board** Bonnie L. Bassler, May R. Berenbaum, Carlos J. Bustamante, Claire M. Fraser, Laura H. Greene, Elizabeth Loftus, Raymond Orbach, Inder M. Verma

AAAS
ADVANCING SCIENCE, SERVING SOCIETY

SENIOR EDITORIAL BOARD

A. Paul Alivisatos, *Lawrence Berkeley Nat'l. Laboratory*
Ernst Fehr, *Univ. of Zurich*
Susan M. Rosenberg, *Baylor College of Medicine*
Michael S. Turner, *University of Chicago*

BOARD OF REVIEWING EDITORS

Adriano Aguzzi, *Univ. Hospital Zürich*
Takuzo Aida, *Univ. of Tokyo*
Leslie Aiello, *Wenner-Gren Foundation*
Sonia Altizer, *Univ. of Georgia*
Virginia Armbrust, *Univ. of Washington*
Sebastian Amigorena, *Institut Curie*
Kathryn Anderson, *Memorial Sloan-Kettering Cancer Center*
Peter Andolfatto, *Princeton Univ.*
Meinrat O. Andreae, *Max Planck Inst., Mainz*
Paola Arlotta, *Harvard Univ.*
Johan Auwerx, *EPFL*
David Awschalom, *Univ. of Chicago*
Jordi Bascompte, *Estación Biológica de Doñana, CSIC*
Facundo Batista, *London Research Inst.*
Ray H. Baughman, *Univ. of Texas, Dallas*
David Baum, *Univ. of Wisconsin*
Mark Bear, *Massachusetts Inst. of Technology*
Kamran Behnia, *Paris-Sud Univ.*
Yasmine Belkaid, *NIAID, NIH*
Philip Benfey, *Duke Univ.*
Stephen J. Benkovic, *Penn State Univ.*
Gabriele Bergers, *Univ. of California, San Francisco*
Christophe Bernard, *Aix-Marseille Univ.*
Gregory C. Beroza, *Stanford Univ.*
Peer Bork, *EMBL*
Bernard Bourdon, *Ecole Normale Superieure de Lyon*
Chris Bowler, *Ecole Normale Supérieure*
Ian Boyd, *Univ. of St. Andrews*
Christian Büchel, *Universitätsklinikum Hamburg-Eppendorf*
Joseph A. Burns, *Cornell Univ.*
William P. Butz, *Population Reference Bureau*
Gyorgy Buzsaki, *New York Univ., School of Medicine*
Blanche Capel, *Duke Univ.*
Mats Carlsson, *Univ. of Oslo*
David Clapham, *Children's Hospital, Boston*
David Clary, *Univ. of Oxford*
Joel Cohen, *Rockefeller Univ., Columbia Univ.*
Jonathan D. Cohen, *Princeton Univ.*
Robert Cook-Deegan, *Duke Univ.*
James Collins, *Boston Univ.*
Alan Cowman, *Walter & Eliza Hall Inst.*
Robert H. Crabtree, *Yale Univ.*
Janet Currie, *Princeton Univ.*
Jeff L. Dangl, *Univ. of North Carolina*
Tom Daniel, *Univ. of Washington*
Frans de Waal, *Emory Univ.*
Stanislas Dehaene, *Collège de France*
Robert Desimone, *MIT*
Claude Desplan, *New York Univ.*
Ap Dijksterhuis, *Radboud Univ. of Nijmegen*
Dennis Discher, *Univ. of Pennsylvania*
Gerald W. Dorn II, *Washington Univ. School of Medicine*
Jennifer A. Doudna, *Univ. of California, Berkeley*
Bruce Dunn, *Univ. of California, Los Angeles*
Christopher Dye, *WHO*
Todd Ehlers, *University of Tuebingen*
David Ehrhardt, *Carnegie Inst. of Washington*
Tim Elston, *Univ. of North Carolina at Chapel Hill*
Gerhard Ertl, *Fritz-Haber-Institut, Berlin*
Barry Everitt, *Univ. of Cambridge*
Ernst Fehr, *Univ. of Zurich*
Michael Feuer, *The George Washington Univ.*
Alain Fischer, *INSERM*
Anne C. Ferguson-Smith, *Univ. of Cambridge*
Peter Fratzl, *Max Planck Inst.*
Elaine Fuchs, *Rockefeller Univ.*
Wulfram Gerstner, *EPFL Lausanne*
Daniel Geschwind, *UCLA*
Andrew Gewirth, *Univ. of Illinois*
Karl-Heinz Glassmeier, *TU Braunschweig*
Julia R. Greer, *Caltech*
Elizabeth Grove, *Univ. of Chicago*
Kip Guy, *St. Jude's Children's Research Hospital*
Taekjip Ha, *Univ. of Illinois at Urbana-Champaign*
Christian Haass, *Ludwig Maximilians Univ.*
Steven Hahn, *Fred Hutchinson Cancer Research Center*
Gregory J. Hannon, *Cold Spring Harbor Lab.*
Michael Hasselmo, *Boston Univ.*
Martin Heimann, *Max Planck Inst., Jena*
Yka Helariutta, *Univ. of Finland*
James A. Hendler, *Rensselaer Polytechnic Inst.*
Janet G. Hering, *Swiss Fed. Inst. of Aquatic Science & Technology*
Michael E. Himmel, *National Renewable Energy Lab.*
Kai-Uwe Hinrichs, *Univ. of Bremen*
Kei Hirose, *Tokyo Inst. of Technology*
David Hodell, *Univ. of Cambridge*
David Holden, *Imperial College*
Lora Hooper, *UT Southwestern Medical Ctr at Dallas*
Thomas Hudson, *Ontario Inst. for Cancer Research*
Raymond Huey, *Univ. of Washington*
Steven Jacobsen, *Univ. of California, Los Angeles*
Kai Johnsson, *EPFL Lausanne*
Peter Jonas, *Inst. of Science & Technolgy (IST) Austria*
Matt Kaeberlein, *Univ. of Washington*
William Kaelin Jr., *Dana-Farber Cancer Inst.*
Daniel Kahne, *Harvard Univ.*
Daniel Kammen, *Univ. of California, Berkeley*
Masashi Kawasaki, *Univ. of Tokyo*
Joel Kingsolver, *Univ. of North Carolina at Chapel Hill*
Robert Kingston, *Harvard Medical School*
Alexander Kolodkin, *Johns Hopkins Univ.*
Roberto Kolter, *Harvard Medical School*
Alberto R. Kornblihtt, *Univ. of Buenos Aires*
Leonid Kruglyak, *Princeton Univ.*
Thomas Langer, *Univ. of Cologne*
Mitchell A. Lazar, *Univ. of Pennsylvania*
David Lazer, *Harvard Univ.*
Virginia Lee, *Univ. of Pennsylvania*
Thomas Lecuit, *IBDM*
Stanley Lemon, *Univ. of North Carolina at Chapel Hill*
Ottoline Leyser, *Cambridge Univ.*
Marcia C. Linn, *Univ. of California, Berkeley*
Jianguo Liu, *Michigan State Univ.*
Luis Liz-Marzan, *CIC biomaGUNE*
Jonathan Losos, *Harvard Univ.*
Ke Lu, *Chinese Acad. of Sciences*
Christian Lüscher, *Univ. of Geneva*
Laura Machesky, *CRUK Beatson Inst. for Cancer Research*
Anne Magurran, *Univ. of St Andrews*
Oscar Marin, *CSIC & Univ. Miguel Hernández*
Charles Marshall, *Univ. of California, Berkeley*
Chris Marshall, *Inst. of Cancer Research*
C. Robertson McClung, *Dartmouth College*
Graham Medley, *Univ. of Warwick*
Yasushi Miyashita, *Univ. of Tokyo*
Richard Morris, *Univ. of Edinburgh*
Sean Munro, *MRC Lab. of Molecular Biology*
Thomas Murray, *The Hastings Center*
Naoto Nagaosa, *Univ. of Tokyo*
James Nelson, *Stanford Univ. School of Med.*
Daniel Neumark, *Univ. of California, Berkeley*
Timothy W. Nilsen, *Case Western Reserve Univ.*
Pär Nordlund, *Karolinska Inst.*
Helga Nowotny, *European Research Advisory Board*
Luke O'Neill, *Trinity College, Dublin*
Ben Olken, *MIT*
N. Phuan Ong, *Princeton Univ.*
Joe Orenstein, *Univ. of California, Berkeley & Lawrence Berkeley National Lab*
Harry Orr, *Univ. of Minnesota*
Andrew Oswald, *Univ. of Warwick*
Steve Palumbi, *Stanford Univ.*
Jane Parker, *Max-Planck Inst. of Plant Breeding Research*
Donald R. Paul, *Univ. of Texas at Austin*
John H. J. Petrini, *Memorial Sloan-Kettering Cancer Center*
Joshua Plotkin, *Univ. of Pennsylvania*
Philippe Poulin, *CNRS*
Colin Renfrew, *Univ. of Cambridge*
Trevor Robbins, *Univ. of Cambridge*
Jim Roberts, *Fred Hutchinson Cancer Research Ctr.*
Barbara A. Romanowicz, *Univ. of California, Berkeley*
Jens Rostrup-Nielsen, *Haldor Topsoe*
Mike Ryan, *Univ. of Texas, Austin*
Mitinori Saitou, *Kyoto Univ.*
Shimon Sakaguchi, *Kyoto Univ.*
Miquel Salmeron, *Lawrence Berkeley National Lab*
Jürgen Sandkühler, *Medical Univ. of Vienna*
Alexander Schier, *Harvard Univ.*
Randy Seeley, *Univ. of Cincinnati*
Vladimir Shalaev, *Purdue Univ.*
Joseph Silk, *Institut d'Astrophysique de Paris*
Denis Simon, *Arizona State Univ.*
Alison Smith, *John Innes Centre*
John Speakman, *Univ. of Aberdeen*
Allan C. Spradling, *Carnegie Institution of Washington*
Jonathan Sprent, *Garvan Inst. of Medical Research*
Eric Steig, *Univ. of Washington*
Molly Stevens, *Imperial College London*
Paula Stephan, *Georgia State Univ. and National Bureau of Economic Research*
V. S. Subrahmanian, *Univ. of Maryland*
Ira Tabas, *Columbia Univ.*
Sarah Teichmann, *Cambridge Univ.*
John Thomas, *North Carolina State Univ.*
Christopher Tyler-Smith, *The Wellcome Trust Sanger Inst.*
Herbert Virgin, *Washington Univ.*
Bert Vogelstein, *Johns Hopkins Univ.*
Cynthia Volkert, *Univ. of Göttingen*
Bruce D. Walker, *Harvard Medical School*
Douglas Wallace, *Dalhousie Univ.*
David Wallach, *Weizmann Inst. of Science*
Ian Wardle, *Univ. of Oxford*
David A. Wardle, *Swedish Univ. of Agric Sciences*
David Waxman, *Fudan Univ.*
Jonathan Weissman, *Univ. of California, San Francisco*
Kathy Willis, *Oxford Univ.*
Ian A. Wilson, *The Scripps Res. Inst.*
Timothy D. Wilson, *Univ. of Virginia*
Rosemary Wyse, *Johns Hopkins Univ.*
Jan Zaanen, *Leiden Univ.*
Kenneth Zaret, *Univ. of Penn. School of Medicine*
Jonathan Zehr, *Univ. of California, Santa Cruz*
Len Zon, *Children's Hospital Boston*
Maria Zuber, *MIT*

BOOK REVIEW BOARD

David Bloom, *Harvard Univ.*
Samuel Bowring, *MIT*
Angela Creager, *Princeton Univ.*
Richard Shweder, *Univ. of Chicago*
Ed Wasserman, *DuPont*

AROUND THE WORLD

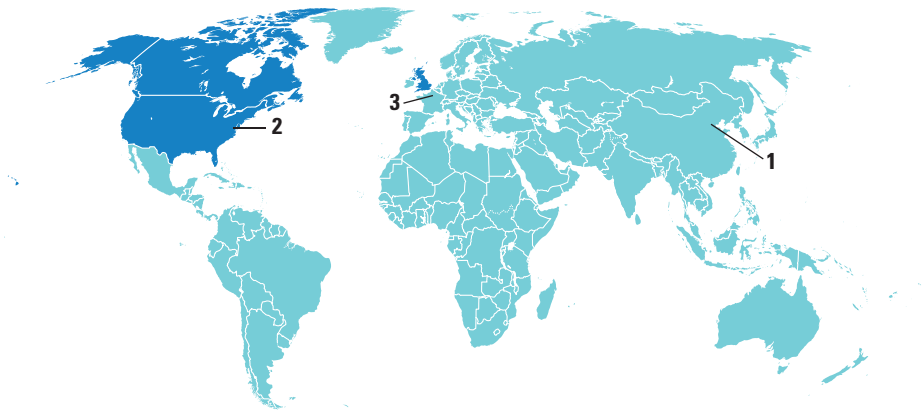

Beijing **1**

Crackdown on Southern Chinese Research Graft Widens

A corruption probe in one of China's wealthiest provinces has so far snared more than 50 scientists and research administrators. On 14 February, a government website for Guangdong province revealed that the provincial science bureau's former deputy director, Wang Kewei, was under investigation for violating antigraft regulations. The bureau's director, Li Xinghua, was removed from his post and stripped of Communist Party membership last month. And 21 employees of the science department of Foshan city were also charged in December with skimming money from government R&D subsidies intended for local companies.

Scrutinized. Guangzhou, capital of Guangdong province.

Guangdong spent nearly $4 billion on science and technology in 2012—a disproportionately large share of the roughly $36 billion in provincial government spending overall. "I think the current national leadership is very serious about corruption," says Cao Cong, an expert on Chinese science policy at the University of Nottingham in the United Kingdom. "They really want to crack down." **http://scim.ag/_graft**

Washington, D.C. **2**

New Website Tracks Forests In Near-Real Time

Scientists, policymakers, and the public have a powerful new tool to study and monitor forests online. Global Forest Watch, launched last week by the World Resources Institute, allows users to access deforestation alerts updated monthly, locate current fires, and track forest loss or growth anywhere in the world.

Underpinning the interactive website are two powerful new data sets based on satellite imaging. The first, with a geographical resolution of 500 meters, has already helped chimp conservationists confirm deforestation events as they occur. The second, highlighted in a paper last fall (*Science*, 15 November 2013, p. 850), offers an annual snapshot of global forests at 30-meter resolution. "In itself, more transparency doesn't lead to stopping deforestation," says Steve Schwartzman, of the Environmental Defense Fund in Washington, D.C., "but this is a terrific step." **http://scim.ag/_forest**

Paris **3**

Europe to Launch Hunt For Earth-Like Planets

The European Space Agency last week added a new mission to its "Cosmic Vision 2015-2025" program: a search for habitable planets outside our solar system. Of about 1000 known exoplanets, only a few dozen are rocky, as opposed to gaseous, and none of these have conditions that would allow liquid water on their surfaces. The PLAnetary Transits and Oscillations of stars (PLATO) mission, to launch in 2024, will try to find more planets that occupy the so-called habitable zone around sunlike stars by measuring the dimming of the light from a star as a planet passes in front of it.

Other space-based observatories have used this technique to search for exoplanets, but to do so have had to monitor very faint stars. That makes it hard to determine an exoplanet's mass, and thereby decide if it is rocky or gaseous. PLATO will use 34 small telescopes to widen its field of view and monitor large numbers of bright, relatively nearby stars for up to 3 years at a time. **http://scim.ag/_plato**

NEWSMAKERS

Three Q's

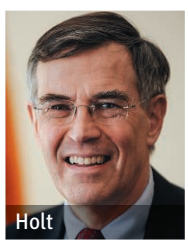

Holt

Last week, one of two research physicists in the U.S. House of Representatives announced he won't run for reelection this fall. **Representative Rush Holt** (D–NJ), 65, isn't saying what he'll do next. But his passion for science-based policies still burns brightly.

Q: How has the level of scientific discourse changed since you first came to Congress in 1999?

R.H.: It has not gotten better, let's put it that way. There are still people who read popular science articles, and most members of Congress say they value science and respect scientists. But I don't see more scientific thinking—evidence-based, critical thinking.

Q: Why would a scientist want to run for Congress?

R.H.: We need all kinds, especially people who can analyze problems and not be bamboozled by technical talk. And scientists bring a skill set that can be useful.

Q: What would it take to regain bipartisan support for science-related legislation?

R.H.: It will take more people who have an allegiance to evidence. And what I'm saying is that many [current members] do not. That's what would have to change.

CREDITS (TOP TO BOTTOM): ESA–C. CARREAU; U.S. HOUSE OF REPRESENTATIVES; AZWARI NUGRAHA/FLICKR

Downloaded from www.sciencemag.org on February 28, 2014

Published by AAAS

Random Sample

Science by the Eyeful

The digital age may offer new ways to make data more eye-catching, but the effort to turn scientific research into a visual story is centuries old. The British Library in London is honoring that effort in a new exhibit called *Beautiful Science: Picturing Data, Inspiring Insight*. The exhibit draws on the library's collections to showcase artful displays of science through the ages, focusing on the themes of weather, evolution, and public health.

The oldest piece on view is a 1617 illustration of the ancient Greek classifications of life forms, the *Great Chain of Being* (left), in which the goddess of wisdom stands atop a hierarchy of animals, plants, and minerals. The newest work, Martin Krzywinski's *Circles of Life* (right), relies on DNA sequencing data to illustrate our relationship to other species using colorful links between the top and bottom halves of the circles—each representing genes arrayed on a chromosome. The exhibit opened last week and will run through 26 May.

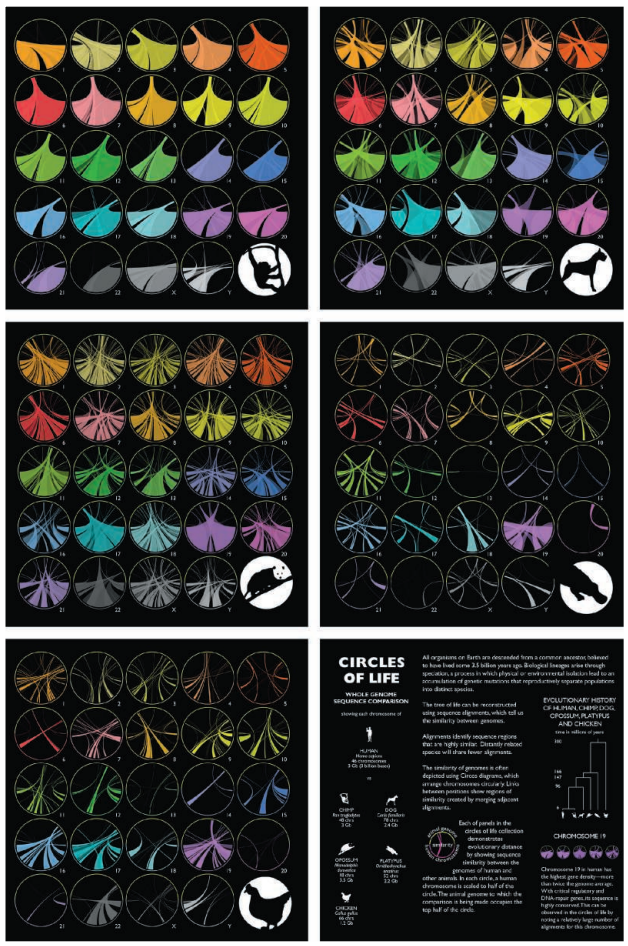

CREDITS: (CLOCKWISE FROM TOP LEFT) © THE BRITISH LIBRARY BOARD; © MARTIN KRZYWINSKI, *CIRCLES OF LIFE*, 2014; BORBALA FERENCZY; CYRIL RUOSO

Revered Primatologist Dies

Primatologist and conservationist **Alison Jolly**, who suggested that social behavior drove the evolution of intelligence, died on 6 February in England at age 76.

American-born Jolly, who studied the lemurs of Madagascar, was the first to report in the 1960s that females are dominant in some primates. This discovery "upended virtually all standing hypotheses about primate social behavior … and didn't go down easily at the time," says Anne Yoder, director of the Duke Lemur Center in Durham, North Carolina. Then, in a seminal *Science* paper (*Science*, 29 July 1966, p. 501), Jolly proposed that complex social interactions, rather than the need for sophisticated tools, drove the evolution of primate intelligence. This is now a leading theory. "[H]er insights transformed our understanding," wrote anthropologist Alison Richard of Yale University in an obituary. Jolly "never described herself as a feminist," Richard wrote, but "lived a life that led and supported feminism."

FINDINGS

Pooch Brains Attuned to Voices

Dog owners can attest to the uncanny canine ability to read a person's tone of voice. New research reveals a surprising mechanism behind this skill: Dog brains have a dedicated "voice area." In humans, this area is activated when we hear others speak, helping us recognize a speaker's identity and pick up on emotional content in her voice.

To find out if the canine brain processes sound similarly, a team of neuroscientists trained 11 dogs to lie motionless in a functional magnetic resonance imaging scanner while wearing headphones that played nearly 200 dog and human sounds, including whines, playful barks, and laughs. The group also scanned the brains of 22 human subjects who listened to the same sounds.

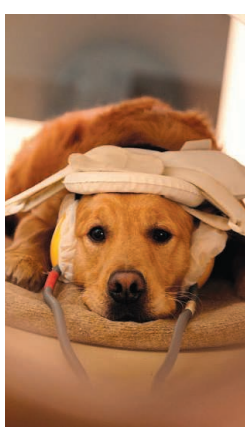

Obedient. A dog fitted with headphones prepares for an MRI.

The researchers found similarities in how dog and human brains process emotionally laden sounds, they reported last week in *Current Biology*. Voice areas were once thought to be unique to primates and tied to the evolution of language, but their presence in dogs suggests they evolved at least 100 million years ago. **http://scim.ag/dogvoice**

Published by AAAS

CREDIT: ASSOCIATED PRESS

Setback. Protests and science failed to stop Uganda's antigay law.

SCIENCE AND POLITICS

Science Misused to Justify Ugandan Antigay Law

On 24 February, Uganda's president, Yoweri Museveni, signed a draconian Anti-Homosexuality Bill into law, after 2 months of declining to do so. Science, he says, changed his mind—in particular, the findings of a special scientific committee his Health Ministry had appointed earlier in the month. "Their unanimous conclusion was that homosexuality, contrary to my earlier thinking, was behavioural and not genetic," Museveni wrote to President Barack Obama on 18 February, in response to Obama's pleas that he not sign the bill. "It was learnt and could be unlearnt."

But some scientists on the committee are crying foul, saying that Museveni and his ruling party—Uganda's National Resistance Movement (NRM)—misrepresented their findings. "They misquoted our report," says Paul Bangirana, a clinical psychologist at Makerere University in Kampala. "The report does not state anywhere that homosexuality is not genetic, and we did not say that it could be unlearnt." Two other committee members have now resigned to protest the use of their report to justify the harsh legislation, which mandates life imprisonment for "aggravated homosexuality," such as sexual acts with a minor, and prison terms of 7 to 14 years for attempted and actual homosexual acts, respectively.

The law was first introduced into Uganda's Parliament in 2009, but withdrawn after widespread objections to provisions that could have included the death penalty. As he signed the new version, passed by Parliament last 20 December, Museveni claimed that "mercenaries" were recruiting young people into gay activities.

The 11-member committee, including officials from the Ministry of Health, scientists at Makerere University, and other medical researchers, was charged with reviewing scientific evidence about the causes of homosexuality. The first draft of the report concluded that "there is no definitive gene responsible for homosexuality"; that homosexuality is not a disease nor abnormal; that being gay can be influenced by environmental factors such as culture and peer pressure; and that both homosexual and heterosexual behavior need "regulation" to "protect the vulnerable."

Dean Hamer, a geneticist emeritus at the National Institutes of Health who discovered the first evidence that homosexuality probably has some genetic basis (*Science*, 16 July 1993, p. 321), says "what's fascinating about the Ugandan report is that it gets so much right about the science of sexual orientation." The committee's report even referred to a recent, genome-wide study confirming Hamer's original findings.

But things began to go wrong for the Ugandan scientists when they presented their findings to Museveni, Prime Minister Amama Mbabazi, and more than 200 NRM members of Parliament at a 14 February NRM meeting. Shortly afterward, NRM put out a press release, signed by NRM spokeswoman Evelyn Anite, summarizing the scientific committee's findings and declaring that Museveni would now sign the bill "since the question of whether one can be born a homosexual or not had been answered"—supposedly in the negative. Anite denies charges that the press release distorted the panel's findings: "I did not change anything. What I put there is what the scientists said," Anite told *Science*. (Anite also asked the reporter on this story if he was a "homo" when he sought further clarification.)

Yet the press release combined and altered the committee's findings that "Homosexuality is not a disease" and "Homosexuality is not an abnormality" to read that "Homosexuality is not a disease but merely an abnormal behavior which may be learned through experiences in life." This change made several committee members see red. "We didn't say homosexuality is an abnormality," Bangirana says. Another member, who asked not to be identified, adds that "many people out there have ignorantly misinterpreted our position, taking it for an outright support for the bill." As a result, committee members Seggane Musisi, a psychiatrist at Makerere's School of Medicine, and Eugene Kinyanda, a mental health researcher for Uganda's Medical Research Council, tell *Science* that they have now resigned from the committee and dissociated themselves from the report. "History is replete with lessons from the mixing of science and politics," Musisi says.

The committee has now produced a final report, dated 23 February—the day before Museveni signed the legislation. It eliminates the language about regulating homosexuality because that "is easily abused or interpreted badly," Bangirana says. The new report also goes into more detail about the relative roles of nature and nurture in producing homosexuality, concluding that both are involved, although nurture could play a bigger role.

Some committee members say they were used to provide cover for a fait accompli. "Regardless of what our report would say, this bill was going to be signed," Bangirana says. J. Michael Bailey, a psychologist at Northwestern University in Evanston, Illinois, who led the recent replication of Hamer's original study, adds that no matter what the science says, it cannot be used to justify punishing gays: "There should be no link between how homosexual people are treated and what causes homosexuality."

–MICHAEL BALTER

Downloaded from www.sciencemag.org on February 28, 2014

Published by AAAS

ENERGY

New Review Slams Fusion Project's Management

ITER, the international fusion reactor project in France, is reeling from an assessment that found serious problems with the project's leadership, management, and governance. The report is so damning, *Science* has learned, that after a 13 February special session that reviewed and accepted the report's conclusions and recommendations, the ITER Council—the project's governing body—restricted its readership to a small number of senior managers and council members. "We feared that if [the assessment] leaked to people who don't know about the ITER agreement, the project could be interpreted as a major failure, which is not what the management assessor intended," says nuclear engineer Bob Iotti of the consulting firm CH2M HILL, who chairs that council.

Backed by China, the European Union, India, Japan, Russia, South Korea, and the United States, ITER aims to build a testbed for fusion energy. Under construction at Cadarache in southern France, it is often described as the most complex machine ever built. In its cavernous doughnut-shaped vacuum vessel, the reactor will heat heavy hydrogen to 150 million °C so that the nuclei will fuse to form helium, releasing energy.

Since the project began in earnest in 2006, the expected completion date has slipped from 2016 to 2018 to 2020, the estimated cost has tripled to at least €16 billion, and there's been a major change of leadership. "ITER had to create a project, a design, a laboratory, and an institutional culture. That's very many things to create at once," says Steve Cowley, head of the Culham Centre for Fusion Energy in the United Kingdom.

The ITER agreement requires management assessments every 2 years. The previous two were critical, but nothing like the latest, conducted by Bill Madia, former director of the Pacific Northwest and Oak Ridge national laboratories. "It didn't mince words," Iotti says. "It could be read as an indictment of the current director general [Osamu Motojima], but one should also look at the obstacles in his path. Some are not under his control."

Because all the partners want to gain experience from building ITER for what could be a lucrative future industry, the ITER agreement carves up the construction of reactor components among partners, each of which has created a "domestic agency" to handle the contracts. The result is far from efficient: Superconducting cable for the reactor's magnets is manufactured in six different nations and the 5000-tonne vacuum vessel is being built partly in Korea and partly in Europe.

ITER management acts as ringmaster, overseeing the reactor design, enforcing technical standards, and resolving conflicts. "The ITER Organization and the seven domestic agencies should work as a single project team," says Jean Jacquinot, scientific adviser to the head of France's Atomic Energy Commission. "But that's not really the case. Communication is not ideal."

The relationship is often acrimonious and when conflicts arise, domestic agencies sometimes go behind the central management's back and put pressure on it via their delegates to the ITER Council. Iotti believes this antagonism is "one of the biggest problems." The assessment found that voting on the council is often swayed by political considerations and that it acts only on unanimous decisions, which has had a devastating effect on the project's cost and schedule. Iotti, who took over the council chair at the start of the year, accepts the criticism. "We need to simplify our activities. … Then we can focus on the controversial issues," he says.

The assessment also found that ITER's day-to-day management team is inflexible and top-heavy, in part because the nationalities of senior management and the staff as a whole must reflect the division of funding. "Inefficiencies were built in with the full consent of the parties," Iotti says. The number of managers should be reduced, the report says, identifying one whole level that, if removed entirely, would improve efficiency and decision-making.

Iotti says that in response to the assessment, Motojima and ITER's senior management have proposed organizational changes that the council has "temporarily endorsed" because it "is not convinced that it is the ultimate answer." The council has asked for more information and justification for the changes. "ITER is still a young organization and it takes a very long time for different cultures to work as a single team," Jacquinot says.

Perhaps most controversially, a source tells *Science*, the assessment calls for the council to "accelerate the transition to a new director general." Brought in as part of a 2010 management reboot, Motojima ends his 5-year term in June 2015. Motojima, who declined comment, insists on consensus in decision-making and has surrounded himself with a coterie of staff, all Japanese, who meet with him daily outside the normal management structure, according to people

CREDIT: ITER ORGANIZATION

Rock bottom. Work on the circular foundations for the ITER fusion reactor was halted last June following disputes over the design. Construction did not begin again for 8 months.

Downloaded from www.sciencemag.org on February 28, 2014

Published by AAAS

who have worked closely with ITER officials.

ITER's schedule continues to slip, which will push up costs. ITER has said its reactor will power up for the first time before the end of 2020, but that date is widely discounted. "We don't have a realistic, believable, very high quality schedule," Iotti says. The council is now planning to announce an updated schedule at its meeting in June 2015. "We need to be sure," Iotti says. "Once we have a schedule, then we can talk about cost." ITER leaders fear that further delays, combined with the damning assessment, could cause backers to pull their funding; the United States has threatened doing so more than once.

Despite the problems, Iotti is optimistic. "The project is making progress; things are being built," he says. This summer, the first items of hardware will start arriving on site. "When stuff comes together, you will see a completely different attitude … [but] there are still going to be difficult times ahead."

–DANIEL CLERY

SOCIAL SCIENCE

Twitter Offers Entire Data Pool, but Some Wary of Diving In

Earlier this month, the social media company Twitter offered academic researchers a chance to play with a vast treasure trove of data—all 500 million of the 140-character "tweets" its 200 million users generate daily, as well as all tweets on record going back to Twitter's creation in 2006. Many scientists, eager to study social dynamics on a massive scale, are scrambling to apply by the company's 15 March deadline. But some, scrutinizing the fine print of the application, worry about legal strings that seem to grant Twitter ownership of their research ideas. "This would be a nonstarter for us," says systems scientist Yaneer Bar-Yam, who is among those reluctant to apply for Twitter's full data set.

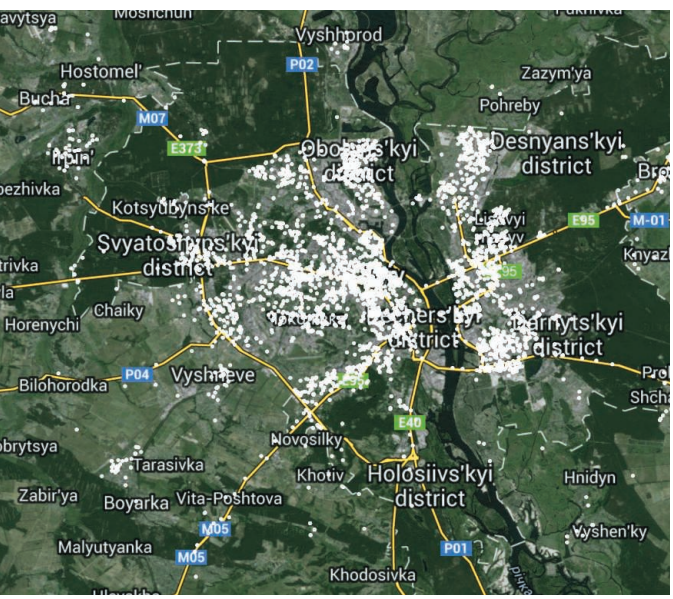

Social unrest. Social scientists can analyze tweets during protests, such as these 7458 from Kiev region over 2 days in mid-February.

Twitter has for several years provided free access to 1% of tweets through an online application programming interface (API). For many research projects, that's enough. Last year, for example, a team led by Bar-Yam, president of the New England Complex Systems Institute in Cambridge, Massachusetts, used the API to harvest 604,000 tweets from people in New York City. Users of Twitter's mobile app have the option to reveal their location when they tweet, and about 3% do so. By analyzing the sentiment in those geolocated tweets, the team mapped out the city's emotional landscape in time and space in exquisite detail. Conclusion: New Yorkers love parks and hate transportation.

When he learned last week that Twitter was granting researchers access to the full "firehose" of its data, Bar-Yam was thrilled. "Twitter data is an incredible resource," he says. "We want to use it to understand society, and also to help solve problems ranging from violence to pandemics."

But the 1% of tweet data now available through Twitter's free API is too limited for some research projects, says Nick Obradovich, a political science Ph.D. student at the University of California, San Diego. Obradovich wants to compare sentiments about climate change in U.S. geolocated tweets with local temperatures; according to one theory, unusually hot days make people more open to the idea that the scientific consensus about climate change is correct. Given that only a small proportion of tweets are geolocated, and an even smaller portion pertain to climate change, he needs a deep dive into Twitter's data.

The contract that researchers must sign to apply for the program, however, includes language that some find troubling. Simply by applying, it states, "you are granting Twitter an unconditional, irrevocable, non-exclusive, royalty-free, fully paid-up, fully transferable, perpetual and worldwide license to evaluate, use, copy, perform, display, publish, transmit, or create derivative works … [and] hereby waive all copyright, trademark, trade secret, patent and other intellectual property right claims you may have against Twitter" related to that content.

Some researchers interpret that as handing ownership of their ideas to Twitter, even if their applications are turned down. In principle, Twitter could then publish those ideas, sell them to third parties, or develop technologies based on them without compensating or even crediting the researchers. "These types of data are useful for my research, but I am not applying because of concerns about the Ownership & License section of the agreement," says Sarita Yardi Schoenebeck, an information scientist at the University of Michigan, Ann Arbor. "It does indeed read like they want to own the ideas," Obradovich agrees, "and any potential derivative ideas they choose to pursue, which is somewhat troubling." But he plans to apply nevertheless.

A Twitter representative did little to clarify the situation for researchers, writing briefly in an e-mail to *Science*: "Just as users own their Tweets, researchers own their ideas. This program is no different: the license pertains to our ability to further explore the contributions of the research community and advance our offerings to the community as a whole."

The confusion over Twitter's legalese is part of a wider debate about intellectual property (IP) and academic research, Bar-Yam says. "The question here is not whether there is IP but who gains the rights." If another company owns your ideas, it's nearly impossible to get commercial funding, he says. "The whole purpose of IP is to allow people with ideas to build on them. … Without IP protections, investors don't give resources to develop those ideas."

Still unclear are Twitter's terms for actual access to its full data trove—the debate so far has been over just the application process. "Since applying is the first step, the submission agreement is the only available agreement at the moment," the company representative notes.

–JOHN BOHANNON

CREDIT: ZACHARY C. STEINERT-THRELKELD/TWITTER

Published by AAAS

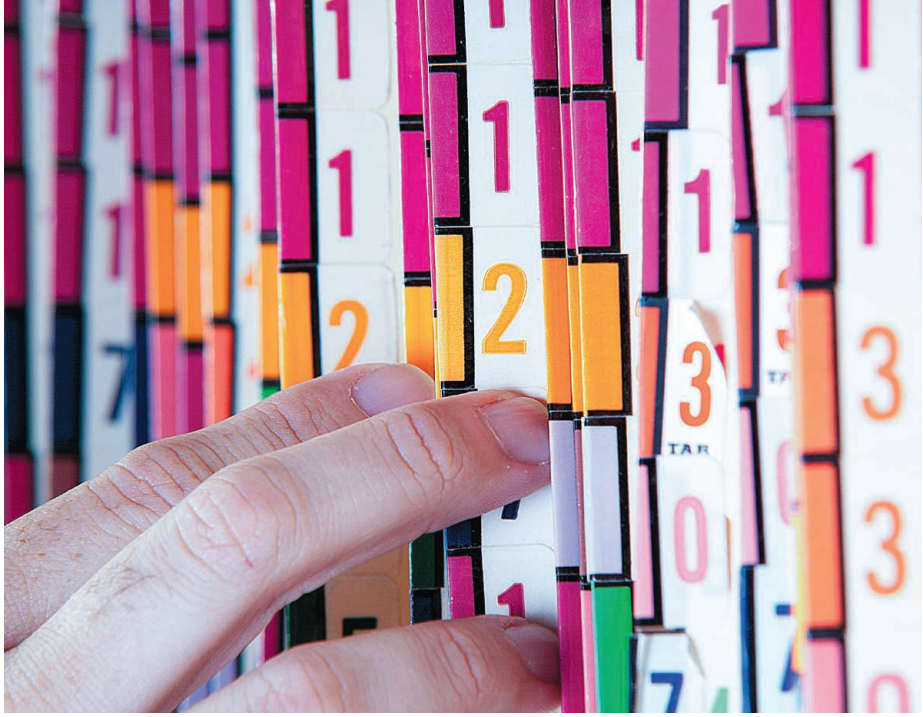

Off limits? Proposed E.U. rules would make it more difficult to use medical records for research.

EUROPE

E.U. Privacy Protection Bill Would Hamper Research, Scientists Warn

BRUSSELS—Neuroscientist Richard Frackowiak co-directs the Human Brain Project, a giant research endeavor that will get €1 billion from the European Union in the next 10 years. One part of the project tries to link up hospital archives across Europe to mine data from hundreds of thousands of patients. The goal is to define diseases by biological and clinical patterns, and ultimately to build computer models of diseased brains and predict the effects of treatment.

But Frackowiak, who also serves as chair of the medical sciences committee of Science Europe, an association of research funders, is worried that such studies may become unworkable if the European Union approves a new bill aimed at better protecting citizens' privacy and harmonizing the current patchwork of data protection rules across the continent. As it stands, scientists say, the bill could make it much harder—and in some cases impossible—to use this kind of data without patients' specific consent, as the Human Brain Project does.

The Wellcome Trust, a major health research charity in the United Kingdom, is leading a campaign urging members of the European Parliament, which is set to vote on the bill next month, to change it. More than 40 European organizations involved in research have joined. They're also targeting national governments, which will negotiate the plan later this year. "The European Union is at risk of getting this dangerously wrong," the leaders of Science Europe, the Max Planck Society, the Institut Pasteur, and others said in an open letter in *The Times* last month.

> "Member States law may provide for exceptions to the requirement of consent for research … that serves a **high public interest, if that research cannot possibly be carried out otherwise**. The data in question shall be anonymised, or if that is not possible for the research purposes, pseudonymised under the highest technical standards. …"
>
> **Article 81(2a) of the proposed E.U. Data Protection Regulation, as amended by the LIBE committee**

Data protection is a hot topic across Europe, where Edward Snowden's revelations about U.S. snooping have caused widespread indignation. Just last week, the U.K. National Health Service announced it will delay the creation of a national database of medical records for 6 months to address patients' privacy concerns and build public confidence in the system, which supporters say will be a boon for medical research.

The European Commission unveiled its data protection proposal, which covers everything from online shopping to e-banking services, in 2012. It replaces a directive from 1995, a time when the Internet had just arrived. Most scientists said they could live with the commission's draft proposal, which defined conditions under which health researchers can use patients' data without their specific, explicit consent. The proposal acknowledged that consent is sometimes difficult to obtain. For instance, one U.K. study into the risk of leukemia for children living close to power lines used cancer registry data from 33,000 patients; seeking individual consent from all of the kids' families would have been impractical, scientists say.

But in October 2013, the European Parliament's civil liberties committee (LIBE) introduced several changes to narrow the exceptions. Research organizations are particularly upset about LIBE's changes to Article 81 of the regulation, which now says that the obligation to get consent can be lifted only if the research serves a "high public interest" and "cannot possibly be carried out otherwise." Even then, the data must be anonymized—that is, stripped of anything that could betray the patient's identity—or, if that's impossible for the study's purpose, pseudonymized, so that patients' names are stored securely but not visible to the researcher.

Consumer groups argue that the changes strike a balance between legitimate privacy concerns and public health needs. But research advocates say the amendment "is setting a disproportionately high bar," as Beth Thompson, a policy adviser at the Wellcome Trust, puts it. Thompson argues that researchers sometimes need data, such as a postal code, age, or disease status, that could identify an individual. For instance, a 63-year-old woman from a small town suffering from a rare disease might be identifiable even if her name isn't used. "At the moment, it's possible in the U.K. to use that kind of identifiable data

CREDIT: DAVEWHITNEY/ISTOCKPHOTO.COM

Downloaded from www.sciencemag.org on February 28, 2014

Published by AAAS

without consent," Thompson says. "We're not saying it should be easy, but it should be an option."

Researchers in some other countries are less concerned. France, for example, already has one of the strictest data protection legislations in Europe, says Charles Persoz, head of the public health unit at France's national health research institute INSERM in Paris. Tougher E.U.-wide data rules would make procedures more burdensome, but would not restrict the work of researchers in France as much as they would in the United Kingdom, he says.

But Persoz does worry that the bill's failure to define a "high public interest" could end up imperiling research even in France. "The absence of definition could have dreadful consequences," he warns. If, for instance, a register of gynecological cancers in a French region isn't deemed to be of high public interest, tapping the data would become illegal because patients don't give explicit consent to have their information entered.

Jan Philipp Albrecht, a Green member of the European Parliament and the lead author of LIBE's opinion on the bill, says researchers shouldn't worry too much. The two criteria laid out in the amended Article 81 are necessary and reasonable safeguards, he says, adding that public health research generally qualifies as a "high public interest" endeavor. (Some private research may not, he says.) But Albrecht says that researchers can still weigh into the debate and suggest better wording if they think it's necessary.

Patients generally support the use of medical data for health research, says Cicely Marston of the London School of Hygiene & Tropical Medicine, who studies patient views on the use of electronic health records in the United Kingdom. But unlike researchers, they may not be aware of all the safeguards currently in place, and they want to know how and for what their data are used. Better informed patients may be more willing to share their information, Marston says.

In the end, there will always be some risk of privacy breaches, Frackowiak says—but he believes that risk is minor, and worth taking given the huge potential health benefits of population-based studies. European countries have developed a strong system of ethical panels to review every study, Frackowiak says, and in his experience most patients trust scientists with their data to advance medical knowledge. "There's a big infrastructure in place, that thus far hasn't created any scandal at all," he says.

–TANIA RABESANDRATANA

ATMOSPHERIC EVOLUTION

New Look at Ancient Mineral Could Scrap a Test for Early Oxygen

Geologists trying to sniff out signs of oxygen in Earth's early air have long struggled with a major obstacle: eons-old rocks that provide only a ragged, fragmentary record of the gas. Even so, some have for decades taken the presence of the mineral hematite in a so-called banded iron formation (BIF) in northwestern Australia as a sign that 2.5 billion years ago, Earth's atmosphere had at least a trace of oxygen. The ruddy mineral was thought to record the moment when photosynthesis first pushed oxygen to levels high enough to fully oxidize iron.

Now, a new study of that BIF, using the latest analytical techniques, suggests that this rock record has been misread. If true, oxygen actually may have appeared in the atmosphere hundreds of millions of years later than this BIF suggested. Geologists say the study raises serious questions about a supposedly reliable test. "People are recognizing that we have to be more careful," says geochemist Timothy Lyons of the University of California, Riverside. "We need to increasingly focus on doing just what [these authors] did, a more careful characterization of samples."

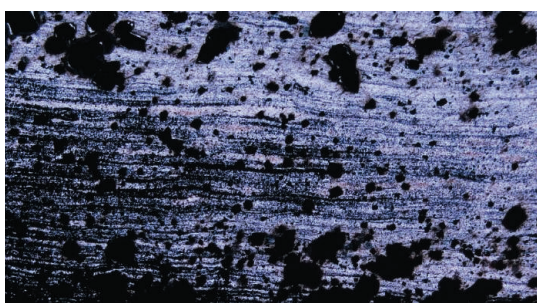

Late oxygen. Thin layers of oxygen-rich hematite formed long after this sediment was deposited.

CREDIT: B. RASMUSSEN *ET AL., GEOLOGICAL SOCIETY OF AMERICA BULLETIN* 8 (3 FEBRUARY 2014)

In a paper in the *Geological Society of America Bulletin* published online on 3 February, geologists Birger Rasmussen, Bryan Krapež, and Daniela Meier of Curtin University, Bentley, Australia, reanalyze the mineral makeup of the Dales Gorge BIF, an ancient ocean bottom now in western Australia. Their original intent was to explain how run-of-the-mill BIFs like Dales Gorge turn into the iron-rich ores so heavily mined worldwide.

The team took 400 translucent slivers of Dales Gorge rock from four deep-drill cores and studied them with several kinds of modern optical microscopes, as well as with a scanning electron microscope equipped with an x-ray spectrometer for elemental analysis. That let the researchers see where each microscopic mineral in the rock formed and get a sense of the order of their creation. Knowing the conditions under which each mineral could form, the researchers could tell a tale about conditions in the ocean beneath which the BIF was first laid down—a time when oxygen gas may have been making its first, tentative appearance on Earth.

Their more detailed look at the rocks focused on hematite, which consists of iron combined with as much oxygen as iron's bonds can hold. Because the Dales Gorge BIF has plenty of oxygen-rich hematite, earlier researchers concluded that oxygen gas from the atmosphere must have already been dissolved in the ocean and in the underlying sediments 2.5 billion years ago, when the makings of this BIF first settled to the ocean bottom.

But the Australian researchers see signs that the BIF's hematite was a Johnny-come-lately. Other iron-rich minerals—ones that, unlike hematite, form in the absence of oxygen gas—were there in the original seafloor sediments, the group argues. But they conclude that this iron was probably not oxidized, producing the hematite, until about 300 million years later, after tectonic forces crumpled the sea floor into mountains and drove oxygen-laden water down into the rock. Given that western Australia hosts the archetypal examples of BIFs in that early time, Rasmussen says, the Dales Gorge formation "probably records fundamental processes that also affected other BIFs at some time in their history."

Others are not ready to go quite that far. BIF geologist Bruce Simonson of Oberlin College in Ohio praises the team's "careful study and reasonable conclusions" but adds that "it would be premature to extrapolate their conclusions to all BIFs everywhere." Even so, both he and Lyons see the new work as a warning shot. "Big stories [of oxygen's history] have been told by small amounts of data," Lyons says. Lately, "by being more careful, we're seeing a more nuanced, more coherent picture."

–RICHARD A. KERR

Published by AAAS

CREDIT: MAURICIO ANTON

Welcome to Beringia

A flurry of studies suggests that instead of being simply a bridge from Asia to the Americas, Beringia may have beckoned the ancestors of the first Americans to linger

ONE SUMMER DAY DURING THE HEIGHT OF the last ice age, a small herd of elk moved through a now-vanished region of lowland above the Arctic Circle, nosing about small woody shrubs like crowberry and Labrador tea. Far to the west lay glacier-capped mountains, and along the plains between, horses, mammoths, and caribou wandered through patches of wildflowers—violet asters, yellow tansies, red burnets. The large animals and other game made good eating for roaming cave lions and cave hyena, as well as this landscape's top predator, humans.

This vision of a land dotted with elk, blooming with wildflowers, and sprinkled with shrubs for firewood is a far cry from traditional views of the ice age north. For decades, researchers considered Beringia—the now partly submerged landmass that once stretched from Siberia's Verkhoyansk Mountains to northern Canada's Mackenzie River (see map, p. 962)—as chiefly a highway. It served as a "land bridge" that large mammals, as well as the ancestors of the first Americans, hurried across on their way from Asia to a new continent.

Now, a flurry of studies, including analyses of seafloor sediments and ancient DNA from plants and animals, are painting a surprising picture of this lost world. They suggest that Beringia, twice the size of Texas, could have been more welcoming than expected during the Last Glacial Maximum (LGM), a period of intensely cold temperatures from about 17,000 to 28,000 years ago. The research "really expands our knowledge of the ecology of Beringia," says archaeologist Michael Waters of Texas A&M University, College Station. And it fits well with one idea about the peopling of the New World, namely that the ancestors of the first Americans holed up in Beringia for 10,000 years during the LGM before continuing into North America.

The findings are far from conclusive, and direct evidence for a long-term human presence in Beringia is scarce. But the results highlight an urgent need to get archaeological teams searching this now partly submerged and remote region, Waters says. "What I'd sure like to see is the archaeological Manhattan Project of Beringia," he says.

The land time forgot. Even during an ice age, Beringia had few glaciers and greenery enough for large game.

Big chill, big pause

Ancient Beringia is lost to us in more ways than one. The mammoths, woolly rhinos, and most other megafauna have vanished, along with most of the glacial-era vegetation that sustained them. And the central Beringian lowlands were drowned some 10,500 years ago, when melting ice raised sea level by about 120 meters. Areas that remain above water are often difficult to reach except by helicopter, so whole chunks of Beringia are terra incognita to archaeologists.

Some of the most compelling hints of a human presence in Beringia have come from the genes of people living thousands

Downloaded from www.sciencemag.org on February 28, 2014

Published by AAAS

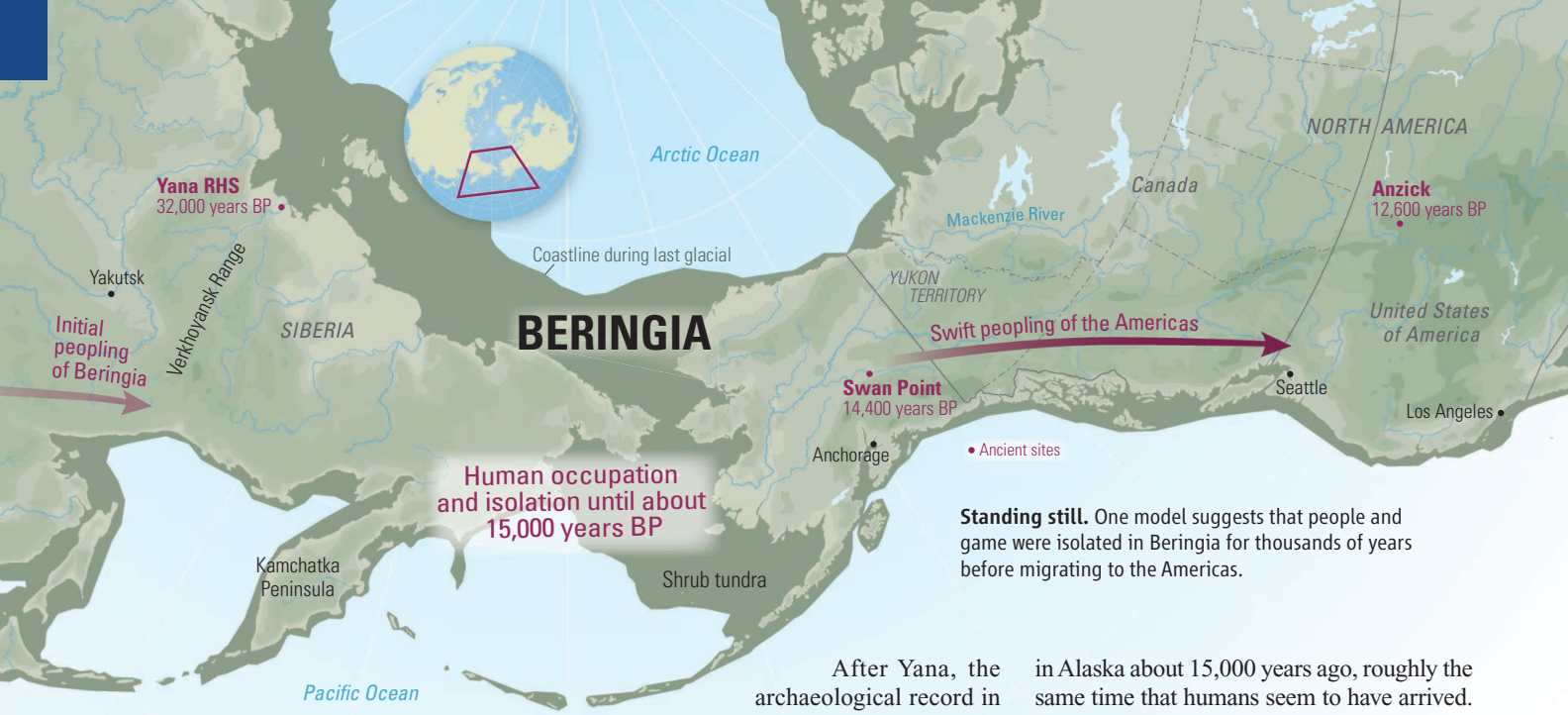

Standing still. One model suggests that people and game were isolated in Beringia for thousands of years before migrating to the Americas.

of miles away. Back in 2007, for example, researchers led by molecular anthropologist Erika Tamm of the Estonian Biocentre in Tartu analyzed mitochondrial DNA from 601 Native Americans and 3764 Asians from geographically diverse populations. The team identified three subclades—C1b, C1c, and C1d—that were widely distributed in Native American groups, but absent in Asians. This pattern, plus a chronology based on mutation rates, strongly suggested that the ancestors of the first Americans were isolated from their Asian kin some 25,000 years ago, diversifying into the C subclades before they entered the Americas some 15,000 years ago.

After analyzing how the genetic signals are distributed geographically, Tamm and her colleagues concluded that the most likely place for this isolation was Beringia. If the ancestors of the Native Americans toughed it out there during the LGM, they would have been well positioned to swiftly people the New World when the cold period ended. Several other analyses of mitochondrial and nuclear DNA have supported this "Beringian standstill" model.

Archaeological evidence for this scenario remains scarce, but some clues come from the Yana RHS locality at 71°N latitude in Beringia's far west in Siberia. This locality, the earliest known in Beringia at 32,000 years old, brimmed with carved ivory ornaments and bone tools such as sewing needles (*Science*, 2 January 2004, p. 52), suggesting a culture well adapted to life in the Arctic interior. Yana's broad-based hunters and foragers appear to have brought down diverse game including steppe bison, reindeer, horses, polar foxes, and birds.

After Yana, the archaeological record in Beringia goes dark. The next site doesn't pop up until 14,400 years ago, at Swan Point, Alaska. Like Yana's occupants, the earliest Alaskans were broad-based hunter-gatherers, targeting everything from horses to hares.

Given the spotty archaeological record, most archaeologists remained skeptical that people occupied northern Beringia throughout the brutally cold LGM. Most of the region escaped glaciation because of its largely arid climate, but winters averaged about 8°C colder than today. "Beringia seemed the last place on Earth that you would put a large population during one of the coldest periods in history," says archaeologist John Hoffecker of the University of Colorado, Boulder.

Light my fire. Woody plants in Beringia's shrub tundra may have supplied firewood and tools for humans.

In search of new clues, a team led by molecular biologists Meirav Meiri of Tel Aviv University and Ian Barnes of the Natural History Museum in London examined another Asian immigrant that passed through Beringia on its way to the New World: the elk, or wapiti (*Cervus elaphus canadensis*). Previous studies had suggested that these temperate and boreal forest dwellers first appeared in Alaska about 15,000 years ago, roughly the same time that humans seem to have arrived. Meiri and Barnes hypothesized that as temperatures rose, the elk swiftly barreled across Beringia and into the Americas.

To test the idea, they collected 113 bone, antler, and teeth samples from ancient elk in museums and 74 specimens from modern elk across North America and Asia. After dating and sequencing most of the samples, they found what Barnes calls an "astonishing" picture, very different from what they had expected, as reported in the 7 February issue of the *Proceedings of the Royal Society B*.

The radiocarbon dates and locality data indicate that elk had pushed into northwestern Beringia by at least 50,000 years ago, but didn't advance into North America until 15,200 years ago. Barnes and colleagues were so surprised that they analyzed hydrogen and oxygen isotopes from the Siberian specimens to double-check the locality data supplied by the museums. (The water and food the elk ingested influenced the isotopes in their bones, and can be used to trace the latitude where the animals lived.) The results confirmed the samples' Arctic origins. The researchers also used DNA data to estimate elk population size, which apparently declined during the LGM. But there was no sign that the population had been wiped out and later replaced.

If the elk stood still in Beringia, perhaps humans did, too. The elk data suggest that humans could have been present in northwestern Beringia "much earlier and longer than we thought," Barnes says. Elk and humans may have migrated into the Americas together, he adds. Some of the oldest known artifacts in North America—13,000-year-old rods buried with Clovis tools and human

CREDIT: (PHOTO) SCOTT ELIAS/ROYAL HOLLOWAY, UNIVERSITY OF LONDON

Published by AAAS

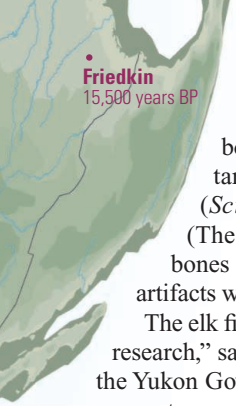

bones at the Anzick site in Montana—are made from elk antler (*Science*, 14 February, p. 716). (The rods are even older than the bones at the site, suggesting that the artifacts were heirlooms when buried.)

The elk findings are "an elegant piece of research," says archaeologist Greg Hare of the Yukon Government in Whitehorse, who was not a member of the team. Hare thinks both elk and humans could have survived in parts of Beringia during the LGM "as long as they had enough to eat."

Early adapters. Denizens of temperate and boreal forests today, elk survived ice age cold in Beringia.

Arctic refuge

The humans could have eaten the elk and any other game. But what were elk and other large herbivores eating? Previous pollen studies of Beringia's vegetation revealed mostly grasses. But grasses make more pollen than other types of plants do, so pollen studies may give a biased view.

To get a more complete picture, an international team led by geneticist Eske Willerslev of the University of Copenhagen used a new technique: They extracted bulk DNA from 18 Beringian permafrost sites and used primers to fish out and sequence fragments of ancient DNA from plants. As they reported in *Nature* this month, their samples spanned the past 50,000 years and came from Beringia and other parts of the Eurasian Arctic. To find out what the megafauna ate, the team also sequenced the gut contents and coprolites of woolly mammoths, woolly rhinoceros, a horse, and a bison.

The data held "a number of surprises," Willerslev says. Broad-leafed herbaceous plants called forbs, including species of thyme, vetch, and anemone, dominated the samples, even during the LGM. More than 60% of the DNA in the giant mammals' guts and poop was from forbs, and these flowering plants may have helped the megafauna survive. Forbs are rich in protein, and "promote easy digestion, so maybe the megafauna were [choosing] the forbs," says Yukon government paleontologist Grant Zazula in Whitehorse, a member of the team.

Willerslev's samples came from areas of Beringia still on dry land. But pollen from what is now the sea floor suggests that different vegetation may have cloaked the lowlands, which would have been slightly warmer and moister than other areas. Pollen from a sediment core drilled near the coast of the central Beringian lowland shows that some trees and shrubs—including spruce, birch, and alder—survived the LGM, as graduate student Rachel Westbrook of the University of Alaska, Fairbanks, and colleagues reported at a 2012 meeting of the Geological Society of America. Pollen, plant, and insect records from other seafloor cores suggest a similar picture.

The now-drowned part of central Beringia was likely covered with shrub tundra—a form of tundra dominated by small woody plants and sprinkled with other vegetation including forbs—according to a Perspective by Hoffecker and colleagues on page 979 of this issue. Hoffecker adds that the woody shrubs, including dwarf birch, dwarf willow, and crowberry, could have been sources of valuable firewood for Beringian hunter-gatherers, helping them survive the ice age cold. Archaeological evidence shows that later indigenous peoples of both Alaska and Northeast Asia often fed their fires with fresh bone, which burns hot and fast, but they also added small quantities of wood. The wood makes the bone easier to ignite and the flames last longer, as shown in experiments reported in 2001 by archaeologist Isabelle Théry-Parisot of CNRS, the French national research agency.

Arctic toolkit. Humans made bone tools as early as 32,000 years ago at Yana RHS in Siberia.

There's no data on whether elk lived in the now-submerged Beringian lowlands, but Hoffecker suspects they might have, noting that wapiti are versatile grazers and browsers. With game to hunt and fuel for fires, "central Beringia could have been a magnet for people during that intense cold period," he says. He, too, thinks Beringia is the most plausible location for the geneticists' standstill model. It "not only gives people the resources to survive, but it's a place that was isolated from everywhere else during the Last Glacial Maximum," he says. Pollen records show that the shrub tundra expanded eastward into Alaska and the Yukon after about 16,000 years ago. Both elk and people could have followed the shifting vegetation into the New World.

Barnes sees a slightly different story in the elk data. Rather than central Beringia being a magnet that caused species to linger, he thinks it was the site of some kind of ecological barrier that kept elk and possibly people in western Beringia—and out of the Americas—during the LGM. "It seems that the land bridge is closed for business before 15,000 years ago, and that humans were affected as well," he says.

Finding out whether central Beringia was refuge or barrier and searching northeastern Siberia's wilderness for traces of ice age Beringian hunters will require a multidisciplinary approach. "Right now we have three stories that have been developing independently in the fields of archaeology, genetics, and paleoecology," says Hoffecker, who's organizing an interdisciplinary workshop on the Beringian standstill to be held in Colorado in the fall. "Now we have to bring the stories together." **–HEATHER PRINGLE**

CREDITS (TOP TO BOTTOM): WAYNE SIMPSON/ALL CANADA PHOTOS/CORBIS; V. V. PITULKO *ET AL.*, *ANTIQUITY* **86**, 333 (SEPTEMBER 2012) © ANTIQUITY PUBLICATIONS LTD.

Published by AAAS

CREDIT: MASSACHUSETTS GENERAL HOSPITAL

Can Down Syndrome Be Treated?

People with Down syndrome are signing up for trials of several drugs aimed at helping their cognitive impairment, even as researchers explore more radical ideas to "cure" the genetic disorder

Brian Skotko remembers clearly when he first became an advocate for people with Down syndrome. It was on the playground in grade school, listening to his classmates use the R-word.

"Someone would just casually say, 'I'm such a retard,' or 'You're such a retard,' " he says. Even at that young age, Skotko found himself speaking up for his younger sister Kristin, who has the typical constellation of physical features and intellectual disability caused by having a third copy of chromosome 21. "I got to see firsthand what it's like to grow up with an extra chromosome," he says. "I learned along the way that some of the struggles are not defined by your chromosomes, but by the community that you live in."

Over time, brotherly concern also developed into an intellectual curiosity about the cause of his sister's disorder, and Skotko became a medical geneticist. Now co-directing the Down Syndrome Program at Massachusetts General Hospital in Boston, he hopes to overturn one of the most entrenched assumptions about the disorder: that its cognitive symptoms are too complex and permanent to treat pharmaceutically.

This spring, Skotko's clinic and others around the world are running two major trials of drugs that may alleviate some of the intellectual impairments in people with Down syndrome. One targets a chemical compound that is elevated in the blood in both Down syndrome and Alzheimer's disease, and may somehow harm the brain. The other takes aim at an inhibitory neurotransmitter system that may put a brake on brain activity in people with Down syndrome. Both trials face some unusual challenges, including recruiting enough people with Down syndrome and gaining their informed consent. But if the drugs work, they could give these individuals—who increasingly survive into middle age thanks to improved treatments for the syndrome's physical symptoms—a better chance at an independent life, Skotko says.

Even as these trials move forward, a number of labs are pursuing a more radical option: addressing Down syndrome at its root. One line of work aims to steer fetal brain development back onto a more typical path; another would address the genetic cause of Down syndrome by inactivating the extra copy of chromosome 21. Although the prospect of treating Down syndrome at an early age, or even in the womb, is still far off, "this is an achievable goal," says Diana Bianchi, an expert on fetal genetic conditions at Tufts University, Boston.

Early origins

In 1946, popular pediatrician Benjamin Spock declared that all babies with Down syndrome should be immediately institutionalized because "if [the infant] merely exists at a level that is hardly human, it is much better for the other children and the parents to have him cared for elsewhere." The statement encapsulated a belief about the disorder that remained entrenched for decades: that Down syndrome is an immutable condition with little prospect of improvement or integration into society.

Downloaded from www.sciencemag.org on February 28, 2014

Published by AAAS

Treatment plan. Brian Skotko (*left*) hopes to help people with Down syndrome, such as Kayla Flinkstrom (*right*), live independently.

In most cases, Down syndrome occurs when the two copies of chromosome 21, the smallest human chromosome, don't separate properly during the formation of sperm or eggs or during their union. Once fertilized, the egg ends up with three, rather than two, copies in each cell. As a result of the extra chromosome, scientists believe, the developing fetus receives an extra dose of the products of hundreds of genes, altering the delicate balance of proteins and other chemicals in the body.

At the time of Spock's recommendation, most children with Down syndrome died before their teenage years from one of the myriad health problems that frequently accompany the disorder, such as congenital heart defects, immune deficiencies, and leukemia. Today, many people with the disorder live into their 60s, but these strides toward better physical health—largely the indirect result of medical advances ranging from antibiotics to heart valve replacement surgery—have greatly outpaced progress toward treating the impairments in IQ, speech, learning, and memory.

The most dramatic changes in how people with Down syndrome are treated since Spock's era have not been medical, but social, says geneticist and cell biologist Robert Schoen of the nonprofit organization Research Down Syndrome in Chicago, Illinois. Now that people with Down syndrome have secured some basic rights—to attend school; to be employed; to be protected from abuse and discrimination—treatment is coming to the forefront, Schoen suggests. "I think this current generation of parents is looking for the next step beyond acceptance and inclusion."

That statement rings true for Elaine Chaisson, mother of Brian, a 22-year-old with Down syndrome in Massachusetts. Brian, who is also legally blind, was the first teenager with significant mental and physical disabilities allowed to attend his local public high school. Getting the extra help he needed was exhausting, and it wasn't easy for him socially, she says. Other students "tried to break him," she says, "but he rose to the occasion."

When they heard about the drug trials at Skotko's Down syndrome clinic at Massachusetts General Hospital, the Chaissons leapt at the opportunity to enroll. Brian is one of roughly 24 patients taking part in the smaller of the two, testing a compound called ELND005, or scyllo-inositol, originally intended for Alzheimer's disease. Researchers had noticed in animal and cell studies that ELND005, a sugar alcohol derived from plants such as the coconut palm, breaks up the β-amyloid plaques that accumulate in the brains of Alzheimer's patients. Further testing by the Dublin-based biotechnology company Elan, now part of Perrigo Co., then revealed that it also lowers levels of myo-inositol, a chemical associated with plaque formation and cognitive impairment.

People with Down syndrome have unusually high levels of myo-inositol in their brains, particularly in the hippocampus, a region vital to memory and learning. By the time they reach their 40s, roughly 75% have also developed Alzheimer's-like plaques and dementia, presumably because they get an extra dose of the amyloid precursor protein gene on chromosome 21. Although ELND005 isn't intended to reverse abnormalities in brain development typical of Down syndrome, Elan proposes that by reducing myo-inositol, the drug will help neurons communicate more effectively and prevent the sticky plaques from forming.

The current study will measure only the drug's short-term effects on Brian's learning, memory, and language abilities, but the Chaissons hope that it will also help their son avoid dementia in later life. Although he is "still struggling" with some aspects of the trial, such as having his blood drawn, the choice to join was ultimately her son's, Chaisson says. "Brian knows he has problems and just wants those things not to be there."

Skotko hopes that the drugs he's testing will indeed help clear some of the cognitive obstacles Brian faces. He acknowledges having some mixed feelings about the trials, however. One lesson he's learned from his sister, and from surveying hundreds of people with Down syndrome, is that the vast majority are happy with their lives, who they are, and how they look. "People with Down syndrome are achieving success in school and employment, and are very satisfied with their lives," he says.

Online

sciencemag.org

Podcast interview with author Emily Underwood (http://scim.ag/pod_6174).

Informed consent

Decorating the walls of Mary Ellen McDonough's office is a lively collection of snapshots. Each smiling face has the almond-shaped eyes, flattened noses, small ears, and slightly protruding tongues that are telltale physical signs of Down syndrome. In one photo, a young man sits on the bed of an MRI scanner and gives the camera a celebratory two thumbs-up. McDonough, Skotko's clinical trial coordinator, explains that he had just had his brain scanned—a mandatory baseline before beginning the Elan trial—and had been so anxious about being rolled inside the machine's claustrophobia-inducing cylindrical gullet that he had to be sedated.

Reassuring patients is only one of the challenges McDonough faces. After realizing that a 21-page, single-spaced legal consent document is inappropriate for people with Down syndrome, she devised a simplified, illustrated version. "A drug company called Elan has a new medicine," reads one caption next to an image of a pillbox. "We want to test how well it works. We need to know how people's bodies react to the new medicine." A "thumbs-up" and a "thumb-down" symbol on another page reads: "You can say YES, or you can say NO."

Although the form mentions the possibility of dizziness, headache, sleepiness, and muscle pain, McDonough says she avoids talking too much about risks with the participants, as they sometimes become frightened and confused. Instead, she saves in-depth discussions of potential side effects for guardians and parents, who in most cases must give consent as well. Because the drug trials require a great deal of time and commitment—clinic visits at least once per week for 10 weeks for the Elan trial—Down syndrome researchers need participants and families "to understand and to trust," she says.

Although Chaisson's family is particularly interested in the Elan trial because of their fear of Alzheimer's disease, Brian's mother also hopes to enroll her son in the second, much larger trial, which will begin in the next few months. The phase II trial, sponsored by Swiss pharmaceutical company Hoffmann-La Roche, will recruit 180 young adults

Although the prospect of treating Down syndrome at an early age, or even in the womb, is still far off, one geneticist now calls it **"an achievable goal."**

Published by AAAS

and adolescents with Down syndrome at sites all over the world, including 33 from Skotko's clinic.

The trial will test a compound called RG1662 that targets memory deficits thought to stem from an imbalance of inhibitory and excitatory activity in the brain. In the early 2000s, neuroscientist William Mobley, then at Stanford University in Palo Alto, California, and several other researchers noticed that mice bred with third copies of genes similar to those tripled in Down syndrome showed an excess of inhibitory brain activity. The inhibition seemed to encumber the rodents' ability to learn. Stanford neuroscientist Craig Garner likens it to driving with the parking brake on. The problem seemed especially pronounced in the hippocampus, where memories are processed and stored.

Mobley wondered if it was possible to release that brake by blocking the activity of GABA, the brain's primary inhibitory neurotransmitter. He applied picrotoxin, a poisonous crystalline plant compound that prevents GABA from binding to a class of receptors called GABAA, to living slices of brain taken from the hippocampi of Down syndrome mice. The compound normalized electrical brain activity in the tissue, but was too dangerous to use as a drug because it causes seizures. Garner began administering other, safer GABA-blocking drugs to Down syndrome mice. In 2007, he and colleagues reported that several compounds, including PTZ, a circulatory and respiratory stimulant, largely reversed the rodents' memory and learning deficits. Once used to treat memory disorders, the Food and Drug Administration (FDA) took PTZ off the market in 1982 due to concerns about its efficacy and safety: Like picrotoxin, it causes seizures.

As these discoveries unfolded, Michael Harpold, chair of the scientific advisory board for the Down Syndrome Research and Treatment Foundation, which had funded much of the laboratory work, decided to try to translate them into a safe treatment. Hoffmann-La Roche, along with several other companies, was already working to develop drugs that target GABA activity for general cognitive impairment, but not for Down syndrome. Tapping into the company's long-running focus on developmental disorders, Harpold helped persuade it to tackle the genetic disorder.

The firm went on to develop its own drug, which selectively blocks brain receptors that contain a specific protein subunit called GABAA α5. In February 2013, it released a study in *The Journal of Neuroscience* showing significant reductions in the cognitive deficits in a mouse model of Down syndrome, without seizures. The company went on to demonstrate the initial clinical safety of the drug in people with and without Down syndrome with two phase I trials.

Buoyed by such developments, Mobley, who is now at the University of California, San Diego, predicts that a pill that alleviates some of the memory and learning deficits of Down syndrome will be available within 5 years. Hoffmann-La Roche isn't the only company now pursuing drugs that target the balance of inhibitory and excitatory brain activity in Down syndrome, Harpold notes. Balance Therapeutics, a California-based company, is now recruiting participants for a phase I clinical trial of a compound commonly used in cough syrup that also has been shown to influence the GABA system.

Neuroscientist Alberto Costa of Case Western Reserve University in Cleveland, Ohio, shares Mobley's excitement. But nearly 2 decades of searching for cognitive treatments for Down syndrome—inspired by his 19-year-old daughter, Tyche, who has the disorder—have taught him to be cautious. The recent flourishing of research into Down syndrome has produced at least 11 potentially interesting new drug leads, including nicotine, green tea extract, and various nerve growth factors, he says, but testing their efficacy and safety will be slow given the relatively low prevalence of the disorder, about one in 1000.

> "I think this current generation of **parents** is looking for the next step **beyond acceptance** and inclusion." —Robert Schoen, Research Down Syndrome

For Costa's own recent trial of memantine, a drug already used to slow cognitive decline in Alzheimer's disease, it took 4 years to recruit 42 people with Down syndrome. The participants scored better on verbal memory tests when they took memantine than they did on a placebo, but the study was too small to be conclusive. Now, Costa is working with researchers in São Paulo, Brazil, to recruit 200 young adults and adolescents for a follow-up trial.

Early intervention

If current clinical drug trials in adults with Down syndrome don't work, it may be because the window of opportunity is already closed in adults, suggests Tufts University's Bianchi. Indeed, Costa believes that previous clinical trials of memantine in adults "completely failed" to show any benefits because the drug was likely administered too late. "You can't really revive neurons, or restore a disturbed neuronal network" if important brain structures "have basically gone away," he says.

Once mature, the brains of people with Down syndrome are about 20% smaller than average and have fewer neurons, as well as abnormal connections between cells. Studies of rodent models of Down syndrome by Costa; Roger Reeves of Johns Hopkins University in Baltimore, Maryland; and Tarik Haydar of Boston University School of Medicine, among others, have revealed aberrations in the earliest stages of brain development. The most affected regions include the hippocampus; the prefrontal cortex, which governs higher level cognitive tasks such as planning; and the cerebellum, which coordinates movement and learning, as well as attention and language.

The cerebellum is Reeves's personal fascination. In normal brain development, he notes, a population of neural stem cells in the cerebellum "has to divide like crazy the day

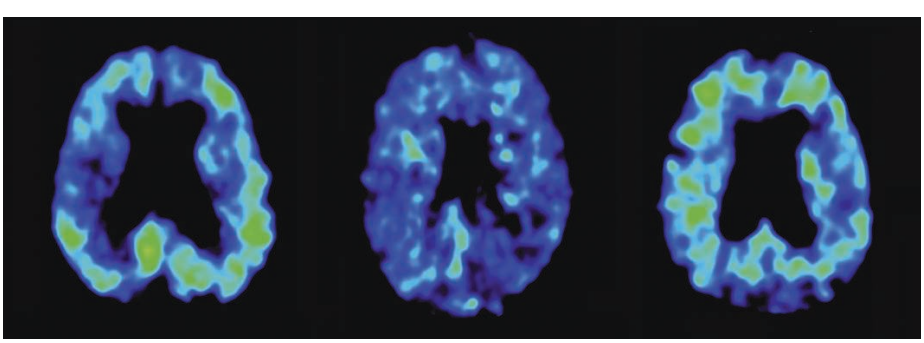

Eerie similarity. Unlike a scan of a normal brain (*center*), those of people with Down syndrome (*left*) and Alzheimer's disease (*far right*) show similar protein plaques.

CREDIT: L. NELSON *ET AL.*, *JAMA NEUROLOGY* **68**, 6 (13 JUNE 2011)

Published by AAAS

after birth." In the Down syndrome mice he studies, these cells seem to miss the starting gun, he says, and the cerebellum never reaches its proper size and function.

Last year, Reeves decided to amplify that "Go" signal. He used Sonic hedgehog, a powerful growth factor responsible for many aspects of development—we have Sonic hedgehog to thank for our symmetrical bodies and distinct fingers and toes, for example. On the day the Down syndrome mice were born, he injected the growth factor into cells in their cerebellum, and was startled to see that just one dose made the brain region develop to a normal size and at a normal pace. When the mice grew up, some of their learning deficits were also lessened, his group reported in *Science Translational Medicine*.

The fact that "a single shot of a drug" at birth could correct an aspect of brain development "was a pretty satisfying and gratifying result," Reeves says. Although Mobley describes the improvements in the rodents' behavior and physiology as "modest," based on the study, "I bet there's something really significant about Sonic hedgehog signaling in Down syndrome," he says. Even subtle tweaks in the growth factor at birth or in the womb could have profound effects on development, he adds.

There's still an enormous gap between such experiments in mice and treating a fetus diagnosed with Down syndrome, however, says cell biologist Jeanne Lawrence of the University of Massachusetts Medical School in Worcester. "Would you ever feel like you could apply this drug to a child or prenatally, based on a mouse study?"

"If I waltzed down to the FDA and said we'd like to squirt Sonic hedgehog in some babies they'd probably just arrest me right there," Reeves acknowledges. The next step, he says, is to start exploring why neural stem cells in humans with an extra chromosome 21 are so reluctant to grow. "It would be a really neat experiment" if we could turn off the extra chromosome in those cells, he says.

Genetic off switch

A few hundred miles to the north of Baltimore, Lawrence is experimenting with exactly that. Last summer in *Nature*, to media fanfare that occasionally suggested a "cure" was at hand, she and her team unveiled a new technique for "silencing" the extra chromosome 21.

Lawrence was trained as a genetic counselor before "falling in love" with chromosomes while working as an assistant in a lab. Her potential Down syndrome treatment involves inserting a gene called *XIST* into one of the copies of chromosome 21. *XIST* normally resides on the X chromosome and serves to shut down one of the two X chromosomes in females—both men and women get along with one X. The gene produces a long strand of RNA, which Lawrence says likely covers the chromosome in an RNA shroud, triggering proteins that block any genes from being transcribed.

Working with pluripotent human stem cells created from people with Down syndrome, Lawrence used proteins that target specific DNA sequences to place *XIST* on one of the copies of chromosome 21. The added gene shut off the entire extra chromosome. Her colleague Jun Jiang, whose job is to try to coax Down syndrome stem cells into differentiating into neurons in a petri dish, says that the "silenced" cells develop normally. Rather than a scarce, neuron-poor moonscape or an unhealthy overgrowth of glial cells, which such stem cells from Down patients typically produce, Jiang sees many flourishing neural "rosettes" in her petri dishes—the early agglomerations of stem cells that ultimately turn into neurons. "Like beautiful flowers," she says.

The *XIST* strategy is already a powerful tool for studying what goes wrong in Down syndrome in humans, Lawrence says. For example, because scientists can switch chromosome 21 off in some cells and not in others, this could provide a controlled model for testing drugs, such as regulators of Sonic hedgehog, that could improve neural stem cell function or differentiation, she says. Long-term, her team plans to extract neural stem cells from mouse models of Down syndrome, treat them with *XIST*, and transplant them back into the rodents' hippocampi to see if the cells proliferate and restore learning and memory, she says. Her lab is also planning to test strategies to deliver the *XIST* gene directly into neural stem cells in mice hippocampi to see if the injected gene can correct fetal brain development and later function in vivo.

Both Lawrence and Reeves agree that the prospect of using *XIST* to treat Down syndrome in humans—either in utero or adulthood—is still extremely remote. Beyond the considerable technical obstacles, there are the ethical hurdles that come with a powerful genetic therapy, especially one that might be deployed in utero. "It's not clear to me how this is going to be translated into humans," Reeves says.

That hasn't stopped the phone at Skotko's Massachusetts General Hospital Down Syndrome Program from ringing off the hook with calls from people wanting to sign up family members with Down syndrome for a trial with *XIST*, however. "We had a lot of untangling and explaining to do," when Lawrence's research was first published last summer, McDonough says.

For Mary Beth Rattey, Lawrence's results generated strong emotions. "I burst into tears and had to pull over to the side of the road," when she heard about the work over the radio, the Townsend, Massachusetts, restaurant manager recalls. She, her husband Ray, and their 19-year-old daughter Genevieve, who has Down syndrome, regularly visit Lawrence's course on human genetics to talk to medical students about the disorder, so she had heard hints about the research before it was published. Even though she knows the advances will likely not benefit Genevieve, the potential for treatments that could help other families in the future is "incredible news," Rattey says. "I don't feel like I missed a boat—our life has been awesome—but for the first time, it seems like they have something to work with."

–EMILY UNDERWOOD

Hopeful result. Jeanne Lawrence points to a cell in which her team has turned off a third copy of chromosome 21, leaving the two others untouched.

CREDIT: JACKIE RICCIARDI

Published by AAAS

LETTERS

edited by Jennifer Sills

Raw Data: Access to Inaccuracy

IN "RAW PERSONAL DATA: PROVIDING ACCESS" (POLICY FORUM, 24 January, p. 373), J. E. Lunshof and colleagues argue that donors should have access to raw data derived from their contribution to research or clinical repositories. Fairness, reciprocity, and respect for autonomy are compelling ethical reasons for access, if not for one major problem: the intrinsic inaccuracy of most research data.

Even the best-documented population studies cannot guarantee accurate data for individual participants. Limited research budgets force researchers to decide between assessing a few variables at high quality or many variables at lower quality, and they typically choose the latter. More data means more research opportunities, and suboptimal data quality is perfect enough when conclusions are drawn for populations at large. Yet, the data cannot be used to inform about individual participants.

To illustrate the moral obligation for granting access, the authors draw an excellent analogy with money banks, but the example actually undercuts their point. Money banks would never provide customers access to their bank accounts if they had even the slightest doubt about the accuracy of the balances. Inaccurate account data not only harm individual customers, who then remain uncertain about their financial position, but also destroy public trust in money banks. This is a risk that banks would not even think of taking, and scientists should not either.

High-quality online genome data interpretation tools, health professionals, and other independent experts cannot make sense of data when they cannot rely on the quality. A disclaimer concerning data accuracy, as the authors propose, does not solve that problem. If researchers respect their participants, take them seriously, and want to do more good than harm (*1*), they do not give them all they have, but give something valuable in a responsible way (*2*). And that is not merely access to data.

A. CECILE J. W. JANSSENS

Department of Epidemiology, Emory University, Atlanta, GA 30322, USA. E-mail: cecile.janssens@emory.edu

References

1. The National Commission for the Protection of Human Subjects of Biomedical and Behavioral Research, Ethical Principles and Guidelines for the Protection of Human Subjects of Research (1979); www.hhs.gov/ohrp/humansubjects/guidance/belmont.html.
2. J. P. Evans, B. B. Rothschild, *Genet. Med*. **14**, 358 (2012).

Raw Data: Research and Health Care Goals Differ

IN THEIR POLICY FORUM "RAW PERSONAL data: Providing access" (24 January, p. 373), J. E. Lunshof *et al.* suggest that more should be done to enable persons who had their genome sequenced, either as research subjects or as patients, to actively access their raw data. They argue that routinely providing them with personal access codes to those data would be a matter of transparency and respect for autonomy. We think Lunshof *et al.* underestimate the dangers of actively handing out data that we know are not fully reliable and can lead to misinterpretation.

In our view, the proposed policy would be at odds with the responsibility of health professionals.

In health care, clinical utility should have priority over social utility. An appeal to reciprocity between donors and users of genomic data does not change this argument. Patients are not the same as data donors. If patients become data donors by consenting to have their data stored in research registries, they should be aware that they have entered a different relationship, in which they primarily contribute to the benefit of future patients.

Lunshof *et al.* ignore the crucial difference between health care and research when they criticize the recent recommendations of the European Society of Human Genetics (ESHG). To avoid the unnecessary generation of incidental findings, these recommendations advise the use of targeted forms of testing if that is sufficient to address the patient's problem (*1*). According to Lunshof *et al.*, this is problematic as it "systematically precludes the possible discovery of complex genetic causation." We disagree: Discovery is the aim of research, not of health care. Conflating these aims risks turning patients into research subjects without their consent.

W. J. DONDORP,[1]* C. G. VAN EL,[2] G. M. W. R. DE WERT,[1,3] M. C. CORNEL[3,4]

[1]Department of Health, Ethics and Society, Research Schools CAPHRI and GROW, Maastricht University, Maastricht, 6200 MD, Netherlands. [2]Section Community Genetics, Department of Clinical Genetics and EMGO Institute for Health and Care Research, VU University Medical Center,

CREDIT: T. POPOVA/ISTOCKPHOTO

Downloaded from www.sciencemag.org on February 28, 2014

Published by AAAS

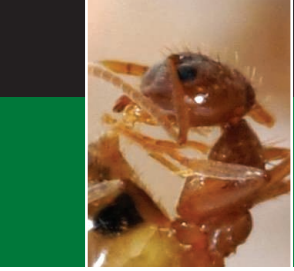

Ant against ant

974

Turning microtubules inside out

981

Amsterdam, 1081 HV, Netherlands. [3]Centre for Society and the Life Sciences, Nijmegen, 6500 GL, Netherlands. [4]Center for Medical Systems Biology, Leiden, 2300 RC, Netherlands.

*Corresponding author. E-mail: w.dondorp@maastrichtuniversity.nl

References and Notes

1. C. G. van El *et al., Eur. J. Hum. Genet*. **21**, 580 (2013).
2. The authors are writing on behalf of the ESHG Public and Professional Policy Committee.

Response

WE FULLY AGREE WITH A. C. J. W. JANSSENS and W. K. Dondorp *et al*. on the importance of considering very carefully what conclusions from analysis of raw data should be returned to data donors. However, that is very different from enabling patients and research participants to access the raw data. The two processes serve different purposes: The returning of findings aims at providing research participants and patients (and their doctors) with analytically valid, clinically relevant, and, if possible, clinically actionable information. Indeed, in this situation, the professional responsibility of health care professionals is a particular one.

The dangers, as perceived by Janssens and by Dondorp *et al*., of communicating imperfect data and an uncertain interpretation to patients, are inherent to the clinical encounter and part of professional liability, as we emphasize in our Policy Forum. This responsibility is very different in enabling access to raw data. Moreover, in any context, personal risk assessments and the balancing with expected benefits are highly individual processes and not just a matter of professional expertise (*1*). It will need to be made very clear to those wanting to access their raw data sets that these may contain mistakes and inaccuracies, and that they may—in most cases—not be actionable in an immediate way. We expect that as a result, many patients and research participants will not actually access their raw data. But this decision needs to be up to them. The same applies to personal raw data in other types of research, such as the social sciences, in which access to individual metadata has no practical utility for participants but serves transparency and is the cornerstone of a reciprocal relationship between participants and researchers.

Dondorp *et al*. raise the issue of conflating research and clinical care. They emphasize, first, that patients need to consent to become research participants and thus data donors. In practice, however, in many clinical settings, becoming a donor of research data or samples may occur by default, and individuals need to be aware of this and opt out if they do not want their data to be included (*2*). This underscores once more the asymmetrical relationship between patients on the one hand and clinicians or researchers on the other. Second, Dondorp *et al*., referring to the need to restrict analyses to avoid the unnecessary generation of incidental findings, state that discovery is the aim of research and not of health care. However, such a dichotomy does not always correspond with the wishes of patients: Many patients want research to be done, for their own benefit and that of others, and they donate their data for research. In particular in genetics, patients and families, as partners in research, often seek the most comprehensive approach to find their disease-causing mutations (*3*, *4*).

JEANTINE E. LUNSHOF,[1,2]* GEORGE M. CHURCH,[1] BARBARA PRAINSACK[3]

[1]Department of Genetics, Harvard Medical School, Boston, MA 02115, USA. [2]Department of Molecular Cell Physiology, VU University Amsterdam, 1081 HV Amsterdam, Netherlands. [3]Department of Social Science, Health and Medicine, King's College London, London WC2R 2LS, UK.

*Corresponding author. E-mail: jelunshof@genetics.med.harvard.edu

References

1. M. N. Meyer, *Admin. Law Rev.* **65**, 237 (2013).
2. K. B. Brothers *et al*., *Per. Med.* **10**, 349 (2013).
3. E. A. Worthey *et al*., *Genet. Med.* **13**, 255 (2011).
4. B. Maher, *Nature* **449**, 773 (2007).

CORRECTIONS AND CLARIFICATIONS

Letters: "Global warming and winter weather" by J. M. Wallace *et al*. (14 February, p. 729). The low-temperature record set at O'Hare Airport equates to –27°C, not –8°C. The PDF and HTML versions online have been corrected.

Reports: "Designing collective behavior in a termite-inspired robot construction team" by J. Werfel *et al*. (14 February, p. 754). A production error resulted in the omission of the end of the second sentence of the abstract. The sentence should read "Predicting high-level results given low-level rules is a key open challenge; the inverse problem, finding low-level rules that give specific outcomes, is in general still less understood." The PDF and HTML versions online have been corrected.

Reports: "An antifreeze protein folds with an interior network of more than 400 semi-clathrate waters" by T. Sun *et al*. (14 February, p. 795). The correct PDB code is 4KE2 (not 4EK2). The HTML and PDF versions online have been corrected.

News Focus: "Selling America's fossil record" by H. Pringle (24 January, p. 364). The date on which the GeoDécor Web site was accessed was incorrect; it was accessed on 6 December 2013, not in December 2014. The HTML and PDF versions online have been corrected.

Editors' Choice: "A question of balance" by H. J. Smith (3 January, p. 7). Lupascu *et al*. reported that in High Arctic tundra, warming alone decreases (not increases) the summertime CO_2 sink strength by up to 55%. The HTML and PDF versions online have been corrected.

Reports: "GRB 130427A: A nearby ordinary monster" by A. Maselli *et al.* (3 January, p. 48; published online 21 November 2013). Author B. Wiegand's name was incorrectly spelled "Weigand." The HTML and PDF versions online have been corrected.

Reports: "Pregnenolone can protect the brain from cannabis intoxication" by M. Vallée *et al*. (3 January, p. 94). In the author list, the dagger indicating that "These authors equally supervised this work" should be deleted from M. Vallée's name and added to G. Marsicano's name, indicating that G. Marsicano and P. V. Piazza were equal supervisors. The HTML and PDF versions online have been corrected.

Letters to the Editor

Letters (~300 words) discuss material published in *Science* in the past 3 months or matters of general interest. Letters are not acknowledged upon receipt. Whether published in full or in part, Letters are subject to editing for clarity and space. Letters submitted, published, or posted elsewhere, in print or online, will be disqualified. To submit a Letter, go to www.submit2science.org.

CREDIT: BILL BRANSON/NATIONAL CANCER INSTITUTE/WIKIMEDIA COMMONS

Published by AAAS

URBAN STUDIES

Connecting Paradigms

Michael Szell

Science is an endeavor of artful simplification, of discovering general principles. Fruit flies, for example, look very different from humans, but the two species share 75% of disease-causing genes. Thus, we can study fruit flies to learn about our own weaknesses under the common framework of genetics. Similarly, the unifying principles of allometry allow us to make sense of most forms of life on Earth, where a cat is just a blown-up mouse and a human is just a blown-up cat. Multiply an animal's size by x, and its heart rate, lifetime, and other features will increase in proportion to specific powers of x. This is the case because the physical rules that govern the formation of circulatory systems hold everywhere. Turning to social phenomena, can we find universal processes underlying them?

The New Science of Cities

by Michael Batty
MIT Press, Cambridge, MA, 2013. 518 pp. $45, £31.95.
ISBN 9780262019521.

Let us take a big leap and consider cities: Perhaps something similar to biology's allometric rules would allow a megacity as complicated as New York to be better understood by looking at what goes on in a small village. Is New York just a blown-up version of Venice? Universal principles that govern urban shapes and growth processes independent of particular history or geography could support a "grand unified theory of cities." What would it take to discover them?

The New Science of Cities presents a herculean attempt to bring together widely fragmented approaches to making sense of human social organization with the goal of eventually establishing a consolidated "science of cities" able to answer our questions. Michael Batty bases his argument on the interplay among space, dynamics, and relations. He holds that "to understand place, we must understand flows, and to understand flows we must understand networks." Batty (a geographer at University College London) also stresses two other principles: an intrinsic order of scale determines a city's form and function, and a science of cities should not merely observe but also predict. The book draws on the work of urbanists, economists, mathematicians, and physicists as well as almost five decades of his own contributions to urban studies.

Batty's approach rests on a physicalist philosophy: He focuses on what can be immediately observed. In a treatise that eventually becomes technical, he simplifies cities as "sets of actions, interactions, and transactions." The book develops a toolbox of mathematical models—well applicable to "big data" that are being increasingly collected about cities—from a mesmerizing potpourri of paradigms. Its foundational part takes us on a fascinating historical journey through these perspectives, from urban economics and transportation to fractal geometry, dynamical systems, and network science. All these aspects can be embedded in complexity theory, the most likely candidate to provide the consistent philosophy for achieving the author's ambitious goal.

The foundations for modern urban studies were laid in the 19th century, with the first analytical, economic approaches and the concept of agglomeration. The closer we live together, the more opportunities of trade we find, creating economies of scale. Today, extensive empirical evidence supports an urban allometry that convincingly shows cities are humanity's socioeconomic reactors, in which citizens produce, consume, and interact more as the city increases in size. These interactions can be explained mechanistically using Newtonian metaphors of cities as entities that exert gravitational-like forces on populations. Such gravity models are used in various social sciences and have recently experienced a boom in the study of human mobility through mobile phone data.

Powerful metaphors populate the histories of urban studies and planning. For a long time, the prevailing line of thinking saw the city as a machine, a model in which a "controller steered the city cybernetically toward a future desired state." Now we know better, realizing that cities are complex systems meandering through a space of configurations, like biological organisms evolving in a Darwinian fitness landscape. Such systems exhibit hallmark features of nonlinear dynamics far from equilibrium. Small interventions can have massive, counterintuitive consequences, making cities almost impossible to control. In a field where planning is essential, this discovery is devastating. It means that monumental top-down plans, which dominated most of 20th-century city planning, are a recipe for failure.

The book provides some better options. Parsimonious bottom-up models and agent-based simulations unveil basic mechanisms of competition and growth. Cutting-edge visualizations facilitate the exploration and the interpretation of empirical and synthetic data. Through a synthesis of the descriptive and the normative and a combination of quantitative modeling with qualitative theories of social exchange and collective action, the author shows how to model urban design to improve the decision processes of authorities and policy-makers.

Batty stresses that the set of approaches he tackles is a first step and by no means exclusive: "it would be presumptuous to think of this effort as the only science of cities, for the city and its planning admits many viewpoints." He concludes that an

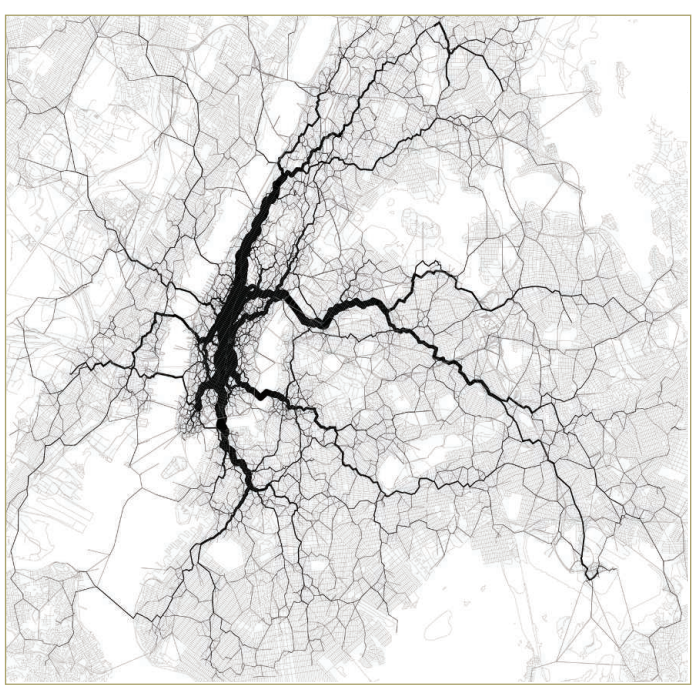

Urban complexity. Human flows (mapped by Eric Fischer using geotagged tweets) illustrate the organic structure of New York City.

CREDIT: ERIC FISCHER/USING DATA FROM THE TWITTER STREAMING API; BASE MAP DATA © OPENSTREETMAP CONTRIBUTORS

The reviewer is at the SENSEable City Laboratory, Massachusetts Institute of Technology, Cambridge, MA 02139, USA. E-mail: mszell@mit.edu

Downloaded from www.sciencemag.org on February 28, 2014

Published by AAAS

integrated, "nicely packaged," and immediately applicable science of cities might never be reached. Nevertheless, *The New Science of Cities* succeeds in clearing a way. It illustrates convincingly the particular promise of mathematical modeling and complexity theory for designing sustainable urban futures.

10.1126/science.1249599

ENVIRONMENT AND HEALTH

Fighting Urban Scourges

Frederick R. Davis

Flies, bedbugs, cockroaches, and rats—ugh. What an ignominious group of animals. Each in its own way proved a bane of city life in the 20th-century United States. Collectively and individually, they carry disease, spoil pantries, and threaten the general well-being of urban residents, particularly the poor and especially people in public housing. How can cities fight these pests? Who is responsible: the federal government or the municipality? the community or the family? Where does agency lie in an urban ecology that pits resident against pests? Dawn Day Biehler examines these sorts of questions in her fascinating *Pests in the City*.

In laying out her history of urban ecology, Biehler (a geographer at the University of Maryland, Baltimore County) develops the notion of "ecologies of social injustice." In case after case, she reveals how wealthier urban residents drew on domestic help to combat pests while impoverished minorities, especially African Americans, remained vulnerable to the incessant onslaught of those unwanted co-inhabitants of our cities.

Lest the reader forget that pestiferous species possess agency, Biehler reveals this independence through a series of vignettes, set off from the main narration by italics. Without anthropomorphizing, Biehler captures the needs and wants of flies, rats, bedbugs, and cockroaches. These sections illustrate the biology and ecology of pests, and they remind readers that context is what characterizes an organism as a pest.

Given the ignominy of these pests, city planners and public health officials have waged truly epic battles with them. Such struggles often amounted to arms races as public officers and individuals launched one chemical after another against a never-ending onslaught. Biehler follows these fights against pests from private homes to public housing.

A family responsibility. In this 1916 drawing, most of the flies come from trash in the yard.

During the Progressive Era, the status of the house fly (*Musca domestica*) shifted from harmless companion to disease vector. Leland Howard, chief of the Bureau of Entomology at the U.S. Department of Agriculture, tried to change the common name to typhoid fly to transform popular perceptions of the fly. Biehler argues that Howard, along with representatives of the progressive Hull House in Chicago and advocates in the District of Columbia, saw homes as part of an urban ecology and called for government to clean up each of the cities, respectively. Yet, she notes, modernization of homes, citizens, and sanitation failed to effectively control flies in the cities. Such control was achieved only following the transformation of urban transportation systems when electrified streetcars and automobiles replaced horsepower.

Pests such as bedbugs (*Cimex lectularius*) did not respect social class—at least not during the early growth of American cities. Biehler demonstrates, however, that in time domestic help enabled wealthier city residents to control bedbugs through cleaning and attacking them with hot water and kerosene. Metal bedframes and cleaning appliances also helped the well to do in their battle with bedbugs. Not so the impoverished, who could not afford the time, help, or new technologies. Could a powerful insecticide tip the balance in this story of ecological injustice? Yes and no, Biehler argues. Hydrocyanic acid (HCN) substantially curbed bedbug infestations while subjecting residents to the risks of accidental exposure (including death, as illustrated by several tragic cases). Before Rachel Carson revealed its deleterious environmental effects, DDT provided a safer alternative to HCN. Yet, that popular insecticide carried risks of its own and once again shifted the burden of bedbug control to the residents (even in public housing).

Control of German cockroaches (*Blattella germanica*) followed a path similar to that of bedbugs (HCN to DDT). But, according to Biehler, it was disinvestment in cities in the aftermath of the federal Housing Act of 1949 that kept public housing budgets low and fostered the conditions wherein roaches (and mice and rats) thrived. Such conditions probably fostered development of ecological resistance to a new insecticide, chlordane, as the offspring of cockroaches that survived DDT also exhibited resistance to chlordane.

Like other pests, Norway rats (*Rattus norvegicus*) exploited the interstices between public policy and private residences. In Baltimore and Chicago, municipal rat control extended as far as alleys and other public spaces. This placed much of the domestic space off limits to exterminators, leaving residents vulnerable to infestation and responsible for control measures that they could not necessarily afford. Biehler shows that some proponents of urban rat control advocated chemical solutions, with all the risks associated with them, while others argued for ecological strategies on the grand scale, which failed to engage citizens. Populations of rats rebounded in the spaces between these strategies.

Pests in the City demonstrates that wonderful studies can emerge from extremely mundane origins. Throughout much of the 20th century, flies, bedbugs, cockroaches, and rats exploited niches within urban ecologies of the United States. Their continued presence challenged authorities and citizens alike. In her meticulous and thoughtful analysis of urban environmental injustice, Biehler deftly illustrates how these pests continue to undermine aspirations for modern and healthy living conditions for all.

10.1126/science.1249016

Pests in the City
Flies, Bedbugs, Cockroaches, and Rats

by Dawn Day Biehler
University of Washington Press, Seattle, 2013. 359 pp. $34.95. ISBN 9780295993010.

The reviewer is at the Department of History, Florida State University, Tallahassee, FL 23206–2200, USA. E-mail: fdavis@fsu.edu

CREDIT: FROM CHICAGO BOARD OF HEALTH'S *CLEAN LIVING* (JULY 1916)

Published by AAAS

INTELLECTUAL PROPERTY

A Better Route to Tech Standards

Prestandard price commitments, as well as government intervention, may help patent licensing and standard setting.

Josh Lerner[1]* and Jean Tirole[2]

Technological standards are ubiquitous, whether they allow consumers to communicate seamlessly across wireless networks or manufacturers to procure goods across complex global supply chains. These standards—shaped by standard-setting organizations (SSOs) and participating engineers, academics, lawyers, and executives—in turn shape how new technologies evolve, specifying rules for how standard-compliant products must work and interact with other components. This standardization process is under tremendous stress. Many disputes roiling courts and administrative bodies around the world—such as those involving Apple, Google, Microsoft, and Samsung—concern commitments made during the standardization process and the ways that firms have sought to "game" the system. We explore why the system is breaking down and propose a way in which standard setting could be redesigned to address these problems.

Standardization assures users that they will not be stuck with an orphan technology largely incompatible with other systems and used by few others. Instead, users will benefit from network externalities, where the technology's value depends on the number of others using the technology. This boosts demand for new technology, which provides researchers with incentives to innovate.

Standard-setting organizations play three roles in this process. First, engineers identify alternative avenues to solve a given technological challenge. Second, in cases where there are conflicting technologies where none is evidently superior, the SSO will frequently coordinate on one approach. This winnowing down of alternatives is important because it greatly simplifies the choices of manufacturers and consumers.

Finally, because stakes are high for firms participating in the standardization process, SSOs seek to regulate the behavior of members. Particular concerns are ensuring that firms disclose relevant patents, so as to provide adequate information to other parties in the standard-setting process, and agree not to price licenses to their patents too aggressively, so as to enable broader adoption of the technology. But SSOs are limited in this regulatory role, because technology owners can seek another SSO if rules are too onerous.

The intellectual property (IP) embodied in standards has two essential characteristics, which can lead to unfortunate outcomes. First, in many cases, new technologies tend to be covered by a wide array of patents issued to the different firms that contribute components to the technology. In this "patent thicket," if each patent owner sets the revenue-maximizing price for its patent licenses without considering the fact that other patent owners benefit from wider diffusion, the resulting price is likely to be far too high. Economists term this "royalty stacking."

Second, in many cases, there are multiple routes to solving a given technological problem. Each one of these may be equally viable, but often an SSO will choose only one avenue. After the decision is made, however, any patent needed to practice the standard becomes a "standard-essential patent" (SEP), and the patent owner can ask for a high royalty even when other patents could have offered comparable value, had the technology been morphed differently. SSOs must therefore regulate licensing of the patents chosen to be part of the standard. SSOs typically eschew any discussion of price before the establishment of the standard. This reluctance largely reflects fear of antitrust authorities: Any price discussions might lead to charges of collusive and anticompetitive behavior, as the SSO could blackmail patentees to accept low prices in exchange for inclusion into the standard.

To restrain firms from taking advantage of the essentiality of their patents that was acquired only from being included in a standard, SSOs commonly require firms to commit in advance to license their patents on fair, reasonable, and nondiscriminatory (FRAND) terms. But FRAND commitments are ambiguous; what exactly is fair and reasonable? This is determined not by the SSO itself, but by a court years after the standard is established. Perceptions of patent value can differ widely when one looks before or after the dispute. Ambiguities associated with FRAND commitments have resulted in dozens of expensive litigations (*1*, *2*).

Even in the absence of a legal dispute, the FRAND requirement has not worked well. Consider the not uncommon case where participants in an SSO establish a patent pool to jointly license key patents covered by the standard. Many pools simply divide royalties in proportion to the number of patents that each firm has contributed to the pool. Such "1/*n* rules" may reflect that patents initially different in their importance are made equally essential by standardization. The process thus over-rewards minor innovations at the expense of major ones. In these settings, selection of patents for the standard (and pool) can be highly contentious. SSOs may include either too many or too few patents in the standard.

Structured Price Commitments

We propose an alternative approach, which we term "structured price commitments." We suggest that SSOs follow this sequence:

1. During a discovery phase, parties explore which technology combinations are technically viable (as is done now by SSOs). This "engineering" phase makes no reference to prices at which patents would be licensed.

2. Before the standard is finalized (and unlike today's practice), there is a recess, during which firms commit to a price cap at which they will grant nondiscriminatory licenses to their patents. Firms make commitments to the maximum price (and most restrictive terms) that they would charge before the patent is included in the standard.

3. Participants choose the standard, without discussing prices, as is currently done.

4. Finally, some or all of the participants may form a patent pool after the standard is set, again following today's practice.

[1]Harvard Business School, Boston, MA 02163, USA. [2]Toulouse School of Economics and Institute for Advanced Study in Toulouse, 31000 Toulouse, France. *Author for correspondence. josh@hbs.edu

Downloaded from www.sciencemag.org on February 28, 2014

CREDIT: STONE/GETTY IMAGES

Published by AAAS

Challenges of implementation, lessons from experience

The international trade association VITA, which develops standards that govern modular embedded computer systems in such products as advanced avionics devices and complex medical instruments, became frustrated when owners of patents that were essential to implementing one of their new standards demanded a higher royalty rate than anticipated after being deemed standard-essential. As a result, VITA proposed a new policy, which the U.S. Department of Justice's Antitrust Division approved in October 2006 (*6*). VITA demanded that members declare the highest royalty rates and most restrictive terms under which they would license these patents for implementation of the given standard. In response to this controversial policy, Motorola launched a campaign to decertify VITA as an SSO recognized by the American National Standards Institute, an effort that ultimately proved unsuccessful. Although VITA ended up moving forward with its standardization process, it was not a spectacular success (*7*). Similarly, the Institute of Electrical and Electronics Engineers and the European Telecommunications Standards Institute encountered stiff resistance and, in the end, had to make price commitments optional. Even if price commitment requirements lead to a good outcome, we cannot expect SSOs to mandate them by themselves or expect patent holders to cooperate with standard bodies that mandate such commitments.

Our theoretical analysis (*3*) looks at consequences of this modified standard-setting process. Initially, it might be thought that this process, too, might lead to a variety of opportunistic behaviors. For instance, a patent-holder might set a high price cap in order to achieve a stronger bargaining stance when it comes to dividing profits from the eventual patent pool formed around the standard. Such behavior might lead to excessively high licensing rates and too little technology adoption. Despite the possibility of such gaming, our analysis shows that structured price commitments achieve the desired "competitive benchmark," with license prices the same as would prevail if there were no network externalities and, thus, no need for a standard, which would free users to adopt whatever mixture of technology they wished. This provides a reasonable balance between incentives for technology innovation and diffusion.

How can price caps selected before standard-setting work? Intuitively, when patents are fairly interchangeable with each other before selection of the standard, the requirement to commit to a cap forces patent owners to choose a lower price than they would afterwards, so as to get their patent included in the standard. Otherwise, the SSO would choose a more affordable option. And when patents are complementary rather than interchangeable, setting one's price away from its competitive level leads to a loss of profit: For instance, if a patent owner opts for a low price cap, other owners will be less willing to give him or her a large share of the proceeds of any patent pool that may form.

Such commitments lower the amount that ultimately will need to be paid to license the key patents to implement the standard, and also better match the rewards to innovations (royalties) with their contributions.

We do not suggest abandoning FRAND. SSOs may make mistakes, and important patents may escape attention at the time the standard is promulgated. However vague and limited, FRAND still imposes some ex post constraints on licensing terms. Thus, we view structured price commitments as a complement, not a substitute, to FRAND.

Can Regulation Work?

The idea that patent owners might commit to prices before standard-setting is not new; both academics and policy-makers [e.g., (*4*)] have mentioned that possibility. Furthermore, this policy has been tested by some SSOs (see text box). Yet there has been little adoption by SSOs in general.

One issue is that economists had no framework for thinking about price commitments. There was no way to predict, even at a theoretical level, what would happen if such commitments were mandated. The theoretical analysis comforts us about the normative impact of commitments (should we expect a good outcome from this new institution?). But thus far, it does not explain why SSOs which, rightly or wrongly, tried them, failed to appeal to IP owners and set a new "standard" for the standard-setting process.

Consistent with historical examples, our model highlights that patent owners prefer to go to an SSO that does not constrain their freedom to license patents as they see fit. Competition between SSOs, which we term "forum shopping," allows IP owners to find more complacent SSOs that do not put such pressure on their prices. Owners of equally important, standard-relevant patents will always opt for a lenient (commitment-free) SSO. Only in specific circumstances will patent owners be attracted by such requirements, e.g., when owners of clearly essential patents fear that an SSO will include a number of more minor patents, with whose owners they will have to share the pie equally.

The corollary is that without a government mandate and/or purchasing preferences, SSOs are unlikely to opt for the "right answer" and demand price commitments. Nevertheless, the suggestion that price commitments be mandated has problems: It could be infeasible or, if feasible, the regulation might do more harm than good.

Concerning feasibility, the rule can be implemented where public procurement is sizable, such as telecommunications. It would suffice to require suppliers to conform to "compliant standards" enacted by SSOs requiring price commitments. Furthermore, antitrust authorities and courts, already involved in regulating standard-setting through reviews and litigation, could favor compliant standards and discourage noncompliant ones.

As for unintended consequences of regulation, the requirement is simply to commit to a price cap. If practice does not work according to theory (only experimentation can tell), the hazard is that IP owners will set too high a cap. But it cannot be worse than the current policy, which is formally an infinite price cap. The combination of a cap with FRAND cannot be worse than only FRAND. So this is rather low-risk.

In recent years, antitrust authorities have wakened to the importance of standardization and the way in which firms can manipulate this process (*5*). Now, the challenge is to create rules that will ensure that standards can effectively promote translation of scientific and technological insights into new products and economic growth. Requiring price commitments is theoretically appealing, rather risk-free, and worth experimenting with.

References and Notes

1. Lemley and Shapiro (*2*) suggest that these disputes be settled via arbitration, making adjudication more expedient, better informed, and overall more consistent.
2. M. A. Lemley, C. Shapiro, *Berkeley Technol. Law J.* **28**, 1135 (2013).
3. J. Lerner, J. Tirole, "Standard-essential patents" (Working paper no. 19664, National Bureau of Economic Research, Cambridge, MA, 2013).
4. D. P. Majoras, "Recognizing the procompetitive potential of royalty discussions in standard setting," Standardization and the Law, Stanford University, 23 September 2005; www.ftc.gov/sites/default/files/documents/public_statements/recognizing-procompetitive-potential-royalty-discussions-standard-setting/050923stanford.pdf.
5. National Academy of Sciences, *Patent Challenges for Standard-Setting in the Global Economy: Lessons From Information and Communications Technology* (National Academy Press, Washington, DC, 2013).
6. T.O. Barnett, "Business Review Letter: VITA," Antitrust Division, U.S. Department of Justice, 30 October 2006.
7. J. L. Contreras, *Jurimetrics* **53**, 163 (2013).

Acknowledgment: J.T. is a member of Industrial Economics Institute, which receives funds from Microsoft, Orange, and Qualcomm.

10.1126/science.1246439

PHOTO CREDIT: HARLAND QUARRINGTON/WIKIMEDIA COMMONS

Published by AAAS

ECOLOGY

Meet the New Boss, Same as the Old Boss

A chemical defense helps an invasive ant species to outcompete an earlier invader that originates from the same native region.

Michael Kaspari and Michael D. Weiser

In Nature's marketplace, there are many ways to compete. Most species carve out a niche where they are particularly effective at turning resources into offspring. Others play a more dangerous game: They win not by outcompeting their adversaries but by killing them. Sometimes this is as simple as applying a little poison. On page 1014 of this issue, LeBrun *et al*. (*1*) reveal how the tawny crazy ant (*Nylanderia fulva*), newly arrived to the United States from South America, may be ending the more than 60-year reign of the red imported fire ant (*Solenopsis invicta*), a competitor armed with a powerful alkaloid venom. The crazy ant's secret? It knows the antidote.

The tawny crazy ant was transported in the early 1980s to the southeastern United States from the savannas of South America (*2*). It is not choosy where it nests; colonies can be found "under or within almost any object or void, including stumps, soil, concrete, rocks [and] potted plants" (*3*). Erratic carpets of tawny crazy ants can be found in the lawns of Houston, Texas. It is replacing native invertebrates, including native ants (*2*), in grasslands and river bottoms. Along the way, tawny crazy ants are doing something rather remarkable. They are battling and, in many cases, wiping out an invasive ant notorious among three generations of U.S. southerners: the red imported fire ant. Crazy ants even take over fire ant nests. One key to the crazy ant's success lies in its ability to detoxify the fire ant's potent and painful alkaloid venom.

Toxins are often used by predators (e.g., spiders and vipers) and by potential prey aiming to deter predators (e.g., monarch butterflies and lionfish). However, the use of poisons to reduce the fitness of competitors—known as antibiosis by microbial ecologists and as allelopathy by botanists—is rarely observed in animals. This is partly a result of the ways in which poisons work. First, poisons work best when they stay where you put them (*4*): You don't spray mace into a headwind, and soil bacteria are more likely to try antibiosis than their aquatic counterparts (*5*). Ants have evolved a diversity of structures that dab, squirt, and otherwise target venom. Second, poisons must be kept away from the rapidly developing embryos that yield future generations (*6*). Ants can overcome this second constraint because their colonies, like those of the red imported fire ant, are superorganisms. The colony's functioning eggs, sperm, and larvae remain back at the nest with the queen(s), leaving sterile workers free to wreak chemical havoc on the edges of their territories. The red imported fire ant's powerful chemical mace has been a key reason for its successful spread through the southeastern United States (*7*).

The fire ant's toxin tends to deter most North American ants—but not, apparently, the crazy ant. When fire ants find a morsel like a dead cricket, some workers begin to carve it up and bring the pieces back to the nest. Others surround the cricket and "gaster flag": They raise their abdomens, extrude a drop of alkaloid venom from the stinger, and splatter or dab it on anything within reach. This venom cocktail, which burns and raises pustules when injected into humans, is a potent contact poison for insects (*7*). Most other ants stay away from gaster flagging fire ants. The risk of death by venom detracts from the benefit of the food. Yet, crazy ants charge into the defensive ring, spraying a mist of pungent formic acid. What keeps this battle from devolving to a simple war of attrition?

First, and a bad omen for the fire ants, both species coexist in the same South American habitats, where crazy ants regularly outcom-

Department of Biology, University of Oklahoma, Norman, OK 73019, USA. E-mail: mkaspari@ou.edu

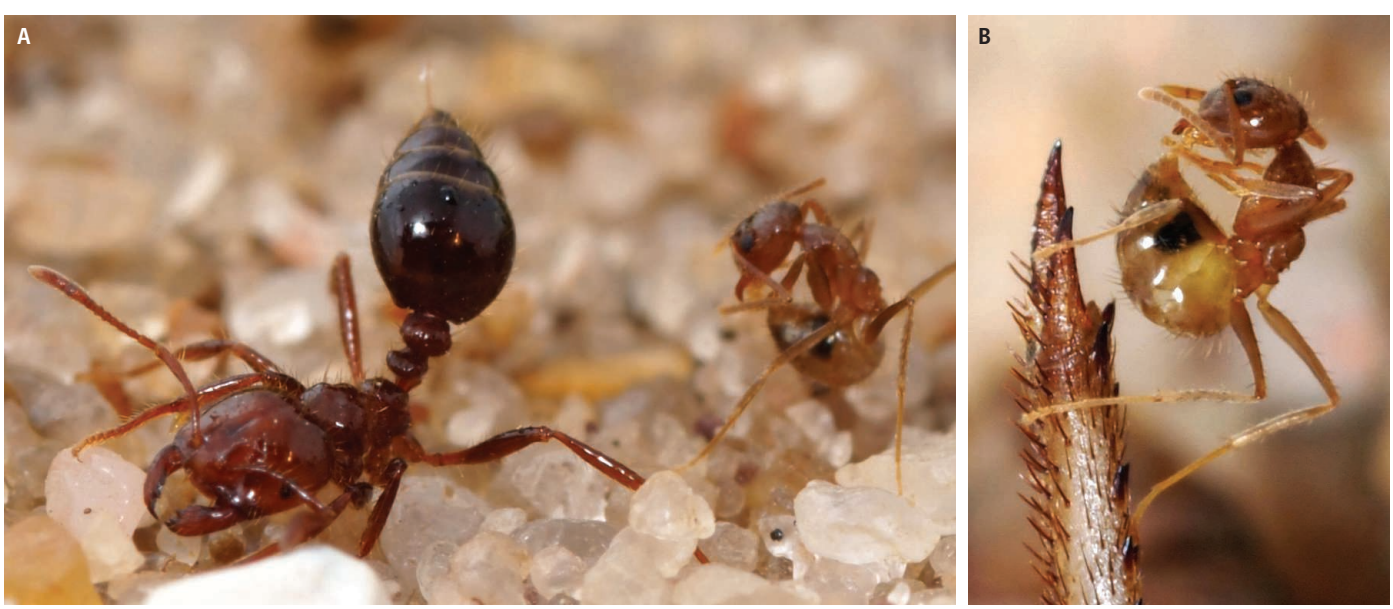

PHOTO CREDITS: LAWRENCE GILBERT

When old foes meet again. (**A**) An imported fire ant dispenses venom from its stinger in the direction of a tawny crazy ant. (**B**) A tawny crazy ant, standing on a cricket's leg, detoxifies after conflict with an imported fire ant.

Published by AAAS

pete fire ants (*8*). A fire ant, when drenched with formic acid, has no apparent defense and falls over dead (*9*). In contrast, the crazy ant, when dabbed with fire ant venom, will use its own weapon as its ultimate defense: It rinses itself clean with its own formic acid. LeBrun *et al*. show that 98% of crazy ants survive fire ant venom; when they are experimentally denied access to their formic acid, survival drops to 48%. Moreover, when crazy ants competed against eight Texas ant species, each of which uses some form of chemical defense, the red imported fire ant triggered seven times more application of formic acid.

The authors hypothesize that formic acid rinses are an adaptive trait in crazy ants, evolved in its native range and employed when the two old foes are reunited. But formic acid rinses don't seal the crazy ant's advantage. Forty years ago, Bhatkar *et al*. (*9*) found that the lowly lawn ant *Lasius neoniger* (which also produces formic acid) can groom away a dose of fire ant poison; it just loses a chemical war of attrition to the more populous colonies of the fire ant. Crazy ants can achieve worker densities that are 100 times as high as those of species in the invaded habitat (*2*). Its antidote gives it the edge.

Biological control efforts often build on the premise that successful invasive species have escaped the parasites and predators of their native ecosystem (*10*). LeBrun *et al*. make a strong case that the red imported fire ant owes its long ride in the American South to its escape from a competitor. The crazy ant may be the fourth in a sequence of ant species that have hit the American Gulf Coast in the past century, each replacing the preceding as common and pernicious (*2*).

Given their ubiquity and impact (*10*), invasive ant species are model ecological systems for studying the many factors that regulate populations. As successive invasions reconstruct the population interactions of a South American ant community in South Texas, a logical next step is to search for the crazy ant's Achilles heel. One fruitful avenue may lie in evolutionary games of rock-paper-scissors (*4*), where round robins of toxins and antidotes make the competitor of your competitor your friend. A more basic puzzle in our homogenizing world is why some—or perhaps all—disruptive invasions eventually crash (*7*, *11*).

References

1. E. G. LeBrun *et al*., *Science* **343**, 1014 (2014).
2. E. G. LeBrun, J. Abbott, L. E. Gilbert, *Biol. Invasions* **15**, 2429 (2013).
3. urbanentomology.tamu.edu/ants/rasberry.html
4. B. Kerr, M. A. Riley, M. W. Feldman, B. J. M. Bohannan, *Nature* **418**, 171 (2002).
5. L. Chao, B. R. Levin, *Proc. Natl. Acad. Sci. U.S.A.* **78**, 6324 (1981).
6. G. H. Orians, D. H. Janzen, *Am. Nat.* **108**, 581 (1974).
7. W. R. Tschinkel, *The Fire Ants* (Harvard Univ. Press, Cambridge, 2006).
8. D. H. Feener Jr. *et al*., *Ecology* **89**, 1824 (2008).
9. A. Bhatkar, W. Whitcomb, W. Buren, P. Callahan, T. Carlysle, *Environ. Entomol.* **1**, 274 (1972).
10. D. Simberloff, *Invasive Species: What Everyone Needs to Know* (Oxford Univ. Press, Oxford, 2013).
11. M. Cooling, S. Hartley, D. A. Sim, P. J. Lester, *Biol. Lett.* **8**, 430 (2012).

10.1126/science.1251272

MATERIALS SCIENCE

The Surface Mobility of Glasses

Surface diffusion on frozen polymer glasses is influenced by the surface dynamics of the glass itself.

Fei Chen,[1] Chi-Hang Lam,[2] Ophelia K. C. Tsui[1,3]

The diffusion of atoms and molecules on a crystal surface plays an important role in myriad applications including thin-film deposition, sintering, and heterogeneous catalysis (*1*, *2*). Surface diffusion is frequently observed at temperatures appreciably below the crystal's melting point, implying a role for enhanced surface mobility in the process. However, understanding the dynamics of surface diffusion in glasses is a research area still in its infancy. On page 994 of this issue, Chai *et al*. (*3*) present an experimental technique that enables detailed quantification of the near-surface mobility of glasses.

Although enhanced surface mobility was found by Chai *et al*. as well as by others in small-molecule and polymer glasses (*4*–*7*), there is a noteworthy distinction between these and the analogous observations in crystals. In crystals, the substrate surface is frequently much less mobile than the surface atoms or molecules (see the figure, panel A). In glasses, however, the first or several surface monolayers are molten even below the glass transition temperature T_g (where the glass freezes), and the change in dynamics from the surface is gradual (see the figure, panels B and C). The reason for such a difference may be that the temperatures commonly used in studies of glass surfaces are close to T_g. This proximity in temperature is attributable to a broad interest in connecting enhanced surface mobility, if present, with the anomalous T_g reduction observed in polymer films (*8*) and, more recently, fast organic crystal growth and the formation of ultrastable glasses (*7*).

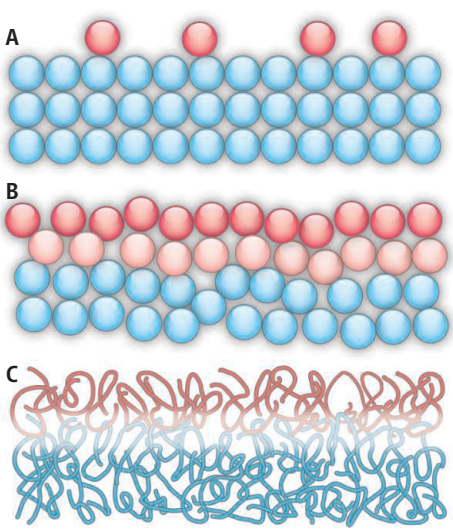

Moving along. Mobile adatoms on a crystal surface (**A**) and their counterparts in the surface mobile layer of an organic glass (**B**) and a polymer glass (**C**). The mobile species are shown in red; the less mobile bulk-like species are in blue.

Computer simulations have consistently revealed the presence of a surface mobile layer in glasses (*9*). Experimental verification has been made only recently. In one method, the relaxation time for the flattening of nano-dimples created on a polymer surface was measured (*4*). In another, polymer films were doped with fluorescent molecules whose dynamics are tied to those of the polymer (*6*); the relaxation time and relative population of the component exhibiting faster dynamics were measured. However, it is generally not straightforward to relate these relaxation times to familiar transport measures such as mobility or diffusivity. Typically, the mobility is determined by monitor-

[1]Department of Physics, Boston University, Boston, MA 02215, USA. [2]Department of Applied Physics, Hong Kong Polytechnic University, Hung Hom, Hong Kong. [3]Division of Materials Science and Engineering, Boston University, Boston, MA 02215, USA. E-mail: okctsui@bu.edu; c.h.lam@polyu.edu.hk

Published by AAAS

ing the evolution of the surface morphology of a specimen and then analyzing the result by means of the Navier-Stokes equation (*5*, *10*) or an equivalent model of fluid flow (*7*). The basic idea is that any nonflat surface structure (artificially or spontaneously created) produces pressure gradients that then drive the specimen to flow. In the lubrication approximation (usually applicable to thin-film specimens with thickness less than ~100 nm), the flow is planar and on average parallel to the pressure gradient. The current (or flow of fluid) per unit width is proportional to the pressure gradient and the film mobility, which can be used to determine the viscosity (*5*).

In one example study, the dynamics for the Brownian height fluctuations of an equilibrated film was monitored and modeled against that of overdamped surface capillary waves (*10*). In two others, surface structures, either shorter (*5*) or taller (*7*) than equilibrium, were created and the dissipative dynamics toward equilibrium (equivalent to that of the former example by the fluctuation-dissipation theorem) was monitored. To discern any anomalous surface mobility, the Navier-Stokes equation was solved for a bilayer film comprising a mobile layer on top of a bulk-like layer. The solution predicts that a crossover from bulk flow to surface flow can occur by either decreasing the thickness or lowering the temperature. The former has been verified by systematically decreasing the thickness from 86 to 2 nm (*5*).

Chai *et al*. measured the flattening dynamics of a step edge created on the surface of polymer films with an average thickness around 100 nm. Upon cooling the films, they observed an analogous flow transition at T_g. A previous experiment (*7*) studying the flattening of surface gratings imprinted on micrometer-thick films of an organic glass also observed a transition from bulk diffusion [a mechanism only feasible in thick films (*2*)] to surface diffusion at T_g + 12 K upon cooling the films. All these findings reinforce the conclusion that surface diffusion is directly tied to the phenomenon of enhanced surface mobility of glasses. Indeed, it becomes the dominant transport process upon lowering the temperature or thinning the specimen.

It remains unknown whether surface diffusion is possible for long-chain polymers, particularly for those with radii of gyration exceeding several nanometers [the thickness of the surface mobile region as derived from surface relaxation time studies (*4*, *6*), which can reveal local motions besides surface flow]. Efforts to understand the dynamics of these materials will have to incorporate material viscoelasticity in the data analysis, which has hitherto been treated sparingly (*11*–*13*).

References and Notes

1. R. Gomer, *Rep. Prog. Phys.* **53**, 917 (1990).
2. W. W. Mullins, *J. Appl. Phys.* **30**, 77 (1959).
3. Y. Chai *et al*., *Science* **343**, 994 (2014).
4. Z. Fakhraai, J. A. Forrest, *Science* **319**, 600 (2008).
5. Z. Yang *et al*., *Science* **328**, 1676 (2010).
6. K. Paeng *et al*., *J. Am. Chem. Soc.* **133**, 8444 (2011).
7. L. Zhu *et al*., *Phys. Rev. Lett.* **106**, 256103 (2011).
8. J. L. Keddie, R. A. L. Jones, R. A. Cory, *Europhys. Lett.* **27**, 59 (1994).
9. J. Baschnagel, F. Varnik, *J. Phys. Condens. Matter* **17**, R851 (2005).
10. H. Kim *et al*., *Phys. Rev. Lett.* **90**, 068302 (2003).
11. S. A. Hutcheson, G. B. McKenna, *Phys. Rev. Lett.* **94**, 076103 (2005).
12. M. Hamdorf, D. Johannsmann, *J. Chem. Phys.* **112**, 4262 (2000).
13. C.-H. Lam, O. K. C. Tsui, D. Peng, *Langmuir* **28**, 10217 (2012).

Acknowledgments: O.K.C.T. is supported by NSF through projects DMR-1004648 and DMR-1310536.

10.1126/science.1248113

CLIMATE CHANGE

The Tropical Pacific Ocean—Back in the Driver's Seat?

Persistent cool conditions in the eastern tropical Pacific may explain the current global warming "hiatus."

Amy Clement[1] and Pedro DiNezio[2]

Average temperatures at Earth's surface are now higher than they were in the mid-19th century, but the rate of warming has not been steady. A pause in surface warming in the mid-20th century coincided with increases in the atmospheric concentrations of sulfate aerosols, which are generally understood to cool the planet. Surface warming resumed in the 1970s, when strong pollution controls were implemented in developed countries. Thus, a balance of warming by greenhouse gases and cooling by aerosols may explain the variable rates of surface warming in the past century. A pause in global warming since 2000—a global warming "hiatus"—has opened up new questions about natural and human activity-driven (anthropogenic) effects on global mean trends in surface temperature. Recent studies point to the importance of the tropical Pacific in driving these changes.

Challenges in CLIMATE SCIENCE
scim.ag/climatechall

A range of factors may have contributed to the current pause in global warming, including changes in stratospheric water vapor, aerosol concentrations (*1*), and reductions in the Sun's output (*2*). The quantitative influence of these factors is still uncertain. However, what is striking about the current hiatus is that while many regions of the globe have continued to warm, the tropical Pacific has been colder than it was during the latter part of the 20th century.

In a recent study, Kosaka and Xie (*3*) showed that by prescribing the cold temperatures in this region (which represents less that 10% of Earth's surface), their model can simulate the pause in global mean temperature since 2000, even when greenhouse gases have been increasing. In another climate model study, Meehl *et al*. found that a cold tropical Pacific increases the heat stored below the ocean surface, thus partially offsetting the warming at the surface (*4*). In the latter model, such hiatus periods arise as a result of natural variations in the climate system, implying that future global surface temperatures will be marked by periods of slowed and accelerated warming as a result of naturally occurring cold and warm periods in the tropical Pacific. Together, the two studies (*3*, *4*) make a compelling case for a modulating effect of the Pacific.

Will these results hold up in other models? The answer depends on the Pacific's natural

[1]Rosenstiel School of Marine and Atmospheric Science, University of Miami, 4600 Rickenbacker Causeway, Miami, FL 33149, USA. [2]School of Ocean and Earth Science and Technology, University of Hawaii at Manoa, Honolulu, HI 96822, USA. E-mail: aclement@rsmas.miami.edu

CREDIT: V. ALTOUNIAN/*SCIENCE*

Published by AAAS

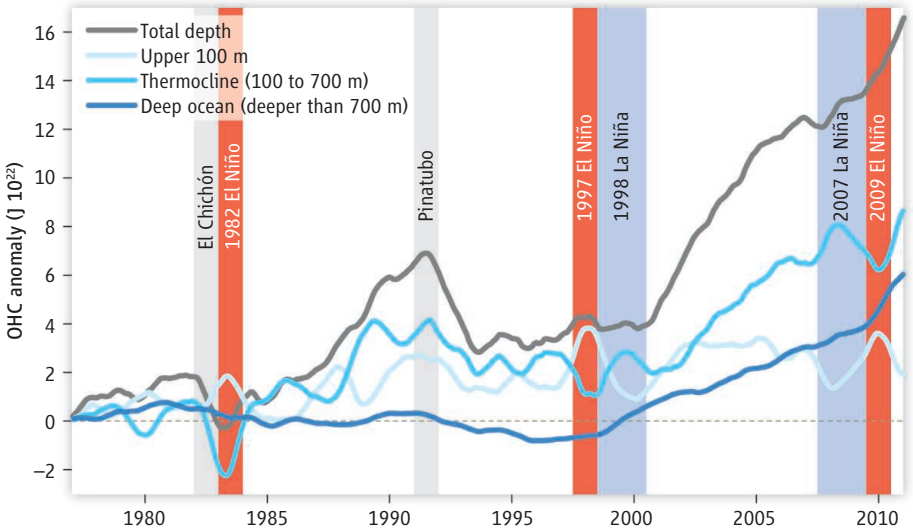

Oceanic heat sink. Evolution of the ocean heat content (OHC) at several depths of the global ocean between 1980 and 2011. Since 2000, the subsurface ocean has warmed much faster than in the preceding two decades; this ocean warming may explain why average atmospheric temperatures have not risen during the past decade. The gray bars show the timing of the El Chichón and Pinatubo volcanic eruptions. The yellow and blue bars show the timing of several key El Niño and La Niña events. Data from the ORAS-4 ocean reanalysis (*10*).

variability, the warming response to greenhouses gases, and the cooling effect of aerosols—a balance of processes that models may not represent accurately. Model-simulated climate sensitivity to anthropogenic greenhouse gases ranges from 2° to 6°C warming, with some models simulating even higher values (*5*). The potential offsetting effects of anthropogenic aerosols are even more uncertain (*6*). The simulation of natural decadal variability is also highly model dependent, with models generally underestimating the magnitude of decadal climate variability in the Pacific (*7*). The interaction among these processes must be represented accurately in a multimodel framework to assess how confident we can be in the attribution of the global warming hiatus.

Examining Earth's energy budget could help to determine whether changes in the tropical Pacific or in aerosols are the main cause of the current hiatus. For instance, there is some observational support for the hypothesis that the missing anthropogenic heat is being stored below the ocean surface (*8*), as proposed by Meehl *et al*. (*4*). Since 2000, the global ocean heat content has increased much faster in the thermocline (between 100 and 700 m) than in the deep ocean (below 700 m), whereas the surface layer (the upper 100 m) has not shown much warming (see the figure) (*9*, *10*). The changes in the thermocline—which is highly responsive to changes in winds—are dominated by the Pacific, where stronger trade winds associated with cold tropical sea-surface temperatures may be instrumental for the penetration of the warming below the ocean surface (*9*, *10*). Although the pathways and rates at which heat is stored in the ocean are still uncertain, these results are consistent with what is expected from a cold tropical Pacific.

If indeed the tropical Pacific is central to the current hiatus, then it may take a while until the Pacific shifts into a warm state and global surface temperatures resume their upward trend. In the past, warm and cold states have lasted for several decades. The last cold period from 1945 to 1975 was followed by a warm period from 1976 to the end of the 20th century (*11*). Some authors have argued that these decadal changes in the Pacific are driven by changes in ocean circulation (*12*), implying some degree of predictability, but others argue that they can arise in response to random forcing from the atmosphere (*13*), with cloud feedbacks potentially playing a role in how long the cold or warm states linger (*14*). The question of what drives decadal changes in the Pacific, as well as their predictability, takes on new urgency in the context of the current hiatus.

Looking back into the past may help to unravel the role of the Pacific Ocean in modulating changes in global mean surface temperature. For example, the mid-20th-century cooling is generally attributed to large increases in sulfate aerosols (*6*), but the cold state of the tropical Pacific may have played a role as well. It is worth reconsidering the balance of natural and anthropogenic effects during this period. Large ensembles of climate models run with historical changes in greenhouse gases and aerosols, as well as natural climate forcings (solar output and volcanoes) (*15*), will allow this balance to be quantified in models. Proxies for past climatic conditions—for example, from corals or tree rings—can also provide more observations of decadal-scale shifts in the tropical Pacific climate and help to determine how well climate models simulate the range of variability of the preindustrial climate (*7*).

The current pause in global mean surface warming has opened new and exciting research questions about the role of the tropical Pacific. A next step is a full attribution of the effects of natural and anthropogenic influences on the Earth's energy budget. How much of the energy gained at the top of the atmosphere is due to greenhouse gases, and how much is reflected back to space by aerosols and clouds or redistributed through the Earth system, in particular stored in the ocean? Is it possible to accurately determine whether aerosols are having an influence on ocean-warming rates during the current hiatus? Answering these questions will require extensive observations and well-tested models to quantify the relative influence of greenhouse gases, anthropogenic aerosols, and internal variability on the Earth's energy budget.

Although high-quality observations of the radiative fluxes at the top of the atmosphere and in the upper 2000 m of the ocean are available for the period since 2000, their estimates of interannual variations in energy gains do not agree (*16*). This issue needs be solved before an attribution of the relative roles played by internal variability versus anthropogenic aerosols can be made. Determining how these rates compare with prior periods of global warming for which climate-quality observations are limited is even more challenging. Furthermore, models and reanalysis data suggest that the upper 700 m of the ocean play a key role storing the excess energy during hiatus periods, whereas the deep ocean may reflect the longer greenhouse gas-driven warming trend. To increase the accuracy of ocean heat content estimates, it is critical that observational capability in the ocean, including arrays of autonomous profiling floats and tropical moorings, is maintained and expanded.

Greenhouse gases are warming the planet, and will continue to do so. Developing a framework for measuring and attributing subtle variations in the global energy budget—from the top of the atmosphere to the depths of the ocean— is one of the out-

Published by AAAS

standing challenges. This research will lead to a more complete and dynamic view of energy flows within the global Earth system, where perhaps the tropical Pacific is indeed in the driver's seat.

References

1. S. Solomon *et al*., *Science* **333**, 866 (2011).
2. K. E. Trenberth, *Curr. Opin. Environ. Sustain.* **1**, 19 (2009).
3. Y. Kosaka, S.-P. Xie, *Nature* **501**, 403 (2013).
4. G. A. Meehl *et al*., *J. Clim.* **26**, 7298 (2013).
5. T. D. Stocker *et al*., Eds., Summary for Policymakers, in *Climate Change 2013: The Physical Science Basis. Contribution of Working Group I to the Fifth Assessment Report of the Intergovernmental Panel on Climate Change* (Cambridge Univ. Press, Cambridge/New York, 2013).
6. D. Rosenfeld, S. Sherwood, R. Wood, L. Donner, *Science* **343**, 379 (2014).
7. T. R. Ault, C. Deser, M. Newman, J. Emile-Geay, *Geophys. Res. Lett.* **40**, 3450 (2013).
8. K. Trenberth, J. T. Fasullo, *Earth's Future* **1**, 19 (2013).
9. M. Balmaseda *et al*., *Geophys. Res. Lett.* **40**, 1754 (2013).
10. M. H. England *et al., Nat. Climate Change* 10.1038/nclimate2106,1758 (2014).
11. C. Deser *et al*., *J. Clim.* **17**, 3109 (2004).
12. D. Gu, S. G. H. Philander, *Science* **275**, 805 (1997).
13. Y. M. Okumura, *J. Clim.* **26**, 9791 (2013).
14. A. C. Clement, R. Burgman, J. Norris, *Science* **325**, 460 (2009).
15. C. Deser, A. S. Phillips, M. A. Alexander, B. V. Smoliak, *J. Clim.* 10.1175/JCLI-D-13-00451.1 (2013).
16. K. Trenberth, J. T. Fasullo, M. Balmaceda, *J. Clim.* 10.1175/JCLI-D-13-00294.1 (2014).

10.1126/science.1248115

NEUROSCIENCE

The Neural Code That Makes Us Human

How does a certain pattern of vibration in the air reliably represent a meaningful speech sound?

Yosef Grodzinsky[1,3] and Israel Nelken[2,3]

Speech provides a fascinating window into brain processes. It is understood effortlessly, and despite a huge variability, manifests both within and across speakers. It is also a stable and reliable carrier of linguistic meaning, complex and intricate as it may be. How speech is encoded and decoded has puzzled those seeking to understand how the brain extracts sense from an ambiguous, noisy environment (see the figure). On page 1006 in this issue, Mesgarani *et al*. (*1*) demonstrate the neural basis of speech perception by combining linguistic, electrophysiological, clinical, and computational approaches.

How do brains use the pattern of pressure waves in the air that is speech ("speech-as-sound") and extract meaning ("speech-as-speech") from it reliably, despite huge variability between speakers and background noise? Studies dating as far back as the 1950s showed that natural speech is highly redundant—speech sounds convey their identity by a large number of disparate acoustic cues (*2*). However, to ensure stable cue-to-speech translation by brains, an invariant code—something like a dictionary of speech units—seems necessary. What, then, is the nature of the representation of speech units in the brain, and how do they combine into larger, meaning-bearing pieces?

In the 1930s, linguists Roman Jakobson and Nikolai Trubetzkoy classified consonants and vowels along articulatory dimensions: Their description of the basic units of speech recognition referred to elements such as the place in the oral cavity where air is compressed on its way out ("labial," "dental," "velar," etc.), the manner of air release ("plosive," "sonorant," etc.), and whether the vocal cords vibrate or not ("voiced," "unvoiced") (*3*). For example, the sound /p/ is a composite of features—[+labial, –voiced, +plosive]—distinguishable from /b/ [+labial, +voiced, +plosive] and from /t/ [+alveolar, –voiced, +plosive]. Distinctive features, then, help to characterize the nature of invariance, while systematically grouping speech units in clusters. These features have therefore played a central role in speech recognition research.

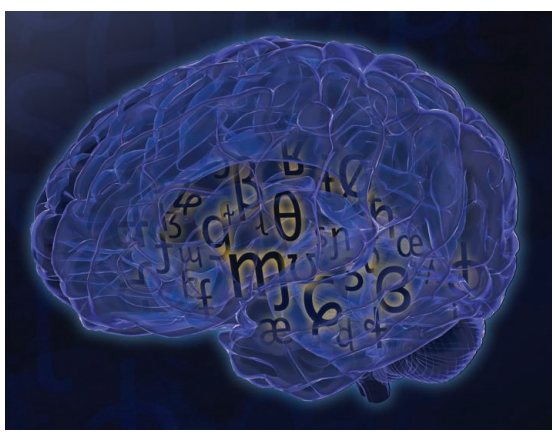

Speech perception. How highly variable speech sounds (vowels and consonants) are represented as stable phonetic units in the brain has not been clear. Acoustic-to-phonetic transformation may involve processing in the superior temporal gyrus of the human brain (*1*). The illustration shows phonetic symbols from the International Phonetic Alphabet superimposed on the language regions of the left cerebral hemisphere.

But what actually happens in human brains during speech perception, and where? It may be that invariance is expressed in terms of articulation-related distinctive features (as proposed by linguists). Invariance may also be reflected already in sensory areas; alternatively, brain processes may achieve invariant representations of speech sounds only outside the auditory system proper. One extreme possibility is that distinctive features correlate with acoustic ones, in which case the invariant coding of sounds may already occur in sensory areas. At the other extreme, as suggested by the influential motor theory of speech perception, speech sounds may well be represented by the articulatory gestures used to produce them (*4*). A recent form of this view actually posits mirror neurons in the brain that do precisely that—map sounds onto motor actions. In that case, the invariant representation of speech would by necessity occur in motor areas, outside of the auditory system (*5*).

Mesgarani *et al*. recorded responses to speech sounds in the brains of human patients who were about to undergo brain surgery for clinical reasons. These recordings give a more detailed view of the electrical activity in the human brain than noninvasive methods such as electroencephalograms or functional magnetic resonance imaging, although they still reflect the average responses of large neuronal populations. Using these electrical signals, the authors demonstrate a high degree of invariance of speech representation as early as in the human auditory cortex by showing that speech sounds of different speakers and

CREDIT: XAVIER STUDIO

[1]Department of Linguistics, McGill University, 1085 Dr. Penfield Avenue Montréal, Québec H3A1A7, Canada. [2]Department of Neurobiology, The Alexander Silberman Institute of Life Sciences, Hebrew University, Jerusalem, 91904 Israel. [3]The Edmond and Lily Safra Center for Brain Sciences, The Hebrew University of Jerusalem, Givat Ram, Jerusalem 91904, Israel. E-mail: yosef.grodzinsky@mcgill.ca

Published by AAAS

in a multitude of contexts nonetheless activate the same brain regions. Moreover, invariance seems to be governed by articulatory distinctive features, thereby supporting the 80-year-old theory of Jakobson and Trubetzkoy. Interestingly, features do not have equal neural representation, and those that induce strong neural invariance have strong acoustic correlates. Speech representation in the auditory cortex, in other words, is governed by acoustic features, but not by just any acoustic feature—the features that dominate speech representation are precisely those that are associated with abstract, linguistically defined distinctive features. Mesgarani *et al*., who base their investigation on linguistic distinctions (*6*), further demonstrate that features are distinguishable by the degree of the neural invariance they evoke, forming an order that is remarkably in keeping with old linguistic observations: Manner of articulation (manifesting early in developing children) produces a neural invariance that is more prominent than that related to place of articulation (manifesting late in children). A hierarchy noted in 1941 for language acquisition is now resurfacing as part of the neural sensitivity to speech sounds (*7*).

But linguistic communication is based on larger pieces than the basic building blocks of speech. It also requires rules that create complex combinations from basic units. Linguistic combinatorics is therefore an essential part of verbal communication, allowing it to be flexible and efficient. Here, too, Mesgarani *et al*. offer some clues. They show that sequencing processes, particularly those that determine voice onset time, tend to be more distributed in neural tissue than the rather localized distinctive features (*8*, *9*). This suggests that combinatorial rules that concatenate basic elements into bigger units might depend on larger, perhaps somewhat more widely distributed, neural chunks, than the stored representations of basic building blocks. How distributed (and speech-specific) such processes are is not revealed by the Mesgarani *et al*. study, but evidence about the neural specificity of language combinatorics at other levels of analysis does exist: Operations involved in building complex expressions—sentences with rich syntax and semantics—are relatively localized in parts of the left cerebral hemisphere (and distinct from other combinatorial processes such as arithmetic), even if the neural chunks that support them may be as large as several cubic centimeters (*10*, *11*).

Although the study of Mesgarani *et al*. was carried out in English, the findings have universal implications. Cross-linguistic evidence for universal neural representation of higher aspects of linguistic communication also exists, at least to some extent (*12*, *13*). These results may suggest a shift in view on brain-language relations: from earlier modality-based models (*14*), we moved to attempts to identify the neural code for specific linguistic units and concatenating operations. This move carries the hope that someday, the complete neural code for language will be identified, thereby making good on the promise that linguistics be "part of psychology, ultimately biology" (*15*).

References and Notes

1. N. Mesgarani *et al*., *Science* **343**, 1006 (2014); 10.1126/science.1245994.
2. A. M. Liberman, F. S. Cooper, D. P. Shankweiler, M. Studdert-Kennedy, *Psychol. Rev.* **74**, 431 (1967).
3. N. Trubetzkoy, *Principles of Phonology* (Univ. of California Press, Berkeley, 1969).
4. A. M. Liberman, I. G. Mattingly, *Cognition* **21**, 1 (1985).
5. L. Fadiga *et al*., in *Broca's Region*, Y. Grodzinsky, K. Amunts, Eds. (Oxford Univ. Press, New York, 2006).
6. N. Chomsky, M. Halle, *The Sound Pattern of English* (Harper & Row, New York, 1969).
7. R. Jakobson, *Kindersprache, Aphasie und allgemeine Lautgesetze* (1941) [English transl.: *Child Language, Aphasia, and Phonological Universals* (Mouton, The Hague, 1968)].
8. E. D. Young, M. B. Sachs, *J. Acoust. Soc. Am.* **66**, 1381 (1979).
9. M. Steinschneider, I. O. Volkov, M. D. Noh, P. C. Garell, M. A. Howard 3rd, *J. Neurophysiol.* **82**, 2346 (1999).
10. Y. Grodzinsky, A. Santi, *Trends Cogn. Sci.* **12**, 474 (2008).
11. S. Heim *et al*., *Front. Evol. Neurosci.* **4**, 4 (2012).
12. M. Makuuchi *et al*., *Cereb. Cortex* **23**, 694 (2013).
13. A. D. Friederici *et al*., *Cereb. Cortex* **16**, 1709 (2006).
14. N. Geschwind, *Science* **170**, 940 (1970).
15. N. Chomsky, *Knowledge of Language, Its Nature, Origin, and Use* (Praeger, New York, 1986).

Acknowledgments: Support by an Insight grant from the Canada Social Sciences and Humanities Council (Y.G.) and by the Canada Research Chairs (Y.G.) and by the Israel Science Foundation (I.N.).

10.1126/science.1251495

ANTHROPOLOGY

Out of Beringia?

John F. Hoffecker,[1] Scott A. Elias,[2] Dennis H. O'Rourke[3]

A shrub tundra refugium on the Bering land bridge may have played a pivotal role in the peopling of the Americas.

Based on the distribution of tundra plants around the Bering Strait region, Eric Hultén proposed in the 1930s that the now-submerged plain between Chukotka and Alaska—the Bering land bridge—became a refugium for shrub tundra vegetation during cold periods (*1*), which include the last glacial maximum (LGM) between ~28,000 and 18,000 cal BP (calibrated radiocarbon years before the present). Adjoining areas to the west and east supported drier plant communities with a higher percentage of grasses during glacial periods. According to Hultén, when warmer and wetter conditions returned to these areas, the land bridge, which he named Beringia, became a center of dispersal for tundra plants. Now it appears that it also may have been a glacial refugium and postglacial center of dispersal for the people who first settled the Americas.

Since 1960, much evidence has accumulated to support the shrub tundra refugium thesis, including data collected from the former surface of the Bering land bridge. Pollen, plant macrofossils, and insect remains from dated sediments extracted from the floor of the Bering Sea indicate a mesic tundra habitat during the LGM (*2*, *3*). Although pollen data from islands in the Bering Sea suggest more steppic vegetation (or "steppe-tundra"), these islands represent former upland areas on the now-submerged land bridge (see the figure). Several tree species, including spruce, birch, and alder, also probably survived locally during the LGM (*3*, *4*). Fossil insect remains from both sides of the Bering Strait suggest surprisingly mild temperatures during the coldest phases of the LGM, despite the high latitude. All of these data presumably reflect the impact of the North Pacific circulation, which brought comparatively moist and warm air to southern Beringia during the LGM (*4*). In fact, the latest study of Beringian vegetation indicates that grasses were less dominant in areas outside the land bridge than previously thought (*5*).

The shrub tundra refugium in Beringia may also have played a pivotal role in the peopling of the Americas. Genetic evidence suggests that most Native Americans are descended from a population that was isolated somewhere between northeast Asia and Alaska during the LGM (*6*). According to the Beringian standstill hypothesis, this popula-

[1]Institute of Arctic and Alpine Research, University of Colorado, Boulder, CO 80309, USA. [2]Department of Geography, Royal Holloway University of London, Egham TW20 0EX, UK. [3]Department of Anthropology, University of Utah, Salt Lake City, UT 84112, USA. E-mail: john.hoffecker@colorado.edu

Published by AAAS

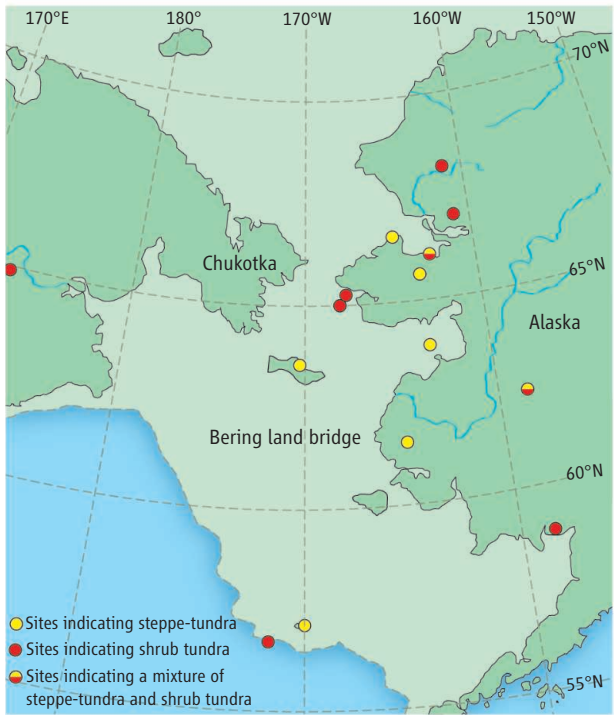

A possible human refugium. Shrub tundra is likely to have covered much of the now-submerged plain that lies between Chukotka and Alaska during the last glacial maximum (LGM), reflecting the effect of moist air from the North Pacific Ocean. Shrub tundra communities also probably extended into parts of western Alaska and Chukotka, whereas drier steppe-tundra covered much of the unglaciated landscape that lay outside central Beringia. Pollen studies indicate that some trees also probably survived in parts of central Beringia during the LGM. These conclusions are based in part on the analysis of sediment cores extracted from the sites shown on this map (*2*, *3*). The shrub tundra zone in central Beringia represents the most plausible home for the people who were genetically isolated from their Asian parent groups during the LGM and later dispersed throughout the Americas.

tion occupied northeast Asia before the LGM, became genetically isolated from its Asian source during the latter, and—following a protracted sojourn in Beringia—dispersed throughout the Western Hemisphere, when retreating glaciers opened access to coastal and interior corridors in northwestern North America (*6*).

Hultén's mesic tundra refugium offers not only a credible home for the Beringians but also a mechanism for their genetic isolation, because other high-latitude regions were apparently abandoned by human populations during the LGM. Wood fuel was probably the key variable in determining which regions remained occupied. People in interior treeless settings relied heavily on fresh bone, but experimental studies have shown that at least a modest quantity of wood is necessary to render bone practical as a fuel (*7*). The woody shrubs and occasional trees of the Beringian shrub tundra zone may have been the only substantive source of wood fuel at higher latitudes during the LGM.

The Beringian standstill hypothesis was first fully articulated in 2007 by Tamm and colleagues, who worked with a large sample of mitochondrial DNA (mtDNA) from living Native Americans. They identified a set of mutations that accumulated after the divergence of the major haplogroups (A, B, C, D, and X) from their Asian parents but before the dispersal throughout the Western Hemisphere. Tamm *et al*. concluded that ancestral Native Americans were isolated genetically from other populations for a least a few thousand years before the dispersal, probably in Beringia. Applying a mutation rate of 3.5×10^{-8} per year per position, they estimated that Asian and American mtDNA haplogroups had diverged more than 25,000 years ago but that the latter dispersed in the New World less than 15,000 years ago (*6*).

Although the Beringian standstill hypothesis is based mainly on mtDNA, analyses of nuclear (including Y chromosome) DNA provide some support for it. Similarly, an allele at a microsatellite locus on chromosome 9 in the nuclear genome (the D9S1120 locus) is found at appreciable frequency in all Native American populations examined, as well as two Northeast Asian populations, but is absent in the rest of the world (*8*). These observations strongly suggest an origin from a single source population for most Native American populations, consistent with the Beringian standstill hypothesis. A large survey of nuclear genetic variation concluded that initial settlement of the Western Hemisphere was followed by at least two separate and later population movements from Asia (*9*). Recent studies of Y-DNA in both North and South American indigenous populations found greater diversity than previously assumed among the initial population, reduced diversity as a function of distance from Beringia, and differentiation of haplogroup Q in Beringia (*10*, *11*).

To what extent is the Beringian standstill hypothesis supported by archaeological data and dated human remains? The analysis of ancient DNA from human skeletal remains dating to 24,000 cal BP from Mal'ta in southern Siberia appears to confirm the pre-LGM divergence of Native Americans from their Asian parent haplogroups (*12*). At the same time, dated archaeological and human remains indicate that settlement of the Western Hemisphere probably took place after the LGM (*13*). At this point, the major outstanding questions are where the standstill population was located during the LGM, and how it was isolated genetically from its Asian source.

The shrub tundra zone in central Beringia represents the most plausible home for the isolated standstill population. Although high-latitude archaeological sites of LGM age are unknown, postglacial submergence of the Bering land bridge would explain the absence of traces of people concentrated in central Beringia. On the other hand, occupation of western Beringia before the LGM is well documented (*14*). The post-LGM archaeological record contains two sets of remains, one of which represents a movement of people from central Siberia into Beringia about 15,000 cal BP (and may be an archaeological proxy for mtDNA subclade D2a) (*6*,*15*). The other lacks obvious antecedents in Asia and might represent the post-LGM standstill population, expanding out of central Beringia with the shrub tundra (*15*). To confirm the hypothesis, archaeological sites of LGM age must be documented in Beringia. Although most such sites presumably would lie underwater, some might be found in areas of the LGM shrub tundra refugium that remain above sea level, such as low-lying portions of southwestern Alaska and eastern Chukotka.

References and Notes

1. E. Hultén, *Outline of the History of Arctic and Boreal Biota During the Quaternary Period* (Lehre J. Cramer, New York, 1937).
2. S. A. Elias, B. Crocker, *Quat. Sci. Rev.* **27**, 2473 (2008).
3. R. Westbrook *et al*., GSA Annual Meeting, 180-10 (Charlotte, NC, 4–7 November 2012).
4. L. B. Brubaker *et al*., *J. Biogeogr.* **32**, 833 (2005).
5. E. Willerslev *et al*., *Nature* **506**, 47 (2014).
6. E. Tamm *et al*., *PLOS ONE* **2**, e829 (2007).
7. I. Théry-Parisot *et al*., in *The Zooarchaeology of Milk and Fats* (Oxbow Books, Oxford, 2005), pp. 50–59.
8. K. B. Schroeder *et al*., *Biol. Lett.* **3**, 218 (2007).
9. D. Reich *et al*., *Nature* **488**, 370 (2012).
10. M. C. Dulik *et al*., *Proc. Natl. Acad. Sci. U.S.A.* **109**, 8471 (2012).
11. V. Battaglia *et al*., *PLOS ONE* **8**, e71390 (2013).
12. M. Raghavan *et al*., *Nature* **505**, 87 (2014).
13. T. Goebel *et al*., *Science* **319**, 1497 (2008).
14. V. Pitulko *et al*., in *Paleoamerican Odyssey,* K. E. Grant *et al*., Eds. (Texas A&M University Press, College Station, 2013), pp. 13–44.
15. J. F. Hoffecker, S. A. Elias, *Human Ecology of Beringia* (Columbia Univ. Press, New York, 2007).

Acknowledgments: We thank N. H. Bigelow, O. K. Mason, G. R. Scott, and two anonymous reviewers who commented on earlier drafts.

10.1126/science.1250768

Published by AAAS

MATERIALS SCIENCE

How Shape Affects Microtubule and Nanoparticle Assembly

Models of nanoparticle assembly can help explain aspects of the inverted structure that forms because of induced change in tubulin protein shape.

Mark J. Stevens

Part of the tantalizing promise of nanoparticles is that they can serve as building blocks of complex systems that could outperform other materials. For example, different structures could form depending on the shape of the nanoparticles. A stimulus, such as a change in temperature or the addition of a small molecule, that changes nanoparticle shape could create a new structure with a different function. Nature provides a large example set of nanoparticles in the form of proteins, which can be studied to gain insight into shape-dependent assembly. In a recent paper, Ojeda-Lopez *et al*. (*1*) describe a new shape-changing mechanism that dramatically alters how a protein system assembles. The α–β tubulin dimer naturally polymerizes to form microtubules. The authors discovered that adding a highly charged small molecule, spermine, causes a shape transformation. The tubules assemble within an inverted structure compared to that of the original microtubules.

Microtubules, the track along which kinesin motor proteins walk, are a key component underlying cellular transport and cell division (*2*). These functions occur in part because of the special properties derived from tubulin, which are of interest to general polymer physics and to the development of synthetic systems, such as ones performing nanoscale transport (*3*). Microtubules assemble, dissociate, and reassemble in cells, and the dynamics of polymerization and depolymerization depends on binding of guanosine triphosphate (GTP) and its dephosphorylation to guanosine diphosphate (GDP). With GTP bound to tubulin, straight growth of the tubule occurs, but the transition to GDP alters the tubulin geometry, tending to cause filaments to peel away in arcs, and leads to catastrophic depolymerization.

Ojeda-Lopez *et al*. stabilized the microtubules using taxol. The subsequent addition of spermine produced arcs peeling away from the tubule, similar to the effect of dephosphorylation (see the figure). However, the spermine-induced structure is an inverted tubulin tubule (ITT)—a spiral tubule with tubulin orientation inverted with respect to the microtubule orientation. The ITT has a larger diameter, 40 nm, versus 24 nm for microtubules.

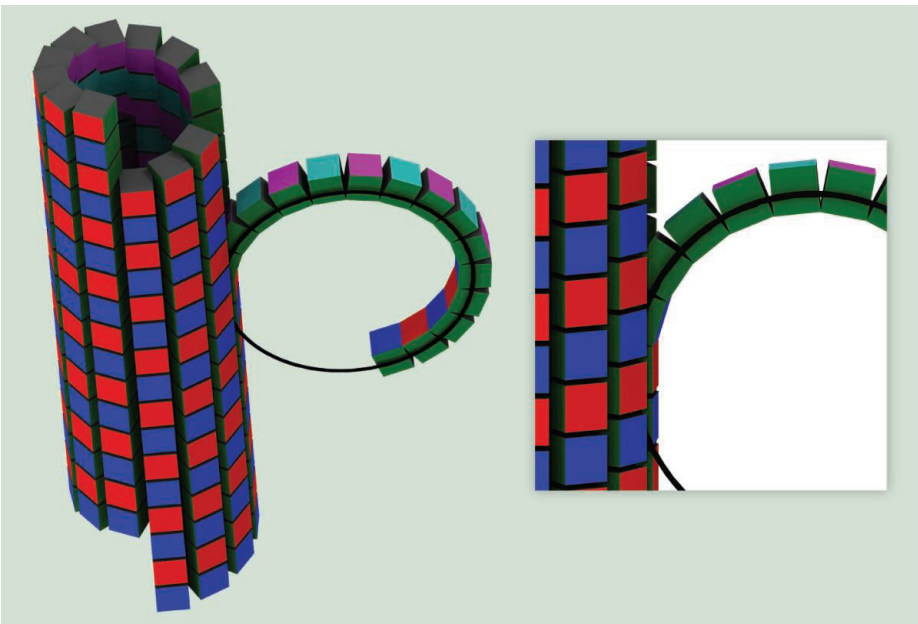

Reversing microtubules. The basic geometry of a microtubule with one ring peeling away that would form the inverted tubulin tubule (ITT) when stabilized by spermine. The red-magenta and blue-cyan cubes represent α- and β-tubulin, respectively. The colors show how what was the inside of the microtubule becomes the outside of the ITT. In the magnified image, the circular black line indicates that the surface contact is different for the tubulin in the ring versus that in the microtubule, implying a change in surface binding and likely a shape change.

Understanding the formation of this new assembly presents many challenges. One is that the assembly of microtubules (and more generally, the assembly of tubular structures from nanoparticles) is not well understood, but progress is being made with minimal coarse-grained models (*4*–*6*). Recent simulations have shown how the interactions between the monomers influence the protofilament number or tubule radius and the chirality of the tubule (*6*). The formation of tubules from nanoparticles requires binding on both their vertical side and lateral sides. Experimental studies have shown that the vertical interaction is stronger than the lateral interaction. This difference is necessary to prevent twist of the tubule, which would yield a wide range of structures and not yield the straight filaments present in biologically functional microtubules (*6*).

The assembly of microtubules from free monomers is heavily influenced by this relative interaction strength. Because the vertical interaction is stronger, the tubulin dimers first form straight protofilaments via vertical binding, and the protofilaments then bind laterally into curved sheets that close to form tubules. In contrast, if the lateral interactions were stronger, the tubule would initiate as a single spiral that would then continue to grow by attaching monomers at the end. In the ITT, the laterally bound surfaces of tubulin are what had been the vertically bound surfaces in the microtubule. The lateral tubulin surfaces (green in the figure) bind together to form a curved assembly, whereas in taxol-stabilized microtubules, they formed straight filaments. In the figure, the cubes represent tubulin contact only at the inner edge of the lateral surfaces, indicating that the contact region changes location in the transition.

Center for Integrated Nanotechnologies, Sandia National Laboratories, Albuquerque, NM 87185–1315 USA. E-mail: msteve@sandia.gov

CREDIT: MARK J. STEVENS

Published by AAAS

These factors imply that the lateral and vertical surfaces in the microtubules change shape to form the ITT structure.

The inversion assembly involves spermine, which is a highly charged +4 cation and is strongly attracted to negatively charged tubulin. Spermine is a well-known "condenser" of double-stranded DNA (dsDNA) into toroids (*7*). In general, a single dsDNA molecule will generically form toroids in the presence of counterions of charge at least +3; the effect is electrostatic in nature and does not require a specific molecular binding (*8*, *9*). The high charge is required to make the electrostatic interactions dominate over entropy. Initially, spermine causes the bundle formation of the microtubules. For bundles of stiff biopolymers (e.g., dsDNA, actin, or microtubules), only divalent ions are needed (*10*, *11*).

In all these cases, because the counterions are localized near the charged polymers, they lose a substantial amount of entropy, which is compensated enthalpically by the strong electrostatic interactions of the multivalent ions. In the bundle geometry, the counterions have more accessible volume and thus lose less entropy than in the smaller-volume toroidal case. Thus, a lower charge and electrostatic interaction strength are needed for bundles. That the ring formation leading to the ITT structure must be induced by highly charged spermine suggests that spermine is being localized in a small volume, possibly between the lateral contacts in the microtubule, or even undergoes specific binding.

The work of Ojeda-Lopez *et al*. brings together many aspects of hierarchical assembly, including strong electrostatics, conformational switches, and nanoparticle-nanoparticle interactions. How spermine produces the ITT structure is still an open and challenging question that involves interactions over multiple length scales. The initial interaction between spermine and tubulin can be studied with atomistic simulations, but any shape change in tubulin is a major challenge to simulate. Understanding how spermine destabilizes taxol-bound microtubules is likely to require atomistic detail while also treating dynamics on the scale of whole tubulin proteins, which is not presently feasible. The path forward for simulations is to attack separately at atomistic and coarse-grained scales and to push them toward each other. More methodological development is needed on the coarse-grained side, and there are many opportunities here and in other nanoparticle systems. For example, new developments in synthesis are creating the patchy nanoparticles whose assembly may be easier to understand (*12*). Theoretical work on patchy particles is providing a fundamental base to study the complex behaviors that occur in these systems (*13*). While understanding nanoparticle systems is complex and very challenging, a foothold for learning the right questions is developing.

References and Notes

1. M. A. Ojeda-Lopez *et al*., *Nat. Mater.* **13**, 195 (2014).
2. H. Lodish *et al*., *Molecular Cell Biology* (Freeman, New York, 2007).
3. H. Hess, *Annu. Rev. Biomed. Eng.* **13**, 429 (2011).
4. V. VanBuren, L. Cassimeris, D. J. Odde, *Biophys. J.* **89**, 2911 (2005).
5. V. Hunyadi, D. Chrétien, H. Flyvbjerg, I. M. Jánosi, *Biol. Cell* **99**, 117 (2007).
6. S. Cheng, M. J. Stevens, *Soft Matter* **10**, 510 (2013).
7. V. A. Bloomfield, *Biopolymers* **44**, 269 (1997).
8. J. Widom, R. L. Baldwin, *J. Mol. Biol.* **144**, 431 (1980).
9. M. J. Stevens, *Biophys. J.* **80**, 130 (2001).
10. J. X. Tang, T. Ito, T. Tao, P. Traub, P. A. Janmey, *Biochemistry* **36**, 12600 (1997).
11. M. J. Stevens, *Phys. Rev. Lett.* **82**, 101 (1999).
12. A. H. Gröschel *et al*., *Nature* **503**, 247 (2013).
13. L. Rovigatti *et al*., *Phys. Rev. Lett.* **111**, 168302 (2013).

Acknowledgments: Supported by the U.S. Department of Energy, Office of Basic Energy Sciences, Division of Materials Sciences and Engineering under Award KC0203010. Sandia National Laboratories is a multiprogram laboratory managed and operated by Sandia Corporation, a wholly owned subsidiary of Lockheed Martin Corporation, for the U.S. Department of Energy's National Nuclear Security Administration under contract DE-AC04-94AL85000.

10.1126/science.1250827

CELL BIOLOGY

Signaling Shifts in Allergy Responses

A mechanism that senses antigen affinity shifts cell signaling and leads to qualitatively different inflammatory responses.

Marc Daëron

Mast cells initiate allergic reactions. These cells express a receptor (FcεRI) that binds to immunoglobulin E (IgE). When antigen binds to receptor-bound IgE, a wide range of responses is triggered that together cause the symptoms of allergy. These include the release of enzymes and a variety of bioactive chemicals from granules, the generation of lipid-derived inflammatory molecules, and the secretion of multiple cytokines and chemokines. However, not all responses are equally induced. On page 1021 of this issue, Suzuki *et al*. (*1*) unravel how a difference in the affinity of antigen favors one response or another by switching between intracellular signaling pathways. Quantitative differences in antigen affinity thus determine the quality of mast cell responses.

FcεRI consists of a subunit (FcRα) that binds to the Fc portion of IgE and two Immunoreceptor tyrosine-based activation motif (ITAM)–containing subunits (FcRβ and FcRγ) that generate activation signals when phosphorylated by Src family tyrosine kinases (see the figure). Phosphorylation occurs when plurivalent allergens (allergy-evoking antigens) bind to receptor-bound IgE antibodies and aggregate FcεRI.

Antigens bind to IgE antibodies with variable affinities. Differences in binding affinity translate into differences in binding kinetics. Antigens that bind with a low affinity indeed dissociate more rapidly from receptor-bound IgE than do antigens that bind with a high affinity. This is a basis for the "kinetic proofreading" concept, according to which the strength of signals depends on the duration of receptor engagement (*2*). Consequently, low-affinity antigens induce mast cell responses of a lower magnitude than high-affinity antigens. All responses, however, are not similarly affected. Unlike cytokine secretion, chemokine secretion was found to be of a similar or greater magnitude when induced by low-affinity than by high-affinity antigens (*3*). Suzuki *et al*. explain this behavior, which the kinetic proofreading concept does not account for, by showing that the affinity of antigen selects both the Src kinase and the transmembrane adapter protein that initiates and organizes proximal signals in FcεRI signalosomes, respectively (signalosomes are protein assemblies in which activation signals are generated). Consequently, different

Institut Pasteur, 75015 Paris, France, and Centre d'Immunologie de Marseille-Luminy, 13009 Marseille, France. E-mail: daeron@pasteur.fr

Published by AAAS

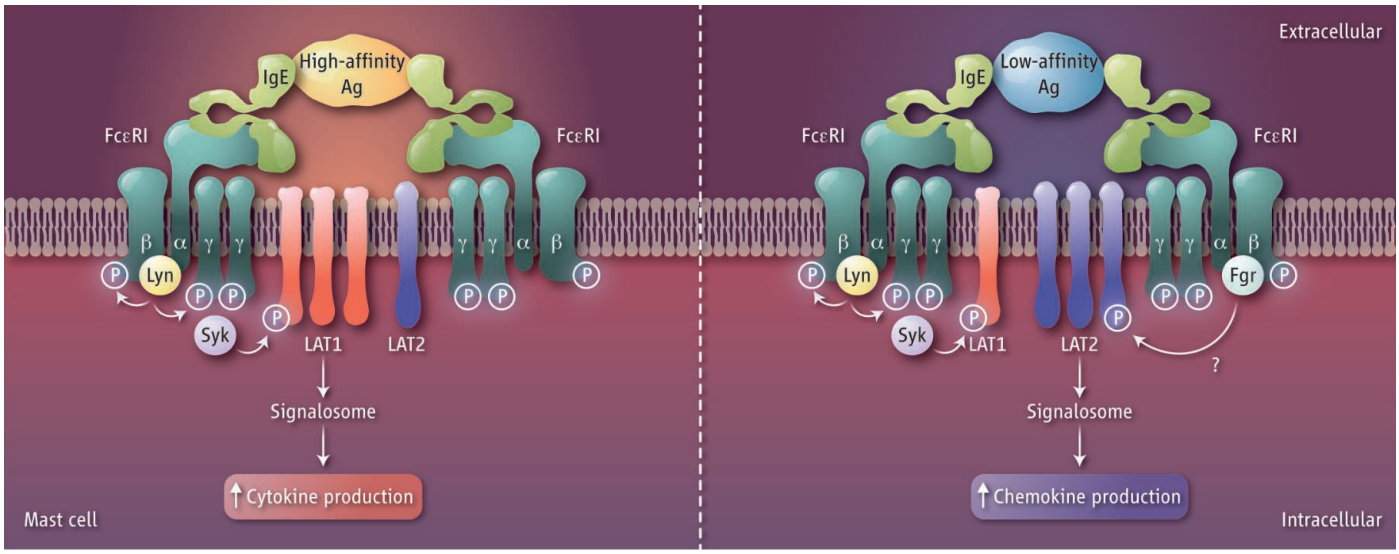

CREDIT: H. MCDONALD/*SCIENCE*

distal signals are generated and genes are differentially transcribed.

Two Src kinases are thought to initiate FcεRI signaling. Fyn phosphorylates the cytosolic adapter Gab2, enabling the recruitment of phosphatidylinositol 3-kinase (*4*). Lyn phosphorylates FcRβ and FcRγ ITAMs, enabling the recruitment of the tyrosine kinase Syk. Syk subsequently phosphorylates the many tyrosines of the transmembrane adapters LAT1 and LAT2 that nucleate the FcεRI signalosome. Although LAT1 (*5*) and LAT2 (*6*) each generate a mixture of positive and negative signals, the two adapters play antagonistic roles: LAT1 positively regulates, whereas LAT2 negatively regulates FcεRI signaling (*7*). The molecular basis of this antagonism is poorly understood.

Suzuki *et al*. compared the effects of a high-affinity antigen [dinitrophenyl-caproate-Fab (DNP)] and of a low-affinity antigen [2-dinitrophenyl-caproate-Fab (2NP)] that are recognized by the same IgE, at concentrations that induce comparable FcεRI phosphorylation in cultured mouse mast cells. As expected, DNP triggered more robust Lyn-Syk-LAT1–dependent signals than 2NP, leading to an increase in the release of a granular enzyme (β-hexosaminidase), the production of a proinflammatory lipid (leukotriene C4), and the secretion of cytokines (tumor necrosis factor and interleukins 6 and 13). By contrast, 2NP induced more chemokine secretion [chemokine motif ligand (CCL) 2, 3, and 4]. Unexpectedly, LAT2 was more phosphorylated upon stimulation by 2NP than by DNP, and the adapter colocalized with FcεRI. Another Src kinase, Fgr, colocalized with FcεRI and could enhance LAT2 phosphorylation. Chemokine secretion was impaired by either Fgr or LAT2 deficiency, whereas degranulation was increased. DNP induced passive cutaneous anaphylaxis (a reaction characterized by increased permeability of blood vessels in the skin) of a greater magnitude than did 2NP. Infiltration of the dermis that follows passive cutaneous anaphylaxis was enriched in neutrophils in response to DNP, but was enriched with monocytes and macrophages in response to 2NP. Thus, the Src kinases that initiate FcεRI signaling differentially control the use of LAT1 and LAT2, which in turn determines the relative abundance of cytokines and chemokines that are produced. This ultimately regulates the cell types that contribute to inflammatory reactions.

Early and late signals triggered by FcεRI are tightly controlled. Early signals depend on antigen affinity through kinetic proofreading. Late signals are controlled by the lipid phosphatase SHIP1 (*8*). How SHIP1 is recruited into FcεRI signalosomes is unclear, but SHIP1 phosphorylation (a consequence of its membrane recruitment) increases with the concentration of antigen (*9*). SHIP1-dependent negative regulation therefore depends on mechanisms that sense the extent of FcεRI aggregation. Suzuki *et al*. unravel an additional mechanism that controls the quality of mast cell responses. Thus, distinct mechanisms sense the concentration and the affinity of antigen and concur to control FcεRI-dependent mast cell activation both quantitatively and qualitatively.

FcεRI resembles antigen receptors expressed by B and T cells, whose signaling depends on the affinity of their interaction with antigen. Kinetic proofreading may in part account for differences in the magnitude and in the quality of T (*10*) and B (*11*) cell responses. No LAT1-LAT2 shift can occur in lymphocytes that express one adapter only (LAT1 in T cells, LAT2 in B cells). Many other cells besides mast cells, including natural killer cells, macrophages, neutrophils, and platelets, express both adapters. All express receptors for the Fc portion of IgG (FcγR) that use the same ITAM-dependent signaling as FcεRI when engaged by antigen-antibody complexes. Like mast cells, they have a wide functional repertoire and they contribute to both protective immunity and inflammatory diseases. One expects the LAT1-LAT2 balance to also control FcγR signaling in these cells. The identification of mechanisms that affect this balance is a key to understanding the protective and pathogenic effects of immune responses, and consequently to designing new therapeutic tools with increased efficacy and decreased toxicity.

Receptor discrimination. Allergy-evoking antigens (Ag), depending on their affinities for IgE antibodies, can elicit different mast cell responses by coupling the IgE receptor (FcεRI) with different Src family kinases (Lyn and/or Fgr). This results in differential use of the adapter proteins LAT1 and LAT2, which promote preferentially cytokine- or chemokine-driven responses, respectively.

References

1. R. Suzuki *et al*., *Science* **343**, 1021 (2014); 10.1126/science.1246976.
2. C. Torigoe, J. K. Inman, H. Metzger, *Science* **281**, 568 (1998).
3. Z. J. Liu, H. Haleem-Smith, H. Chen, H. Metzger, *Proc. Natl. Acad. Sci. U.S.A.* **98**, 7289 (2001).
4. V. Parravicini *et al*., *Nat. Immunol.* **3**, 741 (2002).
5. O. Malbec *et al*., *J. Immunol.* **173**, 5086 (2004).
6. M. Zhu, Y. Liu, S. Koonpaew, O. Granillo, W. Zhang, *J. Exp. Med.* **200**, 991 (2004).
7. J. Rivera, *Trends Immunol.* **26**, 119 (2005).
8. M. Huber *et al*., *Proc. Natl. Acad. Sci. U.S.A.* **95**, 11330 (1998).
9. K. Gimborn, E. Lessmann, S. Kuppig, G. Krystal, M. Huber, *J. Immunol.* **174**, 507 (2005).
10. R. A. Gottschalk *et al*., *Proc. Natl. Acad. Sci. U.S.A.* **109**, 881 (2012).
11. P. K. Tsourkas, W. Liu, S. C. Das, S. K. Pierce, S. Raychaudhuri, *Cell. Mol. Immunol.* **9**, 62 (2012).

10.1126/science.1251425

Published by AAAS

Powerful prototype. Microsoft's Kinect Sign Language Translator could become an important communication tool, but many other technologies have a long way to go before they are truly useful for people with disabilities.

CREDIT: MICROSOFT RESEARCH

HUMAN RIGHTS

Many Technologies Still Fall Short for People with Disabilities

Borrowing the motion-sensing technology of the Xbox gaming system, researchers at Microsoft are developing a sign language translator that captures a signing person's movements and translates them into spoken or written words. An on-screen avatar also translates spoken language into sign language.

The device is still in the prototype stage, but for deaf and hearing people who need to communicate with each other at work or in other aspects of their lives, "the implications of that are pretty immediate and amazing," said James Thurston, director of International Accessibility Policy at Microsoft.

Thurston described this advance at a recent AAAS event on disability rights, providing a powerful illustration of how technology can assist people with disabilities—and a reminder of how much progress remains to be made. Too often, the concept of accessibility is considered as an afterthought or used in ways that do not improve the lives of the people who need assistance, said co-panelist Vinton Cerf, vice president and chief Internet evangelist for Google.

Using a screen reader to navigate through a Web page, for instance, can be awkward and frustrating if audible navigation wasn't considered during the site's design.

"I consider it to be one of the most ironic and almost tragic facts that information technology [and] programmable devices probably have the most facile capacity to adapt to human need for assistance, and yet we have not done a very good job applying that technology for that purpose," said Cerf, who was the keynote speaker for a plenary session at the AAAS Science and Human Rights Coalition meeting, on 27 January. The 2-day event focused on the intersections between the human rights of persons with disabilities and the fields of science and technology.

Companies that are developing technologies for persons with disabilities are not doing it simply out of a desire to help. Clearly, there are social responsibility reasons for providing such technologies, Thurston said, but "Microsoft looks at it as a business opportunity" as well. About 15% of the world—approximately the population of China—is dealing with some form of disability.

Market demand has also increased due to the aging baby boomer population and to the implementation of Section 508, an amendment to the U.S. Rehabilitation Act that requires the government to develop or acquire only accessible technology. The features that make products more accessible are now another area over which companies can compete, Thurston said.

Change has come slowly, however. Technology developers still need to think more about how to integrate accessibility into applications early in the process, Cerf said. "To imagine that you can just overlay some accessibility pixie dust that makes a specific application work all right for a person with hearing impairment or a person with motor problems, I think, is overly optimistic."

Cerf praised Microsoft and Apple for their efforts in this field and admitted that at Google there was room for improvement. But he cited one "fundamentally critical" effort at his company to train every new engineer in accessibility methods.

Hiring engineers and scientists with disabilities and unique experiences would also benefit technology companies. The AAAS Entry Point! program, a partnership with government and industry, provides opportunities for students with disabilities to contribute to a diverse workforce. Ninety percent of alumni pursue graduate studies or employment in science or engineering fields. Partnerships have included NASA, IBM, Merck, Dow Chemical, Lockheed Martin, Ball Aerospace, L´Oréal, and university-based research programs.

On the other hand, more or improved technology should not be the only focus for disability rights, noted Eric Matthews, an advocacy associate at Disability Rights International, who spoke at the AAAS meeting about the need to end segregation for persons with disabilities. Instead of just supplying computers to an orphanage, for example, companies, donors, and nations should think more about how to use technology to get people out of segregated institutions and back with their families or placed in family-based care in the community. We need "to think about the ways that science can challenge the need for institutional care," Matthews said. *–Sarah Zielinski*

Downloaded from www.sciencemag.org on February 28, 2014

Solar Synthesis: Prospects in Visible Light Photocatalysis

Danielle M. Schultz and Tehshik P. Yoon*

READ THE FULL ARTICLE ONLINE
http://dx.doi.org/10.1126/science.1239176

Cite this article as D. M. Schultz, T. P. Yoon, *Science* **343**, 1239176 (2014).
DOI: 10.1126/science.1239176

Background: Interest in photochemical synthesis has been motivated in part by the realization that sunlight is effectively an inexhaustible energy source. Chemists have also long recognized distinctive patterns of reactivity that are uniquely accessible via photochemical activation. However, most simple organic molecules absorb only ultraviolet (UV) light and cannot be activated by the visible wavelengths that comprise most of the solar energy that reaches Earth's surface. Consequently, organic photochemistry has generally required the use of UV light sources.

Advances: Over the past several years, there has been a resurgence of interest in synthetic photochemistry, based on the recognition that the transition metal chromophores that have been so productively exploited in the design of technologies for solar energy conversion can also convert visible light energy into useful chemical potential for synthetic purposes. Visible light enables productive photoreactions of compounds possessing weak bonds that are sensitive toward UV photodegradation. Furthermore, visible light photoreactions can be conducted by using essentially any source of white light, including sunlight, which obviates the need for specialized UV photoreactors. This feature has expanded the accessibility of photochemical reactions to a broader range of synthetic organic chemists. A variety of reaction types have now been shown to be amenable to visible light photocatalysis via photoinduced electron transfer to or from the transition metal chromophore, as well as energy-transfer processes. The predictable reactivity of the intermediates generated and the tolerance of the reaction conditions to a wide range of functional groups have enabled the application of these reactions to the synthesis of increasingly complex target molecules.

Outlook: This general strategy for the use of visible light in organic synthesis is already being adopted by a growing community of synthetic chemists. Much of the current research in this emerging area is geared toward the discovery of photochemical solutions for increasingly ambitious synthetic goals. Visible light photocatalysis is also attracting the attention of researchers in chemical biology, materials science, and drug discovery, who recognize that these reactions offer opportunities for innovation in areas beyond traditional organic synthesis. The long-term goals of this emerging area are to continue to improve efficiency and synthetic utility and to realize the long-standing goal of performing chemical synthesis using the sun.

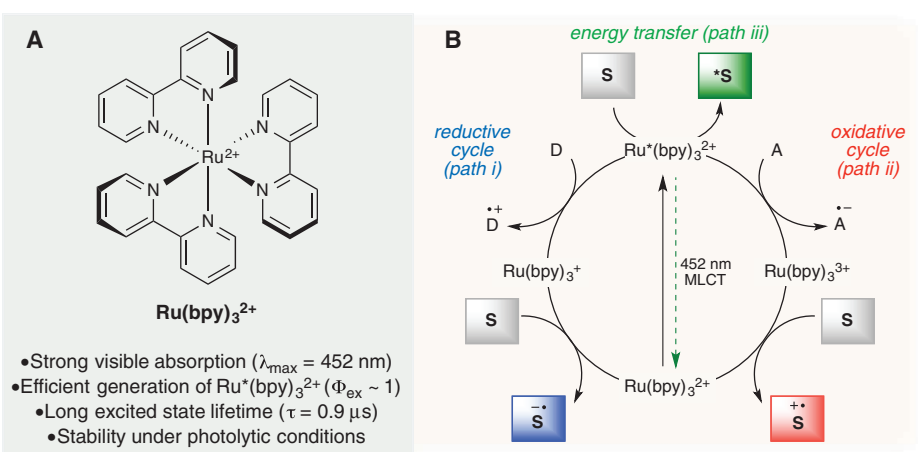

Visible light photocatalysis. (**A**) Transition metal photocatalysts, such as $Ru(bpy)_3^{2+}$, readily absorb visible light to access reactive excited states. (**B**) Photoexcited $Ru^*(bpy)_3^{2+}$ can act as an electron shuttle, interacting with sacrificial electron donors D (path i) or acceptors A (path ii) to yield either a strongly reducing or oxidizing catalyst toward organic substrates S. $Ru^*(bpy)_3^{2+}$ can also directly transfer energy to an organic substrate to yield electronically excited species (path iii). bpy, 2,2'-bipyridine; MLCT, metal-to-ligand charge transfer.

ARTICLE OUTLINE

Mechanisms of Visible Light Photocatalysis
Photogeneration of Organic Radicals
Photocatalytic Activation of Amines
Photogenerated Radical Ions
Triplet Alkenes
Conclusions and Outlook

ADDITIONAL RESOURCES

C. K. Prier, D. A. Rankic, D. W. C. Macmillan, Visible light photoredox catalysis with transition metal complexes: Applications in organic synthesis. *Chem. Rev*. **113**, 5322–5363 (2013).

J. M. R. Narayanam, C. R. J. Stephenson, Visible light photoredox catalysis: Applications in organic synthesis. *Chem. Soc. Rev*. **40**, 102–113 (2011).

T. P. Yoon, M. A. Ischay, J. Du, Visible light photocatalysis as a greener approach to photochemical synthesis. *Nat. Chem*. **2**, 527–532 (2010).

JACS Beta podcast: http://pubs.acs.org/JACSbeta/coverartpodcasts/JACS-Podcast-October-2009.m4a.

RELATED ITEMS IN *SCIENCE*

M. T. Pirnot, D. A. Rankic, D. B. C. Martin, D. W. C. MacMillan, Photoredox activation for the direct β-arylation of ketones and aldehydes. *Science* **339**, 1593–1596 (2013).

D. A. Nicewicz, D. W. C. MacMillan, Merging photoredox catalysis with organocatalysis: The direct asymmetric alkylation of aldehydes. *Science* **322**, 77–80 (2008).

A. McNally, C. K. Prier, D. W. C. MacMillan, Discovery of an α-amino C–H arylation reaction using the strategy of accelerated serendipity. *Science* **334**, 1114–1117 (2011).

Department of Chemistry, University of Wisconsin–Madison, 1101 University Avenue, Madison, WI 53706, USA.
*Corresponding author. E-mail: tyoon@chem.wisc.edu

Solar Synthesis: Prospects in Visible Light Photocatalysis

Danielle M. Schultz and Tehshik P. Yoon*

Chemists have long aspired to synthesize molecules the way that plants do—using sunlight to facilitate the construction of complex molecular architectures. Nevertheless, the use of visible light in photochemical synthesis is fundamentally challenging because organic molecules tend not to interact with the wavelengths of visible light that are most strongly emitted in the solar spectrum. Recent research has begun to leverage the ability of visible light–absorbing transition metal complexes to catalyze a broad range of synthetically valuable reactions. In this review, we highlight how an understanding of the mechanisms of photocatalytic activation available to these transition metal complexes, and of the general reactivity patterns of the intermediates accessible via visible light photocatalysis, has accelerated the development of this diverse suite of reactions.

The year 2012 marked the centennial anniversary of a now-famous article titled "The photochemistry of the future," in which the pioneering chemist Giacomo Ciamician challenged the scientists of his day to imagine a chemical industry that could synthesize chemicals in the same manner that plants do—by using sunlight as a safe, inexpensive, abundant, and renewable source of chemical potential (*1*). In the past several decades, chemists have made remarkable strides toward increasingly efficient conversion of solar energy into electricity and chemical fuels (*2*, *3*). The use of solar energy in the synthesis of value-added, structurally complex organic compounds has, however, been considerably less well investigated, and Ciamician's grand vision has yet to be fully realized (*4*, *5*).

The photochemical synthesis of complex organic molecules is challenging for several reasons. First, organic molecules tend to absorb only photons in the ultraviolet (UV) region that are not abundant in the solar radiation that penetrates the atmosphere (Fig. 1). This has constrained the rate of development in large-scale industrial photochemical synthesis, because energy-efficient sources of UV light have only recently become available. Moreover, UV photons are quite high in energy, on the order of a C–C bond, and can cause considerable unproductive decomposition reactions to occur, particularly when relatively weak bonds are present or when the target compounds possess substantial structural complexity. There are many notable examples of classic syntheses of complex targets that use photochemical key steps, but photochemical synthesis as a whole has long been considered to be the purview of a small community of specialists rather than a core component of the standard synthetic repertoire (*6*, *7*).

Department of Chemistry, University of Wisconsin–Madison, 1101 University Avenue, Madison, WI 53706, USA.

*Corresponding author. E-mail: tyoon@chem.wisc.edu

Recently, there has been a dramatic renaissance of interest in photochemistry among synthetic organic chemists. This development has been inspired in large part by the recognition that the same transition metal complexes that have been so productively used to convert sunlight to electrochemical potential can also be used to catalyze useful and unique organic reactions that are initiated by visible light irradiation (*8*, *9*).

The objective of this review is to explain the features of visible light photocatalysis that have captured the attention of synthetic chemists. First, we will briefly outline the diverse mechanisms by which transition metal photocatalysts can be used to activate organic compounds toward subsequent transformations. Then, we will show that transition metal photocatalysts have been used to generate a wide range of highly reactive intermediates (radicals, amine radical cations, radical ions, and triplet alkenes), each of which display distinctive patterns of reactivity that can be used to access different classes of complex organic structures.

Mechanisms of Visible Light Photocatalysis

A wide variety of transition metal complexes with varying photochemical properties have been examined as photocatalysts for synthetic applications. The majority of these have been ruthenium and iridium complexes, although copper and gold species have also recently been investigated in this context (*10*, *11*). Figure 2 summarizes the key photochemical properties of $Ru(bpy)_3^{2+}$ (bpy is 2,2′-bipyridine) (**1**), the most well-studied transition metal complex in the context of both synthetic photocatalysis as well as solar energy conversion. This complex exhibits a strong, broad absorbance in the visible range that results in the production of a long-lived excited state (*12*, *13*).

This photoexcited complex is both a stronger oxidant and a stronger reductant than its corresponding ground state; remarkably, both electrochemical potentials lie within a range that can perform useful chemical work. Thus, photoactivation of **1** has most commonly been used to drive processes initiated by single-electron transfer. This property of **1** has been instrumental in the development of many strategies for the conversion of solar energy into electricity and

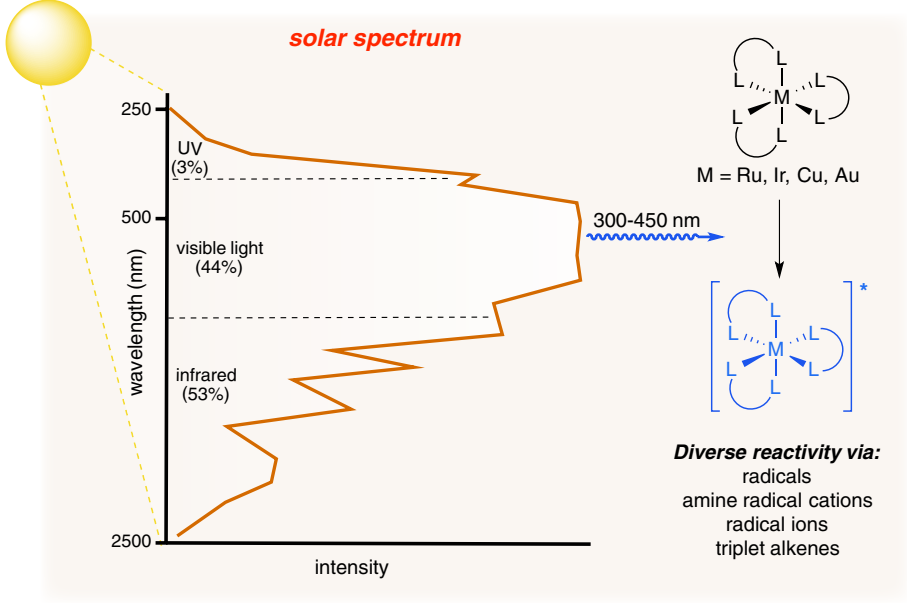

Fig. 1. Converting solar energy into chemical potential. Certain transition metal complexes are strong absorbers of visible light and can thereby harness solar energy for chemical synthesis, particularly by driving radical-mediated transformations from their photoexcited states. Solar spectrum adapted from (*73*).

into electrochemically generated chemical fuels (*14*–*16*). In the context of organic synthesis, $Ru^*(bpy)_3^{2+}$ can initiate the one-electron reduction of a variety of electron-deficient substrates, or it can effect the one-electron oxidation of electron-rich substrates. In other words, the photoinduced electron-transfer properties of **1** can easily be coupled to electrochemically induced transformations of organic molecules (Fig. 2B, paths a and b).

Alternatively, $Ru^*(bpy)_3^{2+}$ can directly transfer energy to a suitable organic substrate (Fig. 2B, path c) (*12*). The resulting electronically excited organic compound reacts quite differently than it would in the ground state. These high-energy intermediates are often useful for reactions that construct strained or otherwise structurally unusual molecular scaffolds that are difficult to assemble by nonphotochemical means (*17*, *18*).

Many terms have been used to describe these various modes of photochemical activation. The photoactivation of organic molecules by electron-transfer processes has been variously referred to as photoinduced electron-transfer (PET) sensitization or, more recently, as photoredox catalysis. Similarly, the indirect generation of electronically excited states of organic substrates has been called photosensitization or energy-transfer photocatalysis. We prefer to use the blanket term "photocatalysis" to describe both modes of activation, because the unambiguous determination of the mechanism of a photochemical reaction can be challenging and the use of a single term highlights the similarities between these two approaches to photochemical synthesis (*19*).

Photogeneration of Organic Radicals

Much of the activity in visible light photocatalysis over the past 5 years has concerned reactions of photogenerated organic radicals (Fig. 3A). The photocatalytic reductive dehalogenation of α-haloketones with dihydroacridine in the presence of **1** was first described by Fukuzumi in 1990; the key intermediate in this transformation is a highly electrophilic α-ketoradical generated by reduction of the bromide by photoexcited $Ru^*(bpy)_3^{2+}$ (Fig. 3B) (*20*). This strategy for the photoreductive generation of highly reactive radical intermediates from alkyl halides is an intriguing complement to more-established methods for the production of carbon-centered radical species; in particular, many of the most common methods for the thermal formation of organic radicals involve highly toxic tin or pyrophoric boron compounds (*21*). Therefore, the ability to access the diverse reactivity of electrophilic radicals via visible light activation is highly attractive.

The synthetic potential of this method for photochemical radical generation was not fully recognized until 2008, when it was exploited by MacMillan to develop an enantioselective α-alkylation of aldehydes with organocatalyst **4** (shown in Fig. 3C) (*22*). This transformation is built on MacMillan's long-standing interest in enantioselective reactions of achiral aldehydes involving the in situ formation of chiral enamines by condensation with secondary amine organocatalysts (*23*–*25*). MacMillan showed that a range of α-ketoradicals, generated from the photoreduction of α-halocarbonyl compounds with **1**, reacts efficiently and with excellent stereocontrol with chiral enamines. Although this initial work focused on the formation of radicals from α-haloketones and α-haloesters, MacMillan has since reported conditions for the formation of highly electrophilic benzyl and trifluoromethyl radicals from the corresponding alkyl halides as well (*26*, *27*).

The direct enantioselective catalytic α-alkylation of carbonyl compounds is synthetically highly useful. An arguably broader impact of MacMillan's initial report was the demonstration that photocatalytic reduction of alkyl halides can be used to access the general complexity-building reactivity of electrophilic organic radicals. This strategy has subsequently been exploited by many research groups and has resulted in the development of a diverse range of new chemical transformations. For example, Stephenson used the reductive dehalogenation of activated alkyl and aryl halides to effect photocatalytic alkylation of heteroarenes (*28*). This is an exceptionally mild and convenient method to construct an important bond type, and Stephenson demonstrated its utility in the context of the total synthesis of the cytotoxic indole alkaloid (+)-gliocladin C (Fig. 3D) (*29*).

The generation of a wide variety of alkyl and aryl radicals by photoreduction of the corresponding halides has been a consistent theme of Stephenson's research program (*30*). An important general feature of this work, and indeed of many of the recent reactions involving photoredox catalysis, is the ready availability of a large number of known photoactive transition metal complexes with well-characterized photochemical and electrochemical properties. Thus, more strongly reducing photocatalysts can be used to compensate for organohalide substrates that are more difficult to reduce than α-haloketones. Stephenson applied iridium complex **2**, which is a significantly more strongly reducing photocatalyst than **1**, in the reduction of simple alkyl and aryl iodides and showed that they participate in synthetically powerful radical cyclization and dehalogenation processes (Fig. 3E) (*31*).

The utility of photocatalytic radical reactions has also been recognized in applications beyond small-molecule synthesis. Recently, Hawker reported an efficient method for photocatalytic atom-transfer radical polymerization (ATRP) that enables the light-controlled synthesis of poly(methylmethacrylate) polymers with **2** (*32*) (Fig. 4A). This reaction showed the same high practical convenience, functional group tolerance, and living nature as other conventional methods for ATRP. However, in contrast to standard copper-initiated reactions, Hawker's method is

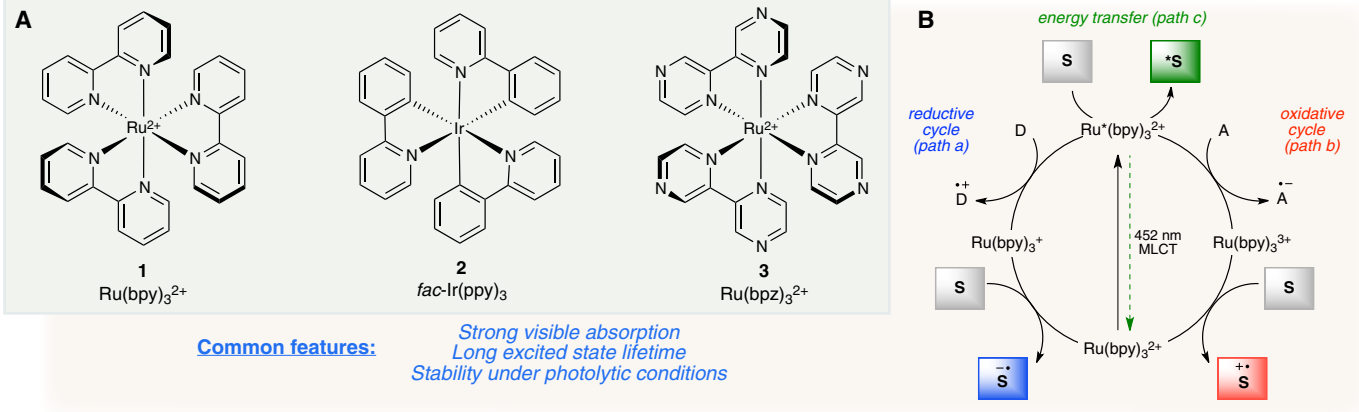

Fig. 2. Visible light photocatalysis. (**A**) Ruthenium and iridium complexes, such as **1** to **3**, readily absorb visible light and can mediate numerous photochemical transformations (*12*, *13*). (**B**) Photoexcited $Ru^*(bpy)_3^{2+}$ can act as an electron shuttle, interacting with sacrificial electron donors D (path a) or acceptors A (path b) to yield either a strongly reducing or a strongly oxidizing catalyst toward organic substrates S. $Ru^*(bpy)_3^{2+}$ can also directly transfer energy to an organic substrate to yield electronically excited species (path c).

subject to a high degree of temporal control; polymerization occurs only under constant irradiation with visible light, but chain growth can be reinitiated after several hours in the dark without loss of the living nature of the polymerization. Moreover, this approach provides a route for block copolymer synthesis, because turning off the light source allows a new monomer to be introduced and incorporated into the growing chain upon reapplication of the light source.

Photogenerated electrophilic radicals have also proven to be important in the development of reactions involving organometallic species. Sanford recently reported new methods for Pd-catalyzed C–H functionalization of arenes and Cu-catalyzed trifluoromethylation of organoboronic acids (Fig. 4B) (*33*, *34*), both of which rely on **1** to generate the key electrophilic radical from

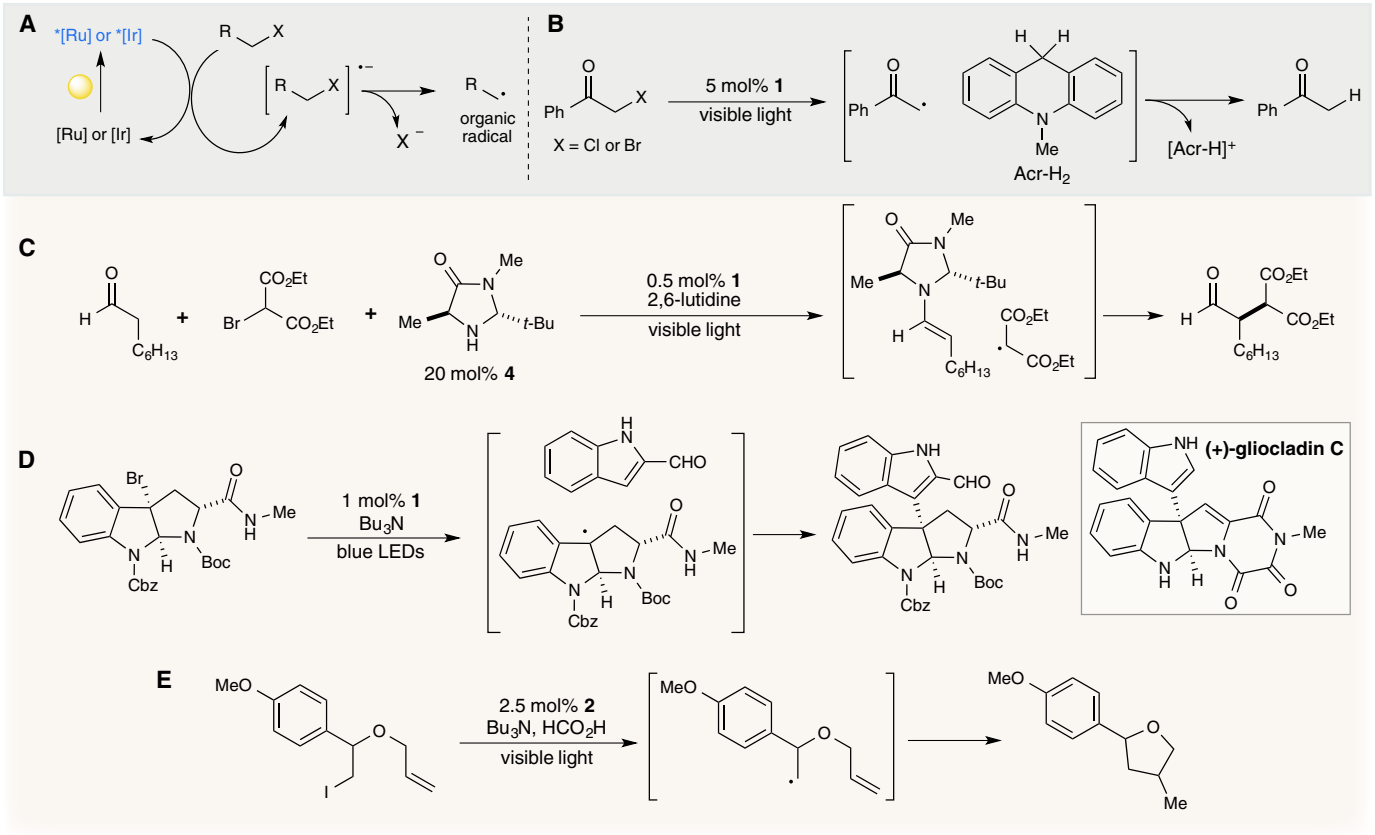

Fig. 3. Photoreduction of alkyl halides for radical reactions. (**A**) Photoexcited ruthenium or iridium complexes can reduce electron-deficient alkyl halides to radical ions that readily undergo fragmentation to an electrophilic organic radical. (**B**) This reactivity was first explored by Fukuzumi in the dehalogenation of α-halocarbonyl compounds (*20*) and later revisited by MacMillan (**C**) in the context of an asymmetric α-alkylation of aldehydes through the merging of photo- and organocatalysis (*22*). (**D**) The generation of radicals through visible light photoreduction of alkyl halides is mild and selective, as demonstrated in the synthesis of (+)-gliocladin C (*29*). (**E**) The range of alkyl and aryl halides susceptible to photoreduction can be extended by tuning the photoelectrochemical properties of the catalyst (*30*). Acr-H_2, 9,10-dihydro-10-methylacridine; Boc, *tert*-butyloxycarbonyl; Bu, butyl; Cbz, carbobenzyloxy; Et, ethyl; LED, light-emitting diode; Me, methyl; Ph, phenyl; *t*-Bu, *tertiary*-butyl.

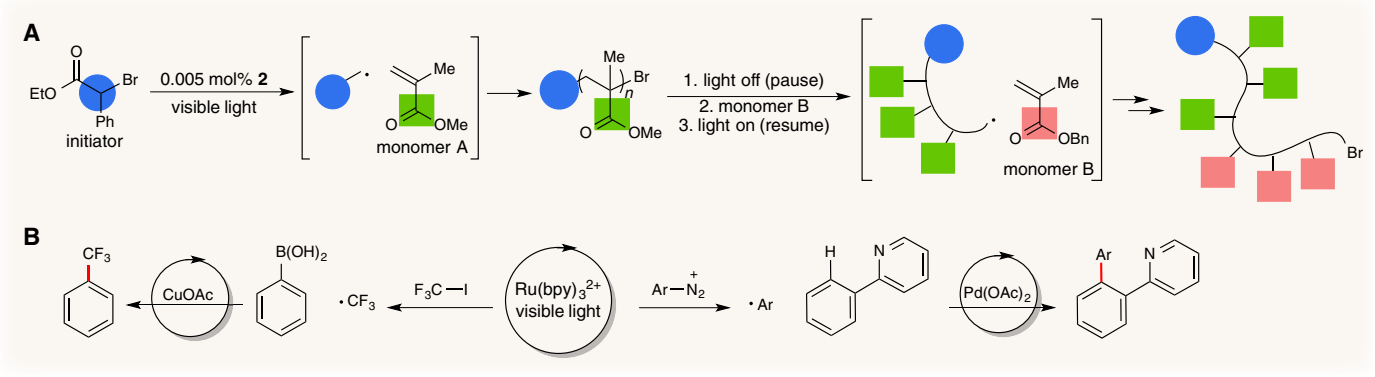

Fig. 4. Applications of photocatalysis in polymerization and organometallic chemistry. (**A**) The ability to temporally control radical formation under photocatalytic conditions has important benefits in ATRP reactions (*32*). Turning off the light source halts polymerization to allow a new monomer to be added (monomer B) before polymerization is reinitialized. (**B**) Likewise, photogenerated radical species can be intercepted with either copper or palladium organometallic complexes in cocatalytic transformations (*33*, *34*). Ar, aryl; Bn, benzyl; OAc, acetate.

photoreduction of an aryl diazonium salt or from CF_3I, respectively. These radicals are proposed to interact with an organometallic intermediate to promote the formation of new C–C bonds.

The ability of photocatalysts to generate organic radicals by selective reduction of carbon-halogen bonds has thus already had a substantial impact in the area of radical chemistry. Many known, synthetically valuable radical reactions can be conducted under exceptionally mild, tin-free conditions by exploiting the ability of transition metal photocatalysts to generate radical species by photoinduced electron transfer.

Photocatalytic Activation of Amines

Amines are common additives in visible light photocatalysis and are generally used as reductants. They assist catalysis either by directly reducing the photoexcited $Ru^*(bpy)_3^{2+}$ catalyst to generate an even more strongly reducing $Ru(bpy)_3^{+}$ complex or by turning over the oxidized $Ru(bpy)_3^{3+}$ photocatalyst after a direct substrate-reduction step (Fig. 2). Several recent reviews have described both mechanisms in detail; however, in either scenario, the amines have generally been sacrificial or catalytic co-reductants in photoredox processes that are not themselves incorporated into the synthetic target (*8*, *35*).

Motivated by the important role that nitrogen-containing compounds play in the chemistry of bioactive small molecules, researchers have recently explored the amine radical cations generated by photocatalytic one-electron oxidation of tertiary amines as substrates for synthetic modification (*36*). One of the most characteristic features of amine radical cations is an observed increase in the acidity of the C–H bond adjacent to the nitrogen, deprotonation of which results in the formation of nucleophilic α-amino radicals that are capable of reacting with a diverse range of electrophilic reaction partners (*37*) (Fig. 5A). The net result of this type of transformation can be viewed as a photochemically induced C–H functionalization of the α-position of amines, an important reaction that has been a long-standing synthetic challenge (*38*, *39*).

For example, Pandey and Reiser described the radical functionalization of nitrogen-containing heterocycles using this approach (*40*). A variety of tetrahydroisoquinolines readily undergoes photooxidation by either **1** or $Ir(ppy)_2(dtbbpy)^+$ (ppy is 2-phenylpyridine; dtbbpy is 4,4′-di-*tert*-butyl-2,2′-bipyridyl) (**5**); the resulting amine radical cation undergoes facile deprotonation to produce the corresponding α-amino radical, which was shown to participate in C–C bond-forming additions to a variety of enone electrophiles in good yields (Fig. 5B). Our laboratory has also studied this transformation, and we reported a mechanistic analysis of this reaction that verifies the nucleophilic nature of the intermediate radical and shows that this reaction can be accelerated by Brønsted acid cocatalysts (*41*).

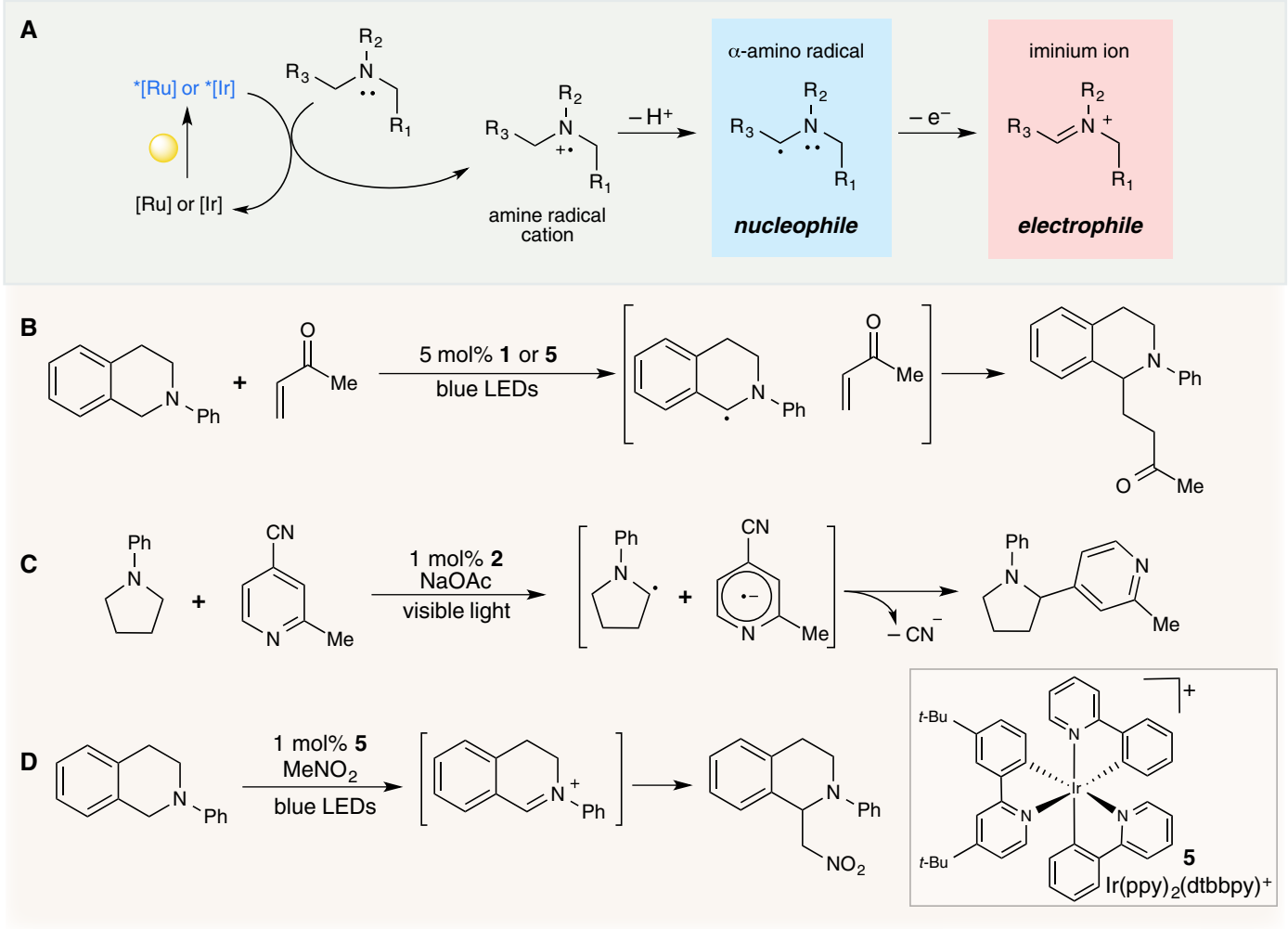

Fig. 5. Diverse reactivity of α-amino radical cations. (**A**) Tertiary amines readily undergo photooxidation to yield a highly versatile amine radical cation intermediate, which can be transformed into a nucleophilic (α-amino radical) or electrophilic (iminium ion) species. (**B**) Pandey and Reiser were able to functionalize tetrahydroisoquinolines through the formation of an α-amino radical that readily intercepted various electrophiles (*40*). (**C**) Through the use of a more strongly reducing iridium photocatalyst (**2**), MacMillan and co-workers were able to intercept α-amino radicals with cyanoarenes, overall providing a route for α-acylating amines (*42*). (**D**) Depending on the reaction conditions, α-amino radicals can undergo further oxidation to electrophilic iminium ions that can subsequently be trapped with nucleophilic reagents (*43*).

MacMillan reported a more complex application of this reactivity to enable the photocatalytic α-arylation of tertiary amines by using electron-deficient cyanoarenes (Fig. 5C) (*42*). The proposed mechanism involves initial photoreduction of the cyanoarene component by photoexcited **2**, coupled with a subsequent oxidation of the amine. Deprotonation of the amine radical cation affords an α-amino radical, which combines with the arene radical anion to expel cyanide and produce the α-arylated amine. The scope of this reaction with respect to both the tertiary amine and the cyanoarene proved to be quite broad, enabling the synthesis of an important class of structures commonly found in bioactive compounds.

The photooxidation of amines has also been used to produce iminium cations, which result formally from a second one-electron oxidation of the α-amino radicals discussed above. These iminium cation intermediates are strong electrophiles that provide reactivity complementary to the nucleophilic reactions of α-amino radicals. Stephenson reported a method for aerobic photocatalytic oxidation of tetrahydroisoquinolines in nitromethane solvent using **5**; under these conditions, the iminium cation is trapped by the solvent to afford the product of formal C–H functionalization of the benzylic position adjacent to the amine (*43*) (Fig. 5D). Subsequently, Stephenson found that a broader range of nucleophiles could be added to these iminium cations in a two-step process involving $BrCCl_3$ as a terminal oxidant (*44*). Under these conditions, the tetrahydroisoquinolines could be substituted with a variety of carbon-based nucleophiles, including copper acetylenes, silyl enol ethers, allyl silanes, and electron-rich heteroarenes.

Depending on reaction conditions, the same family of transition metal photocatalysts has thus been used to generate both nucleophilic α-amino radicals and highly electrophilic iminium cations, and the variety of reactions accessible via photochemical formation of these intermediates is consequently quite broad (*45*, *46*). Moreover, the ability to rapidly modify the environment around an amine holds particular promise in the discovery of structurally complex new bioactive compounds, because nitrogen-containing functional groups are very often important in the binding of a small molecule to a biological target (*47*).

Photogenerated Radical Ions

Compared with the chemistry of neutral organic radicals and amine radical cations, reactions that exploit the reactivity of alkene radical ions have enjoyed substantially fewer applications in organic synthesis (*48*–*50*). The most common methods for the generation of these reactive intermediates have involved either stoichiometric heavy metal oxidants (*51*–*53*) or electrochemical activation (*54*, *55*), which may explain some of the reluctance of chemists to fully explore the synthetic potential of these reactions. Nevertheless, radical ion intermediates exhibit reactivity profiles that are quite distinctive; reactions involving these charged odd-electron species can result in the formation of products that are difficult to assemble by any other means.

Our group has been particularly interested in exploring cycloaddition reactions of alkene radical ion intermediates, given the efficiency with which this class of reactions can construct stereochemically and structurally complex carbocyclic structures from readily available starting materials (*56*, *57*). In 2008, we demonstrated that aryl enones are readily reduced to the corresponding radical anions upon irradiation in the presence of **1**; these photogenerated intermediates can then participate in efficient [2+2] intramolecular cycloaddition reactions (*58*). The extension of this method to intermolecular cycloadditions took advantage of the ability to selectively reduce aryl enones in the presence of less-conjugated Michael acceptors; thus, high selectivity for crossed [2+2] cycloadducts could be achieved for reactions with unsaturated ketones, esters, and thioesters, providing an approach to the synthesis of a broad range of unsymmetrically substituted cyclobutanes (Fig. 6A) (*59*). The same crossed [2+2] cycloadditions could not be effected by direct photoexcitation with UV light, because the electronically excited triplet enones preferentially undergo alkene isomerization processes rather than productive cycloaddition.

Inspired by the ease with which radical anions can be generated by visible light photocatalysis, we have also explored other new reactions involving these reactive intermediates. For example,

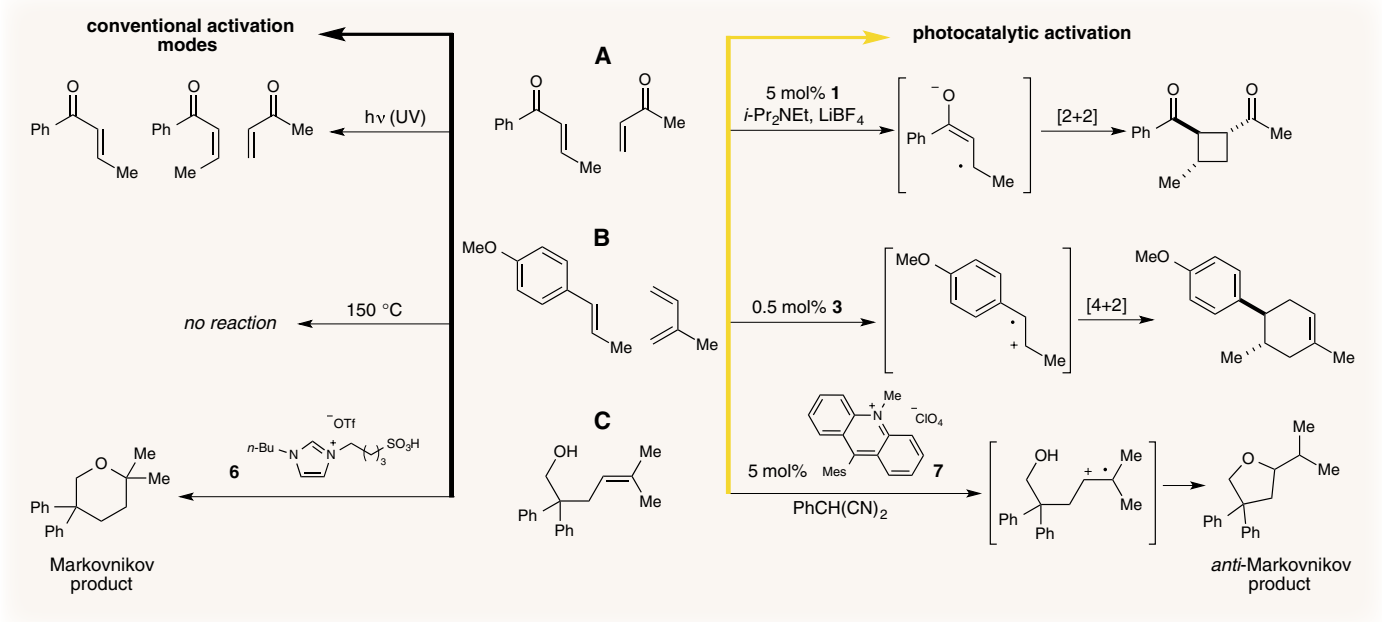

Fig. 6. Unique reactivity of photogenerated radical ions. Radical ions are underused reactive intermediates that can participate in otherwise inaccessible bond formations. (**A**) Yoon has demonstrated that the photocatalytic activation of enones produces radical anions that readily participate in [2+2] cycloadditions to afford cyclobutane products that are not generated upon UV irradiation (*59*). (**B**) Likewise, the photooxidation of electron-rich styrenes yields an electron-deficient radical cation that undergoes facile [4+2] cycloaddition with an electron-rich diene, a reaction that is disfavored under thermal conditions (*62*). (**C**) Radical ion intermediates also afford products with atypical atom connectivities, such as the exclusive formation of the less common anti-Markovnikov product under photochemical conditions (*63*). *i*-Pr, *iso*-propyl; Mes, mesityl; *n*-Bu, normal-butyl; OTf, trifluoromethanesulfonate.

we recently reported that aryl cyclopropyl ketones can engage in [3+2] cycloadditions via formation of radical anion intermediates (*60*). This reaction involves the photoinduced reduction of the aryl cyclopropyl ketone moiety followed by fragmentation to afford a distonic radical anion. This intermediate undergoes a series of subsequent intramolecular bond-forming reactions with a pendant alkene to afford cyclopentane products in good yield.

The ability of photoactive transition metal complexes to promote both oxidation and reduction processes has also enabled the development of photocatalytic cycloadditions involving alkene radical cations. The scope of these reactions is complementary to that of radical anion reactions; one-electron oxidations are most facile with electron-rich alkenes. For example, electron-rich styrenes undergo facile one-electron photooxidation in the presence of ruthenium photocatalysts. We showed that the resulting alkene radical cations undergo efficient [2+2] cycloaddition with a variety of alkene partners to afford cyclobutane products with high diastereoselectivity (*61*).

[4+2] Cycloadditions of electron-rich alkenes can also be promoted by one-electron photooxidation (Fig. 6B) (*62*). These reactions provide a valuable alternative to thermal Diels-Alder cycloaddition reactions, which have been applied to the synthesis of complex carbocyclic organic structures for decades. In particular, thermal [4+2] cycloadditions generally proceed efficiently only when one component of the reaction is electron-rich and the other is electron-deficient such that the frontier molecular orbitals are close in energy; cycloadditions between two electron-rich partners are generally quite slow. However, one-electron oxidation of electron-rich styrenes using $Ru(bpz)_3^{2+}$ [bpz is 2,2′-bipyrazine] (**3**) reverses their electronic character and results in the generation of intrinsically electron-deficient radical cations. These can subsequently undergo rapid [4+2] cycloaddition with simple dienes to afford the formal products of electronically mismatched Diels-Alder cycloadditions. Predictably, under forcing thermal conditions no [4+2] cycloaddition is observed, further highlighting the unique reactivity accessible through photogenerated radical ion intermediates.

Nicewicz has also investigated new reactions of photogenerated alkene radical cations, focusing on the addition of alcohols to olefins to form heterocyclic products (Fig. 6C) (*63*). This type of bond construction commonly relies on acid catalysts, such as **6**, that direct bond formation to the most substituted carbon of the alkene to yield the Markovnikov product. However, in Nicewicz's work, the cyclization process is promoted via photooxidation by a mesityl-substituted acridinium salt **7** originally reported by Fukuzumi (*64*, *65*). This organic photocatalyst has many of the same properties as ruthenium and iridium complexes, including strong visible light absorption and a long excited-state lifetime, but its photoexcited state is sufficiently oxidizing to react with trisubstituted aliphatic alkenes (*65*, *66*). The resulting alkene radical cations can undergo nucleophilic attack by a tethered alcohol; however, because of the polarization of the radical cation, the regioselectivity complements that of acid-catalyzed reactions and results in the exclusive formation of the anti-Markovnikov addition product. Nicewicz has also reported the same regioselectivity in additions of nitrogen nucleophiles to these radical cations (*67*). Although many methods for the Markovnikov functionalization of alkenes are known and widely exploited in synthesis, few methods for the direct anti-Markovnikov addition of nucleophiles to olefins have been reported (*68*). Thus, the chemistry of photogenerated radical cations offers a solution to a long-standing problem of great synthetic importance.

Triplet Alkenes

Almost all of the recent investigations in visible-light photocatalysis have involved photoredox processes that activate a variety of organic substrates by single-electron oxidation or reduction. Thus, the success of these reactions depends on the relative electrochemical properties of the substrates and photoexcited catalysts; reactions involving thermodynamically unfavorable electron-transfer processes are unlikely to occur at efficient rates. However, the transition metal complexes that have proven to be so powerful in the development of photoredox reactions can also be involved in energy-transfer processes that generate highly reactive organic molecules in electronically excited states. In these cases, successful activation depends on the relative triplet-state energies of the catalyst and substrate and not on redox potentials (Fig. 7A).

For instance, our group recently reported that styrenes undergo efficient [2+2] cycloaddition via energy transfer when irradiated in the presence of the iridium complex **8** (Fig. 7B) (*69*). This method involves the formation of electronically excited styrenes in their triplet state, which undergo [2+2] cycloaddition reactions that are superficially similar to the radical cation reactions discussed in the previous section. However, because the mode of substrate activation involves energy transfer rather than electron transfer, the scope of styrenes that participate in this reaction is considerably broader. Highly electron-deficient styrenes and heterostyrenes that cannot be easily photooxidized nevertheless undergo facile cycloaddition.

This alternative approach to visible light photocatalysis is intriguing because it offers convenient access to the reactivity of organic compounds in electronically excited states by using photons of much lower energy than those required for direct photoexcitation. In the absence of sensitization, short-wavelength UV photons are required to excite simple styrenes to a singlet state (black dashed line in Fig. 7A), which then relaxes to the triplet. Because the excited singlet state is more energetic (~115 kcal/mol) than many common bonds found in organic molecules, including C–C bonds, reactions requiring irradiation with these high-energy UV photons often suffer from competitive homolytic photodecomposition processes. Therefore, triplet sensitization using transition metal photocatalysts that are photoexcited with

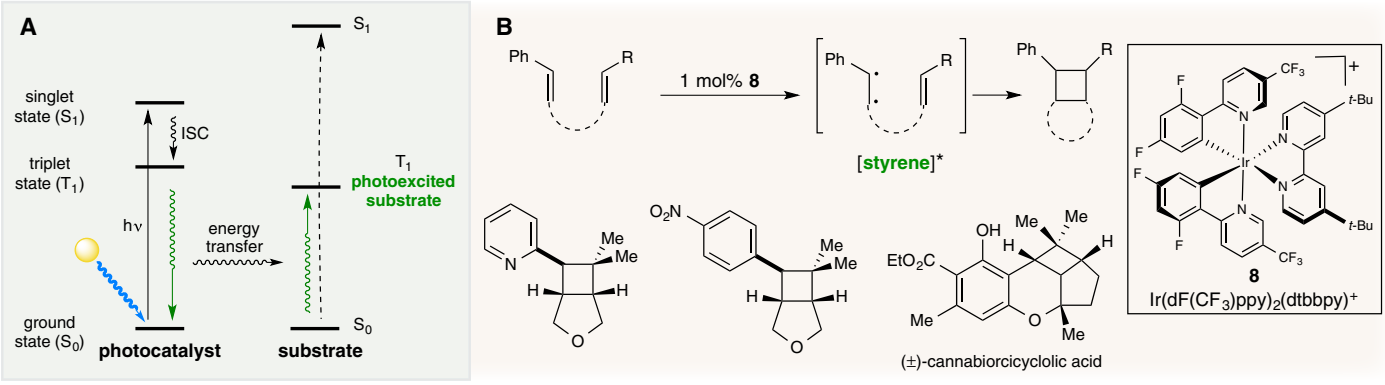

Fig. 7. Visible light photocatalyzed triplet sensitization. (**A**) Visible light–induced energy-transfer sensitization involves coupling the generation of an electronically excited organic substrate to the relaxation of a photoexcited transition metal chromophore (*12*). (**B**) Iridium catalyst **8** mediates the facile [2+2] cycloaddition of styrenes (*69*). Triplet sensitization provides a means to access interesting and highly strained cyclobutane frameworks that are prevalent in natural products and would be difficult to construct through other methods. $dF(CF_3)ppy$, 2-(2,4-difluorophenyl)-5-trifluoromethylpyridine; ISC, intersystem crossing.

lower-energy visible light provides access to the reactivity of electronically excited alkenes that are less susceptible to photoinduced degradation. For example, the cyclobutane cannabanoid cannabiorcicyclolic acid can be synthesized by using a clean, high-yielding [2+2] cycloaddition under photocatalytic conditions. Direct irradiation with UV light, however, results in substantial photodecomposition of the product after 5 hours, and only 19% yield of the cycloadduct is formed along with 9% of unreacted starting material.

Conclusions and Outlook

Synthetic organic chemistry benefits greatly when it can incorporate developments from intellectually adjacent disciplines to advance. For instance, organotransition metal chemistry, biocatalysis, and computational chemistry have all been rapidly adopted and are now tools used by synthetic chemists on a routine basis. Photochemistry has the potential to have an equally substantial impact on the field of chemical synthesis by providing a complementary strategy for the activation of organic substrates; the prospect of doing so with renewable solar radiation has motivated photochemists for over a century and seems increasingly relevant as the chemistry community becomes more cognizant of its environmental responsibilities. The growing recognition that operationally facile visible light–induced photochemical reactions can be conducted by using transition metal photocatalysts is bringing us closer to this long-standing goal.

The pace of development in this area has been remarkable. Recent research in visible light photocatalysis has yielded a generalizable rubric for how organic substrates can undergo photoactivation by transition metal complexes. Both electron-transfer and energy-transfer photocatalysis have been used to generate classes of reactive intermediates whose general reactivity patterns are well understood, inspiring the design of a wide range of new chemical reactions.

Therefore, the immediate goals within this area are to continue advancing the utility of photocatalytic synthesis by exploiting the reactivity of photogenerated intermediates in the construction of increasingly complex organic targets. Current research is also expanding the range of reactive intermediates that are available using photocatalytic activation, which should increase the diversity of transformations accessible to synthetic chemists interested in photochemical activation strategies (*70*). Last, as has been the case with many other advances in synthetic chemistry, the advantages of visible light photocatalysis are being recognized by researchers with interests in areas as diverse as materials science, chemical biology, and drug discovery, suggesting that research in photochemical synthesis will continue to grow in synergistic relationship with intellectually adjacent fields (*32*, *71*, *72*). It seems clear that the future of photochemical synthesis remains bright.

References and Notes

1. G. Ciamician, The photochemistry of the future. *Science* **36**, 385–394 (1912). doi: 10.1126/science.36.926.385; pmid: 17836492
2. V. Balzani, A. Credi, M. Venturi, Photochemical conversion of solar energy. *ChemSusChem* **1**, 26–58 (2008). doi: 10.1002/cssc.200700087; pmid: 18605661
3. K. Kalyanasundaram, *Photochemistry of Polypyridine and Porphyrin Complexes* (Academic Press, London, 1992).
4. S. Protti, S. Manzini, M. Fagnoni, A. Albini, "The contribution of photochemistry to green chemistry," in *Eco-Friendly Synthesis of Fine Chemicals*, R. Ballini, Ed. (2009), pp. 80–111.
5. P. Esser, B. Pohlmann, H. D. Scharf, The photochemical-synthesis of fine chemicals with sunlight. *Angew. Chem. Int. Ed. Engl.* **33**, 2009–2023 (1994). doi: 10.1002/anie.199420091
6. T. Bach, J. P. Hehn, Photochemical reactions as key steps in natural product synthesis. *Angew. Chem. Int. Ed.* **50**, 1000–1045 (2011). doi: 10.1002/anie.201002845; pmid: 21246702
7. N. Hoffmann, Photochemical reactions as key steps in organic synthesis. *Chem. Rev.* **108**, 1052–1103 (2008). doi: 10.1021/cr0680336; pmid: 18302419
8. C. K. Prier, D. A. Rankic, D. W. MacMillan, Visible light photoredox catalysis with transition metal complexes: Applications in organic synthesis. *Chem. Rev.* **113**, 5322–5363 (2013). doi: 10.1021/cr300503r; pmid: 23509883
9. T. P. Yoon, M. A. Ischay, J. Du, Visible light photocatalysis as a greener approach to photochemical synthesis. *Nat. Chem.* **2**, 527–532 (2010). doi: 10.1038/nchem.687; pmid: 20571569
10. M. Pirtsch, S. Paria, T. Matsuno, H. Isobe, O. Reiser, $[Cu(dap)_2Cl]$ as an efficient visible-light-driven photoredox catalyst in carbon-carbon bond-forming reactions. *Chemistry* **18**, 7336–7340 (2012). doi: 10.1002/chem.201200967; pmid: 22581462
11. G. Revol, T. McCallum, M. Morin, F. Gagosz, L. Barriault, Photoredox transformations with dimeric gold complexes. *Angew. Chem. Int. Ed.* **52**, 13342–13345 (2013). doi: 10.1002/anie.201306727; pmid: 24133051
12. A. Juris *et al.*, Ru(II) polypyridine complexes: Photophysics, photochemistry, eletrochemistry, and chemiluminescence. *Coord. Chem. Rev.* **84**, 85–277 (1988). doi: 10.1016/0010-8545(88)80032-8
13. K. Kalyanasundaram, Photophysics, photochemistry and solar energy conversion with tris(bipyridyl)ruthenium(II) and its analogues. *Coord. Chem. Rev.* **46**, 159–244 (1982). doi: 10.1016/0010-8545(82)85003-0
14. H. Takeda, O. Ishitani, Development of efficient photocatalytic systems for CO_2 reduction using mononuclear and multinuclear metal complexes based on mechanistic studies. *Coord. Chem. Rev.* **254**, 346–354 (2010). doi: 10.1016/j.ccr.2009.09.030
15. O. S. Wenger, Proton-coupled electron transfer with photoexcited metal complexes. *Acc. Chem. Res.* **46**, 1517–1526 (2013). doi: 10.1021/ar300289x; pmid: 23402212
16. D. R. Weinberg *et al.*, Proton-coupled electron transfer. *Chem. Rev.* **112**, 4016–4093 (2012). doi: 10.1021/cr200177j; pmid: 22702235
17. T. Bach, Stereoselective intermolecular [2+2]-photocycloaddition reactions and their application in synthesis. *Synthesis* **1998**, 683–703 (1998). doi: 10.1055/s-1998-2054
18. A. Albini, Photosensitization in organic-synthesis. *Synthesis* **1981**, 249–264 (1981). doi: 10.1055/s-1981-29405
19. M. Fagnoni, D. Dondi, D. Ravelli, A. Albini, Photocatalysis for the formation of the C-C bond. *Chem. Rev.* **107**, 2725–2756 (2007). doi: 10.1021/cr068352x; pmid: 17530909
20. S. Fukuzumi, S. Mochizuki, T. Tanaka, Photocatalytic reduction of phenacyl halides by 9,10-dihydro-10-methylacridine - control between the reductive and oxidative quenching pathways of tris(bipyridine) ruthenium complex utilizing an acid catalysis. *J. Phys. Chem.* **94**, 722–726 (1990). doi: 10.1021/j100365a039
21. F. Alonso, I. P. Beletskaya, M. Yus, Metal-mediated reductive hydrodehalogenation of organic halides. *Chem. Rev.* **102**, 4009–4092 (2002). doi: 10.1021/cr0102967; pmid: 12428984
22. D. A. Nicewicz, D. W. MacMillan, Merging photoredox catalysis with organocatalysis: The direct asymmetric alkylation of aldehydes. *Science* **322**, 77–80 (2008); 10.1126/science.1161976. doi: 10.1126/science.1161976; pmid: 18772399
23. S. Mukherjee, J. W. Yang, S. Hoffmann, B. List, Asymmetric enamine catalysis. *Chem. Rev.* **107**, 5471–5569 (2007). doi: 10.1021/cr0684016; pmid: 18072803
24. T. D. Beeson, A. Mastracchio, J. B. Hong, K. Ashton, D. W. C. Macmillan, Enantioselective organocatalysis using SOMO activation. *Science* **316**, 582–585 (2007); 10.1126/science.1142696. doi: 10.1126/science. 1142696; pmid: 17395791
25. T. D. Beeson, D. W. C. Macmillan, Enantioselective organocatalytic α-fluorination of aldehydes. *J. Am. Chem. Soc.* **127**, 8826–8828 (2005). doi: 10.1021/ja051805f; pmid: 15954790
26. H. W. Shih, M. N. Vander Wal, R. L. Grange, D. W. MacMillan, Enantioselective α-benzylation of aldehydes via photoredox organocatalysis. *J. Am. Chem. Soc.* **132**, 13600–13603 (2010). doi: 10.1021/ja106593m; pmid: 20831195
27. P. V. Pham, D. A. Nagib, D. W. MacMillan, Photoredox catalysis: A mild, operationally simple approach to the synthesis of α-trifluoromethyl carbonyl compounds. *Angew. Chem. Int. Ed.* **50**, 6119–6122 (2011). doi: 10.1002/anie.201101861; pmid: 21604347
28. L. Furst, B. S. Matsuura, J. M. Narayanam, J. W. Tucker, C. R. Stephenson, Visible light-mediated intermolecular C-H functionalization of electron-rich heterocycles with malonates. *Org. Lett.* **12**, 3104–3107 (2010). doi: 10.1021/ol101146f; pmid: 20518528
29. L. Furst, J. M. Narayanam, C. R. Stephenson, Total synthesis of (+)-glioccladin C enabled by visible-light photoredox catalysis. *Angew. Chem. Int. Ed.* **50**, 9655–9659 (2011). doi: 10.1002/anie.201103145; pmid: 21751318
30. C. J. Wallentin, J. D. Nguyen, P. Finkbeiner, C. R. Stephenson, Visible light-mediated atom transfer radical addition via oxidative and reductive quenching of photocatalysts. *J. Am. Chem. Soc.* **134**, 8875–8884 (2012). doi: 10.1021/ja300798k; pmid: 22486313
31. J. D. Nguyen, E. M. D'Amato, J. M. Narayanam, C. R. Stephenson, Engaging unactivated alkyl, alkenyl and aryl iodides in visible-light-mediated free radical reactions. *Nat. Chem.* **4**, 854–859 (2012). doi: 10.1038/nchem.1452; pmid: 23001000
32. B. P. Fors, C. J. Hawker, Control of a living radical polymerization of methacrylates by light. *Angew. Chem. Int. Ed.* **51**, 8850–8853 (2012). doi: 10.1002/anie.201203639; pmid: 22807122
33. Y. Ye, S. A. Künzi, M. S. Sanford, Practical method for the Cu-mediated trifluoromethylation of arylboronic acids with CF_3 radicals derived from $NaSO_2CF_3$ and tert-butyl hydroperoxide (TBHP). *Org. Lett.* **14**, 4979–4981 (2012). doi: 10.1021/ol3022726; pmid: 22984900
34. D. Kalyani, K. B. McMurtrey, S. R. Neufeldt, M. S. Sanford, Room-temperature C-H arylation: Merger of Pd-catalyzed C-H functionalization and visible-light photocatalysis. *J. Am. Chem. Soc.* **133**, 18566–18569 (2011). doi: 10.1021/ja208068w; pmid: 22047138
35. J. W. Tucker, C. R. Stephenson, Shining light on photoredox catalysis: Theory and synthetic applications. *J. Org. Chem.* **77**, 1617–1622 (2012). doi: 10.1021/jo202538x; pmid: 22283525
36. L. Shi, W. Xia, Photoredox functionalization of C-H bonds adjacent to a nitrogen atom. *Chem. Soc. Rev.* **41**, 7687–7697 (2012). doi: 10.1039/c2cs35203f; pmid: 22869017
37. U. C. Yoon, P. S. Mariano, Mechanistic and synthetic aspects of amine enone single electron-transfer photochemistry. *Acc. Chem. Res.* **25**, 233–240 (1992). doi: 10.1021/ar00017a005
38. E. A. Mitchell, A. Peschiulli, N. Lefevre, L. Meerpoel, B. U. Maes, Direct α-functionalization of saturated cyclic amines. *Chemistry* **18**, 10092–10142 (2012). doi: 10.1002/chem.201201539; pmid: 22829434
39. K. R. Campos, Direct sp^3 C-H bond activation adjacent to nitrogen in heterocycles. *Chem. Soc. Rev.* **36**, 1069–1084 (2007). doi: 10.1039/b607547a; pmid: 17576475
40. P. Kohls, D. Jadhav, G. Pandey, O. Reiser, Visible light photoredox catalysis: Generation and addition of

N-aryltetrahydroisoquinoline-derived α-amino radicals to Michael acceptors. *Org. Lett.* **14**, 672–675 (2012). doi: 10.1021/ol202857t; pmid: 22260623
41. L. Ruiz Espelt, E. M. Wiensch, T. P. Yoon, Brønsted acid cocatalysts in photocatalytic radical addition of α-amino C-H bonds across Michael acceptors. *J. Org. Chem.* **78**, 4107–4114 (2013). doi: 10.1021/jo400428m; pmid: 23537318
42. A. McNally, C. K. Prier, D. W. MacMillan, Discovery of an α-amino C-H arylation reaction using the strategy of accelerated serendipity. *Science* **334**, 1114–1117 (2011). doi: 10.1126/science.1213920; pmid: 22116882
43. A. G. Condie, J. C. González-Gómez, C. R. Stephenson, Visible-light photoredox catalysis: Aza-Henry reactions via C-H functionalization. *J. Am. Chem. Soc.* **132**, 1464–1465 (2010). doi: 10.1021/ja909145y; pmid: 20070079
44. D. B. Freeman, L. Furst, A. G. Condie, C. R. Stephenson, Functionally diverse nucleophilic trapping of iminium intermediates generated utilizing visible light. *Org. Lett.* **14**, 94–97 (2012). doi: 10.1021/ol202883v; pmid: 22148974
45. Y. Q. Zou *et al.*, Visible-light-induced oxidation/[3+2] cycloaddition/oxidative aromatization sequence: A photocatalytic strategy to construct pyrrolo[2,1-a] isoquinolines. *Angew. Chem. Int. Ed.* **50**, 7171–7175 (2011). doi: 10.1002/anie.201102306; pmid: 21698733
46. S. Zhu *et al.*, Oxygen switch in visible-light photoredox catalysis: Radical additions and cyclizations and unexpected C-C-bond cleavage reactions. *J. Am. Chem. Soc.* **135**, 1823–1829 (2013). doi: 10.1021/ja309580a; pmid: 23330701
47. D. A. Horton, G. T. Bourne, M. L. Smythe, The combinatorial synthesis of bicyclic privileged structures or privileged substructures. *Chem. Rev.* **103**, 893–930 (2003). doi: 10.1021/cr020033s; pmid: 12630855
48. F. Müller, J. Mattay, Photocycloadditions: Control by energy and electron-transfer. *Chem. Rev.* **93**, 99–117 (1993). doi: 10.1021/cr00017a006
49. M. Schmittel, A. Burghart, Understanding reactivity patterns of radical cations. *Angew. Chem. Int. Ed. Engl.* **36**, 2550–2589 (1997). doi: 10.1002/anie.199725501
50. N. L. Bauld, Cation radical cyclo-additions and related sigmatropic reactions. *Tetrahedron* **45**, 5307–5363 (1989). doi: 10.1016/S0040-4020(01)89486-2
51. P. E. Floreancig, Development and applications of electron-transfer-initiated cyclization reactions. *Synlett* **2007**, 0191–0203 (2007). doi: 10.1055/s-2007-968021
52. D. J. Edmonds, D. Johnston, D. J. Procter, Samarium(II)-iodide-mediated cyclizations in natural product synthesis. *Chem. Rev.* **104**, 3371–3404 (2004). doi: 10.1021/cr030017a; pmid: 15250745
53. F. Guo, M. D. Clift, R. J. Thomson, Oxidative coupling of enolates, enol silanes and enamines: Methods and natural product synthesis. *Eur. J. Org. Chem.* **2012**, 4881–4896 (2012). doi: 10.1002/ejoc.201200665; pmid: 23471479
54. J. B. Sperry, D. L. Wright, The application of cathodic reductions and anodic oxidations in the synthesis of complex molecules. *Chem. Soc. Rev.* **35**, 605–621 (2006). doi: 10.1039/b512308a; pmid: 16791332
55. P. I. Dalko, Redox-induced radical and radical ionic carbon-carbon bond-forming reactions. *Tetrahedron* **51**, 7579–7653 (1995). doi: 10.1016/0040-4020(95)00434-A
56. M. A. Ischay, T. P. Yoon, Accessing the synthetic chemistry of radical ions. *Eur. J. Org. Chem.* **2012**, 3359–3372 (2012). doi: 10.1002/ejoc.201101071
57. T. P. Yoon, Visible light photocatalysis: The development of photocatalytic radical ion cycloadditions. *ACS Catal.* **3**, 895–902 (2013). doi: 10.1021/cs400088e; pmid: 23691491
58. M. A. Ischay, M. E. Anzovino, J. Du, T. P. Yoon, Efficient visible light photocatalysis of [2+2] enone cycloadditions. *J. Am. Chem. Soc.* **130**, 12886–12887 (2008). doi: 10.1021/ja805387f; pmid: 18767798
59. J. Du, T. P. Yoon, Crossed intermolecular [2+2] cycloadditions of acyclic enones via visible light photocatalysis. *J. Am. Chem. Soc.* **131**, 14604–14605 (2009). doi: 10.1021/ja903732v; pmid: 19473018
60. Z. Lu, M. Shen, T. P. Yoon, [3+2] cycloadditions of aryl cyclopropyl ketones by visible light photocatalysis. *J. Am. Chem. Soc.* **133**, 1162–1164 (2011). doi: 10.1021/ja107849y; pmid: 21214249
61. M. A. Ischay, M. S. Ament, T. P. Yoon, Crossed intermolecular [2+2] cycloaddition of styrenes by visible light photocatalysis. *Chem. Sci.* **3**, 2807–2811 (2012). doi: 10.1039/c2sc20658g; pmid: 22984640
62. S. Lin, M. A. Ischay, C. G. Fry, T. P. Yoon, Radical cation Diels-Alder cycloadditions by visible light photocatalysis. *J. Am. Chem. Soc.* **133**, 19350–19353 (2011). doi: 10.1021/ja2093579; pmid: 22032252
63. D. S. Hamilton, D. A. Nicewicz, Direct catalytic anti-markovnikov hydroetherification of alkenols. *J. Am. Chem. Soc.* **134**, 18577–18580 (2012). doi: 10.1021/ja309635w; pmid: 23113557
64. S. Fukuzumi *et al.*, Electron-transfer state of 9-mesityl-10-methylacridinium ion with a much longer lifetime and higher energy than that of the natural photosynthetic reaction center. *J. Am. Chem. Soc.* **126**, 1600–1601 (2004). doi: 10.1021/ja038656q; pmid: 14871068
65. K. Ohkubo *et al.*, Simultaneous production of p-tolualdehyde and hydrogen peroxide in photocatalytic oxygenation of p-xylene and reduction of oxygen with 9-mesityl-10-methylacridinium ion derivatives. *Chem. Commun.* **46**, 601–603 (2010). doi: 10.1039/b920606j; pmid: 20062875
66. H. Kotani, K. Ohkubo, S. Fukuzumi, Photocatalytic oxygenation of anthracenes and olefins with dioxygen via selective radical coupling using 9-mesityl-10-methylacridinium ion as an effective electron-transfer photocatalyst. *J. Am. Chem. Soc.* **126**, 15999–16006 (2004). doi: 10.1021/ja048353b; pmid: 15584734
67. T. M. Nguyen, D. A. Nicewicz, Anti-Markovnikov hydroamination of alkenes catalyzed by an organic photoredox system. *J. Am. Chem. Soc.* **135**, 9588–9591 (2013). doi: 10.1021/ja4031616; pmid: 23768239
68. K. D. Moeller, Intramolecular anodic olefin coupling reactions: Using radical cation intermediates to trigger new umpolung reactions. *Synlett* **2009**, 1208–1218 (2009). doi: 10.1055/s-0028-1088126
69. Z. Lu, T. P. Yoon, Visible light photocatalysis of [2+2] styrene cycloadditions by energy transfer. *Angew. Chem. Int. Ed.* **51**, 10329–10332 (2012). doi: 10.1002/anie.201204835; pmid: 22965321
70. E. P. Farney, T. P. Yoon, Visible-light sensitization of vinyl azides by transition-metal photocatalysis. *Angew. Chem. Int. Ed.* **53**, 793–797 (2014). doi: 10.1002/anie.201308820; pmid: 24281908
71. F. A. Leibfarth, K. M. Mattson, B. P. Fors, H. A. Collins, C. J. Hawker, External regulation of controlled polymerizations. *Angew. Chem. Int. Ed.* **52**, 199–210 (2013). doi: 10.1002/anie.201206476; pmid: 23166046
72. Y. Chen, A. S. Kamlet, J. B. Steinman, D. R. Liu, A biomolecule-compatible visible-light-induced azide reduction from a DNA-encoded reaction-discovery system. *Nat. Chem.* **3**, 146–153 (2011). doi: 10.1038/nchem.932; pmid: 21258388
73. M. P. Thekaekara, Solar-radiation measurement - techniques and instrumentation. *Sol. Energy* **18**, 309–325 (1976). doi: 10.1016/0038-092X(76)90058-X

Acknowledgments: We gratefully acknowledge support from the NIH in the form of a research grant (GM095666) and a postdoctoral fellowship to D.M.S.

10.1126/science.1239176

ESCRT Machinery Is Required for Plasma Membrane Repair

Ana Joaquina Jimenez, Paolo Maiuri, Julie Lafaurie-Janvore, Séverine Divoux, Matthieu Piel, Franck Perez*

READ THE FULL ARTICLE ONLINE
http://dx.doi.org/10.1126/science.1247136

Cite this article as A. J. Jimenez *et al.*, *Science* **343**, 1247136 (2014).
DOI: 10.1126/science.1247136

Introduction: Plasma membrane damage can result from numerous threats, including mechanical stress or biochemical agents such as pore-forming toxins. Different mechanisms for plasma membrane repair have been described in a variety of cellular models, including patching with endomembranes, endocytosis, and extracellular budding. We found that the endosomal sorting complex required for transport (ESCRT), which is implicated in numerous membrane fission events (such as during cytokinesis or for the budding of several viruses) was also required for the rapid closure of small wounds made at the plasma membrane.

Methods: We used micropipettes, detergents, pore-forming toxins, and laser wounding to damage the plasma membrane of mammalian cells in tissue culture. Ultraviolet or two-photon lasers were used to induce small, localized wounds, and cell reactions were followed with time-lapse imaging. Propidium iodide (PI) entry in wounded cells was used to allow imaging of the plasma membrane opening and to quantify the rate of closure of single wounds. Mathematical fit of PI entry kinetics was used to estimate the diameter and the rate of closure of individual wounds. Characterization of PI fluorescence and diffusion gave us an estimation of wound sizes. Transfection of small interfering RNA or dominant-negative mutants of ESCRT subunits allowed us to assess their importance during plasma membrane repair. Last, using correlative scanning electron microscopy we examined the ultrastructure of wounded plasma membranes.

Results: The various wounding methods used here revealed a systematic recruitment of ESCRTs to the plasma membrane. Wounding with a laser beam showed that ESCRTs—and in particular, ESCRT-III proteins—were specifically recruited to wound sites and were accumulated until wound closure. This recruitment depended on calcium, which is known to be a crucial signaling molecule for wound repair. The depletion of important ESCRT subunits such as CHMP4B, CHMP2A, or Vps4 was deleterious for a subpopulation of cells bearing small wounds (less than 100 nm in diameter). Correlative scanning electron microscopy and time-lapse imaging revealed that wounding was followed by ESCRT-positive membrane budding and shedding. Energy depletion did not prevent—and rather increased—ESCRT accumulation but prevented both membrane shedding and repair.

Discussion: These results show that ESCRT proteins play an important role in the detection and removal through the extracellular shedding of small wounds present at the plasma membrane. We propose that different mechanisms for membrane repair (patching, budding, or endocytosis) can be used by cells depending on the type and size of the wound. These mechanisms are stimulated by common early signaling events, such as calcium, but downstream events are likely to depend on the physiochemical characteristics of the wounds.

ESCRT-positive plasma membrane shedding has been observed in a variety of normal and pathological conditions. It remains unclear whether these phenomena are linked to local plasma membrane damage and whether ESCRT-III proteins are involved in these processes.

FIGURES IN THE FULL ARTICLE

Fig. 1. CHMP4B is recruited to wounded plasma membrane.

Fig. 2. CHMP4B-recruitment occurs before resealing.

Fig. 3. CHMP2, CHMP3, and the ESCRT-associated protein ALIX are recruited to wounds.

Fig. 4. ESCRT-III proteins and the ESCRT-associated protein ALIX are recruited in a calcium-dependent manner.

Fig. 5. Perturbation of wound resealing after depletion of ESCRT-III and ESCRT disassembly subunits.

Fig. 6. ESCRT-positive cell surface budding upon wounding.

Fig. 7. Energy-independent ESCRT recruitment and energy-dependent shedding of wounded membrane.

SUPPLEMENTARY MATERIALS

Materials and Methods
Figs. S1 to S17
Full Reference List
Movies S1 to S8

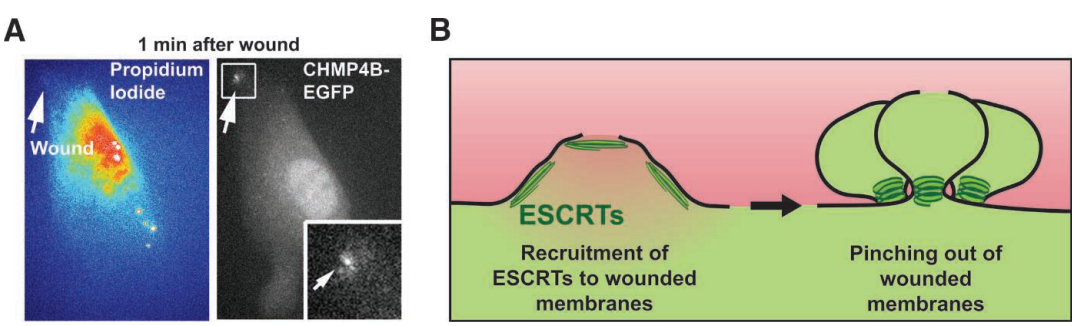

ESCRT recruitment mediates pinching out of wounded plasma membrane. (**A**) Cells expressing the ESCRT subunit CHMP4B-EGFP and wounded (arrow) in the presence of propidium iodide (PI) were observed by means of fluorescence imaging. (**B**) Model for ESCRT-mediated detection and shedding of wounded plasma membrane.

The list of author affiliations is available in the full article online.
*Corresponding author. E-mail: franck.perez@curie.fr

ESCRT Machinery Is Required for Plasma Membrane Repair

Ana Joaquina Jimenez,[1,2] Paolo Maiuri,[1,2]* Julie Lafaurie-Janvore,[1,2]* Séverine Divoux,[1,2] Matthieu Piel,[1,2] Franck Perez[1,2]†

Plasma membrane damage can be triggered by numerous phenomena, and efficient repair is essential for cell survival. Endocytosis, membrane patching, or extracellular budding can be used for plasma membrane repair. We found that endosomal sorting complex required for transport (ESCRT), involved previously in membrane budding and fission, plays a critical role in plasma membrane repair. ESCRT proteins were recruited within seconds to plasma membrane wounds. Quantitative analysis of wound closure kinetics coupled to mathematical modeling suggested that ESCRTs are involved in the repair of small wounds. Real-time imaging and correlative scanning electron microscopy (SEM) identified extracellular buds and shedding at the site of ESCRT recruitment. Thus, the repair of certain wounds is ensured by ESCRT-mediated extracellular shedding of wounded portions.

Endosomal sorting complex required for transport (ESCRT) has been implicated in multivesicular body (MVB) biogenesis, viral budding, cytokinesis, and spontaneous budding of the plasma membrane (*1*). They are involved in local membrane deformation and scission. The topology of the bent membrane is very characteristic, with its concave side facing the cytoplasm. ESCRT subunits are classified in five complexes: ESCRT-0, ESCRT-I, ESCRT-II, ESCRT-III, and ESCRT disassembly subcomplex, which are recruited in a serial fashion during MVB biogenesis (*2*–*4*). ESCRT-III and ESCRT disassembly proteins appear to be involved in every ESCRT-associated function. ESCRT-0 and ESCRT-II have not been implicated in cytokinesis and are dispensable during viral budding (*5*, *6*). It is likely that adaptor proteins such as ALG-2–interacting protein X (ALIX) can fulfill the role of ESCRT-II for the recruitment of the ESCRT-III machinery (*5*, *7*–*14*).

Extracellular budding events have been described during cellular response to plasma membrane wounding by pore-forming toxins (*15*, *16*). Because the topology of these budded membranes was reminiscent of ESCRT-dependent membrane deformation, we decided to explore the role of ESCRTs in plasma membrane repair.

We first analyzed the behavior of the ESCRT-III complex upon localized plasma membrane damage. We followed the dynamics of CHMP4B, an ESCRT-III protein necessary for all known ESCRT functions in mammals. The plasma membrane of HeLa cells was wounded using three different means. In the first assay, we incubated HeLa cells expressing CHMP4B-EGFP (enhanced green fluorescent protein) at endogenous levels (*17*), with two pore-forming molecules (digitonin at 250 μM or saponin at 0.05%) added to the cells for a short time. In both cases, we observed a redistribution of cytosolic CHMP4B-EGFP to localized spots at the cell membrane less than 3 min after the addition of the pore-forming molecules (Fig. 1A). Similar results were obtained with the pore-forming toxins streptolysin O and listeriolysin O (Fig. 1B). Second, we mechanically damaged the plasma membrane using a micropipette in a standard

[1]Institut Curie, 26 rue d'Ulm, 75248 Paris Cedex 05, France. [2]CNRS UMR 144, 26 rue d'Ulm, 75248 Paris Cedex 05, France.

*These authors contributed equally to this work.
†Corresponding author. E-mail: franck.perez@curie.fr

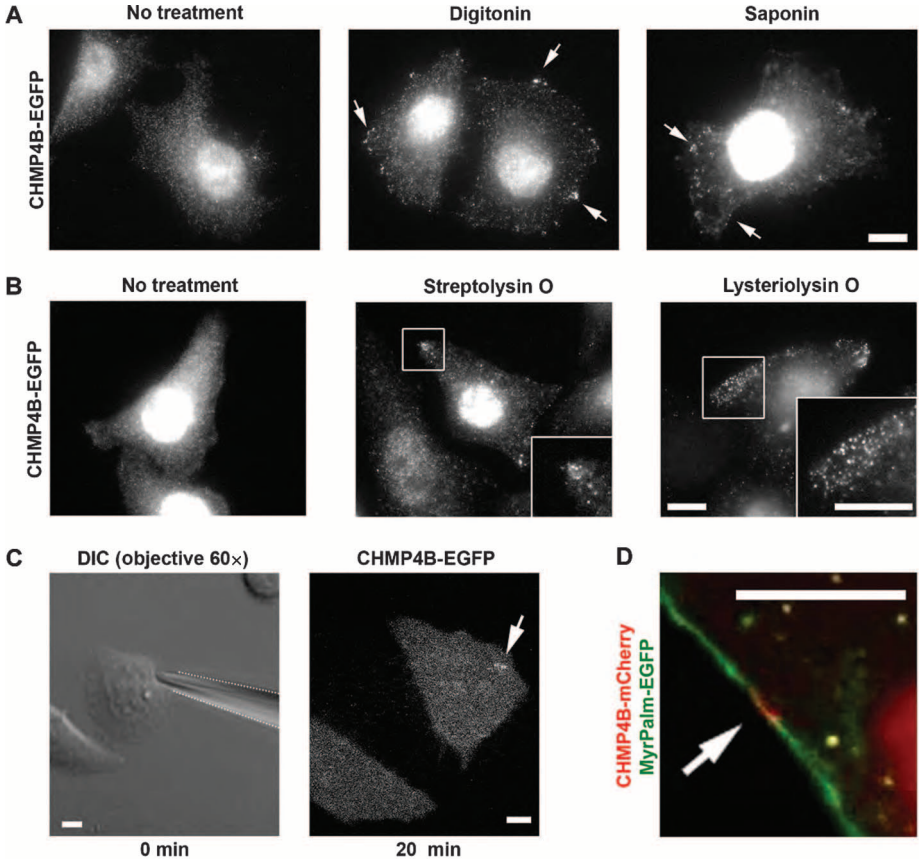

Fig. 1. CHMP4B is recruited to the wounded plasma membrane. (**A** to **C**) HeLa cells stably expressing CHMP4B-EGFP at endogenous levels (referred below as HeLa CHMP4B-EGFP) were used. Cells were treated with digitonin or saponin for 1 min and fixed for 3 min after the beginning of the treatment (A) or were treated with streptolysin O or listeriolysin O for 2.5 min before fixation (B). Cells were fixed and immunolabeled with antibodies to GFP (for better visualization of CHMP4B-EGFP recruitment) (A to C). Plasma membrane wounding with a glass needle (highlighted with dashed lines) was followed by differential interference contrast (DIC) microscopy imaging, and CHMP4B-EGFP recruitment was observed by confocal microscopy in 6 of 20 cells analyzed (C). (**D**) HeLa cells cotransfected with CHMP4B-mCherry and MyrPalm-EGFP constructs were wounded at the plasma membrane with a UV laser/spinning disc microscope system. Scale bars, 10 μm.

microinjection setup. Similarly, CHMP4B-EGFP was recruited to the wounded site in HeLa cells in about 25% of the cells analyzed (n = 20) (Fig. 1C). Finally, to standardize wounding conditions and to couple localized plasma membrane damage to fast imaging of the cellular response, we performed laser-based plasma membrane wounding. We used either a scanning confocal microscope equipped with a two-photon laser or a spinning disc confocal microscope equipped with an ultraviolet (UV) laser. These experiments revealed a very fast (less than 30 s) and localized recruitment of CHMP4B-EGFP to wounded domains (Figs. 1D and 2, A and C). CHMP4B was found on the damaged plasma membrane colocalizing with the plasma membrane marker pMyrPalmEGFP (Fig. 1D). ESCRT-III subunits have been observed before at the plasma membrane when overexpressed or when lacking autoinhibitory domains (*18*, *19*) and during viral budding or uncharacterized nonviral budding events (*1*). Certain ESCRT-III subunits, such as CHMP3, bind with high affinity to phosphatidylinositol 3,4-bisphosphate, a lipid exclusively produced at the plasma membrane (*20*). Because lysosomes/late endosomes (LLEs) were found to be involved in plasma membrane repair (*21*, *22*) and because ESCRT proteins are involved in LLE functions, we tested whether CHMP4 was transported by LLE to the wounded area of the plasma membrane. Cells expressing CHMP4B-EGFP were immunostained with endolysosomal markers [lyso-bisphosphatidic acid (LBPA), lysosomal-associated membrane protein 1 (Lamp1), and early endosome antigen 1 (EEA1)] after localized laser wounding to look for approaching endolysosomal vesicles. No LBPA, Lamp1, or EEA1 vesicular structures were detectable close to the wound in conditions where CHMP4 was strongly recruited (fig. S1). As reported before (*22*), however, the presence of Lamp1 can be revealed by surface staining at the wound (fig. S2A). However, the recruitment of ESCRTs at the wound in cells with depolymerized microtubules suggests that it is mainly independent of vesicular transport (fig. S2B). This is further suggested by the fact that recruitment of CHMP4B on wound sites was energy-independent (see below).

These data suggest that soluble ESCRT-III proteins are directly targeted to physical holes present at the plasma membrane, where they may be involved in repair. The disruption of the membrane and the closure of the wound were monitored following the entry of the impermeant nucleic acid dye propidium iodide (PI) into wounded cells. Reversible physical damage upon laser-based wounding can be efficiently followed in real time, quantifying cellular PI fluorescence. CHMP4B recruitment was triggered by single or sequential and spatially distinct laser wounds (Fig. 2, A to C, and movie S1). The suitability of PI to monitor wound opening and repair was confirmed by comparing PI with other dyes (fig. S3). Using PI as a tracer, or other fluorescent dyes, we observed that wounds could stay open for a few hundreds of seconds (Fig. 2B and fig. S3). This was further confirmed by adding PI to the cells at different time points after wounding, which indicated that some wounds remained open up to 4 min (fig. S4). The recruitment

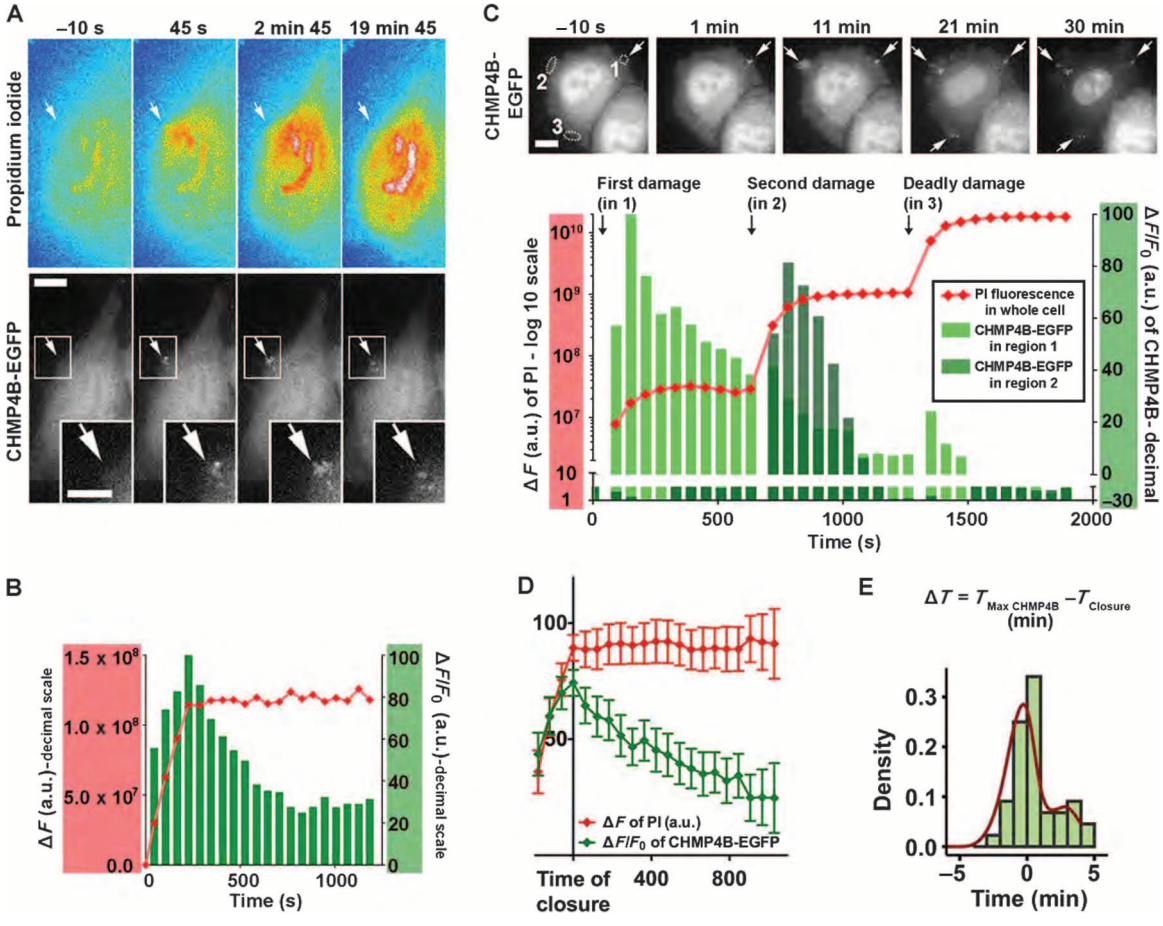

Fig. 2. CHMP4B-recruitment occurs before resealing. (**A** to **E**) The plasma membranes of HeLa CHMP4B-EGFP cells were locally wounded (arrow) in the presence of PI at t = 0 (A, B, D, and E) or at several time points (C), using a UV laser. Time-lapse imaging was performed using a spinning disc microscope system to follow the recruitment of CHMP4B-EGFP and the entry of PI. (A) PI fluorescence is presented using a "royal" look-up table. (B) Corresponding graph for the cell in (A), which is representative of 15 cells analyzed. The red curve represents PI entry, and the green bars represent CHMP4B-EGFP recruitment measured around the wound. (C) Similar experiments were performed for cells subjected to successive wounding. Two localized wounding were performed at 0 and 10 min on two spatially separated spots of the membrane of cells, followed by a deadly wounding at 20 min. The cell presented is representative of 15 cells analyzed. The top panel illustrates CHMP4B recruitment at the wound sites at different time points. CHMP4B-EGFP recruitment measured in regions 1 and 2 is represented by the histograms in light green and dark green, respectively, and PI entry is represented by the red curve. Scales are shown on the right and left of the graph (see corresponding movie S1). (D) Curves of PI entry and CHMP4B-EGFP recruitment were averaged for 15 cells around the time of closure ($T_{closure}$) (time when PI reaches a plateau), with $T_{closure}$ centered at 0. Error bars correspond to the SE of each mean. (E) The difference between $T_{closure}$ and the time of maximum CHMP4B-EGFP recruitment gives a ΔT for each cell analyzed. The distribution of all ΔT was plotted; average = –0.0227, t test not significantly different from 0, P = 0.9421. Arrows point at the wound site to which CHMP4B-EGFP is recruited. Scale bars, 10 μm.

of this ESCRT subunit always preceded the closure of the wound (Fig. 2D). Furthermore, we calculated the difference between the time of closure (time of reach of the PI plateau) and the time of maximum recruitment of CHMP4B, which was not statistically different from 0, strongly suggesting that these two events are correlated (Fig. 2E). Thus, as soon as the wound closes, ESCRT-III starts to dissociate from the wounded area.

We next investigated whether other subunits of the ESCRT-III subcomplex were involved in this targeted response. Immunostaining of digitonin-treated cells revealed that, upon damage, endogenous CHMP3, CHMP2A, and CHMP2B, but not CHMP6, colocalized with CHMP4B-EGFP at the plasma membrane (Fig. 3, A to C, E, and F, and fig. S5). Proteins from other ESCRT subcomplexes, such as hepatocyte growth factor–regulated tyrosine kinase substrate (HRS), were not detected (fig. S6A), although recruitment of overexpressed and endogenous TSG101 was observed (fig. S6, B and C). We investigated whether ALIX, a protein capable of bypassing ESCRT-0, ESCRT-I, and ESCRT-II complexes and recruiting ESCRT-III proteins directly, was involved in the recruitment of ESCRT-III proteins. ALIX colocalized with CHMP4B-EGFP at the plasma membrane of cells treated with digitonin (Fig. 3D) or wounded with a laser beam (Fig. 4C). Polyubiquitination of the plasma membrane wounded by a laser or by digitonin was observed by immunofluorescence (fig. S7). Its belated detection befogs the role of ubiquitin as a potential early signal for ESCRT recruitment via ubiquitin-binding domains (*23*, *24*). Nevertheless, although we cannot exclude that the belated detection is due to a limited antibody sensitivity, the presence of ESCRTs at the wound sites in the absence of energy, as described below, argues in favor of ubiquitin-independent recruitment of ESCRTs. Calcium, an essential molecule for wound repair (*25*), is likely to be involved in early signaling of membrane damage and stimulate the local recruitment of ESCRTs. As expected, calcium depletion enhanced cell necrosis when cells were wounded with a laser (Fig. 4A and fig. S8). These conditions also strongly inhibited ESCRT recruitment (Fig. 4B). This argues for a role of calcium entry at wounded sites in the local recruitment of ESCRT. Accordingly, the recruitment of ALIX mutants lacking calcium-binding domain (*26*) (as well as lipid-binding mutants) was strongly impaired as compared to a control mutant or wild-type proteins (Fig. 4, C and D). Thus, calcium plays a major, and early, role in the direct recruitment of ESCRTs to the wounded plasma membrane, but the presence of both ALIX and TSG101 suggests that redundant pathways may be involved in the recruitment of ESCRTs at the wounded plasma membranes. The lipid-binding domain of ALIX has been described by Bissig *et al.* (*26*) as an LBPA-specific lipid-binding domain. Nevertheless, this study only considers lipids present on MVBs. Our data suggest that ALIX can bind to the plasma membrane through its LBPA-binding domain, suggesting that this domain can also bind other lipids present at the plasma membrane, or that LBPA might be transiently present at the wounded plasma membrane. This finding opens research perspectives concerning ALIX binding properties.

Finally, we analyzed the recruitment of the AAA+ adenosine triphosphatase Vps4 (responsible for the disassembly of ESCRT-III polymers) and also observed the rapid kinetics of recruitment (fig. S9 and movie S2). The timing for Vps4 recruitment and removal from the wounding site was very close to that of CHMP4B recruitment and removal. We did not detect other markers such as annexin A1 that have previously been detected in streptolysin O wounds (*16*).

We then asked whether the ESCRT machinery was recruited at the wounded area following the classical sequential order of events described

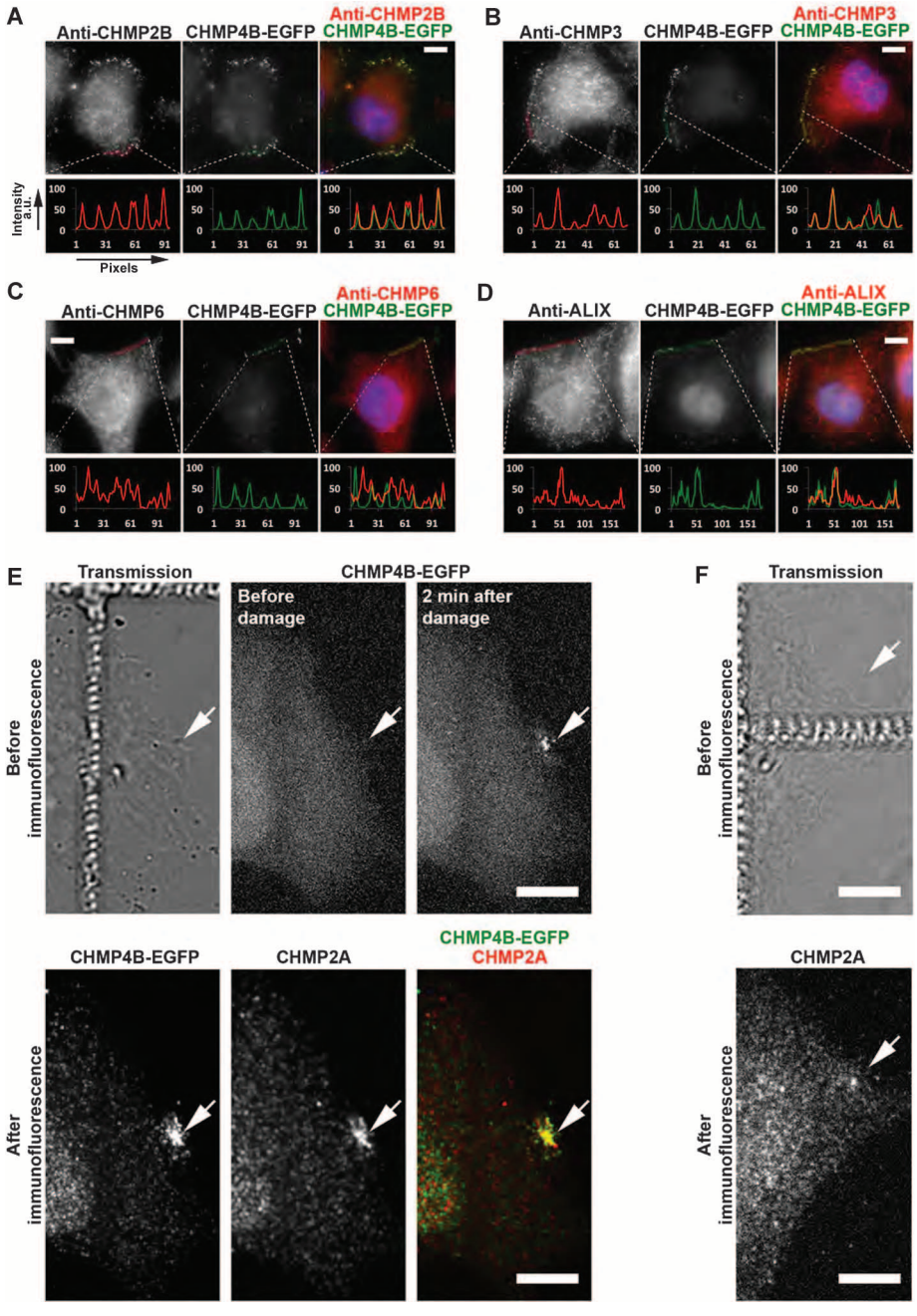

Fig. 3. CHMP2, CHMP3, and the ESCRT-associated protein ALIX are recruited to wounds. (**A** to **D**) HeLa CHMP4B-EGFP cells were treated with digitonin and immunostained for CHMP2B (A), CHMP3 (B) (*37*), CHMP6 (C), and ALIX (D) (*38*). Intensity measurements of CHMP4B-EGFP and the other ESCRT subunits were performed along the lines highlighted at the plasma membrane edge and are represented as intensity spectrums. (**E** and **F**) HeLa CHMP4B-EGFP (E) or HeLa (F) cells were wounded and imaged with a spinning disc microscope equipped with a UV laser. Cells were fixed 2 min after wounding and immunostained for CHMP2A. EGFP signal was enhanced in all experiments as before. White arrows point at the wound where CHMP4B-EGFP is recruited. Scale bars, 10 μm.

for MVB formation. We knocked down CHMP2A in HeLa cells expressing CHMP4B-EGFP (*17*). CHMP2 proteins, in interaction with Vps4, are necessary to recruit the ESCRT disassembly complex (*2*, *3*, *27*–*30*). In control cells, CHMP4B-EGFP local accumulation reached a plateau about 2 to 4 min after wounding and then started to decrease right after wound closure (see Fig. 2, B to D). In contrast, in CHMP2A knockdown cells, CHMP4B continued accumulating up to three times more at the wounded site and reached a plateau only 15 min after wounding (Fig. 5, A and B, fig. S10A, and movie S3). This suggests that ESCRT-III recruitment is the result of a dynamic equilibrium between the assembly and disassembly of the complex on the wound. Knockdown of CHMP3 had a similar, albeit milder, effect on CHMP4B accumulation (figs. S10B and S11A), suggesting a role for CHMP3 in the disassembly of ESCRT-III machinery.

To better understand the role of ESCRT-III proteins in plasma membrane repair processes, we followed the opening and closure of the wound by recording and quantifying the kinetics of entry of PI into wounded cells. A simple model of wound closure was established, and the curves of PI entry after cell damage were fitted using this model. Successive wounding of the same cell showed that the plateau of PI entry reached after each damage was caused by wound closure and not by saturation of PI labeling and thus could be used when fitting the curves (Fig. 2C and fig. S12). Quantitative information about the initial radius of the hole in the plasma membrane (R_{eff}) and its rate of closure (v) could be estimated using the model (see details in supplementary materials and methods and fig. S12). Laser-based plasma membrane damage led to a diversity in wound size (see the cumulative distribution in fig. S13). When we plotted closing rate values against the relative wound size, closure rates increased with wound size. However, two modes were apparent: one for relatively smaller R_{eff} (smaller holes), where rates increased rapidly in function of R_{eff}, and one for relatively larger R_{eff} (larger holes), where closing rate increased more moderately. This suggested that different mechanisms may be used depending on wound sizes. Indeed, inhibition of CHMP2A affected only the closure rate of relatively small holes with no impact on wound size distribution (Fig. 5, C and D, and fig. S13, A and B), whereas no effect was observed for larger holes (fig. S12B). Using quantitative microscopy and calculation, we could estimate that ESCRTs play a role in the repair of wounds of less than 100 nm (fig. S14). No effect on v could be detected upon treatment of cells with small interfering RNA (siRNA) against CHMP3 (figs. S10B and S11, C and D).

ESCRT-III function was further perturbed by transfecting the dominant-negative (DN) mutant Vps4B^{E223Q} (*31*) or by treating cells with an siRNA targeting CHMP4B (*32*) (for siRNA efficiency, see fig. S10C). These treatments inhibit ESCRT-III activity: CHMP4B is the main component of ESCRT-III filaments (*33*), and Vps4B DN blocks depolymerization of ESCRT subunits and therefore their recycling (*3*). In these conditions, we did not detect a reduction in the rate of closure. However, when we plotted the distribution of wound size, we observed that perturbation of Vps4B or CHMP4B functions leads to a reduction in the number of cells displaying a relatively smaller wound (fig. S13, C and D). No such effect was seen upon inhibition of CHMP2A or CHMP3 (figs. S11B and S13A). This suggested that, upon perturbation of Vps4B or CHMP4B functions, cells with smaller wounds did not survive and, thus, could not be analyzed. Accordingly, we observed a significant reduction of cell survival upon laser wounding in these conditions, in comparison to cells treated with a control siRNA or overexpressing wild-type Vps4B (Fig. 5E). This was consistent with the higher levels of PI entry observed (Fig. 5F). This indicates that ESCRT-III activity is essential for cell survival after plasma membrane damage and suggests that the importance of ESCRT-III role in repair is related to the size of the wound.

Our observations indicate that ESCRT-III proteins are rapidly, specifically, and dynamically recruited to damaged areas of the plasma membrane to quickly repair the defect. Knowing the usual topology of ESCRT activity, this suggests a model whereby ESCRT proteins would be involved in extracellular budding of the damaged area and sealing of the plasma membrane.

To directly test this model by observing the wound site at high resolution, we set up a correlative scanning electron microscopy (SEM) assay to (i) get a spatiotemporal control of the wound driven by a laser, (ii) observe CHMP4B-EGFP dynamics and specific recruitment, and (iii) obtain a high-resolution image of the zone where CHMP4B-EGFP was recruited. The surface of

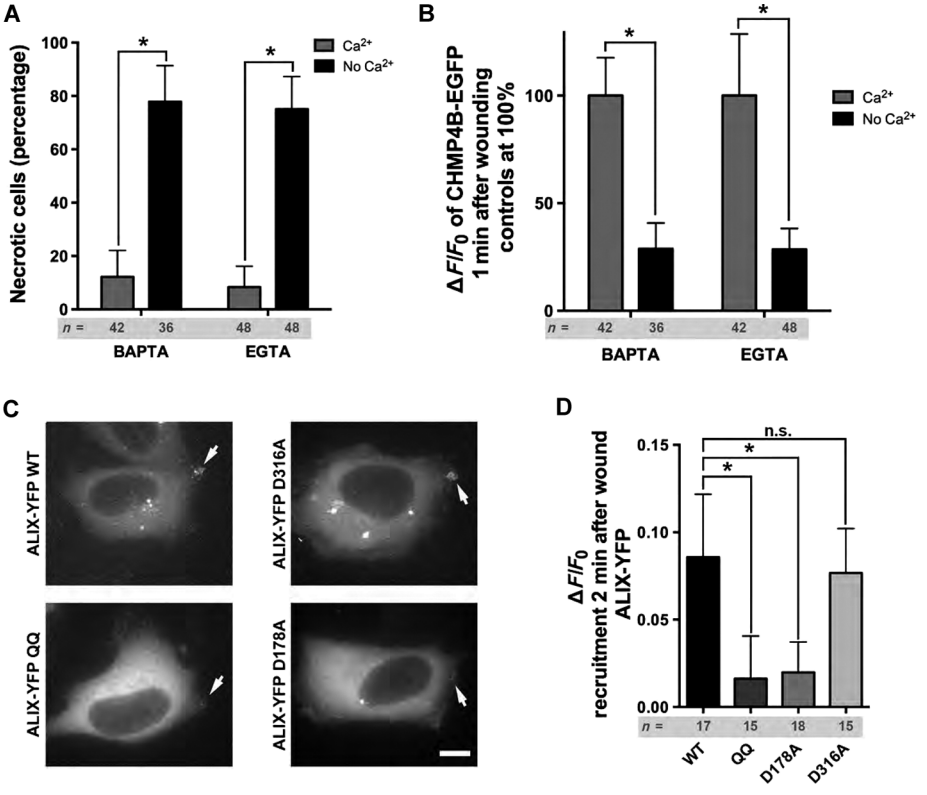

Fig. 4. ESCRT-III proteins and the ESCRT-associated protein ALIX are recruited in a calcium-dependent manner. HeLa CHMP4B-EGFP cells were incubated in media with or without calcium and supplemented with BAPTA [1,2-bis(2-aminophenoxy)ethane-*N*,*N*,*N*′,*N*′-tetraacetic acid] or EGTA. Both media were supplemented with PI at 160 μg/ml. Laser wounding was performed with a UV laser mounted on a spinning disc microscope. Cells were examined for necrosis after wounding on the basis of morphology by transmission light and levels of PI (see fig. S8). (**A**) Surviving and necrotic cells were quantified. Asterisks indicate differences tested by Fisher's exact test: $P > 0.0001$ (for BAPTA); $P > 0.0001$ (for EGTA). (**B**) The amount of recruited CHMP4B-EGFP at the wound was quantified at 1 min after wounding to avoid measurement artifacts due to cell shape changes and blebbing. Asterisks indicate differences tested with the unpaired *t* test with Welch's correction: $P = 0.0013$ (for BAPTA); $P = 0.0219$ (for EGTA). (**C** and **D**) HeLa cells transfected with different forms of split-YFP (yellow fluorescent protein) ALIX plasmids (*26*) were wounded and imaged. (C) Representative cells are presented for each mutant 2 min after wounding. (D) The recruitment of YFP-ALIX wild type (WT) or mutants was quantified at the wound site. Asterisks indicate differences tested with the unpaired *t* test with Welch's correction: $P = 0.0107$ (D178A mutant); $P = 0.6661$ (D316A mutant); $P = 0.0277$ (QQ mutant). Error bars correspond to half 95% confidence intervals. Scale bar, 10 μm.

the CHMP4B-EGFP HeLa cells grown on gridded coverslips was wounded using a UV laser (Fig. 6, A to F, and movie S4). The recruitment of CHMP4B-EGFP was followed by fluorescence time-lapse imaging (Fig. 6A). Lateral projection of image stacks showed that CHMP4B was recruited on plasma membrane protrusions (Fig. 6B). Cells imaged by time-lapse microscopy were then fixed and observed by SEM ($n = 6$). Low-magnification observation allowed the detection of wounded areas (Fig. 6C). At higher magnification, a cluster of extracellular buds of various size was detected on damaged zones and could be aligned with CHMP4B-EGFP–positive areas (Fig. 6, D to F). This suggested that ESCRT-III proteins were involved in extracellular budding at wounded sites.

We observed ESCRT-positive membrane shedding at the cell surface at wounded sites using time-lapse confocal microscopy (Fig. 7A, fig. S15, and movie S5). Accordingly, using spinning disc confocal time-lapse microscopy and SEM, we observed that CHMP4B-EGFP–positive buds were accompanied with shedding (fig. S16). Both membrane repair and ESCRT-positive shedding were adenosine 5′-triphosphate (ATP)–dependent mechanisms (Fig. 7, B to E, and movie S6). ESCRT recruitment itself still occurred in the absence of energy, but pinching of the membrane was only observed when energy production was restored (Fig. 7C and fig. S17). Thus, ESCRT shedding itself appears necessary for the wound closure, and ATP-dependent mechanisms, most likely the ESCRT disassembly machinery, may also be required to resolve the neck constriction, bud detachment, and wound closure.

The precise mechanisms that allow cells to rapidly detect wounds at the plasma membrane will need further investigation, but our results indicate a key role played by calcium increase. In addition, time-lapse imaging of CHMP4B recruitment led to an intriguing observation: We often noticed that plasma membrane wounding was followed by the rapid formation of a localized bleb of a few micrometers in diameter. The bleb rapidly became positive for CHMP4B-EGFP (Fig. 6G). As the bleb regressed, the staining of CHMP4B-EGFP became denser. Previous studies have revealed that events lowering membrane tension (such as exocytosis and local removal of the actin cytoskeleton) occur upon wounding of the plasma membrane (*34*). On the basis of these studies and our observations, we thus propose a model whereby a lesion in the plasma membrane triggers a local drop in membrane tension reinforced by local membrane supply through exocytosis and/or cytoskeleton remodeling. This drop in tension together with calcium entry would promote ALIX and ESCRT-III local recruitment. Other signals such as ubiquitination of proteins at the wound site or loss of lipid asymmetry and the recruitment of lipid-binding proteins may reinforce this binding. The assembly of ESCRT-III into helix-shaped filaments would then trap the damaged portions of plasma membrane on buds, shed them from the plasma membrane, and

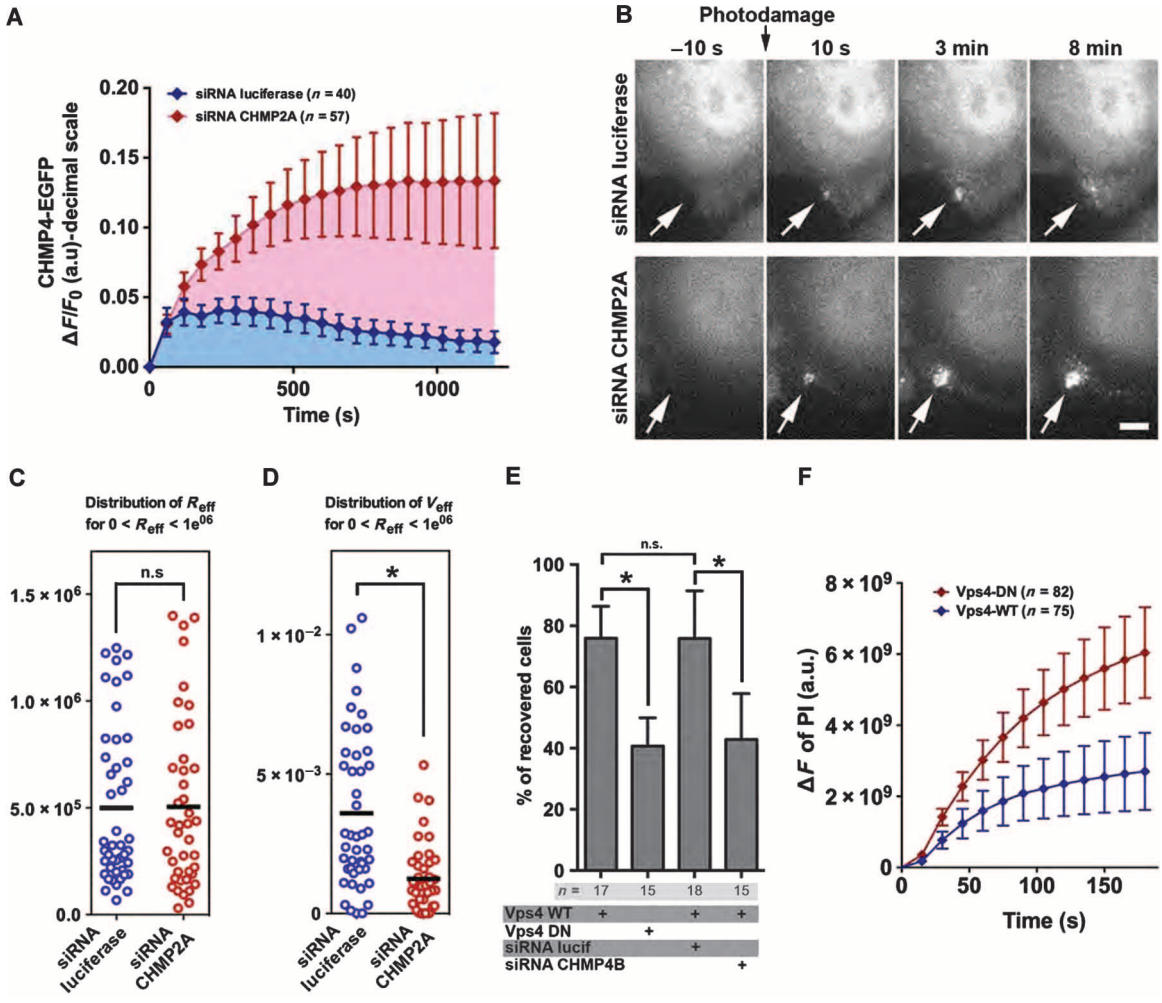

Fig. 5. Perturbation of wound resealing after depletion of ESCRT-III and ESCRT disassembly subunits. Laser wounding and time-lapse acquisition were performed with a UV laser/spinning disc microscope system on cells incubated with PI. (**A** and **B**) HeLa CHMP4B-EGFP cells were treated with siRNA luciferase or CHMP2A; see movie S3. (A) Quantification of CHMP4B recruitment at the wound site. (B) Representative cells for CHMP4B-EGFP recruitment in cells treated with siRNA luciferase or CHMP2A. Arrows point at the wound site. Scale bar, 10 μm. (**C** and **D**) HeLa cells transfected with different plasmids or siRNA were incubated in medium with PI and wounded using a UV laser. The total fluorescence of PI intensity was fitted using a mathematical model (see supplementary materials and methods) to obtain an initial effective radius (R_{eff}) of the wound and an effective rate of closure (v) (see fig. S13 for raw data). The distribution of R_{eff} for $R_{eff} < 1.5 \times 10^6$ was not different between siRNA luciferase and CHMP2A conditions; t test with Welch's correction, $P = 0.9537$ (C). Distribution of v for $R_{eff} < 1.5 \times 10^6$ was significantly different between siRNA luciferase and CHMP2A conditions; t test with Welch's correction, $P = 3.849 \times 10^{-6}$ (D). (**E**) Quantification of cell survival upon plasma membrane damage in HeLa cells transfected with Vps4B-EGFP WT or DN or treated with siRNA against luciferase or CHMP4B. Statistical analysis was performed using a two-sided χ^2 test for proportion comparison ($\alpha = 5\%$). n.s., nonsignificant differences; $^*P < 0.0001$. (**F**) PI entry was quantified and averaged for each time point in each condition. Error bars correspond to 95% confidence intervals.

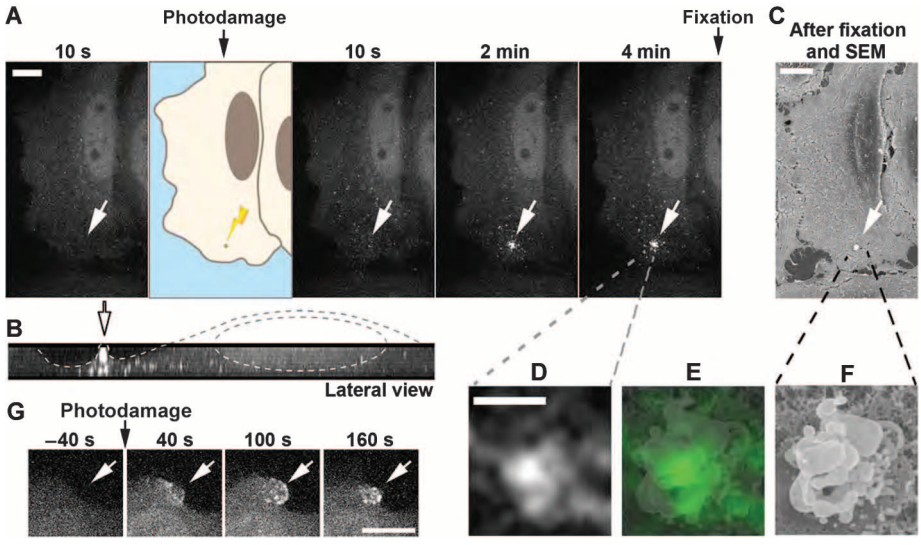

Fig. 6. ESCRT-positive cell surface budding upon wounding. HeLa CHMP4B-EGFP cells were used for these experiments. Wounds and time-lapse acquisition was performed on a spinning disc microscope equipped with a UV laser. (**A**) Time-lapse observation of the recruitment of CHMP4B-EGFP in wounded cells. (**B**) Lateral view of the cell 4 min after wounding. (**C**) Correlative image of the cell fixed and processed for SEM (representative of six cells analyzed). (**D** and **F**) Higher magnification of the areas pointed in (A) and (C). (**E**) Fluorescence to SEM alignment based on cell morphology criteria; see movie S4. (**G**) Recruitment of cytoplasmic CHMP4B-EGFP at blebs generated at the wounded site. The resorption of the bleb is accompanied by concentration of CHMP4B at the wounding site. Lateral views correspond to an orthogonal projection where the z images were separated by 5 pixels and intrapolated. White arrows point at the wound site where CHMP4B is recruited. Scale bars, 10 μm (A, C, and G); 1 μm (D to F).

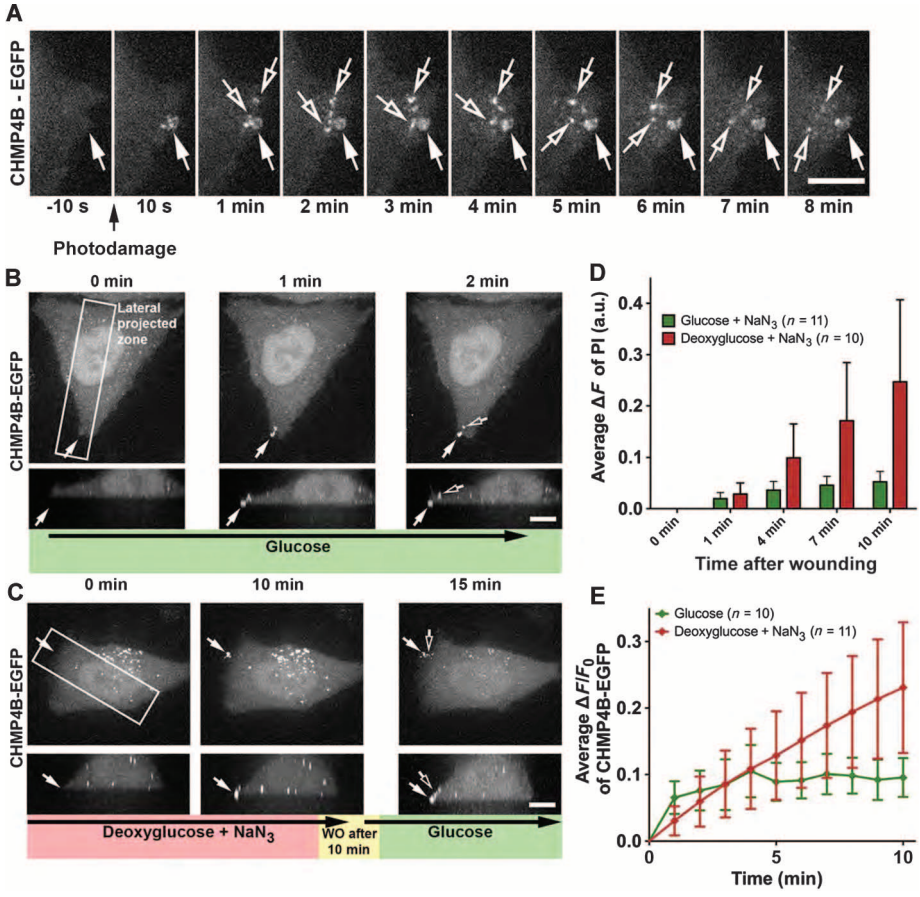

Fig. 7. Energy-independent ESCRT recruitment and energy-dependent shedding of wounded membrane. HeLa CHMP4B-EGFP cells were wounded and imaged on a spinning disc microscope equipped with a UV laser. (**A**) Shedding of ESCRT-positive particles from wound site pointed by the arrow. For corresponding lateral view, see movie S5. (**B** and **C**) Cells were incubated in phosphate-buffered saline (PBS) + PI supplemented with glucose, glucose + sodium azide, or deoxyglucose + sodium azide, as indicated. Cells were wounded as previously described. PBS containing deoxyglucose and sodium azide was washed out in certain assays [(C) and fig. S17] and replaced with PBS-glucose 10 min after wounding (WO). (**D** and **E**) PI entry (D) and CHMP4B (E) recruitment were quantified over time and averaged. Arrows point at the wound site where CHMP4B is recruited. Empty arrows point at CHMP4B-positive shedding particles. Error bars correspond to half 95% confidence intervals. Scale bars, 10 μm.

ensure sealing of nondamaged areas. Rapid binding of ESCRT proteins may also prevent extension of the wound and enhance cell survival. Although these mechanisms would be sufficient to explain localized membrane repair, it may be associated with other mechanisms described previously, such as patching of membrane gaps with intracellular vesicles (fig. S2A). The size of the gap may dictate the choice of the mechanism involved for repair because the patching model has clearly been demonstrated for larger wounds and because we observed critical involvement of ESCRT-III proteins to repair wounds smaller than 100 nm. These wounds were rather long-lasting as compared to what has been observed for larger wounds.

In conclusion, plasma membrane integrity is essential for cell homeostasis and survival. We propose that ESCRT-III proteins play a central role in repairing local injuries by ensuring extracellular shedding of damaged areas. Plasma membrane shedding, sometimes positive for ESCRTs, has been observed in several normal and pathological conditions (*35*, *36*), and it will now be important to test whether this is linked to local plasma membrane damage and whether ESCRT-III proteins are involved in these processes.

References and Notes

1. J. F. Nabhan, R. Hu, R. S. Oh, S. N. Cohen, Q. Lu, Formation and release of arrestin domain-containing protein 1-mediated microvesicles (ARMMs) at plasma membrane by recruitment of TSG101 protein. *Proc. Natl. Acad. Sci. U.S.A.* **109**, 4146–4151 (2012). doi: 10.1073/pnas.1200448109; pmid: 22315426

2. S. Saksena, J. Wahlman, D. Teis, A. E. Johnson, S. D. Emr, Functional reconstitution of ESCRT-III assembly and disassembly. *Cell* **136**, 97–109 (2009). doi: 10.1016/j.cell.2008.11.013; pmid: 19135892
3. T. Wollert, C. Wunder, J. Lippincott-Schwartz, J. H. Hurley, Membrane scission by the ESCRT-III complex. *Nature* **458**, 172–177 (2009). doi: 10.1038/nature07836; pmid: 19234443
4. T. Wollert, J. H. Hurley, Molecular mechanism of multivesicular body biogenesis by ESCRT complexes. *Nature* **464**, 864–869 (2010). doi: 10.1038/nature08849; pmid: 20305637
5. U. K. von Schwedler *et al*., The protein network of HIV budding. *Cell* **114**, 701–713 (2003). doi: 10.1016/S0092-8674(03)00714-1; pmid: 14505570
6. C. Langelier *et al*., Human ESCRT-II complex and its role in human immunodeficiency virus type 1 release. *J. Virol.* **80**, 9465–9480 (2006). doi: 10.1128/JVI.01049-06; pmid: 16973552
7. J. G. Carlton, J. Martin-Serrano, Parallels between cytokinesis and retroviral budding: A role for the ESCRT machinery. *Science* **316**, 1908–1912 (2007). doi: 10.1126/science.1143422; pmid: 17556548
8. E. Morita *et al*., Human ESCRT and ALIX proteins interact with proteins of the midbody and function in cytokinesis. *EMBO J.* **26**, 4215–4227 (2007). doi: 10.1038/sj.emboj.7601850; pmid: 17853893
9. J. G. Carlton, M. Agromayor, J. Martin-Serrano, Differential requirements for Alix and ESCRT-III in cytokinesis and HIV-1 release. *Proc. Natl. Acad. Sci. U.S.A.* **105**, 10541–10546 (2008). doi: 10.1073/pnas.0802008105; pmid: 18641129
10. R. D. Fisher *et al*., Structural and biochemical studies of ALIX/AIP1 and its role in retrovirus budding. *Cell* **128**, 841–852 (2007). doi: 10.1016/j.cell.2007.01.035; pmid: 17350572
11. J. McCullough, R. D. Fisher, F. G. Whitby, W. I. Sundquist, C. P. Hill, ALIX-CHMP4 interactions in the human ESCRT pathway. *Proc. Natl. Acad. Sci. U.S.A.* **105**, 7687–7691 (2008). doi: 10.1073/pnas.0801567105; pmid: 18511562
12. B. Strack, A. Calistri, S. Craig, E. Popova, H. G. Göttlinger, AIP1/ALIX is a binding partner for HIV-1 p6 and EIAV p9 functioning in virus budding. *Cell* **114**, 689–699 (2003). doi: 10.1016/S0092-8674(03)00653-6; pmid: 14505569
13. Y. Usami, S. Popov, H. G. Göttlinger, Potent rescue of human immunodeficiency virus type 1 late domain mutants by ALIX/AIP1 depends on its CHMP4 binding site. *J. Virol.* **81**, 6614–6622 (2007). doi: 10.1128/JVI.00314-07; pmid: 17428861
14. Q. Zhai *et al*., Structural and functional studies of ALIX interactions with YPX_nL late domains of HIV-1 and EIAV. *Nat. Struct. Mol. Biol.* **15**, 43–49 (2008). doi: 10.1038/nsmb1319; pmid: 18066081
15. P. A. Keyel *et al*., Streptolysin O clearance through sequestration into blebs that bud passively from the plasma membrane. *J. Cell Sci.* **124**, 2414–2423 (2011). doi: 10.1242/jcs.076182; pmid: 21693578
16. E. B. Babiychuk, K. Monastyrskaya, S. Potez, A. Draeger, Intracellular Ca^{2+} operates a switch between repair and lysis of streptolysin O-perforated cells. *Cell Death Differ.* **16**, 1126–1134 (2009). doi: 10.1038/cdd.2009.30; pmid: 19325569
17. I. Poser *et al*., BAC TransgeneOmics: A high-throughput method for exploration of protein function in mammals. *Nat. Methods* **5**, 409–415 (2008). doi: 10.1038/nmeth.1199; pmid: 18391959
18. P. I. Hanson, R. Roth, Y. Lin, J. E. Heuser, Plasma membrane deformation by circular arrays of ESCRT-III protein filaments. *J. Cell Biol.* **180**, 389–402 (2008). doi: 10.1083/jcb.200707031; pmid: 18209100
19. G. Bodon *et al*., Charged multivesicular body protein 2B (CHMP2B) of the endosomal sorting complex required for transport-III (ESCRT-III) polymerizes into helical structures deforming the plasma membrane. *J. Biol. Chem.* **286**, 40276–40286 (2011). doi: 10.1074/jbc.M111.283671; pmid: 21926173
20. P. Whitley *et al*., Identification of mammalian Vps24p as an effector of phosphatidylinositol 3,5-bisphosphate-dependent endosome compartmentalization. *J. Biol. Chem.* **278**, 38786–38795 (2003). doi: 10.1074/jbc.M306864200; pmid: 12878588
21. J. K. Jaiswal, N. W. Andrews, S. M. Simon, Membrane proximal lysosomes are the major vesicles responsible for calcium-dependent exocytosis in nonsecretory cells. *J. Cell Biol.* **159**, 625–635 (2002). doi: 10.1083/jcb.200208154; pmid: 12438417
22. A. Reddy, E. V. Caler, N. W. Andrews, Plasma membrane repair is mediated by Ca^{2+}-regulated exocytosis of lysosomes. *Cell* **106**, 157–169 (2001). doi: 10.1016/S0092-8674(01)00421-4; pmid: 11511344
23. O. Pornillos *et al*., Structure and functional interactions of the Tsg101 UEV domain. *EMBO J.* **21**, 2397–2406 (2002). doi: 10.1093/emboj/21.10.2397; pmid: 12006492
24. D. P. Dowlatshahi *et al*., ALIX is a Lys63-specific polyubiquitin binding protein that functions in retrovirus budding. *Dev. Cell* **23**, 1247–1254 (2012). doi: 10.1016/j.devcel.2012.10.023; pmid: 23201121
25. R. A. Steinhardt, G. Bi, J. M. Alderton, Cell membrane resealing by a vesicular mechanism similar to neurotransmitter release. *Science* **263**, 390–393 (1994). doi: 10.1126/science.7904084; pmid: 7904084
26. C. Bissig *et al*., Viral infection controlled by a calcium-dependent lipid-binding module in ALIX. *Dev. Cell* **25**, 364–373 (2013). doi: 10.1016/j.devcel.2013.04.003; pmid: 23664863
27. H. Fujita *et al*., Mammalian class E Vps proteins, SBP1 and mVps2/CHMP2A, interact with and regulate the function of an AAA-ATPase SKD1/Vps4B. *J. Cell Sci.* **117**, 2997–3009 (2004). doi: 10.1242/jcs.01170; pmid: 15173323
28. T. Obita *et al*., Structural basis for selective recognition of ESCRT-III by the AAA ATPase Vps4. *Nature* **449**, 735–739 (2007). doi: 10.1038/nature06171; pmid: 17928861
29. S. Shim, L. A. Kimpler, P. I. Hanson, Structure/function analysis of four core ESCRT-III proteins reveals common regulatory role for extreme C-terminal domain. *Traffic* **8**, 1068–1079 (2007). doi: 10.1111/j.1600-0854.2007.00584.x; pmid: 17547705
30. S. Shim, S. A. Merrill, P. I. Hanson, Novel interactions of ESCRT-III with LIP5 and VPS4 and their implications for ESCRT-III disassembly. *Mol. Biol. Cell* **19**, 2661–2672 (2008). doi: 10.1091/mbc.E07-12-1263; pmid: 18385515
31. N. Bishop, P. Woodman, ATPase-defective mammalian VPS4 localizes to aberrant endosomes and impairs cholesterol trafficking. *Mol. Biol. Cell* **11**, 227–239 (2000). doi: 10.1091/mbc.11.1.227; pmid: 10637304
32. J. Guizetti *et al*., Cortical constriction during abscission involves helices of ESCRT-III–dependent filaments. *Science* **331**, 1616–1620 (2011). doi: 10.1126/science.1201847; pmid: 21310966
33. D. Teis, S. Saksena, S. D. Emr, Ordered assembly of the ESCRT-III complex on endosomes is required to sequester cargo during MVB formation. *Dev. Cell* **15**, 578–589 (2008). doi: 10.1016/j.devcel.2008.08.013; pmid: 18854142
34. P. L. McNeil, R. A. Steinhardt, Plasma membrane disruption: Repair, prevention, adaptation. *Annu. Rev. Cell Dev. Biol.* **19**, 697–731 (2003). doi: 10.1146/annurev.cellbio.19.111301.140101; pmid: 14570587
35. M. Guescini *et al*., C2C12 myoblasts release micro-vesicles containing mtDNA and proteins involved in signal transduction. *Exp. Cell Res.* **316**, 1977–1984 (2010). doi: 10.1016/j.yexcr.2010.04.006; pmid: 20399774
36. D. P. Romancino *et al*., Identification and characterization of the nano-sized vesicles released by muscle cells. *FEBS Lett.* **587**, 1379–1384 (2013). doi: 10.1016/j.febslet.2013.03.012; pmid: 23523921
37. K. G. Bache *et al*., The ESCRT-III subunit hVps24 is required for degradation but not silencing of the epidermal growth factor receptor. *Mol. Biol. Cell* **17**, 2513–2523 (2006). doi: 10.1091/mbc.E05-10-0915; pmid: 16554368
38. A. Cabezas, K. G. Bache, A. Brech, H. Stenmark, Alix regulates cortical actin and the spatial distribution of endosomes. *J. Cell Sci.* **118**, 2625–2635 (2005). doi: 10.1242/jcs.02382; pmid: 15914539

Acknowledgments: We are indebted to the electron microscopy platform of Institut Pasteur and in particular to P. Bomme for their services with correlative light to SEM experiments. We are also indebted to our colleagues who shared materials; I. Poser and A. Hyman for the CHMP4B-GFP cell line; C. Wunder and C. Bissig for ESCRT plasmids; M. Maki for the CHMP6-GFP plasmid; R. Tweten for the streptolysin O plasmid; R. Y. Tsien for the MyrPalm-EGFP plasmid; A. Draeger for the annexin plasmids; H. Stenmark, S. Urbé, and R. Sadoul for the antibodies against ESCRT subunits; G. van der Goot for the listeriolysin O toxin; A. El Marjou for the production of streptolysin O; V. Fraisier, L. Leconte, L. Sengmanivong, and F. Waharte of the Nikon Imaging Center and the PICT-IBiSA of the Institut Curie for technical support in microscopy; A. Pinheiro for quantitative polymerase chain reaction protocols and help; P. Vargas for advice and reagents for calcium experiments; J. B. Manneville, D. Guet, and M. Pinot for technical assistance with micropipette use; and F. Niedergang, G. Boncompain, A. Dimitrov, and F. Brochard for commenting on the results. Funding: This work was supported by the Institut Curie, CNRS, the French Agence Nationale de la Recherche ("ANR") (to F.P.), a Ligue Contre le Cancer grant (to M.P.), a French ministerial fellowship (to J.L.-J.), Fondation pour la Recherche Medicale fellowships (to J.L.-J. and P.M.), and an Institut Curie fellowship (to A.J.J.). F.P.'s team is supported by the LaBex CelTisPhyBio (ANR-10-LBX-0038 part of the IDEX PSL no. ANR-10-IDEX-0001-02). Author contributions: A.J.J. and J.L.-J. began the project. A.J.J. designed and performed all the experiments under the supervision of F.P. and with the help of the electron microscopy platform of Institut Pasteur for the SEM experiments and performed most quantifications. A.J.J. wrote the paper together with F.P. J.L.-J. performed preliminary experiments under the supervision of M.P., was involved in discussions, and participated in the writing of the manuscript. P.M. performed experiments for determining hole size together with A.J.J., performed the computational modeling of PI entry and hole size estimation, performed several quantitative analysis in close interaction with A.J.J. and under the supervision of M.P. and F.P., was involved in discussions, and participated in the writing of the manuscript. S.D. helped A.J.J. with revision experiments. M.P. was involved in discussions, supervised the quantitative analysis, and participated in the writing of the manuscript. F.P. supervised this work and wrote the manuscript together with A.J.J.

Supplementary Materials

www.sciencemag.org/content/343/6174/1247136/suppl/DC1
Materials and Methods
Figs. S1 to S17
Movies S1 to S8
References (*39*–*43*)

11 October 2013; accepted 16 January 2014
10.1126/science.1247136

Lost in Transition: Start-Up of Glycolysis Yields Subpopulations of Nongrowing Cells

Johan H. van Heerden, Meike T. Wortel, Frank J. Bruggeman, Joseph J. Heijnen, Yves J. M. Bollen, Robert Planqué, Josephus Hulshof, Tom G. O'Toole, S. Aljoscha Wahl, Bas Teusink*

READ THE FULL ARTICLE ONLINE
http://dx.doi.org/10.1126/science.1245114

Cite this article as J. H. van Heerden *et al.*, *Science* **343**, 1245114 (2014).
DOI: 10.1126/science.1245114

Introduction: Cells use multilayered regulatory systems to respond adequately to changing environments or perturbations. Failure in regulation underlies cellular malfunctioning, loss of fitness, or disease. How molecular components dynamically interact to give rise to robust and adaptive responses is not well understood. Here, we studied how the model eukaryote *Saccharomyces cerevisiae* can cope with transition to high glucose levels, a failure of which results in metabolic malfunctioning and growth arrest.

Methods: We combined experimental and modeling approaches to unravel the mechanisms used by yeast to cope with sudden glucose availability. We studied growth characteristics and metabolic state at population and single-cell levels (through flow cytometry and colony plating) of the wild type and of mutants unable to transit properly to excess glucose; such mutants are defective in trehalose synthesis, a disaccharide associated with stress resistance. Dynamic ^{13}C tracer enrichment was used to estimate dynamic intracellular fluxes immediately after glucose addition. Mathematical modeling was used to interpret and generalize results and to suggest subsequent experiments.

Results: The failure to cope with glucose is caused by imbalanced reactions in glycolysis, the essential pathway in energy metabolism in most organisms. In the failure mode, the first steps of glycolysis carry more flux than the downstream steps, resulting in accumulating intermediates at constant low levels of adenosine triphosphate (ATP) and inorganic phosphate. We found that cells with such an unbalanced glycolysis coexist with vital cells with normal glycolytic function. Spontaneous, nongenetic metabolic variability among individual cells determines which state is reached and consequently which cells survive. In mutants of trehalose metabolism, only 0.01% of the cells started to grow on glucose; in the wild type, the success rate was still only 93% (i.e., 7% of wild-type yeast did not properly start up glycolysis). Mathematical models predicted that the dynamics of inorganic phosphate is a key determinant in successful transition to glucose, and that phosphate release through ATP hydrolysis reduces the probability of reaching an imbalanced state. ^{13}C-labeling experiments confirmed the hypothesis that trehalose metabolism constitutes a futile cycle that would provide proper phosphate balance: Upon a glucose pulse, almost 30% of the glucose is transiently shuttled into trehalose metabolism.

Discussion: Our work reveals how cell fate can be determined by glycolytic dynamics combined with cell heterogeneity purely at the metabolic level. Specific regulatory mechanisms are required to initiate the glycolytic pathway; in yeast, trehalose cycling pushes glycolysis transiently into the right direction, after which cycling stops. The coexistence of two modes of glycolysis—an imbalanced state and the normal functional state—arises from the fundamental design of glycolysis. This makes the imbalanced state a generic risk for humans as well, extending our fundamental knowledge of this central pathway that is dysfunctional in diseases such as diabetes and cancer.

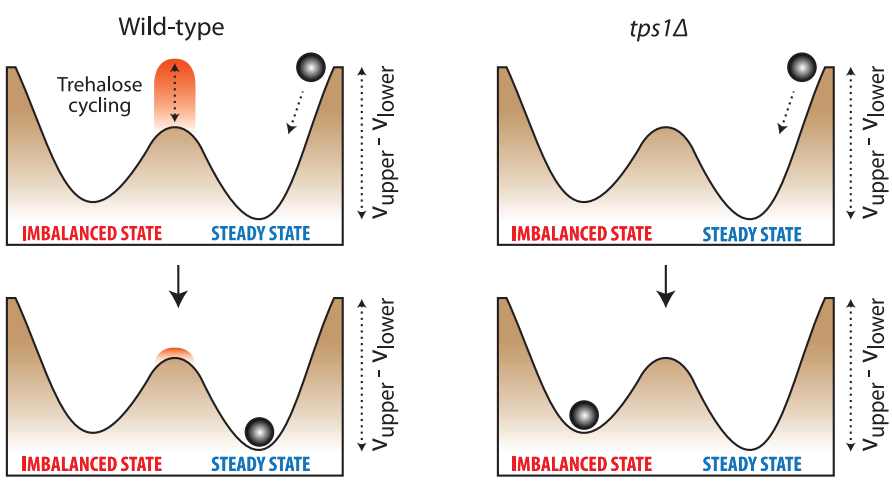

Initiation of glycolysis can have two outcomes. Upon glucose availability, glycolysis can end up in either a functional steady state or an unviable imbalanced state with imbalanced fluxes between ATP-consuming (V_{upper}) and ATP-producing steps (V_{lower}). In wild-type yeast, the transient activation of trehalose cycling pushes glycolysis toward the viable steady state. Failure to do so results in metabolic malfunctioning, as observed in mutants in trehalose biosynthesis (*tps1*Δ).

FIGURES IN THE FULL ARTICLE

Fig. 1. The coexistence of two glycolytic states underlies glucose-tolerant *tps1*Δ subpopulations.

Fig. 2. pH_i reveals distinct metabolic subpopulations.

Fig. 3. Metabolic subpopulations are caused by small variation in metabolic variables, and their sizes can be manipulated.

Fig. 4. Generalized core model of glycolysis can reach two stable, coexisting states.

Fig. 5. ^{13}C tracer enrichment reveals highly dynamic flux distributions through the trehalose cycle.

SUPPLEMENTARY MATERIALS

Supplementary Text
Figs. S1 to S18
Tables S1 to S8
References

The list of author affiliations is available in the full article online.
*Corresponding author. E-mail: b.teusink@vu.nl

Lost in Transition: Start-Up of Glycolysis Yields Subpopulations of Nongrowing Cells

Johan H. van Heerden,[1,2,3] Meike T. Wortel,[1,2,3] Frank J. Bruggeman,[1,3] Joseph J. Heijnen,[2,4] Yves J. M. Bollen,[3,5] Robert Planqué,[6] Josephus Hulshof,[6] Tom G. O'Toole,[7] S. Aljoscha Wahl,[2,4] Bas Teusink[1,2,3]*

Cells need to adapt to dynamic environments. Yeast that fail to cope with dynamic changes in the abundance of glucose can undergo growth arrest. We show that this failure is caused by imbalanced reactions in glycolysis, the essential pathway in energy metabolism in most organisms. The imbalance arises largely from the fundamental design of glycolysis, making this state of glycolysis a generic risk. Cells with unbalanced glycolysis coexisted with vital cells. Spontaneous, nongenetic metabolic variability among individual cells determines which state is reached and, consequently, which cells survive. Transient ATP (adenosine 5′-triphosphate) hydrolysis through futile cycling reduces the probability of reaching the imbalanced state. Our results reveal dynamic behavior of glycolysis and indicate that cell fate can be determined by heterogeneity purely at the metabolic level.

Key properties of biological systems are adaptability and robustness—the ability to maintain the physiological state in response to perturbations or dynamic conditions (*1*). Cells use multilayered regulation to respond adequately to changing environments or sudden perturbations. Failures in regulation underlie cellular malfunctioning, loss of fitness, or disease. In recent years, there has been a revived interest in metabolic processes, because many diseases are associated with metabolic aberrations, such as diabetes and cancer (*2*). Glycolysis is the central pathway in energy metabolism, which converts glucose to pyruvate with a net production of two adenosine 5′-triphosphate (ATP) molecules per glucose molecule. However, this net formation of ATP in "lower glycolysis" (Fig. 1) is preceded by an initial ATP investment at the first steps in the pathway ("upper glycolysis"; Fig. 1). This sequence of enzymatic steps in glycolysis, which is adopted by many organisms (*3*), implies a serious risk. If upper glycolysis outpaces lower glycolysis, a massive accumulation of glycolytic intermediates can occur with much reduced ATP production (*4*). This phenotype is observed in pancreatic β cells overexpressing glucokinase (coined acute glucose intolerance) (*5*), the enzyme that catalyzes the first step of glycolysis. Similarly, *Saccharomyces cerevisiae* mutants defective in the biosynthesis of the disaccharide trehalose, which branches off from glycolysis at the level of glucose-6-phosphate (G6P) (Fig. 1), show accumulation of the glycolytic intermediate fructose 1,6-bisphosphate (FBP) at low concentrations of ATP (*6*). We call this detrimental state of glycolysis an imbalanced state. We find that this imbalanced state is a risk also for normal cells. Through detailed system-level analysis of yeast glycolysis, we explain how phosphate dynamics is at the origin of the imbalance, and reveal how specific regulatory mechanisms affect the probability for cells to get trapped in it.

S. cerevisiae mutants with a defect in trehalose 6-phosphate (T6P) synthase (*tps1*), the first committed step in trehalose biosynthesis (Fig. 1), exhibit the imbalanced-state phenotype and are unable to grow on glucose (*7*). The molecular mechanism underlying this imbalanced phenotype has proven challenging to elucidate [we provide an extensive account of the literature in (*8*)]. T6P, the product of *tps1*, acts in vitro as a competitive inhibitor of the hexokinases (HXK1 and HXK2), with respect to glucose (*9*). This negative feedback loop was hypothesized to slow down the upper part of glycolysis and restore the balance in wild-type cells (*4*), but T6P-insensitive hexokinase mutants do grow on glucose (*10*). An alternative hypothesis assumes a reduced activity of glyceraldehyde-3-phosphate dehydrogenase (GAPDH) because of the low amounts of its substrate, cytosolic phosphate (P_i), in *tps1*Δ mutants. Accordingly, P_i release should enhance GAPDH activity and restore balance. In line with this hypothesis, enhanced glycerol production, which releases P_i, restores growth of *tps1*Δ mutants on glucose (*11*). Trehalose production from G6P also releases P_i (Fig. 1A); however, the capacity of trehalose synthesis was believed to be too low to provide enough P_i for the high flux of glycolysis (*12*).

We used a computational approach to better understand the complex phenotype of *tps1*Δ mutants. We adapted an existing kinetic model of glycolysis (*13*) by (i) introducing P_i as an explicit variable in the model (rather than as a fixed "commodity" metabolite) and (ii) allowing for the mobilization of P_i from vacuolar stores, based on in vivo nuclear magnetic resonance data that describe this behavior (*6*). The latter was necessary because the net accumulation of phosphate-containing glycolytic intermediates that are observed experimentally in the imbalanced state (Fig. 1B) is not possible without the import of P_i [details on these and other small adjustments to the original model are provided in (*8*)].

Two Glycolytic States Coexist

Simulations representing the *tps1*Δ mutant resulted in dynamic metabolite profiles that were qualitatively similar to experimentally observed profiles (Fig. 1B); that is, all metabolites were balanced, except for the intermediates between the upper and lower parts of glycolysis (Fig. 1B and fig. S3). Known experimental rescue mechanisms for the *tps1*Δ mutant, such as reduced activity of hexokinase (*14*) or enhanced glycerol production (*11*), could be reproduced in silico (figs. S11C and S14, C and D).

Our *tps1*Δ mutant model could reach another state, which resembled the wild-type steady state with proper flux, high ATP and P_i levels, and normal FBP levels. Whether this state was reached depended on the initial concentrations of the metabolites, as shown for FBP and P_i (Fig. 1B). Hence, two stable outcomes (states) coexisted in the model, a global steady state and an imbalanced state: the latter is a nontypical stable state, because some variables are not constant in time but rather accumulate. Other systems with more than one stable state, as found in sporulation (*15*) or differentiation (*16*), often result in phenotypically different subpopulations in an isogenic population. We assessed experimentally whether we could find evidence for such subpopulations as well, by asserting that only the functional glycolytic state would support growth. On the basis of serial dilution plating of wild-type and *tps1*Δ cultures on galactose and glucose (*8*), we estimated that about 1 in 10^3 to 10^4 *tps1*Δ cells grew on excess glucose (Fig. 1C). This small subpopulation size is consistent with the very long lag phase we observed in glucose liquid cultures (Fig. 1D). In the past, glucose-positive *tps1*Δ colonies were usually discarded as revertants or rescue mutants. However, when *tps1*Δ colonies were directly picked from glucose plates and subjected to another transition via galactose to glucose, the original subpopulation structure with less than

[1]Systems Bioinformatics/Amsterdam Institute for Molecules, Medicines and Systems (AIMMS)/Netherlands Institute for Systems Biology, VU University, De Boelelaan 1085, 1081 HV Amsterdam, Netherlands. [2]Kluyver Centre for Genomics of Industrial Fermentation/Netherlands Consortium for Systems Biology (NCSB), Delft University of Technology, Julianalaan 67, 2628 BC Delft, Netherlands. [3]Department of Molecular Cell Biology, VU University, 1081 HV Amsterdam, Netherlands. [4]Department of Biotechnology, Delft University of Technology, 2628 BC Delft, Netherlands. [5]LaserLaB Amsterdam, VU University, 1081 HV Amsterdam, Netherlands. [6]Department of Mathematics, VU University, 1081 HV Amsterdam, Netherlands. [7]Department of Molecular Cell Biology and Immunology, Vrije University Medical Center, v/d Boechorststraat 7, 1081 BT Amsterdam, Netherlands.

*Corresponding author. E-mail: b.teusink@vu.nl

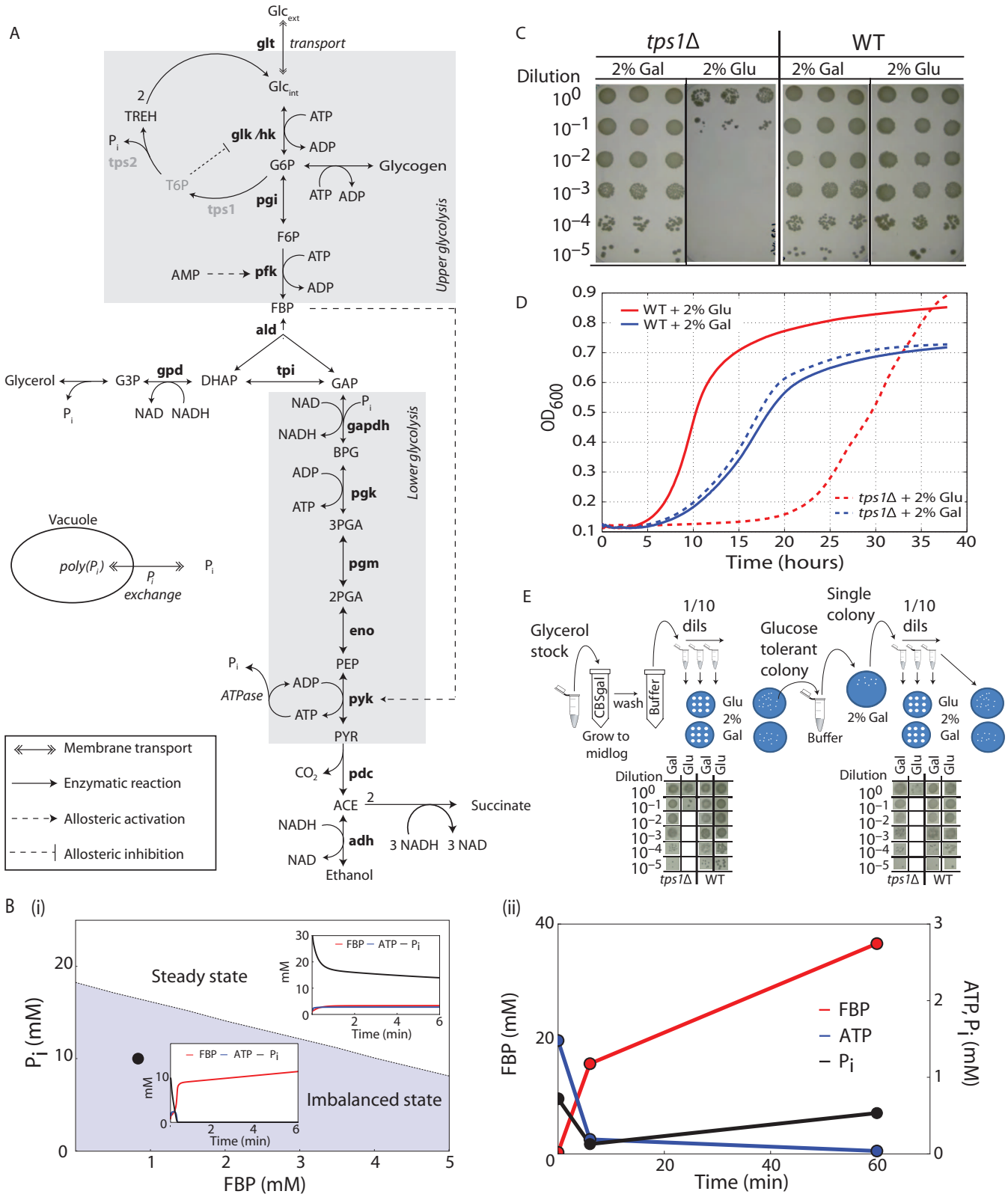

Fig. 1. The coexistence of two glycolytic states underlies glucose-tolerant *tps1*Δ subpopulations. (**A**) Schematic illustration of glycolysis and the trehalose cycle. (**B**) Depending on initial conditions, the *tps1*Δ-like model can reach one of two stable states. (i) Normal steady state (white area) or an imbalanced state (gray area). The black circle indicates the initial values for P_i and FBP used (table S2). (ii) Simulation of the imbalanced state is qualitatively similar to experimentally observed profiles [data reproduced from (*9*)]. (**C**) Serial dilution plating reproducibly shows glucose-tolerant subpopulations of between 1 in 10^3 and 1 in 10^4 *tps1*Δ cells ($n = 3$). (**D**) Growth curves for wild type (WT) and *tps1*Δ on glucose (Glu) and galactose (Gal): Glu *tps1*Δ cells show extended lag phase as a consequence of a large nongrowing background. (**E**) Summary of the propagation scheme and a representative result (see fig. S5C for full scheme) show that glucose tolerance can be reset, because populations derived from a glucose-tolerant colony exhibit subpopulation structures similar to initial populations derived from glycerol stocks.

1 in 10^3 glucose-tolerant colonies was restored (Fig. 1E and fig. S5C). This argues against a genetic basis. We therefore conclude that there is a small subpopulation of glucose-positive *tps1*Δ cells that arises from spontaneous phenotypic—as opposed to genetic—variability.

We reexamined the reported inhibitory effect of low concentrations of glucose on *tps1*Δ mutant growth in the presence of excess galactose (*17*). Plating experiments again showed that the growth inhibition observed at the population level is in fact caused by a glucose-dependent increase in the size of a subpopulation that was unable to grow (fig. S6A). A simple mathematical model of population growth dynamics with different growing and nongrowing subpopulation sizes (*8*) reproduced the experimental data (*17*) very well (fig. S6B).

Intracellular pH Reveals Two Metabolic Subpopulations

To visualize the two subpopulations, we made use of the observation that *tps1*Δ mutants, when exposed to glucose, are unable to maintain pH homeostasis because they produce too little ATP (*6*). Hence, after glucose addition, the intracellular pH (pH_i) of *tps1*Δ populations decreased by more than 1 pH unit compared to that of wild-type cells (Fig. 2A). After confirming that different subpopulations could be distinguished on the basis of pH_i signals (Fig. 2B), we used flow cytometry as a high-throughput approach to study the structure of both *tps1*Δ and wild-type populations exposed to galactose and glucose. We found two subpopulations of *tps1*Δ cells of sizes that agreed with the plating assays and growth lag phases (Fig. 2C). We also tested wild-type cells because analysis of the wild-type version of the model also showed two stable states (fig. S4). Indeed, a subpopulation of wild-type cells with low pH appeared in cultures exposed to glucose, but a similar response was observed for galactose (Fig. 2C). The size of the subpopulation, about 7%, was larger than the model suggested (but not unexpectedly; fig. S4). These results indicate that the imbalanced state is a general property of glycolysis that cannot be fully prevented by regulatory mechanisms operative in wild-type cells.

Metabolic Variability Determines State of Glycolysis

We tested in silico whether the observed phenotypic variability in the response to sugar addition could be reproduced by introducing spontaneous variation in enzyme and initial metabolite concentrations. We sampled these concentrations from Gaussian distributions with realistic coefficients of variation (*18*). The mean of the initial metabolite concentrations was based on metabolite data for wild-type cells grown on galactose (*19*), the sugar on which we grew *tps1*Δ before glucose addition. We generated 10^6 *tps1*Δ-like models each with unique initial conditions and simulated a galactose-to-glucose transition. Less than one in a thousand models actually reached a functional steady state. Thus, heterogeneity in the amounts of glycolytic enzymes and metabolites appears to cause some cells to survive glucose dynamics, whereas others do not. This is striking, because metabolism is often considered to operate in a deterministic regime due to rather high concentrations of enzymes and intermediates. Phenotypic variation by nongenetic variability is usually studied in genetic circuits that naturally operate at a stochastic regime with low copy numbers for key components (*20*).

It is relevant to compare the above observations with frameworks such as fluctuation-induced bistable switching (*21*, *22*), which has previously been linked to the emergence of phenotypic heterogeneity. In contrast to such stochastic switching phenomena, the emergence of the two distinct phenotypes (viable and nonviable) described here does not depend on the coexistence of two qualitatively different physiological states before a glucose perturbation. Our interpretation of the above data is that spontaneous, nongenetic variation between cells creates a continuous probability distribution for metabolite concentrations and metabolic fluxes. Within the space of these initial physiological states, a subspace exists that characterizes the cells that survive a sudden glucose excess exposure (fig. S7) (*8*).

To assess which parameters and initial conditions most affect the probability to reach an imbalanced or functional steady state, we performed a linear discriminant analysis over all our model simulations (*8*). A single discriminant accounted for 99% of the differences in initial conditions that lead to either the balanced or imbalanced states

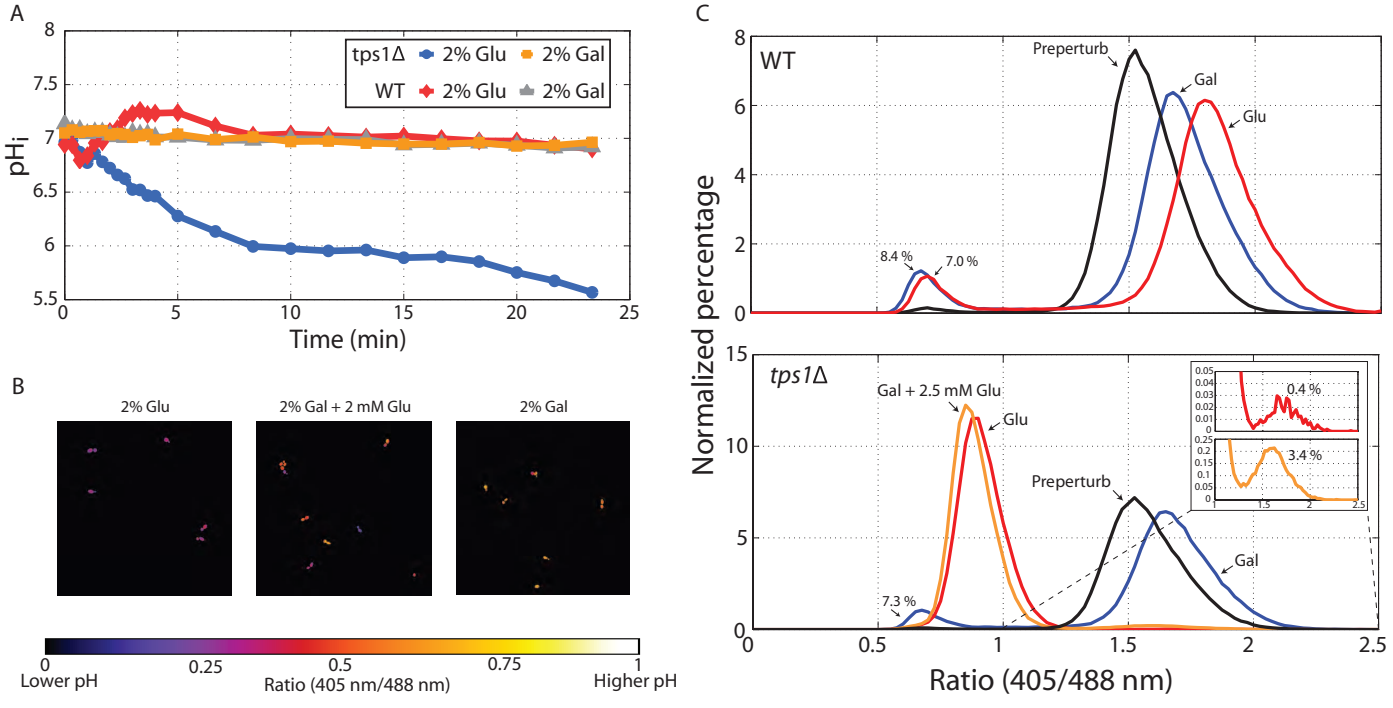

Fig. 2. pH_i reveals distinct metabolic subpopulations. (**A**) Population-level pH_i responses show the disruption of pH homeostasis of *tps1*Δ cells in response to 2% glucose. After a 2% glucose or galactose pulse, the pH_i of WT and *tps1*Δ populations is shown in time. (**B**) Fluorescence microscopy shows that distinct metabolic states can be visualized using pH_i readouts. (**C**) Flow cytometry measurements based on pHluorin signals reveal the presence of distinct subpopulations in both WT (top graph) and *tps1*Δ populations (bottom graph) after perturbations with glucose and galactose (black, preperturbation sample in wash buffer; blue, 2% Gal; red, 2% Glu; orange, 2% Gal + 2.5 mM Glu).

(fig. S11A). This discriminant identified parameters and initial metabolite concentrations that tend to either reduce the flux through the upper part of glycolysis or enhance the flux through lower glycolysis (Fig. 3A). The parameters related to the primary mechanisms known to rescue the *tps1*Δ mutant phenotype (*23*) were all represented.

Size of Subpopulations Can Be Manipulated

We looked for ways to experimentally influence the size of the two subpopulations. Respiratory inhibitors, in particular antimycin A (*24*), have been shown to improve growth in the presence of glucose. However, ethanol, the solvent of antimycin A, produced pronounced decreases in the lag phase (Fig. 3B), completely dominating the antimycin A effect (fig. S5D). These results were confirmed by plating assays (fig. S6C) and flow cytometry measurements of pH_i (fig. S9) (*8*). We repeated the in silico random sampling approach at different ethanol concentrations and reproduced the positive effect of ethanol (Fig. 3C). The model showed that the increase in ethanol concentration increased P_i release through glycerol formation (fig. S11B) driven by an increased NADH (reduced form of nicotinamide adenine dinucleotide)/NAD (oxidized form of nicotinamide adenine dinucleotide) ratio (*25*). This model prediction was experimentally tested in *tps1*Δ mutant cultures by the addition of formate. Although formate cannot be used as a carbon source by yeast, its conversion to CO_2 by formate dehydrogenase (*26*) enhances NADH formation. Indeed, formate additions similarly decreased the lag phase, implying a NADH-driven increase in glycerol production that subsequently increases the proportion of *tps1*Δ cells in the population that could grow on glucose (fig. S5E).

Core Model Explains and Generalizes Dynamics

To generalize our findings and to provide a deeper understanding of the observed coexistence of two stable states, we captured the essential features of the large model in a reduced model. This generalized core model (*8*) only considers the concentrations of FBP, ATP, and P_i and four reactions: (i) a lumped upper glycolysis reaction (v_{upper}), (ii) a lumped lower part of glycolysis (v_{lower}), (iii) an ATP-demand reaction (v_{ATP}), and (iv) a P_i import or export reaction (v_P) (Fig. 4). Detailed mathematical analysis showed that such a generalized glycolytic pathway has two stable states representing a functional steady state and an imbalanced state.

Figure 4 shows the system dynamics that lead to these two states: The difference between the left and right panel is only the initial P_i level (10.4 and 9.4 mM, respectively). How can the different outcomes in these simulations be explained? At the start of the simulation (when glucose is added), $v_{upper} > v_{lower}$, and this difference causes the concentration of the intermediate FBP to increase (as $dFBP/dt = v_{upper} - v_{lower}$). For a balanced steady state, v_{lower} needs to accelerate to equal the rate of v_{upper} (note that this challenge becomes bigger if the activity of v_{upper} is higher). P_i is the phosphate source for FBP, and therefore, FBP accumulation results in a drop in P_i (Fig. 4). Because both FBP and P_i are substrates of v_{lower}, the accumulation of FBP stimulates v_{lower}, whereas the drop in P_i tends to slow it down: Which effect is dominant may determine the fate of the system. If P_i is high initially, a drop in P_i will not affect v_{lower} and the FBP increase will dominate, resulting in the functional steady state being reached (Fig. 4, left panel). Similarly, if P_i is liberated quickly enough directly by storage/uptake (v_P) or indirectly by ATP hydrolysis (v_{ATP}), P_i will drop less quickly and the balanced steady state can also be reached. If, however, P_i is low at the onset of glucose addition or P_i mobilization is too slow, or both, the decrease in P_i will quickly become a limiting factor for v_{lower} and will dominate the stimulating effect of accumulating FBP. In this case, v_{lower} will not accelerate quickly enough to reach the rate of v_{upper}, and the system will collapse to the imbalanced state (Fig. 4, right panel). Once in this imbalanced state, continuous P_i mobilization from uptake or storage paradoxically maintains the imbalance. In this low P_i, low ATP state, imported P_i enhances the rate of v_{lower}, but the concomitant production of ATP will increase v_{upper} two times more (due to the stoichiometric coupling of ATP in glycolysis; Fig. 4B). Hence, the imbalance and, thus, FBP accumulation will only get bigger with faster P_i import, as observed in the core model and the detailed model (fig. S1).

Trehalose Metabolism Constitutes Transient Futile Cycling

The core model predicted that enhanced P_i mobilization through ATP hydrolysis by v_{ATP} could enlarge the set of initial conditions that leads to a functional steady state, or could even result in the disappearance of the imbalanced state altogether (fig. S14). This was confirmed in the detailed model. We realized that, in yeast, the full trehalose cycle (Fig. 1A) could act as a mechanism for ATP hydrolysis through futile cycling. This cycling of trehalose should be able to remove the existence of the imbalanced state or at least reduce the probability to reach it, providing a rationale why trehalose metabolism affects glycolytic function.

To estimate the dynamic fluxes through the trehalose network upon a transition to glucose excess, we used a dynamic ^{13}C-labeling approach (*8*). Wild-type cells were grown in a glucose-limited chemostat and treated with either 110 mM [^{12}C] glucose or uniformly labeled [U-$^{13}C_6$]glucose pulses. The time course of the concentrations and the average carbon labeling enrichments for key intermediates are shown in Fig. 5A. For most metabolites, up to full enrichment was achieved very rapidly; in contrast, the large trehalose pool was enriched to only 14% at the end of the experiment. From these data, the flux of glucose through the different glycolytic enzymes was estimated on the basis of a hybrid modeling approach (*27*). The flux profiles indicated that (i) fluxes changed rapidly after a glucose pulse, at similar time scales as key metabolites, such as ATP (Fig. 5B); (ii) fluxes through TPS1 and TPS2 increased and subsequently decreased between 0 and 5 min; and (iii) at its maximum, as much as 28% of the glucose taken up was branched into trehalose (Fig. 5C). The transient nature of the flux through the trehalose pathway is consistent with the existence of two stable states in glycolysis, that is, once the system has reached the viable steady state, the need for excessive ATP hydrolysis through futile trehalose cycling has disappeared. Thus, we suggest that trehalose cycling constitutes a transient futile

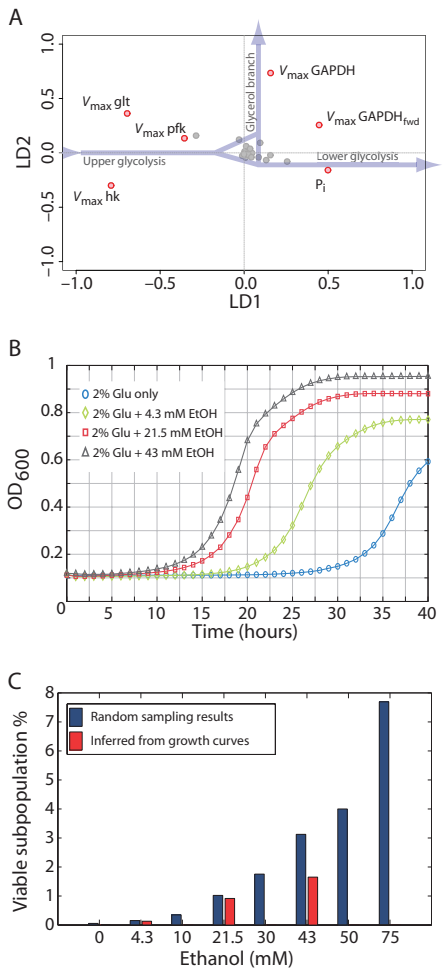

Fig. 3. Metabolic subpopulations are caused by small variation in metabolic variables, and their sizes can be manipulated. (**A**) Linear discriminant analysis of randomly sampled initial conditions (metabolites and V_{maxes}) highlights the variables that most significantly affect the probability of reaching either the normal steady state or the imbalanced state. (**B**) In liquid cultures, lag phases of *tps1*Δ cultures decreased with increasing concentrations of ethanol (EtOH) in the medium. (**C**) The positive effect of ethanol as percentage of viable cells [experimental data: red bars (*8*)] can be reproduced by a population of models with initial conditions sampled from a Gaussian distribution as described in the main text (blue bars).

cycle, large enough to push the system's dynamics into the functional steady state.

Different Mechanisms Contribute to Robustness

Finally, we examined the contribution of various aspects of trehalose metabolism to establish proper glycolytic functioning, through random sampling of initial conditions in the full kinetic model (Fig. 5D). Whereas the combined trehalose cycling and negative (T6P-mediated) feedback on hexokinase resulted in 100% viability in the wild-type version of the model, apparent futile cycling of trehalose alone resulted in a regular steady state in 76% of the sampled cases. Removal of G6P without P_i release (only possible in silico) resulted in a functional state in 4% of the cases. This shows that phosphate recovery is the primary safety mechanism, with hexokinase inhibition also contributing. The reported inhibition of trehalose synthesis by P_i (*28*) reinforces this picture, because low P_i concentrations will relieve inhibition and ensure P_i mobilization. These results provide a strong basis for the interpretation of population-level phenotypes of various mutants in trehalose metabolism and hexokinase (*8*).

Start-Up of Glycolysis Requires Dynamic Regulation

From our work, a dynamic picture emerges where the organization of glycolysis in ATP-investing upper and ATP-producing lower parts provides a major challenge for robust start-up upon activation. After environmental changes (for example, nutrition, hormone, and drug), proper steering through a dynamic landscape consisting of undesired states requires specialized regulatory mechanisms. Our work shows that phosphate dynamics is an essential determinant of the state that is reached. Because existing glycolytic models ignored P_i dynamics, the coexistence of two states in glycolysis was not previously discovered.

The core model demonstrated that mostly generic features of glycolysis give rise to this two state outcomes, in particular, (i) its stoichiometry in ATP consumption and production, and (ii) the (universal) equilibrium constants of phosphofructokinase (large; allowing accumulation of FBP) and GAPDH (small; requiring high P_i levels to drive the reaction). In yeast, trehalose metabolism apparently provides protection against the imbalanced state, albeit not 100% fail-safe based on flow cytometry (Fig. 2C); the observed failure of wild type (~7%) could reflect a trade-off between different aspects of the transition to high sugar, because a higher success rate will require tighter regulation or higher futile cycling that will make start-up slower or more costly, respectively.

Other systems, notably mammalian cell types, have adopted alternative mechanisms that may function to prevent glycolytic imbalance. In human cell types, feedback inhibition of hexokinase or glucokinase, either by the product G6P (muscle) or a glucokinase regulatory protein (liver), is a well-known regulatory mechanism for glycolysis (*29*). Pancreatic β cells seem to have no protective mechanism, but have low glucokinase activity

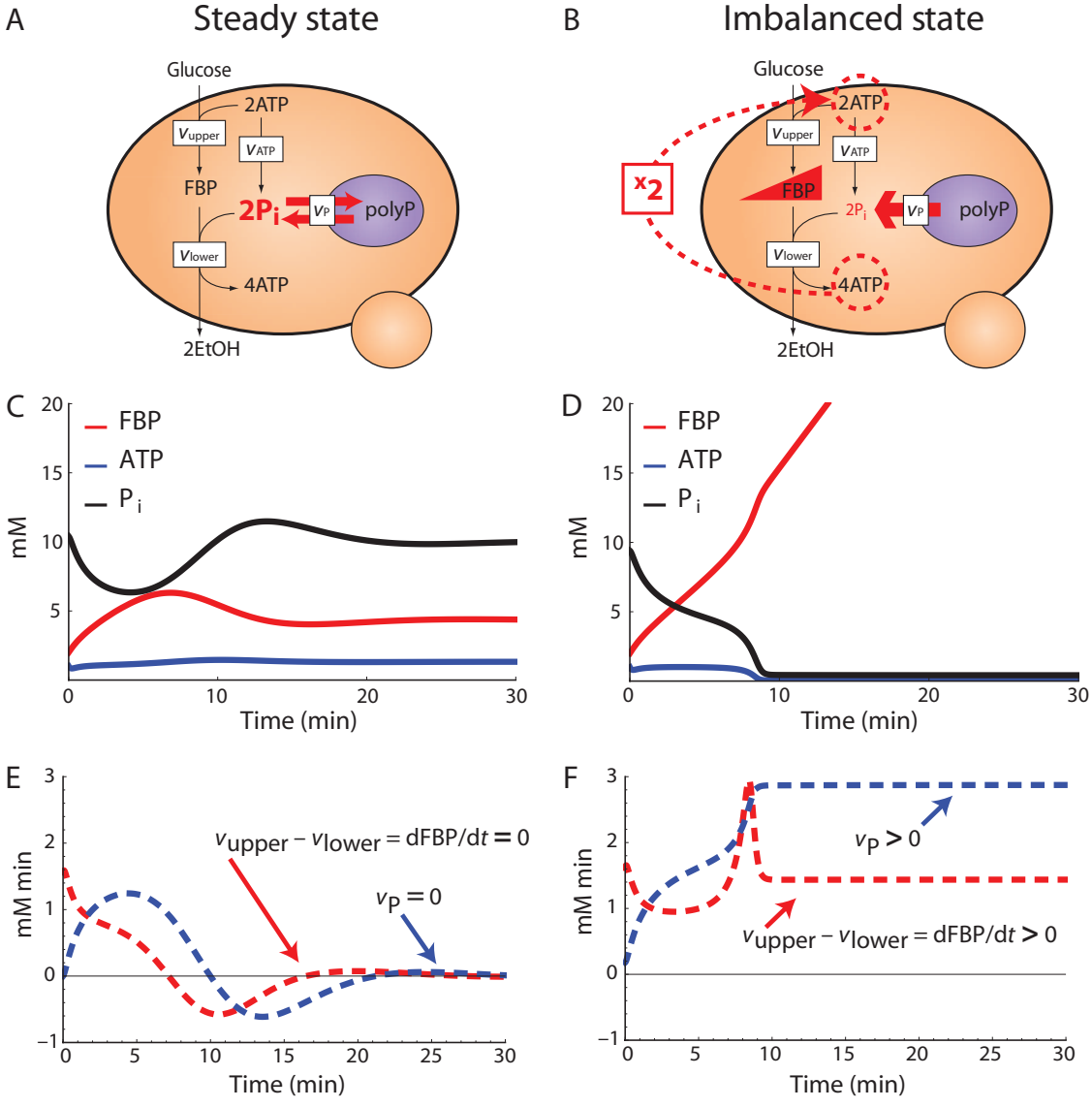

Fig. 4. Generalized core model of glycolysis can reach two stable, coexisting states. The left panel shows the global steady state, and the right panel the imbalanced state. The difference between panels is the initial P_i level (10.4 and 9.4, respectively). (**A** and **B**) Stoichiometry of the core model, with red arrows emphasizing the vacuolar flow of P_i from polyphosphates (polyP). The coupling between the upper and lower part of glycolysis through ATP is emphasized by the red dashed line (B). (**C** and **D**) Metabolite levels for a simulation of the core model, resulting in steady state (metabolite levels constant in time) (C) or imbalance (FBP accumulation at very low P_i and ATP levels) (D). (**E** and **F**) Characteristic rates that specify the states: The red dashed lines indicate the difference in rate between upper and lower glycolysis ($v_{upper} - v_{lower}$), which is zero at steady state (E) and is positive at the imbalanced state (F). The dashed blue lines represent the vacuolar import rate of P_i (v_P), which should be zero at steady state. In (F), the constant positive v_P indicates mobilization of P_i, which sustains accumulation of FBP (red dashed line) through the stoichiometric coupling of ATP.

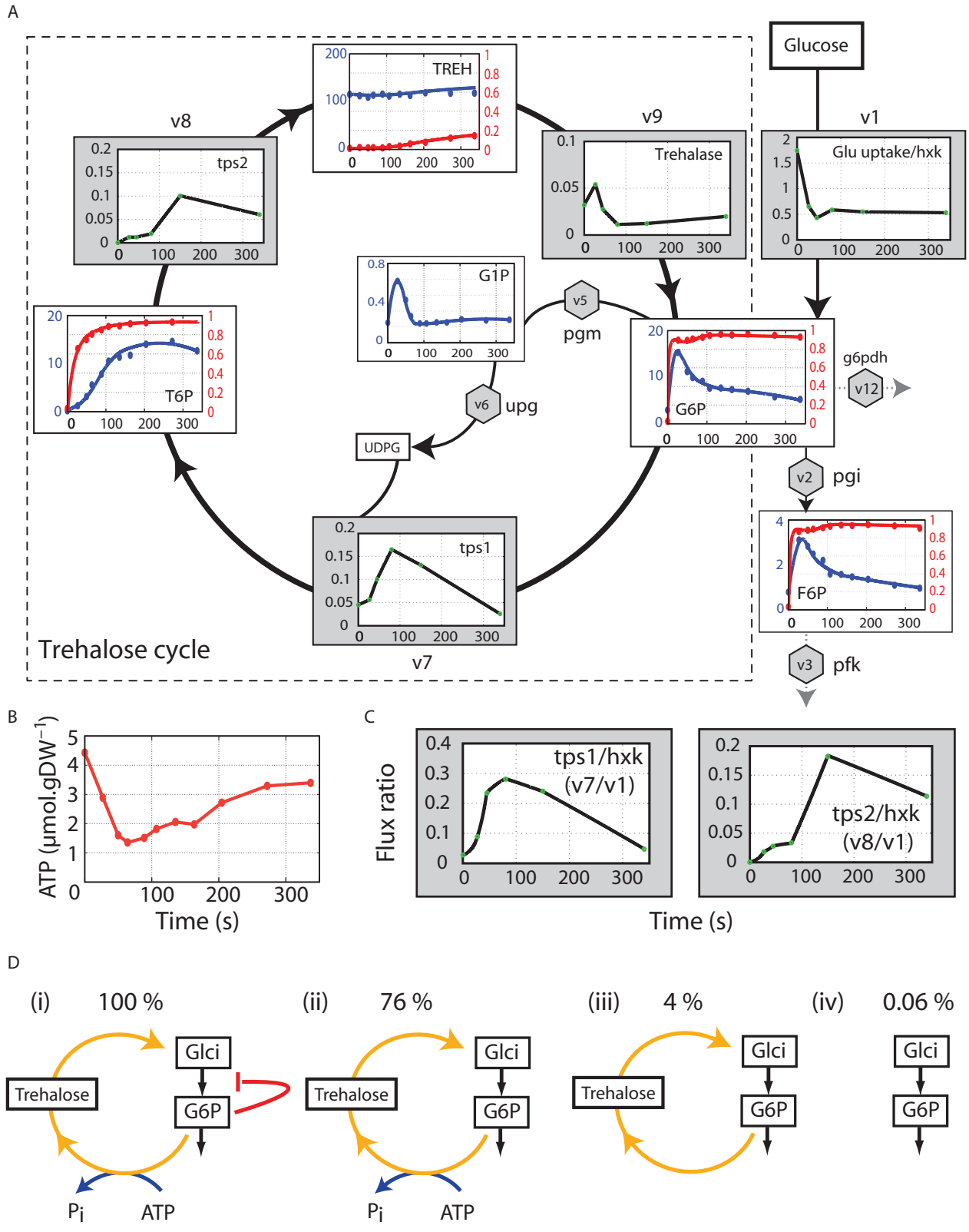

Fig. 5. ^{13}C tracer enrichment reveals highly dynamic flux distributions through the trehalose cycle. (**A**) Selection of data [complete data set in (*8*)] superimposed on the trehalose cycle. White boxes contain metabolite data, with concentrations (µmol gDW^{-1}) in blue and tracer enrichment (fraction) in red (symbols represent measurements, and lines represent model fits); *x* axes show time in seconds. Gray boxes show flux profiles (µmol gDW^{-1} s^{-1}) of the indicated reactions in time (s). (**B**) ATP concentration profile shows a response time similar to that of flux channeling toward the trehalose pool via the tps1 reaction. (**C**) Dynamic flux ratios of tps1 (v7) and tps2 (v8) relative to hxk (v1) show that up to 28% of glucose is dynamically routed into trehalose metabolism. (**D**) Percentage of balanced steady states found with randomly sampled initial conditions as input for different features of the trehalose cycle. Different aspects of trehalose metabolism contribute to the overall probability to reach the functional steady state.

that would prevent the upper part of glycolysis from being too fast. Upon overexpression of hexokinase, these cells exhibit a similar metabolic imbalance to that observed in yeast *tps1*Δ mutants (*5*), providing relevance for this state in mammalian metabolism.

Our findings have major implications for biotechnological applications and disease. In biotechnology, poor mixing in large-scale fermenters causes dynamic conditions, which—often in combination with genetic manipulations—may create conditions in which individual cells behave very differently from the measured population average. In disease, cancer in particular, the regulation of glycolysis has recently regained great interest because of the Warburg effect, characterized by an enhanced glycolytic flux and lactate production (*30*). Our work provides systems-level insight into the dynamic regulation of glycolysis. As an example, feed-forward activation of pyruvate kinase (PK) by FBP is impaired in the PKM2 splice variant that replaces the original PKM1 protein in many cancer cells (*31*). Such feed-forward activation of PK by FBP, observed from bacteria to man, could act as an additional safety mechanism to prevent a metabolic imbalance in glycolysis: FBP activation would help to accelerate the lower part of glycolysis if FBP starts to accumulate. Indeed, in all our models, removing the positive feedback on PK enhanced the probability to reach imbalance. Intriguingly, PKM2 expression in tumors coincides with an alternative phosphoglycerate mutase activity that instead of ATP produces P_i from PEP (*32*). Such an activity would fit with the role of P_i release to ensure robust functioning of glycolysis. Interfering with protective mechanisms against the metabolic imbalance state in tumor cells, or perhaps, counterintuitively, enhancing glucose uptake rather than inhibiting it, may provide a rationale for sophisticated treatment strategies.

Materials and Methods

Strains, Media, and Growth Conditions

All strains used in this study are listed in table S3. The *S. cerevisiae* strains based on the BY4743 background were used to characterize growth behavior and subpopulation dynamics. The W303-1A background was used to evaluate the effects of HXK2 overexpression. All growth experiments were performed at 30°C using a defined mineral medium [see (*33*) for reference] with required amino acid supplements, buffered to pH 5 (30 mM sodium citrate/citric acid buffer) and supplemented with either 2% galactose (CBS-Gal) or 2% glucose (CBS-Glu), with additions as indicated. Defined mineral medium plates were made by addition of 1% agarose to the growth medium. Plates were always incubated for 3 days at 30°C before counting colonies, unless stated otherwise. Medium lacking a carbon source (CBS-C) was used as a wash and resuspension buffer throughout.

For ^{13}C tracer experiments, the haploid prototrophic *S. cerevisiae* strain CEN.PK 113-7D (*34*) was cultured in an aerobic glucose-limited chemostat using a low-salt defined medium (*35*) containing the following: glucose (8.25 g/liter), ethanol (0.39 g/liter), and silicone antifoaming agent (0.05 g/liter) (BDH Chemicals), yielding a steady-state biomass concentration of 4.0 g_{DW}/liter. Ethanol was added to suppress spontaneous oscillations (*36*). The continuous culture was performed in a 7.0-liter bioreactor with 4.0-liter working volume (Applikon) at a dilution rate of 0.1 per hour. Temperature was set to 30°C, and pH was kept constant at 5.0 by automated addition of 4.0 M KOH (aq). Air was sparged through the culture at a rate of 2.0 liter/min, and stirring was set to 800 rpm. Steady-state conditions were assumed when, after five volume changes, dissolved oxygen, off-gas composition, and biomass concentration were stable. Biomass dry weight was measured, in triplicate, by filtering 5.0-ml broth samples on preweighed and predried 0.45-μm cellulose membranes (Supor 450, Gelman Sciences). Next, the membranes were washed with 10.0 ml of demineralized water and placed at 70°C to dry (24 hours), before being weighed.

Strain Constructions

All yeast transformations were performed according to (*37*). The pYES-PACT1-pHluorin plasmid described in (*38*) was supplied by G. Smits. The plasmids for HXK2 overexpression described in (*39*) were supplied by J. Thevelein.

Microtiter Growth Experiments

Growth behavior in response to different carbon sources and various perturbing agents was monitored using 96-well microtiter plates. All inoculums, unless stated otherwise, were derived from single colony isolates. Glycerol stocks were streaked out onto YEP + 2% galactose agar plates (1% yeast extract, 2% peptone, 2% agar) and incubated at 30°C. After 2 to 3 days, single colonies were isolated directly from the plates and resuspended in CBS-C. Optical densities (OD_{600}) were adjusted to be in the order of 0.1. Each suspension (biological replicate) was divided such that it could be subjected to all permutations within a single experiment. Once carbon sources and, where applicable, perturbing agents were added, microtiter wells were filled with 300 μl of prepared culture, and growth was monitored at 600 nm, using either a SpectraMax Plus384 (Molecular Devices) or a Multiskan GO (Thermo Fischer Scientific) microplate spectrophotometer. All experiments were done with at least two biological replicates per condition. All growth profiles are presented as the average of biological replicates, unless stated otherwise.

^{13}C Tracer Enrichment Experiment and Trehalose Cycle Flux Estimations

Glucose Pulse Perturbations

Glucose pulse perturbations were performed by coupling a BioScope reactor (*36*) to the chemostat culture; this facilitated multiple sequential perturbations without disturbing the steady-state reference culture in the chemostat. The BioScope flow was calibrated to a rate of 0.475 ml/min, which allowed for a total sampling time of 5 min 37 s with samples after −0, 27, 50, 64, 89, 107, 135, 163, 204, 272, and 337 s. The culture was perturbed by the addition of 110 mM glucose to the broth flow when entering the BioScope (see fig. S15 for an illustration of the experimental setup). The sampling time was chosen on the basis of a priori expectations of flux dynamics through central carbon metabolism and represents a trade-off between resolving rapid and slow enrichments of the various metabolite pools. Within our system, the main challenge was to ensure that the tracer was sufficiently propagated to the large trehalose pool while maintaining some degree of resolution for the much smaller and rapidly labeled upper glycolytic metabolite pools. The experiments were performed in duplicate from the same chemostat culture for both glucose perturbation (for concentration measurements) and a perturbation with uniformly labeled ^{13}C [U-$^{13}C_6$]glucose (for labeling enrichment measurements).

Sample extractions, processing, and analysis were performed as in (*35*) and were briefly described below.

Metabolite Extraction and Sample Storage

Tubes with 100% methanol (5 ml) were taken from the cryostat (−40°C), and 1 ml of broth was sampled directly into this quenching solution. The biomass is separated from the quenching solution by centrifugation. To remove the broth supernatant, an additional washing step is included. In the case of concentration measurements, ^{13}C extract was added. The washed pellet is then extracted by the addition of 5 ml of 75% (v/v) boiling ethanol. Samples were immediately vortexed and placed in a water bath at 95°C for 3 min and then returned to the cryostat. Ethanol was evaporated using a RapidVap N2 (Labconco). The dried residues were stored at −80°C until further processing.

Metabolite Concentration and Mass Isotopomer Quantifications

Mass isotopomer fractions—as well as concentrations of G6P, fructose 6-phosphate (F6P), glucose 1-phosphate (G1P), FBP, T6P, uridine diphosphoglucose (UDP-glucose), and 6-phosphogluconate (6PG)—were determined using anion exchange liquid chromatography–tandem mass spectrometry (LC-MS/MS) (*35*). The concentration of ATP was determined by ion-pair reversed-phase LC-MS/MS (*35*). Additionally, G6P, F6P, FBP, T6P, and trehalose were measured, as methoxime-trimethylsilyl derivatives, by gas chromatography–MS. The intracellular concentrations were determined on the basis of isotope dilution mass spectrometry (*35*). Where applicable, metabolite values determined by more than one platform were combined.

Hybrid Modeling Approach

The estimation of intracellular fluxes based on the concentration and ^{13}C enrichment data was

performed according to the procedure outlined by (*27*). A definition of the network with indicated C atom transitions that was used to automatically generate the concentration and labeling enrichment balances is shown in table S8; the notation introduced by (*40*) was used. Figure S16 provides a graphical illustration of reactions and metabolite pools included in our analysis.

Population-Level pHluorin Measurements

pHluorin-transformed cells (*38*) (see table S3) were inoculated into CBS-Gal and grown overnight to an OD_{600} of 0.8 to 1. Cells were collected by centrifugation, washed twice with ice-cold CBS-C, and resuspended to an OD_{600} of about 1. Cell suspensions (200 µl) were transferred to black polystyrene clear-bottom 96-well microtiter plates (Greiner Bio-One), and pHluorin fluorescence emission was measured at 510 nm using an Omega FLUOstar microtiter plate spectrofluorometer (BMG LABTECH GmbH), with excitation bands of 10 nm centered about 390 and 470 nm, respectively. Glucose was added to a final concentration of 2% by automated injection. Additionally, pHluorin signals were collected for cultures growing on 2% galactose (OD_{600} ~0.8).

Calibration curves were constructed exactly as described in (*38*). Background fluorescence for a wild-type culture not expressing pHluorin was measured in triplicate and subsequently subtracted from all measurements. The background-corrected ratio of emission intensity ($Em510_{390ex}/Em510_{470ex}$) was converted to pH by a function derived from the constructed calibration curve.

pHluorin Microscopy

Sample Preparation and Data Acquisition

*Tps1*Δ cells were grown to an OD_{600} of about 0.8. Cells were harvested by centrifugation at 4000 rpm for 5 min and washed twice in CBS-C. Samples were resuspended in CBS-C to an OD_{600} of about 1 and kept on ice until the addition of carbon sources. After addition of either 2% glucose, 2% galactose, or 2% galactose + 2 mM glucose, cells were incubated on a shaker for 30 min at 30°C, whereas microscope slides were prepared with 1% agarose pads. Agarose was dissolved in CBS-C. Once set, 20 µl of cell culture was pipetted directly onto the agarose and sealed with a cover slip and VALAP (a mixture of equal amounts of Vaseline, lanolin, and paraffin wax).

pHluorin fluorescence images were collected on a Nikon Ti-E inverted microscope using a CFI Plan Apochromat 60× oil immersion objective (Nikon Instruments). pHluorin was excited using either a 30-mW, 405-nm diode laser or a 90-mW, 488-nm diode laser from an Agilent MLC400 laserbox (Agilent Technologies). Both lasers were attenuated to 7% of their maximal power using an acousto-optical tunable filter. Emission light was selected using a 525-nm filter with 45-nm band width (Semrock) and recorded on a cooled back-illuminated electron-multiplying (EM) charge-coupled device camera (iXon DU897, Andor) using exposure times of 100 ms and an EM gain of 100 V.

Image Processing and Data Analysis

Images were processed and analyzed using ImageJ version 1.45s (*41*). General background correction was applied by the built-in function, with a rolling ball radius of 50 pixels and smoothing enabled. False-color images were generated from the ratio of emission intensities resulting from excitation at 405 and 488 nm ($Em525_{405ex}/Em525_{488ex}$).

pHluorin Flow Cytometry

Sample Preparation and Perturbation

Wild-type and *tps1*Δ cells were cultured, harvested, washed, and resuspended as described for above for microscopy. Carbon sources (wild type: 2% Glu or 2% Gal; *tps1*Δ: 2% Glu, 2% Gal or 2% Gal + 2.5 mM Glu) were added about 45 min before data acquisition. In addition, signals for cells suspended in CBS-C (unperturbed) were also collected about 45 min after resuspension.

A second set of experiments was performed to evaluate whether the presence of ethanol leads to the enrichment of the functional steady-state fraction of a *tps1*Δ population when challenged with glucose. Single colonies were picked directly from a galactose plates and resuspended in CBS-C. Suspension was perturbed as before, with either 2% Glu, 2% Gal, 2% Glu + 40 mM ethanol, or 2% Gal + 1 mM Glu. Samples not expressing pHluorin were always included to estimate background fluorescence signals.

Data Acquisition

Flow cytometry data were acquired on a CyAn ADP 9 Color flow cytometer (Beckman Coulter). pHluorin was excited by a 50-mW, 405-nm laser and a 25-mW solid-state 488-nm laser, respectively, and emission was detected through a 530/40-nm filter. Laser voltages were set at a minimum value that displayed the entire unperturbed wild-type population on a linearly scaled bivariate plot. The acquisition limit was 10^6 events per sample.

Data Analysis

Raw data files (.fcs) were processed and analyzed using MATLAB R2012b. Data were extracted from FCS (flow cytometry standard) files using the fcsread.m function, available in the MATLAB File Exchange repository (www.mathworks.nl/matlabcentral/fileexchange/8430-flow-cytometry-data-reader-and-visualization/content/fcsread.m). The channel-specific average background values were calculated from samples not expressing pHluorin and subtracted from each individual data point. In the first set of experiments (Fig. 2C), this threshold was 25 times the channel-specific background signal, and for the second set of experiments (fig. S9), this was 5 times the channel-specific background signal. This difference is a consequence of lower overall signal in the second set of experiments. The chosen thresholds resulted in an average of about 200,000 events being retained for each sample, in both experiments.

Fluorescence signals for each event were calculated as the ratio of emission intensity resulting from excitation at 405 and 488 nm ($Em530_{405ex}/Em530_{488ex}$). Frequency data (bins = 101) for each sample were normalized to sample-specific total post-filter events and expressed as percentages.

Kinetic Modeling

All models were implemented and analyzed using Mathematica 9.0 (Wolfram Research). The time simulations were performed with the NDSolve function. A steady state is defined as a state, characterized by the metabolite concentrations, where all time derivatives of internal metabolite concentrations are equal to zero. Steady states were calculated by solving these equalities with the FindRoot function. Metabolite concentrations from the time simulations, after 250 simulation minutes, were used as initial values for the steady-state estimations with the FindRoot function.

The detailed kinetic model and the core model described in this paper are available as supplementary files in SBML (Systems Biology Markup Language) format. In addition, an interactive Web application is provided at www.ibi.vu.nl/sysbio/tpsmodel/, and demonstrates the effects of several parameters on the detailed kinetic model.

Modeling Metabolic Heterogeneity

Model Variations and Random Sampling Descriptions

The kinetic model, as detailed in (*8*), was used to explore the relationship between initial conditions and the probability of obtaining a regular steady state with a model representing the *tps1*Δ state. We took enzyme expression levels and metabolite concentrations as two sources of interindividual metabolic variation in a population. To simulate this heterogeneity, we assumed Gaussian distributions for both enzyme expression levels (represented by V_{max} values) and initial metabolite concentrations. Variance was set such that the probability of a sampled value deviating more than 20% from the reference value is less than 1 in 10^3; this equals a coefficient of variation (that is, a mean-normalized SD) of 6.1% (3.29 SDs = mean ± 20%, for Gaussian distributions). To additionally evaluate the effect of ethanol on the probability of reaching a steady state, we performed samplings at varying ethanol concentrations: 0, 4.3, 10, 21.5, 30, 43, 50, 62.5, 75, 100, 200, and 500 mM.

We randomly drew more than 10^6 unique V_{max} and initial metabolite concentration sets, at each ethanol concentration, and used these as input for the kinetic model. We performed a numerical time simulation for 250 min and evaluated the system to check whether a regular or an imbalanced state was obtained. An imbalanced state was defined when the final FBP concentration was higher than the concentration at 90% of the evaluation time (indicating long-term accumulation). In addition, to score a viable state, free phosphate concentra-

tion >1 mM was used to avoid incorrectly identifying zero flux states as vital steady states, a scenario that would arise when no free phosphate is available to drive FBP accumulation. On the basis of the evaluation outcome, each randomly drawn data set was categorized and saved.

Random sampling, time simulations, and steady-state evaluations were performed, as above, using Mathematica 9.0 (Wolfram Research).

Discriminant Analysis

Using the output from the random sampling evaluations, 5000 samples were drawn (randomly) from the saved data sets, for both imbalanced and regular steady-state solutions, at each ethanol concentration, yielding a data set with 28 variables (14 initial metabolite and 14 V_{max} values) and 24 independent classes (two groups: imbalanced versus steady state, at 12 different ethanol concentrations, see above). The discriminant analysis was performed with the lda function of the MASS package in the R (version 2.14.2) statistical environment (*42*).

References and Notes

1. J. Stelling, U. Sauer, Z. Szallasi, F. J. Doyle III, J. Doyle, Robustness of cellular functions. *Cell* **118**, 675–685 (2004). doi: 10.1016/j.cell.2004.09.008; pmid: 15369668
2. R. J. DeBerardinis, C. B. Thompson, Cellular metabolism and disease: What do metabolic outliers teach us? *Cell* **148**, 1132–1144 (2012). doi: 10.1016/j.cell.2012.02.032; pmid: 22424225
3. A. Flamholz, E. Noor, A. Bar-Even, W. Liebermeister, R. Milo, Glycolytic strategy as a tradeoff between energy yield and protein cost. *Proc. Natl. Acad. Sci. U.S.A.* **110**, 10039–10044 (2013). doi: 10.1073/pnas.1215283110; pmid: 23630264
4. B. Teusink, M. C. Walsh, K. van Dam, H. V. Westerhoff, The danger of metabolic pathways with turbo design. *Trends Biochem. Sci.* **23**, 162–169 (1998). doi: 10.1016/S0968-0004(98)01205-5; pmid: 9612078
5. P. B. Iynedjian, Glycolysis, turbo design and the endocrine pancreatic β cell. *Trends Biochem. Sci.* **23**, 467–468 (1998). doi: 10.1016/S0968-0004(98)01317-6; pmid: 9868365
6. L. Van Aelst *et al.*, Molecular cloning of a gene involved in glucose sensing in the yeast *Saccharomyces cerevisiae*. *Mol. Microbiol.* **8**, 927–943 (1993). doi: 10.1111/j.1365-2958.1993.tb01638.x; pmid: 8355617
7. J. M. Thevelein, S. Hohmann, Trehalose synthase: Guard to the gate of glycolysis in yeast? *Trends Biochem. Sci.* **20**, 3–10 (1995). doi: 10.1016/S0968-0004(00)88938-0; pmid: 7878741
8. See supplementary materials on *Science* Online.
9. S. Hohmann, W. Bell, M. J. Neves, D. Valckx, J. M. Thevelein, Evidence for trehalose-6-phosphate-dependent and -independent mechanisms in the control of sugar influx into yeast glycolysis. *Mol. Microbiol.* **20**, 981–991 (1996). doi: 10.1111/j.1365-2958.1996.tb02539.x; pmid: 8809751
10. B. M. Bonini, P. Van Dijck, J. M. Thevelein, Uncoupling of the glucose growth defect and the deregulation of glycolysis in *Saccharomyces cerevisiae tps1* mutants expressing trehalose-6-phosphate-insensitive hexokinase from *Schizosaccharomyces pombe*. *Biochim. Biophys. Acta* **1606**, 83–93 (2003). doi: 10.1016/S0005-2728(03)00086-0; pmid: 14507429
11. K. Luyten *et al.*, Fps1, a yeast member of the MIP family of channel proteins, is a facilitator for glycerol uptake and efflux and is inactive under osmotic stress. *EMBO J.* **14**, 1360–1371 (1995). pmid: 7729414
12. J. François, J. L. Parrou, Reserve carbohydrates metabolism in the yeast *Saccharomyces cerevisiae*. *FEMS Microbiol. Rev.* **25**, 125–145 (2001). doi: 10.1111/j.1574-6976.2001.tb00574.x; pmid: 11152943
13. B. Teusink *et al.*, Can yeast glycolysis be understood in terms of in vitro kinetics of the constituent enzymes? Testing biochemistry. *Eur. J. Biochem.* **267**, 5313–5329 (2000). doi: 10.1046/j.1432-1327.2000.01527.x; pmid: 10951190
14. S. Hohmann *et al.*, The growth and signalling defects of the *ggs1* (*fdp1/byp1*) deletion mutant on glucose are suppressed by a deletion of the gene encoding hexokinase PII. *Curr. Genet.* **23**, 281–289 (1993). doi: 10.1007/BF00310888; pmid: 8467527
15. J. W. Veening, L. W. Hamoen, O. P. Kuipers, Phosphatases modulate the bistable sporulation gene expression pattern in *Bacillus subtilis*. *Mol. Microbiol.* **56**, 1481–1494 (2005). doi: 10.1111/j.1365-2958.2005.04659.x; pmid: 15916600
16. L. Wang *et al.*, Bistable switches control memory and plasticity in cellular differentiation. *Proc. Natl. Acad. Sci. U.S.A.* **106**, 6638–6643 (2009). doi: 10.1073/pnas.0806137106; pmid: 19366677
17. M. J. Neves *et al.*, Control of glucose influx into glycolysis and pleiotropic effects studied in different isogenic sets of *Saccharomyces cerevisiae* mutants in trehalose biosynthesis. *Curr. Genet.* **27**, 110–122 (1995). doi: 10.1007/BF00313424; pmid: 7788713
18. J. R. S. Newman *et al.*, Single-cell proteomic analysis of *S. cerevisiae* reveals the architecture of biological noise. *Nature* **441**, 840–846 (2006). doi: 10.1038/nature04785; pmid: 16699522
19. S. M. Fendt, U. Sauer, Transcriptional regulation of respiration in yeast metabolizing differently repressive carbon substrates. *BMC Syst. Biol.* **4**, 12 (2010). doi: 10.1186/1752-0509-4-12; pmid: 20167065
20. A. Raj, A. van Oudenaarden, Nature, nurture, or chance: Stochastic gene expression and its consequences. *Cell* **135**, 216–226 (2008). doi: 10.1016/j.cell.2008.09.050; pmid: 18957198
21. N. Q. Balaban, J. Merrin, R. Chait, L. Kowalik, S. Leibler, Bacterial persistence as a phenotypic switch. *Science* **305**, 1622–1625 (2004). doi: 10.1126/science.1099390; pmid: 15308767
22. S. F. Levy, N. Ziv, M. L. Siegal, Bet hedging in yeast by heterogeneous, age-correlated expression of a stress protectant. *PLOS Biol.* **10**, e1001325 (2012). doi: 10.1371/journal.pbio.1001325; pmid: 22589700
23. C. Gancedo, C. L. Flores, The importance of a functional trehalose biosynthetic pathway for the life of yeasts and fungi. *FEMS Yeast Res.* **4**, 351–359 (2004). doi: 10.1016/S1567-1356(03)00222-8; pmid: 14734015
24. M. A. Blázquez, C. Gancedo, Mode of action of the *qcr9* and *cat3* mutations in restoring the ability of *Saccharomyces cerevisiae tps1* mutants to grow on glucose. *Mol. Gen. Genet.* **249**, 655–664 (1995). doi: 10.1007/BF00418035; pmid: 8544831
25. K. M. Overkamp *et al.*, Metabolic engineering of glycerol production in *Saccharomyces cerevisiae*. *Appl. Environ. Microbiol.* **68**, 2814–2821 (2002). doi: 10.1128/AEM.68.6.2814-2821.2002; pmid: 12039737
26. J. M. A. Geertman, J. P. van Dijken, J. T. Pronk, Engineering NADH metabolism in *Saccharomyces cerevisiae*: Formate as an electron donor for glycerol production by anaerobic, glucose-limited chemostat cultures. *FEMS Yeast Res.* **6**, 1193–1203 (2006). doi: 10.1111/j.1567-1364.2006.00124.x; pmid: 17156016
27. A. Abate, R. C. Hillen, S. A. Wahl, Piecewise affine approximations of fluxes and enzyme kinetics from in vivo ^{13}C labeling experiments. *Int. J. Robust Nonlinear Control* **22**, 1120–1139 (2012). doi: 10.1002/rnc.2798
28. J. Londesborough, O. E. Vuorio, Purification of trehalose synthase from baker's yeast. Its temperature-dependent activation by fructose 6-phosphate and inhibition by phosphate. *Eur. J. Biochem.* **216**, 841–848 (1993). doi: 10.1111/j.1432-1033.1993.tb18206.x; pmid: 8404904
29. B. Teusink, H. V. Westerhoff, F. J. Bruggeman, Comparative systems biology: From bacteria to man. *Wiley Interdiscip. Rev. Syst. Biol. Med.* **2**, 518–532 (2010). doi: 10.1002/wsbm.74; pmid: 20836045
30. W. H. Koppenol, P. L. Bounds, C. V. Dang, Otto Warburg's contributions to current concepts of cancer metabolism. *Nat. Rev. Cancer* **11**, 325–337 (2011). doi: 10.1038/nrc3038; pmid: 21508971
31. H. R. Christofk, M. G. Vander Heiden, N. Wu, J. M. Asara, L. C. Cantley, Pyruvate kinase M2 is a phosphotyrosine-binding protein. *Nature* **452**, 181–186 (2008). doi: 10.1038/nature06667; pmid: 18337815
32. M. G. Vander Heiden *et al.*, Evidence for an alternative glycolytic pathway in rapidly proliferating cells. *Science* **329**, 1492–1499 (2010). doi: 10.1126/science.1188015; pmid: 20847263
33. K. van Eunen *et al.*, Measuring enzyme activities under standardized in vivo-like conditions for systems biology. *FEBS J.* **277**, 749–760 (2010). doi: 10.1111/j.1742-4658.2009.07524.x; pmid: 20067525
34. J. P. van Dijken *et al.*, An interlaboratory comparison of physiological and genetic properties of four *Saccharomyces cerevisiae* strains. *Enzyme Microb. Technol.* **26**, 706–714 (2000). doi: 10.1016/S0141-0229(00)00162-9; pmid: 10862876
35. A. B. Canelas, C. Ras, A. ten Pierick, W. M. van Gulik, J. J. Heijnen, An in vivo data-driven framework for classification and quantification of enzyme kinetics and determination of apparent thermodynamic data. *Metab. Eng.* **13**, 294–306 (2011). doi: 10.1016/j.ymben.2011.02.005; pmid: 21354323
36. M. R. Mashego, W. M. van Gulik, J. L. Vinke, D. Visser, J. J. Heijnen, In vivo kinetics with rapid perturbation experiments in *Saccharomyces cerevisiae* using a second-generation BioScope. *Metab. Eng.* **8**, 370–383 (2006). doi: 10.1016/j.ymben.2006.02.002; pmid: 16618549
37. R. H. Schiestl, R. D. Gietz, High efficiency transformation of intact yeast cells using single stranded nucleic acids as a carrier. *Curr. Genet.* **16**, 339–346 (1989). doi: 10.1007/BF00340712; pmid: 2692852
38. R. Orij, J. Postmus, A. Ter Beek, S. Brul, G. J. Smits, In vivo measurement of cytosolic and mitochondrial pH using a pH-sensitive GFP derivative in *Saccharomyces cerevisiae* reveals a relation between intracellular pH and growth. *Microbiology* **155**, 268–278 (2009). doi: 10.1099/mic.0.022038-0; pmid: 19118367
39. J. R. Ernandes *et al.*, During the initiation of fermentation overexpression of hexokinase PII in yeast transiently causes a similar deregulation of glycolysis as deletion of Tps1. *Yeast* **14**, 255–269 (1998). doi: 10.1002/(SICI)1097-0061(199802)14:3<255::AID-YEA228>3.0.CO;2-N; pmid: 9580251
40. W. Wiechert, M. Möllney, N. Isermann, M. Wurzel, A. A. de Graaf, Bidirectional reaction steps in metabolic networks: III. Explicit solution and analysis of isotopomer labeling systems. *Biotechnol. Bioeng.* **66**, 69–85 (1999). doi: 10.1002/(SICI)1097-0290(1999)66:2<69::AID-BIT1>3.0.CO;2-6; pmid: 10567066
41. C. A. Schneider, W. S. Rasband, K. W. Eliceiri, NIH Image to ImageJ: 25 years of image analysis. *Nat. Methods* **9**, 671–675 (2012). doi: 10.1038/nmeth.2089; pmid: 22930834
42. R. Ihaka, R. Gentleman, R: A language for data analysis and graphics. *J. Comput. Graph. Stat.* **5**, 299–314 (1996). doi: 10.2307/1390807

Acknowledgments: We thank G. Smits for pHluorin plasmids; J. Thevelein for W303-1A strains and HXK2 overexpression plasmids; M. Walsh for fruitful discussions; D. Molenaar and H. Hoefsloot for valuable assistance with statistical methods; J. Pronk for experimental suggestions; K. Hellingwerf, R. Leurs, and I. Stulemeijer for critical reading of the manuscript; and L. da Cruz, Z. Zhao, and A. Deshmukh for assistance with tracer experiments. **Funding:** This work was supported by funding from AIMMS, FP7 UNICELLSYS, and Kluyver Centre for Genomics of Industrial Fermentation and NCSB, funded by the Netherlands Genomics Initiatives.

Supplementary Materials

www.sciencemag.org/content/343/6174/1245114/suppl/DC1
Supplementary Text
Figs. S1 to S18
Tables S1 to S8
References (*43*–*57*)

23 August 2013; accepted 7 January 2014
Published online 16 January 2014;
10.1126/science.1245114

Global Anisotropies in TeV Cosmic Rays Related to the Sun's Local Galactic Environment from IBEX

N. A. Schwadron,[1,2]* F. C. Adams,[3] E. R. Christian,[4] P. Desiati,[5] P. Frisch,[6] H. O. Funsten,[7] J. R. Jokipii,[8] D. J. McComas,[2,9] E. Moebius,[1] G. P. Zank[10]

Observations with the Interstellar Boundary Explorer (IBEX) have shown enhanced energetic neutral atom (ENA) emission from a narrow, circular ribbon likely centered on the direction of the local interstellar medium (LISM) magnetic field. Here, we show that recent determinations of the local interstellar velocity, based on interstellar atom measurements with IBEX, are consistent with the interstellar modulation of high-energy (tera–electron volts, TeV) cosmic rays and diffusive propagation from supernova sources revealed in global anisotropy maps of ground-based high-energy cosmic-ray observatories (Milagro, Asγ, and IceCube). Establishing a consistent local interstellar magnetic field direction using IBEX ENAs at hundreds to thousands of eV and galactic cosmic rays at tens of TeV has wide-ranging implications for the structure of our heliosphere and its interactions with the LISM, which is particularly important at the time when the Voyager spacecraft are leaving our heliosphere.

The heliosphere—the region surrounding our solar system that is carved out by the supersonic solar wind—moves through the local interstellar cloud (LIC), which is the part of the galactic environment surrounding the Sun. The heliosphere deflects much of the harmful cosmic-ray radiation from the local galactic environment, thereby regulating the radiation environment throughout the solar system, which likely has important implications for Earth's atmosphere and life (*1*). The Interstellar Boundary Explorer (IBEX) recently provided updated values for the velocity vector of the heliosphere through the LIC (*2*) and direction for the local interstellar medium (LISM) magnetic field (Table 1 and Fig. 1) from the center of the IBEX ribbon of energetic neutral atom (ENA) emission (*3*–*9*). These results show that the interstellar flow, after removing the motion of the Sun through the local standard of rest (LSR), is nearly perpendicular (87.6 ± 3.0°) to the LISM magnetic field. The LSR describes the velocity frame in which the mean motion of the oldest stars in the Milky Way in the neighborhood of the Sun is zero and is the reference frame in which cosmic rays assume near uniformity (in velocity direction). The local interstellar magnetic field direction from the IBEX ribbon center is within ~33 ± 20° of the magnetic field direction derived by interstellar polarization data from stars within 40 pc (*10*, *11*). Here, we show that the anisotropy maps of high-energy (TeV) cosmic rays likely provide independent confirmation of the interstellar magnetic field orientation inferred from the IBEX ribbon center.

The flux of high-energy (TeV) galactic cosmic rays (GCRs) varies as a function of look direction in the sky. The large-scale structure in the TeV GCR sky consists of two broad asymmetries with flux variations of ~0.2%: a deficit of GCR flux at high galactic latitudes (the "loss cone") and an excess of flux in the heliotail (*12*) direction [the "tail-in" excess (*13*–*21*)]. Small-scale TeV anisotropies (<~10°) in cosmic-ray arrival directions possibly arise from cosmic-ray propagation in a turbulent magnetic field (*22*). Because TeV GCRs have gyroradii of <700 astronomical units (AUs) (<0.005 parsec or pc; 1 pc = 3 × 10^{18} cm = 200,000 AU) in the LISM, the observed GCR asymmetries must originate in the immediate interstellar environment of the Sun. This study extends and builds on increasing knowledge of the LISM magnetic field (*3*, *4*, *10*, *11*, *23*, *24*) and interstellar flow (*2*, *25*–*28*) to understand the origin of the large-scale high-energy (TeV) cosmic-ray anisotropy, which has remained uncertain.

The observed cosmic-ray anisotropy has a number of features that may reflect ordering both by the entry of cosmic rays into the heliosphere and by the interstellar magnetic field. It has been found (*13*) that the tail-in excess weakens above 10 TeV because of the relative sizes of the GCR gyroradius and heliotail. Data from underground detectors in both hemispheres has led to precise positions of the asymmetries (*14*). Additionally, the underground muon observatory Super-Kamiokande I obtained similar asymmetries for the 10-TeV GCR flux, with a deficit toward the constellation of Virgo representing the northern galactic deficit, and an excess in the direction of the heliotail, toward the constellation of Taurus (*15*). The direction of the Taurus excess is within 29° of the local interstellar magnetic field defined by the IBEX ribbon (Table 1) and within 23° from the local interstellar downwind direction (*2*). Milagro observations in the Northern Hemisphere (*19*), in combination with IceCube observations in the Southern Hemisphere (*20*), have confirmed that the galactic deficit is centered at high galactic latitudes and extends into both hemispheres (*21*). A global GCR anisotropy model constructed with unidirectional and bidirectional components and applied to results of the Tibet Asγ experiment attributed the bidirectional flow to GCRs drifting parallel to the local interstellar magnetic field.

The cosmic-ray anisotropy, according to standard diffusion theory [e.g., (*29*, *30*)], is proportional to the average streaming of cosmic rays. Here, we take a small [0.3% (*31*)] ratio of perpendicular to parallel diffusion, as well as an interstellar flow direction to be nearly perpendicular to the magnetic field on the basis of IBEX observations.

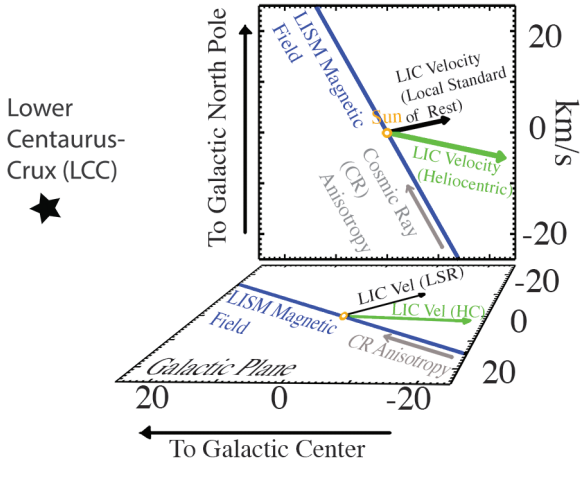

Fig. 1. LIC velocities and LISM magnetic field directions. The LIC velocities inferred from IBEX (*2*) in the heliocentric (HC; green vector) rest frame and the local standard of rest (LSR; black vector) in the galaxy. These vectors are shown in both the galactic plane (lower plane) and the plane containing the galactic poles (upper plane) relative to the magnetic field of the local interstellar medium (LISM; blue lines). The LIC velocity and magnetic field are a part of the Loop I superbubble roughly centered on the Lower Centaurus Crux subgroup of the Scorpius-Centaurus Association. The cosmic-ray anisotropy (gray vector) indicates average streaming of cosmic rays.

[1]University of New Hampshire, Space Science Center, Durham, NH 03824, USA. [2]Southwest Research Institute, San Antonio, TX 78228, USA. [3]University of Michigan, Physics Department, Ann Arbor, MI 48109, USA. [4]Goddard Space Flight Center, Greenbelt, MD 20771, USA. [5]University of Wisconsin, IceCube Observatory and Astronomy Department, Madison, WI 53706, USA. [6]University of Chicago, Department of Astronomy and Astrophysics, Chicago, IL 60637, USA. [7]Los Alamos National Laboratory, Space Science and Applications, Los Alamos, NM 87545, USA. [8]University of Arizona, Department of Planetary Sciences, Tucson, AZ 85721, USA. [9]University of Texas at San Antonio, San Antonio, TX 78249, USA. [10]University of Alabama, Huntsville, AL 35805, USA.

*Corresponding author. E-mail: n.schwadron@unh.edu

In this parameter regime, cosmic rays are largely guided by the interstellar magnetic field because both the anisotropic and perpendicular components of the anisotropy (fig. S1) are small compared to the field-aligned component.

We consider two scenarios for the formation of the cosmic-ray anisotropy. In the first scenario, the magnitude of the anisotropy is determined in part by spatial gradients in the average cosmic-ray density in response to the interstellar flow (eq. S6 in supplementary text). For example, an outward plasma flow from the center of the Lower Centaurus Crux (LCC) cluster (Fig. 1) pushes some cosmic rays out of the local interstellar environment in which the heliosphere resides. This creates a spatial gradient in the cosmic-ray density in the direction of the source and flow, which the average streaming (gray vector, Fig. 1) of cosmic rays tends to oppose.

The streaming direction of cosmic rays is determined on relatively small scales (on the scale of the cosmic-ray gyroradii, less than 1% of a pc), whereas the streaming magnitude is determined over much larger scales of tens of pc (*32*, *33*) controlled by the scattering (random changes in direction) of cosmic rays caused by interactions with the turbulent interstellar magnetic field.

It is important to differentiate (*34*, *35*) between the interstellar magnetic field on local scales (thousands of AU or ~0.005 to 0.01 pc) and on larger (parsec) scales owing to the presence of turbulence (*36*–*41*). Turbulence disrupts steady flows by random motion. In the interstellar medium, turbulent motion causes tangling and complexity in the structure of the interstellar magnetic field. The coherence scale length in the interstellar medium—the approximate distance along which the magnetic field appears relatively ordered—is typically 1 to 10 pc (*37*). Hence, the average magnetic field direction at these scales could be very different than in the vicinity of the heliosphere. At the large field-to-flow angle (87.6 ± 3.0°) found by IBEX (excepting the small region within 0.3° of exact perpendicularity, where perpendicular diffusion dominates for the 0.3% ratio of perpendicular to parallel diffusion taken here), the cosmic-ray density gradient becomes large so that the projection of the cosmic-ray streaming into the flow plane opposes the interstellar velocity. The cosmic-ray gradient in this case depends largely on the ratio of perpendicular to parallel diffusion. Reduced levels of perpendicular diffusion cause increased density gradients and thus stronger interstellar modulation of cosmic rays.

The ~0.2% high-energy (TeV) cosmic-ray anisotropy suggests a magnitude for the ratio of perpendicular to parallel diffusion of only 0.3% (fig. S1). This ratio is compatible with recent results (*31*), but an order-of-magnitude smaller than the derived ~4% ratio of perpendicular to parallel diffusion (*41*) based on cosmic-ray lifetimes in the galaxy (*39*). Simulations of cosmic-ray diffusion (*42*) similarly predicted a ratio of perpendicular to parallel diffusion of ~2 to 4% at MeV to GeV energies, which are lower than the TeV energies considered here. The relatively small ratio of perpendicular to parallel diffusion of ~0.3% may be a result of lower turbulence levels in the LIC compared to other portions of the galaxy.

In our second scenario for the cosmic-ray anisotropy, we consider the contributions of supernova remnants (SNRs) to the local cosmic-ray gradient (*43*–*48*). A statistical model of cosmic rays originating from SNR sources based on the temporal and spatial distributions of supernova sources (*43*) suggests that cosmic rays are injected locally by different sources and time dependently diffuse throughout the galaxy. In the case of the convective anisotropy (supplementary text, section 2), the cosmic-ray gradient is created by steady cosmic-ray diffusion against the interstellar flow. Therefore, the cosmic-ray gradient driven by SNRs depends on the time and spatial distribution of SNR sources. Because parallel diffusion in the LISM is far more rapid than perpendicular diffusion, cosmic rays have a strong tendency to stream along the interstellar magnetic field. Provided that the GCR density gradient along the LISM magnetic field has the same sign as that of the convective gradient and that the cosmic-ray density gradient produces a maximum anisotropy magnitude similar to that in observations, the anisotropy associated with diffusion from SNR sources has a global morphology similar to that of the convective anisotropy (supplementary text, section 5). That is, the dominance of parallel diffusion in the LISM can result in a similar global morphology for both the convective anisotropy and that driven by SNR sources.

We developed a model of the LISM magnetic field that is deflected around the heliosphere (supplementary text, section 3) and analyzed its influence on high-energy (TeV) cosmic-ray anisotropies. We constructed a sky map (Fig. 2) of cosmic-ray flux as viewed from the Sun, using Monte-Carlo calculations of 10^4 individual cosmic-ray trajectories in this perturbed magnetic field structure.

General ordering about the magnetic equator deduced from the IBEX ribbon is apparent in the high-energy (TeV) cosmic-ray observations (Fig. 2, left). Some features absent in the simulation results can be attributed to the model's lack of interstellar turbulence (*22*) that should cause small-scale

Table 1. LISM velocity and magnetic field direction.

	Magnitude (km/s)	Galactic longitude (°)	Galactic latitude (°)	Equatorial right ascension (°)	Equatorial declination (°)
LISM flow velocity* (HC frame)	23.2 ± 0.3	185.25 ± 0.24	−12.0 ± 0.5	78.5 ± 0.6	18.0 ± 0.5
LISM flow velocity (LSR frame†)	18.0 ± 0.9	47.9 ± 2.9	23.8 ± 2.0	267.0 ± 3.0	23.2 ± 3.1
Interstellar magnetic field‡		210.5 ± 2.6	−57.1 ± 1.0	48.5 ± 1.5	−21.2 ± 1.6

*Heliocentric (HC) rest frame (*2*). †Heliocentric velocities are converted to the local standard of rest (LSR) using the solar apex motion in (*54*). ‡Field directions and uncertainty inferred from the IBEX highest-energy steps [1.79 and 2.73 keV (*55*)] in which the ribbon maintains coherence and has the largest line-of-sight.

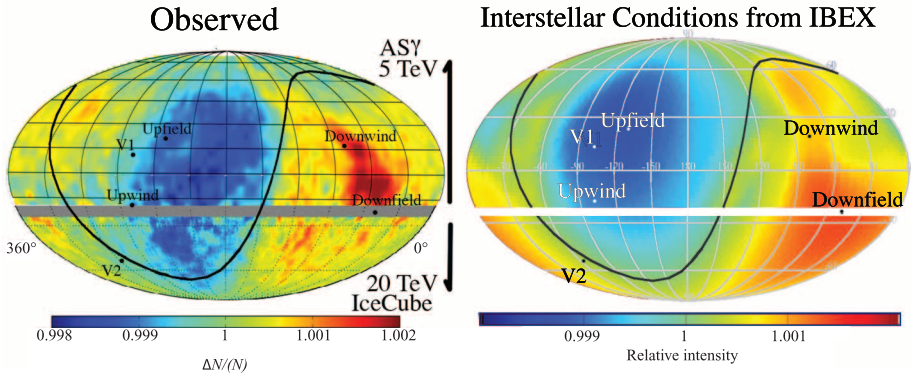

Fig. 2. TeV cosmic-ray anisotropies compared with predictions. Comparison between observed (**left**) and modeled (**right**) cosmic-ray relative intensities across the sky (J2000 coordinates). Black curves show the magnetic equator with a magnetic field direction derived from the center of the IBEX ribbon. On the left, the region below 25°S latitude is the anisotropy map from IceCube with a median energy of 20 TeV (*18*) and above 20°S latitude is the anisotropy map from ASγ with 5-TeV median energy (*15*). Similarly, the modeled map (right) at 20 TeV is shown below 25°S latitude and at 5 TeV above 20°S latitude. Both portions of the maps are smoothed over 3° to 5°. Labels indicate upwind and downwind directions (*2*), the current locations of Voyager 1 (V1), and Voyager 2 (V2) directions, and the "upfield" and "downfield" directions. Downfield is along the LISM magnetic field determined by IBEX in the direction closest to the interstellar velocity, and upfield is in the opposite direction. Plots are in equatorial coordinates with 0 hours at the right and increasing longitudes toward the left.

anisotropic structures, local GCR acceleration that may result in a more defined excess near the heliotail (*21*), and asymmetric influences on the heliosphere by the interstellar magnetic field (*49*–*53*). The modeled and observed anisotropies show some differences (e.g., the region from right ascension = –30 to 90° shows weaker modeled than observed anisotropies).

That a similar ordering of the global cosmic-ray anisotropy maps is generated simply by taking into account IBEX observations of low-energy interstellar neutral atoms to deduce the interstellar velocity, and the IBEX ribbon to deduce the local interstellar magnetic field direction reveals consistency with independent observations across 10 orders of magnitude in particle energy (keV energies in the IBEX ribbon compared to 10-TeV cosmic ray energies). Thus, local interstellar conditions play a key role in ordering very-high-energy (TeV) cosmic rays in the immediate interstellar environment of the Sun.

References and Notes

1. N. A. Schwadron, H. E. Spence, R. Came, *Eos* **92**, 297 (2011).
2. D. J. McComas *et al*., *Science* **336**, 1291–1293 (2012).
3. D. J. McComas *et al*., *Science* **326**, 959–962 (2009).
4. N. A. Schwadron *et al*., *Science* **326**, 966–968 (2009).
5. H. O. Funsten *et al*., *Science* **326**, 964–966 (2009).
6. S. A. Fuselier *et al*., *Science* **326**, 962–964 (2009).
7. J. Heerikhuisen *et al*., *Astrophys. J.* **708**, L126–L130 (2010).
8. J. Heerikhuisen, N. V. Pogorelov, *Astrophys. J.* **738**, 29 (2011).
9. N. A. Schwadron, D. J. McComas, *Astrophys. J.* **764**, 92 (2013).
10. P. C. Frisch *et al*., *Astrophys. J.* **760**, 106 (2012).
11. P. C. Frisch, N. A. Schwadron, http://arxiv.org/abs/1310.2922 (2013).
12. D. J. McComas, M. A. Dayeh, H. O. Funsten, G. Livadiotis, N. A. Schwadron, *Astrophys. J.* **771**, 77 (2013).
13. K. Nagashima, K. Fujimoto, R. M. Jacklyn, *J. Geophys. Res.* **103**, 17429 (1998).
14. D. L. Hall *et al*., *J. Geophys. Res.* **104**, 6737 (1999).
15. G. Guillian *et al*., *Phys. Rev. D Part. Fields Gravit. Cosmol.* **75**, 062003 (2007).
16. M. Amenomori *et al*., in *Proceedings of the 9th Annual International Astrophysics Conference*, *AIP Conference Proceedings*, J. Le Roux, G. P. Zank, A. J. Coates, V. Florinski, Eds. (American Institute of Physics, College Park, MD, 2010), vol. 1302, p. 285.
17. M. Amenomori; The Tibet ASγ Collaboration, *Astrophys. Space Sci. Trans.* **6**, 49–52 (2010).
18. A. A. Abdo *et al*., *Phys. Rev. Lett.* **101**, 221101 (2008).
19. A. A. Abdo *et al*., *Astrophys. J.* **698**, 2121–2130 (2009).
20. R. Abbasi *et al*., *Astrophys. J.* **740**, 16 (2011).
21. P. Desiati, A. Lazarian, *Astrophys. J.* **762**, 44 (2013).
22. G. Giacinti, G. Sigl, *Phys. Rev. Lett.* **109**, 071101 (2012).
23. R. Lallement *et al*., *Science* **307**, 1447–1449 (2005).
24. M. Opher, E. C. Stone, T. I. Gombosi, *Science* **316**, 875–878 (2007).
25. M. Witte, *Astron. Astrophys.* **426**, 835–844 (2004).
26. E. Möbius *et al*., *Science* **326**, 969–971 (2009).
27. E. Möbius *et al*., *Astrophys. J. Suppl. Ser.* **198**, 11 (2012).
28. M. Bzowski *et al*., *Astrophys. J. Suppl. Ser.* **198**, 12 (2012).
29. L. J. Gleeson, W. I. Axford, *Astrophys. J.* **154**, 1011 (1968).
30. M. A. Forman, L. J. Gleeson, *Astrophys. Space Sci.* **32**, 77–94 (1975).
31. A. Shalchi, I. Büsching, A. Lazarian, R. Schlickeiser, *Astrophys. J.* **725**, 2117–2127 (2010).
32. I. Büsching, M. S. Potgieter, *Adv. Space Res.* **42**, 504–509 (2008).
33. V. S. Ptuskin, I. V. Moskalenko, F. C. Jones, A. W. Strong, V. N. Zirakashvili, *Astrophys. J.* **642**, 902–916 (2006).
34. J. R. Jokipii, *Science* **307**, 1424–1425 (2005).
35. J. R. Jokipii, *Science* **316**, 839–840 (2007).
36. L. C. Lee, J. R. Jokipii, *Astrophys. J.* **206**, 735 (1976).
37. A. H. Minter, S. R. Spangler, *Astrophys. J.* **458**, 194 (1996).
38. S. Chandrasekhar, G. Munch, *Astrophys. J.* **115**, 103 (1952).
39. J. R. Jokipii, E. N. Parker, *Astrophys. J.* **155**, 799 (1969).
40. J. W. Armstrong, B. J. Rickett, S. R. Spangler, *Astrophys. J.* **443**, 209 (1995).
41. J. R. Jokipii, in *Proceedings of the 2nd Guillermo Haro Conference*, J. Franco, A. Carraminana, Eds. (Cambridge Univ. Press, Cambridge, 1999), p. 70.
42. J. Giacalone, J. R. Jokipii, *Astrophys. J.* **520**, 204–214 (1999).
43. P. Blasi, E. Amato, *J. Cosmol. Astropart. Phys.* **2012**, 011 (2012).
44. A. D. Erlykin, A. W. Wolfendale, *Astropart. Phys.* **25**, 183–194 (2006).
45. I. Büsching, M. Pohl, R. Schlickeiser, *Astron. Astrophys.* **377**, 1056 (2001).
46. M. Pohl, D. Eichler, *Astrophys. J.* **766**, 4 (2013).
47. I. Busching *et al*., *Astrophys. J.* **619**, 314–326 (2005).
48. C. Evoli, D. Gaggero, D. Grasso, L. Maccione, *Phys. Rev. Lett.* **108**, 211102 (2012).
49. G. P. Zank, *Space Sci. Rev.* **89**, 413–688 (1999).
50. R. Ratkiewicz *et al*., *Astron. Astrophys.* **335**, 363 (1998).
51. N. V. Pogorelov, G. P. Zank, *Astrophys. J.* **636**, L161–L164 (2006).
52. M. Opher, E. C. Stone, P. C. Liewer, *Astrophys. J.* **640**, L71–L74 (2006).
53. N. V. Pogorelov, J. Heerikhuisen, G. P. Zank, S. N. Borovikov, *Space Sci. Rev.* **143**, 31–42 (2009).
54. R. Schönrich, J. Binney, W. Dehnen, *Mon. Not. R. Astron. Soc.* **403**, 1829–1833 (2010).
55. H. O. Funsten *et al*., *Astrophys. J.* **776**, 30 (2013).

Acknowledgments: We thank all those who made IBEX possible. IBEX is primarily funded by NASA's Explorers Program (Contract no. NNG05EC85C). IBEX data are available at http://ibex.swri.edu/researchers/publicdata.shtml. IceCube cosmic ray data are available from http://icecube.wisc.edu/science/data.

Supplementary Materials

www.sciencemag.org/content/343/6174/988/suppl/DC1
Supplementary Text
References (*56*–*67*)

21 August 2013; accepted 29 January 2014
Published online 13 February 2014;
10.1126/science.1245026

Nanoporous $BiVO_4$ Photoanodes with Dual-Layer Oxygen Evolution Catalysts for Solar Water Splitting

Tae Woo Kim and Kyoung-Shin Choi*

Bismuth vanadate ($BiVO_4$) has a band structure that is well-suited for potential use as a photoanode in solar water splitting, but it suffers from poor electron-hole separation. Here, we demonstrate that a nanoporous morphology (specific surface area of 31.8 square meters per gram) effectively suppresses bulk carrier recombination without additional doping, manifesting an electron-hole separation yield of 0.90 at 1.23 volts (V) versus the reversible hydrogen electrode (RHE). We enhanced the propensity for surface-reaching holes to instigate water-splitting chemistry by serially applying two different oxygen evolution catalyst (OEC) layers, FeOOH and NiOOH, which reduces interface recombination at the $BiVO_4$/OEC junction while creating a more favorable Helmholtz layer potential drop at the OEC/electrolyte junction. The resulting $BiVO_4$/FeOOH/NiOOH photoanode achieves a photocurrent density of 2.73 milliamps per square centimenter at a potential as low as 0.6 V versus RHE.

N-type bismuth vanadate ($BiVO_4$) has recently emerged as a promising photoanode for use in water-splitting photoelectrochemical cells because it absorbs a substantial portion of the visible spectrum (bandgap energy, ~2.4 eV) and has a favorable conduction band (CB) edge position very near the thermodynamic H_2 evolution potential (*1*, *2*). However, the solar-to-hydrogen (STH) conversion efficiency achieved with $BiVO_4$ to date has been far below what is expected because the material suffers from poor electron-hole separation yield (ϕ_{sep}) (*2*–*6*). Previous efforts to improve the ϕ_{sep} of $BiVO_4$ mainly focused on doping studies, which were intended to improve its poor electron transport properties (*2*, *6*–*12*).

Here, we demonstrate that a high-surface-area, nanoporous $BiVO_4$ electrode composed of particles smaller than its hole diffusion length can effectively increase ϕ_{sep} without additional doping. Furthermore, we investigated the effect of an oxygen evolution catalyst (OEC) layer on the interfacial recombination at the $BiVO_4$/OEC junction, water oxidation kinetics, and the Helmholtz layer potential drop at the OEC/electrolyte junction using two different OECs, FeOOH and NiOOH. Our understanding of the $BiVO_4$/OEC/electrolyte junction resulted in the development of a new strategy to serially apply dual layers of OECs that can optimize both the $BiVO_4$/OEC and the OEC/electrolyte junctions simultaneously, enabling efficient utilization of surface-reaching holes for solar water oxidation.

Department of Chemistry, University of Wisconsin–Madison, Madison, WI 53706, USA.

*Corresponding author. E-mail: kschoi@chem.wisc.edu

Nanoporous $BiVO_4$ electrodes were prepared by first electrochemically depositing BiOI electrodes and then applying a dimethyl sulfoxide (DMSO) solution of vanadyl acetylacetonate [$VO(acac)_2$] onto their surface and heating in air at 450°C for 2 hours (experimental deatails are available in the supplementary materials, materials and methods). A schematic overview of the synthesis procedure is shown in fig. S1. The specific advantage of using BiOI is that its two-dimensional (2D) crystal structure enables electrodeposition of extremely thin plates (~20 nm) with sufficient voids between them (Fig. 1A). These voids inhibit grain growth of $BiVO_4$ during the conversion process, resulting in nanoporous $BiVO_4$ electrodes.

In a previous attempt to prepare nanoporous $BiVO_4$ (*13*), we used an NH_4OH solution of V_2O_5 as the vanadium source, which could not easily wet the BiOI surface because air in the voids between the BiOI plates renders the surface highly hydrophobic (fig. S2). Thus, the distribution of V_2O_5 was uneven, few $BiVO_4$ nucleation processes were induced within a single 2D BiOI sheet, and the resulting electrodes manifested limited porosity (Fig. 1, B and C). The use of comparatively hydrophobic $VO(acac)_2$/DMSO solution overcame this problem and resulted in a remarkable increase in surface area. The top-view and side-view scanning electron microscopy (SEM) images show the formation of much smaller $BiVO_4$ nanoparticles (mean particle size = 76 ± 5 nm) (fig. S3) creating a 3D nanoporous network (Fig. 1, D to F).

N_2 adsorption-desorption-isotherm measurements show that the nanoporous $BiVO_4$ electrode contains micropores within $BiVO_4$ particles as well as mesopores and macropores between $BiVO_4$ nanoparticles (fig. S4 and table S1) (*14*). The specific surface area of the nanoporous $BiVO_4$ electrode was estimated to be 31.8 ± 2.3 m^2/g based on a fitting analysis using the Brunauer-Emmett-Teller equation (*14*). $BiVO_4$ electrodes prepared by using other synthesis methods (such as metal organic decomposition, spray deposition, or direct electrodeposition of $BiVO_4$) possess limited surface areas, and no attempts to measure surface areas of these samples were reported (*2*).

The purity and crystal structure of the nanoporous $BiVO_4$ electrode (monoclinic scheelite structure) were confirmed with x-ray diffraction (fig. S5). The bandgap of the nanoporous $BiVO_4$ electrode was estimated to be ~2.50 to 2.55 eV, using ultraviolet-visible absorption spectra (fig. S6), which is slightly larger than the bandgap of $BiVO_4$ samples prepared by other methods that result in larger grain composition (~2.4 eV) (*13*, *15*).

The photoelectrochemical properties were first examined in the presence of 1 M sodium sulfite (Na_2SO_3), which served as the hole scavenger. The oxidation of sulfite is thermodynamically and kinetically more facile than oxidation of water (*11*, *13*, *15–18*), and therefore, measuring photocurrent for sulfite oxidation enables investigation of the photoelectrochemical properties of $BiVO_4$ independently of its poor water oxidation kinetics. A typical photocurrent-potential (*J-V*) curve of the sulfite oxidation with nanoporous $BiVO_4$ is shown in Fig. 2A. A very early photocurrent onset potential, 0.1 V versus reversible hydrogen electrode (RHE), and a rapid increase in photocurrent in the 0.2 V < E versus RHE < 0.6 V region, representing an excellent fill factor, resulted in a photocurrent density of 3.3 ± 0.3 mA/cm^2 at a potential as low as 0.6 V versus RHE. The incident photon-to-current conversion efficiency (IPCE) and the absorbed photon-to-current conversion efficiency (APCE) of the nanoporous $BiVO_4$ at 0.6 V versus RHE are 60 and 72%, respectively, at 420 nm (Fig. 2B).

Photocurrent density obtained for sulfite oxidation was used to calculate ϕ_{sep} by using Eq. 1, where J_{PEC} is the measured photocurrent density and J_{abs} is the photon absorption rate expressed as current density, which is calculated assuming 100% APCE (calculation details are available in the supplementary materials, materials and methods) (*4*, *6*, *19–21*). J_{abs} of the nanoporous $BiVO_4$ electrode was calculated to be 4.45 mA/cm^2. ϕ_{sep} is the yield of the photogenerated holes that reach the surface, and ϕ_{ox} is the yield of the surface reaching holes that are injected into the solution species (*21*).

$$J_{PEC} = J_{abs} \times \phi_{sep} \times \phi_{ox} \quad (1)$$

For sulfite oxidation with extremely fast oxidation kinetics, surface recombination is negligible, and ϕ_{ox} is ~1. Therefore, ϕ_{sep} is obtained by dividing J_{PEC} by J_{abs} (Fig. 2A, inset). The result shows that the nanoporous $BiVO_4$ electrode achieves ϕ_{sep} = 0.70 ± 0.03 and 0.90 ± 0.03 at 0.6 V and 1.23 V versus RHE, respectively, which is remarkable because a typical ϕ_{sep} value for a $BiVO_4$ photoanode is below 0.3 at 1.23 V versus RHE (*4*, 6). The highest ϕ_{sep} achieved recently by Abdi and coworkers using gradient doping was ~0.6 at 1.23 V versus RHE (*12*). The hole diffusion length of $BiVO_4$ was recently reported to be ~100 nm when using single-crystal $BiVO_4$ (*22*). The mean particle size of $BiVO_4$ composing the nanoporous $BiVO_4$ electrode shown in Fig. 1D is 76 ± 5 nm (fig. S3), and the particle size obtained from the XRD peaks (fig. S5) when using the Scherrer equation is 27 ± 2 nm. Therefore, the nanoporosity incorporated into $BiVO_4$ electrodes in this study appears to be ideal for effectively suppressing bulk carrier recombination, resulting in a record high ϕ_{sep}.

Photocurrent from the nanoporous $BiVO_4$ for water oxidation shown in Fig. 3A (black line) is considerably lower than the photocurrent for sulfite oxidation (Fig. 2A), indicating that the majority of the surface-reaching holes were lost to surface recombination because of the poor catalytic nature of the $BiVO_4$ surface for water oxidation (*2*). To improve water oxidation kinetics, we photodeposited a thin FeOOH or NiOOH layer on the nanoporous $BiVO_4$ surface as an OEC layer in order to assemble $BiVO_4$/FeOOH and $BiVO_4$/NiOOH electrodes. Their thicknesses were optimized so as to maximize photocurrent generation (fig. S7). It has been previously demonstrated that FeOOH interfaces well with $BiVO_4$ (*13*, *15*), whereas NiOOH is known to be a more active OEC than FeOOH (less overpotential required to

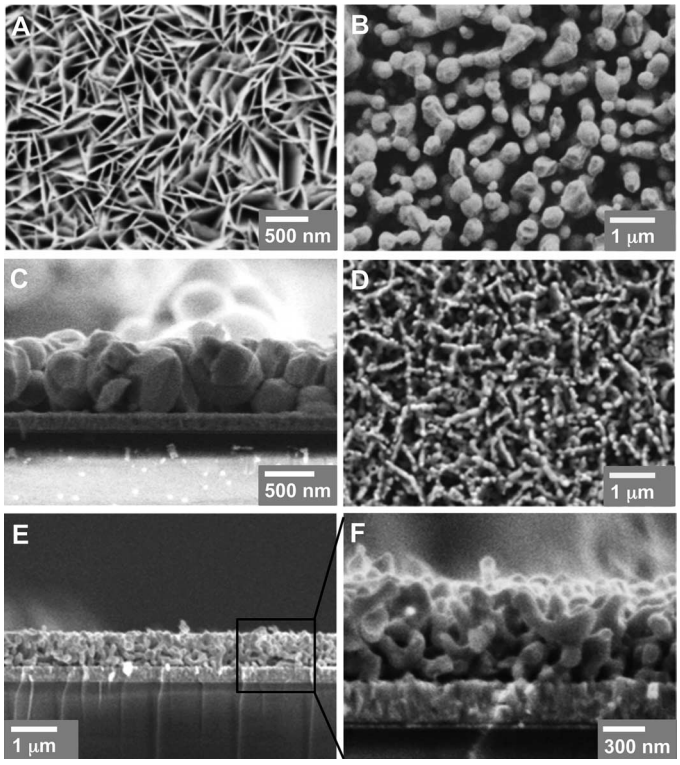

Fig. 1. Morphologies of nanoporous $BiVO_4$ electrodes. (**A**) SEM image of BiOI. (**B** and **C**) Top-view and side-view SEM images of $BiVO_4$ electrode prepared using NH_4OH/V_2O_5. (**D** to **F**) Top-view and side-view SEM images of nanoporous $BiVO_4$ prepared using $DMSO/VO(acac)_2$.

achieve the same current density) as a dark electrocatalyst on a conducting substrate (fig. S8) (*23*–*25*).

The photocurrents for water oxidation from the resulting $BiVO_4$/FeOOH and $BiVO_4$/NiOOH photoanodes were markedly higher than those from the bare $BiVO_4$ electrode (Fig. 3A and table S2), but their photocurrents were still lower than that generated for sulfite oxidation at the bare $BiVO_4$ electrode. This comparison suggested that neither $BiVO_4$/FeOOH nor $BiVO_4$/NiOOH engages all surface-reaching holes in the oxygen evolution reaction, instead losing a portion to surface recombination at the $BiVO_4$/OEC junction. The interface states formed at the $BiVO_4$/OEC junction can serve as recombination centers and cause surface recombination. The fact that $BiVO_4$/FeOOH generated higher photocurrent than did $BiVO_4$/NiOOH, although NiOOH shows faster water oxidation kinetics as an electrocatalyst, suggests that the interface recombination at the $BiVO_4$/NiOOH junction is more substantial than that at the $BiVO_4$/FeOOH junction. This can be easily confirmed by comparing photocurrents for sulfite oxidation by $BiVO_4$, $BiVO_4$/FeOOH, and $BiVO_4$/NiOOH (Fig. 3, B and C, and table S3). Because the interfacial hole transfer rates for sulfite oxidation on the $BiVO_4$, FeOOH, and NiOOH surfaces should be equally fast, any difference observed in photocurrents for sulfite oxidation by $BiVO_4$, $BiVO_4$/FeOOH, and $BiVO_4$/NiOOH should be mainly due to the recombination at the $BiVO_4$/OEC junction. The comparison shows that photocurrent for $BiVO_4$/FeOOH is very close to that for $BiVO_4$, whereas the photocurrent for $BiVO_4$/NiOOH is considerably lower, which indicates that the interface recombination at the $BiVO_4$/NiOOH junction is indeed more substantial.

In addition to the interface recombination at the $BiVO_4$/OEC junction, slow water oxidation kinetics at the OEC/solution junction can cause additional surface recombination during water oxidation (*26*, *27*). This additional surface recombination can be shown as the difference in photocurrent for sulfite oxidation and water oxidation (Fig. 3, B and C). When the rate of interfacial hole transfer for water oxidation is slower than the rate of holes entering the OEC layer, holes are accumulated in the OEC layer and at the $BiVO_4$/OEC junction, which in turn increases the electron current from the CB of $BiVO_4$ to the OEC layer for surface recombination (*27*). Because FeOOH has slower water oxidation kinetics than that of NiOOH, the difference in photocurrent for water oxidation and sulfite oxidation is more pronounced for $BiVO_4$/FeOOH than $BiVO_4$/NiOOH (Fig. 3, B and C). However, when the effects of interface recombination at the $BiVO_4$/OEC junction and water oxidation kinetics are combined, $BiVO_4$/NiOOH loses more surface-reaching holes to surface recombination and generates lower photocurrent than does $BiVO_4$/FeOOH for water oxidation (Fig. 3A).

Regardless of more substantial surface recombination, $BiVO_4$/NiOOH shows an earlier photocurrent onset and generates higher photocurrent than does $BiVO_4$/FeOOH in the low bias region ($E < 0.44$ V versus RHE) for water oxidation (Fig. 3A and table S2). This means that $BiVO_4$/NiOOH has a more negative flatband potential (E_{FB}) than that of $BiVO_4$/FeOOH. The photocurrent onset potential for sulfite oxidation with fast oxidation kinetics should be very close to E_{FB}. The results show that $BiVO_4$ has the most negative onset potential (0.11 ± 0.02 V versus RHE), followed by $BiVO_4$/NiOOH (0.12 ± 0.02 V versus RHE), and then $BiVO_4$/FeOOH (0.18 ± 0.02 V versus RHE) (table S3 and fig. S9A). The E_{FB}s obtained by Mott-Schottky plots of $BiVO_4$, $BiVO_4$/FeOOH, and $BiVO_4$/NiOOH show the same trend; $BiVO_4$ has the most negative E_{FB} (0.10 ± 0.03 V versus RHE), followed by $BiVO_4$/NiOOH (0.11 ± 0.03 V versus RHE), and then $BiVO_4$/FeOOH (0.15 ± 0.02 V versus RHE) (table S4 and fig. S10).

It is unlikely that the shift in E_{FB} is due to the change in charge carrier density of $BiVO_4$ because the addition of an extremely thin OEC layer should not affect the doping level or carrier density within the $BiVO_4$ electrode. This assumption is also supported by the comparable slopes in the Mott-Schottky plots for these three electrodes at each frequency (table S4). Then, the difference in E_{FB} should be caused by the change in the Helmholtz layer potential drop (V_H), which is the only other factor that can affect the E_{FB}, as shown in Eq. 2, where ϕ_{SC} is the work function of the semiconductor versus vacuum, and 4.5 is the scale factor relating the H^+/H_2 redox level to vacuum (*28*). At the $BiVO_4$/electrolyte junction, the dominant charges that affect the solid side of the Helmholtz double layer come from the adsorption of H^+ and OH^- ions on the $BiVO_4$ surface, which depends on the solution pH and the point of zero ζ potential (pH_{PZZP}) of $BiVO_4$ (Eq. 3) (*28*, *29*).

$$E_{FB}\ (\text{NHE}) = \phi_{SC} + V_H - 4.5 \quad (2)$$

$$V_H = 0.059\ (pH_{PZZP} - pH) \quad (3)$$

The pH_{PZZP} of $BiVO_4$ is reported to be between 2.5 and 3.5, and therefore, V_H should be negative in a pH 7 solution (*30*, *31*). However, when a thin layer of FeOOH or NiOOH is deposited on $BiVO_4$, because the Helmholtz double layer is now formed at the OEC/solution junction the V_H at the solid/solution interface is no longer determined by the pH_{PZZP} of $BiVO_4$ but by the pH_{PZZP} of the OEC layer. This means that the pH_{PZZP} of OEC is an important factor to consider in optimizing the photoanode/OEC junction because it can affect the E_{FB} of the photoanode.

The pH_{PZZP} of FeOOH is reported to be between 7 and 9 (*32*, *33*). Thus, the resulting more positive V_H at the FeOOH/solution junction will shift the E_{FB} of $BiVO_4$/FeOOH positively, which is in agreement with the observed shift direction of the E_{FB}. The pH_{PZZP} of NiOOH cannot be straightforwardly determined because chemical composition of NiOOH varies with pH. However, it is known that NiOOH has a

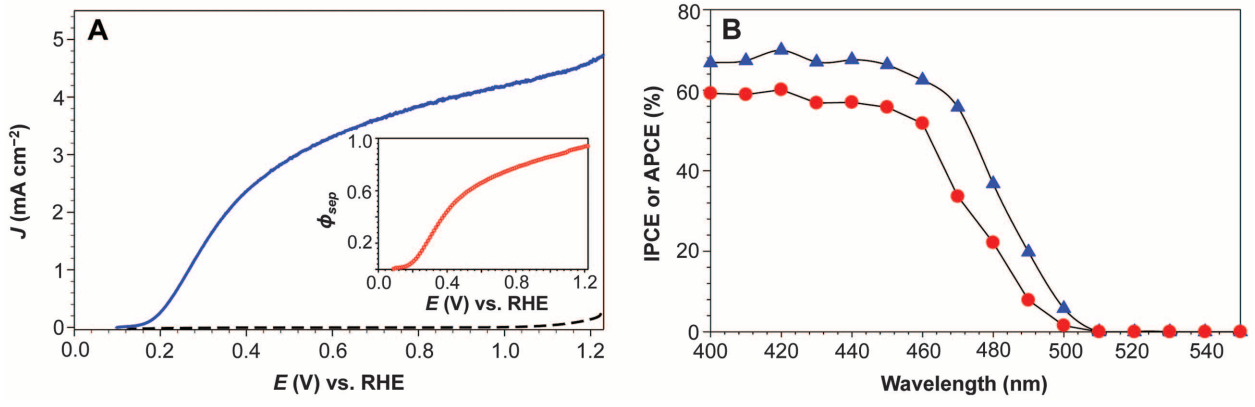

Fig. 2. Photoelectrochemical properties of nanoporous $BiVO_4$ electrode for sulfite oxidation. (**A**) *J-V* curve of nanoporous $BiVO_4$ electrode measured in a 0.5 M phosphate buffer (pH 7) containing 1 M Na_2SO_3 as hole scavenger under AM 1.5 G, 100 mW/cm^2 illumination (scan rate, 10 mV/s). Dark current is shown as a dashed line. (Inset) ϕ_{sep} calculated from the *J-V* curve after dark current is subtracted. (**B**) IPCE (red circles) and APCE (blue triangles) measured in the same solution at 0.6 V versus RHE.

negative ζ potential (~–20 mV) in a pH 7 solution (*34*), meaning that pH_{PZZP} of NiOOH is lower than 7, and the E_{FB} of $BiVO_4$/NiOOH is expected to be more negative than that of $BiVO_4$/FeOOH, which again agrees with the observed E_{FB} shift.

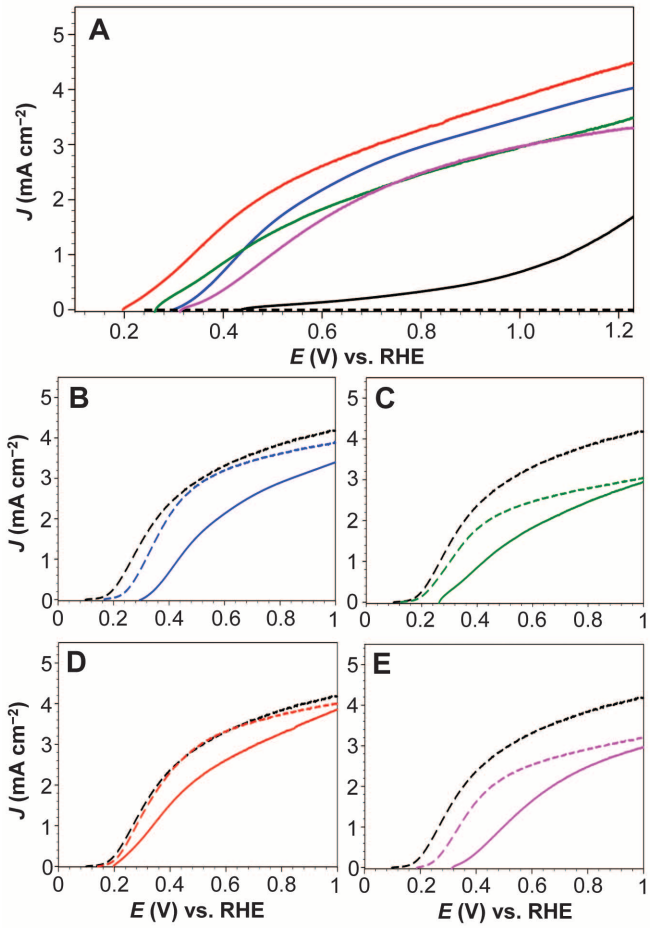

Fig. 3. Effect of OECs on photocurrents for water oxidation and sulfite oxidation. (**A**) *J-V* curves of $BiVO_4$ (black solid line), $BiVO_4$/FeOOH (blue), $BiVO_4$/NiOOH (green), $BiVO_4$/FeOOH/NiOOH (red), and $BiVO_4$/NiOOH/FeOOH (pink) for water oxidation measured in a 0.5 M phosphate buffer (pH 7) under AM 1.5 G illumination. Dark current is shown as a dashed line. (**B** to **E**) *J-V* curves of (B) $BiVO_4$/FeOOH, (C) $BiVO_4$/NiOOH, (D) $BiVO_4$/FeOOH/NiOOH, and (E) $BiVO_4$/NiOOH/FeOOH comparing photocurrent for sulfite oxidation (dashed) and water oxidation (solid) measured with and without the presence of 1.0 M Na_2SO_3 as hole scavenger. Photocurrent for sulfite oxidation by $BiVO_4$ is shown as the black dashed line for comparison. The mean values and SDs of photocurrent onset potentials and photocurrent densities are summarized in tables S2 and S3.

The pH_{PZZP} of a material depends on its specific surface termination and solution composition. Therefore, the most reliable estimations of the V_Hs of electrodes discussed in this study can be obtained when the ζ potential measurement is performed by using the electrodes and the solution that were used in this study. The ζ potentials measured for our nanoporous $BiVO_4$, $BiVO_4$/FeOOH, and $BiVO_4$/NiOOH in a 0.5 M phosphate buffer (pH 7) were –36 ± 3, –8 ± 3, and –36 ± 4 mV, respectively. These results indicate that the V_Hs at the $BiVO_4$/solution and the NiOOH/solution junctions should indeed be more negative than that at the FeOOH/solution junction.

On the basis of our new understanding of the $BiVO_4$/OEC and the OEC/electrolyte interfaces, we deposited consecutive layers of FeOOH and NiOOH, simultaneously optimizing the $BiVO_4$/OEC and the OEC/electrolyte junctions. The FeOOH at the $BiVO_4$/OEC junction will reduce the interface recombination, whereas the NiOOH at the OEC/electrolyte junction will decrease V_H to achieve a more negative E_{FB} for $BiVO_4$ while realizing faster water oxidation kinetics than if FeOOH was used as the outermost layer.

The photocurrent onset for sulfite oxidation (fig. S9A and table S3) as well as the Mott-Schottky plot (fig. S10 and table S4) of the resulting $BiVO_4$/FeOOH/NiOOH photoanode shows that its E_{FB} is comparable with that of $BiVO_4$/NiOOH, indicating that the E_{FB} of the $BiVO_4$ photoanode is indeed affected by the pH_{PZZP} of the outermost OEC layer. In addition, $BiVO_4$/FeOOH/NiOOH and $BiVO_4$/FeOOH show comparable *J-V* curves for sulfite oxidation, confirming that the $BiVO_4$/FeOOH junction effectively reduces the interface recombination at the $BiVO_4$/OEC junction (Fig. 3, B and D). As a result, $BiVO_4$/FeOOH/NiOOH shows

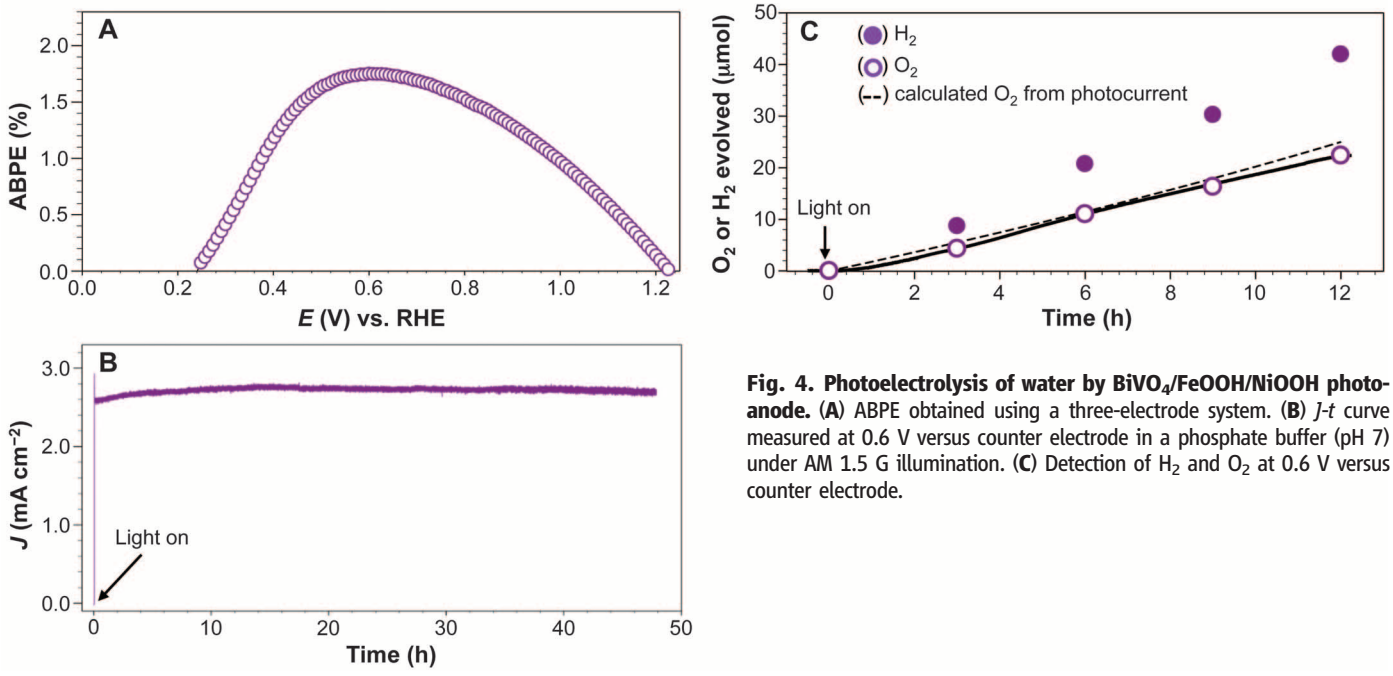

Fig. 4. Photoelectrolysis of water by $BiVO_4$/FeOOH/NiOOH photoanode. (**A**) ABPE obtained using a three-electrode system. (**B**) *J-t* curve measured at 0.6 V versus counter electrode in a phosphate buffer (pH 7) under AM 1.5 G illumination. (**C**) Detection of H_2 and O_2 at 0.6 V versus counter electrode.

impressive overall performance for water oxidation, reaching a photocurrent density of 2.8 ± 0.2 mA/cm^2 at 0.6 V versus RHE (Fig. 3A and table S2), which is markedly better than those of $BiVO_4$/FeOOH and $BiVO_4$/NiOOH and is almost comparable with the performance of bare $BiVO_4$ for sulfite oxidation.

When NiOOH was first deposited on the $BiVO_4$ surface and FeOOH was added as the outermost layer to form $BiVO_4$/NiOOH/FeOOH (reversed OEC junction), the resulting E_{FB}s determined by sulfite photocurrent onset (fig. S9A and table S3) and Mott-Schottky plot (fig. S10 and table S4) are comparable with those of $BiVO_4$/FeOOH, again confirming that the E_{FB} of the $BiVO_4$ photoanode is affected by the pH_{PZZP} of the outermost OEC. Also, the *J-V* curve for sulfite oxidation by $BiVO_4$/NiOOH/FeOOH was comparable with that by $BiVO_4$/NiOOH, confirming that a $BiVO_4$/NiOOH junction is not favorable for interface recombination (Fig. 3, C and E). As a result, $BiVO_4$/NiOOH/FeOOH shows the lowest photocurrent for water oxidation. These results prove that the photocurrent enhancement achieved by the $BiVO_4$/FeOOH/NiOOH photoanode for photoelectrolysis of water is truly due to the simultaneous optimization of the $BiVO_4$/OEC and OEC/electrolyte junctions, using an optimum dual OEC structure.

The applied bias photon-to-current efficiency (ABPE) of the $BiVO_4$/FeOOH/NiOOH electrode calculated by using its *J-V* curve, assuming 100% Faradaic efficiency, is plotted in Fig. 4A (*35*). The maximum ABPE of 1.75% achieved by the system is impressive because it is obtained by using unmodified $BiVO_4$ as a single photon absorber. Moreover, this efficiency is achieved at a potential as low as 0.6 V versus RHE, which is a highly favorable feature for assembling a tandem cell or a photoelectrochemical diode (*12*, *36*, *37*). The ABPE obtained by using a two-electrode system (working electrode and a Pt counter electrode), which achieves the maximum ABPE of 1.72%, is also shown in fig. S11 (*35*). The long-term stability of $BiVO_4$/FeOOH/NiOOH was tested by obtaining a *J-t* curve. A photocurrent density of 2.73 mA/cm^2, obtained by applying 0.6 V between the working and counter electrodes, was maintained for 48 hours without showing any sign of decay, proving its long-term stability (Fig. 4B). The O_2 measurement made by using a fluorescence O_2 sensor confirmed that the photocurrent generated at 0.6 V versus counter-electrode was mainly associated with O_2 production (> 90% photocurrent-to-O_2 conversion efficiency) (Fig. 4C). The same results were obtained when the measurement was performed at 0.6 V versus RHE. H_2 production at the Pt counter electrode was also detected with gas chromatography (GC) (Fig. 4C). The molar ratio of the produced H_2:O_2 was 1.85:1. The slight deviation from the stoichiometric ratio of 2:1 is due to our imperfect manual sampling method of H_2 for GC analysis.

Because this outstanding performance was achieved by using simple, unmodified $BiVO_4$ (no extrinsic doping and no composition tuning) as the only photon absorber, further improvement of the cell efficiency is expected when various strategies of tuning compositions or forming heterojunctions and tandem cells are used to enhance photon absorption and electron-hole separation.

References and Notes

1. A. Kudo, K. Omori, H. Kato, *J. Am. Chem. Soc.* **121**, 11459–11467 (1999).
2. Y. Park, K. J. McDonald, K.-S. Choi, *Chem. Soc. Rev.* **42**, 2321–2337 (2013).
3. Y. Liang, T. Tsubota, L. P. A. Mooij, R. van de Krol, *J. Phys. Chem. C* **115**, 17594–17598 (2011).
4. F. F. Abdi, R. van de Krol, *J. Phys. Chem. C* **116**, 9398–9404 (2012).
5. F. F. Abdi, T. J. Savenije, M. M. May, B. Dam, R. van de Krol, *J. Phys. Chem. Lett* **4**, 2752–2757 (2013).
6. D. K. Zhong, S. Choi, D. R. Gamelin, *J. Am. Chem. Soc.* **133**, 18370–18377 (2011).
7. H. S. Park *et al.*, *J. Phys. Chem. C* **115**, 17870–17879 (2011).
8. W. J. Jo *et al.*, *Angew. Chem. Int. Ed. Engl.* **51**, 3147–3151 (2012).
9. S. P. Berglund, A. J. E. Rettie, S. Hoang, C. B. Mullins, *Phys. Chem. Chem. Phys.* **14**, 7065–7075 (2012).
10. K. Zhang, X. J. Shi, J. K. Kim, J. H. Park, *Phys. Chem. Chem. Phys.* **14**, 11119–11124 (2012).
11. Y. Park, D. Kang, K.-S. Choi, *Phys. Chem. Chem. Phys.* **16**, 1238–1246 (2014).
12. F. F. Abdi *et al.*, *Nat. Commun* **4**, 2195 (2013).
13. K. J. McDonald, K.-S. Choi, *Energy Environ. Sci* **5**, 8553–8557 (2012).
14. T. Allen, *Particle Size Measurement* (Chapman and Hall, London, 1997).
15. J. A. Seabold, K.-S. Choi, *J. Am. Chem. Soc.* **134**, 2186–2192 (2012).
16. R. Sarala, M. A. Islam, S. B. Rabin, D. M. Stanbury, *Inorg. Chem.* **29**, 1133–1142 (1990).
17. D. M. Stanbury, *Adv. Inorg. Chem.* **33**, 69–138 (1989).
18. J.-F. Reber, K. Meier, *J. Phys. Chem.* **88**, 5903–5913 (1984).
19. H. Dotan, K. Sivula, M. Grätzel, A. Rothschild, S. C. Warren, *Energy Environ. Sci* **4**, 958–964 (2011).
20. J. M. Foley, M. J. Price, J. I. Feldblyum, S. Maldonado, *Energy Environ. Sci* **5**, 5203–5220 (2012).
21. M. Zhou *et al.*, *ChemSusChem* **5**, 1420–1425 (2012).
22. A. J. E. Rettie *et al.*, *J. Am. Chem. Soc.* **135**, 11389–11396 (2013).
23. L. Trotochaud, J. K. Ranney, K. N. Williams, S. W. Boettcher, *J. Am. Chem. Soc.* **134**, 17253–17261 (2012).
24. R. D. L. Smith *et al.*, *Science* **340**, 60–63 (2013).
25. M. W. Louie, A. T. Bell, *J. Am. Chem. Soc.* **135**, 12329–12337 (2013).
26. C. Y. Cummings, F. Marken, L. M. Peter, A. A. Tahir, K. G. Wijayantha, *Chem. Commun. (Camb.)* **48**, 2027–2029 (2012).
27. L. M. Peter, K. G. Wijayantha, A. A. Tahir, *Faraday Discuss.* **155**, 309–322, discussion 349–356 (2012).
28. J. Nozik, *Annu. Rev. Phys. Chem.* **29**, 189–222 (1978).
29. S. R. Morrison, in *Electrochemistry at Semiconductor and Oxidized Metal Electrodes* (Plenum Press, New York, 1980), pp. 49–78.
30. N. C. Castillo, A. Heel, T. Graule, C. Pulgarin, *Appl. Catal. B* **95**, 335–347 (2010).
31. S. Obregón, G. Colón, *J. Mol. Catal. Chem.* **376**, 40–47 (2013).
32. R. M. Cornell, U. Schwertmann, *The Iron Oxides: Structure, Properties, Reactions, Occurrences and Uses* (Wiley VCH, New York, 2003).
33. D. M. Sherman, *Geochim. Cosmochim. Acta* **69**, 3249–3255 (2005).
34. N. Hernández, R. Moreno, A. J. Sánchez-Herencia, J. L. Fierro, *J. Phys. Chem. B* **109**, 4470–4474 (2005).
35. Z. Chen *et al.*, *J. Mater. Res.* **25**, 3–16 (2010).
36. M. G. Walter *et al.*, *Chem. Rev.* **110**, 6446–6473 (2010).
37. L. Tong *et al.*, *Energy Environ. Sci* **5**, 9472–9475 (2012).

Acknowledgments: We acknowledge support from the Center for Chemical Innovation of the National Science Foundation (POWERING THE PLANET: grant CHE-1305124). We thank M. A. Woo for electrodepositing FeOOH and NiOOH on FTO substrates and testing their electrochemical water oxidation performances.

Supplementary Materials

www.sciencemag.org/content/343/6174/990/suppl/DC1
Materials and Methods
Figs. S1 to S11
Tables S1 to S4
References (*38*–*41*)

7 October 2013; accepted 31 January 2014
Published online 13 February 2014;
10.1126/science.1246913

A Direct Quantitative Measure of Surface Mobility in a Glassy Polymer

Y. Chai,[1] T. Salez,[3] J. D. McGraw,[4]* M. Benzaquen,[3] K. Dalnoki-Veress,[3,4] E. Raphaël,[3] J. A. Forrest[1,2]†

Thin polymer films have striking dynamical properties that differ from their bulk counterparts. With the simple geometry of a stepped polymer film on a substrate, we probe mobility above and below the glass transition temperature T_g. Above T_g the entire film flows, whereas below T_g only the near-surface region responds to the excess interfacial energy. An analytical thin-film model for flow limited to the free surface region shows excellent agreement with sub-T_g data. The system transitions from whole-film flow to surface localized flow over a narrow temperature region near the bulk T_g. The experiments and model provide a measure of surface mobility in a simple geometry where confinement and substrate effects are negligible. This fine control of the glassy rheology is of key interest to nanolithography among numerous other applications.

The last decades have seen a considerable interest in the dynamical and rheological properties of glassy materials (*1*, *2*). Recent efforts (*1*, *3*–*5*) have focused on elucidating the nature of glassy dynamics both in the bulk and in systems, such as thin films or colloids,

where the interfaces play a dominant role and can induce strong dynamical heterogeneities. Higher mobility near interfaces has often been suggested as the cause of anomalous glass transition temperature (T_g) in thin polymer films (*3*–*5*). The presence of a more mobile surface has practical implications for thin-film coatings related to lubrication, wear, and friction. Flow on a near-surface layer can also place strict lower limits on feasible length scales for nanolithography (*6*–*8*). Although earlier investigations provided some contradictory conclusions (*9*, *10*), most recent reports are consistent with a region of enhanced mobility on the surface of glassy polymer films. There have also been reports of enhanced surface mobility in small-molecule glasses (*11*, *12*). The parallels between polymeric and small-molecule glasses suggest that enhanced surface mobility is a more general property of glass-forming materials. Most current research efforts have a goal of providing a quantitative description, including the temperature dependence, of the properties of the near-surface region. Surface response to nanoparticle embedding has been used to probe anomalous surface dynamics in both polymeric and small-molecule glasses (*13*–*17*). That work showed that small molecules can flow on the surface, whereas larger polymers have enhanced segmental mobility but do not flow owing to their larger molecular size. Relaxation of an imposed surface topography has been used to demonstrate enhanced mobility in polymeric (*18*–*21*) and small-molecule systems (*11*). For small-molecule glasses, the enhanced surface mobility is often discussed in terms of surface diffusion (*22*), where the molecules at the free surface have a diffusion time that can be orders of magnitude smaller than the bulk value (*11*, *12*). For polymers, the most complete description comes from studies of low-molecular-weight polystyrene (*23*).

The use of capillary leveling as a probe of rheology on the nanometer scale (*24*–*26*) has been successfully used to study polymer rheology for films at temperatures much greater than the T_g value of the polymer. Stepped films were annealed, and a decrease in the surface area was monitored to probe dissipation of the system's free energy, with a complete quantification of the rheological properties (*24*–*26*). The low-molecular-weight films considered here are sufficiently thin that gravitational effects can be ignored, yet thick enough that van der Waals interactions resulting in a disjoining pressure can be neglected. Gradients in the curvature of the free surface result in Laplace pressure gradients that drive viscous flows. When the height gradients are sufficiently small, and the typical height of the profile is sufficiently smaller than its typical width, the flow can be described by the Stokes equations in the lubrication approximation (*27*). For homogenous viscous films, the evolution of the profile $h(x,t)$ is described by the capillary-driven thin-film equation (TFE) (*28*)

$$\partial_t h + \frac{\gamma}{3\eta_b}\partial_x(h^3\partial_x^3 h) = 0 \qquad (1)$$

where η_b is the bulk viscosity, γ is the surface tension, x is the horizontal coordinate, and t is the time. The TFE can be solved numerically for a stepped initial profile (*25*), and the solution has been shown to converge in time toward a self-similar profile in the variable $xt^{-1/4}$.

For the case of films with $T < T_g$, the majority of the film is unable to flow. Because previous studies have shown an evolution of the free surface to minimize surface area and energy in polymeric (*18*, *19*) and nonpolymeric glasses (*12*, *17*), there must be some flow localized over a thin layer near the free surface. At a given temperature, we will assume the thickness h_m of this mobile layer, with viscosity η_m, to be constant (see Fig. 1B). Of course, the present two-layer model is an approximation, and one would expect a continuous variation from surface to bulk dynamics through the sample (*29*). However, this simple description provides a first-order approach with a single free parameter, as shown below. Invoking Stokes equations in the lubrication approximation for the surface layer, and assuming no slip between the glassy and surface layers and no shear at the free surface, leads to

$$\partial_t h + \frac{\gamma h_m^3}{3\eta_m}\partial_x^4 h = 0 \qquad (2)$$

which we will refer to as the glassy thin-film equation (GTFE). It is mathematically identical to the linearized TFE. The GTFE thus has an exact analytical solution for a stepped initial profile (*26*), which is self-similar in the variable $xt^{-1/4}$. This solution can be used to extract a single free parameter describing the flow: $\gamma h_m^3/3\eta_m$. The form of Eq. 2 is mathematically identical to the Mullins model (*22*) describing the evolution of profiles by surface diffusion of molecules. However, for flow of macromolecules where all the segments must move together, the GTFE interpretation in terms of surface flow in a layer of size h_m is more relevant than this collective surface diffusion scenario. Figure 1 displays a schematic diagram of the two flow regimes studied. The first is for $T > T_g$ with homogeneous viscosity (TFE), and the second for $T < T_g$, where there is only a thin layer of mobile fluid atop an immobile glassy film (GTFE). The self-similar nature of both Eqs. 1 and 2 implies that, by fitting their solutions to the experimental profiles, one can determine the physical quantities of the problem through a single free parameter. This method of investigation can be carried out with films thick enough that chain confinement and polymer-substrate effects can be ignored.

Films were prepared by spin-coating from a dilute solution of polystyrene (PS) dissolved in toluene onto two types of substrates: silicon (Si) with the native oxide layer, and freshly cleaved mica substrates. The PS had weight-averaged molecular weight $M_w = 3.0$ kg mol^{-1}, and polydispersity index 1.09 (Polymer Source Inc., Dorval, Québec). Samples were annealed at 348 K, which is 5 K above bulk T_g, in an oven flushed with dry N_2 for 12 hours. Films with thickness h_2 on mica substrates were floated onto the surface of purified water in order to separate the films from the mica. The previously coated Si substrates, coated with PS of thickness h_1, were then dipped into the water and used to pick up the floating films. These low-molecular-weight films are fragile when floating on the water surface and break into smaller sections with several straight vertical edges. Thus, when transferred, these "float-gaps" form perfect steps of height h_2 over bottom films of height h_1 (see Fig. 1A). The dilatometric T_g of independent, annealed flat films on Si was measured by ellipsometry. For $h \geq 40$ nm, we found $T_g = 343 \pm 2$ K.

We first demonstrate that the stepped film samples level at temperatures much less than the

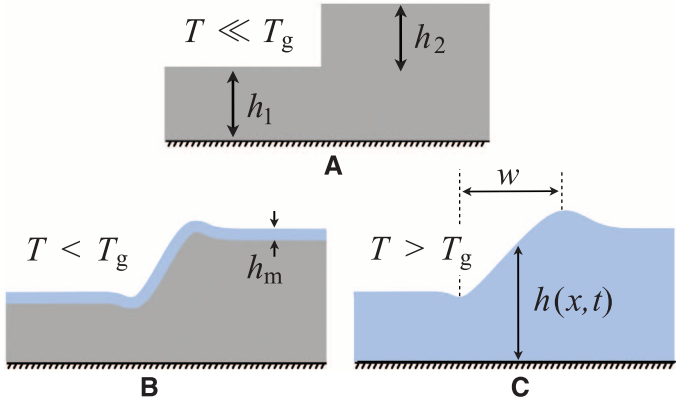

Fig. 1. Schematic diagram of the simple geometry and flow regions. (**A**) An as-prepared sample at room temperature. (**B** and **C**) The two flow mechanisms discussed in the paper. (**C**) describes the evolution of the total height profile $h(x,t)$ through whole-film flow (TFE) (see Eq. 1), and (**B**) shows the evolution of the total height profile through flow localized in a small region near the free surface (GTFE) (see Eq. 2). The flow region is indicated in blue and is assumed to vanish far below T_g.

[1]Department of Physics and Astronomy and Guelph-Waterloo Physics Institute, University of Waterloo, Waterloo, Ontario N2L 3G1, Canada. [2]Perimeter Institute for Theoretical Physics, 31 Caroline Street North, Waterloo, Ontario N2L 2Y5, Canada. [3]Laboratoire de Physico-Chimie Théorique, UMR CNRS Gulliver 7083, École Supérieure de Physique et de Chimie Industrielles (ESPCI), Paris, France. [4]Department of Physics and Astronomy, McMaster University, Hamilton, Ontario L8S 4M1, Canada.

*Present address: Department of Experimental Physics, Saarland University, 66041 Saarbrücken, Germany.
†Corresponding author. E-mail: jforrest@uwaterloo.ca

bulk T_g. We performed a simple width evolution experiment where three types of stepped polymer films were prepared with the same bottom-layer thickness, h_1 = 90 nm, and top-layer thicknesses of h_2 = 14, 23, and 42 nm (see Fig. 1A). The stepped films were collectively heated in a N_2 filled oven and removed after various annealing times for measurement at room temperature with atomic force microscopy (AFM) (JPK Instruments, Berlin). Scan lines were averaged to produce a profile, and the width w (see Fig. 1C) was obtained by fitting this profile to a tanh[x/(w/2)] function. Figure 2A shows the temporal evolution of w for this series of stepped films at five different temperatures. There is an increase with time of the width at temperatures as much as 30 K below the bulk T_g value. This indicates enhanced mobility in the glassy film. Furthermore, as suggested by both Eqs. 1 and 2, the width varies as $w = (at)^{1/4}$ at all temperatures, where a is a factor that depends a priori on temperature and initial geometry. This 1/4 power law demonstrates the existence of a capillary-driven flow both above and below T_g. By analogy with the scaling analysis of Stillwagon and Larson (*30*), a simple determination of the effective viscosity η_{eff} of the sample can be obtained by the vertical offset between the lines in Fig. 2A, using $\eta_{eff} \propto a^{-1}$. The effective viscosity corresponds to the viscosity of the sample calculated as if flow occurs in the entire film, within the lubrication approximation. For a given geometry, it is then possible to compare the η_{eff} values obtained at all temperatures to one, η_0, at a particular reference temperature T_0, to get a relative measure of the effective viscosity of the entire film. Setting $T_0 = T_g$, Fig. 2B shows the relative effective viscosity, $\eta_{eff}/\eta_0 = a_0/a$, for all film geometries. The solid line in this plot is the Vogel-Fulcher-Tammann (VFT) law for PS (*31*). When $T > T_g$, the temperature dependence of the effective viscosity agrees quantitatively with the bulk VFT law. However, for $T < T_g$, there is significant deviation away from this line. There are two ways in which this difference can be interpreted: Either (i) the entire film flows with viscosity reduced below that predicted by the VFT law (either because the viscosity is reduced from the bulk one or because the bulk viscosity deviates from the VFT law for $T < T_g$), or (ii) the assumption of whole-film flow is invalid.

To distinguish between these two possibilities, we turn to a more quantitative investigation based on the TFE and GTFE. Stepped polymer films with $h_1 = h_2 = 90$ nm were used. Typically, AFM images were collected over a square region of size ~1 μm by 1 μm for glassy samples and up to ~50 μm by 50 μm for melt samples. This measurement was repeated until the shape of the profile was self-similar in the variable $xt^{-1/4}$ or, for cases of the two temperatures in the transition region, until a sample was heated for a total of 90 hours. All AFM measurements were carried out at room temperature. For the TFE (see Eq. 1) and GTFE (see Eq. 2), the long-time solutions have been shown to be self-similar in the variable $xt^{-1/4}$ (*24*–*26*). Therefore, if we plot the film height $h(x,t)$ as a function of $xt^{-1/4}$ for several times, the profiles should superimpose. Figure 3, A and B, shows a number of measured profiles over a large time window, both for temperatures below T_g (left) and above T_g (right). Figure 3, C and D, shows that the profiles are indeed self-similar. Although the data obeys this self-similarity for $T < T_g$ and $T > T_g$, there are important differences between the two temperature regimes. In particular, the shapes of the self-similar profiles are different. See, for example, Fig. 3, C and D, where one can see that above T_g the magnitude of the bump (first top oscillation) is larger than that of the dip (first bottom oscillation). Below T_g, it is similarly evident that the bump and dip extrema are equal in magnitude. To be more precise, above T_g these features depend quantitatively on h_1 and h_2, whereas below T_g the surface flows without sensitivity to the substrate for the considered thicknesses. In the latter case, samples with same h_2 but different h_1 show bumps and dips that are all equal in magnitude (fig. S1). This simple qualitative feature of the profiles shows that it is the surface alone that flows below T_g. Fits of the sub-T_g profiles to solutions of both the TFE and GTFE quantitatively highlight the differences. The left plots of Fig. 3 are for $T < T_g$. The blue solid line in Fig. 3C is a best fit of the self-similar experimental profile to the GTFE analytical solution (*26*). The residuals of the fit are also shown as a blue solid line in Fig. 3E. The red dashed line in Fig. 3E corresponds to the fit of the sub-T_g data to the TFE numerical solution (*25*). In the sub-T_g case, the experimental profiles are thus much better described by the GTFE than by the TFE, as the residuals are much lower and do not exhibit the systematic variation seen in the dashed residuals. Similarly, the experimental data on the right side of Fig. 3 are for $T > T_g$ and are much better represented by the TFE than by the GTFE.

Because the TFE and GTFE correspond to different physical pictures, we can define a single metric, χ, for the goodness of fit to each model. χ is used to characterize the transition from where the system is best described by whole-film flow to where it is best described by surface flow over thickness h_m. We define this quantity by the correlation function

$$\chi = \frac{\int dx (h_{EXP} - h_{TFE})^2}{\int dx (h_{GTFE} - h_{TFE})^2} \quad (3)$$

where h_{EXP} is the self-similar experimental profile, h_{TFE} is the numerical solution (*25*) of the TFE, and h_{GTFE} is the analytical solution (*26*) of the GTFE. This function equals 1 if the experimental data are exactly described by the GTFE solution and 0 if the experimental data are exactly described by the TFE solution. Figure 4 shows the temperature dependence of χ as well as the temperature dependence of the thermal expansivity dh/dT derived from ellipsometry measurements for an independent flat 87-nm-thick film. This type of ellipsometry data is often used to find the dilatometric T_g value in thin films (*4*), and in this case gives rise to $T_g = 343 \pm 2$ K. It is remarkable that $\chi(T)$ undergoes an abrupt transition at a temperature indistinguishable from the bulk T_g value. This means that the system undergoes

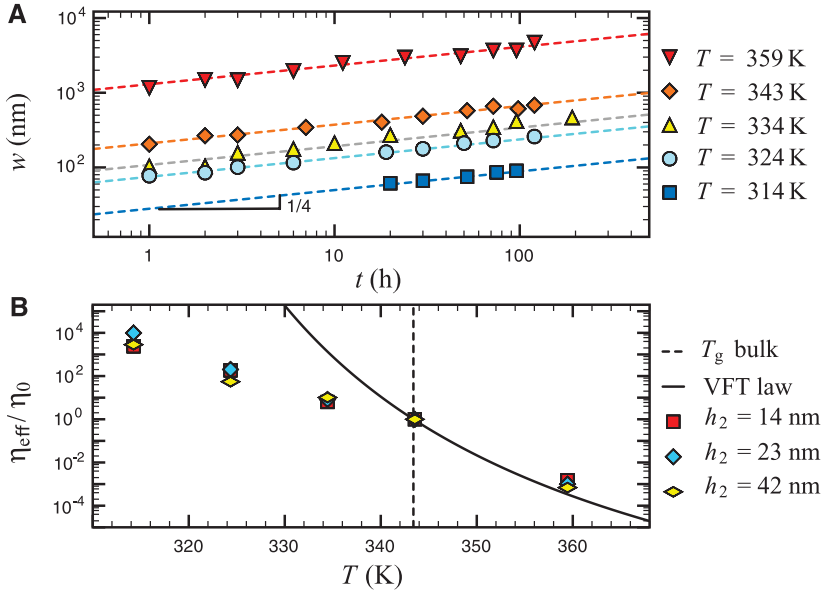

Fig. 2. Temporal evolution of the width of stepped films and temperature dependence of the effective viscosity. (**A**) The temporal evolution of the width w (see Fig. 1C), obtained by fitting the profile to a tanh[x/(w/2)] function, for h_1 = 90 nm and h_2 = 42 nm, at temperatures near the bulk T_g = 343 K. The dashed lines have slope 1/4. (**B**) Effective viscosities (see definition in text) normalized to the one at $T_0 = T_g$ for a given geometry, for films with h_1 = 90 nm and h_2 as indicated. Errors are comparable to the symbol size.

a sharp transition from bulk flow to surface-dominated flow as the temperature is lowered through the bulk T_g value. The transition temperature should be interpreted as the one below which most of the film exhibits no flow on the 90-hour time scale.

Polystyrene is a model glass-forming material, and through our measurements, we should be able to probe other aspects of the glassy dynamics. In particular, while the data shown in Fig. 4 are for profiles having reached steady state or after 90 hours of annealing, whichever occurs first, we can measure the time dependence of the shape of the profile at temperatures near the transition. For temperatures in this range, we might expect to see evidence of the time-dependent mechanical properties of the glassy material. In particular, glass-forming materials behave like elastic solids on short time scales and like viscous materials on much larger time scales. We thus might expect that for short times the system would behave like a glassy material, with flow only occurring in the surface region and the profile well described by the GTFE, and for long times the system would be well characterized by flow of the entire film with a profile well described by the TFE. The inset shows the temporal evolution of χ for the particular 343 K and 348 K data, which lie in the transition region. For the case of $T = 343$ K, the initial χ value is near 1, meaning that the system is initially dominated by flow localized in a surface region. As the system evolves in time, this correlation decreases, and the system becomes less well described by the GTFE. The sample at $T = 348$ K shows even more striking behavior. In this case, one can see that over a period of 3×10^5 s the system goes from being well described by flow localized in the surface region ($\chi \sim 1$), to being well described by flow in the entire film ($\chi \sim 0$). In this transition region, because the shape of the profile is changing from glass-like to fluid-like, the profiles cannot be self-similar over a large time window.

The time dependences of χ at $T = 343$ and 348 K show that the height profiles can be used to monitor the system as it changes from glass-like to liquid-like behavior. This also implies that we could probe in a single sample more than one temperature, as long as we waited for the profile to reach a self-similar state at each temperature. The data shown with diamond symbols in Fig. 4 show that a single sample, with a film thickness large enough so that chain confinement and substrate effects can safely be neglected, can exhibit a transition from bulk flow to surface flow. This thickness range can also be used for molecular glasses where other experiments requiring thinner films would not be appropriate, because dewetting is too rapid above T_g.

The numerical fits to the data can be used to extract meaningful physical parameters. In both the TFE and GTFE cases, there is a single free horizontal stretching parameter that determines the fit of the self-similar experimental profile to the dimensionless theoretical solution. Knowing the tabulated (*32*) surface tension γ, the GTFE fitting parameter (see Eq. 2) gives the surface mobility $h_m^3/(3\eta_m)$, and the TFE fitting parameter (see Eq. 1) gives the bulk viscosity η_b. As a more direct comparison, we plot the GTFE mobility $h_m^3/(3\eta_m)$ and the average TFE mobility $\left(h_1 + \frac{h_2}{2}\right)^3/(3\eta_b)$ on the single composite plot of Fig. 5. The result is consistent with that of Yang *et al.* (*23*) but with two differences in the methodology: We use films that are thick enough to prevent chain confinement and substrate effects, and we have the possibility of using a single sample to obtain the entire curve. The solid line is obtained from using the bulk VFT law for PS of the same M_w (*31*). The agreement we obtain for $T > T_g$ (left side of Fig. 5) is consistent with the previous success of the stepped-film technique in polymer melts (*24*). Of more importance for the present work is the sub-T_g mobility (right side of Fig. 5), for which we observe a strong deviation from the bulk VFT law. In this temperature range, the single-fit parameter $h_m^3/(3\eta_m)$ combines the two relevant physical quantities of the mobile surface layer: its size and viscosity. Using reasonable constraints, we now estimate each parameter individually. For any flow to occur, the size of the surface region has to be large enough so that the polymer molecules fit into it. Molecules larger than the surface region size will have segments in the glassy region and will thus be unable to flow. For PS with $M_w = 3$ kg mol^{-1}, the root-mean-squared end-to-end distance of the molecule satisfies $\langle R_{EE}\rangle_{RMS} \sim 3$ nm, and we can use this as a first estimate for the surface region size that is similar to the one in (*33*, *34*). This length scale coupled with the data in Fig. 5 suggests a surface viscosity of $\eta_m \sim 2 \times 10^8$ Pa · s at 323 K. We note that we used only an estimate for h_m, and the subsequent estimated value of η_m is very sensitive to this chosen thickness. In particular, the constraint $h_m > \langle R_{EE}\rangle_{RMS}$ may be too strong, as this is an average of the molecular size, and it is only necessary that there is a significant fraction of the molecules that have all segments in the surface region in order to have surface flow. Alternatively, if we used the value of $h_m \sim 1$ nm suggested as a lower limit in (*17*), we would predict a surface viscosity of 7.7×10^6 Pa · s at 323 K, which is 20 K below T_g. This surface viscosity is more than 3 orders of magnitude lower than the bulk viscosity at T_g. Finally, the observed linear trend (in log-lin scale) of Fig. 5 below T_g allows us to infer an Arrhenius behavior of the surface mobility below T_g, with

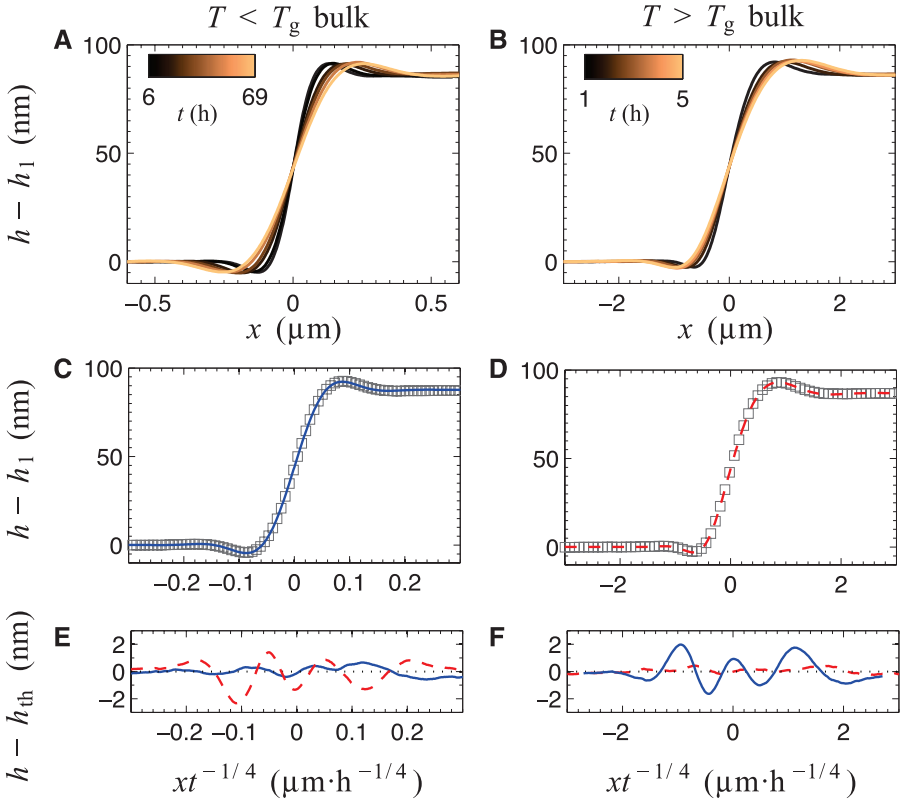

Fig. 3. Height profiles and fits below and above T_g. In both the glassy (left) ($T = 333$ K) and melt (right) ($T = 353$ K) cases, the top (**A** and **B**) shows the temporal evolutions of experimental profiles with $h_1 = h_2 = 90$ nm; the center (**C** and **D**) are the collapsed experimental profiles (white squares) showing self-similar behavior in the variable $xt^{-1/4}$; and the bottom (**E** and **F**) demonstrates the goodness of fit of each collapsed profile to either the TFE numerical solution or the GTFE analytical solution. In (C), (D), (E), and (F), the blue solid line corresponds to the GTFE and the red dashed line corresponds to the TFE.

activation energy $E_a \sim 337 \pm 20$ kJ mol^{-1}, in agreement with existing literature (*18*, *20*, *23*).

In conclusion, by employing the stepped-film geometry and analyzing the resulting flow, we report quantitative evidence for the existence of a thin layer of liquid-like material at the free surface of glassy, low-molecular-weight polystyrene films. The sample thicknesses and preparation are such that annealing effects, chain confinement, and substrate effects can be neglected. The transition from whole-film flow to flow localized in a thin surface layer has been measured and observed to occur sharply at the bulk T_g value. For temperatures inside the transition region, we were able to measure time-dependent evolutions from glassy to liquid behavior. This technique provides an opportunity to accurately follow the transition from surface flow to bulk flow within a single sample. Below T_g, a fit to the measured profile gives a surface mobility parameter $h_m^3/(3\eta_m)$ that can be used to estimate a surface viscosity. In particular, we obtain $\eta_m \sim 10^8$ Pa · s at 20 K below T_g. Independent determination of either the size $h_m(T)$ of the surface region or its viscosity $\eta_m(T)$ would allow a complete determination of the temperature-dependent properties of the near-surface region.

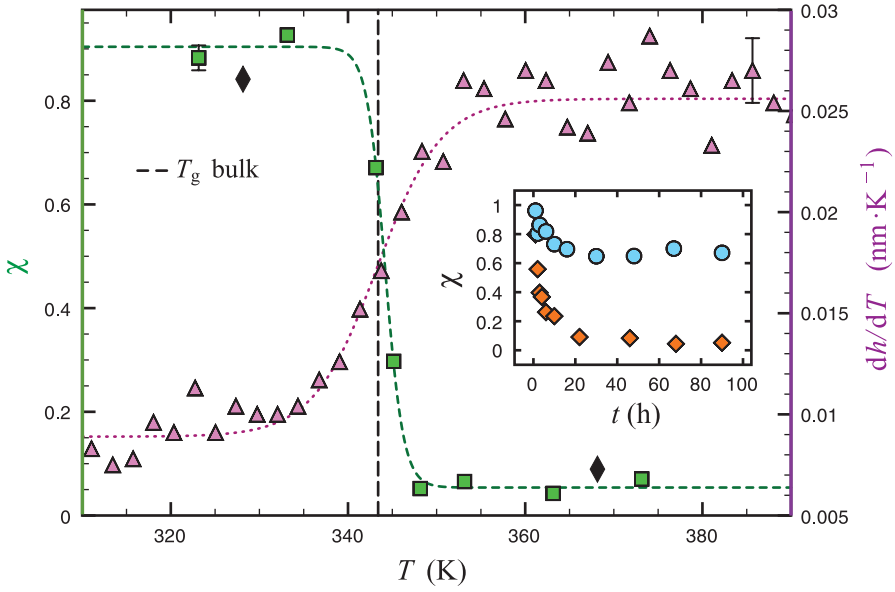

Fig. 4. Temperature dependence of the correlation function and thermal expansivity. The correlation function $\chi(T)$ defined in Eq. 3 is given by the green square and black diamond symbols (left axis) for samples with $h_1 = h_2 = 90$ nm. The thermal expansivity for an independent flat 87-nm sample is given by the purple triangles (right axis). The black diamond symbols are $\chi(T)$ for a single sample that was held first for 90 hours at $T < T_g$, then measured and heated to $T > T_g$ until the self-similar profile was reached. The inset shows the temporal evolution of χ for $T = 343$ K and 348 K data that lie in the transition region (blue circles are for $T = 343$ K; orange diamonds are for $T = 348$ K). Error bars are indicated once for each subplot.

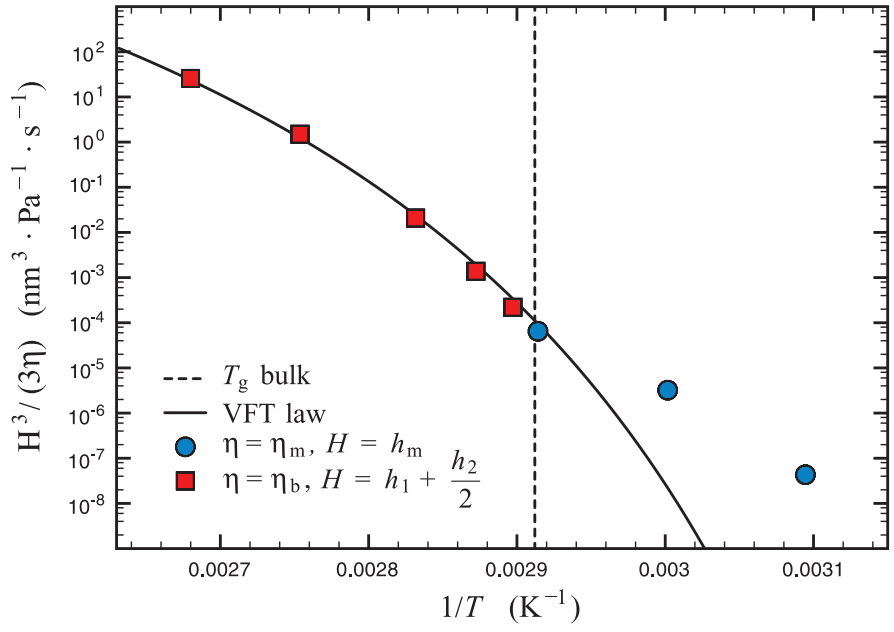

Fig. 5. Temperature dependence of the mobility. This figure is made of two subplots representing $h_1 = h_2 = 90$-nm samples. The mobility $H^3/(3\eta)$ is determined by a fit to either the analytical GTFE solution (blue circles) or the numerical TFE solution (red squares), with η and H as defined in the legend.

References and Notes

1. M. D. Ediger, P. Harrowell, *J. Chem. Phys.* **137**, 080901 (2012).
2. P. W. Anderson, *Science* **267**, 1615–1616 (1995).
3. J. A. Forrest, *Eur. Phys. J. E* **8**, 261–266 (2002).
4. J. A. Forrest, K. Dalnoki-Veress, *J. Coll. Int. Sci.* **94**, 167–195 (2001).
5. M. Alcoutlabi, G. B. McKenna, *J. Phys. Condens. Matter* **17**, R461–R524 (2005).
6. J. Teisseire, A. Revaux, M. Foresti, E. Barthel, *Appl. Phys. Lett.* **98**, 013106 (2011).
7. E. Rognin, S. Landis, L. Davoust, *Phys. Rev. E Stat. Nonlin. Soft Matter Phys.* **84**, 041805 (2011).
8. E. Rognin, S. Landis, L. Davoust, *J. Vac. Sci. Technol. B* **30**, 011602 (2012).
9. T. Kerle, Z. Lin, H. Kim, T. P. Russell, *Macromolecules* **34**, 3484–3492 (2001).
10. S. Ge *et al.*, *Phys. Rev. Lett.* **85**, 2340–2343 (2000).
11. L. Zhu *et al.*, *Phys. Rev. Lett.* **106**, 256103 (2011).
12. R. Malshe, M. D. Ediger, L. Yu, J. J. de Pablo, *J. Chem. Phys.* **134**, 194704 (2011).
13. J. H. Teichroeb, J. A. Forrest, *Phys. Rev. Lett.* **91**, 016104 (2003).
14. M. Ilton, D. Qi, J. A. Forrest, *Macromolecules* **42**, 6851–6854 (2009).
15. D. Qi, M. Ilton, J. A. Forrest, *Eur. Phys. J. E* **34**, 56 (2011).
16. D. Qi, Ph.D. thesis, University of Waterloo, Ontario, Canada, 2009.
17. C. R. Daley, Z. Fakhraai, M. D. Ediger, J. A. Forrest, *Soft Matter* **8**, 2206 (2012).
18. Z. Fakhraai, J. A. Forrest, *Science* **319**, 600–604 (2008).
19. D. Qi, Z. Fakhraai, J. A. Forrest, *Phys. Rev. Lett.* **101**, 096101 (2008).
20. R. M. Papaléo *et al.*, *Phys. Rev. B* **74**, 094203 (2006).
21. E. Buck, K. Petersen, M. Hund, G. Krausch, D. Johannsmann, *Macromolecules* **37**, 8647–8652 (2004).
22. W. W. Mullins, *J. Chem. Phys.* **30**, 77 (1959).
23. Z. Yang, Y. Fujii, F. K. Lee, C.-H. Lam, O. K. C. Tsui, *Science* **328**, 1676–1679 (2010).
24. J. D. McGraw, T. Salez, O. Bäumchen, E. Raphaël, K. Dalnoki-Veress, *Phys. Rev. Lett.* **109**, 128303 (2012).
25. T. Salez *et al.*, *Eur. Phys. J. E* **35**, 114 (2012).
26. T. Salez, J. D. McGraw, O. Bäumchen, K. Dalnoki-Veress, E. Raphaël, *Phys. Fluids* **24**, 102111 (2012).
27. Materials and methods are available as supplementary materials on *Science* Online.
28. R. Blossey, *Thin Liquid Films: Dewetting and Polymer Flow* (Springer, Dordrecht, 2012).
29. J. A. Forrest, *J. Chem. Phys.* **139**, 084702 (2013).
30. L. E. Stillwagon, R. G. Larson, *J. Appl. Phys.* **63**, 5251 (1988).
31. J.-C. Majeste, J.-P. Montfort, A. Allal, G. Marin, *Rheol. Acta* **37**, 486–499 (1998).
32. S. Wu, *J. Chem. Phys.* **74**, 632–638 (1970).
33. J. Mattsson, J. A. Forrest, L. Borjesson, *Phys. Rev. E Stat. Phys. Plasmas Fluids Relat. Interdiscip. Topics* **62**, (4 Pt B), 5187–5200 (2000).

34. J. A. Forrest, J. Mattsson, *Phys. Rev. E Stat. Phys. Plasmas Fluids Relat. Interdiscip. Topics* **61**, R53–R56 (2000).

Acknowledgments: The authors acknowledge the École Normale Supérieure of Paris, the Fondation Langlois, the Chaire Total–ESPCI ParisTech, as well as the Natural Sciences and Engineering Research Council of Canada, for financial support. We also thank O. Bäumchen for interesting discussions.

Supplementary Materials
www.sciencemag.org/content/343/6174/994/suppl/DC1
Materials and Methods
Figs. S1 and S2
Database S1
References (*35*, *36*)

19 August 2013; accepted 3 February 2014
10.1126/science.1244845

Rapid Thinning of Pine Island Glacier in the Early Holocene

J. S. Johnson,[1]*† M. J. Bentley,[2,1]† J. A. Smith,[1] R. C. Finkel,[3,4] D. H. Rood,[3,5]‡ K. Gohl,[6] G. Balco,[7] R. D. Larter,[1] J. M. Schaefer[8,9]

Pine Island Glacier, a major outlet of the West Antarctic Ice Sheet, has been undergoing rapid thinning and retreat for the past two decades. We demonstrate, using glacial-geological and geochronological data, that Pine Island Glacier (PIG) also experienced rapid thinning during the early Holocene, around 8000 years ago. Cosmogenic ^{10}Be concentrations in glacially transported rocks show that this thinning was sustained for decades to centuries at an average rate of more than 100 centimeters per year, which is comparable with contemporary thinning rates. The most likely mechanism was a reduction in ice shelf buttressing. Our findings reveal that PIG has experienced rapid thinning at least once in the past and that, once set in motion, rapid ice sheet changes in this region can persist for centuries.

Ice mass loss from the Pine Island–Thwaites sector dominates the contemporary contribution to sea level from the West Antarctic Ice Sheet (WAIS) (*1*, *2*). Pine Island Glacier (PIG) (Fig. 1A) in particular is currently experiencing considerable acceleration, thinning, and retreat (*3*–*6*). This has raised concerns over how much ice will be lost to the ocean before the ice stream stabilizes (*5*–*8*). Satellite altimetry measurements show an increase in rates of thinning of ice close to the PIG grounding line from 1.2 to 6 m year^{-1} between 2002 and 2007 (*4*, *9*). In addition, thinning has been detected 150 km upstream of the grounding line (*10*). The pattern of change is best explained by a dynamic response to increased influx of warm water to the cavity under the ice shelf at the glacier front (*11*–*14*). However, the record of change—and our understanding of dynamic changes—over longer time scales of centuries to millennia is still limited. Consequently, there is considerable uncertainty associated with model projections of the future evolution of PIG and hence the rate and timing of future ice loss (*15*). The geological record provides evidence of styles and rates of past ice sheet change that can provide constraints on the bounds of possible future change (*16*). In the PIG region, the existing geological record consists largely of marine geological data describing grounding line retreat across the continental shelf (*17*–*21*). In contrast, little is known about the terrestrial thinning

[1]British Antarctic Survey, Natural Environment Research Council, High Cross, Madingley Road, Cambridge CB3 0ET, UK. [2]Department of Geography, Durham University, South Road, Durham DH1 3LE, UK. [3]Center for Accelerator Mass Spectrometry, Lawrence Livermore National Laboratory, Post Office Box 808 L-397, Livermore, CA 94550, USA. [4]Earth and Planetary Science Department, University of California, Berkeley, CA 94720, USA. [5]Earth Research Institute, University of California, Santa Barbara, CA 93106, USA. [6]Alfred Wegener Institute Helmholtz–Centre for Polar and Marine Research, Am Alten Hafen 26, 27568 Bremerhaven, Germany. [7]Berkeley Geochronology Center, 2455 Ridge Road, Berkeley, CA 94709, USA. [8]Lamont-Doherty Earth Observatory (LDEO), Columbia University, Route 9W, Palisades, NY 10964, USA. [9]Department of Earth and Environmental Sciences, Columbia University, New York, NY 10027, USA.

*Corresponding author. E-mail: jsj@bas.ac.uk
†These authors contributed equally to this work.
‡Present address: Scottish Universities Environmental Research Centre, Rankine Avenue, Scottish Enterprise Technology Park, East Kilbride G75 0QF, UK.

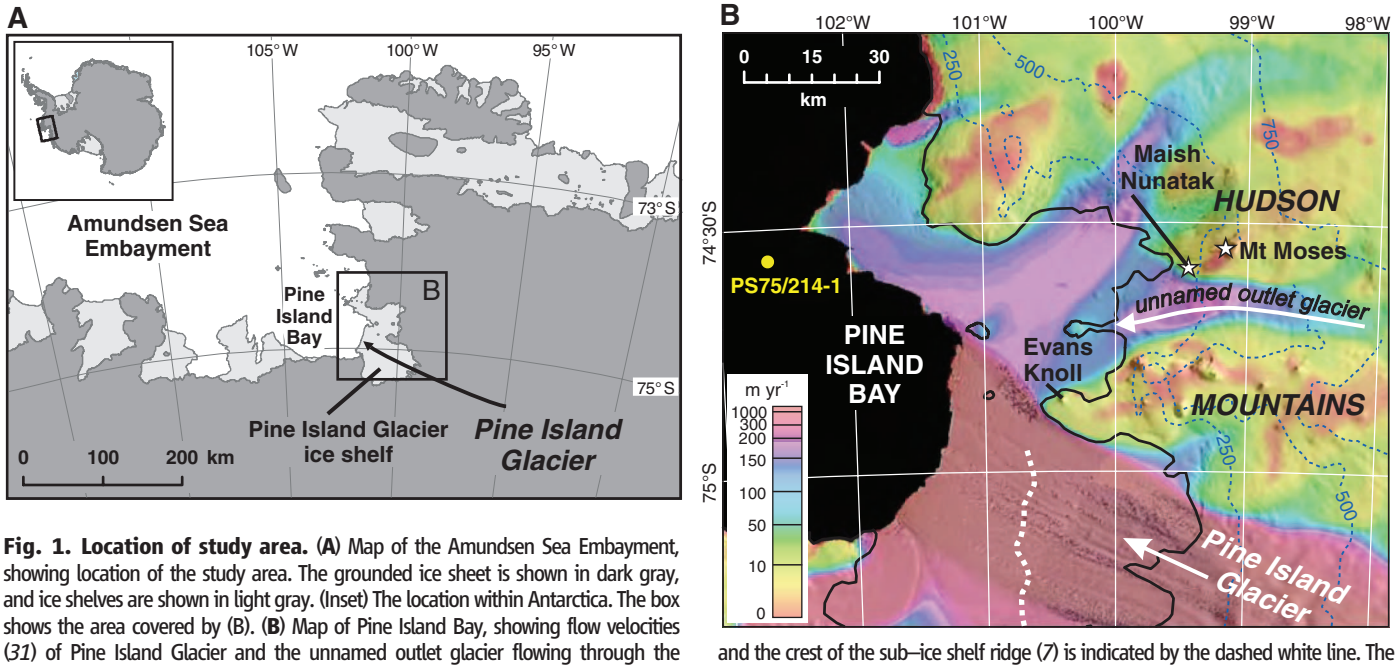

Fig. 1. Location of study area. (**A**) Map of the Amundsen Sea Embayment, showing location of the study area. The grounded ice sheet is shown in dark gray, and ice shelves are shown in light gray. (Inset) The location within Antarctica. The box shows the area covered by (B). (**B**) Map of Pine Island Bay, showing flow velocities (*31*) of Pine Island Glacier and the unnamed outlet glacier flowing through the Hudson Mountains, overlaid on Landsat Image Mosaic of Antarctica imagery (gray scale). Contours are in meters. The grounding line is indicated by the solid black line, and the crest of the sub–ice shelf ridge (*7*) is indicated by the dashed white line. The yellow circle indicates marine sediment core site PS75/214-1, which constrains grounding line retreat (before 11.7 ± 0.7 ka) from Pine Island Bay (*21*).

history of PIG (*22*) or how the ice stream evolved through the Holocene to the onset of present-day thinning.

Here, we report detailed glacial-geological evidence from the Hudson Mountains (Fig. 1B) for rapid thinning in the PIG system ~8 thousand years ago (ka). We studied two nunataks, Mount Moses and Maish Nunatak, located close to the northern margin of PIG within 50 km of its present grounding line (Fig. 1B). An unnamed outlet glacier flows through the Hudson Mountains and feeds into Pine Island Glacier ice shelf (Fig. 1B). In common with many of the ice shelf–tributary glaciers along the Amundsen Sea coast, the outlet glacier is presently thinning rapidly (at a rate of 80 to 150 cm year^{-1}) (fig. S1) (*4*). At times when the PIG grounding line was beyond Evans Knoll (~45 km seaward of its current position) (Fig. 1B), the glacier would have been a tributary to PIG, and thus, changes in its elevation provide a proxy for past elevation changes of PIG. In this way, the Hudson Mountains provide a "dipstick" record of PIG thinning during formerly more advanced positions.

Glacial deposits at both sites consist of scattered erratic cobbles and boulders of granitic lithology resting on basaltic bedrock (fig. S2) (*23*). High-sensitivity ^{10}Be surface exposure dating (*24*) was undertaken on 12 erratics collected between 0 and 142 m above the present ice surface on the two nunataks (fig. S3). Details of chemical procedures, isotopic data, and age calculations are given in (*23*) and tables S1 to S3. All but one sample—whose anomalously old exposure age (~15,800 years) (table S2) we attribute to reworking of a previously exposed cobble—yielded early Holocene ^{10}Be ages, in a narrow time interval from 6.0 ± 0.2 to 8.1 ± 0.3 ka (Fig. 2, A, B, and C). At Maish Nunatak, exposure ages at all elevations—a range of 100 m—are indistinguishable. At Mount Moses, the three highest samples yielded exposure ages that are not only indistinguishable over an elevation range of 60 m but are also indistinguishable from the ages at Maish Nunatak. By "indistinguishable," we mean that we cannot reject the hypothesis that the scatter of each group of ages around the mean results from measurement uncertainty alone (table S3) (*23*). We interpret the ages as a record of thinning of the outlet glacier flowing through the Hudson Mountains. Given that an ice surface cannot lower infinitely fast, samples at higher elevations must have been exposed for longer than were samples at lower elevations. Our observation of indistinguishable exposure ages over a wide elevation range from two nearby nunataks can therefore only be explained by ice-sheet thinning that was sufficiently rapid to expose the samples instantaneously with respect to the precision of their exposure ages.

In order to determine the thinning rate at our sites, we fitted separate linear age-elevation models to the data from each nunatak (*23*). Less than 20 km upstream of the modern grounding line, modeled thinning rates that best fit the exposure age data are 112 and 167 cm year^{-1} (Fig. 2D). Our uncertainty analysis shows that these cannot be distinguished from contemporary thinning rates (fig. S1). The early Holocene thinning rates are thus sufficiently high that they imply ice-dynamic change rather than thinning resulting from changes in accumulation and ablation. We infer that previous rapid thinning of the PIG system must have been sustained for several decades, and possibly centuries; our uncertainty analysis indicates 95% confidence that rapid thinning lasted longer than 25 years (*23*). If we assume that the early Holocene thinning was monotonic, the results of our fitting procedure suggest that by 7.9 ka, the ice sheet surface at Maish Nunatak had lowered to its present-day elevation, and rapid thinning at Mount Moses had ended (fig. S4). The Maish Nunatak data place some constraint on the onset of contemporary thinning. If present rapid thinning rates

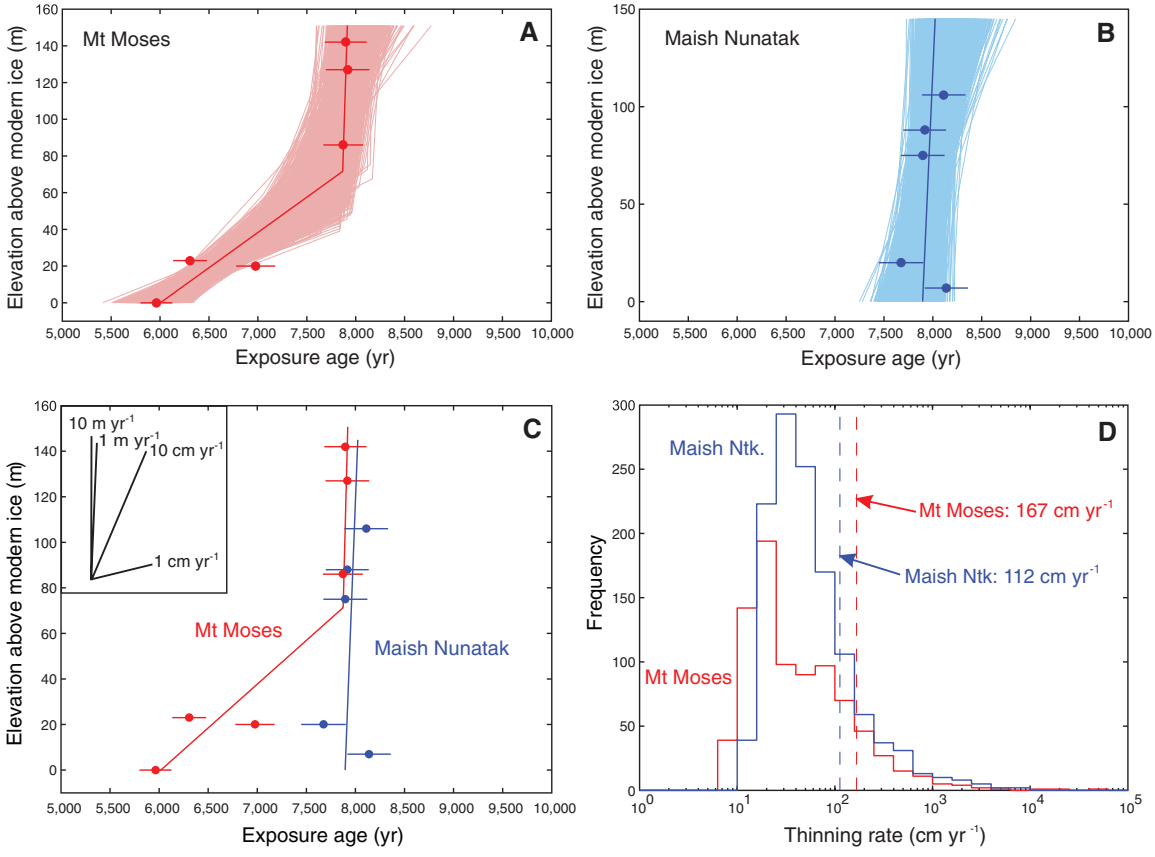

Fig. 2. Thinning history of the Pine Island Glacier system. (**A** and **B**) ^{10}Be exposure ages of erratics from Mount Moses and Maish Nunatak relative to the local ice surface. Error bars show 1σ measurement uncertainties. Dark lines are linear age-elevation relationships that best fit the exposure age data, and the bundles of lighter lines show age-elevation relationships generated by the Monte Carlo uncertainty analysis (*23*). (**C**) Relationship between ^{10}Be exposure ages from both nunataks. (Inset) Representative thinning rates on same axes. One sample from Maish Nunatak with an anomalously old age (~15,800 years) is not shown because its age likely reflects prior cosmic ray exposure (*16*). (**D**) Uncertainty distributions for thinning rates for each nunatak, derived from Monte Carlo simulations. Dashed lines are best-fit thinning rates. Histogram bins are logarithmically spaced for clarity. 95% of the Monte Carlo results fell between 8 and 590 cm year^{-1} for the period of rapid thinning at Mount Moses, and between 13 and 550 cm year^{-1} for thinning at Maish Nunatak. In (A) to (D), the uncertainty distributions do not include systematic uncertainty on ^{10}Be production rate; errors in estimating production rate would act to shift the entire array of ages equally, without changing the relationship between them.

have been sustained for several decades, then the ice surface must have been considerably higher when it started. However, if the ice surface was even a few meters above present for a substantial period of the late Holocene, then we would observe erratics with much younger exposure ages at sites adjacent to the modern ice surface than those at higher elevations. Given that this is not the case, if the ice surface was above these samples between 7.9 ka and recent decades, it can only have been so for a time comparable with the precision of the exposure ages (~100 years). Thus, the most likely scenario consistent with our data is that the ice surface was near its present elevation (or possibly lower, because our observations cannot detect periods of thinner ice) between 7.9 ka and the onset of contemporary thinning.

The high thinning rates determined from our exposure ages imply an ice-dynamic change because drivers such as a decrease in accumulation rate or increase in atmospheric temperature would produce a slower response. Marine geological and geophysical studies show that the PIG grounding line had retreated to within, but had not stabilized at, 112 km of its present position (the core site is shown in Fig. 1B and fig. S5) by 11.7 ± 0.7 ka (*21*), and that a ridge beneath PIG ice shelf (Fig. 1B and fig. S5) acted as a pinning point for the grounding line before the 1970s (*7*). Therefore, potential hypotheses for the mechanism of an early Holocene ice-dynamic change could be (i) rapid migration of the PIG grounding line resulting from decoupling from a topographic high or (ii) reduction in ice shelf buttressing.

First, we discuss the effect of subglacial topography. This can influence the style of ice stream retreat—for example, by providing topographic highs on which pinning can occur (*25*) and by constraining ice stream width (*26*, *27*). Although the marine geological data constrain retreat of the grounding line landward from the core site to the sub–ice shelf ridge only to sometime between 11.7 ka and the 1970s, they do not preclude that the retreat was associated with inland thinning at ~8 ka. However, there are no topographic highs seaward of the sub–ice shelf ridge where the grounding line might have been pinned after 11.7 ka (fig. S5) and from which detachment could have triggered the dynamic thinning inland. Therefore, although grounding line retreat may have been associated with the early Holocene thinning, decoupling of the PIG grounding line from a topographic high [hypothesis (i)] is unlikely to have been the trigger for it.

Alternatively, thinning may have been the consequence of reduction in buttressing by an ice shelf. Marine sediments have been used to infer the presence of an ice shelf across the middle shelf of the Amundsen Sea before ~10.6 ± 0.3 ka (fig. S5A) (*19*). Although the available chronological data cannot resolve when that ice shelf finally retreated into inner Pine Island Bay, one study suggests that it persisted there until ~7 ka (*19*). Glaciers in the Amundsen Sea Embayment and elsewhere in Antarctica have responded to recent ice shelf thinning with acceleration of flow, grounding line retreat, and thinning (*14*). Similarly, subsequent retreat or weakening (such as by thinning) of a buttressing ice shelf in Pine Island Bay could have triggered the dynamic thinning in the Hudson Mountains at ~8 ka. Reduction in ice shelf buttressing would most likely have been initiated by enhanced basal melting in response to inflow of warm Circumpolar Deep Water, as is suggested to account for present thinning (*11*). We favor hypothesis (ii) as the most likely mechanism for early Holocene ice-dynamic change, but we cannot rule out more complicated mechanisms. For example, it is possible that thinning of the outlet glacier may be related to its separation from PIG.

These results have implications for understanding how the Pine Island–Thwaites sector of the WAIS is likely to evolve in coming decades to centuries. The knowledge that PIG has previously undergone sustained dynamic thinning, followed by relative stabilization over several millennia before the onset of contemporary thinning, suggests that the PIG system can respond quickly to environmental change by abrupt, discontinuous, and stepwise retreat. Continued thinning may lead to an even more dramatic response if a dynamic threshold, such as a critical ice shelf thickness or ice flow rate, is exceeded. In addition, the rate and magnitude of early Holocene thinning is consistent with model-based estimates of future PIG thinning sustained over the coming century (*28*, *29*), a time scale over which the magnitude of sea-level rise most concerns policymakers. In a wider context, the pattern of abrupt past thinning of PIG contrasts with evidence for slower and steadier Holocene deglaciation of other regions of the WAIS (*16*, *30*), hinting that a considerable part of any WAIS contribution to sea-level rise in the early Holocene may have come from its Amundsen Sea sector.

The data presented here demonstrate that thinning of PIG at a rate comparable with that over the past two decades is rare but not unprecedented in the Holocene. Moreover, in contrast to previous glacial-geological work in Antarctica that has provided average thinning rates only over millennial time scales, our data are precise enough to show that rapid thinning of PIG was sustained for at least 25 years, and most likely for much longer. These data provide a long-term context for contemporary thinning of PIG, suggesting that ongoing ocean-driven melting of PIG ice shelf can result in continued rapid thinning and grounding line retreat for several more decades or even centuries.

References and Notes

1. M. A. King *et al.*, *Nature* **491**, 586–589 (2012).
2. A. Shepherd *et al.*, *Science* **338**, 1183–1189 (2012).
3. E. Rignot, *Geophys. Res. Lett.* **35**, L12505 (2008).
4. H. D. Pritchard, R. J. Arthern, D. G. Vaughan, L. A. Edwards, *Nature* **461**, 971–975 (2009).
5. D. Wingham, D. W. Wallis, A. Shepherd, *Geophys. Res. Lett.* **36**, L17501 (2009).
6. J. W. Park *et al.*, *Geophys. Res. Lett.* **40**, 2137–2142 (2013).
7. A. Jenkins *et al.*, *Nat. Geosci.* **3**, 468–472 (2010).
8. I. Joughin, R. B. Alley, *Nat. Geosci.* **4**, 506–513 (2011).
9. R. Thomas *et al.*, *Science* **306**, 255–258 (2004).
10. A. Shepherd, D. J. Wingham, J. A. D. Mansley, H. F. Corr, *Science* **291**, 862–864 (2001).
11. S. S. Jacobs, A. Jenkins, C. F. Giulivi, P. Dutrieux, *Nat. Geosci.* **4**, 519–523 (2011).
12. A. J. Payne, A. Vieli, A. Shepherd, D. J. Wingham, E. Rignot, *Geophys. Res. Lett.* **31**, L23401 (2004).
13. A. Shepherd, D. Wingham, E. Rignot, *Geophys. Res. Lett.* **31**, L23402 (2004).
14. H. D. Pritchard *et al.*, *Nature* **484**, 502–505 (2012).
15. Intergovernmental Panel on Climate Change, in *Climate Change 2007: The Physical Science Basis. Contribution of Working Group I to the Fourth Assessment Report of the Intergovernmental Panel on Climate Change*, S. Solomon, *et al.*, Eds. (Cambridge Univ. Press, Cambridge, 2007).
16. J. O. Stone *et al.*, *Science* **299**, 99–102 (2003).
17. A. L. Lowe, J. B. Anderson, *Quat. Sci. Rev.* **21**, 1879–1897 (2002).
18. A. G. C. Graham *et al.*, *J. Geophys. Res.* **115**, F03025 (2010).
19. A. E. Kirshner *et al.*, *Quat. Sci. Rev.* **38**, 11–26 (2012).
20. M. Jakobsson *et al.*, *Quat. Sci. Rev.* **38**, 1–10 (2012).
21. C.-D. Hillenbrand *et al.*, *Geology* **41**, 35–38 (2013).
22. J. S. Johnson, M. J. Bentley, K. Gohl, *Geology* **36**, 223–226 (2008).
23. Materials and methods are available as supplementary materials on *Science* Online.
24. J. M. Schaefer *et al.*, *Science* **324**, 622–625 (2009).
25. K. J. Tinto, R. E. Bell, *Geophys. Res. Lett.* **38**, L20503 (2011).
26. S. S. R. Jamieson *et al.*, *Nat. Geosci.* **5**, 799–802 (2012).
27. G. H. Gudmundsson, J. Krug, G. Durand, L. Favier, O. Gagliardini, *Cryosphere* **6**, 1497–1505 (2012).
28. I. Joughin, B. E. Smith, D. M. Holland, *Geophys. Res. Lett.* **37**, L20502 (2010).
29. R. M. Gladstone *et al.*, *Earth Planet. Sci. Lett.* **333-334**, 191–199 (2012).
30. M. J. Bentley *et al.*, *Geology* **38**, 411–414 (2010).
31. E. Rignot, J. Mouginot, B. Scheuchl, *MEaSUREs InSAR-Based Antarctica Ice Velocity Map* (National Snow and Ice Data Center, Boulder, CO, 2011).

Acknowledgments: The data presented here are archived in the supplementary materials. The project was conceived and developed by M.J.B. and R.D.L. Fieldwork and sampling were planned and undertaken by M.J.B., J.A.S., and J.S.J. K.G. led the cruise (RV *Polarstern* Expedition ANT-XXVI/3). J.S.J. processed the samples and interpreted the data, with direction from J.M.S., and analyses were performed by R.C.F. and D.H.R. G.B. developed the Monte Carlo simulations for Fig. 2 and fig. S4. M.J.B. and J.S.J. wrote the first draft, and all authors contributed to the interpretation and writing of the paper. This work forms part of the British Antarctic Survey program "Polar Science for Planet Earth," funded by the Natural Environment Research Council, and was made possible by a Marie Tharp Fellowship in Earth, Environmental, and Ocean Sciences at Columbia University Earth Institute/Lamont-Doherty Earth Observatory, awarded to J.S.J. The fieldwork was supported by the research program PACES, Topic 3 "Lessons from the Past" of the Alfred Wegener Institute. This is LDEO publication 7577.

Supplementary Materials

www.sciencemag.org/content/343/6174/999/suppl/DC1
Materials and Methods
Figs. S1 to S5
Tables S1 to S3
References (*32*–*41*)

18 October 2013; accepted 5 February 2014
Published online 20 February 2014;
10.1126/science.1247385

Promoter-Bound Trinucleotide Repeat mRNA Drives Epigenetic Silencing in Fragile X Syndrome

Dilek Colak,[1] Nikica Zaninovic,[2] Michael S. Cohen,[1]* Zev Rosenwaks,[2] Wang-Yong Yang,[3] Jeannine Gerhardt,[4] Matthew D. Disney,[3] Samie R. Jaffrey[1]†

Epigenetic gene silencing is seen in several repeat-expansion diseases. In fragile X syndrome, the most common genetic form of mental retardation, a CGG trinucleotide–repeat expansion adjacent to the *fragile X mental retardation 1* (*FMR1*) gene promoter results in its epigenetic silencing. Here, we show that *FMR1* silencing is mediated by the *FMR1* mRNA. The *FMR1* mRNA contains the transcribed CGG-repeat tract as part of the 5′ untranslated region, which hybridizes to the complementary CGG-repeat portion of the *FMR1* gene to form an RNA•DNA duplex. Disrupting the interaction of the mRNA with the CGG-repeat portion of the *FMR1* gene prevents promoter silencing. Thus, our data link trinucleotide-repeat expansion to a form of RNA-directed gene silencing mediated by direct interactions of the trinucleotide-repeat RNA and DNA.

Fragile X syndrome (FXS) results from the absence of the fragile X mental retardation protein (FMRP), which is encoded by the *fragile X mental retardation 1* (*FMR1*) gene on the X chromosome (*1*). Impaired FMRP expression is caused by an inherited CGG trinucleotide–repeat expansion adjacent to the *FMR1* promoter (*2*). *FMR1* alleles that contain >200 CGG repeats undergo epigenetic silencing of the *FMR1* promoter at ~11 weeks of gestation (*2*–*4*). It remains unclear how the CGG-repeat expansion leads to gene silencing.

The mechanism of gene silencing in FXS has been particularly difficult to dissect. Transgenes containing expanded CGG-repeat *FMR1* alleles are not silenced in cell lines or mice (*5*). Furthermore, overexpression of expanded CGG-repeat sequences is complicated by sequence instability in plasmids (*6*). Recently, human embryonic stem cells (hESCs) harboring an *FMR1* allele with >200 CGG repeats (FXS hESCs) were shown to undergo *FMR1* gene silencing upon differentiation (*7*). The switch from active *FMR1* gene expression to *FMR1* silencing in FXS hESCs resembles the switch that occurs in FXS embryos (*4*), which provides an in vitro system to study *FMR1* silencing.

To monitor *FMR1* silencing, we used two FXS lines, WCMC-37 and SI-214 (*8*, *9*) (referred to throughout the text as FXS-1 and FXS-2, respectively); each contains >400 CGG repeats (fig. S1). We monitored *FMR1* silencing after inducing neuronal differentiation over 60 days (fig. S2). In neurons derived from FXS hESCs, FMRP and *FMR1* mRNA were readily detected until ~48 days, at which point the levels dropped and were absent

[1]Department of Pharmacology, Weill Cornell Medical College, Cornell University, New York, NY 10065, USA. [2]Center for Reproductive Medicine and Infertility, Weill Cornell Medical College, Cornell University, New York, NY 10065, USA. [3]Department of Chemistry, The Scripps Research Institute, Scripps Florida, Jupiter, FL 33458, USA. [4]Department of Cell Biology, Albert Einstein College of Medicine, Bronx, NY 10461, USA.

*Present address: Department of Pharmacology, Oregon Health Sciences University, Portland, OR 97239–3098, USA.
†Corresponding author. E-mail: srj2003@med.cornell.edu

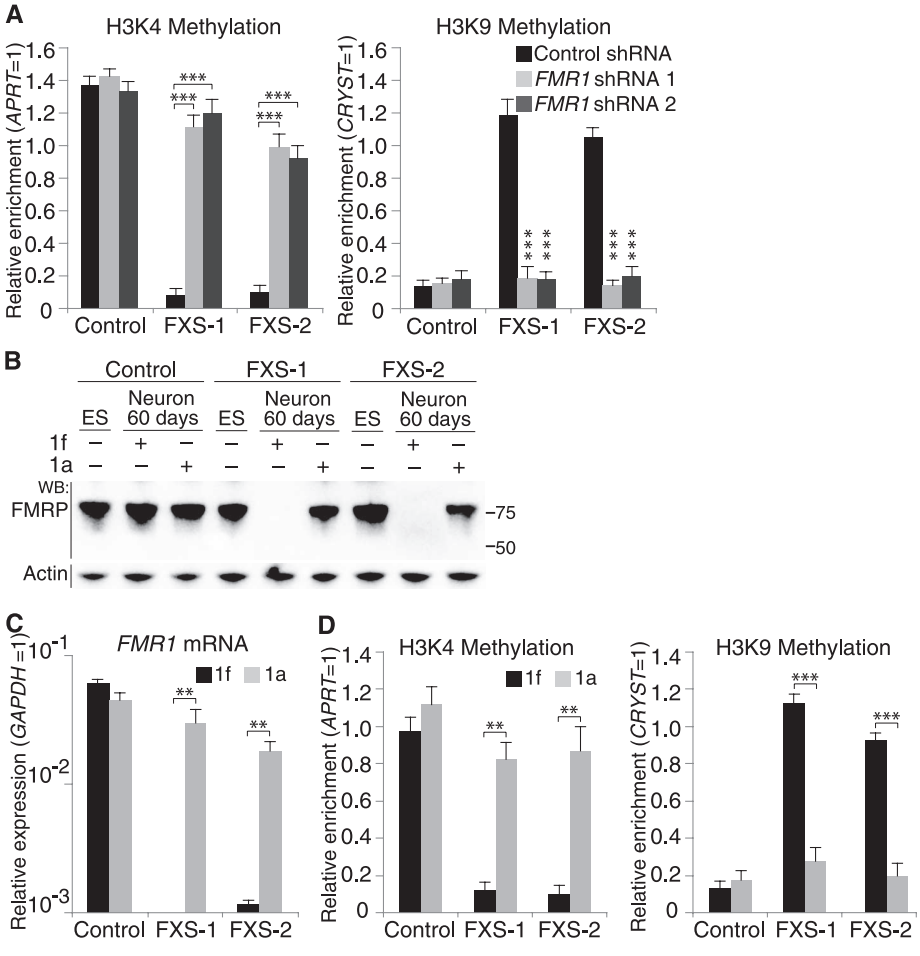

Fig. 1. The *FMR1* transcript and its CGG-repeat tract are required for *FMR1* silencing. (**A**) *FMR1* mRNA is required for *FMR1* silencing in differentiating FXS hESCs. shRNA-expressing lentivirus was applied at day 1, and histone marks at *FMR1* promoters were measured at day 60. FXS hESCs expressing control shRNA showed high levels of transcriptionally repressive marks (H3K9me2) and low levels of transcriptionally active marks (H3K4me2). *FMR1*-specific shRNA prevented the appearance of repressive marks and maintained the expression of transcriptionally active marks (n = 4 per condition). ES, hESCs; WB, Western blot; *APRT*, *adenine phosphoribosyltransferase*; *GAPDH*, *glyceraldehyde-3-phosphate dehydrogenase*; *CRYST*, *crystallin*. (**B** to **D**) The CGG-repeat RNA-binding small molecule 1a blocks *FMR1* silencing. Differentiating FXS hESCs treated with 10 μM 1a did not lose FMRP (B) or *FMR1* mRNA (C) (n = 3 per condition) and retained active *FMR1* promoters (D) (n = 3 per condition). Data are means ± SEM. Statistical analysis was performed using Student's t test (two-tailed distribution, $^{**}P < 0.01$, $^{***}P < 0.001$). When comparing different cell lines, we considered the samples as two samples with unequal variance. When comparing different conditions on the same cell line, we considered the samples as two samples with equal variance.

by day 51 (fig. S3 to S5). The *FMR1* promoters in the undifferentiated FXS hESC lines contain high levels of histone H3 dimethylated on lysine 4 (H3K4me2, associated with gene expression) and low levels of histone H3 dimethylated on lysine 9 (H3K9me2, associated with gene repression) (fig. S6). However, in differentiated FXS cells, the *FMR1* promoter switched to the repressive H3K9me2 mark, with a concomitant reduction in the levels of H3K4me2 (fig. S6). Taken together, these data indicate that the loss of FMRP and *FMR1* mRNA in FXS hESC lines correlates with the epigenetic silencing of the *FMR1* promoter.

The expanded CGG repeat influences DNA structure, which may be recognized by pathways that induce epigenetic silencing (*10*). However, the expanded CGG repeat is also transcribed as the 5′ untranslated region (UTR) of the *FMR1* mRNA, which makes it possible that the mRNA could induce promoter silencing. We therefore tested whether the *FMR1* transcript is required for silencing. Knockdown of *FMR1* mRNA in FXS hESCs prevented differentiation-induced *FMR1* silencing, as measured by the retention of transcriptionally active histone marks at the *FMR1* promoter (Fig. 1A). The effect of the *FMR1*-specific short hairpin RNAs (shRNAs) was not due to knockdown of a previously described antisense *FMR1* transcript that partially overlaps with the *FMR1* mRNA (*11*) (fig. S7B). These data indicate that the *FMR1* transcript is required for *FMR1* silencing.

CGG repeats in mRNA form a hairpin structure (*10*) (fig. S7C), which may be unfolded and linearized in order to mediate *FMR1* silencing. To test the role of the mRNA CGG repeat in *FMR1* gene silencing, we used 1a, a small molecule that selectively binds the repeating G-G internal loops in the RNA hairpin and inhibits its thermal melting (*12*) (fig. S7D). Application of 1a (10 μM) throughout the differentiation prevented differentiation-induced *FMR1* silencing in FXS hESCs (Fig. 1, B to D, and fig. S8). Application of the structurally related control compound 1f (10 μM), which does not bind CGG repeats (*12*), did not affect *FMR1* silencing. The effect of 1a was not due to impaired differentiation, as the 1a-treated cells expressed the neuronal marker β-III tubulin (fig. S9). Together, these data suggest that linearization of the CGG-repeat hairpin in the *FMR1* transcript is required for silencing.

Dicer processes CGG-repeat RNAs into small RNAs in vitro (*13*) and may contribute to *FMR1* silencing (*14*). However, knockdown of *Dicer*,

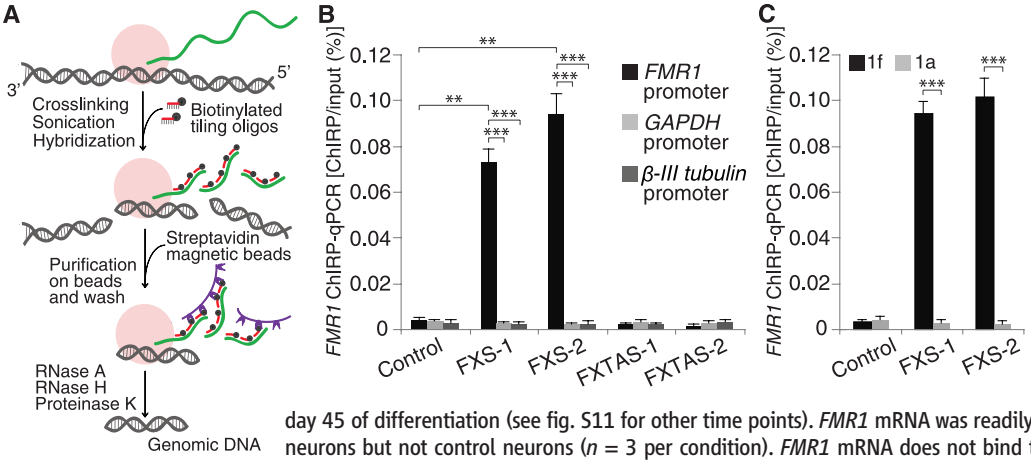

Fig. 2. *FMR1* mRNA interacts with the *FMR1* promoter in a CGG repeat–dependent manner. (**A**) Schematic representation of ChIRP technique [adapted from (*15*)]. RNA (green) and protein complexes (pink) are cross-linked to the DNA (gray) in cells by glutaraldehyde. The cell lysate is sonicated to shear DNA to ~500 bp. Streptavidin beads (purple) are used to pull down biotinylated oligonucleotides hybridized to RNA. Bound DNA sequences are detected by qPCR. (**B**) *FMR1* mRNA interacts with the *FMR1* promoter. *FMR1* mRNA bound to the *FMR1* gene was measured by ChIRP at day 45 of differentiation (see fig. S11 for other time points). *FMR1* mRNA was readily detectable on the *FMR1* promoter in FXS neurons but not control neurons ($n = 3$ per condition). *FMR1* mRNA does not bind to *FMR1* promoters in *FMR1* premutation lines, FXTAS-1 and FXTAS-2, that contain 70 and 73 CGG repeats, respectively. *GAPDH* and *β-III tubulin* promoters were used as controls. (**C**) The CGG-repeat portion of the transcript is required for the binding of *FMR1* mRNA to the *FMR1* gene. *FMR1* binding to the *FMR1* gene was markedly reduced in FXS hESC-derived neurons cultured in the presence of 1a. The control compound 1f did not block the *FMR1* transcript–*FMR1* gene interaction. Data are means ± SEM; Student's *t* test (two-tailed distribution, $^{**}P < 0.01$, $^{***}P < 0.001$). Different conditions on the same cell line were considered as two samples with equal variance; different cell lines were considered as two samples with unequal variance.

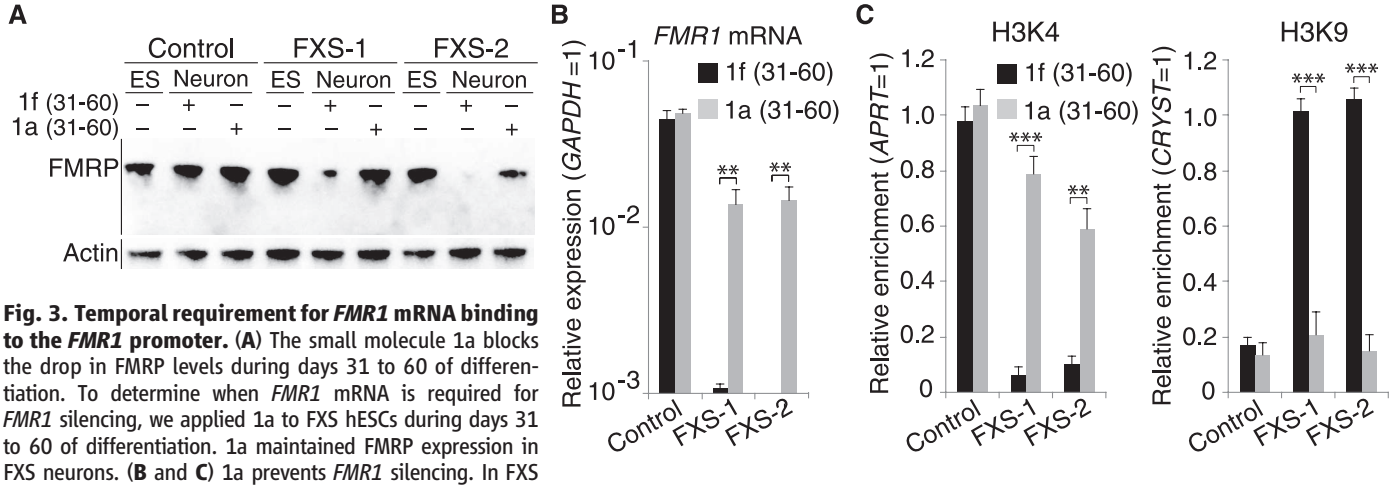

Fig. 3. Temporal requirement for *FMR1* mRNA binding to the *FMR1* promoter. (**A**) The small molecule 1a blocks the drop in FMRP levels during days 31 to 60 of differentiation. To determine when *FMR1* mRNA is required for *FMR1* silencing, we applied 1a to FXS hESCs during days 31 to 60 of differentiation. 1a maintained FMRP expression in FXS neurons. (**B** and **C**) 1a prevents *FMR1* silencing. In FXS neurons, application of 1a during days 31 to 60 of differentiation was sufficient to maintain *FMR1* mRNA levels [(B), quantitative reverse transcription polymerase chain reaction (qRT-PCR), $n = 4$ per condition], high levels of H3K4me2 and low levels of H3K9me2 histone modifications [(C), chromatin immunoprecipitation, $n = 4$ per condition]. Control hESCs were unaffected by 1a. Application of 1a (10 μM) during days 1 to 30 of differentiation failed to prevent *FMR1* silencing (see fig. S12). Data are means ± SEM; Student's *t* test (two-tailed distribution, $^{**}P < 0.01$, $^{***}P < 0.001$). Different conditions on the same cell line were considered as two samples with equal variance.

Ago1, or *Ago2* did not prevent differentiation-induced *FMR1* silencing (fig. S10). Thus, *FMR1* silencing does not require a Dicer-directed pathway.

We next asked if the *FMR1* transcript directs silencing by binding, directly or indirectly, to the promoter. To test this, we measured *FMR1* mRNA binding to the *FMR1* gene using the chromatin isolation by RNA purification (ChIRP) technique (Fig. 2A) (*15*, *16*). After cross-linking endogenous RNA to its binding partners, we pulled down *FMR1* mRNA using biotinylated oligonucleotides that hybridize along the length of the transcript. The amount of *FMR1* promoter pulled down was quantified by quantitative polymerase chain reaction (qPCR) with promoter-specific primers. In control hESC-derived neurons, there was minimal *FMR1* transcript bound to the *FMR1* promoter at any time point during differentiation (Fig. 2B and fig. S11). Similarly, in FXS hESC-derived neurons at 12, 24, 36, and 60 days, minimal *FMR1* transcript was bound to the promoter (fig. S11). However, at 45 days in FXS hESC-derived neurons, *FMR1* mRNA was readily detectable on the *FMR1* promoter (Fig. 2B). Linearization of the CGG hairpin is required for binding of the FXS *FMR1* mRNA to the FXS *FMR1* promoter, as treatment of both FXS hESC lines with 1a, but not 1f, reduced binding of the *FMR1* RNA to the promoter during differentiation (Fig. 2C).

The length of the CGG-repeat tract is the major determinant for *FMR1* gene silencing (*17*). Normal alleles (less than 55 repeats) and "premutation" alleles (55 to 200 repeats) do not lead to *FMR1* silencing (*17*). We therefore asked if the *FMR1* transcript binds to the *FMR1* promoter in normal and premutation lines. In normal (~30 repeats) and premutation (70 and 73 repeats) hESC lines (fig. S1), the *FMR1* transcripts were not bound to the promoter (Fig. 2B). Thus, the lack of *FMR1* silencing in normal and premutation hESC lines may reflect the absence of *FMR1* mRNA binding to the promoter.

To more precisely define the temporal sensitivity of *FMR1* silencing to 1a, we selectively applied 1a during days 1 to 30 (fig. S12) or 31 to 60 of differentiation (Fig. 3). Only application of 1a during days 31 to 60 blocked silencing (Fig. 3). Similarly, application of *FMR1*-specific shRNA during days 31 to 60 also prevented differentiation-induced silencing (fig. S13). These data suggest that *FMR1* mRNA does not trigger gene silencing dur-

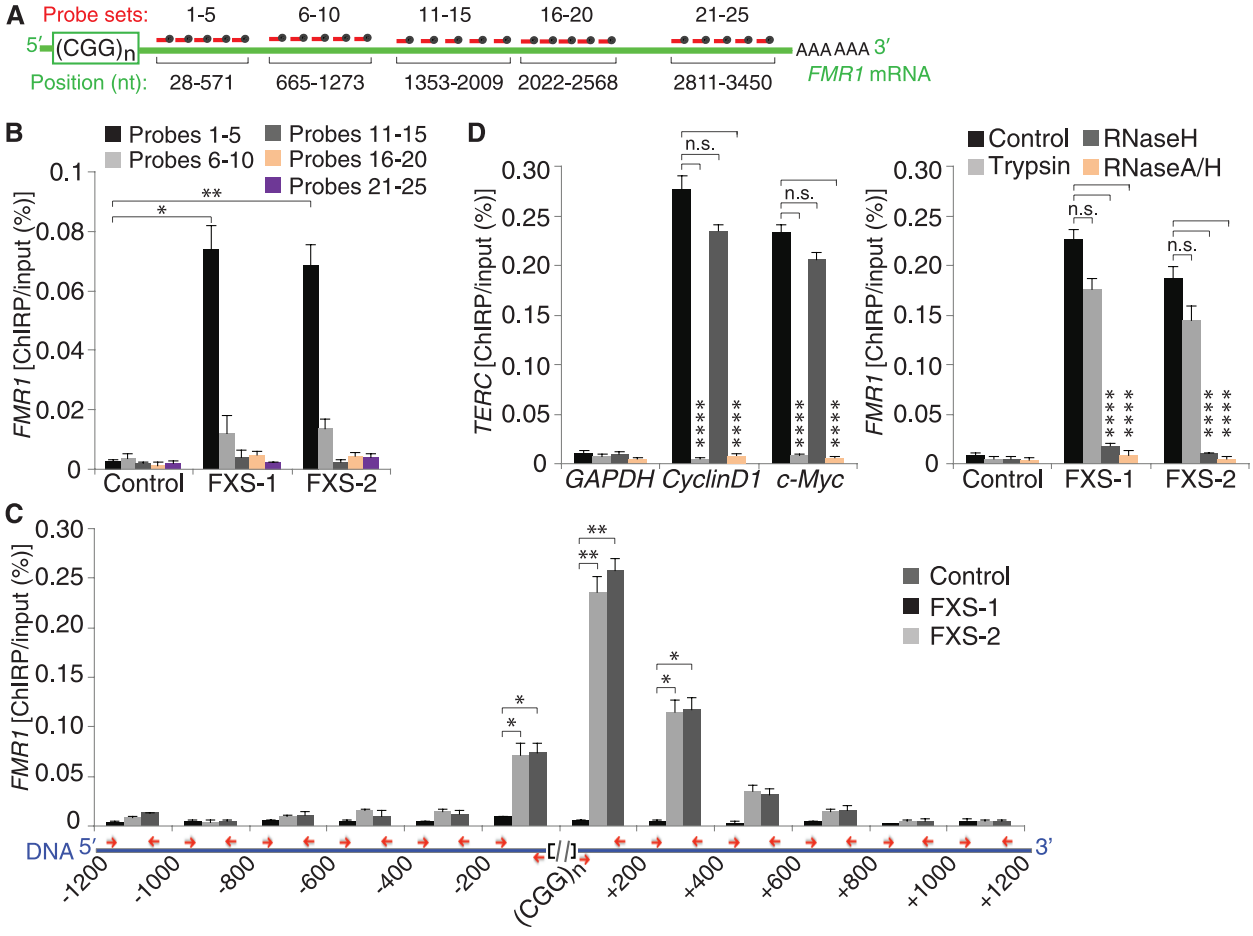

Fig. 4. The CGG-repeat portion of the *FMR1* mRNA hybridizes to the complementary region of the *FMR1* DNA. (**A**) Schematic of the hybridization sites of the different biotinylated-oligonucleotide sets used to pull down sheared RNA in ChIRP experiments (see methods for further details on probe design). (**B**) The 5′ UTR portion of the *FMR1* transcript binds to the *FMR1* gene. ChIRP was performed using the probe sets shown in (A). Only probes that bind the CGG repeat–proximal portion of the *FMR1* transcript pulled down the *FMR1* promoter in FXS neurons ($n = 4$ per condition). (**C**) The *FMR1* transcript binds to the CGG-repeat portion of the *FMR1* gene. To determine where the *FMR1* mRNA binds on the *FMR1* gene, we measured the ChIRP signal along a 1200-bp region both upstream and downstream of the genomic CGG repeat. The positions of the primers used to amplify portions of the *FMR1* gene (blue) are indicated (red arrows) (referred to as bp relative to the 5′ or 3′ end of the CGG repeat). The ChIRP signal was highly enriched adjacent to the genomic CGG repeat ($n = 3$ per condition) (see also fig. S16). (**D**) The *FMR1* mRNA binds to the *FMR1* DNA in a protein-independent and RNase H–sensitive manner. The binding of the control noncoding-RNA *TERC* to its target promoters (*CyclinD1* and *c-Myc*) was abolished after trypsin treatment ($n = 3$), whereas the binding of the *FMR1* transcript to the *FMR1* gene was unaffected by trypsin in FXS hESC-derived neurons ($n = 3$ per condition). In contrast, RNase H treatment only blocked the *FMR1* ChIRP signal ($n = 3$ per condition). RNase A–RNase H treatment, which digests all RNA, is used as a control to demonstrate the RNA-dependence of the ChIRP signal. Data are means ± SEM; Student's *t* test (two-tailed distribution, $*P < 0.05$, $**P < 0.01$, $****P < 0.0001$). Different conditions on the same cell line were considered as two samples with equal variance; different cell lines were considered as two samples with unequal variance.

ing the first 30 days but is required in the second 30-day period when it binds to the *FMR1* gene and leads to gene silencing.

We next asked whether *FMR1* gene silencing can occur after the 48- to 51-day time point of the differentiation protocol. In these experiments, we inhibited *FMR1* silencing by culturing differentiating FXS hESCs in the presence of 1a for 60 days. Withdrawal of 1a for 10 days triggered *FMR1* silencing (fig. S14), which suggests that sustained 1a treatment is required to maintain *FMR1* in the transcriptionally active state. The small molecule 1a appears to function to prevent silencing, rather than reverse silencing, as application of 1a to cells with an already silenced *FMR1* promoter did not reverse silencing (fig. S15).

We next mapped the part of the *FMR1* transcript that binds to the *FMR1* gene. To do this, we performed ChIRP using biotinylated primers that hybridize to different regions of the *FMR1* transcript (Fig. 4A). Primers that hybridize adjacent to the CGG repeat pulled down the *FMR1* promoter, whereas primers directed elsewhere along the *FMR1* transcript resulted in markedly reduced pull down (Fig. 4B). Together with the finding that 1a blocks the binding of *FMR1* mRNA to the *FMR1* gene, these data suggest that the CGG-repeat region of the *FMR1* transcript interacts with the *FMR1* gene.

We next mapped the part of the *FMR1* gene that is bound to the *FMR1* mRNA. In our previous ChIRP experiments, we measured the binding of the *FMR1* mRNA to a portion of the *FMR1* promoter that lies 92 to 196 base pairs (bp) upstream of the CGG-repeat sequence. To more precisely define the binding site, we measured the ChIRP signal both upstream and downstream of the genomic CGG-repeat sequence in differentiating FXS hESCs. Because of the high G/C content of the repeat sequence, binding to this region cannot be tested. We found that the ChIRP signal was detectable on both sides of the ~1200-bp genomic CGG repeat and is markedly reduced at sites away from the repeat (Fig. 4C). This pattern of binding is consistent with the genomic CGG-repeat sequence being the binding site for the *FMR1* mRNA (see fig. S16).

Some noncoding RNAs have been shown to interact with promoters indirectly through a protein intermediate (*18*). To determine if *FMR1* mRNA binds to its promoter through a protein intermediate, we performed ChIRP experiments, except we treated the cross-linked lysate with trypsin to digest any protein intermediates. For the control *TERC* noncoding RNA (*15*), the binding to its target promoters was abolished after trypsin treatment (Fig. 4D). However, *FMR1* mRNA binding to the *FMR1* gene was not affected by trypsin (Fig. 4D).

We next asked if *FMR1* mRNA binds to the *FMR1* gene by forming an RNA•DNA heteroduplex. To test this, we used ribonuclease H (RNase H), which selectively degrades RNA hybridized to DNA. Treatment of the cross-linked DNA fragments with RNase H selectively prevented the pull down of the *FMR1* promoter but did not affect the *TERC* pull downs (Fig. 4D). These data indicate that *FMR1* mRNA binds the *FMR1* gene through a direct RNA•DNA duplex and does not require a protein intermediate.

The *FMR1* mRNA CGG repeat may bind to the complementary CCG portion of the DNA that becomes accessible while it is being transcribed. Indeed, transcription through G-rich sequences causes stalling in vitro and in vivo (*19*, *20*). Conceivably, the nascent *FMR1* CGG-repeat RNA interacts with the template strand of the unwound DNA to form a RNA•DNA duplex that is highly stabilized by its G/C content. This would require that the CGG-repeat sequence in the RNA achieves a sufficient length to reach back and interact with the DNA and may contribute to the requirement for >200 CGG repeats for silencing. In addition, the length of the resulting RNA•DNA duplex may need to be of sufficient length to activate downstream pathways that induce *FMR1* silencing.

The initial step in *FMR1* silencing is the binding of the *FMR1* mRNA to the genomic repeat. The inability of the *FMR1* transcript to bind to the DNA before day 45 may relate to DNA accessibility during transcription. The expression of diverse DNA helicases, which are known to regulate DNA accessibility (*21*, *22*), is reduced during hESC differentiation (*23*). Conceivably, helicase activity may contribute to the temporal interaction of *FMR1* mRNA and DNA. However, the exact mechanisms underlying the temporal nature of *FMR1* silencing remain unknown.

The formation of the *FMR1* RNA•DNA duplex coincides with the initiation of epigenetic silencing in the *FMR1* gene. Because this causes a drop in *FMR1* mRNA expression, subsequent maintenance of *FMR1* silencing is unlikely to be *FMR1* mRNA–dependent. It remains to be determined which mechanisms maintain epigenetic silencing of *FMR1* throughout the patient's lifetime.

FXS hESCs allow the characterization of the endogenous *FMR1* transcript transcribed from the endogenous promoter. This is important because RNA-directed gene silencing frequently occurs in cis with the nascent transcript affecting a promoter within the gene locus (*24*). Indeed, only *FMR1* and not other CGG repeats in the genome are silenced in FXS (*25*). Thus, rather than overexpressing CGG-repeat RNAs, which is complicated by plasmid instability, pharmacologic targeting of the endogenous CGG repeat provides insight into its role in promoter silencing.

Our data demonstrate that an mRNA can mediate promoter silencing and links trinucleotide repeat expansion to a novel form of RNA-directed promoter silencing. Epigenetic changes are seen in diverse repeat-expansion diseases (*26*, *27*). The prevalence of repeat expansion–associated epigenetic changes raises the possibility that aspects of the mRNA-directed gene silencing pathway described here may contribute to gene expression alterations in other repeat-expansion diseases as well.

References and Notes

1. A. J. Verkerk *et al.*, *Cell* **65**, 905–914 (1991).
2. I. Oberlé *et al.*, *Science* **252**, 1097–1102 (1991).
3. B. Coffee, F. Zhang, S. Ceman, S. T. Warren, D. Reines, *Am. J. Hum. Genet.* **71**, 923–932 (2002).
4. R. Willemsen, C. J. Bontekoe, L. A. Severijnen, B. A. Oostra, *Hum. Genet.* **110**, 601–605 (2002).
5. J. R. Brouwer *et al.*, *Exp. Cell Res.* **313**, 244–253 (2007).
6. G. Sandberg, M. Schalling, *Nucleic Acids Res.* **25**, 2883–2887 (1997).
7. R. Eiges *et al.*, *Cell Stem Cell* **1**, 568–577 (2007).
8. J. Gerhardt *et al.*, *Mol. Cell* **53**, 19–31 (2014).
9. Y. Verlinsky *et al.*, *Reprod. Biomed. Online* **10**, 105–110 (2005).
10. K. Usdin, K. J. Woodford, *Nucleic Acids Res.* **23**, 4202–4209 (1995).
11. P. D. Ladd *et al.*, *Hum. Mol. Genet.* **16**, 3174–3187 (2007).
12. M. D. Disney *et al.*, *ACS Chem. Biol.* **7**, 1711–1718 (2012).
13. V. Handa, T. Saha, K. Usdin, *Nucleic Acids Res.* **31**, 6243–6248 (2003).
14. P. Jin, R. S. Alisch, S. T. Warren, *Nat. Cell Biol.* **6**, 1048–1053 (2004).
15. C. Chu, K. Qu, F. L. Zhong, S. E. Artandi, H. Y. Chang, *Mol. Cell* **44**, 667–678 (2011).
16. M. D. Simon *et al.*, *Proc. Natl. Acad. Sci. U.S.A.* **108**, 20497–20502 (2011).
17. Y. Feng, L. Lakkis, D. Devys, S. T. Warren, *Am. J. Hum. Genet.* **56**, 106–113 (1995).
18. J. T. Lee, *Science* **338**, 1435–1439 (2012).
19. B. P. Belotserkovskii *et al.*, *Proc. Natl. Acad. Sci. U.S.A.* **107**, 12816–12821 (2010).
20. E. Grabczyk, M. C. Fishman, *J. Biol. Chem.* **270**, 1791–1797 (1995).
21. M. L. Bochman, K. Paeschke, V. A. Zakian, *Nat. Rev. Genet.* **13**, 770–780 (2012).
22. S. G. Mackintosh, K. D. Raney, *Nucleic Acids Res.* **34**, 4154–4159 (2006).
23. J. Q. Wu *et al.*, *Proc. Natl. Acad. Sci. U.S.A.* **107**, 5254–5259 (2010).
24. S. Guil, M. Esteller, *Nat. Struct. Mol. Biol.* **19**, 1068–1075 (2012).
25. R. S. Alisch *et al.*, *BMC Med. Genet.* **14**, 18 (2013).
26. M. V. Evans-Galea, A. J. Hannan, N. Carrodus, M. B. Delatycki, R. Saffery, *Trends Mol. Med.* **19**, 655–663 (2013).
27. Z. Xi *et al.*, *Am. J. Hum. Genet.* **92**, 981–989 (2013).

Acknowledgments: We thank members of the Jaffrey lab for helpful comments and suggestions, E. Ferretti for assistance with chromatin immunoprecipitation, Q. Zhan for help with hESC cultures, S.L. Nolin and C. Dobkin for PCR on premutation lines. hESC lines are available from N.Z. and Z.R. (Weill Cornell Medical College hESC lines, nizanin@med.cornell.edu, zrosenw@med.cornell.edu) and S.R.J. (SI-214 hESC line, srj2003@med.cornell.edu), subject to approval by the Embryonic Stem Cell Research Oversight Committee (ESCRO) of Weill Cornell Medical College. M.D.D. previously consulted for SMaRT (Small Molecule Approach to Targeting RNA) Therapeutics. A patent (U.S. Patent and Trademark Office application no. 61/694,977) was filed on 30 August 2012 by the Scripps Research Institute governing composition and use of 1f and 1a. This work was supported by the Tri-Institutional Stem Cell Initiative (Tri-I SCI) grant 2008-019 (S.R.J., N.Z., and Z.R.), New York Stem Cell Foundation-Druckenmiller Fellowship (D.C.), Life Sciences Research Foundation Fellowship and Tri-I SCI postdoctoral fellowship (M.S.C.), and a FRAXA postdoctoral fellowship (W.-Y.Y.). Portions of this project not involving non-NIH registry stem cells were supported by NIH R01 MH80420 (S.R.J.) and NIH R01 GM079235 (M.D.D.).

Supplementary Materials

www.sciencemag.org/content/343/6174/1002/suppl/DC1
Materials and Methods
Figs. S1 to S16
Tables S1 to S3
References (*28*–*34*)

11 September 2013; accepted 30 January 2014
10.1126/science.1245831

Phonetic Feature Encoding in Human Superior Temporal Gyrus

Nima Mesgarani,[1]* Connie Cheung,[1] Keith Johnson,[2] Edward F. Chang[1]†

During speech perception, linguistic elements such as consonants and vowels are extracted from a complex acoustic speech signal. The superior temporal gyrus (STG) participates in high-order auditory processing of speech, but how it encodes phonetic information is poorly understood. We used high-density direct cortical surface recordings in humans while they listened to natural, continuous speech to reveal the STG representation of the entire English phonetic inventory. At single electrodes, we found response selectivity to distinct phonetic features. Encoding of acoustic properties was mediated by a distributed population response. Phonetic features could be directly related to tuning for spectrotemporal acoustic cues, some of which were encoded in a nonlinear fashion or by integration of multiple cues. These findings demonstrate the acoustic-phonetic representation of speech in human STG.

Phonemes—and the distinctive features composing them—are hypothesized to be the smallest contrastive units that change a word's meaning (e.g., /b/ and /d/ as in bad versus dad) (*1*). The superior temporal gyrus (Brodmann area 22, STG) has a key role in acoustic-phonetic processing because it responds to speech over other sounds (*2*) and focal electrical stimulation there selectively interrupts speech discrimination (*3*). These findings raise fundamental questions about the representation of speech sounds, such as whether local neural encoding is specific for phonemes, acoustic-phonetic features, or low-level spectrotemporal parameters. A major challenge in addressing this in natural speech is that cortical processing of individual speech sounds is extraordinarily spatially discrete and rapid (*4*–*7*).

We recorded direct cortical activity from six human participants implanted with high-density multielectrode arrays as part of their clinical evaluation for epilepsy surgery (*8*). These recordings provide simultaneous high spatial and temporal resolution while sampling population neural activity from temporal lobe auditory speech cortex. We analyzed high gamma (75 to 150 Hz) cortical surface field potentials (*9*, *10*), which correlate with neuronal spiking (*11*, *12*).

Participants listened to natural speech samples featuring a wide range of American English speakers (500 sentences spoken by 400 people) (*13*). Most speech-responsive sites were found in posterior and middle STG (Fig. 1A, 37 to 102 sites per participant, comparing speech versus silence, $P < 0.01$, t test). Neural responses demonstrated a distributed spatiotemporal pattern evoked during listening (Fig. 1, B and C, and figs. S1 and S2).

We segmented the sentences into time-aligned sequences of phonemes to investigate whether STG sites show preferential responses. We estimated the mean neural response at each electrode to every phoneme and found distinct selectiv-

[1]Department of Neurological Surgery, Department of Physiology, and Center for Integrative Neuroscience, University of California, San Francisco, CA 94143, USA. [2]Department of Linguistics, University of California, Berkeley, CA 94720, USA.

*Present address: Department of Electrical Engineering, Columbia University, New York, NY 10027, USA.

†Corresponding author. E-mail: changed@neurosurg.ucsf.edu

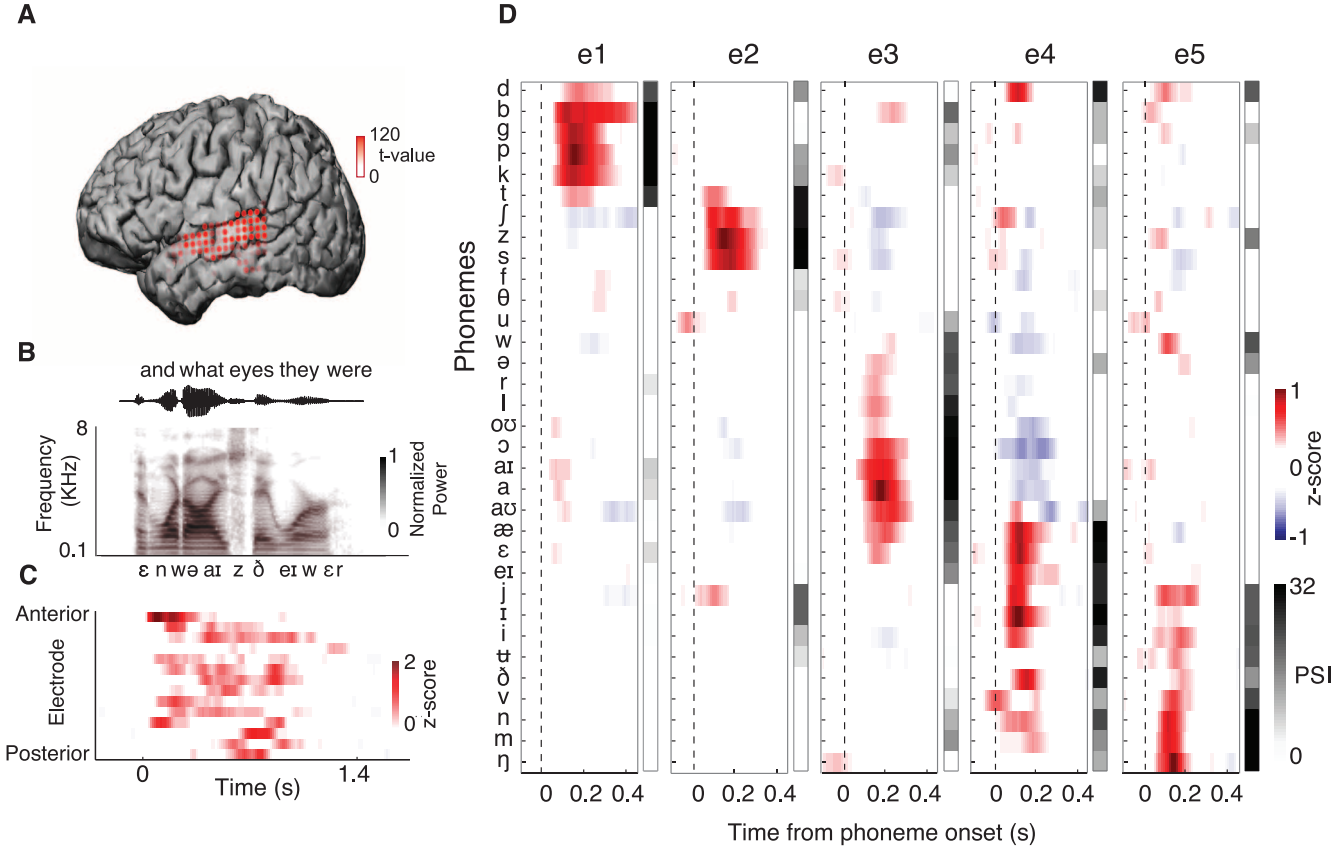

Fig. 1. Human STG cortical selectivity to speech sounds. (**A**) Magnetic resonance image surface reconstruction of one participant's cerebrum. Electrodes (red) are plotted with opacity signifying the t test value when comparing responses to silence and speech ($P < 0.01$, t test). (**B**) Example sentence and its acoustic waveform, spectrogram, and phonetic transcription. (**C**) Neural responses evoked by the sentence at selected electrodes. z score indicates normalized response. (**D**) Average responses at five example electrodes to all English phonemes and their PSI vectors.

ity. For example, electrode e1 (Fig. 1D) showed large evoked responses to plosive phonemes /p/, /t/, /k/, /b/, /d/, and /g/. Electrode e2 showed selective responses to sibilant fricatives: /s/, /ʃ/, and /z/. The next two electrodes showed selective responses to subsets of vowels: low-back (electrode e3, e.g., /a/ and /aʊ/), high-front vowels and glides (electrode e4, e.g., /i/ and /j/). Last, neural activity recorded at electrode e5 was selective for nasals (/n/, /m/, and /ŋ/).

To quantify selectivity at single electrodes, we derived a metric indicating the number of phonemes with cortical responses statistically distinguishable from the response to a particular phoneme. The phoneme selectivity index (PSI) is a dimension of 33 English phonemes; PSI = 0 is nonselective and PSI = 32 is extremely selective (Wilcox rank-sum test, $P < 0.01$, Fig. 1D; methods shown in fig. S3). We determined an optimal analysis time window of 50 ms, centered 150 ms after the phoneme onset by using a phoneme separability analysis (f-statistic, fig. S4A). The average PSI over all phonemes summarizes an electrode's overall selectivity. The average PSI was highly correlated to a site's response magnitude to speech over silence ($r = 0.77$, $P < 0.001$, t test; fig. S5A) and the degree to which the response could be predicted with a linear spectrotemporal receptive field [STRF, $r = 0.88$, $P < 0.001$, t test; fig. S5B (*14*)]. Therefore, the majority of speech-responsive sites in STG are selective to specific phoneme groups.

To investigate the organization of selectivity across the neural population, we constructed an array containing PSI vectors for electrodes across all participants (Fig. 2A). In this array, each column corresponds to a single electrode, and each row corresponds to a single phoneme. Most STG electrodes are selective not to individual but to specific groups of phonemes. To determine selectivity patterns across electrodes and phonemes, we used unsupervised hierarchical clustering analyses. Clustering across rows revealed groupings of phonemes on the basis of similarity of PSI values in the population response (Fig. 2B). Clustering

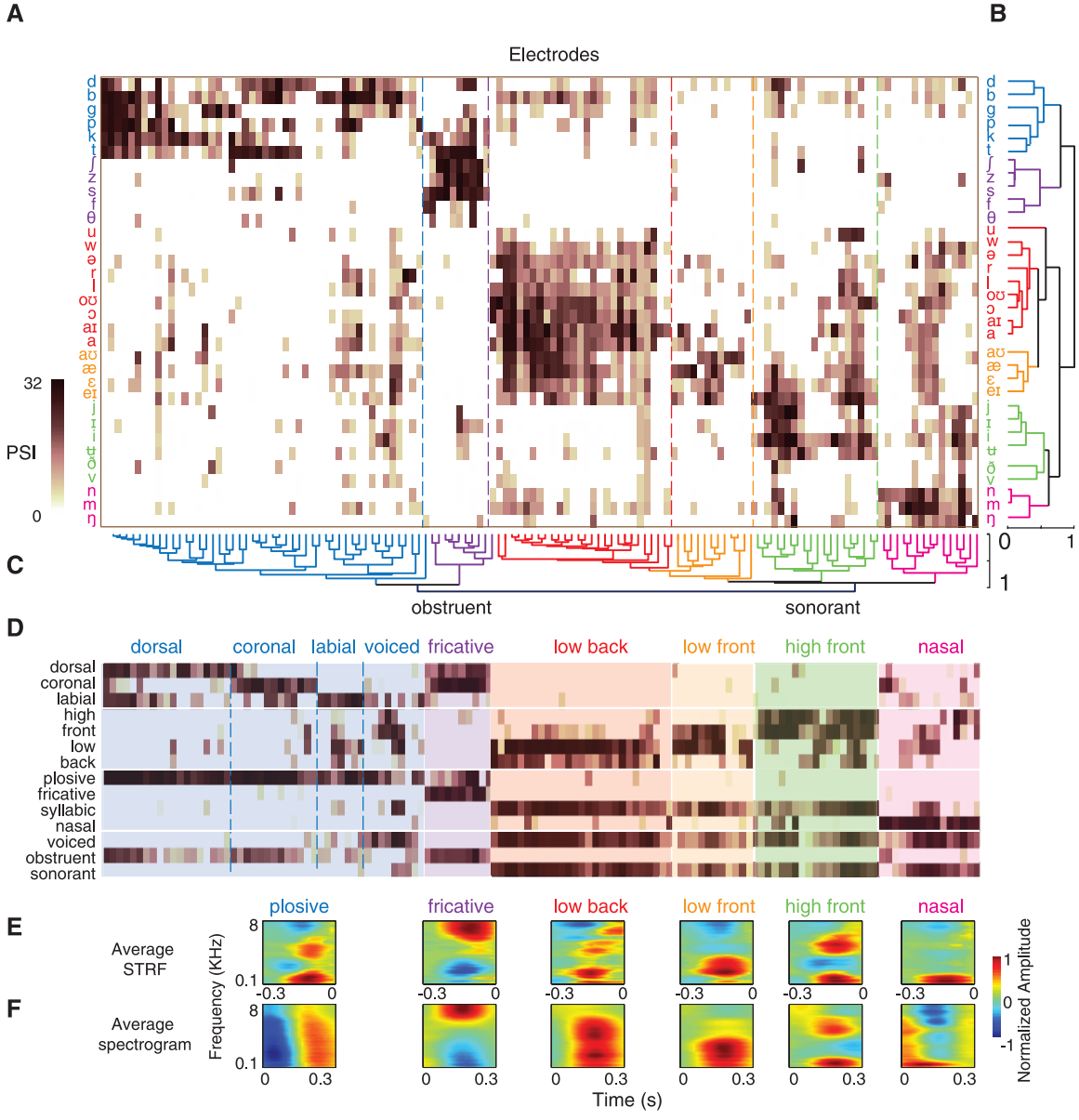

Fig. 2. Hierarchical clustering of single-electrode and population responses. (**A**) PSI vectors of selective electrodes across all participants. Rows correspond to phonemes, and columns correspond to electrodes. (**B**) Clustering across population PSIs (rows). (**C**) Clustering across single electrodes (columns). (**D**) Alternative PSI vectors using rows now corresponding to phonetic features, not phonemes. (**E**) Weighted average STRFs of main electrode clusters. (**F**) Average acoustic spectrograms for phonemes in each population cluster. Correlation between average STRFs and average spectrograms: $r = 0.67$, $P < 0.01$, t test. ($r = 0.50$, 0.78, 0.55, 0.86, 0.86, and 0.47 for plosives, fricatives, vowels, and nasals, respectively; $P < 0.01$, t test).

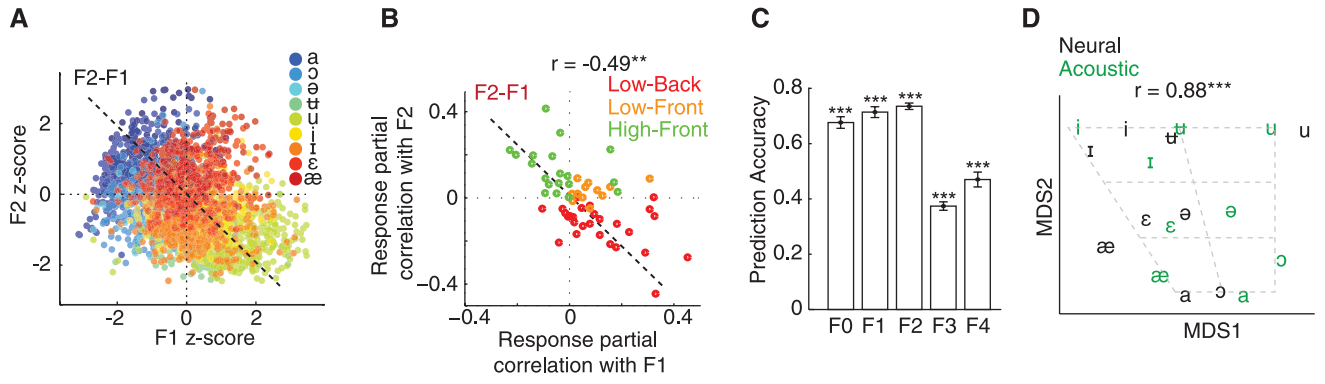

Fig. 3. Neural encoding of vowels. (**A**) Formant frequencies, F1 and F2, for English vowels (F2-F1, dashed line, first principal component). (**B**) F1 and F2 partial correlations for each electrode's response (**$P < 0.01$, *t* test). Dots (electrodes) are color-coded by their cluster membership. (**C**) Neural population decoding of fundamental and formant frequencies. Error bars indicate SEM. (**D**) Multidimensional scaling (MDS) of acoustic and neural space (***$P < 0.001$, *t* test).

across columns revealed single electrodes with similar PSI patterns (Fig. 2C). These two analyses revealed complementary local- and global-level organizational selectivity patterns. We also replotted the array by using 14 phonetic features defined in linguistics to contrast distinctive articulatory and acoustic properties (Fig. 2D; phoneme-feature mapping provided in fig. S7) (*1*, *15*).

The first tier of the single-electrode hierarchy analysis (Fig. 2C) divides STG sites into two distinct groups: obstruent- and sonorant-selective electrodes. The obstruent-selective group is divided into two subgroups: plosive and fricative electrodes (similar to electrodes e1 and e2 in Fig. 1D) (*16*). Among plosive electrodes (blue), some were responsive to all plosives, whereas others were selective to place of articulation (dorsal /g/ and /k/ versus coronal /d/ and /t/ versus labial /p/ and /b/, labeled in Fig. 2D) and voicing (separating voiced /b/, /d/, and /g/ from unvoiced /p/, /t/, and /k/; labeled voiced in Fig. 2D). Fricative-selective electrodes (purple) showed weak, overlapping selectivity to coronal plosives (/d/ and /t/). Sonorant-selective cortical sites, in contrast, were partitioned into four partially overlapping groups: low-back vowels (red), low-front vowels (orange), high-front vowels (green), and nasals (magenta) (labeled in Fig. 2D, similar to e3 to e5 in Fig. 1D).

Both clustering schemes (Fig. 2, B and C) revealed similar phoneme grouping based on shared phonetic features, suggesting that a substantial portion of the population-based organization can be accounted for by local tuning to features at single electrodes (similarity of average PSI values for the local and population subgroups of both clustering analyses is shown in fig. S8; overall $r = 0.73$, $P < 0.001$). Furthermore, selectivity is organized primarily by manner of articulation distinctions and secondarily by place of articulation, corresponding to the degree and the location of constriction in the vocal tract, respectively (*16*). This systematic organization of speech sounds is consistent with auditory perceptual models positing that distinctions are most affected by manner contrasts (*17*, *18*) compared with other feature hierarchies (articulatory or gestural theories) (*19*).

We next determined what spectrotemporal tuning properties accounted for phonetic feature selectivity. We first determined the weighted average STRFs of the six main electrode clusters identified above, weighting them proportionally by their degree of selectivity (average PSI). These STRFs show well-defined spectrotemporal tuning (Fig. 2E) highly similar to average acoustic spectrograms of phonemes in corresponding population clusters (Fig. 2F; average correlation = 0.67, $P < 0.01$, *t* test). For example, the first STRF in Fig. 2E shows tuning for broadband excitation followed by inhibition, similar to the acoustic spectrogram of plosives. The second STRF is tuned to a high frequency, which is a defining feature of sibilant fricatives. STRFs of vowel electrodes show tuning for characteristic formants that define low-back, low-front, and high-front vowels. Last, STRF of nasal-selective electrodes is tuned primarily to low acoustic frequencies generated from heavy voicing and damping of higher frequencies (*16*). The average spectrogram analysis requires a priori phonemic segmentation of speech but is model-independent. The STRF analysis assumes a linear relationship between spectrograms and neural responses but is estimated without segmentation. Despite these differing assumptions, the strong match between these confirms that phonetic feature selectivity results from tuning to signature spectrotemporal cues.

We have thus far focused on local feature selectivity to discrete phonetic feature categories. We next wanted to address the encoding of continuous acoustic parameters that specify phonemes within vowel, plosive, and fricative groups. For vowels, we measured fundamental (F0) and formant (F1 to F4) frequencies (*16*). The first two formants (F1 and F2) play a major perceptual role in distinguishing different English vowels (*16*), despite tremendous variability within and across vowels (Fig. 3A) (*20*). The optimal projection of vowels in formant space was the difference of F2 and F1 (first principal component, dashed line, Fig. 3A), which is consistent with vowel perceptual studies (*21*, *22*). By using partial correlation analysis, we quantified the relationship between electrode response amplitudes and F0 to F4. On average, we observed no correlation between the sensitivity of an electrode to F0 with its sensitivity to F1 or F2. However, sensitivity to F1 and F2 was negatively correlated across all vowel-selective sites (Fig. 3B; $r = -0.49$, $P < 0.01$, *t* test), meaning that single STG sites show an integrated response to both F1 and F2. Furthermore, electrodes selective to low-back and high-front vowels (labeled in Fig. 2D) showed an opposite differential tuning to formants, thereby maximizing vowel discriminability in the neural domain. This complex sound encoding matches the optimal projection in Fig. 3A, suggesting a specialized higher-order encoding of acoustic formant parameters (*23*, *24*) and contrasts with studies of speech sounds in nonhuman species (*25*, *26*).

To examine population representation of vowel parameters, we used linear regression to decode F0 to F4 from neural responses. To ensure unbiased estimation, we first removed correlations between F0 to F4 by using linear prediction and decoded the residuals. Relatively high decoding accuracies are shown in Fig. 3C ($P < 0.001$, *t* test), suggesting fundamental and formant variability is well represented in population STG responses (interaction between decoder weights with electrode STRFs shown in fig. S9). By using multidimensional scaling, we found that the relational organization between vowel centroids in the acoustic domain is well preserved in neural space (Fig. 3D; $r = 0.88$, $P < 0.001$).

For plosives, we measured three perceptually important acoustic cues (fig. S10): voice-onset time (VOT), which distinguishes voiced (/b/, /d/, and /g/) from unvoiced plosives (/p/, /t/, and /k/); spectral peak (differentiating labials /p/ and /b/ versus coronal /t/ and /d/ versus dorsal /k/ and /g/); and F2 of the following vowel (*16*). These acoustic parameters could be decoded from population STG responses (Fig. 4A; $P < 0.001$, *t* test). VOTs in particular are temporal cues that are perceived categorically, which suggests a nonlinear encoding (*27*). Figure 4B shows neural responses for three example electrodes plotted for all plosive instances (total of 1200), aligned to their release

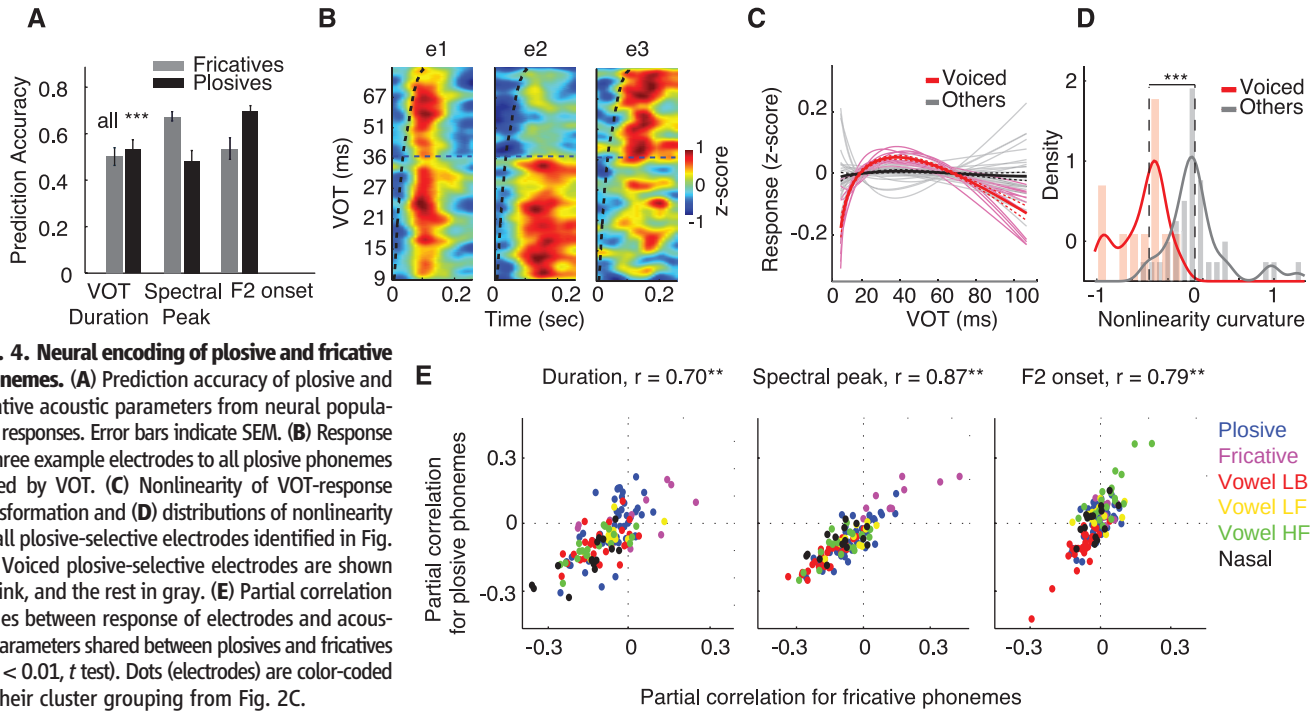

Fig. 4. Neural encoding of plosive and fricative phonemes. (**A**) Prediction accuracy of plosive and fricative acoustic parameters from neural population responses. Error bars indicate SEM. (**B**) Response of three example electrodes to all plosive phonemes sorted by VOT. (**C**) Nonlinearity of VOT-response transformation and (**D**) distributions of nonlinearity for all plosive-selective electrodes identified in Fig. 2D. Voiced plosive-selective electrodes are shown in pink, and the rest in gray. (**E**) Partial correlation values between response of electrodes and acoustic parameters shared between plosives and fricatives (**$P < 0.01$, *t* test). Dots (electrodes) are color-coded by their cluster grouping from Fig. 2C.

time and sorted by VOT. The first electrode responds to all plosives with same approximate latency and amplitude, irrespective of VOT. The second electrode responds only to plosive phonemes with short VOT (voiced), and the third electrode responds primarily to plosives with long VOT (unvoiced).

To examine the nonlinear relationship between VOT and response amplitude for voiced-plosive electrodes (labeled voiced in Fig. 2D) compared with plosive electrodes with no sensitivity to voicing feature (labeled coronal, labial and dorsal in Fig. 2D), we fitted a linear and exponential function to VOT-response pairs (fig. S11B). The difference between these two fits specifies the nonlinearity of this transformation, shown for all plosive electrodes in Fig. 4C. Voiced-plosive electrodes (pink) all show strong nonlinear bias for short VOTs compared with all other plosive electrodes (gray). We quantified the degree and direction of this nonlinear bias for these two groups of plosive electrodes by measuring the average second-derivative of the curves in Fig. 4C. This measure maps electrodes with nonlinear preference for short VOTs (e.g., electrode e2 in Fig. 4B) to negative values and electrodes with nonlinear preference for long VOTs (e.g., electrode e3 in Fig. 4B) to positive values. The distribution of this measure for voiced-plosive electrodes (Fig. 4D, red distribution) shows significantly greater nonlinear bias compared with the remaining plosive electrodes (Fig. 4D, gray distribution) ($P < 0.001$, Wilcox rank-sum test). This suggests a specialized mechanism for spatially distributed, nonlinear rate encoding of VOT and contrasts with previously described temporal encoding mechanisms (*26*, *28*).

We performed a similar analysis for fricatives, measuring duration, which aids the distinction between voiced (/z/ and /v/) and unvoiced fricatives (/s/, /ʃ/, /θ/, /f/); spectral peak, which differentiates /f/ and /v/ versus coronal /s/ and /z/ versus dorsal /ʃ/; and F2 of the following vowel (*16*) (fig. S12). These parameters can be decoded reliably from population responses (Fig. 4A; $P < 0.001$, *t* test).

Because plosives and fricatives can be subspecified by using similar acoustic parameters, we determined whether the response of electrodes to these parameters depends on their phonetic category (i.e., fricative or plosive). We compared the partial correlation values of neural responses with spectral peak, duration, and F2 onset of fricative and plosive phonemes (Fig. 4E), where each point corresponds to an electrode color-coded by its cluster grouping in Fig. 2D. High correlation values ($r = 0.70$, 0.87, and 0.79; $P < 0.001$; *t* test) suggest that electrodes respond to these acoustic parameters independent of their phonetic context. The similarity of responses to these isolated acoustic parameters suggests that electrode selectivity to a specific phonetic features (shown with colors in Fig. 4E) emerges from combined tuning to multiple acoustic parameters that define phonetic contrasts (*24*, *25*).

We have characterized the STG representation of the entire American English phonetic inventory. We used direct cortical recordings with high spatial and temporal resolution to determine how selectivity for phonetic features is correlated to acoustic spectrotemporal receptive field properties in STG. We found evidence for both spatially local and distributed selectivity to perceptually relevant aspects of speech sounds, which together appear to give rise to our internal representation of a phoneme.

We found selectivity for some higher-order acoustic parameters, such as examples of nonlinear, spatial encoding of VOT, which could have important implications for the categorical representation of this temporal cue. Furthermore, we observed a joint differential encoding of F1 and F2 at single cortical sites, suggesting evidence of spectral integration previously speculated in theories of combination-sensitive neurons for vowels (*23*–*25*, *29*).

Our results are consistent with previous single-unit recordings in human STG, which have not demonstrated invariant, local selectivity to single phonemes (*30*, *31*). Instead, our findings suggest a multidimensional feature space for encoding the acoustic parameters of speech sounds (*25*). Phonetic features defined by distinct acoustic cues for manner of articulation were the strongest determinants of selectivity, whereas place-of-articulation cues were less discriminable. This might explain some patterns of perceptual confusability between phonemes (*32*) and is consistent with feature hierarchies organized around acoustic cues (*17*), where phoneme similarity space in STG is driven more by auditory-acoustic properties than articulatory ones (*33*). A featural representation has greater universality across languages, minimizes the need for precise unit boundaries, and can account for coarticulation and temporal overlap over phoneme-based models for speech perception (*17*).

References and Notes

1. N. Chomsky, M. Halle, *The Sound Pattern of English* (Harper and Row, New York, 1968).
2. J. R. Binder *et al.*, *Cereb. Cortex* **10**, 512–528 (2000).
3. D. Boatman, C. Hall, M. H. Goldstein, R. Lesser, B. Gordon, *Cortex* **33**, 83–98 (1997).
4. E. F. Chang *et al.*, *Nat. Neurosci.* **13**, 1428–1432 (2010).

5. E. Formisano, F. De Martino, M. Bonte, R. Goebel, *Science* **322**, 970–973 (2008).
6. J. Obleser, A. M. Leaver, J. Vanmeter, J. P. Rauschecker, *Front. Psychol.* **1**, 232 (2010).
7. M. Steinschneider *et al.*, *Cereb. Cortex* **21**, 2332–2347 (2011).
8. Materials and methods are available as supplementary materials on *Science* Online.
9. N. E. Crone, D. Boatman, B. Gordon, L. Hao, *Clin. Neurophysiol.* **112**, 565–582 (2001).
10. E. Edwards *et al.*, *J. Neurophysiol.* **102**, 377–386 (2009).
11. M. Steinschneider, Y. I. Fishman, J. C. Arezzo, *Cereb. Cortex* **18**, 610–625 (2008).
12. S. Ray, J. H. R. Maunsell, *PLOS Biol.* **9**, e1000610 (2011).
13. J. S. Garofolo, TIMIT: Acoustic-Phonetic Continuous Speech Corpus (Linguistic Data Consortium, Philadelphia, 1993).
14. F. E. Theunissen *et al.*, *Network* **12**, 289–316 (2001).
15. M. Halle, K. Stevens, in *Music, Language, Speech, and Brain*, J. Sundberg, L. Nord, R. Carlson, Eds. (Wenner-Gren International Symposium Series vol. 59, Macmillan, Basingstoke, UK, 1991).
16. P. Ladefoged, K. Johnson, *A Course in Phonetics* (Cengage Learning, Stamford, CT, 2010).
17. K. N. Stevens, *J. Acoust. Soc. Am.* **111**, 1872–1891 (2002).
18. G. Clements, *Phonol. Yearb.* **2**, 225–252 (1985).
19. C. A. Fowler, *J. Phonetics* **14**, 3–28 (1986).
20. G. E. Peterson, H. L. Barney, *J. Acoust. Soc. Am.* **24**, 175 (1952).
21. J. D. Miller, *J. Acoust. Soc. Am.* **85**, 2114–2134 (1989).
22. A. K. Syrdal, H. S. Gopal, *J. Acoust. Soc. Am.* **79**, 1086–1100 (1986).
23. H. M. Sussman, *Brain Lang.* **28**, 12–23 (1986).
24. I. Nelken, *Curr. Opin. Neurobiol.* **18**, 413–417 (2008).
25. N. Mesgarani, S. V. David, J. B. Fritz, S. A. Shamma, *J. Acoust. Soc. Am.* **123**, 899–909 (2008).
26. C. T. Engineer *et al.*, *Nat. Neurosci.* **11**, 603–608 (2008).
27. L. Lisker, A. S. Abramson, *Lang. Speech* **10**, 1–28 (1967).
28. M. Steinschneider *et al.*, *Cereb. Cortex* **15**, 170–186 (2005).
29. G. Chechik, I. Nelken, *Proc. Natl. Acad. Sci. U.S.A.* **109**, 18968–18973 (2012).
30. A. M. Chan *et al.*, *Cereb. Cortex*, published online 16 May 2013 (10.1093/cercor/bht127).
31. O. Creutzfeldt, G. Ojemann, E. Lettich, *Exp. Brain Res.* **77**, 451–475 (1989).
32. G. A. Miller, P. E. Nicely, *J. Acoust. Soc. Am.* **27**, 338 (1955).
33. A. M. Liberman, *Speech: A Special Code* (MIT Press, Cambridge, MA, 1996).

Acknowledgments: We thank A. Ren for technical help with data collection and preprocessing. S. Shamma, C. Espy-Wilson, E. Cibelli, K. Bouchard, and I. Garner provided helpful comments on the manuscript. E.F.C. was funded by NIH grants R01-DC012379, R00-NS065120, and DP2-OD00862 and the Ester A. and Joseph Klingenstein Foundation. E.F.C., C.C., and N.M. collected the data. N.M. and C.C. performed the analysis. N.M. and E.F.C. wrote the manuscript. K.J. provided phonetic consultation. E.F.C. supervised the project.

Supplementary Materials

www.sciencemag.org/content/343/6174/1006/suppl/DC1
Materials and Methods
Figs. S1 to S12
Reference (*34*)

16 September 2013; accepted 17 January 2014
Published online 30 January 2014;
10.1126/science.1245994

Detection of a Recurrent *DNAJB1-PRKACA* Chimeric Transcript in Fibrolamellar Hepatocellular Carcinoma

Joshua N. Honeyman,[1,2]* Elana P. Simon,[1,3]* Nicolas Robine,[4]* Rachel Chiaroni-Clarke,[1] David G. Darcy,[1,2] Irene Isabel P. Lim,[1,2] Caroline E. Gleason,[1] Jennifer M. Murphy,[1,2] Brad R. Rosenberg,[5] Lydia Teegan,[1] Constantin N. Takacs,[1] Sergio Botero,[1] Rachel Belote,[1] Soren Germer,[4] Anne-Katrin Emde,[4] Vladimir Vacic,[4] Umesh Bhanot,[6] Michael P. LaQuaglia,[2] Sanford M. Simon[1]†

Fibrolamellar hepatocellular carcinoma (FL-HCC) is a rare liver tumor affecting adolescents and young adults with no history of primary liver disease or cirrhosis. We identified a chimeric transcript that is expressed in FL-HCC but not in adjacent normal liver and that arises as the result of a ~400-kilobase deletion on chromosome 19. The chimeric RNA is predicted to code for a protein containing the amino-terminal domain of DNAJB1, a homolog of the molecular chaperone DNAJ, fused in frame with PRKACA, the catalytic domain of protein kinase A. Immunoprecipitation and Western blot analyses confirmed that the chimeric protein is expressed in tumor tissue, and a cell culture assay indicated that it retains kinase activity. Evidence supporting the presence of the *DNAJB1-PRKACA* chimeric transcript in 100% of the FL-HCCs examined (15/15) suggests that this genetic alteration contributes to tumor pathogenesis.

Fibrolamellar hepatocellular carcinoma (FL-HCC) is a rare liver tumor that was first described in 1956 and that historically has been considered a variant of hepatocellular carcinoma (*1*, *2*). It is histologically characterized by well-differentiated neoplastic hepatocytes and thick fibrous bands in a noncirrhotic background (*3*, *4*). FL-HCC has a clinical phenotype distinct from conventional hepatocellular carcinoma and usually occurs in adolescents and young adults. Patients have normal levels of alpha fetoprotein without underlying liver disease or history of viral hepatitis (*3*–*6*). Little is known of its molecular pathogenesis. FL-HCC tumors do not respond well to chemotherapy (*7*, *8*), and surgical resection remains the mainstay of therapy, with overall survival reported to be 30 to 45% at 5 years (*1*, *6*, *8*, *9*).

To investigate the molecular basis of FL-HCC, we performed whole-transcriptome and whole-genome sequencing of paired tumor and adjacent normal liver samples. To determine whether there were tumor-specific fusion transcripts among the coding RNA, we ran the program FusionCatcher (*10*) on RNA sequencing (RNA-Seq) data from 29 samples, including primary tumors, metastases, recurrences, and matched normal tissue samples, derived from a total of 11 patients (table S1). There was only one recurrent candidate chimeric transcript detected in every tumor sample. This candidate transcript is predicted to result from the in-frame fusion of exon 1 from the *DNAJB1* gene, which encodes a member of the heat shock 40 protein family, with exons 2 to 10 from *PRKACA*, the gene encoding the adenosine 3′,5′-monophosphate (cAMP)–dependent protein kinase A (PKA) catalytic subunit alpha. This fusion transcript was not detected in any of the available paired normal tissue samples ($n = 9$). This fusion is not found in the COSMIC database (*11*) and has not previously been reported in the literature.

To further characterize the candidate fusion transcript, we directly examined those RNA-Seq reads that mapped to *PRKACA* and *DNAJB1*. We examined *PRKACA* transcript levels with DESeq2 (*12*) and found that they were increased relative to normal in tumors from all nine patients tested [P value adjusted for multiple testing (pAdj) $< 10^{-12}$, range three- to eightfold]. To determine whether the increased expression was attributable to a specific isoform of PRKACA, we quantified reads mapping to different exons and evaluated differential expression using DEXSeq (*13*). In all nine patients, there was an increase in the expression of exons 2 to 10 of *PRKACA* in the tumor relative to exon 1 and relative to the expression in normal tissue (Fig. 1A, left). This exon expression pattern does not correspond to a known isoform of PRKACA. Rather, it reflects an increase in *PRKACA* transcripts lacking the first exon, which encodes the domain that engages the regulatory subunits of PKA. All reads mapping to *PRKACA* in normal tissue were either contained within exons or bridged the junctions between adjacent exons at annotated splicing sites (Fig. 1B, left, blue). All tumor samples additionally had reads mapping from the start of the second exon of

[1]Laboratory of Cellular Biophysics, Rockefeller University, 1230 York Avenue, New York, NY 10065, USA. [2]Division of Pediatric Surgery, Department of Surgery, Memorial Sloan-Kettering Cancer Center, 1275 York Avenue, New York, NY 10065, USA. [3]The Dalton School, 108 East 89th Street, New York, NY 10128, USA. [4]New York Genome Center, 101 Avenue of the Americas, New York, NY 10013, USA. [5]Whitehead Presidential Fellows Program, The Rockefeller University, 1230 York Avenue, New York, NY 10065, USA. [6]Pathology Core Facility Memorial Sloan-Kettering Cancer Center, 1275 York Avenue, New York, NY 10065, USA.

*These authors contributed equally to this work.
†Corresponding author. E-mail: simon@rockefeller.edu

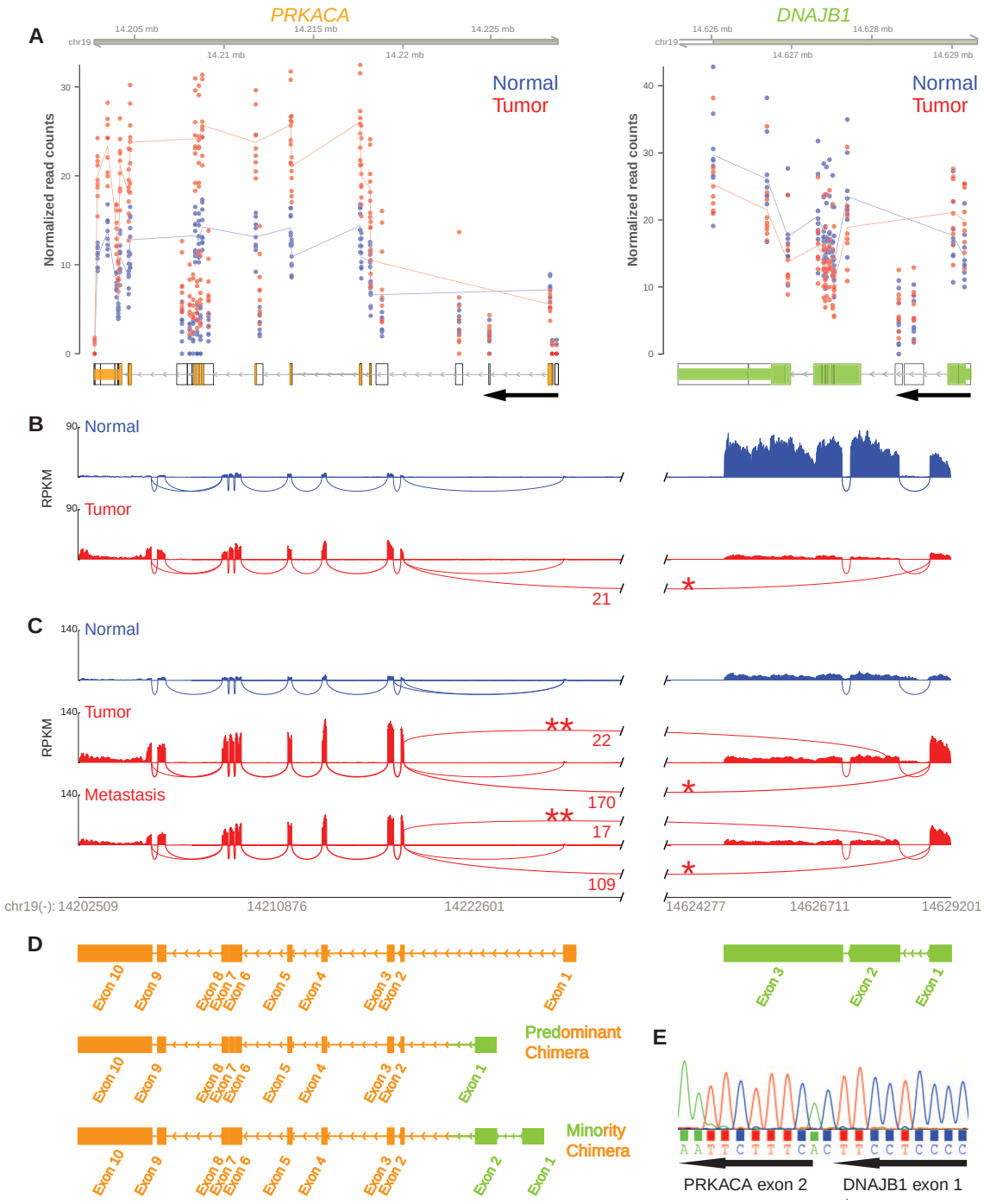

Fig. 1. RNA-Seq read coverage from fibrolamellar hepatocellular carcinoma and adjacent healthy liver tissue. (**A** to **C**) Plot of reads mapped to chromosome 19 in the region encoding, on the negative strand, the genes *PRKACA* (chr19:14,202,499 to 14,228,558) and *DNAJB1* (chr19:14,625,580 to 14,640,086) from the normal tissue (blue) and FL-HCC tissue (red). (A) Normalized RNA-Seq read counts from nine pairs of tumor and adjacent tissue demonstrate a consistent increase in tumor relative to normal in the reads mapping to exons 2 through 10 of *PRKACA* and a decrease in the reads of exon 1. Exons are shown as orange and green blocks [see (D)]. Normalized read counts are plotted per exon part (nonoverlapping portions of exons in all isoforms in ENSEMBL annotation; indicated by empty boxes). Transcript structure (solid color boxes) indicates most likely dominant isoform as inferred by RNA-Seq read coverage. Lines indicate the average normalized read count per exon part (in dominant isoform) for normal and tumor samples. (B) Sashimi plot (*39*) of RNA-Seq read coverage at *PRKACA* and *DNAJB1* loci for patient 9. Solid peaks depict reads per kilobase per million reads mapped (RPKM) within individual exons. Reads that bridge different exons are shown as arcs. In every tumor sample (nine out of nine) and in none of the normal tissue sample (zero out of nine), there are reads mapped from the end of exon 1 of *DNAJB1* to the start of exon 2 of *PRKACA* (read counts indicated for patient 9). (C) There is an additional set of reads from patient 4 that map from the second exon of DNAJB1 to the start of the second exon of *PRKACA* (read counts indicated). Indistinguishable results are observed in metastasis tissue from this same patient. (**D**) RNA-Seq read mapping predicts the production of four transcripts: a native *DNAJB1* (green); a native isoform 1 *PRKACA* (orange); a predominant chimera with the first exon of *DNAJB1* and exons 2 to 10 of *PRKACA*; and, in a subset of patients, a minority transcript with the first exon and part of the second of *DNAJB1* and exons 2 to 10 of *PRKACA*. (**E**). Sanger sequencing of RT-PCR products from FL-HCC samples confirmed in seven out of seven patients a chimera transcript joining the end of exon 1 of *DNAJB1* and the start of exon 2 of *PRKACA*.

PRKACA to a point ~400 kilobases (kb) upstream of the coding region, which corresponded to the end of the first exon of DNAJB1 (marked with an asterisk in Fig. 1B). Examination of the exon expression of *DNAJB1* in tumor samples revealed a decrease in the number of reads in exons 2 and 3 relative to exon 1 (Fig. 1, A and B, right). The data on the differential exon expression and the data on the RNA-Seq reads spanning the 400-kb distance that bridges these two genes further support a structural variation resulting in a chimeric transcript incorporating *DNAJB1* and *PRKACA* sequences.

In tumor samples from patients 4 and 14, there were indications of a second splice variant spanning *PRKACA* and *DNAJB1* (Fig. 1C). In addition to the reads from the end of exon 1 of *DNAJB1* to the start of exon 2 of *PRKACA* (Fig. 1C, middle red plot marked with an asterisk and Fig. 1D, the predominant chimera), there were reads that started in the middle of exon 2 of *DNAJB1* and mapped to the start of exon 2 of *PRKACA* (Fig. 1C, middle red plot marked with a double asterisk and Fig. 1D, the minority chimera). For patient 4, we also sequenced four different metastases and observed reads that spanned the same regions (Fig. 1C, bottom red plot). These findings predict the presence of one predominant chimera incorporating only the first exon of *DNAJB1* and a second, minority chimera, incorporating both the first and a portion of the second exon of *DNAJB1*. Both chimeras continue with exons 2 to 10 of *PRKACA*.

The presence of the predicted dominant chimeric RNA transcript was validated by Sanger sequencing of reverse transcription polymerase chain reaction (RT-PCR) products in all seven tumor samples tested from six patients (Fig. 1E), including one tumor and recurrence pair. The same chimeric transcript was confirmed by Sanger sequencing in an eighth newly acquired primary tumor from a patient whose samples were not previously analyzed by RNA-Seq or whole-genome sequencing.

In every tumor sample, in addition to the presence of one or both predicted RNA chimeras, we also observed RNA-Seq reads consistent with transcripts covering the entire length of *PRKACA*, which suggested that the cells still contain a wild-type (WT) copy of the gene. These results are most consistent with a heterozygous deletion in chromosome 19 resulting in a single copy of the chimeric transcript and single copies of both the WT *DNAJB1* and the WT *PRKACA*.

We next searched for potential structural variants in the FL-HCC genome by performing whole-genome sequencing on paired tumor and adjacent normal liver. We used the program Delly (*14*) to search for structural variations on chromosome 19. In 8 of 10 tumor samples, there were between 2 and 23 paired-end reads that spanned ~400 kb and mapped to both *DNAJB1* and *PRKACA*. In addition, in all eight of these tumor samples, split reads mapped to the deletion fusion point (table S2). The program, SplazerS (*15*) identified 3 to 17 split reads mapping between these genes in all 10 tumor samples. The predicted deletions ranged in size from 401,552 to 409,262 base pairs (bp), with a telomeric breakpoint between chr19: 14,218,306 and 14,226,300 (hg19) and a centromeric breakpoint between chr19:14,627,567 and 14,628,632. These deletions were not detected in adjacent normal liver samples.

The presence of the predicted deletion in the tumor DNA was validated by PCR and Sanger sequencing in eight out of eight samples tested

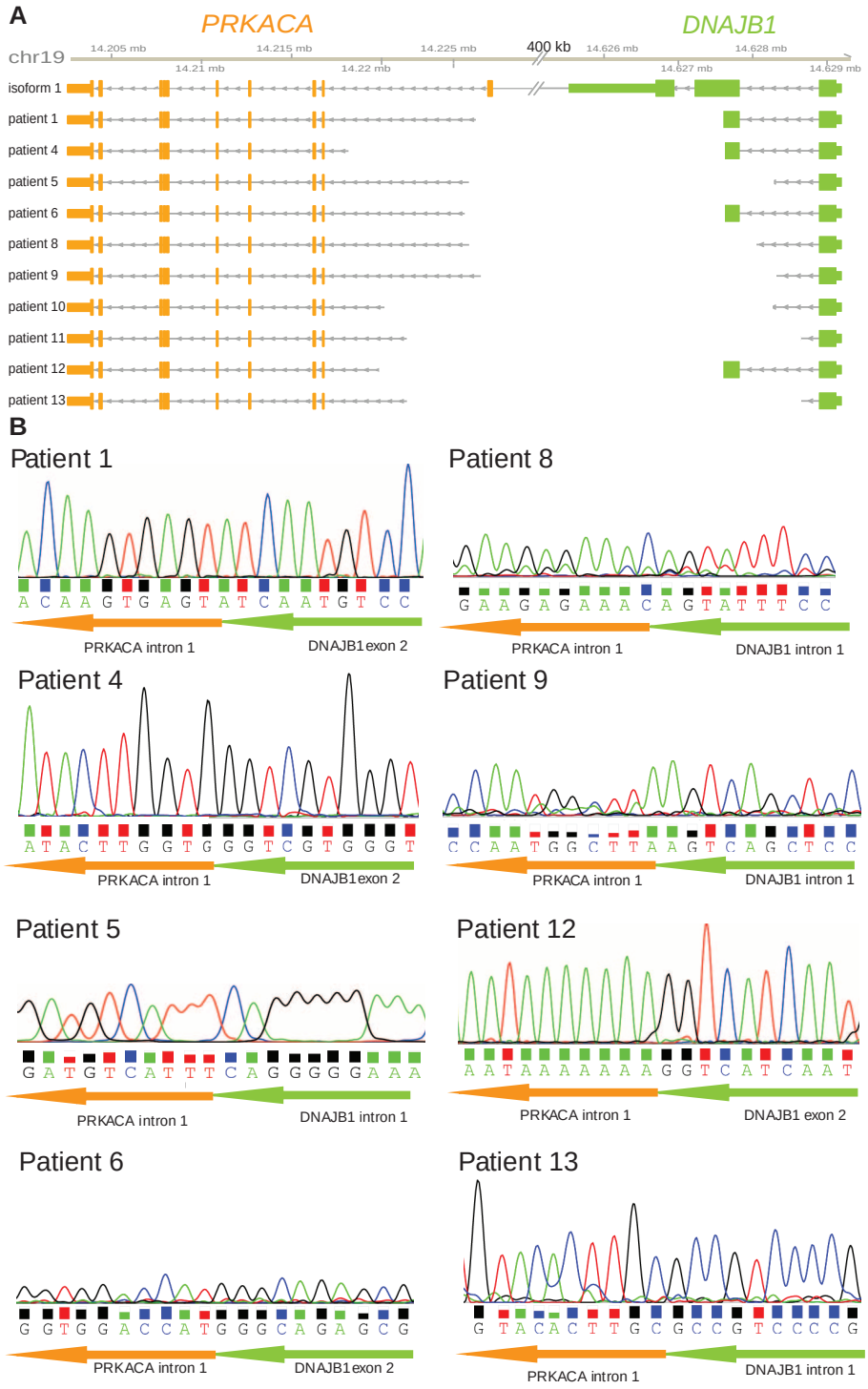

Fig. 2. DNA sequence analysis of fibrolamellar hepatocellular carcinoma DNA. (**A**) Mapping of the size and location of the breaks in the DNA between the *DNAJB1* and the *PRKACA* genes. (**B**). PCR followed by Sanger sequencing confirmed a deletion of ~400 kD in each patient. Each deletion results in a fusion that starts either in intron 1 or exon 2 of *DNAJB1* and ends in intron 1 of *PRKACA*. The break is in a different location in all patients. Note that the sequencing reads are shown for the positive strand. However, both *DNAJB1* and *PRKACA* are coded off the negative strand.

(Fig. 2B). In all patients, the precise breakpoints of the deletion mapped to different genomic coordinates (table S2). For all patients, the data were consistent with a deletion originating in the first intron (n = 6) or the second exon (n = 4) of *DNAJB1* and terminating in the first intron of *PRKACA* (Fig. 2A).

To determine whether the chimeric RNA transcript was translated into a chimeric protein, we performed Western blot analysis. Proteins extracted from tumor and adjacent normal liver samples were separated by SDS–polyacrylamide gel electrophoresis (SDS-PAGE) and probed with an antibody to the carboxyl terminus of PRKACA. Normal and tumor samples showed a band corresponding to a size of 41 kD (Fig. 3A), the predicted size of isoform 1 of WT PRKACA protein. In nine of nine previously sequenced tumor samples, there was a slower moving band at ~46 kD, consistent with the predicted larger molecular size of the predominant chimeric protein (patients 1, 3, 4, 5, 6, 7, 10, 11, and 12). This higher molecular mass band was not observed in any of the normal samples. Additional pairs of tumor and normal tissue not originally sequenced (patients 13, 14, and 17) were analyzed and showed the same larger band in the tumor but not in the normal tissue. The larger band was also seen in two metastases from patient 2.

We observed a third immunoreactive band in samples from two patients that migrated at ~50 kD (Fig. 3A, patients 4 and14), consistent with the minority chimera predicted by the RNA-Seq analysis. This larger band was present in addition to the bands corresponding to the native PRKACA protein and the predominant DNAJB1-PRKACA chimeric protein. This slower-mobility, apparently higher molecular mass band is consistent with a chimeric protein that includes amino acids corresponding to the first exon and portion of exon 2 of *DNAJB1*, as well as exons 2 to 10 of *PRKACA* (Fig. 1C, patient 4 shown).

To confirm that the higher molecular mass bands were the chimeric proteins, we tested reactivity with an antibody to the amino terminus of DNAJB1 and an antibody to the carboxyl terminus of PRKACA. Protein was immunoprecipitated with an antibody to DNAJB1, separated by SDS-PAGE alongside a sample of the total solubilized tissue, and then probed on a Western blot with an antibody to the carboxyl terminus of PRKACA (Fig. 3B). The whole-cell lysate again showed bands corresponding to both WT PRKACA and the chimeric protein. However, the sample immunoprecipitated with DNAJB1 showed only the higher molecular mass band (lanes labeled IP-DNAJB1, Fig. 3B) corresponding to the chimera. The WT PRKACA band was not present in the immunoprecipitate. Thus, the higher molecular mass band that is present only in tumor samples is a true chimeric protein resulting from the fusion of the amino terminus of DNAJB1 and carboxyl terminus of PRKACA.

To determine whether the DNAJB1-PRKACA chimeric protein retains kinase activity, we transfected human embryonic kidney–293T (HEK-293T) cells with plasmids encoding either WT PRKACA or the DNAJB1-PRKACA chimera. Control cells were transfected with an "empty" plasmid lacking the PRKACA or chimera genes, which provided a measure for the background activity level of PKA in the cells. PKA activity was measured by the ability of cell lysate to phosphorylate the fluorescent PKA substrate peptide LRRASLG, whose mobility shifts on a gel upon phosphorylation. In cells expressing either WT PRKACA or the chimera (Fig. 3C), PKA activity was significantly greater than controls ($P < 0.001$) (Fig. 3C). Both PRKACA and the chimera were each expressed from the same promoter, and the PKA activity was indistinguishable in cells expressing either protein. This demonstrates that the chimeric protein retains full PKA activity. Finally, we examined the expression of PRKACA protein in tumor and adjacent normal tissue by confocal

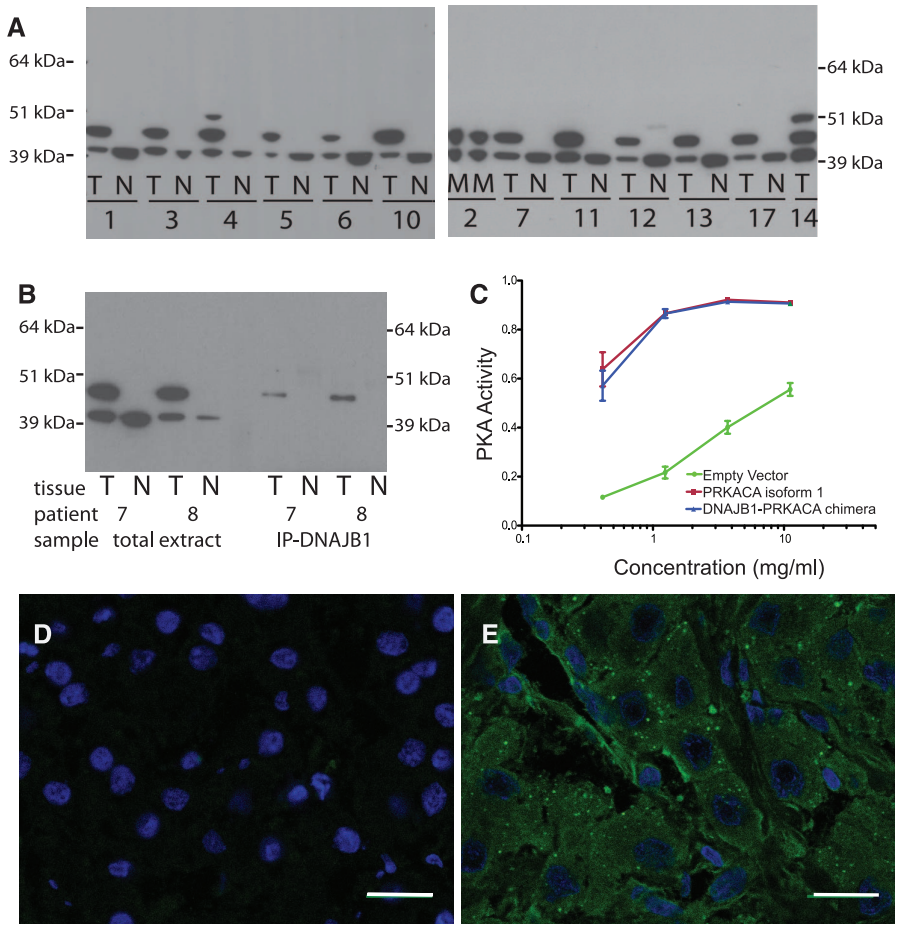

Fig. 3. Tumor-specific expression of a protein consistent with the predicted *DNAJB1-PRKACA* chimera. (**A**) Immunoblot analysis. Protein extracts of fibrolamellar carcinoma (T) and adjacent liver tissue (N) were separated on SDS-PAGE and subjected to immunoblot analysis using an antibody to the carboxyl terminus of PRKACA. This analysis revealed the presence of the native PRKACA in all tumor, metastasis, and normal samples and the presence of one additional, apparent higher molecular mass band in all tumor samples (the predominant chimera). There is a second even higher molecular mass band, the minority chimera, in the two tumor samples that had demonstrated a second set of RNA reads mapping between exon 2 of DNAJB1 and exon 2 of PRKACA (patients 4 and 14). (**B**) Confirmation of chimeric protein. Protein extracts of fibrolamellar carcinoma (T) and adjacent liver tissue (N) were immunoprecipitated with an antibody to the amino terminus of DNAJB1 and run adjacent to total-cell extract on SDS-PAGE. These samples were then subjected to immunoblot analysis with an antibody to the carboxyl terminus of PRKACA (**C**) PKA activity of WT PRKACA and chimera are indistinguishable. HEK-293T cells were transfected with an empty control plasmid, a plasmid encoding WT PRKACA, or a plasmid encoding the chimeric DNAJB1-PRKACA. Cell extracts were diluted and assayed for PKA activity. The activity of the WT PRKACA and the chimera PRKACA-DNAJB1 are significantly higher [$P < 0.001$, two-way analysis of variance (ANOVA)] than background kinase activity. Samples were processed in triplicate ± SEM. (**D** and **E**) Immunofluorescence assay. The presence and distribution of PRKACA protein was examined with an antibody against the carboxyl terminus in (D) adjacent normal tissue and (E) FL-HCC liver tissue from patient 11, both imaged by confocal microscopy. The green areas correspond to PRKACA and the blue areas correspond to nuclei, which were stained with Hoechst stain. Similar results were seen in samples from additional patients (fig. S1). Scale bar, 20 μm.

fluorescence microscopy. Analysis with an antibody against the carboxyl terminus of PRKACA revealed a fluorescent signal that was consistently brighter throughout the cells in FL-HCC (Fig. 3E and fig. S1) than in the adjacent tissue normal liver (Fig. 3D).

In summary, we have provided evidence for a 400-kb heterozygous deletion on chromosome 19 in 10 out of 10 FL-HCC patients tested. We detected a chimeric *DNAJB1-PRKACA* RNA transcript in 12 of 12 patients tested and a putative chimeric DNAJB1-PRKACA protein in 14 of 14 patients tested. The genomic deletion, the chimeric transcript, and the chimeric protein were not present in any normal liver samples tested. This chimera is predicted to incorporate the J domain of DNAJB1 and the catalytic domain of PRKACA. The promoter is from the *DNAJB1* gene, which could explain why the chimeric transcript is expressed at higher levels than the WT PRKACA transcript (Fig. 1, A, B, and C).

PKA is a heterotetramer composed of two regulatory subunits and two catalytic subunits. In this configuration, the catalytic subunit is inactive until cAMP binding causes its release from the regulatory units. The DNAJB1-PRKACA chimera retains the functional catalytic domain and maintains full kinase activity, but it is missing the domain that binds the regulatory subunits of PKA. PKA phosphorylates numerous cytoplasmic and nuclear substrates, including members of the Ras, mitogen-activated protein kinase (*16*), estrogen signaling (*17*), and apoptosis pathways (*18*). PKA is also involved in signaling via endothelial growth factor receptor (*19*) and regulation of aromatase expression (*20*), both of which can be overexpressed in FL-HCC (*21*–*24*). PRKACA has been implicated in epithelial-mesenchymal transition, migration, and invasion of lung cancer cells (*25*). A review of publicly available data sets from the Cancer Genome Atlas (*26*, *27*) suggests that PRKACA is amplified in 12% of ovarian serous cystadenocarcinoma (*28*); 5% of uterine corpus endometrial carcinoma (*29*); 3% of adenoid cystic carcinoma (*30*); 2% of lung squamous cell carcinoma (*31*); 1% of sarcoma (*32*), colon and rectum adenocarcinoma (*33*) and breast invasive carcinoma (*34*). In FL-HCC, the deletion we observe in chromosome 19 has not been reported in comparative genomic hybridization of FL-HCC (*35*–*38*), perhaps because of the limited resolution of the approach at the time those studies were performed.

There are currently no molecular diagnostic tests for FL-HCC. Because previous studies have detected PKA in the peripheral blood of cancer patients (*39*), this chimera may represent a diagnostic marker for FL-HCC. Surgical resection remains the cornerstone of therapy and patients who present with advanced-stage or metastatic disease have few treatment options. While the role of the DNAJB1-PRKACA chimera in the pathogenesis of FL-HCC has yet to be addressed, our observations raise the possibility that it contributes to the pathogenesis of the tumor and may represent a therapeutic target.

References and Notes

1. H. B. El-Serag, J. A. Davila, *Hepatology* **39**, 798–803 (2004).
2. H. A. Edmondson, *AMA J. Dis. Child.* **91**, 168–186 (1956).
3. M. Torbenson, *Adv. Anat. Pathol.* **14**, 217–223 (2007).
4. J. R. Craig, R. L. Peters, H. A. Edmondson, M. Omata, *Cancer* **46**, 372–379 (1980).
5. F. Stipa *et al.*, *Cancer* **106**, 1331–1338 (2006).
6. M. N. Mavros, S. C. Mayo, O. Hyder, T. M. Pawlik, *J. Am. Coll. Surg.* **215**, 820–830 (2012).
7. V. B. Weeda *et al.*, *Eur. J. Cancer* **49**, 2698–2704 (2013).
8. H. M. Katzenstein *et al.*, *Cancer* **97**, 2006–2012 (2003).
9. S. Kakar *et al.*, *Mod. Pathol.* **18**, 1417–1423 (2005).
10. H. Edgren *et al.*, *Genome Biol.* **12**, R6 (2011).
11. S. Bamford *et al.*, *Br. J. Cancer* **91**, 355–358 (2004).
12. S. Anders, W. Huber, *Genome Biol.* **11**, R106 (2010).
13. S. Anders, A. Reyes, W. Huber, *Genome Res.* **22**, 2008–2017 (2012).
14. T. Rausch *et al.*, *Bioinformatics* **28**, i333–i339 (2012).
15. A.-K. Emde *et al.*, *Bioinformatics* **28**, 619–627 (2012).
16. D. G. Adams, N. A. Sachs, R. R. Vaillancourt, *Arch. Biochem. Biophys.* **407**, 103–116 (2002).
17. D. Chen, P. E. Pace, R. C. Coombes, S. Ali, *Mol. Cell. Biol.* **19**, 1002–1015 (1999).
18. S. R. Datta *et al.*, *Mol. Cell* **6**, 41–51 (2000).
19. G. Tortora *et al.*, *Oncogene* **14**, 923–928 (1997).
20. M. F. Bouchard, H. Taniguchi, R. S. Viger, *Endocrinology* **146**, 4905–4916 (2005).
21. K. Muramori *et al.*, *J. Pediatr. Hematol. Oncol.* **33**, e195–e197 (2011).
22. A. Patonai *et al.*, *Pathol. Oncol. Res.* **19**, 63–70 (2013).
23. C. S. Ang *et al.*, *Gastrointest. Cancer Res.* **6**, 3–9 (2013).
24. A. F. Buckley, L. J. Burgart, S. Kakar, *Hum. Pathol.* **37**, 410–414 (2006).
25. D. Shaikh *et al.*, *Cell. Signal.* **24**, 2396–2406 (2012).
26. E. Cerami *et al.*, *Cancer Discov.* **2**, 401–404 (2012).
27. J. Gao *et al.*, *Sci. Signal.* **6**, pl1 (2013).
28. D. Bell *et al.*, *Nature* **474**, 609–615 (2011).
29. C. Kandoth *et al.*, *Nature* **497**, 67–73 (2013).
30. A. S. Ho *et al.*, *Nat. Genet.* **45**, 791–798 (2013).
31. P. S. Hammerman *et al.*, *Nature* **489**, 519–525 (2012).
32. J. Barretina *et al.*, *Nat. Genet.* **42**, 715–721 (2010).
33. D. M. Muzny *et al.*, *Nature* **487**, 330–337 (2012).
34. Cancer Genome Atlas Network, *Nature* **490**, 61–70 (2012).
35. S. Kakar *et al.*, *Mod. Pathol.* **22**, 134–141 (2009).
36. L. Wilkens *et al.*, *Am. J. Clin. Pathol.* **114**, 867–874 (2000).
37. S. C. Ward, S. Waxman, *Semin. Liver Dis.* **31**, 61–70 (2011).
38. A. Marchio *et al.*, *Oncogene* **19**, 3733–3738 (2000).
39. M. V. Nesterova *et al.*, *Cancer Res.* **66**, 8971–8974 (2006).

Acknowledgments: Two coauthors on this study are patients with FL-HCC. We thank S. Tavazoie and H. Goodarzi for trouble-shooting, recommending protocols and software, and for helpful discussions of the data and the manuscript. We thank R. Darnell for support, insightful discussions of the data, and critical comments on the manuscript. We also thank the Pathology core facility at Memorial Sloan-Kettering Cancer Center (MSKCC), the Molecular Cytology core facility (MSKCC), and members of the fibrolamellar community for support. This work was funded by a grant from The Fibrolamellar Cancer Foundation, The Rockefeller University Center for Clinical and Translational Science grant 2UL1RR024143, and by an anonymous donor. We thank J. Panda for fund-raising efforts. C.N.T was supported by a Howard Hughes Medical Institute International Student Predoctoral Fellowship. The New York Genome Center and the authors (N.R., S.G., A.-K.E., and V.V.) have filed a patent application related to the use of the chimeric transcript in the detection of human cancers. Sequence data have been deposited into the database of Genotypes and Phenotypes, dbGaP (accession no. phs000709.v1.p1).

Supplementary Materials

www.sciencemag.org/content/343/6174/1010/suppl/DC1
Materials and Methods
Fig. S1
Tables S1 to S3
References (*40*–*48*)

9 December 2013; accepted 29 January 2014
10.1126/science.1249484

Chemical Warfare Among Invaders: A Detoxification Interaction Facilitates an Ant Invasion

Edward G. LeBrun,* Nathan T. Jones, Lawrence E. Gilbert

As tawny crazy ants (*Nylanderia fulva*) invade the southern United States, they often displace imported fire ants (*Solenopsis invicta*). After exposure to *S. invicta* venom, *N. fulva* applies abdominal exocrine gland secretions to its cuticle. Bioassays reveal that these secretions detoxify *S. invicta* venom. Further, formic acid from *N. fulva* venom is the detoxifying agent. *N. fulva* exhibits this detoxification behavior after conflict with a variety of ant species; however, it expresses it most intensely after interactions with *S. invicta*. This behavior may have evolved in their shared South American native range. The capacity to detoxify a major competitor's venom probably contributes substantially to its ability to displace *S. invicta* populations, making this behavior a causative agent in the ecological transformation of regional arthropod assemblages.

When multiple species invade a region, they often originate from common source assemblages (*1*). As a consequence, species interactions in invaded regions may reflect deep evolutionary histories. The emerging invasion of the southern United States by tawny crazy ants (*Nylanderia fulva*) and resulting intense competitive conflict with red imported fire ants (*Solenopsis invicta*) provide an example of interacting invaders with shared evolutionary histories. The native ranges of *S. invicta* and *N. fulva* overlap in northern Argentina, Paraguay, and southern Brazil (*2*–*6*), and within this expansive region, these species compete directly for resources (*7*–*9*).

Since the 1930s, *S. invicta* has spread throughout the southern United States, ecologically dominating most grassland ant assemblages (*10*). In the

Brackenridge Field Laboratory, Department of Integrative Biology, The University of Texas at Austin, 2907 Lake Austin Boulevard, Austin, TX 78703, USA.

*Corresponding author. E-mail: edwardlebrun@austin.utexas.edu

early 2000s, *N. fulva* was introduced into Texas and Florida and is now spreading through U.S. Gulf Coast states. Where these species meet, high-density *N. fulva* populations are displacing *S. invicta* (*11*). This displacement constitutes an emerging transformative change in the organization of regional arthropod assemblages, which were previously dominated by *S. invicta*.

The displacement of *S. invicta* populations by *N. fulva* apparently stems in part from a surprisingly strong competitive asymmetry. At recently invaded sites, *N. fulva* easily ousts *S. invicta* from food items it controls. In fact, at locations where foragers of both species were similarly abundant, *N. fulva* captured 93% of contested resources (fig. S1). Further, at *N. fulva* invasion fronts, most *N. fulva* colonies were located inside *S. invicta* mounds, often still partially occupied by *S. invicta*, suggesting that *N. fulva* can usurp their nests (*11*).

Other competing ant species typically avoid large aggregations of *S. invicta* because their venom is a potent topical insecticide (*12*). In contrast, *N. fulva* workers will charge into masses of *S. invicta* surrounding food items, spraying venom. In response, *S. invicta* workers gaster flag (extruding and vibrating a venom droplet from their stinger) and dab venom onto nearby attackers (Fig. 1A and movie S1). As a result, many *N. fulva* workers are smeared with *S. invicta* venom, an event usually fatal for ants (*13*).

After contacting *S. invicta* venom, an *N. fulva* worker immediately engages in a highly stereotyped behavioral sequence. Standing on its hind and middle legs, the worker curls its gaster (the modified abdomen of ants) underneath its body, touching its acidopore (the specialized exocrine gland opening at the tip of the gaster) to its mandibles. The *N. fulva* worker then runs its front legs through its mandibles and grooms itself vigorously, periodically reapplying its acidopore to its mandibles (Fig. 1B and movie S1). Apparently, these ants apply an exocrine gland secretion in what seems to be an attempt to detoxify *S. invicta* venom. We refer to this sequence of behaviors as "detoxification behavior."

We performed a series of experiments: (i) testing whether this behavior detoxifies *S. invicta* venom, (ii) testing the glandular source and chemical nature of the detoxifying agent, and (iii) evaluating the species-level specificity of this detoxification behavior.

To evaluate potential detoxification of *S. invicta* venom, we staged antagonistic interactions between *S. invicta* and *N. fulva* workers. *N. fulva* were treated by sealing their acidopore with nail polish, blocking secretions, or sham treated by applying nail polish to the side of their gaster. In *S. invicta* conflict treatments, a single *N. fulva* worker was introduced into a vial containing two *S. invicta* workers. Once an *S. invicta* worker dabbed the *N. fulva* worker with its stinger, the *S. invicta* were removed and the survivorship of the *N. fulva* was monitored for 8 hours (*14*).

Survivorship differed strongly across treatments (Wilcoxon: $\chi^2 = 48.6$, df = 2, $P < 0.0001$), with no mortality in acidopore-sealed controls that were not exposed to *S. invicta* venom. *N. fulva* workers with sealed acidopores exposed to *S. invicta* died at a high rate, with 48% surviving. In contrast, 98% of sham-treated *N. fulva* workers dabbed by *S. invicta* with venom survived (Wilcoxon: $\chi^2 = 28.0$, df = 1, $P < 0.0001$) (Fig. 2). These ants employed their detoxification behavior frequently after exposure to venom. Thus, detoxification behavior is an extremely effective countermeasure to *S. invicta* venom.

The Dufour's and venom glands (exocrine glands used for communication and defense) both duct to the acidopore of *N. fulva* workers. To assess which produces the detoxifying agent, we applied solutions of *S. invicta* venom and *N. fulva* glandular products to Argentine ants (*Linepithema humile*). Argentine ants cannot detoxify *S. invicta* venom (*13*), are approximately the same size as *N. fulva* workers, and have similarly scleroticized exoskeletons. Application of *N. fulva* gland-product solutions (Dufour's or venom), followed immediately by the carrier solution, provided controls. The treatments were (i) application of *S. invicta* venom solution followed by the carrier solution and (ii) application of *S. invicta* venom solution followed by one of the *N. fulva* gland-product solutions (*14*).

N. fulva Dufour's glands contain 2-ketones and alkanes (*15*); for ants in the subfamily Formicinae, the contents of this gland typically serve as alarm pheromones (*16*). In tests of the Dufour's gland contents, survival times differed across treatments (Wilcoxon: $\chi^2 = 39.4$, df = 2, $P < 0.0001$), with no mortality in the Dufour's-treated control group.

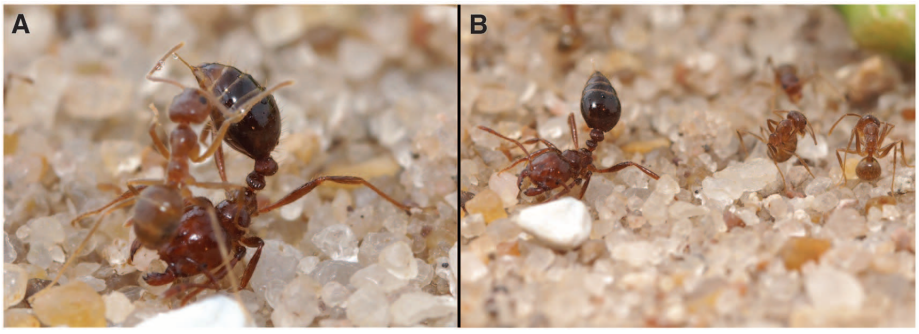

Fig. 1. Interaction of *N. fulva* and *S. invicta*, illustrating the detoxification behavior. (**A**) A larger *S. invicta* worker dabs venom droplets from its sting onto antennae of an attacking *N. fulva* worker. (**B**) Two *N. fulva* workers, previously smeared with *S. invicta* venom, engage in detoxification behavior. The worker in the middle stands on its hind and middle legs, dispensing fluid from its acidopore onto its mandibles. The worker on the right distributes the fluid with its front legs. On the left, an *S. invicta* worker gaster flags.

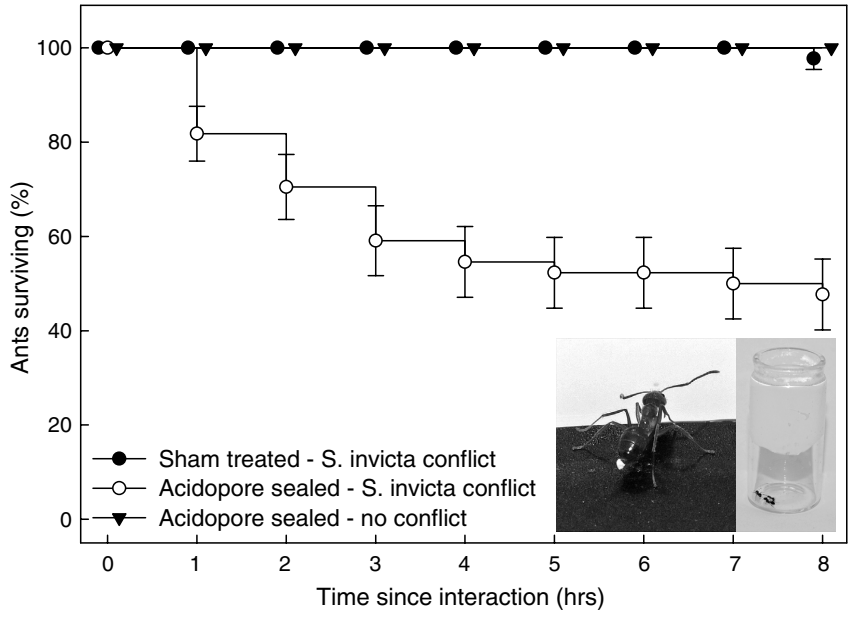

Fig. 2. Demonstration of detoxification. Survivorship curves for *N. fulva* workers after staged interactions with *S. invicta*. Triangular symbols denote controls, and circular symbols denote experimental treatments. Bars present standard errors of the Kaplan-Meier survivorship estimator. The images at the bottom show an ant with a sealed acidopore (left) and an interaction vial (right).

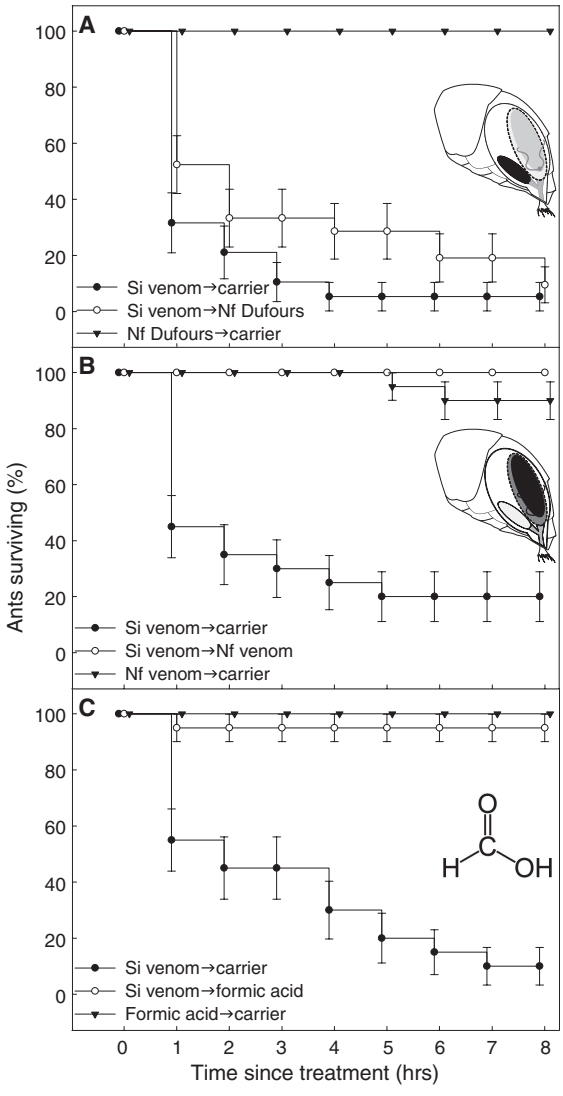

Fig. 3. Results of bioassays. Survivorship curves for topically treated *L. humile* workers. Legends at bottom left identify the sequence of solutions applied. Solutions consisted of the test agent diluted in a carrier solution of water plus surfactant. Si denotes *S. invicta*; Nf denotes *N. fulva*. (**A**) Test of *N. fulva* Dufour's gland as the source of the detoxifying agent. (**B**) Test of *N. fulva* venom gland as the source of the detoxifying agent. (**C**) Test of formic acid as the detoxifying agent. Triangular symbols denote controls, and circular symbols denote experimental treatments. Error bars present standard errors of the Kaplan-Meier survivorship estimator. The inset illustrations detail internal gland anatomy and chemical structures. The source gland is shaded dark.

However, the *S. invicta* venom solution alone and *S. invicta* venom solution followed by Dufour's solution groups died at similar, very high rates (Wilcoxon: $\chi^2 = 2.1$, df = 1, $P = 0.15$) (Fig. 3A). Dufour's gland products do not detoxify *S. invicta* venom.

When *N. fulva* venom was tested, survival times differed between groups (Wilcoxon: $\chi^2 = 44.1$, df = 2, $P < 0.0001$), with very low mortality in the *N. fulva* venom–treated control group (10%). The fate of workers in the *S. invicta* venom followed by carrier solution group differed dramatically from those in the *S. invicta* venom solution followed by *N. fulva* venom solution group (Wilcoxon: $\chi^2 = 25.7$, df = 1, $P < 0.0001$). Only 20% of workers treated with *S. invicta* venom alone survived, as compared to the survival of 100% of workers treated with both venoms sequentially (Fig. 3B). Therefore, the venom gland of *N. fulva* contains the detoxifying agent.

As is clear from the odor and respiratory trauma resulting from collecting *N. fulva* with an aspirator, *N. fulva* venom consists primarily of concentrated formic acid (*15*). Using the same Argentine ant–based bioassay, we tested whether formic acid is the detoxifying agent. We used a formic acid solution with a pH equivalent to that of the *N. fulva* venom solution used in the previous assay. Controls were application of formic acid solution followed by carrier solution. Treatments were application of *S. invicta* venom solution followed by carrier solution, and application of *S. invicta* venom solution followed by formic acid solution (*14*).

Treatments and controls differed in survivorship (Wilcoxon: $\chi^2 = 51.1$, df = 2, $P < 0.0001$), with no mortality among formic acid–treated control workers. Again, workers treated with *S. invicta* venom followed by carrier solution suffered high

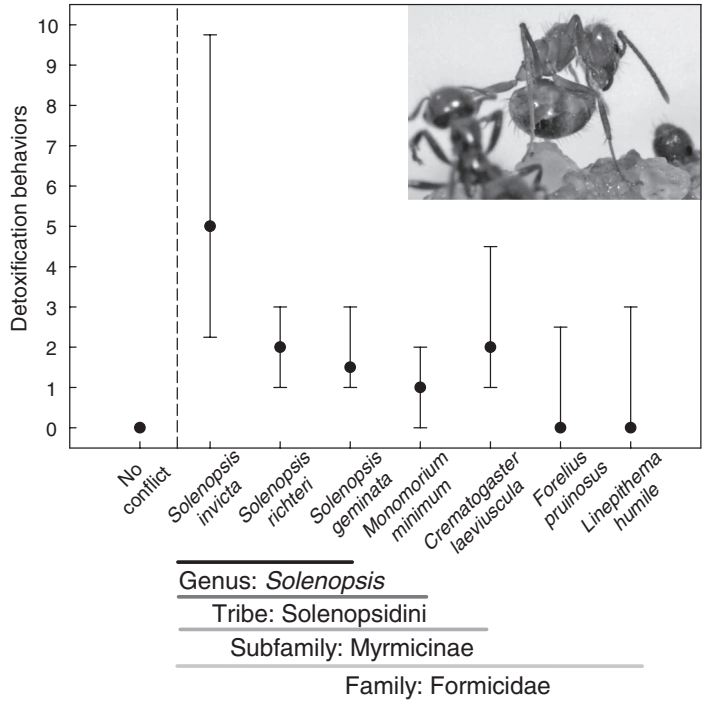

Fig. 4. Evaluation of the specificity of detoxification behavior. The dependent variable is a 2-min count of *N. fulva* detoxification behaviors after chemical conflict with a variety of test species (*x* axis). Symbols indicate the median number of detoxification behaviors expressed. Error bars present interquartile ranges. The horizontal dashed line separates no conflict from post-interaction data. Interactions terminated when the test species deployed its defensive compounds against the *N. fulva* worker. Horizontal lines and text at bottom indicate species progressively less related to *S. invicta*. The inset image shows an *N. fulva* worker performing the detoxification behavior.

mortality. In stark contrast, 95% of workers treated with *S. invicta* venom solution followed by formic acid solution survived (Wilcoxon: $\chi^2 = 25.4$, df = 1, $P < 0.0001$) (Fig. 3C). Thus, formic acid appears to be the compound responsible for detoxifying *S. invicta* venom.

How formic acid renders fire ant venom nontoxic is unresolved. Five principal piperidine alkaloids (2,6-dialkylpiperidines) and some of their stereoisomers primarily make up *S. invicta* venom (*10*). Suspended in this are small amounts of proteins (approximately 1% of the total), primarily the enzymes phospholipase A and hyaluronidase (*17*). The insecticidal properties of *S. invicta* venom derive directly from its alkaloids (*13*). However, associated enzymes function as cell membrane disruptors (*18*) and may be critical for gating alkaloids through intercuticular membranes and cell walls. Formic acid denatures these enzymes. This indirect effect seems the most likely detoxification mechanism. It is unknown whether formic acid alters the bioactivity of the alkaloid fraction.

N. fulva and other formicines use formic acid as a chemical weapon because it is highly caustic. Self-applying formic acid is thus costly, favoring selectivity in the expression of the detoxification behavior. We evaluated the specificity of detoxification expression by measuring its intensity after interactions with *S. invicta* versus after interactions with a series of seven test species that employ defensive compounds in interspecific conflicts. In vials, two-on-one interactions (test species versus *N. fulva*) were staged, ending when test ants applied defensive compounds to *N. fulva* (*14*). After chemical conflict with any test species, *N. fulva* workers performed significantly more detoxification behaviors than they did when there was no conflict (Fig. 4 and table S1). However, after chemical conflict with *S. invicta*, *N. fulva* workers performed the detoxification behavior with much higher frequency than after conflict with any other species (Fig. 4 and table S2). In fact, the median detoxification response after conflict with *S. invicta* was performed 6.7 times more frequently than the average response after conflicts with non–fire ant species. Curiously, detoxification behaviors were not unusually elevated after exposure to *S. richteri* workers, a closely related South American fire ant.

N. fulva and *S. invicta* share an evolutionarily ancient interaction. Although it is broadly expressed after chemical conflicts, the intense expression of detoxification behavior appears specific to interactions with *S. invicta*. We suggest that the behavior of *N. fulva* of applying toxic formic acid to its own cuticle may constitute an adaptation to competition with *S. invicta* in South America. In some South American ant assemblages, *N. fulva* is dominant to *S. invicta* but subordinate to species below *S. invicta* in the assemblage dominance hierarchy (*8*). This intransitive interaction, rare in ant assemblages, may be a hallmark, from their ancestral range, of this competitor-specific defensive adaptation.

The use of defensive compounds to achieve competitive dominance is widespread and amazingly varied in ants (*19*, *20*). Particularly potent defensive chemistries can even protect native species from extirpation by dominant invaders (*21*). However, achieving competitive dominance by self-applying a chemical as an antidote to a competitor's venom is remarkable. The ability of *N. fulva* to detoxify fire ant venom is probably a key factor contributing to the ecologically important population-level displacement of imported fire ants by *N. fulva* that is underway in areas of the southern United States (*11*).

References and Notes

1. G. J. Vermeij, *Science* **253**, 1099–1104 (1991).
2. W. F. Buren, G. E. Allen, W. H. Whitcomb, F. E. Lennartz, R. N. Williams, *J. N.Y. Entomol. Soc.* **82**, 113 (1974).
3. J. P. Pitts, thesis, University of Georgia, Athens, GA (2002).
4. A. L. Wild, *Zootaxa* **1622**, 1–55 (2007).
5. G. L. Mayr, *Verh. Zool. -Bot. Ges. Wien* **12**, 649 (1862).
6. C. Emery, *Boll. Soc. Entomol. Ital.* **37**, 107 (1906).
7. L. A. Calcaterra, F. Cuezzo, S. M. Cabrera, J. A. Briano, *Ann. Entomol. Soc. Am.* **103**, 71–83 (2010).
8. D. H. Feener Jr. *et al.*, *Ecology* **89**, 1824–1836 (2008).
9. E. G. LeBrun *et al.*, *Ecology* **88**, 63–75 (2007).
10. W. R. Tschinkel, *The Fire Ants* (Belknap Press of Harvard Univ. Press, Cambridge, MA, 2006).
11. E. G. LeBrun, J. Abbott, L. E. Gilbert, *Biol. Invas.* **15**, 2429–2442 (2013).
12. M. S. Blum, J. R. Walker, P. S. Callahan, A. F. Novak, *Science* **128**, 306–307 (1958).
13. L. Greenberg *et al.*, *Ann. Entomol. Soc. Am.* **101**, 1162–1168 (2008).
14. Methods are described in the supplementary materials.
15. J. Chen *et al.*, *Toxicon* **76**, 160–166 (2013).
16. B. D. Jackson, E. D. Morgan, *Chemoecology* **4**, 125–144 (1993).
17. M. S. Blum, *J. Toxicol. Toxin Rev.* **11**, 115–164 (1992).
18. L. D. dos Santos *et al.*, *J. Proteome Res.* **9**, 3867–3877 (2010).
19. A. N. Andersen, M. S. Blum, T. H. Jones, *Oecologia* **88**, 157–160 (1991).
20. A. Buschinger, U. Maschwitz, in *Defensive Mechanisms in Social Insects,* H. R. Hermann, Ed. (Praeger, New York, 1984), pp. 95–150.
21. T. R. Sorrells *et al.*, *PLOS ONE* **6**, e18717 (2011).

Acknowledgments: We thank M. Marischen and P. Diebold for technical assistance and N. Youssef and J. Oliver for providing *S. richteri*. E. Sarnat provided a technical drawing, and S. Stokes assisted in formulating the formic acid solution. R. Plowes provided useful discussion. Funding was provided by the Helen C. Kleberg and Robert J. Kleberg Foundation and the Lee and Ramona Bass Foundation. Data are archived at the Dryad Digital Repository, doi: 10.5061/dryad.5t110.

Supplementary Materials

www.sciencemag.org/content/343/6174/1014/suppl/DC1
Materials and Methods
Fig. S1
Tables S1 and S2
References (*22*–*33*)
Movie S1

11 September 2013; accepted 22 January 2014
10.1126/science.1245833

Resurrecting Surviving Neandertal Lineages from Modern Human Genomes

Benjamin Vernot and Joshua M. Akey*

Anatomically modern humans overlapped and mated with Neandertals such that non-African humans inherit ~1 to 3% of their genomes from Neandertal ancestors. We identified Neandertal lineages that persist in the DNA of modern humans, in whole-genome sequences from 379 European and 286 East Asian individuals, recovering more than 15 gigabases of introgressed sequence that spans ~20% of the Neandertal genome (false discovery rate = 5%). Analyses of surviving archaic lineages suggest that there were fitness costs to hybridization, admixture occurred both before and after divergence of non-African modern humans, and Neandertals were a source of adaptive variation for loci involved in skin phenotypes. Our results provide a new avenue for paleogenomics studies, allowing substantial amounts of population-level DNA sequence information to be obtained from extinct groups, even in the absence of fossilized remains.

Hybridization between closely related species, and the concomitant transfer or introgression of DNA, is widespread in nature (*1*, *2*). In hominin evolution, the sequencing of Neandertals (*3*) and their sister lineage, Denisovans (*4*, *5*), provided evidence for introgression of these lineages into modern humans. Specifically, ~1 to 3% of each non-African human genome is estimated to have been inherited from Neandertals (*3*, *5*). Although initial inferences of introgression between Neandertals and humans may not have been robust to alternative explanations—most notably, archaic population structure (*3*, *6*)—subsequent analyses have provided evidence for gene flow (*7*–*9*).

We hypothesized that a substantial amount of the Neandertal genome may be recovered from the analysis of contemporary humans despite the limited amounts of admixture, as introgressed sequences may vary among individuals (Fig. 1A). Coalescent simulations for a broad range of admixture models suggest that 35 to 70% of the Neandertal genome persists in the DNA of present-day humans (figs. S1 and S2) (*10*). By identifying Neandertal sequences from a large sample of modern humans, we hope to discover surviving

Department of Genome Sciences, University of Washington, Seattle, WA 98195, USA.

*Corresponding author. E-mail: akeyj@uw.edu

lineages that may come from multiple archaic ancestors (Fig. 1A), allowing for the recovery of population-level data.

To identify surviving Neandertal lineages, we developed a two-stage computational strategy (fig. S3) (*10*). First, we identify candidate introgressed sequences by using an extension of a previously developed summary statistic referred to as S^* (*11*), which is sensitive to the signatures of introgression (Fig. 1B) and is calculated without using the Neandertal reference genome. We performed coalescent simulations for a wide variety of demographic scenarios and found that our implementation of S^* can distinguish introgressed from nonintrogressed sequences (Fig. 1C and fig. S4). Second, we refine the set of candidate introgressed sequences using an orthogonal approach by comparing them to the Neandertal reference genome and testing whether they match significantly more than expected by chance (*10*). We estimate that the use of S^* alone, as compared to our two-staged approach, would recover ~30% of Neandertal lineages at a false discovery rate (FDR) = 20% (fig. S5) (*10*).

We applied this framework to whole-genome sequences from 379 Europeans and 286 East Asians from the 1000 Genomes Project (table S1) (*12*). Specifically, we calculated S^* in 50-kb sliding windows (tables S2 to S8) (*10*) and used a computationally efficient approach to determine statistical significance through coalescent simulations (fig. S6) (*10*). At an S^* threshold corresponding to $P \leq 0.01$, we identified ~40 Gb of candidate introgressed sequence. Note that S^* P values are robust to demographic uncertainty (fig. S7). The distribution of Neandertal-match P values for this set of candidate introgressed sequences (Fig. 1D) demonstrates a strong skew toward zero, consistent with the hypothesis that these sequences are strongly enriched for Neandertal lineages. The distribution of Neandertal-match P values for sequences that do not possess significant evidence of introgression, as revealed by S^*, is approximately uniform (Fig. 1D) (*10*), indicating that our statistical approach is able to distinguish between introgressed and nonintrogressed lineages (fig. S8) (*10*).

At FDR = 5%, we identified more than 15 Gb of introgressed sequence across all individuals, spanning ~20% (600 Mb) of the Neandertal genome (Fig. 1E and table S9). Of the 600 Mb of distinct sequence, ~25% (149 Mb) was shared between Europeans and East Asians. On average, we found 23 Mb of introgressed sequence per individual (Fig. 1F), with East Asian individuals inheriting 21% more Neandertal sequence than Europeans. Within subpopulations, we found small but statistically significant variation in the amount of introgressed sequence among Europeans (Kruskal-Wallis rank sum test, $P = 4.2 \times 10^{-12}$), but not among East Asians ($P = 0.43$).

The average length of introgressed haplotypes was ~57 kb (Fig. 2A), and ~26% of all protein-coding genes had one or more exons that overlapped a Neandertal sequence (Fig. 2B). On a broad scale, the genomic distribution of Nean-

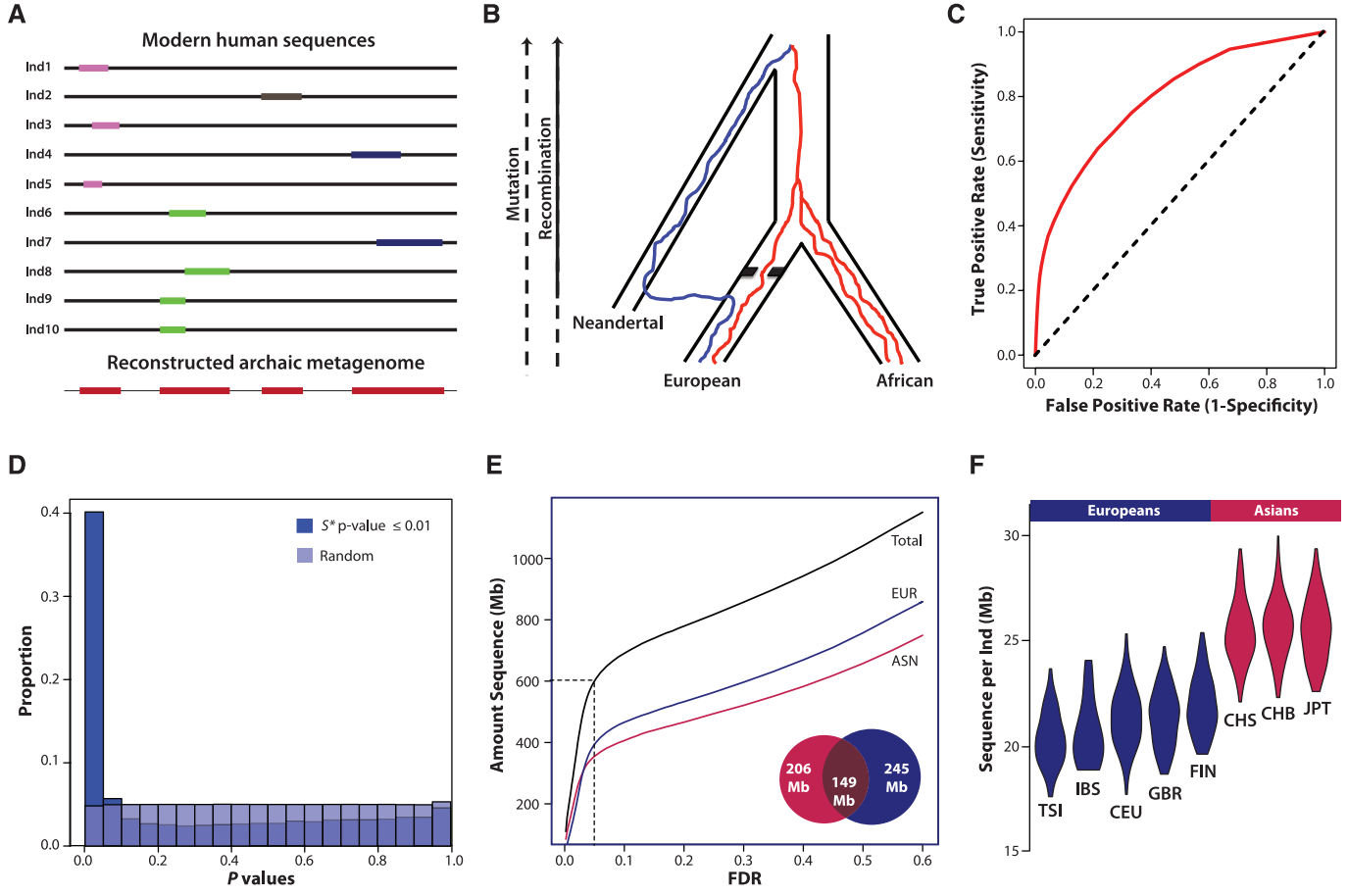

Fig. 1. Recovering Neandertal lineages from the DNA of modern humans. (**A**) Schematic representation illustrating that low levels of introgression may facilitate the recovery of substantial amounts of archaic sequence. Lines represent DNA from contemporary individuals, and colored boxes indicate archaic sequences. Different colored boxes represent sequences inherited from distinct archaic ancestors. (**B**) Genealogies of loci in Europeans and Africans in the presence of introgression. The expected signature of an introgressed lineage (blue) that our method exploits is high levels of divergence that persists over relatively long haplotype blocks. (**C**) Receiver operator curve (red) illustrating the performance of S^* for detecting an introgressed sequence in simulated data (*10*). The black diagonal dashed line represents random predictions. (**D**) Distribution of P values testing for an enrichment of Neandertal variants for S^* candidate and randomly selected regions. (**E**) Amount of Neandertal sequence recovered as a function of FDR. The inset Venn diagram shows the amount of sequence overlap between East Asians (ASN) and Europeans (EUR) at a FDR of 5%. (**F**) Violin plots showing the distribution of the amount of introgressed sequence identified per individual for East Asian and European populations (population abbreviations are described in table S1).

dertal lineages exhibits marked heterogeneity, with particular chromosomal arms, such as 8q and 17q, depleted of Neandertal sequence (Fig. 2A). These qualitative patterns were confirmed by multiple logistic regression, which showed that chromosomal arm was a significant predictor ($P < 10^{-16}$) of the odds that a 50-kb window possessed introgressed sequence (*10*) (Fig. 2C and figs. S9 and S10). Furthermore, odds ratios were negatively correlated with fixed differences between modern humans and Neandertals (Fig. 2D) (Spearman's $\rho = -0.80$, $P < 5.8 \times 10^{-8}$). A strong depletion of Neandertal lineages spanning ~17 Mb on 7q encompasses the *FOXP2* locus (Fig. 2A), a transcription factor that plays an important role in human speech and language (*13*). The observed negative correlation between odds ratio and divergence remained significant when East Asians and Europeans were analyzed separately (fig. S11) and when explicitly controlling for the presence of Neandertal lineages in modern humans (*10*) (figs. S12 and S13). These results suggest that sequence divergence between modern humans and Neandertals was a barrier to gene flow in some regions of the genome and was associated with deleterious fitness consequences (*14*).

We next leveraged the catalog of introgressed sequences in East Asians and Europeans to refine admixture models and infer parameters of gene flow between modern humans and Neandertals (figs. S14 and S15). Specifically, with the use of an approximate Bayesian computation framework (*10*), we statistically tested a model with a single pulse of introgression into the common ancestor of Europeans and East Asians (*3*), as well as a second model with gene flow both in the common ancestor and a second, smaller pulse into East Asians shortly after the two populations split (Fig. 3A). Consistent with recent inferences (*5*, *9*), observed patterns of introgression were incompatible with a one-pulse model (Fig. 3B), suggesting that gene flow between Neandertals and humans occurred multiple times. Although we varied many parameters of each model (*10*) (fig. S14), only the ratio of ancestral effective population size between Europeans and East Asians (N_e^{EUR}/N_e^{ASN}) and the relative amount of introgression between the second and first pulse (m_2/m_1) had appreciable effects on model fit (Fig. 3B). We estimate that

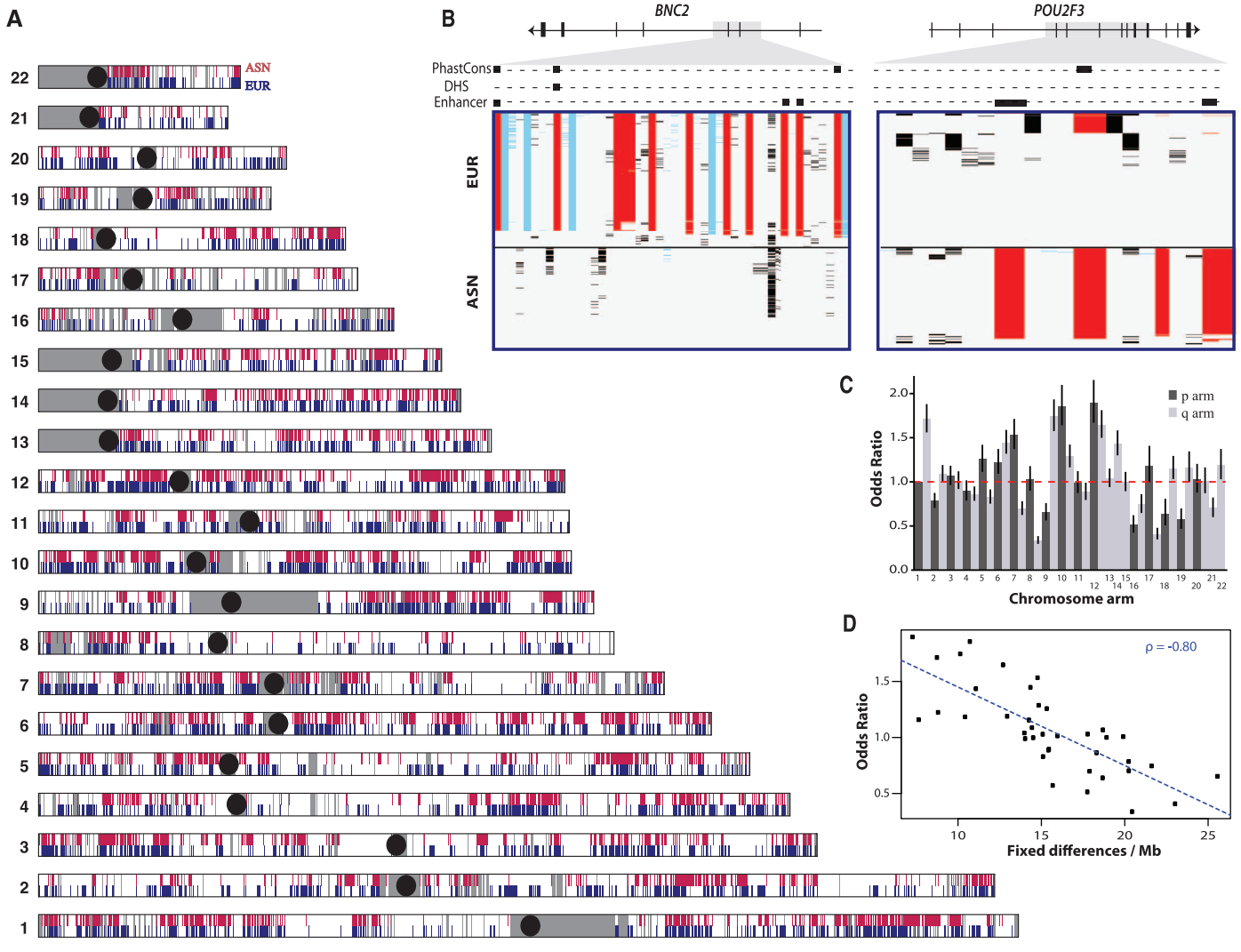

Fig. 2. Genomic distribution of surviving Neandertal lineages. (**A**) Neandertal lineages identified in East Asians (ASN, red) and Europeans (EUR, blue). Gray shading denotes regions that did not pass filtering criteria (*10*); black circles represent centromeres. (**B**) Visual genotype illustrations of introgressed sequences identified in the *BNC2* and *POU2F3* genes. Rows denote individuals, columns indicate variant sites, and rectangles are colored according to genotype (red, predicted Neandertal variant that matches the allele present in the Neandertal reference genome; blue, predicted Neandertal variant that does not match the allele present in the Neandertal reference genome; black, other variants). Introgressed variants that overlap a PhastCons conserved element, DNaseI hypersensitive site (DHS), or putative enhancer elements are shown as boxes (*10*). (**C**) Odds of finding an introgressed lineage on each chromosomal arm calculated from a logistic regression model (*10*). Odds ratios (ORs) are expressed using chromosome 1p as the baseline level. Horizontal bars represent 95% CIs. (**D**) Relation between the OR and the number of fixed differences per megabase between humans and Neandertals. ρ, Spearman's rank correlation coefficient.

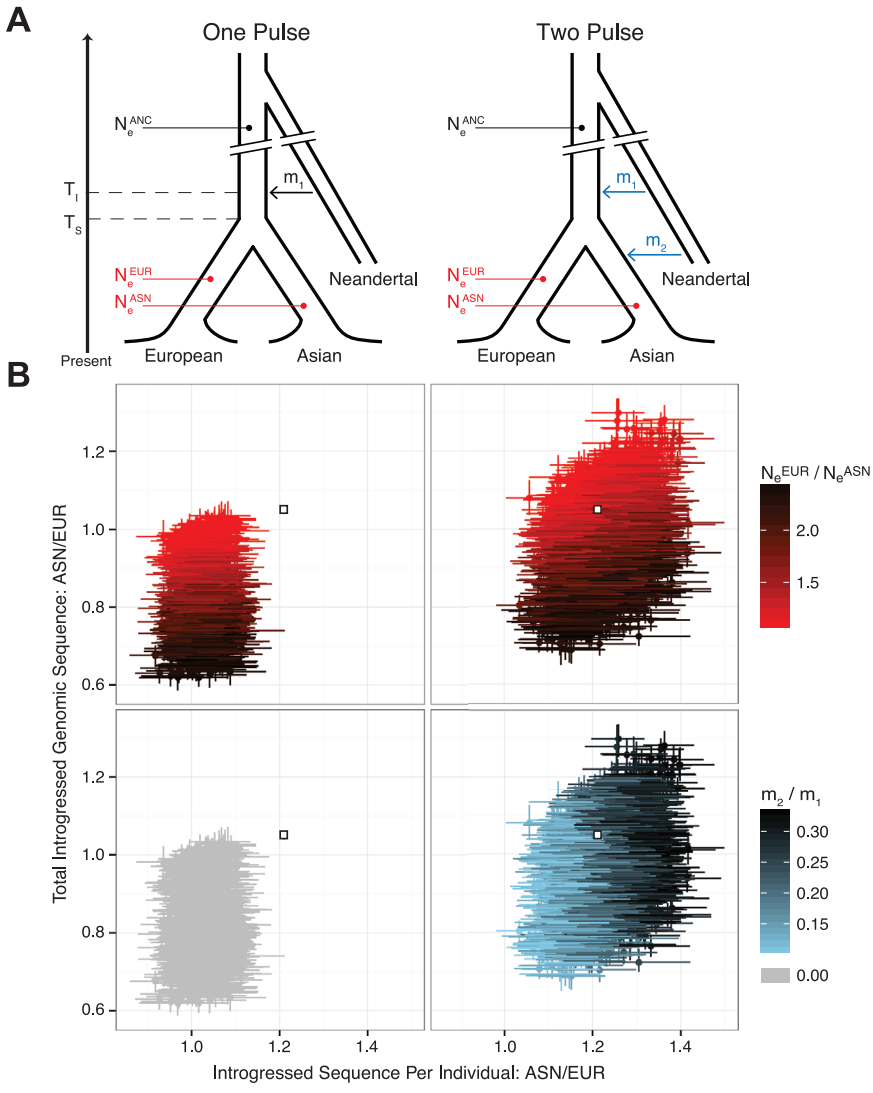

Fig. 3. Organization and characteristics of Neandertal sequence in Europeans and East Asians suggests at least two admixture events. (**A**) Schematic diagrams of the one- and two-pulse admixture models. N_e^{ANC}, N_e^{ASN}, and N_e^{EUR} denote effective population sizes of the ancestral, East Asian, and European populations, respectively. In the one-pulse model, gene flow (m_1) between Neandertals and the ancestors of Europeans and East Asians occurs at time T_I. In the two-pulse model, a second pulse of gene flow (m_2) occurs into East Asians shortly after the divergence of Europeans and East Asians at time T_S. (**B**) Values of summary statistics calculated from 2000 simulations under each model (red, blue, and grey points; horizontal and vertical bars denote 95% CIs) show that a single-pulse model is incompatible with the observed data (white box, corrected for sample size differences between populations; limits of box denote 95% CI). Simulations that varied N_e^{ASN}/N_e^{EUR} are shown in red, and those with variable m_2/m_1 are shown in blue (color bars indicate parameter values).

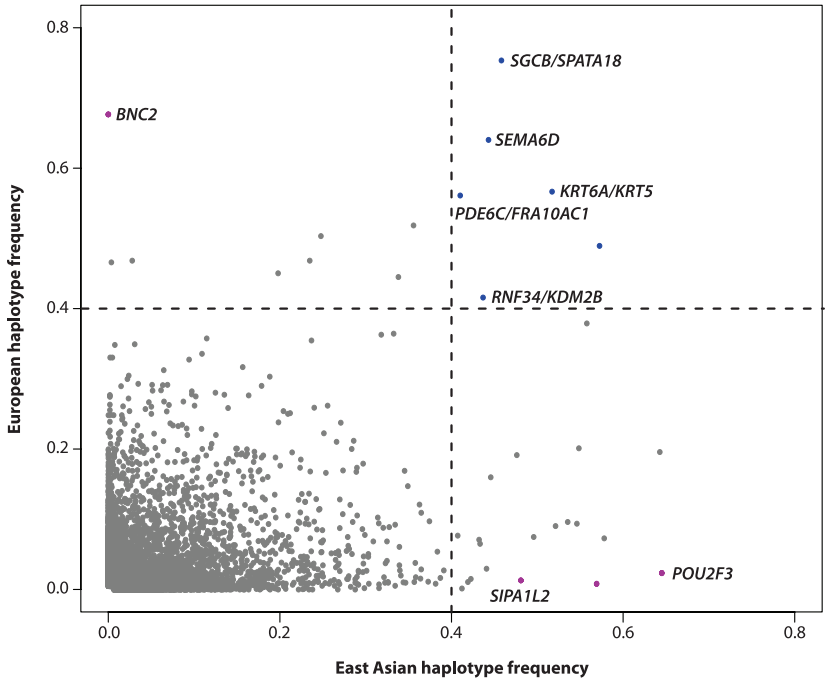

Fig. 4. Signatures of adaptive introgression. A scatter plot of introgressed haplotype frequency in Europeans and East Asians is shown. Significantly differentiated and common shared haplotypes are represented in magenta and blue, respectively. Protein-coding genes that overlap candidate adaptively introgressed loci are also shown.

N_e^{EUR}/N_e^{ASN} is 1.29 [95% confidence interval (CI) of 1.15 to 1.57] and that East Asians received 20.2% (95% CI of 13.4 to 27.1%) more Neandertal sequence in the second pulse (*10*). We note that additional unexplored models may provide a better fit to the data, and refining demographic models of hominin evolution is an important area for future work.

The collection of surviving Neandertal lineages that we identified allows us to search for signatures of adaptive introgression (*15*, *16*). First, we used introgressed variants that exhibit large allele frequency differences between Europeans and East Asians ($F_{ST} > 0.40$, $P < 0.001$ by simulation) (*10*) to identify four significantly differentiated regions (Fig. 4 and table S10) (*10*). Introgressed haplotypes in two of these regions span genes that play important roles in the integumentary system: *BNC2* on chromosome 9 and *POU2F3* on chromosome 11. *BNC2* encodes a zinc finger protein expressed in keratinocytes and other tissues (*17*) and has been associated with skin pigmentation levels in Europeans (*18*). The adaptive haplotype has a frequency of ~70% in Europeans and is completely absent in East Asians (Fig. 2B). *POU2F3* is a homeobox transcription factor expressed in the epidermis and mediates keratinocyte proliferation and differentiation (*19*, *20*). The adaptive haplotype in East Asians has a frequency of ~66% and is found at less than 1% frequency in Europeans (Fig. 2B). No coding introgressed variants were found in *BNC2* or *POU2F3*, although several highly differentiated introgressed variants were located in functional noncoding elements (*21*) (Fig. 2B), suggesting that modern humans acquired adaptive regulatory sequences at these loci. We also searched for shared signatures of adaptive introgression between East Asians and Europeans, identifying six distinct regions that have introgressed haplotype frequencies greater than 40% in both populations (Fig. 4 and table S11) ($P < 10^{-4}$ by simulation) (*10*). One of these regions lies in the type II cluster of keratin genes on 12q13 (table S11), further suggesting that Neandertals provided modern humans with adaptive variation for skin phenotypes. In total, 8 of the 10 candidate introgressed regions overlap protein-coding genes (Fig. 4).

This study shows that the fragmented remnants of the Neandertal genome carried in the DNA of modern humans can be robustly identified, allowing, in aggregate, substantial amounts of Neandertal sequence to be recovered. In principle, our approach can be used in the absence of an archaic reference sequence, potentially allowing the discovery and characterization of previously unknown hominins that interbred with modern humans (*22*–*24*). This fossil-free paradigm of sequencing archaic genomes holds considerable promise for revealing insights into hominin evolution, the population genetics characteristics of archaic hominins, how introgression has influenced extant patterns of human genomic diversity, and narrowing the search for genetic changes that endow distinctly human phenotypes.

References and Notes

1. A. D. Twyford, R. A. Ennos, *Heredity* **108**, 179–189 (2012).
2. D. Zinner, M. L. Arnold, C. Roos, *Evol. Anthropol.* **20**, 96–103 (2011).
3. R. E. Green *et al.*, *Science* **328**, 710–722 (2010).
4. D. Reich *et al.*, *Nature* **468**, 1053–1060 (2010).
5. M. Meyer *et al.*, *Science* **338**, 222–226 (2012).
6. A. Eriksson, A. Manica, *Proc. Natl. Acad. Sci. U.S.A.* **109**, 13956–13960 (2012).
7. M. A. Yang, A. S. Malaspinas, E. Y. Durand, M. Slatkin, *Mol. Biol. Evol.* **29**, 2987–2995 (2012).
8. S. Sankararaman, N. Patterson, H. Li, S. Pääbo, D. Reich, *PLOS Genet.* **8**, e1002947 (2012).
9. J. D. Wall *et al.*, *Genetics* **194**, 199–209 (2013).
10. Supplementary materials are available on *Science* Online.
11. V. Plagnol, J. D. Wall, *PLOS Genet.* **2**, e105 (2006).
12. G. R. Abecasis *et al.*, *Nature* **491**, 56–65 (2012).
13. W. Enard *et al.*, *Nature* **418**, 869–872 (2002).
14. M. Currat, L. Excoffier, *Proc. Natl. Acad. Sci. U.S.A.* **108**, 15129–15134 (2011).
15. F. L. Mendez, J. C. Watkins, M. F. Hammer, *Am. J. Hum. Genet.* **91**, 265–274 (2012).
16. L. Abi-Rached *et al.*, *Science* **334**, 89–94 (2011).
17. A. Vanhoutteghem, P. Djian, *Proc. Natl. Acad. Sci. U.S.A.* **103**, 12423–12428 (2006).
18. L. C. Jacobs *et al.*, *Hum. Genet.* **132**, 147–158 (2013).
19. A. Cabral, D. F. Fischer, W. P. Vermeij, C. Backendorf, *J. Biol. Chem.* **278**, 17792–17799 (2003).
20. H. Takemoto *et al.*, *J. Dermatol. Sci.* **60**, 203–205 (2010).
21. B. E. Bernstein *et al.*, *Nature* **489**, 57–74 (2012).
22. J. D. Wall, K. E. Lohmueller, V. Plagnol, *Mol. Biol. Evol.* **26**, 1823–1827 (2009).
23. M. F. Hammer, A. E. Woerner, F. L. Mendez, J. C. Watkins, J. D. Wall, *Proc. Natl. Acad. Sci. U.S.A.* **108**, 15123–15128 (2011).
24. J. Lachance *et al.*, *Cell* **150**, 457–469 (2012).

Acknowledgments: We thank members of the Akey laboratory, S. Browning, B. Browning, and J. Duffy for critical feedback related to this work; S. Pääbo for providing access to high-coverage Neandertal sequence data; and L. Jáuregui for help in figure preparation. A description of where sequence data used in our analyses can be found in the supplementary materials. Introgressed regions and variants can be downloaded from http://akeylab.gs.washington.edu/downloads.shtml. J.M.A. is a paid consultant of Glenview Capital.

Supplementary Materials

www.sciencemag.org/content/343/6174/1017/suppl/DC1
Materials and Methods
Figs. S1 to S15
Tables S1 to S11
References (*25*–*45*)

12 September 2013; accepted 6 December 2013
Published online 29 January 2014;
10.1126/science.1245938

Molecular Editing of Cellular Responses by the High-Affinity Receptor for IgE

Ryo Suzuki,[1] Sarah Leach,[1] Wenhua Liu,[2] Evelyn Ralston,[2] Jörg Scheffel,[1] Weiguo Zhang,[3] Clifford A. Lowell,[4] Juan Rivera[1]*

Cellular responses elicited by cell surface receptors differ according to stimulus strength. We investigated how the high-affinity receptor for immunoglobulin E (IgE) modulates the response of mast cells to a high- or low-affinity stimulus. Both high- and low-affinity stimuli elicited similar receptor phosphorylation; however, differences were observed in receptor cluster size, mobility, distribution, and the cells' effector responses. Low-affinity stimulation increased receptor association with the Src family kinase Fgr and shifted signals from the adapter LAT1 to the related adapter LAT2. LAT1-dependent calcium signals required for mast cell degranulation were dampened, but the role of LAT2 in chemokine production was enhanced, altering immune cell recruitment at the site of inflammation. These findings uncover how receptor discrimination of stimulus strength can be interpreted as distinct in vivo outcomes.

It has long been recognized that there are many subtleties in how receptors function to determine a cell's response. For example, vegetative growth of the yeast *Saccharomyces cerevisiae* is elicited by low pheromone concentrations recognized by the pheromone receptor Ste2, whereas intermediate and high pheromone concentrations sensed by this receptor lead to chemotropic growth or mating, respectively (*1*). Mathematical modeling suggests that yeast translate pheromone concentration as the duration of the transmitted signal (*2*).

We explored how the high-affinity immunoglobulin E (IgE) receptor FcεRI discriminates high- from low-affinity stimulation to modulate the mast cells' effector responses. Engagement of FcεRI on mast cells and basophils is central to allergic responses (*3*, *4*). Allergic individuals may produce IgE antibodies to offending allergens (a term used for allergy-inducing antigens). These IgE antibodies bind [via their crystallizable

[1]Laboratory of Molecular Immunogenetics, National Institute of Arthritis and Musculoskeletal and Skin Diseases, Bethesda, MD 20892, USA. [2]Light Imaging Section, Office of Science and Technology, National Institute of Arthritis and Musculoskeletal and Skin Diseases, Bethesda, MD 20892, USA. [3]Department of Immunology, Duke University School of Medicine, Durham, NC 27710, USA. [4]Department of Laboratory Medicine, University of California, San Francisco, CA 94143, USA.

*Corresponding author. E-mail: juan_rivera@nih.gov

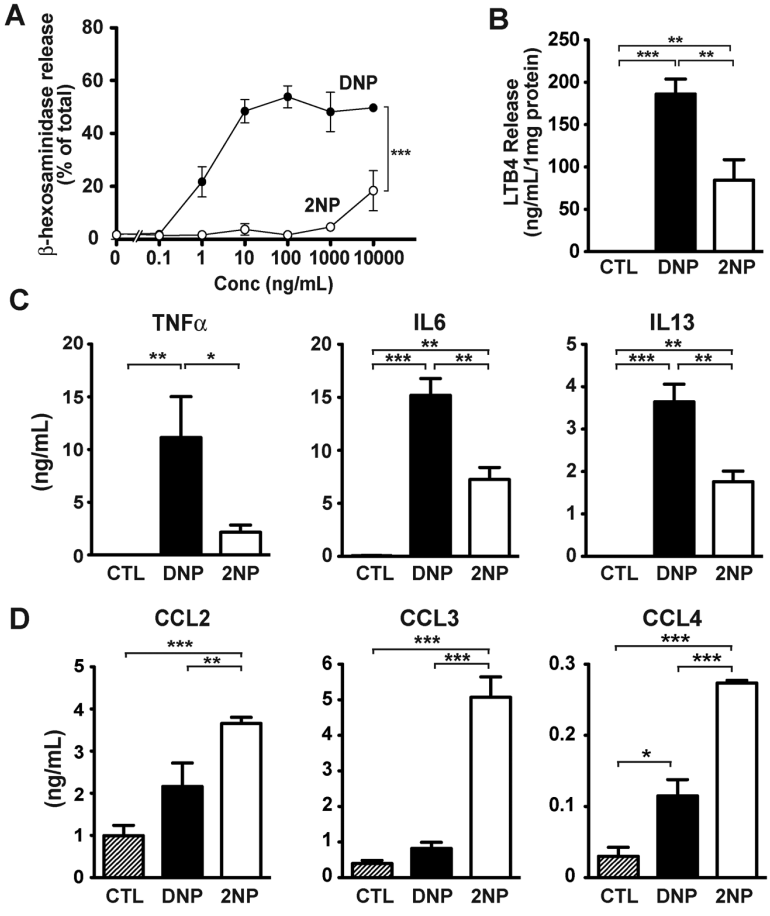

Fig. 1. Mast cell responses differ following DNP or 2NP stimulation of FcεRI. (**A**) Degranulation (as measured by β-hexosaminidase release) of wild-type (WT) BMMCs after stimulation with indicated concentrations of DNP or 2NP. ***$P < 0.001$; two-way analysis of variance (ANOVA). (**B**) Leukotriene B_4 (LTB_4) secretion from BMMCs induced by treatment with 2NP (3000 ng/ml) is less than that with DNP (30 ng/ml). **$P < 0.01$, ***$P < 0.001$; one-way ANOVA. (**C**) Tumor necrosis factor−α (TNFα), interleukin-6 (IL6), and IL13 are similarly affected at the concentrations of DNP and 2NP indicated in (B). *$P < 0.05$, **$P < 0.01$, ***$P < 0.001$; one-way ANOVA. (**D**) Release of CCL2, CCL3, and CCL4 is increased after stimulation with 2NP relative to DNP [conditions as in (B)]. **$P < 0.01$, ***$P < 0.001$; one-way ANOVA. Data were collected from four to eight individual experiments.

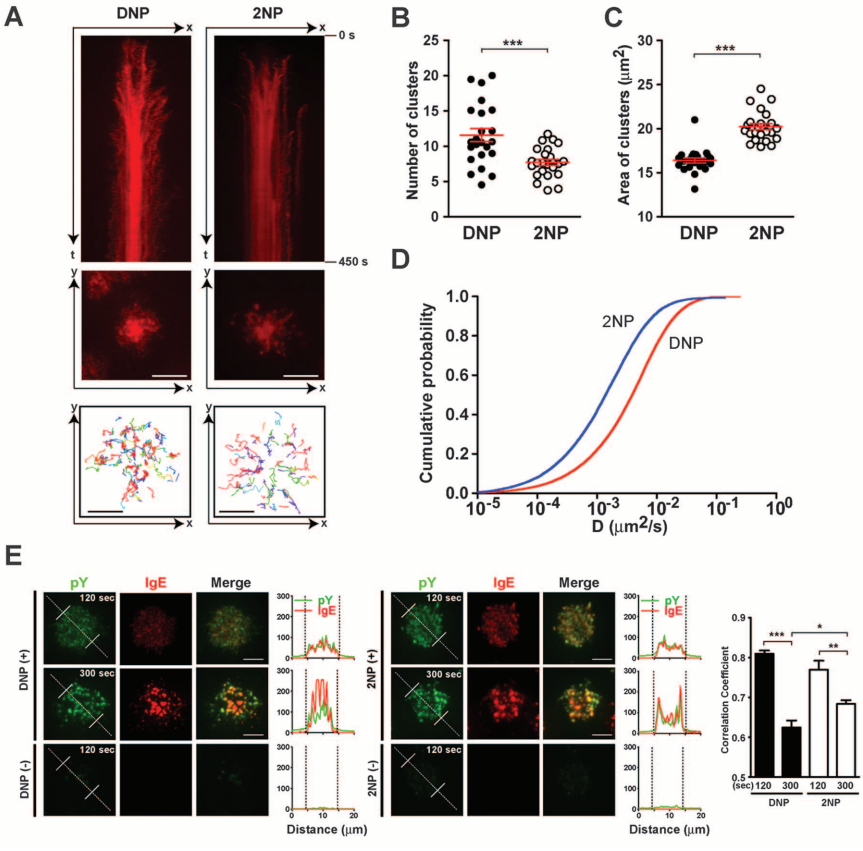

Fig. 2. Characteristics of FcεRI clusters differ with 2NP or DNP stimulation of BMMCs. (**A**) Kymographs of a mast cell labeled with Alexa Fluor 568–labeled IgE (as an FcεRI marker) as captured by TIRF microscopy. Static view of IgE-FcεRI microcluster dynamics (trajectory) captured upon cell contact with DNP or 2NP imbedded in a planar supported lipid bilayer (see supplementary materials) is shown in two dimensions (*x* and *y*) of movement. Movement of receptors clusters with time (t) is also shown. Sequential image sections for 0.5 to 450 s are shown in chronological order. Scale bars, 5 μm. (**B**) The average number of IgE-FcεRI clusters on DNP- or 2NP-imbedded planar supported lipid bilayer is different. Red bars are means ± SE from 24 individual cells. ***$P < 0.001$, Student's *t* test. (**C**) Average area of IgE-FcεRI clusters on DNP- or 2NP-imbedded planar supported lipid bilayers differs. Red bars are means ± SE from 24 individual cells. ***$P < 0.001$, Student's *t* test. (**D**) Cumulative probability distribution of the diffusion coefficient of individual FcεRI clusters at any given time from analysis of 7835 to 11,198 FcεRI clusters on 24 different cells for DNP and 2NP. (**E**) Tyrosine phosphorylation with IgE-FcεRI microclusters in DNP- or 2NP-treated cells as determined by intracellular staining with antibodies to phosphotyrosine. Fluorescence intensity in cross section (white dotted line) is shown. Localization was analyzed for more than 40 cells in each condition. Scale bars, 5 μm. *$P < 0.05$, **$P < 0.01$, ***$P < 0.001$; one-way ANOVA. Data are representative of at least three independent experiments.

fragment (Fc)] to FcεRI with high affinity, with the half-life of IgE bound to FcεRI measured in days (*5*). Interaction of antigen with FcεRI-bound antigen-specific IgE clusters the individual receptors (*6*, *7*); this step is required for generation of intracellular signals that cause mast cells and basophils to release allergic mediators (*3*, *8*). The antigen-binding (Fab) portion of FcεRI-bound IgE antibodies may differ in their affinity for the antigen [as seen in allergic individuals (*9*)], presumably affecting the duration of the transmitted signal and subsequent outcome. Whether FcεRI functionally distinguishes differences in the affinity of IgE antibody and antigen interactions is not clear. To investigate this, we used two previously described antigens (*10*): dinitrophenyl-caproate-Fab (DNP, high affinity) and 2-nitrophenyl-caproate-Fab (2NP, low affinity). These differ in their relative affinities for binding to FcεRI-bound DNP-specific IgE by approximately three orders of magnitude. In bone marrow–derived mouse mast cells (BMMCs) (*11*), FcεRI phosphorylation was similar with approximately 100 times as much 2NP (3000 ng/ml) as DNP (30 ng/ml) (fig. S1A); the kinetics of FcεRI phosphorylation were unaltered at these concentrations (fig. S1B). However, cellular responses differed as 2NP elicited less than 20% of the DNP-induced degranulation response (Fig. 1A) at 3000 ng/ml and 30 ng/ml, respectively, and showed reduced leukotriene B4 (Fig. 1B) and cytokine production (Fig. 1C) but enhanced chemokine production (Fig. 1D). DNP- and 2NP-induced responses required the presence of DNP-specific IgE (fig. S2, A and B), and 2NP treatment had no effect on responses initiated through ovalbumin (OVA)–specific IgE (fig. S2, C and D).

To explore the differences in DNP- and 2NP-induced FcεRI clustering, we used total internal reflection fluorescence (TIRF) microscopy to study DNP-specific IgE-bearing mast cells after their contact with either a DNP- or 2NP-imbedded planar supported lipid bilayer, while maintaining equal receptor phosphorylation and differences in mast cell degranulation (fig. S3, A and B). Exposure to DNP resulted in highly mobile receptor clusters that moved from the cell periphery toward the cell center to form a synapse-like localization as described for the T cell receptor (*12*, *13*) (movie S1). In contrast, treatment with 2NP revealed slower movement of receptor clusters and a diffuse distribution with a loosely organized synapse-like structure at the cell center (movie S2). Analysis of receptor cluster movement with time (Fig. 2A) revealed greater numbers of receptor clusters at the periphery in 2NP-treated cells. The total number of clusters formed at any given time was greater upon DNP treatment (Fig. 2B), but the area occupied by these clusters was larger after 2NP treatment (Fig. 2C). The relative mobility of receptor clusters in cells treated with 2NP was on average one-third that of clusters formed by DNP treatment (Fig. 2D). Phosphotyrosine (a hallmark of intracellular signaling) was localized with both DNP- and 2NP-formed receptor clusters, although stronger colocalization was evident after 2NP treatment (Fig. 2E). These findings demonstrate that the FcεRI clusters induced by DNP or 2NP differ spatiotemporally.

We explored whether differences in the spatiotemporal behavior of receptor clustering by DNP

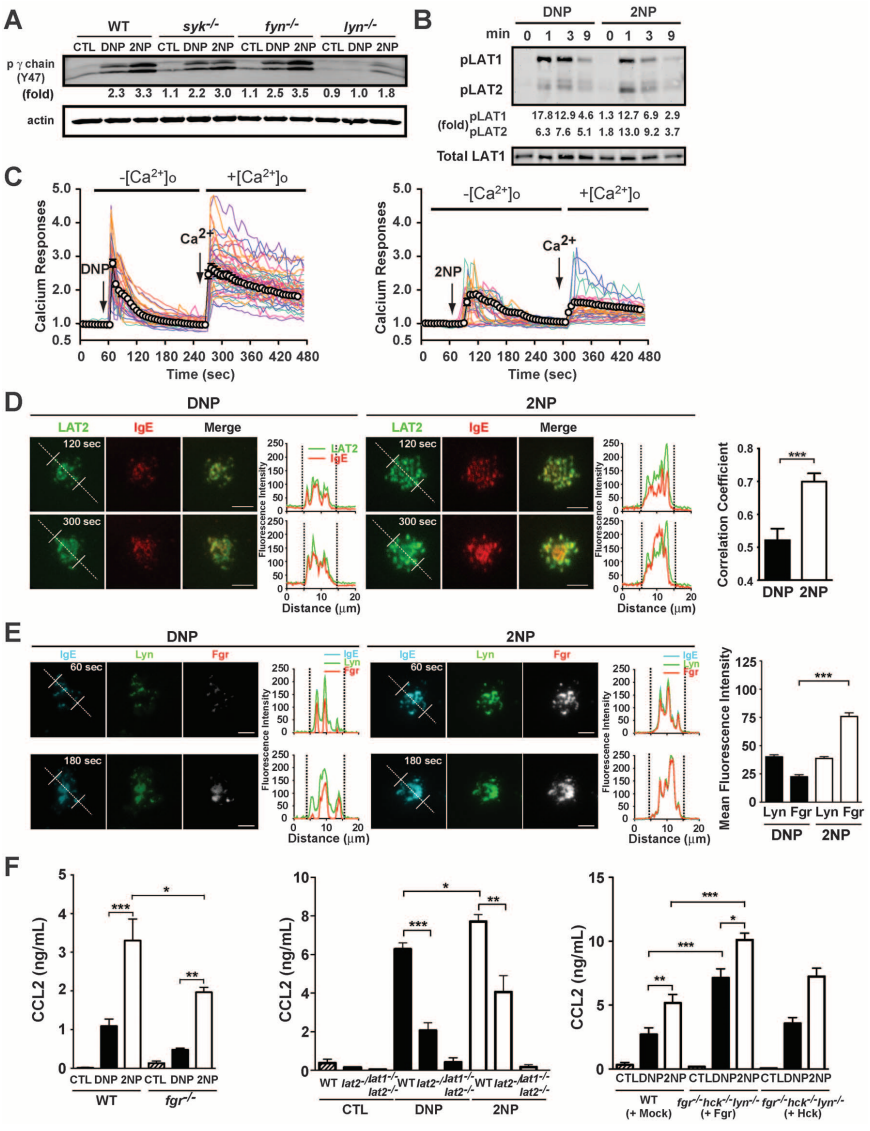

Fig. 3. Distinct molecular signals are induced in 2NP-treated BMMCs: Enhanced role for Fgr and LAT2. (**A**) Phosphorylation of the FcεRI (ITAMγ Y47) in WT, *syk*$^{-/-}$, *fyn*$^{-/-}$, and *lyn*$^{-/-}$ BMMCs after DNP (30 ng/ml) or 2NP (3000 ng/ml) treatment. Relative increase is normalized to the control (CTL) for WT. (**B**) Kinetics of LAT1 and LAT2 phosphorylation detected by Western blot differ in cells treated with DNP or 2NP. Relative increase is normalized to DNP (0 min). (**C**) Single cell analysis of BMMC calcium responses in the absence or presence of extracellular Ca (–[Ca^{2+}]$_o$; +[Ca^{2+}]$_o$) as indicated. Fluorescence intensity of a single cell with time (more than 300 cells were monitored in total) was measured and shown as the "calcium response" normalized to the baseline fluorescence. Single cells, solid colored lines; averaged responses, black line with open circles. (**D**) Localization of the LAT2-RFP (green) in *lat2*$^{-/-}$ BMMCs with Alexa Fluor 647–conjugated IgE (red, marking FcεRI) after DNP or 2NP treatment. Images were captured by TIRF microscopy at 120 or 300 s. Fluorescence intensities of IgE-FcεRI microclusters and LAT2-RFP are shown in the graphs. Colocalization was analyzed in 15 to 30 cells for each condition. ***$P < 0.001$, Student's t test. Scale bar, 5 μm. (**E**) Fluorescence intensities of Lyn-YFP (green), Fgr-RFP (white), IgE-FcεRI microclusters (cyan) in BMMCs derived from *fgr*$^{-/-}$ *hck*$^{-/-}$ *lyn*$^{-/-}$ mice treated with DNP or 2NP for 60 or 120 s. Mean fluorescence intensity was measured from at least 50 cells for each condition. ***$P < 0.001$, Student's t test. Scale bar, 5 μm. (**F**) CCL2 secretion by BMMCs from the indicated mice. *$P < 0.05$, **$P < 0.01$, ***$P < 0.001$; one-way ANOVA. Data are means ± SE from at least four individual experiments.

or 2NP were translated into changes in FcεRI-generated intracellular signals. Analysis of the phosphorylation of FcεRIγ at Tyr^{47} (Y47) showed increased phosphorylation at this site (Fig. 3A) after cell treatment with 2NP, relative to DNP, and the increased phosphorylation was not dependent on Syk, Fyn, or Lyn; however, Lyn deficiency reduced the overall phosphorylation of FcεRI for both stimuli (*14*). In contrast, phosphorylation of Syk on the activation loop tyrosines (Y519 and Y520), a marker of its activity, was reduced with 2NP treatment (fig. S4A). The adapter molecule LAT1 (linker for activation of T cells–1) is a target of Syk and scaffolds multiple signaling molecules at the plasma membrane, including the phospholipases PLCγ1 and PLCγ2, whose activity is essential for initiating release of calcium from intracellular stores. Phosphorylation of LAT1 (Fig. 3B) and of PLCγ1 and PLCγ2 (fig. S4B) was greater in DNP-treated cells than in 2NP-treated cells. Calcium mobilization, a key regulator of degranulation (*15*), from intracellular or extracellular sources was also greater upon DNP treatment (Fig. 3C), consistent with the better degranulation of DNP-treated cells relative to 2NP-treated cells. Phosphorylation of the LAT1-related adapter LAT2 was increased (Fig. 3B) in 2NP-treated mast cells. Greater colocalization of LAT2 with FcεRI was observed in 2NP-treated cells relative to DNP-treated cells (movies S3 and S4), and these differences (as determined by fluorescence intensity) were quantifiable (Fig. 3D). Thus, the differences in FcεRI clustering by DNP or 2NP alter the balance of molecular signaling, dampening some (i.e., LAT1 and PLCγ phosphorylation) but enhancing others (i.e., LAT2 phosphorylation).

Although the absence of Lyn in mast cells caused decreased phosphorylation of FcεRIγ on Y47 (Fig. 3A), phosphorylation at this site was greater in 2NP-treated cells relative to DNP-treated cells, which suggested the possible phosphorylation of FcεRI by another tyrosine kinase after 2NP treatment. FcεRI phosphorylation was completely inhibited by the Src family kinase selective inhibitor 4-amino-5-(4-chlorophenyl)-7-(*t*-butyl)pyrazolo[3,4-d]pyrimidine (also known as AG1879 or PP2) (fig. S5A). Multiple Src family kinases are expressed in mast cells including Fgr, Fyn, Hck, Lyn, and Yes, although Yes is seemingly restricted to transformed mast cell lines (*16*). Hck deficiency in mast cells results in enhanced FcεRI phosphorylation, and Fyn does not contribute to FcεRI phosphorylation (*17*, *18*), but recent work has suggested that Fgr can associate with FcεRI (*19*) (fig. S5B) and contribute to its function. In mast cells derived from $fgr^{-/-}$ $hck^{-/-}$ $lyn^{-/-}$ mice, we found no phosphorylation of FcεRI, LAT1, or LAT2 (fig. S5C). Reconstitution of these cells with a retrovirus encoding Hck also failed to restore phosphorylation of the aforementioned molecules. However, retroviral reconstitution with Fgr restored the phosphorylation of FcεRI, LAT1, and LAT2, even in the absence of Lyn. Phosphorylation of LAT2 was increased relative to LAT1 (fig. S5C). Localization of FcεRI with Fgr or Lyn in cells reconstituted with both proteins revealed increased colocalization of Fgr in 2NP-treated cells relative to DNP-treated cells but no significant change in Lyn colocalization with FcεRI (movies S5 and S6). The amount of Fgr associated with FcεRI (as determined by fluorescence intensity) in 2NP-treated cells was more than twice that in DNP-treated cells (Fig. 3E). Thus, differences in FcεRI clustering result in changes in the balance of receptor-associated kinases and subsequent downstream signaling. To determine whether Fgr or LAT2 contributed to the enhanced chemokine response observed after 2NP stimulation, we analyzed the chemokine (C-C motif) ligand 2 (CCL2) response of Fgr- or LAT2-deficient mast cells after treatment with DNP or 2NP. Fgr or LAT2 deficiency impaired CCL2 secretion in response to both DNP and 2NP (Fig. 3F). Conversely, overexpression of Fgr enhanced production of CCL2 in response to both DNP and 2NP (Fig. 3F). Fgr or LAT2 deficiency enhanced 2NP-induced mast cell degranulation (fig. S5D), demonstrating negative regulatory control of this response.

Subtle changes in cell signaling may have consequences in vivo. To test this, we used a passive cutaneous anaphylaxis (PCA) model, which

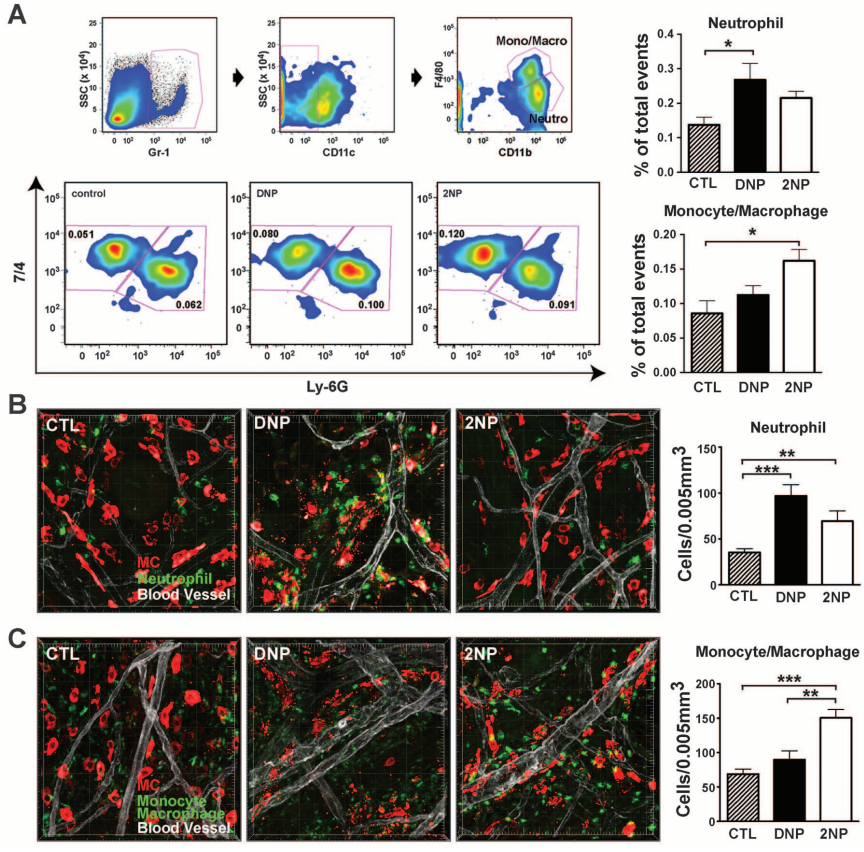

Fig. 4. Immune cell recruitment at the site of inflammation differs in mice treated with DNP or 2NP after passive cutaneous anaphylaxis (PCA). (**A**) Fluorescence-activated cell sorter identification of cell types recruited to the site of inflammation. Monocytes or macrophages and neutrophils were identified as Gr-1^+ (hi) CD11c^- CD11b^+ F4/80^+ (intermediate) neutrophil [7/4]$^+$ Ly-$6G^-$ and Gr-1^+ (hi) CD11c^- CD11b^+ F4/80^+ (intermediate) neutrophil [7/4]$^+$ Ly-$6G^+$, respectively. Data are means ± SE from at least six individual experiments. *P < 0.05; one-way ANOVA. (**B** and **C**) Whole-mount ear tissue immunostaining after PCA reaction reveals differential immune cell recruitment after DNP or 2NP treatment. Mast cells (red) are located along blood vessel (white); degranulation was observed under DNP challenge (middle panel). Total number of neutrophils [green in (B)] or monocyte or macrophages [green in (C)] in random images from six to eight ears per group were counted and normalized per 0.005 mm^3. Data are means ± SE. **P < 0.01, ***P < 0.001; one-way ANOVA. One representative image of at least three independent experiments is shown for (B) and (C).

provides a localized assessment of mast cell responses, maintaining the factor of 100 times the 2NP concentration relative to that of DNP. At 30 min after exposure to DNP or 2NP, vascular permeability as measured by extravasation of Evans blue dye (see supplementary materials) was significantly higher in DNP- than 2NP-treated mice (fig. S6A). Consistent with this result, more mast cells were degranulated in animals treated with DNP. Ear swelling was significantly different 30 min after DNP or 2NP treatment but narrowed with time (fig. S6B), and the increase in the thickness of the dermis was similar at 3 hours after stimulation (fig. S6C). Immune cell infiltration was similarly increased in animals exposed to DNP or 2NP (fig. S6D). By 12 hours after stimulation, the thickness of the dermis returned to that of control mice (fig. S6E) but immune cell infiltrates were still elevated relative to control mice (fig. S6F). Given that an inflammatory response was initiated by either DNP or 2NP, we explored the cell types involved. Gr-1$^+$ CD11c$^-$ CD11b$^+$ cells were distinguished on the basis of the myeloid marker 7/4 [Ly-6B.2, which is somewhat more highly expressed by recently generated inflammatory macrophages (*20*)] from neutrophils as marked by Ly-6G (Fig. 4A). Exposure to DNP caused increased numbers of neutrophils relative to inflammatory macrophages, whereas this ratio was reversed in animals treated with 2NP, consistent with the increased secretion of monocyte- or macrophage-attracting chemokines, such as CCL2, CCL3, and CCL4, after treatment of mast cells with 2NP (Fig. 1D). Whole-mount immunohistochemical analysis of the skin also revealed these differences (Fig. 4, B and C), and skin mast cells from 2NP-treated mice produced greater amounts of CCL2 than did those in the skin of DNP-treated mice (fig. S7). Thus, low-affinity stimulation of FcεRI results in an inflammatory response marked by a shift in the monocyte or macrophage/neutrophil ratio.

Collectively, our findings demonstrate that differences in the affinity of antigen and antibody interactions are discriminated by receptors through qualitative changes in molecular signals resulting in distinct outcomes. This discriminatory ability of receptors may extend beyond the immune system.

References and Notes

1. H. G. Dohlman, J. W. Thorner, *Annu. Rev. Biochem.* **70**, 703–754 (2001).
2. M. Behar, N. Hao, H. G. Dohlman, T. C. Elston, *PLOS Comput. Biol.* **4**, e1000197 (2008).
3. J. P. Kinet, *Annu. Rev. Immunol.* **17**, 931–972 (1999).
4. S. J. Galli, M. Tsai, A. M. Piliponsky, *Nature* **454**, 445–454 (2008).
5. C. Isersky, J. Rivera, S. Mims, T. J. Triche, *J. Immunol.* **122**, 1926–1936 (1979).
6. H. Metzger, *J. Immunol.* **149**, 1477–1487 (1992).
7. N. L. Andrews *et al.*, *Immunity* **31**, 469–479 (2009).
8. U. Blank, J. Rivera, *Trends Immunol.* **25**, 266–273 (2004).
9. D. R. Jackola, L. K. Pierson-Mullany, C. L. Liebeler, M. N. Blumenthal, A. Rosenberg, *Mol. Immunol.* **39**, 367–377 (2002).
10. C. Torigoe, J. K. Inman, H. Metzger, *Science* **281**, 568–572 (1998).
11. E. Razin, *Methods Enzymol.* **187**, 514–520 (1990).
12. C. R. Monks, B. A. Freiberg, H. Kupfer, N. Sciaky, A. Kupfer, *Nature* **395**, 82–86 (1998).
13. A. Grakoui *et al.*, *Science* **285**, 221–227 (1999).
14. V. Parravicini *et al.*, *Nat. Immunol.* **3**, 741–748 (2002).
15. M. Vig *et al.*, *Nat. Immunol.* **9**, 89–96 (2008).
16. A. M. Gilfillan, J. Rivera, *Immunol. Rev.* **228**, 149–169 (2009).
17. H. Hong *et al.*, *Blood* **110**, 2511–2519 (2007).
18. G. Gomez *et al.*, *J. Immunol.* **175**, 7602–7610 (2005).
19. J. H. Lee *et al.*, *J. Immunol.* **187**, 1807–1815 (2011).
20. M. Rosas, B. Thomas, M. Stacey, S. Gordon, P. R. Taylor, *J. Leukoc. Biol.* **88**, 169–180 (2010).

Acknowledgments: Supported by the intramural research program of the National Institute of Arthritis and Musculoskeletal and Skin Diseases and by its Laboratory Animal Care and Use Section and Flow Cytometry Group, Office of Science and Technology. All data are provided in the main paper and supplementary materials. The authors declare no conflicts of interest.

Supplementary Materials

www.sciencemag.org/content/343/6174/1021/suppl/DC1
Materials and Methods
Figs. S1 to S7
Movies S1 to S6
References (*21*–*34*)

8 October 2013; accepted 17 January 2014
Published online 6 February 2014;
10.1126/science.1246976

Cell Surface ABP1-TMK Auxin-Sensing Complex Activates ROP GTPase Signaling

Tongda Xu,[1,2,3] Ning Dai,[4]* Jisheng Chen,[1] Shingo Nagawa,[1,3] Min Cao,[2] Hongjiang Li,[1,5,6] Zimin Zhou,[2] Xu Chen,[5,6] Riet De Rycke,[5] Hana Rakusová,[5,6] Wuyi Wang,[3,7]† Alan M. Jones,[8] Jiří Friml,[5,6,9] Sara E. Patterson,[7] Anthony B. Bleecker,[4]‡ Zhenbiao Yang[1,3,10]§

Auxin-binding protein 1 (ABP1) was discovered nearly 40 years ago and was shown to be essential for plant development and morphogenesis, but its mode of action remains unclear. Here, we report that the plasma membrane–localized transmembrane kinase (TMK) receptor–like kinases interact with ABP1 and transduce auxin signal to activate plasma membrane–associated ROPs [Rho-like guanosine triphosphatases (GTPase) from plants], leading to changes in the cytoskeleton and the shape of leaf pavement cells in *Arabidopsis*. The interaction between ABP1 and TMK at the cell surface is induced by auxin and requires ABP1 sensing of auxin. These findings show that TMK proteins and ABP1 form a cell surface auxin perception complex that activates ROP signaling pathways, regulating nontranscriptional cytoplasmic responses and associated fundamental processes.

Auxin regulates nearly all aspects of plant development and behavior and impinges on a great variety of responses involving cell polarization, expansion, division and differentiation. Exactly how this small-molecule hormone achieves this multitude of diverse roles is largely unexplained, although it may be perceived by multiple functionally distinct auxin perception and signaling systems (*1*–*6*). Members of the nuclear TIR1/AFB F-box protein auxin receptor and AUX/ IAA co-receptor families modulate nuclear gene transcription in response to various auxin concentrations (*1*–*4*).

Independently of the TIR1 family, auxin-binding protein 1 (ABP1) was proposed to perceive extracellular auxin to regulate a plethora of plasma membrane or cytoplasmic responses not necessarily involving gene transcription (*6*–*18*). ABP1 may also coordinate with the TIR1/AFB pathway to regulate gene transcription (*16*, *19*). ABP1 is essential for early embryogenesis, root development, leaf expansion, cell morphogenesis, and subcellular distribution of PIN auxin transporters (*6*, *8*, *9*, *12*, *13*, *15*–*18*, *20*, *21*). ABP1 is required for the auxin-dependent activation of ROPs [Rho-like guanosine triphosphatases (GTPases) from plants] at the plasma membrane,

[1]Center for Plant Cell Biology, Department of Botany and Plant Sciences, University of California, Riverside, CA 92521, USA. [2]Temasek Life Sciences Laboratory, 1 Research Link, National University of Singapore, 117604 Singapore. [3]Shanghai Center for Plant Stress Biology, Shanghai Institutes for Biological Sciences, The Chinese Academy of Sciences, Shanghai 200032, China. [4]Department of Botany, University of Wisconsin, Madison, WI 53706, USA. [5]Department of Plant Systems Biology, VIB and Department of Plant Biotechnology and Bioinformatics, Ghent University, 9052 Gent, Belgium. [6]Bertalanffy Foundation Building, Institute of Science and Technology Austria, Am Campus 1, 3400 Klosterneuburg, Austria. [7]Department of Horticulture, University of Wisconsin, Madison, WI 53706, USA. [8]Departments of Biology and Pharmacology, University of North Carolina, Chapel Hill, Chapel Hill, NC 27599, USA. [9]Mendel Centre for Plant Genomics and Proteomics, Masaryk University, CEITEC MU, CZ-625 00 Brno, Czech Republic. [10]Shanghai Institute of Plant Physiology and Ecology, Shanghai Institutes for Biological Sciences, The Chinese Academy of Sciences, Shanghai 200032, China.

*Present address: Department of Molecular Biology, Massachusetts General Hospital, Boston, MA 02114, USA.
†Present address: Ceres, 1535 Rancho Conejo Boulevard, Thousand Oaks, CA 91320, USA.
‡Deceased.
§Corresponding author. E-mail: yang@ucr.edu

which subsequently regulates cytoskeletal organization and clathrin-mediated endocytosis of PIN proteins (*5*, *17*, *18*, *22*, *23*). However, it is not known how ABP1 transmits the auxin signal to regulate these cytoplasmic responses. Here, we demonstrate that the transmembrane kinase (TMK) members of the receptor-like kinase family interact with ABP1 on the cell surface in an auxin-dependent manner and are required for the auxin-mediated activation of ROP GTPase signaling.

To transduce extracellular auxin to the cytoplasmic responses, secreted ABP1 is expected to communicate with the cytoplasm through a transmembrane docking protein (*17*, *18*, *24*). We hypothesized that TMKs serve as ABP1 docking proteins. TMKs belong to a clade of receptor-like kinases with four functionally overlapping members whose founding member is TMK1. They contain an intracellular kinase domain, a single transmembrane pass, and an extracellular domain with two regions of leucine-rich repeats (LRRs) separated by a non-LRR region. TMKs affect multiple auxin-mediated processes (*25*). We found that *tmk* mutants are affected in the same responses regulated by ABP1. The *tmk1*$^{-/-}$;*tmk2*$^{-/-}$;*tmk3*$^{-/-}$;*tmk4*$^{-/-}$ mutant (*tmk1*$^{-/-}$;*tmk234*) displayed embryo lethality, though with a lower penetrance of lethality as conferred by *abp1* null mutations (fig. S1). Both *tmk1*$^{-/-}$;*tmk234* and *tmk1*$^{-/+}$;*tmk234* seedlings displayed single cotyledons and fused leaf-cups, typically found in *pin1-1* mutants (Fig. 1, A to C; fig. S2A; and table S1). Some PINs (including PIN1) modulate auxin efflux, are polarly distributed to the plasma membrane, and are regulated by ABP1- and ROP GTPase–dependent auxin signaling (*17*, *18*, *26*–*28*). PIN1 localization is also affected in *tmk1*$^{-/+}$*tmk234* mutant (fig. S1, E to G), as in *abp1* or *rop* mutants (*18*, *28*). A weak *abp1* allele (*abp1-5*) greatly enhances cotyledon defects in *tmk1*$^{-/+}$;*tmk234*, suggesting a functional interaction between ABP1 and TMKs (table S1).

Auxin promotes the development of interdigitated pavement cells in the *Arabidopsis* leaf epidermis through ABP1 and ROP GTPases (*18*). The pavement cells of *tmk1*$^{-/-}$;*tmk234* showed interdigitation defects similar to but stronger than those observed in the *abp1-5* mutant (Fig. 1, D and F). Just as in *abp1-5*, the pavement cell defects in *tmk1*$^{-/-}$;*tmk234* mutants were not rescued by auxin (Fig. 1, D to G) (*18*). The *abp1-5;tmk1*$^{-/-}$*tmk234* quintuple mutant displayed a phenotype similar to that of the *tmk1*$^{-/-}$;*tmk234* mutant (fig. S2C). These results suggest that TMKs are required for auxin promotion of pavement cell interdigitation and support an overlapping function with ABP1 in this process.

Auxin activates both the ROP2- and ROP6-dependent pathways in an ABP1-dependent manner in leaf pavement cells (*18*). We determined whether TMKs were also required for the rapid activation of ROP2 and ROP6 GTPases by auxin, similar to ABP1 (*18*). Green fluorescent protein (GFP)–ROP2 and GFP-ROP6 transgenic plants were crossed with the *tmk1*$^{-/+}$;*tmk234* mutant, and *tmk1*$^{-/-}$*tmk234* plants containing GFP-ROP2 or -ROP6 were isolated for ROP activity assays (Fig. 2, A to D) (see supplementary materials and methods). In *GFP-ROP2* and *GFP-ROP6* transgenic lines, the amount of active GFP-ROP2 and GFP-ROP6 proteins increased nearly fourfold upon treatment with 100 nM naphthaleneacetic acid (NAA), as previously shown (Fig. 2, A to D) (*18*). However, in *tmk1*$^{-/-}$*tmk234;GFP-ROP2* or *tmk1*$^{-/-}$*tmk234;GFP-ROP6* mutants, auxin-mediated activation of GFP-ROP2 and GFP-ROP6 was largely abolished (Fig. 2, A to D), as in the *abp1-5* mutant (*18*).

We next assessed the effect of *tmk* mutations on ROP2 and ROP6 signaling targets in leaf pavement cells. The ROP2 effector RIC4, localized to the plasma membrane especially at the tip of the lobes, promotes the accumulation of cortical actin microfilaments (F-actin) (Fig. 2E) (*18*, *22*, *23*). In the *tmk1*$^{-/-}$;*tmk234* mutant, the lobe tip and plasma membrane distribution of GFP-RIC4 was abolished, as in *abp1-5* and *rop2RNAi;rop4-1* mutants (Fig. 2F) (*18*, *22*). Furthermore, cortical F-actin, which normally accumulates at lobe sites (fig. S3A), was absent from the cortical regions of *tmk1*$^{-/-}$;*tmk234* mutant pavement cells, just as in *abp1-5* mutants (*18*, *22*) (fig. S3B). The ROP6 effector RIC1 associates with cortical microtubules and promotes their organization upon activation by ROP6. The association of yellow fluorescent protein (YFP)–RIC1 with cortical microtubules was abolished in the *tmk1*$^{-/-}$;*tmk234* quadruple mutants, causing the disorganization of cortical microtubules, as observed in the *abp1-5* and *rop6-1* mutants (*18*, *23*) (Fig. 2, G to H; and fig. S3, C and D). These results indicate that TMKs participate in auxin perception or signaling that activates both the ROP2 and ROP6 pathways in leaf pavement cells, similar to ABP1.

Given the occurrence of both ROP2 and ROP6 activation at the plasma membrane (*18*, *22*, *23*), their upstream signaling components are expected to localize to the cell surface as well. In both the leaf pavement cells and mesophyll cells of a *pTMK1::TMK1-GFP* transgenic line, TMK1-GFP was localized to the plasma membrane (fig. S4, A and B; and fig. S2, H and I). Although ABP1 is mostly found in the endoplasmic reticulum (ER), a fraction of ABP1 was observed on the cell surface in maize (*8*, *10*, *11*, *24*, *29*, *30*). To determine ABP1 distribution, we performed immunogold histochemistry in conjunction with transmission electron microscopy (TEM) (fig. S5, B to H) and epifluoresence microscopy of GFP-tagged ABP1 (fig. S5I). The TEM analysis indicates that the majority of ABP1 localized to the ER, whereas ~22% ABP1 is detected on the plasma membrane in *Arabidopsis* root cells,

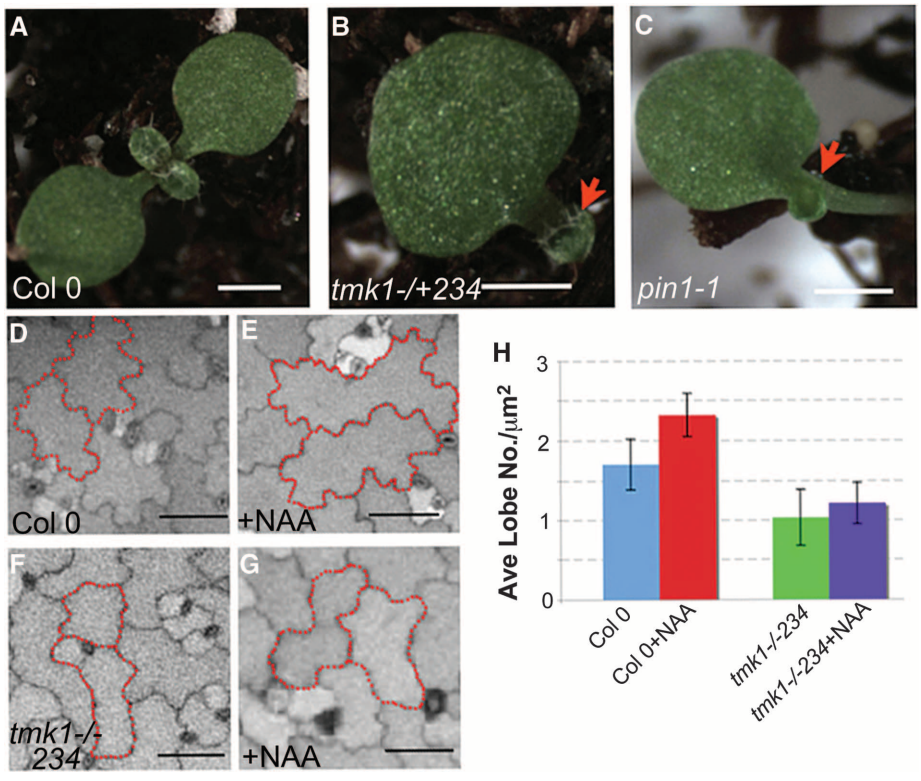

Fig. 1. Transmembrane kinase genes are required for auxin-mediated pavement cell interdigitation. (**A** to **C**) The cotyledon phenotype in the wild type (A), *tmk1*$^{-/+}$;*tmk234* mutant (B), and *pin1-1* mutant (C). Scale bars, 500 μm. (**D** to **H**) Pavement cell phenotype of the wild type with (D) or without (E) auxin (20 nM NAA) treatment, and *tmk1*$^{-/-}$;*tmk234* quadruple mutant with (F) or without (G) auxin (20 nM NAA) treatment. Scale bars, 10 μm. The degree of pavement cell interdigitation was quantified by determining the average number of lobes per square micrometer of pavement cells (Ave Lobe No./μm^2) (H). Error bars indicate SD.

consistent with ABP1 distribution in maize. ABP1-GFP was found both in the ER and on the plasma membrane in *Arabidopsis* pavement cells (fig. S5I). When these cells were plasmolyzed to detach the plasma membrane from the cell wall, ABP1 signal was observed in strands connecting the apoplast and the plasma membrane (fig. S5I). As a negative control, cytoplasmic dominant-negative ROP2 and ER-localized Calnexin did not show comparable apoplastic signal (fig. S5, K and L). These results support the hypothesis that TMK1 and ABP1 are localized to the cell surface suitably for the activation of ROP2 and ROP6.

Our data suggest that TMKs and ABP1 are both required for the activation of plasma membrane–localized ROP2 and ROP6 GTPases in leaf pavement cells (Fig. 2) (*18*). In addition, plasma membrane–localized TMKs are required for cell expansion in several other cell types, including mesophyll cells (fig. S2I) (*25*). ABP1 is also known to promote cell expansion in mesophyll cells; in particular, the cell surface–localized ABP1 has been implicated in the promotion of auxin-mediated expansion of mesophyll cells (*12*, *13*). Thus, we hypothesized that secreted ABP1 and the plasma membrane–localized TMK1 physically form a complex in the perception and signaling of extracellular auxin. To test this, we used an antibody to GFP (anti-GFP) to immunoprecipitate the TMK1-GFP protein complex from the protoplasts of *pTMK1::TMK1-GFP* transgenic plants, which were isolated from expanding leaves and contained both mesophyll cells (92%) and epidermal cells (8%). The ABP1 antibody was used to detect the presence of ABP1 in the complex. ABP1 was detected in the TMK1-GFP protein complex but not in the control BRI1-GFP immunoprecipitates, indicating that ABP1 specifically associates with the TMK1 protein complex (Fig. 3A). Treatments with auxin NAA or IAA increased the amount of ABP1 detected in the TMK1-GFP protein complex (Fig. 3A). The auxin dosage response was similar to that for the activation ROP2 and ROP6 (*18*). Furthermore, the chosen range of concentrations was between 0.2 and 2 times the dissociation constant of NAA binding to ABP1 (*7*). In a reciprocal experiment using the ABP1 antibody to immunoprecipitate the ABP1 protein complex, we also found that auxin treatment increased the amount of TMK1 protein in this complex (Fig. 3B). These results demonstrate that auxin promotes the formation of the ABP1-TMK1 protein complex.

We next assessed whether auxin promotion of the ABP1-TMK1 complex formation involves ABP1 perception of auxin using the ABP1-5 mutant protein. The *abp1-5* point mutation in the auxin-binding pocket of ABP1 greatly reduces its sensitivity to auxin for the activation of ROP2 and ROP6 (*18*). Anti-ABP1 detected the ABP1-5 mutant protein in the TMK1 complex only after extended exposure, suggesting that the ABP1-5 mutant protein is, at best, weakly associated with TMK1 (fig. S6, A and B). Moreover, auxin (both NAA and IAA) treatment only weakly enhanced the association of the ABP1-5 mutant protein with the TMK1 complex (Fig. 3C and fig. S6, A and B). These results indicate that ABP1 sensing of auxin is important for the ABP1-TMK1 complex formation.

On the basis of the above results, we propose that the secreted form of ABP1 associates with the extracellular domain of TMK1 at the cell surface. If the extracellular domain associates with ABP1, overexpression of truncated TMK1 (EX-TMK1, AA1~520), in which the intracellular domain is deleted, would act as a dominant-negative mutant (DN-TMK1) by trapping ABP1 and compromising the function of ABP1 and endogenous TMKs. The *35S::EX-TMK1* construct induced a similar pavement cell phenotype to that of *tmk1*$^{-/-}$*;tmk234* and *abp1-5* mutants (fig. S7, A and B). Furthermore, EX-TMK1 partially or totally blocked the activation of ROP6 and ROP2 by IAA treatment (fig. S7C).

We next tested the physical interaction between ABP1 and EX-TMK1 coexpressed in *Nicotiana benthamiana* tobacco leaves. Coimmunoprecipitation showed that ABP1 associated with both TMK1 and EX-TMK1 fused with HPB (HA-PreScission-Biotin; HA, GE Healthcare Life Sciences) in tobacco leaves (Fig. 4A). The kinase domain, a mutant with the N-terminal LRR repeats removed, or HPB alone did not associate with ABP1 (fig. S6C). ABP1 appeared to immunoprecipitate a greater amount of EX-TMK1 compared with full-length TMK1. Furthermore, the interaction between ABP1 and EX-TMK1 was induced by NAA or IAA in a concentration-dependent manner, very similar to that observed for the association of ABP1 with TMK1-GFP in *Arabidopsis* (Fig. 4A). Finally, the ABP1-5 mutant protein interacted weakly with EX-TMK1-HPB, and the interaction was not promoted by the addition of NAA or IAA (Fig. 4B). Therefore, auxin mediates the interaction between ABP1 and the extracellular domain of TMK1.

Our findings demonstrate that the plasma membrane–localized TMK1 receptor–like kinase

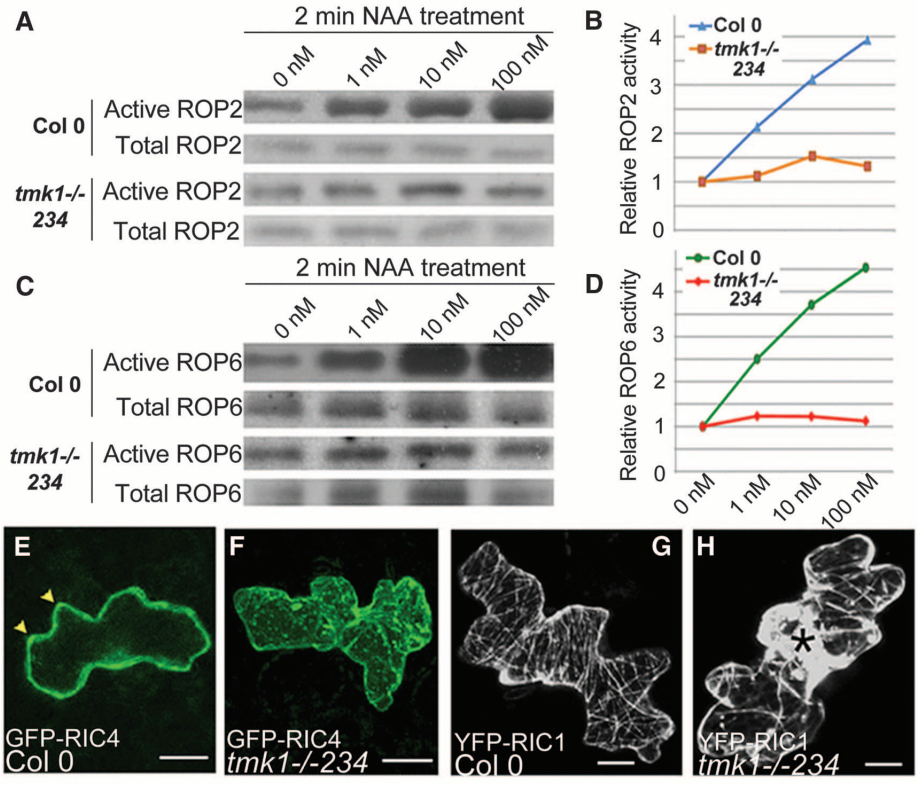

Fig. 2. Transmembrane kinases are required for the auxin-mediated activation of ROP2 and ROP6. (**A** and **B**) ROP2 activation by auxin in the wild type and the *tmk1*$^{-/-}$*;tmk234* mutant was analyzed by pull-down assay, as described previously (*18*) (A). Quantification of relative active GFP-ROP2 level (amount of GTP-bound GFP-ROP2 divided by amount of total GFP-ROP2) to control (as "1") is shown (B). ROP6 activation by auxin in the wild type and the *tmk1*$^{-/-}$*;tmk234* mutant was tested (**C**) and quantified (**D**) as above. Data shown represent one of the three replicates. (**E** to **H**) The activation of ROP2 was analyzed by using GFP-RIC4 subcellular distribution in the wild type (E) and the *tmk1*$^{-/-}$*;tmk234* mutant (F). The ratio of plasma membrane–localized RIC4 to cytosolic RIC4 decreased from 3.14 ± 0.62 in the wild type to 0.68 ± 0.31 (n = 30 cells; $P < 0.001$) in the *tmk1*$^{-/-}$*;tmk234*, indicating lower ROP2 activity in the mutant. (G and H) The activation of ROP6 was analyzed by using YFP-RIC1 localization in the wild type (G) and the *tmk1*$^{-/-}$*;tmk234* mutant (H). The microtubule-localized RIC1 (ratio of RIC1 bundle length to cell size) decreased dramatically from 0.92 ± 0.26 μm^{-1} in the wild type to 0.22 ± 0.12 μm^{-1} (n = 30 cells; $P < 0.001$) in the *tmk1*$^{-/-}$*;tmk234* mutant, indicating lower ROP6 activity level in the mutant. Scale bars, 5 μm.

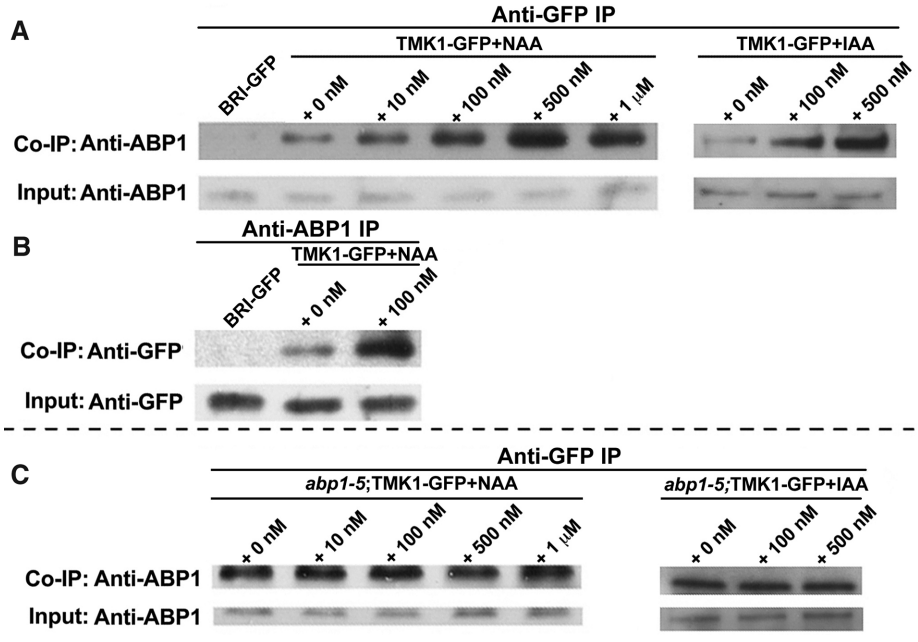

Fig. 3. Auxin promotes the association of TMK1 with ABP1 in *Arabidopsis*. (**A** and **B**) The association of ABP1 with TMK1-GFP in *Arabidopsis* leaves was determined by coimmunoprecipitation (Co-IP) assay. Plasma membrane–localized BRI1-GFP was used as a negative control. The protein complex from leaf protoplasts treated with different concentrations of auxin (NAA and IAA) was immunoprecipitated by GFP antibody (A) or ABP1 antibody (B). ABP1 was detected in the TMK1-GFP complex in an auxin-dependent manner (A). TMK1-GFP was detected in the ABP1 complex, also in an auxin-dependent manner (B). Input ABP1 indicates the total amount of ABP1 in protein samples before coimmunoprecipitation. (**C**) A weak association of TMK1-GFP with an ABP1-5 mutant protein in the *abp1-5;TMK1-GFP* mutant was not induced by auxin addition. The signal shown here (B) was obtained by extended exposure, compared with that shown in (A) (see fig. S6, A and B).

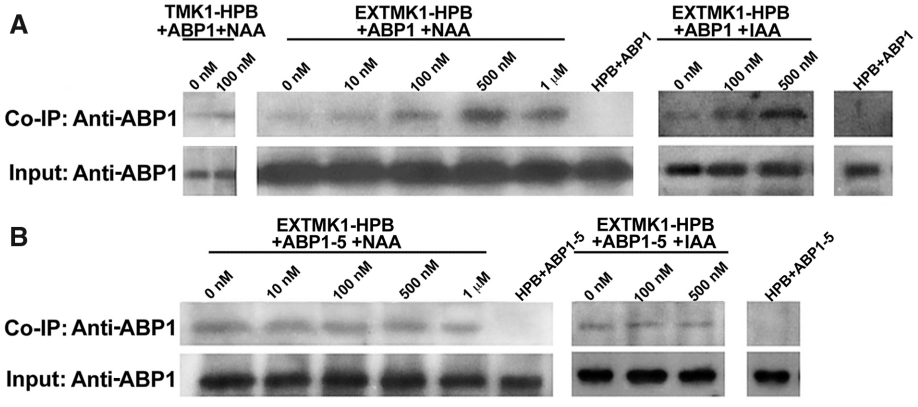

Fig. 4. Auxin promotes the interaction of ABP1 with the extracellular domain of TMK1. (**A**) The association of ABP1 with TMK1 or EX-TMK1 was analyzed by coimmunoprecipitation in tobacco leaves that transiently expressed ABP1 and EX-TMK1 tagged with HPB. Streptavidin-coated magnetic beads were used to immunoprecipitate TMK1-HPB or EXTMK1-HPB protein complexes, which were immunoblotted with the ABP1 antibody. The same assay was carried out for ABP1-5 and EX-TMK1 (**B**).

is functionally and physically associated with ABP1 at the cell surface to regulate auxin- and ABP1-mediated activation of ROP GTPase signaling. TMK1 is at least one of the long-sought docking proteins coupling extracellular auxin and its perception by ABP1 to cytoplasmic signaling (*6*, *14*, *24*). This discovery solves the mystery of the cell surface–cytoplasmic auxin perception and signaling system and opens up a new horizon in auxin biology. Clearly, the TIR1/AFB-based nuclear pathways are essential for various auxin responses (*1*, *2*). The pleiotropic phenotypes of the *tmk* and *abp1* mutants also indicate an essential role for the extracellular auxin perception (*12*, *13*, *15*, *17*, *18*, *25*). The functions of ABP1 and TMKs agree with their role in regulating PIN distribution but also point to unexplored roles for extracellular auxin in other pathways (*6*, *17*, *18*, *21*, *26*–*28*). Therefore, the discovery of the ABP1-TMK complex underlies many exciting prospects of elucidating the roles of cell surface auxin perception and its relation with the TIR1/AFB-based nuclear auxin perception.

References and Notes

1. N. Dharmasiri, S. Dharmasiri, M. Estelle, *Nature* **435**, 441–445 (2005).
2. S. Kepinski, O. Leyser, *Nature* **435**, 446–451 (2005).
3. X. Tan *et al.*, *Nature* **446**, 640–645 (2007).
4. K. Mockaitis, M. Estelle, *Annu. Rev. Cell Dev. Biol.* **24**, 55–80 (2008).
5. Z. Yang, *Annu. Rev. Cell Dev. Biol.* **24**, 551–575 (2008).
6. J. H. Shi, Z. B. Yang, *Mol. Plant* **4**, 635–640 (2011).
7. P. M. Ray, U. Dohrmann, R. Hertel, *Plant Physiol.* **59**, 357–364 (1977).
8. A. M. Jones, E. M. Herman, *Plant Physiol.* **101**, 595–606 (1993).
9. A. M. Jones, *Annu. Rev. Plant Physiol. Plant Mol. Biol.* **45**, 393–420 (1994).
10. H. Tian, D. Klämbt, A. M. Jones, *J. Biol. Chem.* **270**, 26962–26969 (1995).
11. S. C. Oliver, M. A. Venis, R. B. Freedman, R. M. Napier, *Planta* **197**, 465–474 (1995).
12. A. M. Jones *et al.*, *Science* **282**, 1114–1117 (1998).
13. J. G. Chen, S. Shimomura, F. Sitbon, G. Sandberg, A. M. Jones, *Plant J.* **28**, 607–617 (2001).
14. G. O. Badescu, R. M. Napier, *Trends Plant Sci.* **11**, 217–223 (2006).
15. N. Braun *et al.*, *Plant Cell* **20**, 2746–2762 (2008).
16. A. Tromas *et al.*, *PLOS ONE* **4**, e6648 (2009).
17. S. Robert *et al.*, *Cell* **143**, 111–121 (2010).
18. T. Xu *et al.*, *Cell* **143**, 99–110 (2010).
19. A. Tromas *et al.*, *Nat. Commun.* **4**, 2496 (2013).
20. J. G. Chen, H. Ullah, J. C. Young, M. R. Sussman, A. M. Jones, *Genes Dev.* **15**, 902–911 (2001).
21. Y. Effendi, S. Rietz, U. Fischer, G. F. Scherer, *Plant J.* **65**, 282–294 (2011).
22. Y. Fu, Y. Gu, Z. Zheng, G. Wasteneys, Z. Yang, *Cell* **120**, 687–700 (2005).
23. Y. Fu, T. Xu, L. Zhu, M. Wen, Z. Yang, *Curr. Biol.* **19**, 1827–1832 (2009).
24. D. Klämbt, *Plant Mol. Biol.* **14**, 1045–1050 (1990).
25. N. Dai, W. Wang, S. E. Patterson, A. B. Bleecker, *PLOS ONE* **8**, e60990 (2013).
26. X. Chen *et al.*, *Curr. Biol.* **22**, 1326–1332 (2012).
27. D. Lin *et al.*, *Curr. Biol.* **22**, 1319–1325 (2012).
28. S. Nagawa *et al.*, *PLOS Biol.* **10**, e1001299 (2012).
29. W. Diekmann, M. A. Venis, D. G. Robinson, *Proc. Natl. Acad. Sci. U.S.A.* **92**, 3425–3429 (1995).
30. N. Leblanc *et al.*, *J. Biol. Chem.* **274**, 28314–28320 (1999).

Acknowledgments: We are grateful to X. Chen, N. Raikhel, V. Gonehal, and members of the Yang laboratory for their stimulating discussion and critical comments on this manuscript. This work is supported by grants from the U.S. National Institute of General Medical Sciences to Z.Y. (GM081451) and A.M.J. (GM065989), the European Research Council (project ERC-2011-StG-20101109-PSDP) and CEITEC – Central European Institute of Technology (CZ.1.05/1.1.00/02.0068) to J.F., and University of Wisconsin HATCH support to S.E.P. Requests for *tmk* mutant seeds described in this work must be sent to N.D. (ning@molbio.mgh.harvard.edu). Predoctoral fellowship from the Agency for Innovation by Science and Technology (IWT) to H.R.

Supplementary Materials

www.sciencemag.org/content/343/6174/1025/suppl/DC1
Materials and Methods
Supplementary Text
Figs. S1 to S7
Table S1
References (*31*–*39*)

26 August 2013; accepted 27 January 2014
10.1126/science.1245125

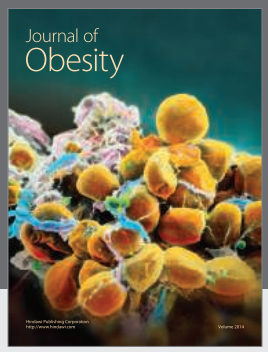

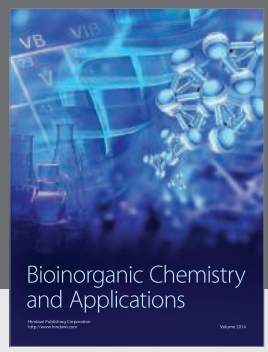

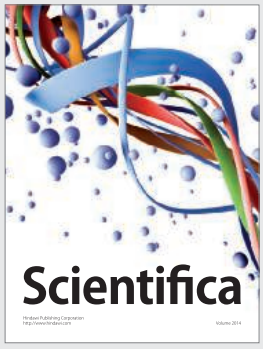

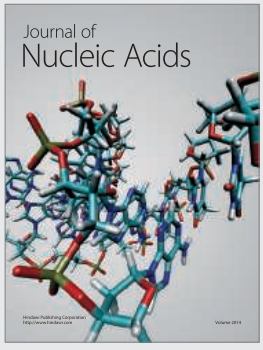

Hindawi

Submit your manuscripts at
http://www.hindawi.com

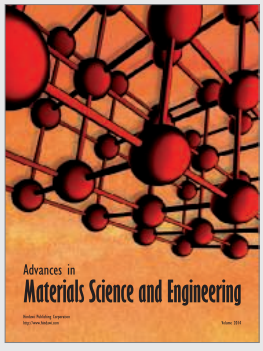

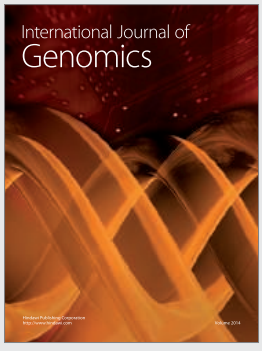

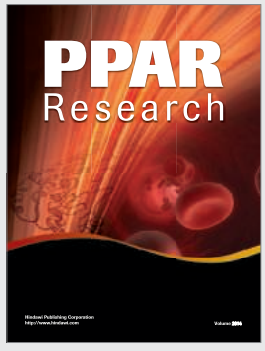

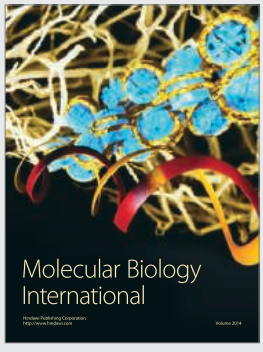

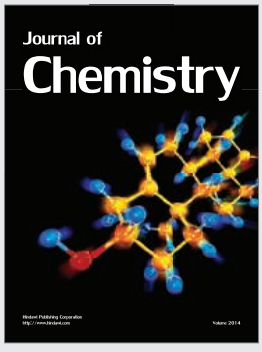

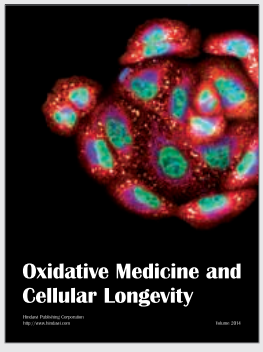

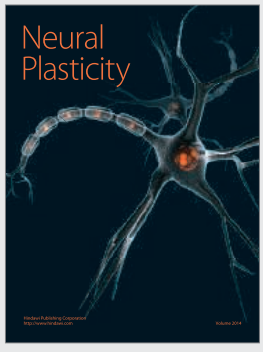

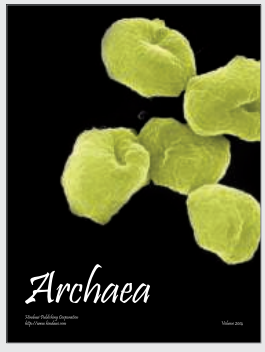

Defining the Future of the Public Research University

UC San Diego

#5 for total R&D expenditures among U.S. universities

National Science Foundation

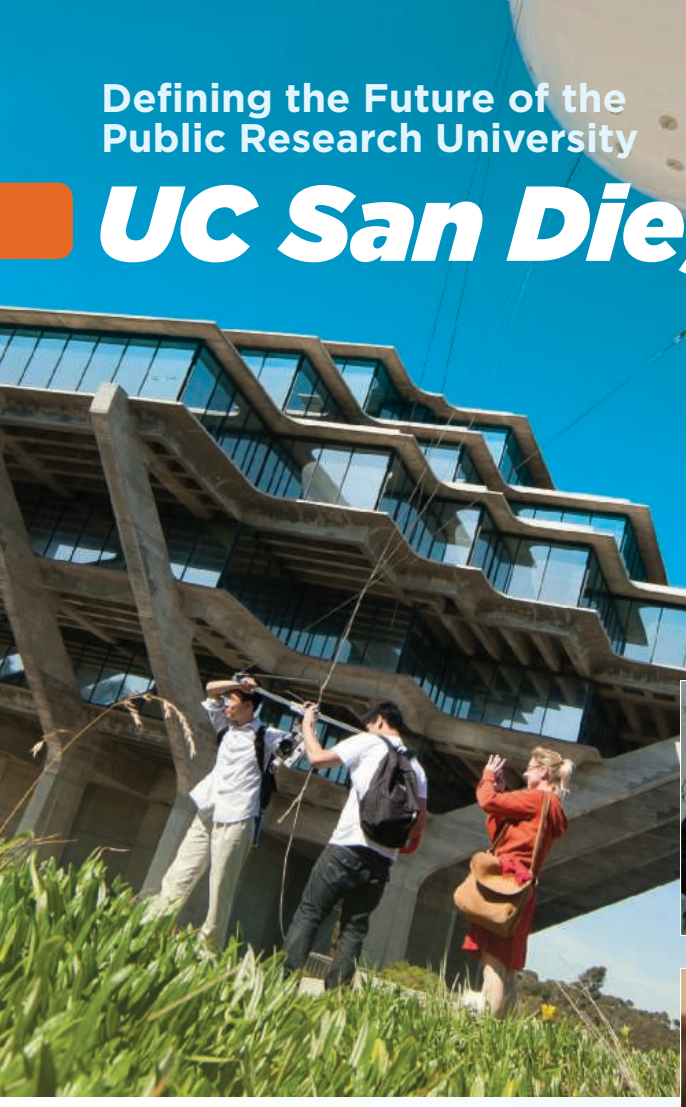

Undergraduates in UC San Diego's Jacobs School of Engineering launch an experimental balloon.

Building a Model of Autism

Alysson Muotri and colleagues have used stem cells from patients with Rett syndrome, one of the most aggressive forms of autism, to create the first human cellular model of the disorder that could be used for drug screening, diagnosis and personalized treatment.

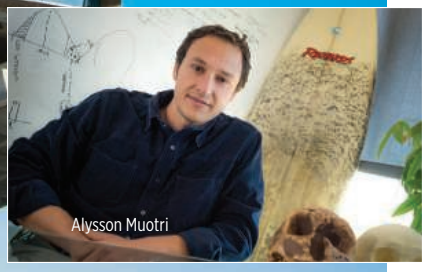

Alysson Muotri

Exploring the Frontier of Drug Delivery

Adah Almutairi directs the Center for Excellence in Nanomedicine and Engineering. Researchers in the center are creating nanoparticles that promise new levels of precision in treating disease. They will be able to deliver drugs under highly specific conditions—when triggered by light or when they encounter a disease-related condition.

Adah Almutairi

Fighting Malaria on Multiple Fronts

Malaria affects anywhere from 250 to 500 million people annually. **Elizabeth Winzeler**'s innovative research at the interface of chemistry and genetics employs advanced screening programs to create novel candidates for possible treatment. Her work investigates new classes of drugs that appear to target the disease parasite at all stages of its development and transition.

Elizabeth Winzeler

Transmitting Data via Tattoos

Todd Coleman's research focuses on wireless tattoo technology that will transmit vital medical data, bringing yesterday's science fiction into today's reality. His ultrathin devices can monitor brain waves, heart rates and other vital signs without tying a patient to a machine, an especially promising advance for neonatal care.

Todd Coleman

Breakthroughs to Better Our World

From its inception, the University of California, San Diego has attracted leading scholars with an entrepreneurial spirit and a penchant for risk-taking. The freedom to cross boundaries and to create new disciplines fuels breakthrough research with global impact. Our visionaries are looking for the next discoveries that will benefit people around the world in all walks of life.

#1 for positive impact on the nation

Washington Monthly

UC San Diego

Learn more at ucsd.edu.

NEW ENGLAND BioLabs® Inc.

Clone with Confidence.

Whether you are performing your first cloning experiment, or constructing multi-fragment gene assemblies, NEB® has the solution for you. Our high quality reagents are available for every workflow, and include specialized enzymes, competent cells, and novel solutions – such as Gibson Assembly®. When you are looking to clone with confidence, think of NEB.

Explore the wise choice at **CloneWithNEB.com.**

Visit CloneWithNEB.com to view online tutorials describing various cloning workflows.

NEW ENGLAND BIOLABS® and NEB® are registered trademarks of New England Biolabs, Inc.
GIBSON ASSEMBLY® is a registered trademark of Synthetic Genomics, Inc.

AAAS 2014 ANNUAL MEETING

13-17 FEBRUARY • CHICAGO

MEETING GLOBAL CHALLENGES:
DISCOVERY AND INNOVATION

AAAS, publisher of *Science*, thanks the sponsors and supporters of the 2014 Annual Meeting

European Commission

SUBARU

ACS Chemistry for Life®
American Chemical Society

HELMHOLTZ ASSOCIATION

NANYANG TECHNOLOGICAL UNIVERSITY

AMERICAN ACADEMY OF ARTS & SCIENCES

Johnson & Johnson
INNOVATION

THE NORWEGIAN ACADEMY OF SCIENCE AND LETTERS

the Lemelson foundation
improving lives through invention

AAAS thanks

THE KAVLI FOUNDATION

for its generous support of
the Science Journalism Awards

Sponsors as of 10 February 2014

Join the Conversation!

Twitter is a great way to connect with AAAS members and staff about the issues that matter to you most. Be a part of the discussion while staying up-to-date on the latest news and information about your personal member benefits.

Follow us @AAASmember and join the conversation with #AAAS

AAAS MemberCentral
MemberCentral.aaas.org

LAMBDA VF-5
Tunable filter changer

NEW!

Introducing the world's first filter changer to use tunable thin-film optical filters. The Sutter **LAMBDA VF-5** allows you to quickly access any center bandpass from 330 to 800nm in nanometer increments. Building on the VersaChrome® filters from Semrock®, the **LAMBDA VF-5** maintains transmission over the tuning range of each filter.

Easy Wavelength Selection
- Wavelength range as wide as 330-800nm
- Keypad or computer interface (USB or serial)

Flexible
- Suitable for excitation or emission
- Easily switch between fluorophore combinations
- Optional liquid light guide offers absolute vibration isolation
- Images pass through filters

Thin filter advantage
- High transmission
- Steep spectral edges
- High out-of-band blocking
- Polarization independence (s and p nearly identical)

SUTTER INSTRUMENT

PHONE: 415.883.0128 | FAX: 415.883.0572
EMAIL: INFO@SUTTER.COM | WWW.SUTTER.COM

STAY INFORMED! STAY CONNECTED!

Get more from your AAAS membership

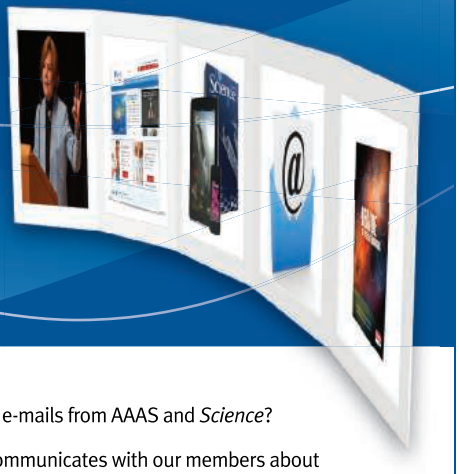

Are you currently registered to receive e-mails from AAAS and *Science*?

E-mail is the primary way that AAAS communicates with our members about AAAS programs, new member benefits, invitations to special events, and, of course, the latest news and research being published in *Science*.

Sign up today to receive e-mails from AAAS and ensure that you are getting the most out of your membership and *Science* subscription.*

To get started visit: **promo.aaas.org/stayconnected** You'll need your AAAS Member number. Find it above your name on your *Science* mailing label.

Don't miss a thing. Sign up for e-mail communications from AAAS today!

Science AAAS

*AAAS follows CAN-SPAM and European Safe Harbor guidelines for protecting your privacy. We will never sell your e-mail address and you can opt-out of receiving e-mails at any time.

AAAS Travels

MONGOLIA
July 4-18, 2014
Genghis Khan to the Gobi Desert

Discover the expansive landscapes and the proud heritage of Mongolia. Explore the Orkhon Valley Cultural Landscape, the Gun-Galuut Nature Reserve, and Gobi Desert, site of the Flaming Cliffs dinosaur site. Horse racing, archery, and other activities of the Naadam Festival will be a treat! $3,995 + air.

For a detailed brochure, please call (800) 252-4910
All prices are per person twin share + air

BETCHART EXPEDITIONS Inc.
17050 Montebello Rd, Cupertino, CA 95014
Email: AAASInfo@betchartexpeditions.com
www.betchartexpeditions.com

LABEL-FREE BIOSENSORS SYSTEM

The DRX 2400 system is a new tool for the measurement of molecular interactions and for the biophysical characterization of proteins. It is based on Dynamic Biosensors' proprietary switchSENSE technology and is the first and only dynamic biosensor system, as it uses actuated DNA layers to actively move the analyte on the surface of the biochip. Even minimal changes in this movement can be detected and used to determine binding affinity and kinetics and allows researchers to analyze a multitude of additional parameters such as molecular size, aggregation, conformational changes, and much more. The DNA nanolevers are electrically actuated at high frequency on microelectrodes, while their orientation is monitored by time-resolved single-photon counting. The binding of analyte molecules slows the switching dynamics in a characteristic way. Hence, the switchSENSE system offers an unprecedented wealth of information at superior sensitivity, all in one label-free measurement.

Dynamic Biosensors GmbH
For info: +49-(0)-89-89-74-544-0 | www.dynamic-biosensors.com

MICROCARRIER CELL CULTURE

A new method of using microcarriers with the ambr micro bioreactor enables scientists to produce uniform microcarrier samples and perform automated media exchange to rapidly optimize parameters for culturing adherent cell lines on microcarriers, thus shortening timelines for successfully scaling up manufacturing of vaccines and cell therapies. Scientists at TAP have utilized the ambr workstation to develop an automated method for providing highly consistent dispensing of microcarriers to multiple 10–15 mL ambr microbioreactors. This means scientists can then rapidly test up to 24 cell-specific culture parameters in parallel including stirring, media formulation, or feed strategies to determine the optimum conditions for cell attachment, growth rate, and vaccine titre, for example. The new method, which has been developed using Vero adherent cells attached to Cytodex 1 microcarriers, allows a 20% media exchange to be performed at any time of the day or night on 24 ambr vessels in approximately four hours.

TAP Biosystems
For info: +44-(0)-1763-227200 | www.tapbiosystems.com

SAMPLE STORAGE SYSTEMS

The new, next generation automated systems are designed for sample and biological storage and include standardized control software that offers a best-in-class user experience. The sample storage platform's flexibility comes from its modular architecture and control software. Each system has six bays that can be populated with the industry's widest range of modules for picking, imaging, and input/output functions. Additional sample banks can be added to the initial system via an internal bridge for future expansion. The control software offers simplified operation and installation. This versatility makes the platform easy to configure and operate, plus highly scalable to meet changing customer requirements. Built-in Dynamic Storage Optimization technology allocates storage space whenever samples are loaded, eliminating the need to predefine the mix of sample containers. High-density trays increase tube storage up to 65% in the same footprint versus 96-tube racks. A high throughput configuration can process over 100,000 tube picks per day.

Brooks Automation
For info: 978-262-2400 | www.brooks.com

VIAL/TUBE HANDLERS

BioMicroLab is introducing a new labeling module for Tube and Vial Handling Instruments. Integrated with the XL100, XL20, or XL9, the new XL LabelPro offers tube and vial labeling automation alongside current modules: barcode decoding, weighing, decapping screw cap vials, recapping screw cap vials, and liquid handling. Integrated labeling offers laboratories even more applications for increasing vial handling throughput. The instrument applies labels to tubes and vials while processing print on demand with unique ID, date, and data; prints 1-D and 2-D barcodes; prints human readable text; labels up to 180 vials per hour; has a 3,000 label capacity; and offers 300 and 600 dpi print modes for crisp text and barcodes. The automated system offers project-based or LIMS-driven sample labeling, integrates with other robotics, has a small footprint (10" x 14"), and is easy to use. It is compatible with common vials and freezer or cryo type labels.

BioMicroLab
For info: 925-689-1200 | www.biomicrolab.com

DNA FRAGMENT SELECTION

The new Microlab NIMBUS Select workstation with Ranger Technology workstation provides a faster and more economical automated solution to agarose gel selection of DNA fragments, generating high-quality material for downstream use in next generation sequencing, cloning, and gene synthesis applications. Ranger Technology targets DNA and isolates fractions with high sensitivity and accuracy; recovery yields typically exceed 80% of the intrinsic content in the targeted range. Agarose gel size selection is a key component in sample preparation and quality control used throughout the life sciences. By automating pipetting steps, the system eliminates manual gel preparation, which is considered one of the most labor-intensive and error-prone steps. In an average two-hour run, the workstation can accurately process up to 96 samples and then place the fragments in destination labware. The NIMBUS Select Workstation with Ranger Technology offers numerous performance and quality control benefits over manual processing and other automated platforms.

Coastal Genomics
For info: 604-620-1332 | www.coastalgenomics.com

Electronically submit your new product description or product literature information! Go to **www.sciencemag.org/products/newproducts.dtl** for more information.

Newly offered instrumentation, apparatus, and laboratory materials of interest to researchers in all disciplines in academic, industrial, and governmental organizations are featured in this space. Emphasis is given to purpose, chief characteristics, and availability of products and materials. Endorsement by *Science* or AAAS of any products or materials mentioned is not implied. Additional information may be obtained from the manufacturer or supplier.

immunogenomics 2014

September 29 - October 1, 2014

HudsonAlpha Biotechnology Campus
Huntsville, Alabama, USA

Bringing together preeminent leaders and thinkers at the intersection of genomics and immunology

Our Keynote Speakers:

Christophe Benoist
Professor, Department of Microbiology and Immunobiology, *Harvard Medical School*

Mary Ellen Conley
Federal Express Chair of Excellence and Professor, Department of Pediatrics, *University of Tennessee, College of Medicine, Memphis*

Mark Davis
Investigator, Howard Hughes Medical Institute; Professor, Department of Microbiology and Immunology; Director, Institute for Immunity, Transplantation, and Infections, *Stanford University School of Medicine*

Register today at haig.aaas.org

presented by

HUDSONALPHA INSTITUTE FOR BIOTECHNOLOGY

Science AAAS

Promega

CellTox™ Green

More Biology, Less Work

CellTox™ Green enables real-time mechanistic toxicity monitoring with a simple Add & Read protocol. Multiplexing with CellTiter-Glo® allows investigators to monitor temporal changes of membrane-modulated cytotoxicity in parallel with the key cell viability biomarker, ATP.

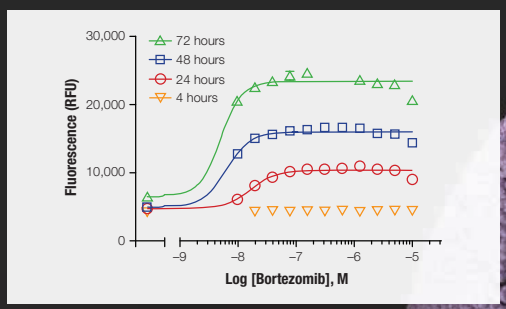

Easily monitor temporal changes in a key cytotoxicity biomarker for IC_{50} determinations.

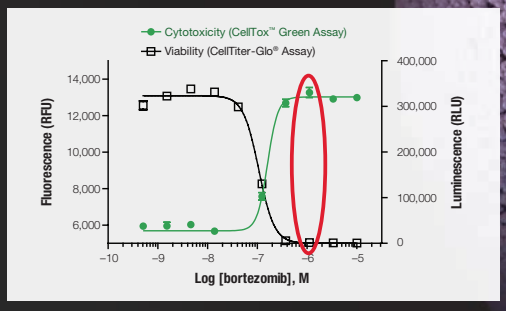

Get more informative data from same-well multiplexing of cytotoxicity and viability assays.

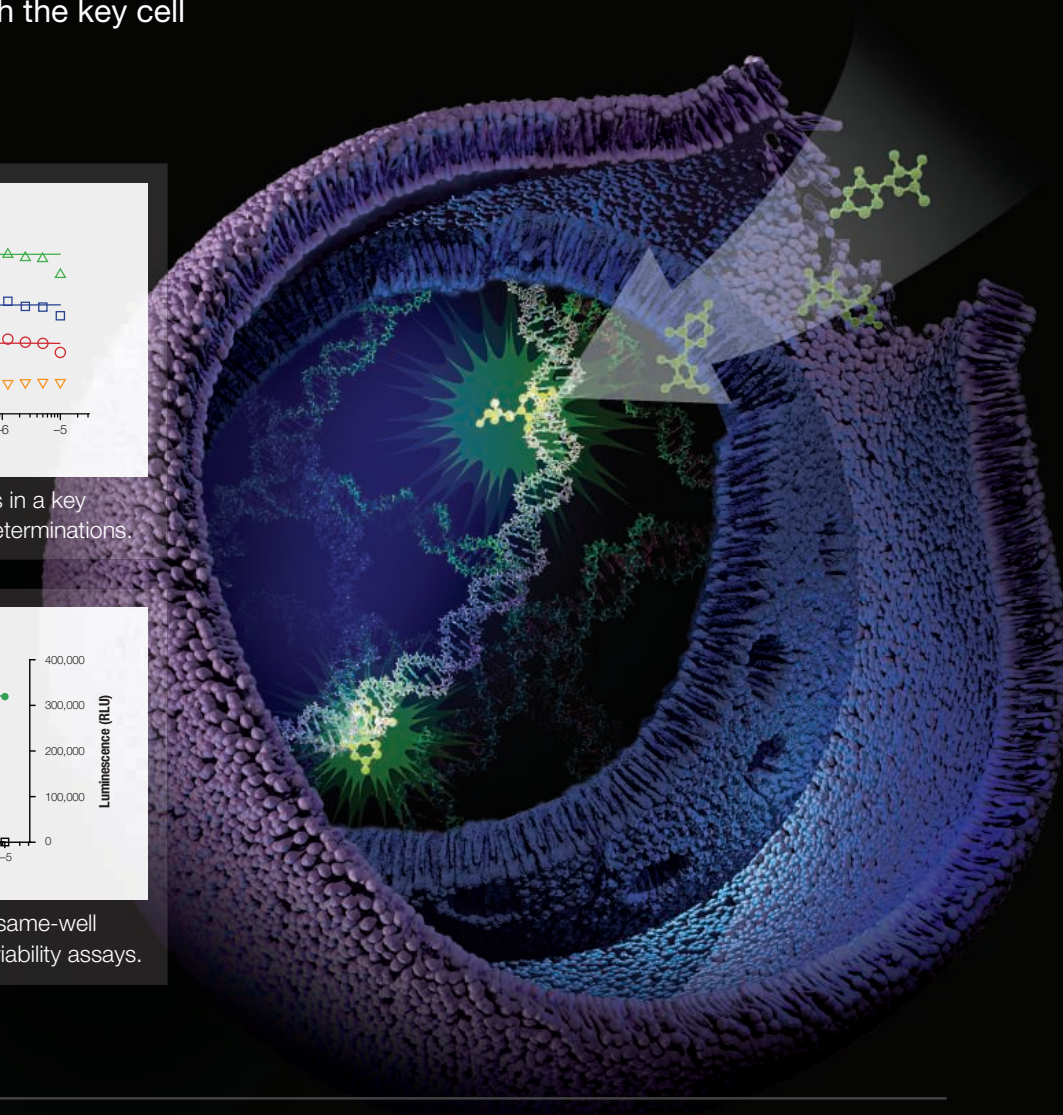

To see how easy better biology can be, request a free sample at:
www.promega.com/realtimecytotoxicity

©2014 Promega Corporation. All rights reserved. 22410-5471

Science Careers Advertising

For full advertising details, go to ScienceCareers.org and click For Employers, or call one of our representatives.

Tracy Holmes
Worldwide Associate Director
Science Careers
Phone: +44 (0) 1223 326525

THE AMERICAS
E-mail: advertise@sciencecareers.org
Fax: 202-289-6742

Tina Burks
Phone: 202-326-6577

Marci Gallun
Phone: 202-326-6582

Online Job Posting Questions
Phone: 202-312-6375

EUROPE / INDIA / AUSTRALIA / NEW ZEALAND / REST OF WORLD
E-mail: ads@science-int.co.uk
Fax: +44 (0) 1223 326532

Axel Gesatzki
Phone: +44 (0)1223 326529

Sarah Lelarge
Phone: +44 (0) 1223 326527

Kelly Grace
Phone: +44 (0) 1223 326528

JAPAN
Yuri Kobayashi
Phone: +81-(0)90-9110-1719
E-mail: ykobayas@aaas.org

CHINA / KOREA / SINGAPORE / TAIWAN / THAILAND
Ruolei Wu
Phone: +86-1367-1015-294
E-mail: rwu@aaas.org

All ads submitted for publication must comply with applicable U.S. and non-U.S. laws. *Science* reserves the right to refuse any advertisement at its sole discretion for any reason, including without limitation for offensive language or inappropriate content, and all advertising is subject to publisher approval. *Science* encourages our readers to alert us to any ads that they feel may be discriminatory or offensive.

Science Careers
From the journal *Science* AAAS

ScienceCareers.org

Stony Brook University

POSTDOCTORAL POSITIONS
Spring 2014

Stony Brook anticipates the following postdoctoral positions being available

- **BIOCHEMISTRY AND CELL BIOLOGY**

  Cellular & molecular mechanisms underlying the autism spectrum disorder Rett syndrome;
  Dr. Nurit Ballas, WC-R-8461-14-02-S.

- **NEUROBIOLOGY AND BEHAVIOR**

  Cortical processing of chemosensory information and reward;
  Dr. Alfredo Fontanini, WC-R-8474-14-02-S.

  Developmental Molecular Cellular Neurobiology;
  Dr. Maya Shelly, WC-R-8475-14-02-S.

  Experience-dependent plasticity in cortical circuits;
  Dr. Arianna Maffei, WC-R-8476-14-02-S.

  Functional Capacity of the Damaged Spinal Cord;
  Dr. Lorne Mendell, WC-R-8477-14-02-S.

  Molecular Structure of Glutamate Signaling;
  Dr. Lonnie Wollmuth, WC-R-8478-14-02-S.

  Regulation of Neural Gene Expression;
  Dr. Howard Sirotkin, WC-R-8479-14-02-S.

  Synaptic Mechanisms in the Retina;
  Dr. Gary Matthews, WC-R-8480-14-02-S.

  Motoneuron Physiology and Plasticity;
  Dr. William Collins, WC-R-8481-14-02-S.

  Electrophysiological and Optogenetic Studies of Central Cholinergic Circuits;
  Dr. Lorna Role, WC-R-8482-14-02-S.

  Molecular Mechanisms of Neuronal Phenotype Control;
  Dr. Simon Halegoua, WC-R-8483-14-02-S.

- **PSYCHIATRY & BIOMEDICAL ENGINEERING**

  Acquisition and Analysis of Diffusion MRI;
  Dr. Christine DeLorenzo, HS-R-7373-13-10-F.

- **SCHOOL OF MARINE AND ATMOSPHERIC SCIENCES (SoMAS)**

  Trace gas isotopic analysis & methods development for paleo-climatic studies;
  Dr. John Mak, WC-R-8347-14-01-F.

  Climate change effects on fish & shellfish ecology & ecosystems;
  Dr. Michael Frisk, WC-S-8456-14-02-S.

- **LAUFER CENTER FOR PHYSICAL AND QUANTITATIVE BIOLOGY**

  Computational/physical biology: Regulatory networks in growing & evolving cell populations;
  Dr. Gabor Balazsi, WC-S-8486-14-02-S

  Statistical physics of cells or proteins;
  Dr. Ken Dill, WC-S-8487-14-02-S

  Interface of synthetic and evolutionary biology;
  Dr. Gabor Balazsi, WC-S-8488-14-02-S

To apply online and for information, visit www.stonybrook.edu/jobs under category "K" or mail résumés to:
Human Resource Services, 390 Administration Building
Stony Brook University, Stony Brook, NY 11794-0751

Stony Brook University/SUNY is an affirmative action, equal opportunity educator and employer.

Postdoc and research **opportunities** in Brazil

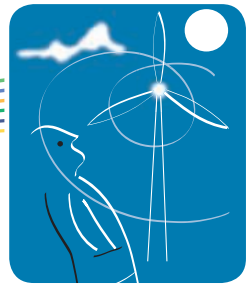

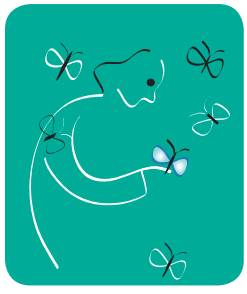
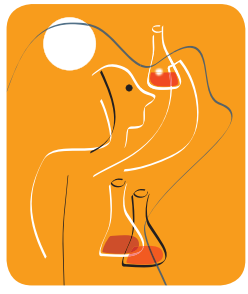

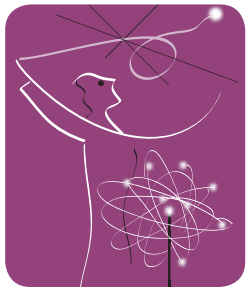

About us

Fifty percent of all science created in Brazil is produced in the State of São Paulo. The state hosts three of the most important Latin American universities: USP, UNICAMP and UNESP. Other universities and 19 research institutes are also located in São Paulo, among them the renowned Instituto Tecnológico de Aeronáutica (ITA), Instituto Nacional de Pesquisas Espaciais (INPE) and Laboratório Nacional de Luz Síncrotron, besides most of Brazilian Industrial P&D.

The São Paulo Research Foundation (FAPESP), one of the leading Brazilian agencies dedicated to the support of research, has ongoing programs and support mechanisms to bring researchers from abroad to excellence centers in São Paulo.

The **Young Investigators Awards** is part of FAPESP's strategy to strengthen the State research institutions, favoring the creation of new research groups. See more about it at www.fapesp.br/yia.

FAPESP **Post-Doctoral Fellowship** is aimed at distinguished researchers with a recent doctorate degree and a successful research track record. The fellowship enables the development of research within higher education and research institutions in São Paulo. Postdoc fellowships are available when calls for applications are issued internationally, or as individual fellowships requested on demand.

In the first case, positions are advertised at www.fapesp.br/oportunidades/ and candidates are selected through international competition. In the second, the proposal must represent an addition to a pre-existent research group and should be developed in association with faculty in higher education and research institutions in São Paulo. More information at www.fapesp.br/en/postdoc.

Location: São Paulo, SP, Brazil

Primary Contact Details:
Rua Pio XI, 1500 – Alto da Lapa
05468-901
São Paulo, SP – Brazil
Phone: +55-11-3838-4224
URL: www.fapesp.br

FAPESP 50 YEARS

FAPESP
SÃO PAULO RESEARCH FOUNDATION

Science Careers online @sciencecareers.org
POSTDOCTORAL OPPORTUNITIES

A Scientist's Guide to Social Media

Social networking sites like Facebook, LinkedIn, and Twitter can be intimidating for introverted scientists—all that interaction, 24/7. But actually, online communities are perfect for people who want to cogitate before they comment. Social networks also give extroverts a channel for real-time global intercommunication. No matter your personality type, career advisors recommend that postdocs use online networking tools to make connections, exchange scientific ideas, and advance a career. This guide is designed to nudge reluctant networkers to get started with an online professional profile and help social media experts get even more out of social networking. **By Chris Tachibana**

"You simply must have an online presence."
—Karen Peterson

In 2009, **Kaan Akşit** (@kaanaksit) found himself surrounded by Dutch Facebook enthusiasts. Akşit was a visiting student at Philips Research in the Netherlands at the time and "not the kind of guy to use social media." After initially resisting invitations to online communities from coworkers, Akşit says, "my supervisor finally said, 'at least use LinkedIn.'" The professional networking site was his social media gateway.

Today, Akşit is finishing an electrical engineering Ph.D. at Koç University in Istanbul, Turkey, and using social media to explore his postdoctoral options. He also shares about his work and life on Facebook, Twitter, Instagram, Google+, and his own blog. He has 500+ LinkedIn connections and self-describes as "kind of a sharefreak."

But even researchers who aren't daily visitors to online social spaces benefit from occasionally dropping by. Networking sites can help scientists stay current in their field, keep track of colleagues, and build a community of advisors and collaborators. Social media lets researchers participate in conferences remotely, sparing travel time and budgets. Professional networking services make it easy for reluctant scientific networkers to create an online profile, which career consultants say is a professional obligation.

IS IT FOR EVERYBODY?

"You simply must have an online presence," says **Karen Peterson,** director of Scientific Career Development at Fred Hutchinson Cancer Research Center; in fact, she adds, you already have one (just try an Internet search of your name), so you might as well curate it. This advice is especially important for researchers who are thinking ahead to a transition: graduate to postgraduate work, postgraduate to job, or perhaps a career change.

Peterson recommends that, like Akşit, researchers start with LinkedIn. A complete, updated LinkedIn profile conveys your background, experience, and accomplishments to potential employers and people with common interests. Peterson says that LinkedIn is especially useful for setting up informational interviews, which are informal conversations with experts in careers or research areas in which you're interested. Use LinkedIn to find personal or institutional connections to someone you want to talk with and use those ties to ask for an introduction. (Or use SciVal Experts if your institution has a subscription.) Set up a meeting or phone conversation and be prepared with a short summary—an elevator pitch—about your research and some specific, open-ended questions. Ask about others you might talk with and follow up with a written thank-you note. This is a classic way to grow your network, says Peterson. LinkedIn and similar services just make the initial contact easier because the major networking sites have a surprisingly vast membership representing all scientific careers and both young and established researchers.

A common assumption is that early career scientists are the most enthusiastic users of social media. However, preliminary results hint that established researchers are also quite active. A study of computer scientists, which mainly focused on methods for determining online activity, found that many scientists with an online presence were tenure-level, judging from their high-impact publications; they also used multiple networking sites. Plus, participation in online communities is growing. "The scientific discourse is moving online," says **Paul Groth** (@pgroth), assistant professor, Department of Computer Science, VU University Amsterdam, and one of the study's coauthors. "And it's going to keep continued>

Upcoming Features

Cancer Research Careers—March 28
Biotech and Pharma—June 13
Postdocs —August 22

CREDIT: (FROM TOP) © SHUTTERSTOCK.COM/NOPPORN; © SHUTTERSTOCK.COM/ROMAN SOTOLA

Roche Postdoc Fellowship (RPF) Program

The RPF Program has built up a world-wide reputation and became a continuous source of innovation. This is reflected not only in high-quality publications in peer-reviewed journals, but is also shown in the influence of the RPF findings on pharmaceutical research and early development at Roche.

"In choosing a postdoc position in the industry, I saw the possibility for me to work in a large, multinational team with a lot of different expertise and to have access to various methods with less limiting budget to achieve my goals. In addition, unlike at a university, I wanted to get a more holistic view on neurosciences, and not only focus on a part of a disease or a single protein."

Anja (33) from Germany

"After my PhD in biomedicine at the University of Würzburg, I was particularly looking for a postdoc position in Switzerland. I had only been doing research in an academic environment and wanted to get an insight in industrial research. Research in industry focuses a lot on immediate results that can be applied for drug discovery."

Eva (29) from Germany

"The RPF program provided me a unique opportunity to utilize knowledge and skills I acquired during my PhD into drug discovery projects. This experience helped me take the next career step, to assume a scientist position within Roche. Along the proposed Roche RPF project, I foresaw an exceptional chance to gain industrial experience; the choice was further driven by the scientific expertise and reputation of the imaging groups in Antwerp and Roche Basel."

Dany (33) from India

Key facts

We currently have ~100 RPF Postdocs working at one of our Roche Research sites or one of the 119 academic collaborators in 18 different countries. Each Postdoc has two mentors, one from Roche & one at the partnering university. The annual Postdoc Symposium, held for all Postdocs at one of the Roche locations worldwide, as well as Postdoc lunches and journal clubs provide additional networking opportunities for our Postdocs.

Duration: Initially for 2 years, with the option of extension for another 1-2 years.

Location: RPFs can be located at Roche in Basel, Zurich, Penzberg, Shanghai, or at the partnering universities.

Main areas: Oncology, Neuroscience, Infectious Diseases, Ophthalmology, Pharmaceutical Sciences (DMPK, Non-Clinical Safety, Modelling & Simulation, Translational Technologies, Bioinformatics), Therapeutic Modalities (Small & Large Molecules Research, Discovery Technologies).

How to apply? All positions will be posted on our Roche Careers Website. Please apply online. New positions may be expected to be online from May 2014 on.

To apply online for positions visit www.careers.roche.ch

Roche is an Equal Opportunity Employer.

The next step is yours.

"I use social media to get scientific inspiration," —Kaan Akşit

moving in that direction." This means that networking sites are virtual venues where students and postdocs can connect to leaders in their field.

People of all ages, experience levels, and career paths are embracing online tools, says **Karyn Traphagen** (@kTraphagen), cofounder and executive director of ScienceOnline, a nonprofit organization for science outreach, networking, and community building. She sees advanced networkers, novices, media mavens, students, postdocs, and professors at national and local ScienceOnline meetings and says that social media sites can create genuine, interactive, and far-reaching communities. Social media is a great equalizer.

Most social networking sites are global, so they are excellent tools for making and maintaining international connections. For early career scientists trying to make a splash with their work, no platform has a greater reach than the big three networking sites: LinkedIn, Facebook, and Twitter. Compare a talk at a conference attended by a thousand people to the potential online audience: LinkedIn has nearly 260 million members and Facebook and Twitter have hundreds of millions of users a month.

FACEBOOK AND TWITTER FOR SCIENTISTS? REALLY?

Social network services emerge, evolve, and go extinct like influenza viruses. But right now, researchers use Facebook for personal contacts. Early career scientists, who move often, might use Facebook to maintain friendships with former lab members. Facebook can reveal fun, nonprofessional insights about a colleague—maybe a potential collaborator is an especially good fit because of a common love of fly fishing, knitting, or manga. Universities, corporations, and even research groups have public Facebook pages that can be useful for news about former and potential employers. However, Facebook is static compared to the real-time interaction of Twitter.

"The number one area for the ScienceOnline community is Twitter," says Traphagen. Twitter use is growing in academia, across disciplines, for scholarly and nonscholarly use. And if you think Twitter is just for celebrity gossip, you might be surprised at the range of professional applications.

"I use social media to get scientific inspiration," says Akşit. His thesis project is improving motion capture, for example for films, so he follows the electronics industry on Twitter to hear about new products and developments. Other scientists follow research groups to avoid overlapping projects or to find collaboration opportunities. Twitter is supplementing or replacing automated search and alert services, for example for relevant literature. "I often hear about important papers on Twitter as soon as they are released or even before," says **Jonathan Jacobs** (@bioinformer), principal scientist in biosurveillance at MRI Global, a nonprofit contract research organization. "Especially in the bioinformatics community, tweeting communicates not just news but actual science."

"The easiest way to see the power of Twitter," says Traphagen, "is to follow a conference hashtag." (For example, search for #AAASmtg for news about the annual American Association for the Advancement of Science conference.) If you are attending a meeting, Twitter and other networking tools can connect you, before arrival, to people who share your research interests. If you can't attend, Twitter can tell you what talks and posters caught people's attention and where to find shared resources such as websites or slides. Jacobs says he gets almost as much information from following a conference via Twitter as actually attending. If you're presenting, Groth advises having a Twitter account and putting your handle on slides and posters. That helps people tweet about your presentation, which increases your impact, maybe even attracting the attention of potential collaborators or group and department leaders.

Somewhat unexpectedly, Twitter is recommended for shy people. "The Internet lets you follow a conversation without physically stepping into a group of people," says Traphagen. "You can sit back and listen and get involved when you're ready by inserting a comment and seeing how people respond." New Twitter users are often intimidated by the billions of tweets, but Traphagen says that if you want specific information, use a hashtag search (e.g., #sharks). If you are still overwhelmed, says Traphagen, think of Twitter as a river: "Every now and then, go put your feet in and see what is flowing by right now."

BUT WAIT, THERE'S MORE?

If Facebook and Twitter are for conversations and LinkedIn presents your credentials, what are the benefits of up-and-coming and specialty sites? The ScienceOnline community increasingly uses Google+ for broadcasting and archiving conversations with researchers, says Traphagen. Another resource for following talks and conferences is Storify, where attendees or hosts collect presentation materials, comments, and notes. Groth recommends posting presentations on Slideshare, if your institution allows. This extends the reach of a seminar far beyond people who can attend. Sites like Slideshare also track views, downloads, and recommendations that document the impact of your research.

Groth used ImpactStory, a science-sharing site, for a midterm review of a European Union project. Publications from the work hadn't had time to build a substantial citation record, says Groth, so he used metrics from ImpactStory to demonstrate the influence of the work in progress. Still, publications are not going away, either as a permanent research record or a measure for hiring, promotion, and tenure, he says.

Since the scientific world orbits around peer-reviewed articles, science-sharing sites such as Mendeley and ResearchGate revolve around publications. By allowing researchers to share and comment on papers and ask and answer questions, these sites add networking functions to a typical publication list. Publication-oriented sites make requests for electronic reprints easy for postdocs at institutions without extensive journal subscriptions. Specialized sites such as GitHub for computer scientists or BioMedExperts for life scientists serve the needs of specific scientific communities. But don't be overwhelmed. "The Internet is a big place," says Jacobs. "How you use it depends on what you have time for and what kind of itch you're trying to scratch." Jacobs and other experienced online networkers say a little exploring will uncover networks with a community and functions that enhance your work.

FEATURED PARTICIPANTS

Fred Hutchinson Cancer Research Center
www.fhcrc.org

Koç University
www.ku.edu.tr/en

MRIGlobal
mriglobal.org

Philips Research
www.research.philips.com

ScienceOnline
scienceonline.com

VU University Amsterdam
www.vu.nl/en

ADDITIONAL RESOURCES

BioMedExperts
www.biomedexperts.com

Facebook
www.facebook.com

Additional Resources Cont.

GitHub
github.com

Google+
plus.google.com

ImpactStory
impactstory.org

LinkedIn
www.linkedin.com

Mendeley
www.mendeley.com

ResearchGate www
researchgate.net

SciVal Experts
scival.com

Slideshare
www.slideshare.net

Storify
storify.com

Twitter
www.twitter.com

Karyn Traphagen often travels with Camilla Corona (@CamillaSpace), a rubber chicken who advocates for Space Education and STEM using social media.

"The number one area for the ScienceOnline community is Twitter."

— Karyn Traphagen

SHOULD I BLOG?

Then there's blogging, which is varsity-level online sharing. Blogs require a regular time commitment and a deep passion about a topic. If you're considering a blog, try guest posts on other sites. **Kiran Dhillon** (@Indigal9), a postdoctoral researcher at Fred Hutchinson Cancer Research Center, started blogging about her breast cancer work when Angelina Jolie spoke about inheriting a BRCA mutation and having prophylactic surgery. Dhillon considers her blog to be professional development: "It's a good exercise in finding my voice and learning how to communicate science to the public."

Even if you don't blog, Dhillon encourages all scientists to have a professional website to highlight accomplishments and show examples of soft skills such as leadership and management. "LinkedIn is good for connecting and summarizing your research, but it's limited. Your own website gives people a better sense of who you are. Plus, you can post videos or images, like great immunofluorescence results." Some researchers modestly say they want their science to speak for itself, but Dhillon says to think about the buzz around certain talks or posters at a conference. In those cases, the scientists worked hard to present their work in a way that got people excited. A professional website can pay off in the same way.

IS REAL LIFE STILL NECESSARY?

Yes, say social media experts. For all the linking, sharing, and networking that online resources offer, Peterson says, "For a true connection, you still need to meet face-to-face." LinkedIn and other sites just facilitate what early career scientists should be doing anyway, says Peterson: meeting people with common interests, professional and otherwise. Even networking with nonscientists is part of career development, she says, because you never know who is connected to whom. Jacobs found jobs through LinkedIn, mainly by finding events to attend and people to contact for in-person interactions.

So go forth and connect, say social media experts, but start slowly. Think about what should be private and public. Traphagen says experienced online networkers advise treating everything you post as potentially becoming public. Follow online etiquette, which is essentially like any social interaction: be friendly, collegial, and respectful. Think of social networking as a conversation, but if you get ignored or rejected, don't take it personally. Find the sites that work for you. Don't pester people, but remember that most people want to help and most researchers love to talk about their work, says Dhillon. "Scientists are passionate about our research—that's why we do it."

If you don't feel like you have time for online networking, Traphagen suggests thinking of it as just another scheduled work activity. "Lots of things can be time sucks," she says, "including social media. But when a task is professionally important, we're disciplined about doing it." But again, says Traphagen, don't be discouraged by the constant influx of information: "Remember: you don't have to pay attention to everything. It's okay to miss things."

When you leave the computer and meet an online contact in person, keep the same open attitude. The late Ken Metzler, who was a professor at the University of Oregon, in his book *Creative Interviewing,* said sincerity, curiosity, and listening ability are all you need for an informative conversation. Scientists are naturally curious and when we find something genuinely interesting about a new colleague, sincerity and listening follow. This is the type of old-fashioned networking that even a young scientist like Dhillon says is most effective.

"Talk to people, even if you're not naturally outgoing," says Dhillon. "Get involved in activities for students and postdocs at your institute. Just going to meetings makes you part of the community, and as you build confidence you'll find ways to contribute." Volunteering for presentations, committees, and workshops is work, admits Dhillon, but pays off in a strong network that reaches into diverse research areas and administration, which helps new researchers learn what it takes to run a laboratory, a group, or a research center. Echoing the first rule of improvisational theater, Dhillon says, "when people ask you to do something, say yes."

Chris Tachibana (@ChrisTachibana) is a science writer based in Seattle, USA, and Copenhagen, Denmark.

DOI: 10.1126/science.opms.r1400141

CREDIT: © RUSS CREECH

University of Michigan
Medical School

POSTDOCTORAL
TRAINING OPPORTUNITIES
www.med.umich.edu/postdoc

The University of Michigan Medical School is an outstanding training environment that combines world-class faculty and innovative programs of research with a rich academic tradition. For two decades Michigan has ranked among the top 10 medical schools in NIH research funding. This research effort is enhanced by 27 NIH-sponsored training programs that support Postdoctoral Scholars.

The University of Michigan recognizes the essential contributions Postdoctoral Scholars make to the University's research mission. We offer a comprehensive career development program for our Postdoctoral Scholars to help guide their choices as they prepare themselves for independent careers. We welcome inquiries from graduate students nearing completion of the Ph.D. degree regarding opportunities for postdoctoral training in the following areas:

- Alcoholism Research
- Biology of Aging
- Biology of Drug Abuse
- Cancer Biology
- Cardiovascular Research
- Cell and Molecular Dermatology
- Clinical and Basic Neuroscience
- Endocrine Dysfunction
- Endocrinology and Metabolism
- Environmental Toxicology
- Experimental Immunology
- Genome Sciences
- Hearing, Balance and Chemical Senses
- Imaging Science in Biomedicine
- Lung Disease
- Lung Immunopathology
- Medical Rehabilitation Research
- Microbial Pathogenesis
- Molecular Hematology
- Nephrology Research
- Organogenesis
- Reproductive Sciences
- Research in Gastroenterology
- Substance Abuse
- Tissue Engineering and Regeneration
- Urology Research
- Vision Research

One way to explore these programs is to attend the *Postdoc Preview* on U-M's campus on June 12-13, 2014. The all expense paid *Preview* visit will introduce outstanding upper-level graduate students in the biomedical sciences to the breadth and excitement of postdoctoral research and training at Michigan.

Apply online by April 15, 2014 at
www.med.umich.edu/postdoc/preview

The University of Michigan is an equal opportunity, affirmative action employer.

NATIONAL RESEARCH COUNCIL
OF THE NATIONAL ACADEMIES
Research Associateship Programs

Graduate, Postdoctoral and Senior Research Awards
offered for research at
US Federal Laboratories and affiliated institutions

Opportunities for graduate, postdoctoral and senior research in all areas of science and engineering

- Awards for independent research at over 100 participating laboratory locations
- 12-month awards renewable for up to 3 years
- Annual stipend $42,000 to $80,000 - higher for senior researchers; graduate entry level stipend begins at $30,000
- Relocation, professional travel, health insurance
- Annual application deadlines Feb. 1, May 1, Aug. 1, Nov. 1
- Open to US and non-US citizens

Detailed program information, including instructions on how to apply online, is available on the NRC Web site at :
www.nationalacademies.org/rap

Applicants must contact Adviser(s) at the lab(s) prior to application deadline to discuss research interests and funding opportunities

Questions should be directed to the :
National Research Council Fellowships Office
TEL: (202) 334-2760
E-MAIL: rap@nas.edu

Qualified applicants will be reviewed without regard to race, religion, color, age, sex or national origin.

THE NATIONAL ACADEMIES
Advisers to the Nation on Science, Engineering, and Medicine

POSTDOCTORAL FELLOW IN CANCER GENETICS

Penn State College of Medicine - Hershey, PA

Postdoctoral fellowship position is open at Penn State College of Medicine in Dr. Carla Gallagher's laboratory. The focus of the research will be the study of genetic variants for the involvement in cancer risk in human populations. Large case-control populations will be screened in genetic association studies, in vivo measurements of metabolite levels in human samples will be compared to genotype, and in vitro activity assays and expression studies will be performed to assess function of genetic variants. See the following link for more information: http://www.pennstatehershey.org/web/phs/people/faculty/epidemiology

Successful candidates should have received a recent Ph.D. or M.D. and have a strong record of training in genetics, molecular biology, biochemistry, and/or cancer epidemiology. Please send your CV and letter of interest by email to: cgallagher@hmc.psu.edu.

Penn State is committed to affirmative action, equal opportunity and the diversity of its workforce.

ASM Postdoctoral Fellowship Programs

The American Society for Microbiology (ASM) Headquarter Fellowship is an intense and multi-faceted training experience for individuals interested in exploring careers outside the traditional academic environment.

There are three opportunities being offered:

- **American Academy of Microbiology Colloquium Fellowship** - The goal of this fellowship is to provide an opportunity for a recent microbiology PhD graduate to develop skills in in science communication and public outreach while working on colloquia to address critical issues in microbiology.
- **Communications and Marketing Fellowship** - The Communication and Marketing Strategy Department provides a variety of communication services for the Society including press relations, public outreach and social media management. The fellow in this office will improve his/her skills in a wide range of communication approaches and develop new outreach projects for the Society.
- **Education Curriculum Fellowship** - The ASM Fellow in Education will deepen his/her understanding of ASM; curriculum guidelines and course design; active learning and laboratory biosafety. He/she will develop skills to shepherd projects from conception to implementation and eventually commercialization.

Applicants for the fellowship should have a broad interest in the field of microbiology and a willingness to learn about topics outside their own area of expertise. Applicants need either to complete a doctoral degree (M.D., Ph.D., D.V.M., D.D.S., or equivalent) by June 2014 or to be currently in post-doctoral degree training. Exceptional writing and communication skills are essential.

The fellowships are for 12-consecutive months and are in residency at the ASM in Washington, DC. They may require some travel. The fellowships offer a $50,000 annual stipend, medical benefits, and a public transportation subsidy. Start date must be between June 1, 2014 and September 1, 2014.

Applications will be reviewed on a rolling basis through **April 1, 2014**. You can find more information and the online applications for all three opportunities at **http://bit.ly/HQopp**

Join the Minds of Janelia Junior Fellow

Janelia Farm Research Campus

A One-of-a-kind Scientific Opportunity

Janelia Farm Research Campus, a pioneering research complex near Washington, DC, is recruiting for Junior Fellow positions.

Janelia Junior Fellows are independent, early career scientists engaged in hands-on research projects of their own design, exploring how the brain processes information and developing imaging technologies to see smaller, deeper, and faster.

Highlights

- Unparalleled technical facilities
- Highly interactive culture
- Internally funded
- No formal teaching

Application deadline: 2pm ET May 15, 2014

www.janelia.org/jf14/sci

HHMI janelia farm research campus

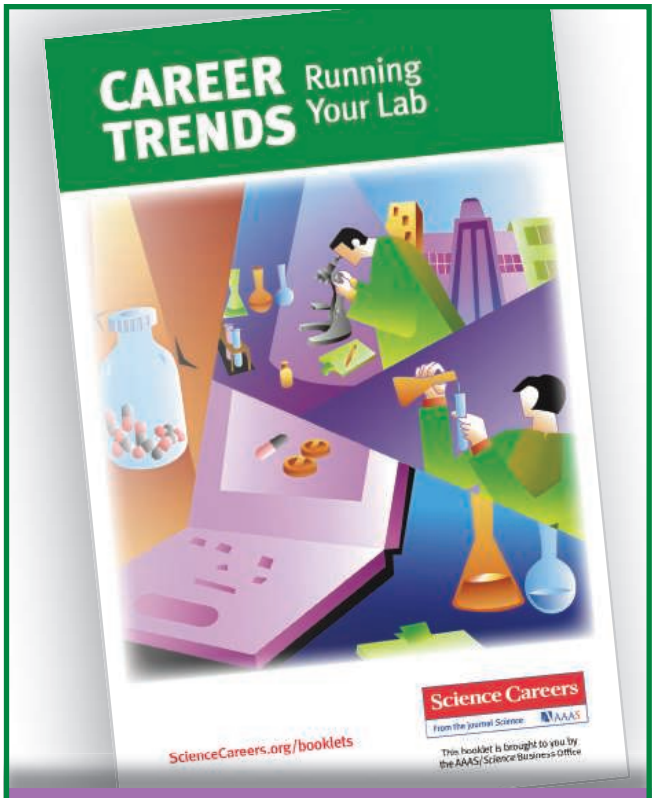

Download your free copy today at ScienceCareers.org/booklets

PRIZE

The 2014 Martha T. Muse Prize for Science and Policy in Antarctica

The "Martha T. Muse Prize for Science and Policy in Antarctica" is a US$100,000 unrestricted award presented to an individual in the fields of Antarctic science or policy who has demonstrated potential for sustained and significant contributions that will enhance the understanding and/or preservation of Antarctica. The Prize is inspired by Martha T. Muse's passion for Antarctica and is intended to be a legacy of the International Polar Year 2007-2008.

The prize-winner can be from any country and work in any field of Antarctic science or policy. The goal is to provide recognition of the important work being done by the individual and to call attention to the significance of understanding Antarctica in a time of change. A website with further details, including the process of nomination and selection of the Prize recipients is available at **www.museprize.org**.

The Prize is awarded by the Tinker Foundation and administered by the Scientific Committee on Antarctic Research (SCAR)

TFI TINKER FOUNDATION INCORPORATED

Nominations open until 22 May 2014

SCAR

University at Buffalo
The State University of New York

DIRECTOR OF RENEW

Research and Education in eNergy, Environment and Water

The University at Buffalo (UB), The State University of New York, is seeking an outstanding researcher, scholar and visionary leader to serve as the Inaugural Director of the newly launched signature UB RENEW Institute, a comprehensive, multidisciplinary organization dedicated to research and education on globally pressing problems in energy, environment, and water. To lead the development of UB RENEW most effectively, the Director, in addition to having outstanding research credentials in an appropriate area, will also have a successful track record of developing and leading interdisciplinary teams. As well as expanding his/her own research program, the Director will lead the hiring of approximately 20 UB RENEW faculty and their integration with the existing 100 faculty, and programs and departments across the Schools of Architecture and Planning, Engineering and Applied Sciences, Law, Management and Public Health and Health Professions, and the College of Arts and Sciences.

UB RENEW is a central component of the Realizing UB 2020 Initiative, which is focused on building UB's reputation as a leader in research, scholarship and innovation in the global community of scholars, and consequently it will be established with a significant university investment. UB RENEW will increase the visibility and stature of UB by integrating its activities with those of community partners and parallel efforts across the 64-campus SUNY system, including participation in the SUNY Network of Excellence in Energy, Environment, Economics, and Education.

The Director will serve as the executive officer responsible for the overall management of UB RENEW, and in this capacity will report to the Vice President for Research and Economic Development. She/He will hold the highest level of academic appointment, potentially in multiple departments or schools, and will work with faculty and university leadership to attract additional external support from granting agencies, foundations, and private donors. Candidates should thus have a track record of productive and well-funded basic and/or applied research and demonstrated ability in working collaboratively within the academy, and also with state and local governments, not-for-profit organizations, and the business community.

For more information on this opportunity go to:
http://www.buffalo.edu/leadership-searches/current-searches/RENEW-director.html

Review of applications will begin March 1, 2014 and will continue until the position is filled. The search will be conducted in strict confidence until finalists participate in campus visits. References will not be contacted without the prior knowledge and approval of the candidates.

To apply, please submit a letter of application, curriculum vita, statements of teaching philosophy and research goals along with the names and contact information for five references. Further enquiries, applications or nominations should be addressed to: **Bruce D. McCombe, SUNY Distinguished Professor, and Chair, UB RENEW Director Search Committee, 516 Capen Hall, University at Buffalo, Buffalo, New York 14260, UB-renew-search@buffalo.edu**.

All qualified individuals are encouraged to apply including women, minorities, persons with disabilities and disabled veterans. University at Buffalo is an Affirmative Action/Equal Opportunity Employer.

Staff Scientific Research Opportunities - Pathway Engineering and Plant Genomics

The Genomics Division at Berkeley Lab invites applications for career scientist positions at the DOE Joint Genome Institute (JGI, www.jgi.doe.gov). We are seeking individuals to direct cutting edge research programs one in pathway engineering, and the second in plant genomics. These positions are open to both established researchers as well as early career investigators who have demonstrated outstanding promise and creative ability.

The JGI is a large-scale genome science facility supported by the US Department of Energy with an emphasis on topics related to energy and environmental issues. The selected individuals will receive support for their research program as well as have access to the JGI's large-scale capabilities including those in genomics, computational biology, and DNA synthesis. Will be expected to develop a strong independent research program as well as interface with ongoing activities at the institute. In addition they will have the opportunity to participate in large multidisciplinary research programs in collaboration with scientists throughout the JGI, LBNL, and the neighboring University of California, Berkeley campus.

How to Apply: To apply, please go to **http://bit.ly/LBL77313Science** and locate "Staff Scientist". Then follow the application instructions. Please include a CV, summary of research interests, and references.
For informal inquiries, contact wrcannan@lbl.gov

Berkeley Lab is an affirmative action/equal opportunity employer committed to the development of a diverse workforce.

JGI JOINT GENOME INSTITUTE DEPARTMENT OF ENERGY

POSTDOC OPPORTUNITIES

CNRS advancing the frontiers
UNIVERSITÉ PARIS DESCARTES

Postdoctoral position with a CNRS laboratory at Paris Descartes University for a project relating structure to function in mouse visual cortex using state-of-the-art technology in optogenetics, imaging and electrophysiology.

Competitive salary is provided initially for one year with possibility of renewal, with a start date no later than June 2014. The candidate must have extensive experience in either in vivo patch clamp electrophysiology or in vivo 2-photon imaging.

The position is in a collaborative interdisciplinary environment; in particular a strong interest in working with theorists towards modelling cortical networks is encouraged.

Please send CV, motivation letter and 2-3 reference letters to Dr Lyle Graham at **lyle@biomedicale.univ-paris5**

AAAS is here –
promoting universal science literacy.

In 1985, AAAS founded Project 2061 with the goal of helping all Americans become literate in science, matematics, and technology. With its landmark publications *Science for All Americans* and *Benchmarks for Science Literacy*, Project 2061 set out recommendations for what all students should know and be able to do in science, mathematics, and technology by the time they graduate from high school.

As a AAAS member, your dues help support Project 2061. If you are not yet a member, join us. Together we can make a difference.

To learn more, visit
aaas.org/plusyou/project2061

AAAS + U = Δ

AAAS is here –
helping scientists achieve career sucess.

Every month, over 400,000 students and scientists visit ScienceCareers.org in search of the information, advice, and opportunities they need to take the next step in their careers.

A complete career resource, free to the public, *Science* Careers offers hundreds of career development articles, webinars and downloadable booklets filled with practical advice, a community forum providing answers to career questions, and thousands of job listings in academia, government, and industry. As a AAAS member, your dues help AAAS make this service available to the scientific community. If you're not a member, join us. Together we can make a difference.

To learn more, visit
aaas.org/plusyou/sciencecareers

AAAS + U = Δ

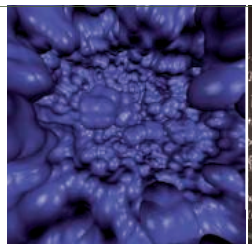
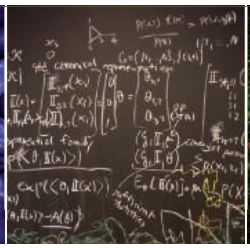
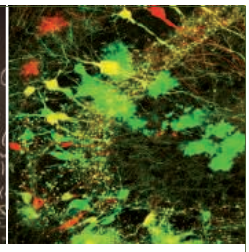

ISTFELLOW: Call for Postdoctoral Fellows

Are you a talented, dynamic, and motivated scientist looking for an opportunity to conduct research in the fields of **BIOLOGY**, **COMPUTER SCIENCE**, **MATHEMATICS**, **PHYSICS**, or **NEUROSCIENCE** at a young, thriving institution that fosters scientific excellence and interdisciplinary collaboration?

Apply to the ISTFellow program. Deadlines March 15 and September 15

www.ist.ac.at/istfellow

ISTFELLOW is partially funded by the European Union

European Commission

IST AUSTRIA
Institute of Science and Technology

ÉCOLE POLYTECHNIQUE FÉDÉRALE DE LAUSANNE

Medtronic Chair in Neuroengineering

at the Wyss Center & Center for Neuroprosthetics of the Ecole polytechnique fédérale de Lausanne (EPFL)

Within the framework of an EPFL initiative to promote groundbreaking translational research in neuroprosthetics, neuroengineering, and neuroscience, EPFL's School of Life Sciences and School of Engineering invite applications for a faculty position at the level of tenure-track assistant professor, although more senior candidates will also be considered. The Medtronic Chair will join the striving community of EPFL's new Geneva campus, which consists of the newly founded Wyss Center (http://epfl.ch/) and Center for Neuroprosthetics (http://cnp.epfl.ch/) in addition to being home to Europe's largest neuroscience initiative, the Human Brain project (https://humanbrainproject.eu/). EPFL seeks outstanding individuals – neuroscientists, neuroengineers, or clinician-scientists – using state-of-the-art neuroengineering approaches to investigate neurological or psychiatric diseases with strong, laboratory-based or clinical research programs. Areas of interest include, but not limited to, neuromodulation, deep brain stimulation, cortical recording and stimulation, closed-loop control, optogenetics to understand diseases, neural interfaces, electrode design and modeling. The main clinical research fields include epilepsy, stroke, neurodegenerative disease, and psychiatric disease.

Internationally competitive salaries, substantial start-up and ongoing resources, and benefits are offered. Full access to all facilities at EPFL's Center for Neuroprosthetics and the Wyss Center will be granted. Development of intensive clinical collaborations with the Department of Clinical Neurosciences and/or the Department of Psychiatry at Geneva University Hospital will be promoted. A commitment to graduate or undergraduate education is expected.

Applications should include a curriculum vitae with a list of publications, a concise statement of research and teaching interests, and the names and addresses (including e-mail) of at least five referees. Applications should be uploaded to :

https://academicjobsonline.org/ajo/jobs/3866

While the committee will start analyzing applications on **April 1st 2014**, the search will remain open until the position is filled.

Enquiries may be addressed to:.

Prof. Olaf Blanke
Chair of the Search Committee
E-mail: cnp@epfl.ch

For additional information on EPFL, the Schools of Engineering and Life Sciences, the Wyss Center, the Center for Neuroprosthetics, the University of Geneva, and Geneva University Hospital, please consult the following web sites:
http://www.epfl.ch, http://sti.epfl.ch, http://sv.epfl.ch, http://cnp.epfl.ch, and http://www.unige.ch/.

EPFL aims to increase the presence of women amongst its faculty, and qualified female candidates are strongly encouraged to apply.

National Research Foundation

DEPUTY CEO: ASTRONOMY

South Africa's astronomy landscape and its scientific community have evolved dramatically with exciting developments over the past years. Starting with the construction of SALT nearly a decade ago, one of the major recent highlights is the award of a major share of the Square Kilometre Array (SKA) project, one of the largest global 'big science' investments. Together with on-going South African and international investments in radio astronomy (the African VLBI Network), optical astronomy (SALT) and gamma-ray astronomy, this increasingly places Africa in a pivotal position in the global astronomy arena.

Strategic decisions associated with these increased investments and internationalisation of astronomy in South Africa prompted the Minister of Science and Technology to support the establishment of a focused Astronomy Sub-Agency within the National Research Foundation (NRF). This Sub-Agency will operate as a separate cluster from the other non-astronomy related National Research Facilities to optimise the benefits that will accrue from the considerable national and international investments already made and expected to be made in astronomy in South Africa.

The NRF is seeking a visionary leader for this new sub-agency. We invite suitably qualified and experienced individuals to apply for the position of Deputy CEO: Astronomy. This position presents a wonderful opportunity to guide and stimulate the development of the rapidly growing astronomy community in South Africa in the interest of national, continental and global astronomy interests.

Key aspects of the position include:

- playing a key role in implementing and coordinating the national strategy for astronomy and related future national investments;
- overseeing the astronomy national facilities and the SKA-SA project within the NRF, and ensuring their synergistic interactions as well as the transfer of best practices amongst them, the rest of the NRF and other elements of the National System of Innovation (NSI);
- developing synergies between the astronomy facilities, universities and science councils, and the astronomy community at large, to address the country's transformation imperatives in terms of skilled resources and research capacity;
- playing a key role in creating a national long range planning culture for multi-wavelength astronomy infrastructure and equipment;
- promoting public awareness through appropriate outreach initiatives; and
- liaising with international partners, boards, and other major international facilities.

Requirements

The ideal candidate will have:

- a record of research excellence in the fields of astronomy, physics or engineering with a minimum of a PhD qualification in any of these fields;
- a sound knowledge of the national science system, including an understanding of the governance requirements for public entities;
- demonstrated ability to consult with and gain the respect of the science community;
- keen insight into the key issues confronting astronomy facilities within the unfolding dynamics of the National System of Innovation and its global dimensions;
- a demonstrable record of leadership and research management capabilities, through having worked with researchers in facility environments and/or university management structures. A record of engagement with the policy environment will be an advantage; and
- a thorough awareness and understanding of science and technology research infrastructure and equipment development and maintenance, their effective utilisation, and challenges involved.

Information

The NRF offers a competitive total remuneration package, which, together with the terms of appointment, will be negotiated with the successful candidate. Candidates who could be based in Pretoria would be preferred.

The position will entail a 5 year term appointment with the possibility of renewal for a further 5 years depending on performance and availability.

The successful candidate will report to the CEO of the NRF. The role of the NRF, amongst other duties, is to provide state of the art national research facilities and infrastructure. In addition, the NRF promotes research ties between National Research Facilities which include the astronomy facilities, and higher education institutions, to maximise the development of skilled human capacity and to promote effective research while in pursuit of a transformed science workforce for the country.

The incumbent DCEO will serve as a member of the Corporate Executive Management team. S/he will provide leadership in the organisation and play a key role leading and co-ordinating all efforts and strategies across the various astronomy platforms and investments. This includes contributing to the transformation imperative, so as to maximise the contribution of astronomy investments to national priorities. In this endeavour the DCEO will be supported by the Astronomy Advisory Council.

The NRF is established by an Act of Parliament and mandated as the national agency to promote and support the development of skilled human capacity, to support knowledge generation and to provide science infrastructure in the country. The web site **www.nrf.ac.za** provides more background details on the NRF and its initiatives.

Applications

Applicants should submit a comprehensive CV, accompanied by a letter of motivation indicating the applicant's suitability for the position. The names and contact details of at least three referees should be provided.

Applications must be forwarded to Mr P Thompson, Group Executive: HR & Legal Services, National Research Foundation, P O Box 2600, Pretoria, 0001. RSA
Tel: +27 (12) 481-4073, Fax: +27 (12) 481-4006, E-mail: **patrick@nrf.ac.za**.

Correspondence will only be conducted with short-listed candidates.

Closing date

The closing date for applications is **25 April 2014**.

The NRF is committed to employment equity and redress.

WOMEN IN SCIENCE

forging new pathways in green science

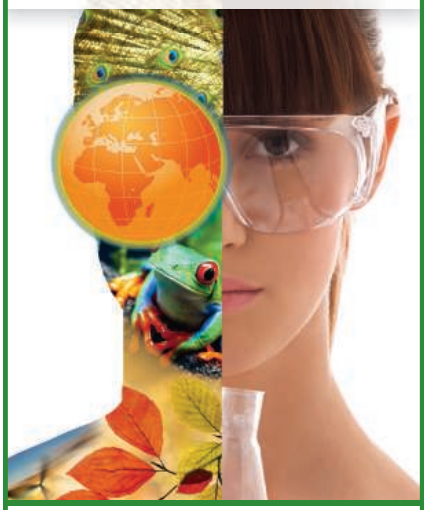

Read inspiring stories of women working in "Green Science" who are blending a unique combination of enthusiasm for science and concern for others to make the world a better place.

Download this free booklet ScienceCareers.org/LOrealWiS

Science AAAS

FOR WOMEN IN SCIENCE L'ORÉAL FOUNDATION

This booklet is brought to you by the AAAS/*Science* Business Office in partnership with the L'Oreal Foundation

if you are looking for research funding, apply today.

If your work is in need of funding, today - maybe the two of us should meet.
Please go to www.lls.org to find out more.

someday is today | LEUKEMIA & LYMPHOMA SOCIETY®
fighting blood cancers

Founding Director, Penn Institute for Biomedical Informatics

Perelman School of Medicine
University of Pennsylvania

The Perelman School of Medicine at the University of Pennsylvania invites applications for the position of Founding Director of the newly established Institute for Biomedical Informatics (IBI), enabled by a recent philanthropic gift. The Institute is focused on the science of biomedical informatics and will integrate informatics disciplines from bioinformatics to translational, clinical, and public health informatics. The Founding Director will lead and develop the Institute, bring together current informatics-related faculty throughout the Penn community, and in partnership with our Department Chairs, recruit new faculty to the Institute and the Perelman School of Medicine.

The mission of IBI is to:

- Establish an outstanding basic and applied sponsored research program in biomedical informatics,
- Recruit faculty and promote career development of biomedical informatics faculty at the Perelman School of Medicine,
- Launch educational programs in biomedical informatics,
- Support programmatic growth in biomedical informatics at the broader University of Pennsylvania, and
- Provide key guidance to the leadership of Penn Medicine on strategic investments in IT.

The IBI, in partnership with the Schools of Engineering and Applied Sciences, Arts and Sciences, Nursing, and Veterinary Medicine, as well as The Children's Hospital of Philadelphia, will tackle challenges directly relevant to patient care, as well as improve basic research that leads to more personalized care. The Institute will also focus on educating the next generation of biomedical informaticians by incorporating a new Masters in Biomedical Informatics degree program with the existing PhD program in Genomics and Computational Biology and by creating additional graduate and medical training programs as the field evolves.

Applicants for the position of Director must have a PhD and/or MD, have a distinguished national/international record in biomedical informatics, and possess dynamic leadership skills, as well as a distinguished research record and a commitment to education and mentorship of students, fellows and faculty. The applicant must have the background and skills to enable strong collaborations among bioinformatics and medical informatics activities. The candidate should express a clear vision of the future of biomedical informatics, and the role of an Institute that is part of a renowned academic medical center. The candidate must be qualified for appointment as Full Professor in the Tenure track of the standing faculty in an appropriate department in the Perelman School of Medicine.

All interested applicants are invited to send their curriculum vitae and letter of interest to Chi Van Dang, MD, PhD, Chair, IBI Director Search Committee, c/o Margaret M. Lizotte, Search Committee Liaison, **lizotte@exchange.upenn.edu**.

We seek candidates who embrace and reflect diversity in the broadest sense. The University of Pennsylvania is an equal opportunity, affirmative action employer.

Qualified applicants should apply to **http://www.med.upenn.edu/apps/faculty_ad/index.php/d3547**

CityU 30
香港城市大學
City University of Hong Kong
30th Anniversary

Worldwide Search for Talent

City University of Hong Kong is a dynamic, fast-growing university that is pursuing excellence in research and professional education. As a publicly-funded institution, the University is committed to nurturing and developing students' talents and creating applicable knowledge to support social and economic advancement.

The Department of Biomedical Sciences has recently been established by the University to develop strategic growth areas of life sciences. It aims to become one of leading centers in the Asia-Pacific region specializing in professional education and cutting-edge research in targeted areas of biomedical sciences. The Department has programs leading to MPhil and PhD degrees, and plans to offer a BSc program and a taught MSc program in biomedical sciences in the coming years. Involvement in pre-clinical teaching is being planned in connection with a proposed School of Veterinary Medicine.

Applications and nominations are invited for:

Chair Professor/Professor/ Associate Professor/Assistant Professor Department of Biomedical Sciences *[Ref. A/133/29]*

Requirements : A PhD/MD/DVM or an equivalent degree in the broadly-defined areas of biomedical sciences. Excellent academic records and English communication skills are essential. Successful candidates are expected to teach at both undergraduate and postgraduate levels, conduct original research, attract external research funding, and publish in high-impact journals. The Department currently has active research in molecular, cellular and systems study of neuroscience, cancer, or regenerative biology, and the development of novel therapeutics and nanomedicine. Candidates with strong background in these and other biomedical science-related areas, especially zoonotic infectious diseases, public health, and food safety, are welcome to apply. Preference will be given to qualified candidates whose activities can contribute to multidisciplinary and collaborative biomedical research. The Department is committed to the professional development of its faculty, enabling them to become next-generation leaders in basic and translational biomedical sciences. Priority will be given to qualified candidates who can contribute through their research, teaching, and service to the diversity and excellence of the University and its community.

Candidates for the post of Professor and above should have a distinguished academic record including significant external funding support, demonstrated leadership skills, and a strong commitment to graduate and undergraduate education. Successful candidates are expected to develop internationally competitive research programs; and assume academic and administrative leadership in the Department by assisting in faculty development, promoting collaboration in cross-disciplinary teaching and research programs within the University, and facilitating the translation of basic biomedical research to practices of health services and healthcare-related industries.

Salary and Conditions of Service
Remuneration package will be driven by market competitiveness and individual performance. Excellent fringe benefits include gratuity, leave, medical and dental schemes, and relocation assistance (where applicable). Initial appointment will be made on a fixed-term contract.

Information and Application
Further information on the posts and the University is available at http://www.cityu.edu.hk or from the Human Resources Office, City University of Hong Kong, Tat Chee Avenue, Kowloon Tong, Hong Kong [Email: hrojob@cityu.edu.hk/ Fax: (852) 2788 1154 or (852) 3442 0311]. Please send the nomination or application with a current curriculum vitae and at least 3 reference reports to Prof. Michael YANG, Faculty Search Committee, Department of Biomedical Sciences via email at bms@cityu.edu.hk. Please quote the reference number in the application. **Applications and nominations will receive full consideration until the positions are filled**, and only shortlisted applicants will be contacted and invited to visit the Department. The University's privacy policy is available on the homepage.

The University also offers a number of visiting positions through its "CityU International Transition Team" scheme for current graduate students, postdoctoral scholars, and for early-stage and established scholars, as described at http://www.cityu.edu.hk/provost/cityu_international_transition.htm.

City University of Hong Kong is an equal opportunity employer and we are committed to the principle of diversity. We encourage applications from all qualified candidates, especially those who will enhance the diversity of our staff.

THE UNIVERSITY OF ARIZONA COLLEGE OF MEDICINE

ASSISTANT/ASSOCIATE PROFESSORS
Bacteria- and virus-host interactions, pathogenesis, commensalism and latency
Department of Immunobiology

The Department of Immunobiology at the University of Arizona (UA) College of Medicine (COM) invites applications for tenure-track faculty positions in bacteriology and virology at the Assistant or Associate Professor level. We seek outstanding scientists who will establish competitive, front-rank, independent research programs on the interactions of bacteria and viruses with their hosts at the molecular, cellular, or organismal level. The UA and the Department of Immunobiology recognize the power of a diverse community and strongly encourages applications from individuals with varied experiences, perspectives, and backgrounds. Candidates who use multidisciplinary approaches to probe microbe-host interactions that impact intrinsic or innate responses to infection, commensalism, persistence, and/or host metabolism, particularly at the respiratory or gut mucosal surfaces, are strongly encouraged to apply. Applicants must have a Ph.D., M.D. or equivalent degree in the relevant field of study and postdoctoral experience. The successful candidates are expected to obtain extramural funding for their research programs and participate in graduate and medical student teaching. Salary and start-up funds are attractive and commensurate with qualifications and experience. Information on the Department of Immunobiology, UA centers and institutes, core facilities and the interdepartmental ABBS graduate training program can be found at (http://immunobiology.arizona.edu) and (http://medicine.arizona.edu/about-college/centers). UA is in the midst of bold investment into doubling its research capacity as a part of the Never Settle strategic plan. Coupled with outstanding climate, lifestyle and cultural environment (http://immunobiology.arizona.edu/content/about-tucson), this makes UA the place to be in the next few decades. Please submit applications containing (i) CV; (ii) a 2-page summary of current research and teaching interests and long-term goals; and (iii) three letters of recommendation; electronically at the following URL address (applications will not be reviewed unless all letters are received): **https://www.uacareertrack.com/applicants/jsp/shared/frameset/Frameset.jsp?time=1392219433886** and search postings for job number **54209**.

THE UNIVERSITY OF ARIZONA IS AN EEO/AA/ADA EMPLOYER. WOMEN AND MINORITIES ARE ENCOURAGED TO APPLY.

MUSC
MEDICAL UNIVERSITY of SOUTH CAROLINA

Charleston, SC

Professor and Chair
Department of Regenerative Medicine and Cell Biology

The Medical University of South Carolina College of Medicine invites applications and nominations for the position of PROFESSOR AND CHAIR of its Department of Regenerative Medicine and Cell Biology (formerly "Cell Biology and Anatomy"). Applicants must possess a PhD and/or MD and are expected to have a history of continued funding and an active research program, a strong record of accomplishment in mentoring postdoctoral fellows and junior faculty, administrative and leadership skills, and a commitment to education and academic excellence. The department currently has research strengths in regenerative medicine, tissue engineering, and cardiovascular development and disease (see http://regmed.musc.edu). The selected individual will report directly to the Dean of the College of Medicine and will be expected to foster new areas of research within the department while supporting and enhancing current research strengths.

The Medical University of South Carolina is in the midst of an exciting period of growth with NCI designation for the Hollings Cancer Center, a CTSA award, and two new research buildings. This is an outstanding opportunity for the right candidate in a city known for its enviable quality of life.

Nominations, expressions of interest and applications may be submitted confidentially via email to the University's consultant, Witt/Kieffer, to the attention of Karen Otto and Donna Padilla at MUSCREGEN@wittkieffer.com. Interested individuals may also submit a letter of interest, curriculum vitae, and the names and contact information of three references via the MUSC employment website at https://www.jobs.musc.edu/postings/23053.

MUSC is an equal opportunity employer, promoting workplace diversity.

WITT / KIEFFER

NWAFU Professorship's Recruitment

Northwest A&F University (NWAFU) is a national key comprehensive university directly under the jurisdiction of the Ministry of Education of the People's Republic of China and supported by its "Project 985" and "Project 211". The University is located in Yangling, Shaanxi Province, 80 km west of Xi'an, a historic city of China. Yangling is not only the location of the University, is also the birth place of Chinese agricultural civilization and the location of the state-level Agricultural Hi-tech Industries Demonstration Zone. The University recruits distinguished professors and full-time professors in various academic disciplines.

I. Academic Disciplines:

Biology, Agricultural Engineering, Food Science and Engineering, Crop Science, Horticulture, Pedology, Plant Pathology, Entomology, Pesticide Science, Animal Husbandry, Veterinary, Machinery Design & Manufacture, Computer Science & Technology, Agricultural & Forestry Economic Management, etc.

II. Applicant's Eligibility

didates must possess a position at Assistant professor or higher ranking in a recognized college or university, and has achieved significant accomplishments or contributions, or evidence of success in the respective discipline.

III. Facilities and Conditions

The University provides sufficient start-up funds and facilities, highly competitive salary, and an apartment with individual property right after serving the University for 10 years. The University will actively help and recommend the hired professors to apply "Global Experts Program" and "Chang Jiang Scholars Program", and many others.

IV. Procedure

For full consideration, interested applicants should send a letter of interest, a recently updated CV with a list of publications, faculty position application form (http://rcb.nwsuaf.edu.cn/sort.php?sortid=8), and three letters of recommendations to: rencaike@nwsuaf.edu.cn. The University will arrange an interview after verifying of the materials and application materials. The University will cover the expenses of international travel when the candidate is invited for an interview. Please visit http://rcb.nwsuaf.edu.cn/ for more information.

http://rcb.nwsuaf.edu.cn/

Faculty Positions Available in Southwest University, Chongqing, China

Southwest University is a national key university of the "211" project directly under the Ministry of Education. It is located in Chongqing, the youngest municipality of China. The university hosts approximately 50,000 students, covering undergraduate, postgraduate and other programs. **For more detailed information, please visit the website: http://www.swu.edu.cn/#**

Applications for full-time professors, associate professors and distinguished scientists are welcome. Competitive salaries and start-up funds will be provided to successful candidates, in line with the national Recruitment Program of Young Experts.

The Recruitment Program of Young Experts (i.e. the Plan for Recruiting 1,000 Professorship for Young Talents): The candidates are required to be under the age of 40 and have obtained a PhD degree in a world-renowned university with at least 3 years of research experience abroad, or have obtained a PhD degree in Mainland China with at least 5 years of research and teaching experience abroad. Special offers will be granted to those who have excellent research achievements during their doctoral study.

Further information is available at http:// renshi.swu.edu.cn/rcgzbgs/ The Talents Recruitment Office, Southwest University,Beibei, Chongqing 400715, P. R. China. 0086-23-68254265.

Please kindly send applications or nominations in the form of an application letter enclosing a current CV to rencai@swu.edu.cn.

首都师范大学 CAPITAL NORMAL UNIVERSITY

Faculty Positions Available at Capital Normal University

Capital Normal University invites applications for full-time positions in research and academics.

Established in 1954, Capital Normal University (CNU) is a comprehensive university offering majors in arts and humanities, sciences, technology, business management, laws, education, foreign languages, and art. CNU is a key university under the administration of Beijing Municipal Government, and a Project 211 institution.

For more detailed information, please visit the website http://www.cnu.edu.cn /pages/info_details.jsp?seq=20433&boardid=71002&classcode=71002

Eligible applicants:

Young scholars with PhDs or postdoctoral research experiences with a specific area of expertise and outstanding research achievements. The applicant must be physically healthy, and demonstrate good teamwork skills.

Professors are required to be under 45 years of age, exceptions can be made for holders of high-level academic titles; PhDs are expected to be under 35 years of age, and post-docs under 40.

Employee benefits:

CNU provides different levels of competitive salaries and start-up research funding. Housing and relocation allowances will be provided for the professors. Post-docs or PhDs from overseas universities with vice senior academic titles who have made significant academic achievements can apply for temporary housing.

To apply:

Please submit the following items to the related colleges or departments, and forward it to the Personnel Department of CNU : Curriculum Vitae; proposed work plan for 3 years; a list of papers and publications in the last 5 years; a list of awards won; a list of research projects participated or led by the applicants; and reference letters from experts in the applicant's field of study.

Please also sent paper copies of the application package to:

Personnel Department, Capital Normal University, 105 Xisanhuanbeilu, Haidian District, Beijing 100048, P.R. China
Contact: Zhou Quan, Chen Wenxin
Email: cnursc2013@163.com
Tel: 86-10-68902824
Fax: 86-10-68902240

Science Careers online @sciencecareers.org
OPPORTUNITIES IN CHINA

NATIONAL CANCER INSTITUTE
Center for Cancer Research

STAFF CLINICIAN
IN MEDICAL ONCOLOGY AND THORACIC ONCOLOGY
Application Deadline: March 17, 2014

The Thoracic and Gastrointestinal Oncology Branch (TGIB), Center for Cancer Research (CCR), National Cancer Institute (NCI), Department of Health and Human Services (DHHS) is seeking candidates for a Staff Clinician position. The position is located on the NIH campus in Bethesda, Maryland. The successful candidate will focus on translational research in thoracic cancers with an emphasis on malignant mesothelioma. The position involves close collaboration with basic scientists and performing innovative early-phase clinical trials of novel targeted agents being developed at the National Cancer Institute. These trials will use immunotherapy-based approaches to treat mesothelioma.

We are seeking individuals interested in an academic career committed to advancing translational research. The candidate is expected to have strong background in translational research, management of malignant mesothelioma and in early-phase clinical trials. Prior experience with clinical development of immunotherapeutic agents is desirable. For further information about the Thoracic and Gastrointestinal Oncology Branch, NCI programs, faculty and training, or the NIH, please visit our respective web sites: http://ccr.cancer.gov/labs/lab.asp?labid=997, http://ccr.nci.nih.gov/, and http://www.nih.gov.

Candidates must have an M.D. degree and be board certified or board eligible in medical oncology. Salary will be commensurate with experience. Applications should include: a personal statement of clinical and research experience and interests; a current curriculum vitae and complete bibliography; and the names, addresses and phone numbers of five (5) references. Applications must be received by COB: March 14, 2014; to the attention of Aaron Bell via e-mail at **bella@mail.nih.gov**; or mail: **National Cancer Institute, 9000 Rockville Pike, Building 3, Room 4E17, Bethesda, MD 20892-1904**.

DHHS, NIH and NCI are Equal Opportunity Employers.

U.S. DEPARTMENT OF HEALTH AND HUMAN SERVICES
National Institutes of Health

NIH

E.O. WILSON
BIODIVERSITY SYMPOSIUM
April 22-24, 2014
The University of Alabama
Tuscaloosa, AL, USA

Registration: www.biodiversity.ua.edu

Beginning on Earth Day at The University of Alabama

Join Dr. Edward O. Wilson and international biodiversity experts for three days of research briefings and forums on the state and future of biodiversity on our planet.

Featuring the international release of Dr. Wilson's new book, *A Window on Eternity: Gorongosa National Park, Mozambique*.

Distinguished Speakers

E. Virginia Armbrust
P. Dee Boersma
R. Scot Duncan
Ryan Earley
Scott V. Edwards
Harry W. Greene
Juan M. Lopez-Bautista
Jonathan B. Losos
Meg Lowman
D. Bruce Means
Michael B.A. Oldstone
Richard A. Richards
Leslie J. Rissler
Sahotra Sarkar
Diana H. Wall
Edward O. Wilson

Join Dr. Wilson and the College of Arts and Sciences as we explore biodiversity from a range of perspectives: biological, evolutionary, cultural, and philosophical.

Registration: www.biodiversity.ua.edu

THE UNIVERSITY OF ALABAMA
COLLEGE OF ARTS AND SCIENCES

AAAS is here –
Science Funding,
Climate Regulation,
Human Rights.

Around the world, governments turn to AAAS as an objective, multidisciplinary scientific authority to educate public officials and judicial figures on today's most pressing issues. And this is just one of the ways that AAAS is committed to advancing science to support a healthy and prosperous world. Join us. Together we can make a difference.

To learn more, visit
aaas.org/plusyou/policy

AAAS + U = Δ

AWARDS

HUMAN FRONTIER SCIENCE PROGRAM (HFSP)

CALL FOR NOMINATIONS FOR THE 2015 HFSP NAKASONE AWARD

In keeping with its mission to promote innovative international research, HFSP invites nominations for the 2015 Nakasone Award which honors ground-breaking contributions in the life sciences. Typically these will be breakthroughs in understanding the complex mechanisms of living organisms that have important consequences for scientists throughout the world. Experimental, conceptual and technological contributions are eligible. This award recognizes the vision of former Prime Minister Nakasone of Japan in the creation of HFSP.

The winner of the 2014 award was Uri Alon of the Weizmann Institute of Science, Rehovot, Israel, for his pioneering work in discovering network motifs in genetic circuits.

The competition is open; it is not limited to HFSP awardees and there is no age limit for candidates. However the jury will pay particular attention to recent breakthroughs by younger scientists. Nominations should be made before 4th April 2014 by submitting the one-page nomination form and the nominee's CV (see the HFSP website for more information). The selection will be made by the HFSP Council of Scientists at its meeting in July 2014. The awardee will receive an unrestricted research grant of 10.000 USD, a commemorative medal and an invitation to deliver the Nakasone lecture at the 2015 HFSP Awardees Meeting.

HFSP, 12 quai Saint-Jean, 67080 STRASBOURG Cedex, France, **www.hfsp.org/awardees**

POSITIONS OPEN

NANYANG TECHNOLOGICAL UNIVERSITY · NUS National University of Singapore · SUTD Singapore University of Technology and Design

TEMASEK RESEARCH FELLOWSHIP (TRF)

A globally connected cosmopolitan city, Singapore provides a supportive environment for a vibrant research culture. Its universities Nanyang Technological University (NTU), National University of Singapore (NUS) and Singapore University of Technology and Design (SUTD) invite outstanding young researchers to apply for the prestigious TRF awards.

Under the TRF scheme, selected young researchers with a PhD degree have an opportunity to conduct and lead defence-related research. It offers:

- A 3-year research grant of up to S$1 million commensurate with the scope of work, with an option to extend for another 3 years
- Postdoctoral or tenure-track appointment (eligibility for tenure-track will be determined by the university)
- Attractive and competitive remuneration

Fellows may lead, conduct research and publish in these areas:

- Beamless RF Generator
- High Power Laser Diodes
- Cognitive Science for Machine Intelligence
- Cyber Security
- Machine Intelligence – Software Architecture as Autonomy Enabler

For more information and application procedure, please visit:

NTU – http://www3.ntu.edu.sg/trf/index_trf.html
NUS – http://www.nus.edu.sg/dpr/funding/trf.html
SUTD – http://www.sutd.edu.sg/trf

Closing date: 21 April 2014 (Monday)

Shortlisted candidates will be invited to Singapore to present their research plans, meet local researchers and identify potential collaborators in July / August 2014.

CONFERENCE

AIDS 2014

20th International AIDS Conference

Melbourne, Australia

July 20-25, 2014

WWW.AIDS2014.ORG

STEPPING UP THE PACE

GET INVOLVED IN AIDS 2014!

Join more than 14,000 community leaders, scientists, youth, researchers, and advocates, and play your part to change the course of the HIV epidemic.

To register for AIDS 2014 and to see the list of plenary speakers and plenary sessions themes, visit:

www. AIDS2014.org

POSTDOCTORAL POSITIONS

POSTDOCTORAL FELLOW

Protein Structure and Function. Position available at the University of Alabama at Birmingham in the laboratory of **Dr. Margaret Johnson.** We use solution NMR spectroscopy to study proteins involved in the metabolism and molecular recognition of poly(ADP-ribose), a key biomolecule in the maintenance of genome integrity, chromatin structure, and the cell cycle. Areas of research include determining high-resolution structures of proteins and protein complexes, enzymatic synthesis, and computational simulations.

Enthusiastic, motivated researchers are encouraged to apply. Candidates should have recently received a Ph.D. in a related discipline and have a strong background in structural biology or biochemistry. To apply please send a cover letter, curriculum vitae, and contact information for three references to **e-mail: maggiejohnson@uab.edu.** *UAB is an Equal Opportunity/Affirmative Action Employer.*

POSTDOCTORAL POSITIONS

Two postdoctoral positions are immediately available for the study of lipid signaling, with an emphasis of cholesterol and nuclear lipid signaling. Our interdisciplinary research includes quantitative imaging of cellular lipids, genomic-scale analysis of membrane binding proteins, and small molecule modulation of membrane-protein interactions. Our group provides a highly challenging and supportive environment with state-of-the-art imaging and biophysical facilities. Motivated candidates with a strong background in cell biology, microscopy, and chemical biology are encouraged to apply.

Please electronically send curriculum vitae and names of three references to: **Wonhwa Cho, Department of Chemistry (M/C 111), University of Illinois at Chicago, 845 W. Taylor Street Chicago, IL 60607; e-mail: wcho@uic.edu. Website: http://brahms.chem.uic.edu.**

ANNOUNCEMENT

CAREER OPPORTUNITY

Doctor of Optometry (O.D.) degree in 27 months for Ph.D.s in science and M.D.s. Excellent career opportunities for O.D./Ph.D.s and O.D./M.D.s in research, education, industry, and clinical practice. This unique program starts in March of each year, features small classes, and 12 months devoted to clinical care.

Contact the Admissions Office, **telephone: 800-824-5526** at the **New England College of Optometry, 424 Beacon Street, Boston, MA 02115.** Additional information at website: **http://www.neco.edu** or at **e-mail: admissions@neco.edu.**

Find your future here.

↓

Science Careers
From the journal *Science* AAAS

www.ScienceCareers.org

Download your free copy today.

ScienceCareers.org/booklets

From technology specialists to patent attorneys to policy advisers, learn more about the types of careers that scientists can pursue and the skills needed in order to succeed in nonresearch careers.

Science Careers
From the journal *Science* AAAS